58th Scientific Conference for Students of Physics and Natural Sciences

Open Readings 2015

March 24-27, 2015

Vilnius, LITHUANIA

Programme and Abstracts

Faculty of Physics
Vilnius University
Saulėtekio Ave. 9-III, LT-10222 Vilnius
LITHUANIA

www.ff.vu.lt
www.openreadings.eu

ISSN 2029-4425

Contents

Conference programme

24 March, TUESDAY

	INVITED LECTURE		
15:00	**Prof. Peter E. Andersen**, Technical University of Denmark, Denmark **HOW TO PUBLISH YOUR MANUSCRIPT**		
	INVITED LECTURE		
16:00	**Dr. Rachel Won**, Nature Photonics, United Kingdom **HOW TO PUBLISH YOUR MANUSCRIPT. EDITORIAL POINT OF VIEW**		
17:00-18:30	**POSTER SESSION P1**		
18:30	SOCIAL EVENT		

25 March, WEDNESDAY

	INVITED LECTURE		
9:00	**Prof. Wolfgang Kautek**, University of Vienna, Austria **MOVE INTO NANO-WORLD BY FEMTOSECOND LASERS**		
	ORAL SESSION O1		
10:00	Rafael Omar, Torres Mendieta, Rosa Mondragón Cazorla, José Enrique Julía Bolívar, Omel Mendoza Yero, Jesús Lancis Saéz, Gladis Mínguez Vega **IMPROVEMENT OF STABILITY PROPERTIES IN HEAT TRANSFER NANOFLUIDS FABRICATED BY PULSED LASER ABLATION IN LIQUIDS**	*O1-1*	**23**
10:15	Mantas Garliauskas, Evaldas Stankevičius, Gediminas Račiukaitis **LASER PULSE PEAK INTENSITY INFLUENCE ON THE GEOMETRY OF PERIODIC POLYMER NANOSTRUCTURES FABRICATED BY INTERFERENCE LITHOGRAPHY**	*O1-2*	**24**
10:30	Natalie Tarasenka, Andrei Butsen **PROPERTIES OF GOLD NANOPARTICLES GENERATED BY LASER ABLATION IN IONIC LIQUIDS**	*O1-3*	**25**
10:45	Tomas Jonavičius, Sima Rekštytė, Mangirdas Malinauskas **LIGHT POLARIZATION INDUCED PECULIARITIES IN DIRECT LASER WRITING 3D NANOLITOGRAPHY**	*O1-4*	**26**
11:00	COFFEE BREAK		
	ORAL SESSION O2		
11:30	Linas Jonušauskas, Mangirdas Malinauskas **COMBINING 3D PRINTING AND DIRECT LASER WRITING FOR MICROFLUIDIC DEVICE FABRICATION**	*O2-1*	**28**
11:45	Paulius Stanislovaitis, Viktorija Pyragaitė **ANALYSIS OF OPTICAL PARAMETRIC AMPLIFICATION BY INCOHERENT PUMP IN TRAPPING REGIME**	*O2-2*	**29**
12:00	Tomas Andrijauskas, Gediminas Juzeliūnas, Ian Spielman **CREATING OPTICAL FLUX LATTICE USING MULTI-FREQUENCY RADIATION**	*O2-3*	**30**
12:15	Nortautas Ulevičius, Aleksej M. Rodin **PICOSECOND LASER WITH 11 W OUTPUT POWER FOR SELECTIVE MICROMACHINING AT 1342 NM WAVELENGTH**	*O2-4*	**31**

12:30	Dominykas Bričkus, Alexander S. Dement'ev **A POSSIBILITY TO REDUCE SPHERICAL THERMAL ABERRATIONS IN DIODE PUMPED SOLID-STATE LASERS**	*O2-5*	**32**
12:45	Rimantas Budriūnas, Tomas Stanislauskas, Jonas Adamonis, Arūnas Varanavičius **DEVELOPMENT OF TW-CLASS, FEW-CYCLE, PASSIVELY CEP-STABILIZED OPCPA SYSTEM BASED ON YB:KGW AND ND:YAG LASERS**	*O2-6*	**33**
13:00	LUNCH		
13:30-15:00	**POSTER SESSION P2**		
	INVITED LECTURE		
15:00	**Dr. Mikas Vengris**, Vilnius university, Lithuania **ULTRAFAST PROCESSES EXPLORED BY MULTI-PULSE TRANSIENT ABSORPTION SPECTROSCOPY**		
	ORAL SESSION O3		
16:00	Mantas Šimėnas, Merten Kobalz, Harald Krautscheid, Jūras Banys, Andreas Pöppl **ELECTRON PARAMAGNETIC RESONANCE STUDY OF A MIXED VALENT METAL-ORGANIC FRAMEWORK CONTAINING CU2 PADDLEWHEEL UNITS**	*O3-1*	**35**
16:15	Ilya Yakovets, Igor Yankovsky, Vladimir Zorin, Lina Bezdetnaya **SPECTRAL METHOD FOR CONTROLLING OF MTHPC REDISTRIBUTION BETWEEN CYCLODEXTRINS AND BIOLOGICAL STRUCTURES**	*O3-2*	**36**
16:30	Edvardas Golovinas, Laura Abariūtė, Gintaras Valinčius, Gediminas Niaura **STUDY OF THE EFFECTS OF LIPID MONOLAYER COMPOSITION AND PHASE ON INTERFACIAL WATER STRUCTURE BY SUM-FREQUENCY SPECTROSCOPY**	*O3-3*	**37**
16:45	Martynas Velička, Milda Pučetaitė, Vidita Urbonienė, Valdas Šablinskas **APPLICATION OF SURFACE ENHANCED RAMAN SPECTROSCOPY FOR STRUCTURAL STUDIES OF BIOLOGICAL FLUIDS**	*O3-4*	**38**
17:00	COFFEE BREAK		
	ORAL SESSION O4		
17:30	Asta Lučiūnaitė, Indrė Dalgėdienė, Aurelija Žvirblienė **THE INFLUENCE OF OLIGOMERIC PROTEINS AND THEIR IMMUNE COMPLEXES ON THE PHENOTYPE OF MACROPHAGES**	*O4-1*	**40**
17:45	Aleksandr Osipenko, Alexandra Plotnikova, Viktoras Masevičius, Giedrius Vilkaitis, Saulius Klimašauskas **APPLICATION OF METHYLTRANSFERASE HEN1 FOR ANALYSIS OF SMALL NON-CODING RIBONUCLEIC ACIDS**	*O4-2*	**41**
18:00	Goda Milinavičiūtė, Justina Kazokaitė, Daumantas Matulis **THE ANALYSIS OF FLUORINATED BENZENESULFONAMIDES BINDING TO CARBONIC ANHYDRASE VI PURIFIED FROM BACTERIA E. COLI AND HUMAN SALIVA**	*O4-3*	**42**
18:15	Diāna Džabijeva, Ilva Nakurte, Kārlis Bērziņš **PHOTOSTABILITY OF NITROFURAN DERIVATIVES IN SOLUTIONS**	*O4-4*	**43**
18:30	Joanna Lach, Pawel Rodziewicz **ANALYSIS OF THE RESULTS FROM CAR-PARRINELLO MOLECULAR DYNAMICS SIMULATIONS OF BIS(2-CHLOROETHYL) SULFIDE WITH THE HELP OF PYTHON PROGRAMMING**	*O4-5*	**44**
18:45	Paulius Imbrasas, Gediminas Kreiza, Marytė Daškevičienė, Vytautas Getautis, Karolis Kazlauskas, Saulius Juršėnas **STRUCTURALLY-MODIFIED SPIRO COMPOUNDS FOR THERMALLY ACTIVATED DELAYED FLUORESCENCE**	*O4-6*	**45**

26 March, THURSDAY

	INVITED LECTURE		
9:00	**Prof. Peter E. Andersen**, Technical University of Denmark, Denmark **SEMICONDUCTOR LASERS: PRINCIPLES AND APPLICATIONS**		
	ORAL SESSION O5		
10:00	Mantas Dmukauskas, Arūnas Kadys **GROWTH AND CHARACTERIZATION OF INGAN/GAN QUANTUM WELLS ON SHORT PERIOD SUPERLATTICE**	*O5-1*	**47**
10:15	Kristina Gelzinyte **STUDY OF EXCESS CARRIER DYNAMICS IN NONPOLAR INGAN/GAN QUANTUM WELLS**	*O5-2*	**48**
10:30	Justinas Aleknavičius, Darius Dobrovolskas, Gintautas Tamulaitis **SPATIALLY RESOLVED PHOTOLUMINESCENCE OF GABIAS EPITAXIAL LAYERS AND GABIAS/GAAS QUANTUM WELLS**	*O5-3*	**49**
10:45	Sandra Stanionytė, Vaidas Pačebutas **GROWTH AND CHARACTERIZATION OF QUATERNARY (GAIN)(ASBI) LAYERS ON GAAS**	*O5-4*	**50**
11:00	COFFEE BREAK		
	ORAL SESSION O6		
11:30	Andrius Rimkus, Evelina Pozingytė, Ramūnas Nedzinskas, Bronislovas Čechavičius **COMPARATIVE SPECTROSCOPIC STUDY OF INAS DOTS-IN-A-WELL QUANTUM STRUCTURES WITH / WITHOUT INGAAS CAP LAYER**	*O6-1*	**52**
11:45	Evelina Pozingytė, Andrius Rimkus, Ramūnas Nedzinskas **TEMPERATURE-DEPENDENT PHOTOREFLECTANCE SPECTROSCOPY OF INAS DOTS-IN-A-WELL STRUCTURES**	*O6-2*	**53**
12:00	Lukasz W. Golacki, Artur Podhorodecki, Nikolai V. Gaponenko, Grzegorz Zatryb, Igor S. Molchan, Liudmila S. Khoroshko, Jan Misiewicz, George E. Thompson **EMISSION DYNAMICS IN THE MICRO SCALE IN THE TWO DIMENSIONAL NANOPOROUS ALUMINA FILLED WITH CUBIC YALO3:TB3+ MATRIX**	*O6-3*	**54**
12:15	Andrii Gudyma, Gregori Astrakharchik, Mikhail Zvonarev **BREATHING MODES OF ONE-DIMENSIONAL TRAPPED QUANTUM GAS**	*O6-4*	**55**
12:30	Ieva Beleckaitė, Ramūnas Adomavičius, Aloyzas Šiušys, Anna Reszka, Janusz Sadowski, Arūnas Krotkus **TERAHERTZ EMISSION FROM GAMNAS AND INGAAS NANOWIRES**	*O6-5*	**56**
12:45	Kazimieras Nomeika **SPECTRAL CHARACTERISTICS OF (IN,GA)N QUANTUM STRUCTURES WITH DIFFERENT DESIGN AND GROWTH PARAMETERS**	*O6-6*	**57**
13:00	LUNCH		
13:30-15:00	**POSTER SESSION P3**		
	INVITED LECTURE		
15:00	**Dr. Gregory J. Quarles**, The Optical Society, USA **TRANSPARENT POLYCYSTALLINE MATERIALS: FROM NANOPOWDER SCIENCE TO NEXT GENERATION LASERS**		
	ORAL SESSION O7		
16:00	Wojciech Wegner, Tomasz Jaroń, Wojciech Grochala **METAL BOROHYDRIDES: THE COMPREHENSIVE NOVEL FUNCTIONAL MATERIALS**	*O7-1*	**59**
16:15	Rafał Owarzany, Karol Jan Fijałkowski, Wojciech Grochala **ALKALI METAL AMIDOBORANES AS ONBOARD HYDROGEN STORAGE MATERIALS AND BORON NITRIDE PRECURSORS**	*O7-2*	**60**
16:30	Jelena Kosmaca, Liga Jasulaneca, Raimonds Meija, Jana Andzane, Justin D. Holmes, Donats Erts **TUNING GERMANIUM NANOWIRE RESONANT FREQUENCY WITH CLAMPING, MECHANICAL DEFORMATION AND MASS DEPOSITION**	*O7-3*	**61**

27 March, FRIDAY

	INVITED LECTURE		
9:00	**Assoc. Prof. Paul R. Stoddart**, Swinburne University of Technology, Australia **OPTICAL STIMULATION OF NEURONS**		
	ORAL SESSION O9		
10:00	Simona Rinkevičiūtė, Andrej Spiridonov **THE IMPACT OF MULDE (WENLOCK: LOWER SILURIAN) MASS EXTINCTION EVENT ON THE ECOLOGICAL DYNAMICS OF OSTRACODES**	*O9-1*	71
10:15	Simona Skyraitė, Donatas Pupienis **SEA SURFACE TEMPERATURE FRONTS IN THE BALTIC SEA**	*O9-2*	72
10:30	Karola Panke, Aiga Svede, Wolfgang Jaschinski, Gunta Krumina **ACCOMMODATION LAG UNDER MONOCULAR AND BINOCULAR CONDITIONS IN SYMPTOMATIC AND ASYMPTOMATIC EMMETROPES**	*O9-3*	73
10:45	Sabina Brazevic, Magdalena Grajek, Tomasz Kopyciuk **THE IMPACT OF DIABETES ON EJECTION FRACTION IN PATIENTS WITH ADVANCED CORONARY ARTERY DISEASE**	*O9-4*	74
11:00	COFFEE BREAK		
	ORAL SESSION O10		
11:30	Ignas Jurčiukonis, Urtė Statkutė, Ieva Mikalauskaitė, Vilius Poderys, Vitalijus Karabanovas, Aldona Beganskienė, Ričardas Rotomskis **OPTIMIZATION OF NAYF4:YB3+,ER3+ UP-CONVERTING NANOPARTICLES FOR CANCER CELL RESEARCH: COLLOIDAL STABILITY, CYTOTOXICITY AND CELL IMAGING**	*O10-1*	76
11:45	Dominyka Dapkute, Simona Steponkiene, Vytautas Kaseta, Una Riekstina, Ricardas Rotomskis **QUANTUM DOT-LOADED MESENCHYMAL STEM CELLS FOR TUMOR-TROPIC THERAPY**	*O10-2*	77
12:00	Greta Jarockyte, Urte Statkute, Vilius Poderys, Vitalijus Karabanovas, Shan-hui Hsu, Ricardas Rotomskis **ACCUMULATION AND TOXICITY OF MAGNETIC NANOPARTICLES FE3O4 IN MOUSE EMBRYONIC FIBROBLASTS**	*O10-3*	78
12:15	Egle Povilaityte, Karolina Zilionyte, Agata Mlynska, Dr. Vita Pasukoniene **POTENTIAL DRUG RESISTANCE BIOMARKERS FOR OVARIAN CANCER**	*O10-4*	79
12:30	Igor Yankovsky, Ilya Yakovets, Ivan Khludeyev, Lina Bezdetnaya, Vladimir Zorin **INFLUENCE OF METHYL-B-CYCLODEXTRIN ON MTHPC INTERACTION WITH BLOOD COMPONENTS**	*O10-5*	80
12:45	Maryna Hliatsevich, Pavel Bulai, Taras Pitlik **DETERMINATION OF HIDDEN PARAMETERS OF SIGNAL TRANSDUCTION IN SYNAPSES**	*O10-6*	81
13:00	LUNCH		
13:30-15:00	**POSTER SESSION P4**		
	INVITED LECTURE		
15:00	**Dr. Kastytis Zubovas**, Center for Physical Sciences and Technology, Lithuania **SUPERMASSIVE BLACK HOLES AND THEIR GALAXIES**		
	ORAL SESSION O11		
16:00	Krzysztof Domogała **THE SEARCH FOR T-TYPE BROWN DWARFS**	*O11-1*	83
16:15	Rokas Naujalis, Kastytis Zubovas **SUPERMASSIVE BLACK HOLE ACCRETION DISC WINDS**	*O11-2*	84
16:30	Katarzyna Rusinek **UNUSUAL MORPHOLOGIES OF GIANT RADIO SOURCES**	*O11-3*	85
16:45	Kostas Sabulis, Kastytis Zubovas **EVOLUTION OF INTERSTELLAR MEDIUM IN ISOLATED DWARF GALAXIES**	*O11-4*	86
17:00	COFFEE BREAK		

ORAL SESSION O12

17:30	Monika Venčkauskaitė, Karolis Tamošiūnas **A STUDY OF THE FLUCTUATING INITIAL STATES OF THE HEAVY ION COLLISIONS AT LHC ENERGIES**	*O12-1*	**88**
17:45	Paula Swierska **BFKL FORMALISM IN QUANTUM CHROMODYNAMICS APPLIED FOR THE JET-GAP-JET PROCESSES IN HADRON COLLISIONS AT HIGH ENERGIES**	*O12-2*	**89**
18:00	Vytautas Dūdėnas, Thomas Gajdosik **DEVELOPING WEYL SPINOR FORMALISM FOR SEESAW NEUTRINOS**	*O12-3*	**90**
18:15	Vaidas Juknevicius **LONG-RANGE SCALING IN GENERALIZED KURAMOTO-SIVASHINSKY EQUATIONS**	*O12-4*	**91**
18:30	Adam Mielnik-Pyszczorski, Krzysztof Gawarecki, Paweł Machnikowski **INFLUENCE OF THE STRAIN DISTRIBUTION ON NON-RADIATIVE TRANSITIONS IN A QUANTUM WELL-QUANTUM DOT SYSTEM**	*O12-5*	**92**
18:45	Tomas Marčiulionis, Darius Abramavičius, Gediminas Trinkūnas **SIMULATION OF EXCITON EVOLUTION IN A SINGLE LIGHT-HARVESTING COMPLEX LH2**	*O12-6*	**93**
19:00	CONFERENCE PARTY		

List of poster presentations

24 March, TUESDAY

17:00-18:30 **POSTER SESSION P1**

25 March, WEDNESDAY

13:30-15:00 **POSTER SESSION P2**

26 March, THURSDAY

13:30-15:00 **POSTER SESSION P3**

27 March, FRIDAY

13:30-15:00 **POSTER SESSION P4**

Oral session 1

Laser physics and optical technologies

IMPROVEMENT OF STABILITY PROPERTIES IN HEAT TRANSFER NANOFLUIDS FABRICATED BY PULSED LASER ABLATION IN LIQUIDS

Rafael Omar Torres Mendieta[1*], Rosa Mondragón Cazorla[2], José Enrique Julía Bolívar[2], Omel Mendoza Yero[1], Jesús Lancis Saéz[1], Gladis Mínguez Vega[1]

[1] GROC·UJI, Institut de Noves Tecnologies de la Imatge (INIT), Universitat Jaume I., 12080, Castelló, Spain
[2] Departmento de Ingeniería Mecánica y Construcción, Universitat Jaume I., 12071, Castelló, Spain.
mendieta@uji.es

The use of nanofluids (fluids with dispersed nanoparticles in it) is an emerging technique for the enhancement of harvesting of energy in solar power plants (SPP) through increasing the thermal conductivity of heat transfer fluids [1]. In this context, it has been proved that the fabrication of gold nanoparticles in fluids commonly used in SPP like Therminol VP-1 [2] can provide an enhancement of its thermal conductivity by up to 6.5% [3], unfortunately the stability of this kind of nanofluid is poor and it can't be used in real application yet; it doesn't matter if the nanofluid is produced by chemical techniques or physical ones such as Pulsed Laser Ablation in Liquids (PLAL), the nanoparticles tend to agglomerate trough the time [4]. Nevertheless, if in PLAL method, a stabilizer like tetra-n-octylammonium bromide ((C8H17)4NBr, TOAB, > 98%) is used, is possible to obtain a stable nanofluid which keeps the thermal conductivity enhancement. In this way, gold nanoparticles were produced in Therminol VP-1 by Pulsed Laser Ablation in Liquids using as stabilizer TOAB. In particular this kind of chemical specie have demonstrated that it can be used for practical applications, insomuch as TOAB doesn't degrade at temperatures over 200ºC.

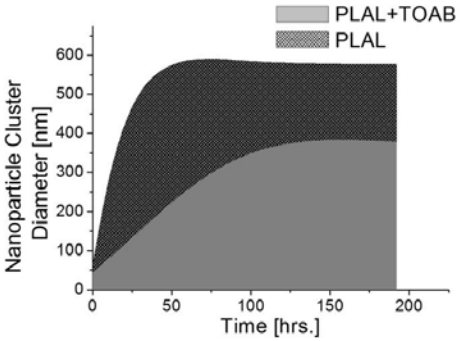

Fig. 1. Agglomeration dynamics of nanofluids through the time.

The process to produce the nanofluid involves two stages, the ablation and post-fragmentation stage. A Ti:Sapphire laser that emits pulses of 30fs FWHM, with mean wavelength of 800nm, and repetition rate of 1kHz, was used as light source; the fluence for both stages was 1Jcm^2. The nanoparticles produced just after the physical method promote an enhancement in the thermal conductivity of Therminol VP-1 by up to 4%; in the other hand, without the use of any stabilizer the particles reach sizes around 58.8 nm, but immediately start an agglomeration process of nanoparticles, forming in this way, nanoparticle clusters which stabilization size is 600nm. TOAB was used as stabilizer to alleviate the agglomeration phenomenon, successfully we have reach sizes around 39nm and nanoparticle cluster's size stabilization at 300nm an enhancement in the thermal conductivity of Therminol VP-1 by up to 3.6%. In contrast, the nanoparticles produced by PLAL method using TOAB as stabilizer reach a similar thermal conductivity enhancement but the stability of the nanofluid through the time is highly improved, making it more suitable for crossing the edge between research and applied technology.

[1] A. Lenert, E. N. Wang, Optimization of nanofluid volumetric receivers for solar thermal energy conversions, Solar Energy **86**, 253-265 (2012).
[2] R. Torres-Mendieta, R. Mondragón, E. Julía, O. Mendoza-Yero, E. Cordoncillo, J. Lancis, G. Minguez-Vega, Fabrication of gold nanoparticles in Therminol VP-1 by laser ablation and fragmentation with fs pulses, Laser Physics Letters **11**, 126001 (2014).
[3] Cingarapu S., Singh D., Timofeeva E. V., Moravek M. R., Nanofluids with encapsulated tin nanoparticles for advanced heat transfer and thermal energy storage, International Journal of Energy Research **38**, 15-59 (2014).
[4] Wang C., Yang J., Ding Y. L., Phase transfer based synthesis and thermophysical properties of Au/Therminol VP-1 nanofluids, Progress in Natural Science-Materials International **23**, 338-342 (2013).

LASER PULSE PEAK INTENSITY INFLUENCE ON THE GEOMETRY OF PERIODIC POLYMER NANOSTRUCTURES FABRICATED BY INTERFERENCE LITHOGRAPHY

Mantas Garliauskas[1,2], Evaldas Stankevičius[2], Gediminas Račiukaitis[2]

[1] Faculty of Physics, Vilnius University, Lithuania
[2] Center for Physical Sciences and Technology, Lithuania
garliauskas.mantas@gmail.com

Nanostructures can have quite amazing linear and especially nonlinear optical properties. Metallic nanoparticles, for instance, can localize visible light on a scale of a few nanometers only in the form of surface plasmon excitations [1]. Fabricating polymeric nanostructures on metal surface could induce such surface plasmon resonance (SPR) which has been intensively exploited for a variety of innovative bioapplications, ranging from biosensing, bioimaging, controlled drug/gene delivery, to photothermal cancer therapy, etc. [2]. The geometry of periodic structures strongly influences the wavelength at witch plasmon resonance occurs, so it is very important to conveniently control geometrical parameters of these structures. In this work, it is implemented by interference lithography, which is a efficient, cost-effective, and maskless optical lithography technique for realizing large area periodic patterning at a subwavelength scale resolution [3].

The aim of this research is to investigate the influence of laser pulse peak intensity on periodic polymer nanostructures geometrical properties.

Figure 1 shows two atomic force microscope (AFM) profiles of fabricated nanostructure arrays using different laser pulse peak intensities: a) 18.1 GW/cm^2 and b) 0.91 GW/cm^2. In figure 1 c) and d), surface profiles of encircled structures are shown. As we see, laser pulse peak intensity strongly influences the shape of fabricated structures: c) 18.1 GW/cm^2 irradiation intensity forms structures with ~8 nm depth pit at the center, whereas ~20 times lower intensity (0.91 GW/cm^2) forms spherical surface structure (Fig. 1c) which is the shape of plano-convex lens. The height of this fabrication is ~120 nm, diameter ~510 nm, and the radius of curvature, measured by circle function approximation (dotted curve), is ~350 nm.

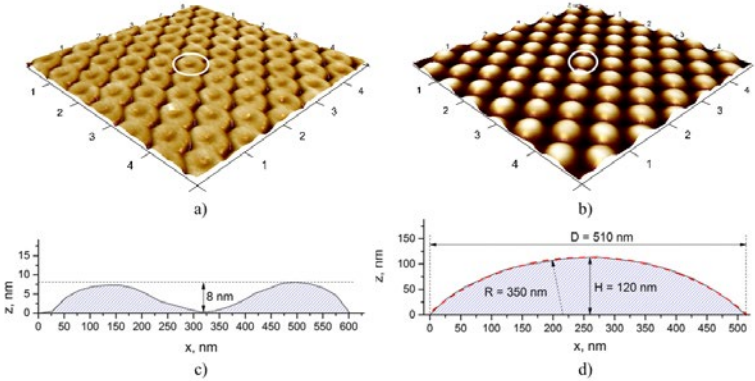

Fig. 1. AFM profiles of periodic nanostructres arrays fabricated using different laser pulse peak intensities: a) 18.1 GW/cm^2; b) 0.91 GW/cm^2 and their surface profiles with geometrical parameters: c) nanostructures with the pit at the center; d) plano-convex lens shape nanostructure.

In conclusion, it was demonstrated that using interference lithography technique, laser pulse peak intensity strongly influences geometrical properties of periodic polymer nanostructures. Spherical surface nanostructures are expected to function as nanolenses [4] for focusing infrared and longer wavelength waves, beyond Abbe's diffraction limit. Further investigation is being carried out to test plasmonic effects of these nanostructures fabricated on thin metal layer.

[1] S. Sakabe, C. Lienau, R. Grunwald, *Progress in Nonlinear Nano-Optics* (Springer, Switzerland, 2015).
[2] Y. Jin, Engineering Plasmonic Gold Nanostructures and Metamaterials for Biosensing and Nanomedicine, Adv. Mater. **24** (38), 5153–5165, (2012).
[3] K. V. Sreekanth, J. K. Chua, and V. M. Murukeshan, Interferometric lithography for nanoscale feature patterning: a comparative analysis between laser interference, evanescent wave interference, and surface plasmon interference, Appl. Opt. **49** (35), 6710-6717, (2010).
[4] J. Y. Lee, B. H. Hong, W. Y. Kim, S. K. Min, Y. Kim et al., Near-field focusing and magnification through self-assembled nanoscale spherical lenses, Nature **460**, 498-501, (2009).

PROPERTIES OF GOLD NANOPARTICLES GENERATED BY LASER ABLATION IN IONIC LIQUIDS

Natalie Tarasenka, Andrei Butsen

B.I. Stepanov Institute of Physics, National Academy of Sciences of Belarus
n.tarasenko@ifanbel.bas-net.by

In this paper we used laser assisted techniques for production of gold and alloyed gold-silver nanoparticles (NPs) in ionic liquid (IL) (1-n-butyl-3-methylimidazolium bis(trifluoromethylsulfonyl)imide [C4C1Im] [Tf2N]). Gold NPs have a wide range of applications, ranging from charge storage systems, sensing of organic and biomolecules, to photonic device fabrications. Studying of Ag-Au alloys is of special interest due to the possibility of altering of their physical properties by varying the composition and atomic arrangement.

To prepare NPs we used laser irradiation processes in several ways: first, laser ablation of metal target immersed into IL, second, laser induced sputtering of the preliminarily prepared gold NPs deposited on glass and placed under IL layer and finally additional laser irradiation of the NPs formed in IL with laser light at frequency of the surface plasmon resonance. In order to synthesize nanoparticles of Ag-Au alloy the Ag and Au colloids, prepared by laser ablation in ethanol, were mixed in the proportion 1:1 and deposited on the glass substrate. After complete drying of the powder it was sputtered by the unfocused beam of the second harmonic (wavelength 532 nm, pulse duration 10 ns) of the Nd:YAG laser in IL. The produced colloidal solution was additionally subjected to laser irradiation by the second harmonic of the Nd:YAG laser with fluence of 400 mJ/cm^2.

The optical properties, morphology and size distributions of the synthesized nanoparticles were investigated using UV/VIS absorption spectroscopy and transmission electron microscopy (TEM). To determine the temperature of the laser irradiated NPs their thermal radiation spectra were fitted by a Planck curve, taking into account the emissivity function of NPs.

Optical extinction spectra of the synthesized gold colloids exhibited the characteristic peaks of the surface plasmon resonance (SPR) on the tail of the broad band extending toward the UV-wavelength range and originating from the interband transitions in NPs. The SPR peak position was around 550 nm indicating the formation of particles with dimensions of 5–20 nm. The plasmon peak position was found to be sensitive to the additional laser irradiation. The blue shift of the SPR maximum and narrowing of the red tail of the band after 532 nm irradiation can be attributed to the depletion of the particle aggregates and fragmentation of parent NPs into smaller ones after the additional laser irradiation. These spectra findings were confirmed by TEM data.

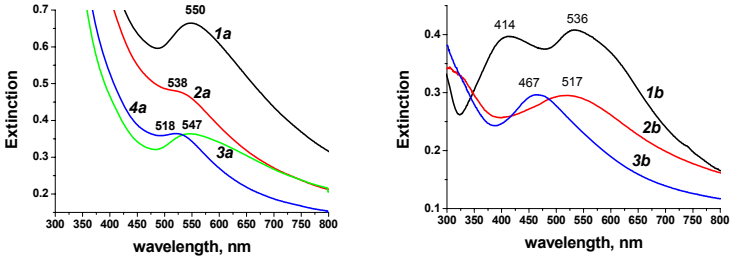

a b

Fig. 1. Extinction spectra of the Au and Ag-Au NPs in IL: 1a – Au NPs prepared by laser ablation, 2a – Au NPs prepared by laser ablation after 532 nm laser modification, 3a – Au NPs prepared by laser sputtering into IL, 4a – Au NPs prepared by laser sputtering into IL after 532 nm laser irradiation, 1b – Ag-Au mixture in ethanol, 2b – Ag-Au NPs after laser sputtering into IL, 3b – Au NPs after laser sputtering in IL and laser irradiation

The optical absorption spectra of Ag-Au colloidal solutions before and after laser modification are presented in Figure 1b. As can be seen from the spectra of the mixture of gold and silver colloidal solutions, two distinct plasmon peaks appear in the spectrum (curve 1b). Laser sputtering of the Ag-Au powder under the layer of IL results in the sufficient changes of the absorption spectrum (curve 2b): instead of two plasmon bands only one is seen in the spectrum with a maximum at 517 nm that is indicative of the alloying of NPs [1]. The plasmon band is rather broad and red shifted that is indicative of the formation of Au-rich alloys with a relatively broad size distribution. After 532 nm laser irradiation a sufficient blue shift of the plasmon band takes place (curve 3b) that can be result of the change of Ag:Au ratio in the nanoparticle.

[1] Q. Zhang, J.Y. Lee, J. Yang, et.al., Size and composition tunable Ag–Au alloy nanoparticles by replacement reactions, Nanotechnology **18**, 1-8 (2007).

LIGHT POLARIZATION INDUCED PECULIARITIES IN DIRECT LASER WRITING 3D NANOLITOGRAPHY

Tomas Jonavičius, Sima Rekštytė and Mangirdas Malinauskas

Laser Research Center, Department of Quantum Electronics, Physics Faculty, Vilnius University, LT-10223 Vilnius, Lithuania
nanopolimerizacija@gmail.com

Direct laser writing based (DLW) true 3D lithography (also known as two-photon polymerization (2PP)) is a technique offering unmatched flexibility in creating arbitrary shape free-form structures of various cross-linkable materials [1-4]. During the last decade it has covered application fields of photonics, microoptics, microfluidics, and biomedicine. Currently it is being implemented as a *high-end 3D printer* ensuring nanoscale resolution and wide material spectrum ranging from metals to proteins. Despite that, several photo-physical and photo-chemical mechanisms are intensively discussed and sometimes contradictory (see references for details [1-3]). The majority of the efforts were targeted towards improving structuring spatial resolution and investigation of novel materials. Up to date exists only a single report [4] related to polarization's influence on DLW based photo-polymerization at nanoscale.

Thus, we present a systematic study on femtosecond laser light polarization's influence to polymerizable features. We chose SZ2080 (Si and Zr containing organic-inorganic hybrid) and PETA (pentaerythritol triacrylate) as photoresists sensitized with 1% *w.t.* Michlers ketone. Ti:Sapphire oscillator (800 nm, 80 MHz, 100 fs) and Yb:KGW amplified laser system (1030 nm, 1 - 200 kHz, 300 fs) were employed as irradiation sources, 100 μm/s sample translation velocity was kept constant. The chosen experimental parameters represent materials, setups and nanostructuring conditions commonly used in DLW nanolithography. By varying the polarization we aimed to distinguish its influence on photo-polymerized features namely: the fabrication window, the line width, height and aspect ratio. Typical test structure micrographs and spatial resolution dependence on irradiation polarization (in respect to sample translation direction) are shown in Fig. 1(a,b) and (c), respectively.

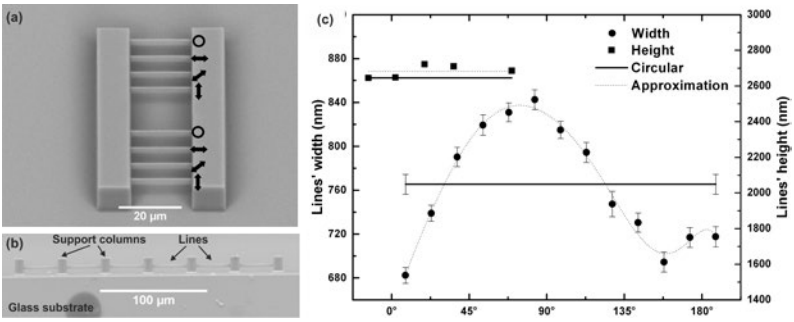

Fig. 1. (a,b)-SEM micrographs of the DLW fabricated 3D test microstructure of SZ2080 consisting of suspended free-hanging lines. It consists of components oriented at various angles in respect to the laser exposure's polarization direction. Arrows show direction of light polarization. (c)-graphed lines' width and height dependences on light polarization ($100^{\times}$ 1.4 NA objective, λ=1030 nm, f=200 kHz, τ=300 fs, E_p=1.102 nJ).

In brief, we report on investigation of *fs* pulsed-light polarization influence to the 3D polymer nanostructuring spatial resolution. We show that the orientation of electric field at the focus induces peculiarities significant for the final polymerized features. Physical mechanisms responsible for it are modeled and presented as well as compared to the ripple formation in metals and transparent dielectrics [5]. Practical issues regarding reaching the highest spatial resolution and optimization of reproducibility in DLW lithography are discussed.

[1] T. Baldacchini, S. Snider, R. Zadoyan, Two-photon polymerization with variable repetition rate bursts of femtosecond laser pulses, Opt. Express **20**, 29890 (2012).
[2] M. Malinauskas, M. Farsari, A. Piskarskas, S. Juodkazis, Ultrafast-laser micro/nano-structuring of photo-polymers: a decade of advances, Phys. Rep. **533**, 1 (2013).
[3] P. Mueller, M. Thiel, M. Wegener, 3D direct laser writing using a 405 nm diode laser, Opt. Lett. **39**, 6847 (2014).
[4] H.-B. Sun, M. Maeda, K. Takada, J.W.M. Chon, M. Gu, S. Kawata, Experimental investigation of single voxels for laser nanofabrication via two-photon photopolymerization, Appl. Phys. Lett. **83**, 813 (2003).
[5] R. Buividas, M. Mikutis, and S. Juodkazis, Surface and bulk structuring of materials by ripples with long and short laser pulses: recent advances, Prog. Quant. Electron. **38**, 119 (2014).

Oral session 2

Laser physics and optical technologies

COMBINING 3D PRINTING AND DIRECT LASER WRITING FOR MICROFLUIDIC DEVICE FABRICATION

Linas Jonušauskas and Mangirdas Malinauskas

Department of Quantum Electronics, Vilnius University, Saulėtekio Ave., 9,
Vilnius LT-10222, Lithuania
linas.jon@gmail.com

Microfluidics is a science branch that investigates liquid behavior in ultra-small volumes (from micro- to femtolitres) and liquid interaction with various micro- and nanostructures. Achievements in this field pave the way for creation of great number of sophisticated microstructures that, combined with other components, could become independent multifunctional device also known as lab-on-chip (LOC) [1]. However, advancements of microfluidics greatly depend on what kind of structures can be created for liquid guidance and interactions in aforementioned scale. Requirements for these structures sometimes might be relatively contradictive: for example, channel system needed for experiments might be millimetres or even centimetres in overall size, but with micrometre sized channels or other features of this scale. Also, in order for structures like these to become widely used they have to be cheap and easy to produce in huge quantities. This puts most fabrication technologies to their limit and makes microfluidic research difficult and costly.

The goal of this work was to show possibility to produce microfluidical millimetre-sized components with integrated functional microelements combining fused filament fabrication 3D printing (3DP) [2] and direct laser writing (DLW) using femtosecond laser [3]. In this case, 3DP guarantees rapid and cheap fabrication of microchannels with size of hundreds of micrometres inside a structure that has overall dimensions in range from millimetres to centimetres. DLW, on the other hand, allows integrating intricate 3D microstructures into channels produced with 3DP. Structure fabrication utilizing only 3DP or DLW would lead to either insufficient spatial resolution if only 3DP is used or costly and long fabrication process if all structure is formed only with DLW.

Results of this work include demonstration what types of channels could be produced using commercially available 3D printer Ultimaker original and polylactic acid (PLA) as main material for channel fabrication [4]. Channel characteristics, best fabrication parameters and arising problems are addressed. In case of DLW, we show fabrication of various microfilters. These components, when integrated in 3DP fabricated channels, could act as passive particle sorters [Fig. 1 (a)]. Filter geometry best suited for integration using DLW as well as filtering is discussed. Finally, novel method for sealing PLA channels with glass covers without using any additional glue is proposed and tested.

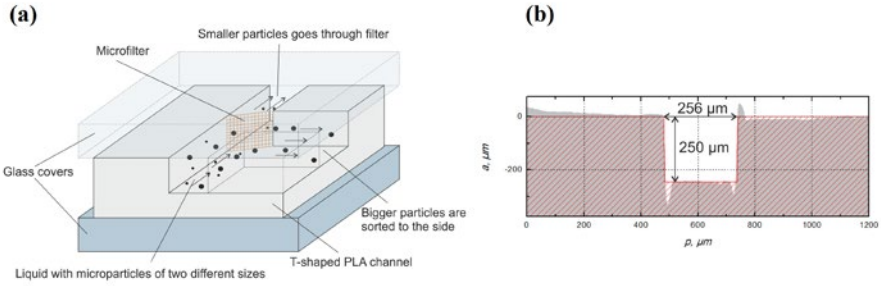

Fig. 1. (a) Schematic representation of microparticle sorter utilizing T-shaped channel (produced using 3DP) and microfilter (integrated with DLW); (b) a nearly square profile of microchannel produced utilizing 3DP. Grey area and arrows shows measured profile, red lines - theoretical profile with both channel width and depth equal to 250 m.

[1] P. Abgrall and A.-M. Gue, Lab-on-chip technologies: making a microfluidic network and coupling it into a complete microsystema review, J. Micromech. Microeng. **17**, R15-R49 (2007).
[2] M. Malinauskas, S. Rekštytė et. al., 3D Microporous Scaffolds Manufactured via Combination of Fused Filament Fabrication and Direct Laser Writing Ablation, Micromachines **5**(12), 839-858 (2014).
[3] K. Sugioka and Y. Cheng, Femtosecond laser three-dimensional micro- and nanofabrication, Appl. Phys. Rev **1**, 041303 (2014).
[4] V. Melissinaki, A. A. Gill et al., Direct laser writing of 3D scaffolds for neural tissue engineering applications, Biofabrication **3**, 045005 (2011).

ANALYSIS OF OPTICAL PARAMETRIC AMPLIFICATION BY INCOHERENT PUMP IN TRAPPING REGIME

Paulius Stanislovaitis, Viktorija Pyragaitė

Department of Quantum Electronics, Vilnius University, Lithuania
paulius.stanislovaitis@ff.stud.vu.lt

In this work we theoretically investigate temporal effects in optical parametric amplifier (OPA) pumped by incoherent wave in trapping regime. Analytical calculations have been performed as well as numerical simulations.

Trapping regime is a term for a situation, when signal and idler group velocities have different directions with respect to the pump wave. In Ref. [1], the parametric interaction of three coherent waves was investigated in cases when directions of signal and idler group velocities with respect to the pump wave coincide and when one of the relative group velocities of idler or signal are equal to zero. However, some of the formulas presented in Ref. [1] can be used in our analysis.

As initial conditions, we chose the signal and pump waves to be incoherent with the same correlation time τ_c. We demonstrate through the numerical experiments, that in the case of trapping regime, the spectrum of signal and idler waves narrows in the process of OPA, thus the coherence of these waves is improved. The strength of this narrowing effect depends on the magnitudes of relative group velocities of signal and idler waves with respect to pump. The larger the magnitude of signal group velocity, the more spectrum narrowing manifests. Howerer, as these group velocities grow, the amplification efficiency is also reduced.

In case of pump depletion, it is shown that the central part of pump spectrum is depleted, since the signal and idler spectra andergo narrowing in the amplification process. The width of that depleted central part depends on the spectral width of the idler wave. With the broader idler spectrum, the pump spectrum is used more effectively. This conclusion can be based on the phase matching conditions. The phase matching conditions are as follows :

$$\begin{aligned} k_1+k_2&=k_3;\\ \Omega_1+\Omega_2&=\Omega_3; \end{aligned} \qquad (1)$$

where the numbers 1,2,3 stand for signal,idler and pump waves respectively. Ω_j is the frequency and k_j – the wave number of the j'th wave. If we expand the wavenumbers k_j in Taylor series and consider that the first condition is satisfied at the central frequencies of pump, signal and idler waves, we obtain :

$$\begin{aligned} \Omega_1&=-\frac{\kappa_2}{\kappa_1}\Omega_2;\\ \Omega_3&=\left(1-\frac{\kappa_2}{\kappa_1}\right)\Omega_2; \end{aligned} \qquad (2)$$

where κ_j is defined as $\kappa_j = L_n/L_{vj}$, where L_{vj} is the group walk-off length and L_n is the nonlinear interaction length. The ratio κ_2/κ_1 can be expressed simply as $\kappa_2/\kappa_1 = L_{v1}/L_{v2}$. It is seen from Eq. (2) that the width of the idler spectrum depends on the ratio of relative group velocities. When $\kappa_2/\kappa_1 = -1$, the idler spectrum narrows along with the signal, and only the central part of the pump spectrum is depleted. In case when κ_2/κ_1 approaches zero, the idler spectrum remains broad and the larger portion of the pump spectrum is depleted.

The numerical simulations have been carried out with various values of κ_2/κ_1, with only the first order of dispersion taken into account, as well as under real conditions in ADP crystal with second-order dispersion. Results of the first case are shown in Fig. 1. Is is evident from the numerical results that the narrowing of pump spectrum depends on the ratio κ_2/κ_1. As can bee seen from the Fig. 1, with the smallest value of $|\kappa_2/\kappa_1|$, the resulting idler spectrum is the broadest.

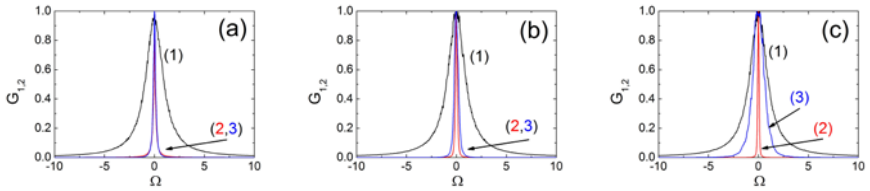

Fig. 1. Spectra of resulting pump (1), signal (2) and idler (3) waves without pump depletion. $Z = 10$ mm, $L_n = 1.5$ mm, $\kappa_1 = 9$. $\kappa_2/\kappa_1 = -1$ (a), -0.5 (b) and -0.1 (c).

[1] A. Picozzi, P. Aschieri. Influence of dispersion on the resonant interaction between three incoherent waves. Phys. Rev. E **72**, 046606 (2005)

CREATING OPTICAL FLUX LATTICE USING MULTI-FREQUENCY RADIATION

Tomas Andrijauskas[1], Gediminas Juzelūnas[1], Ian Spielman[2,3]

[1]Institute of Theoretical Physics and Astronomy, Vilnius university, A. Goštauto 12, Vilnius LT-01108, Lithuania
[2]Joint Quantum Institute, University of Maryland, College Park, Maryland 20742-4111, 20742, USA
[3]National Institute of Standards and Technology, Gaithersburg, Maryland 20899, USA
tomas.andrijauskas@tfai.vu.lt

Ultracold atomic gases are systems exhibiting various condensed matter phenomena. The ultracold atoms are neutral, so under usual circumstance they do not exhibit important magnetic phenomena, like the quantum Hall effect. Possible ways to create artificial magnetic field for ultracold atoms include rotation of an atomic cloud, laser-assisted tunnelling, shaking of optical lattices [1]. Yet it is difficult to reach considerable magnetic fluxes required for achieving the fractional Hall effect.

Here we theoretically analyse another way of creating a non-staggered magnetic flux for ultra-cold atoms by using a periodic sequence of short laser pulses providing a multi-frequency perturbation. In particular, we consider a possibility to create a square flux lattice for ultra-cold atom characterized by two internal states. The energies of the two internal states have opposite gradients in one spatial direction. Hamiltonian of such system reads,

$$H_0 = \frac{\boldsymbol{p}^2}{2m} I + bx\sigma_z, \tag{1}$$

where b is coefficient of linear dependence of the spatial gradient and σ_z is the z-th Pauli matrix. The driving consists of periodic in time pulses that couple the internal states and propagate in a direction perpendicular to the energy gradient. Such pulses can be created using mult-frequency radiation:

$$V(t) = \hbar\Omega|1\rangle\langle 2|\left(\mathrm{e}^{-\mathrm{i}ky}\sum_n \mathrm{e}^{-\mathrm{i}2n\gamma t} + \mathrm{e}^{\mathrm{i}ky}\sum_n \mathrm{e}^{-\mathrm{i}(2n+1)\gamma t}\right) + \mathrm{H.c.} \tag{2}$$

Here Ω is the coupling strength in frequency units, γ is the comb frequency and k is the wave-number. The time-depent perturbation effectively creates a square optical lattice, described by the periodic coupling $V_{\mathrm{eff}} = \boldsymbol{\sigma}\cdot\boldsymbol{B}$, where $\boldsymbol{B}$ is a real three dimensional vector field and $\boldsymbol{\sigma}$ is a vector of Pauli matrices. We show that this effective optical lattice produces a non-staggered magnetic flux [2], described by a geometric vector potential, which contains Aharonov-Bohm type singularities (See figure 1). Finally we explore topological properties of such a lattice.

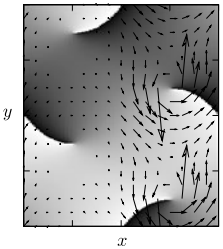

Fig. 1. Spherical angle ϕ of the spherical parametrisation of $\boldsymbol{B} \equiv (B,\theta,\phi)$ and the geometric potential over a single elementary cell in the case of a weak coupling Ω. The scalar field $\phi(\boldsymbol{r})$ is represented by the colour intensity: the range from black to white colours corresponds to the angle range from $-\pi$ to π. The geometric potential is represented by the arrows. There are two singular points in the right side of the elementary cell. Near these points the geometric potential approximately equals to $\nabla\phi$. Since the geometric potential rotates in the same direction around thsese two points, the singularitites do not compensate each other and produce a non-zero magnetic flux over an elementary cell.

[1] Jean Dalibard, Fabrice Gerbier, Gediminas Juzeliūnas and Patrick Öhberg, *Colloquium: Artificial gauge potentials for neutral atoms*, Rev. Mod. Phys. **83**, 1523-1543 (2011).
[2] Gediminas Juzeliūnas and Ian Spielman, *Flux lattices reformulated*, New J. Phys, **14**, 123022 (2012).

PICOSECOND LASER WITH 11 W OUTPUT POWER FOR SELECTIVE MICROMACHINING AT 1342 NM WAVELENGTH

Nortautas Ulevičius[1,2], Aleksej M. Rodin[1]

[1] Department of Laser Technology, Center for Physical Sciences and Technology, Lithuania
[2]Vilnius University, Faculty of Physics, Lithuania
n.ulevicius@gmail.com

Efficient power scaling of ~ 10 ps pulses at 1342 nm wavelength is important for selective scribing of thin film copper InGaSe solar cell (CIGS). Lower silicon absorption at 1.3 μm [1] reduces damage to Si layer [2]. Processing speed is defined by average output power and pulse repetition rate. We demonstrate the generation of ~ 13 ps laser pulses at 1342 nm wavelength with output energy > 35 μJ at 300 kHz repetition rate and diffraction limited beam quality M^2 ~ 1.1. Such a set of output laser parameters satisfy the stringent requirements for industrial microprocessing with high yield and throughput.

The experimental setup for investigation of high average power picosecond laser operating at 1342 nm wavelength is shown in Fig. 1 (left). This laser is comprised of mode locked master oscillator, regenerative amplifier and output pulse control module. End pumped Nd:YVO_4 crystals are used in the both oscillator and amplifier.

Passively mode locked by means of semiconductor saturable absorber mirror (SSA) and pumped through the focusing system (FS1) by fiber coupled laser diode (LD) emitting 808 nm wavelength master oscillator provides pulses of ~ 13 ps FWHM (Fig. 1 – right) at repetition rate of 55 MHz with average output power of ~ 140 mW. The four-pass confocal delay line (CDL) forms a longest part of the oscillator cavity in order to suppress thermo-mechanical misalignment. Optimization of the intracavity pulse fluence ensures significant lifetime improvement for the saturable absorber.

This oscillator was used as the seeder for regenerative amplifier based on composite diffusion-bonded Nd:YVO_4 rod pumped with 880 nm wavelength through the focusing system (FS2). The absorbed pump power at optimum laser diode (LD) temperature approached to 63 W. The seed pulses transmitted by output coupler (OC) pass the beam forming telescope (BFT) to match the diameter and divergence of the beam circulating inside the cavity of regenerative amplifier. Amplifier cavity is formed by rear spherical mirrors (SM1 and SM2), thin film polariser (TFP2) and dichroic separation mirror (DS). Faraday rotator (FR) together with half-wave retardation plate (HW2) and thin film polariser (TFP1) ensure reliable protection from the residual backward emission of regenerative amplifier. Another oscillator beam is directed to the InGaAs photodiode (FD) to launch electrical signal for Pockels cell (PC) synchronization from control electronics module (PCE).

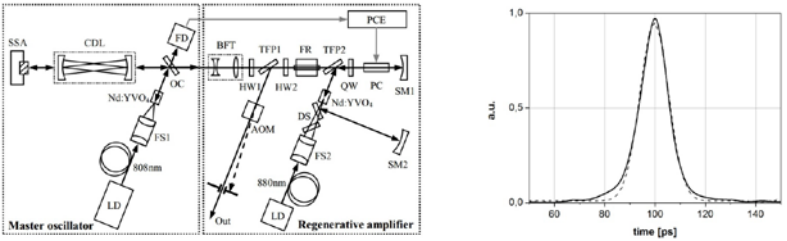

Fig. 1. Experimental set-up (left) and temporal profile of oscillator output pulse (right – solid line) measured by means of Hamamatsu C5680-22 streak camera with Gaussian fit (dashed line).

When operating at 300 kHz repetition rate the amplifier delivered high quality output beam of M^2 ~ 1.1 with average power of 11.6 W at 1342 nm wavelength providing over 16 % efficiency. Acousto-optic modulator (AOM) serves as a high contrast pulse-picker providing pulse on demand or burst operation (scanner or mechanical stage) and allows laser pulse repetition rate to be imposed by external devices. Without seeding the regenerative amplifier transforms to electro-optically cavity-dumped Q-switched laser producing 10 ns FWHM pulses at 10 – 300 kHz repetition rates with up to 11 W of average power and nearly diffraction limited beam quality. In continuous wave operation we achieved more than 17.5 W of average power in TEM_{00} mode radiation providing the slope efficiency of nearly 26 %.

High peak intensity ns or ps pulses with average power in excess of 10 W at 1342 nm wavelength facilitate efficient conversion to 671 nm and 447 nm harmonics as well as OPO. Thus laser may find other applications in high brightness colour display or laser TV, laser scan and printing, medical treatment, spectroscopy and optical storage.

[1] M.A.Green, M.J.Keevers, Optical properties of intrinsic silicon at 300 K, Progress in Photovoltaics: Research and Applications **3**, 189-192(1995).
[2] Y.Ito, H.Sakashita, R.Suzuki, M.Uewada, K.P.Luong, R.Tanabe, Modification and Machining on Back Surface of a Silicon Substrate by Femtosecond Laser Pulses at 1552 nm, JLMN-Journal of Laser Micro/Nanoengineering **9**, 98-102(2014).

A POSSIBILITY TO REDUCE SPHERICAL THERMAL ABERRATIONS IN DIODE PUMPED SOLID-STATE LASERS

Dominykas Brička[1,2], Alexander S. Dement'ev[1]

[1]Center for Physical Sciences and Technology, Savanorių av. 231, Vilnius 02300, Lithuania
[2] Department of Quantum Electronics, Vilnius University, Saulėtekio av. 9, Vilnius 10222, Lithuania
dominykus@gmail.com

Thermally induced spherical aberrations in solid state lasers are one of the main issues for high average power scaling possibilities. Therefore, we take a closer look at the possibility to reduce the spherical aberration by the use of certain pump distribution taking into account temperature dependence of the thermal conductivity coefficient $k(T) = a/T$, where $a = k_0 T_r$ and k_0 is the coefficient of thermal conductivity at reference temperature T_r. We discuss a case of steady-state radial heat flow in cylindrical rods with radially symmetric heating distribution. This allows to simplify the problem enough to obtain simple analytic solutions for various heat load distributions $Q_0(r,z)$ and the following boundary condition $-k(T)(\partial T/\partial r)_{r=R} = h(T - T_a)$, where R is the radius of the rod and h is the convective heat transfer coefficient [1]. A particularly simple solution can be found for the polynomial radial heating distribution

$$Q_h(r,z) = Q_0(z)\sum_{i=0}^{m} b_i \left(\frac{r}{R}\right)^i, \; T(r,z) = T(0,z)\exp\left[-\frac{T_k(z)}{T_r}\sum_{i=0}^{m}\frac{b_i}{(i+2)^2}\left(\frac{r}{R}\right)^{i+2}\right], \tag{1}$$

where $T_k(z) = Q_0(z)R^2/k_0$. By certain choice of coefficients b_i the particular solutions may be obtained [1,2].

It is important to note that due to non-linear heat conductivity coefficient even uniform heat load distribution will give rise to higher than second order terms in (1). In general, a temperature change in the active medium can modify light beam phase by three different mechanisms: refractive index change due to temperature directly, due to temperature gradient induced strains and stresses and due to end face bulging. Additionally, we have to consider that throughout the long rod the light will be bent by thermal lens, so simply integrating the refractive index along the rod at constant radius will not suffice. We attempt to account for this by modelling the beam with geometric rays which are traced through the active medium and the phase change is calculated over the path of the ray. Thus, using fitting procedure, the optical path difference can be written as $\delta\Lambda(r) = r^2/2\tilde{f}_T - C_4 r^4$. This means that the pumped crystal acts as a lens with focal length and has a spherical aberration defined by the coefficient C_4. The effect of spherical phase aberration on the beam quality has been analyzed in [3,4]. It was shown that final beam quality with the quartic-aberration can be written as

$$M_f^2 = \sqrt{(M_i^2)^2 + (M_q^2)^2}, \; M_q^2 = \frac{8\pi\beta_r}{\lambda} C_4 \overline{r^4}, \; \beta_r = \sqrt{\overline{r^2}\,\overline{r^6}/\overline{r^4}^2 - 1}, \tag{2}$$

in which M_i^2 is the beam quality factor of the initial unaberrated beam, M_q^2 is the additional contribution to the beam quality factor caused by the quartic-phase aberration effects and $\overline{r^2}$, $\overline{r^4}$, and so on are radial moments on the transverse intensity profile. It may be shown that for super-Gaussian beams with intensity profile $I(r) = I_0 \exp[-2(r/w_L)^n]$ intensity moments and coefficient β_r for quartic aberration may be expressed as

$$\overline{r^s} = w_L^s \left(\frac{1}{2}\right)^{\frac{s}{n}} \Gamma\left(\frac{s+2}{n}\right)/\Gamma\left(\frac{2}{n}\right), \; s = 2, 4, 6, \; \beta_r = \sqrt{\Gamma(4/n)\Gamma(8/n)/\Gamma^2(6/n) - 1}, \tag{3}$$

where $\Gamma(z)$ is gamma-function. Beam quality factor has been obtained previously [4] for more general polynomial phase aberration $\Phi_L(r) = \alpha_m (r/w_L)^m$. For super-Gaussian beams with $n = 4$ and $n = 6$ the initial beam quality factors are $M_i^2 = 2/\sqrt{\pi} \approx 1.13$ and $M_i^2 \approx 1.30$ respectively. Thus, using formulae (2) and (3), the beam propagation coefficient may be calculated not only for Gaussian beam with quartic phase aberration, but also for super-Gaussian beams. For spherical aberration the beam propagation coefficient increases strongly with increasing width of probe beam. However, it can be shown that for certain combination of b_i coefficients in the pump beam the fourth order aberration term could be completely removed taken into account the temperature dependence of the total change of the thermal refractive index due to thermo-optic and photoelastic effects. Thus, the degradation of beam quality will only depend on the higher order aberrations, and therefore will be not so strong.

[1] A.S. Dement'ev, A. Jovaiša, K. Račkaitis, F. Ivanauskas, J. Dabulytė-Bagdonavičienė, Numerical treatment of the temperature distribution in end-pumped composite laser rods, Lithuanian J. Phys., **47**, 279-288 (2007).
[2] G.L. Bourdet and C. Gouédard, Simple analytical derivations of thermal lensing in longitudinally *Q*-CW pumped Yb:YAG, Appl. Opt., **49**, 4160-4167 (2010).
[3] W.A. Clarkson, Thermal effects and their mitigation in end-pumped solid-state lasers, J. Phys. D: Appl. Phys., **34**, 2381-2395 (2001).
[4] A.S. Dement'ev, A. Jovaiša, G. Šilko, R. Čiegis, On alternative methods for measuring the radius and propagation ratio of axially symmetric laser beams, Quantum Electronics, 35, 1045-1052 (2005).

DEVELOPMENT OF TW-CLASS, FEW-CYCLE, PASSIVELY CEP-STABILIZED OPCPA SYSTEM BASED ON YB:KGW AND ND:YAG LASERS

Rimantas Budriūnas[1,2], Tomas Stanislauskas[1,2], Jonas Adamonis[3], Arūnas Varanavičius[1]

[1] Department of Quantum Electronics, Vilnius University, Lithuania
[2] Light Conversion Ltd., Lithuania
[3] Ekspla Ltd., Lithuania
rimantas.budriunas@ff.stud.vu.lt

Optical parametric chirped pulse amplification (OPCPA) is an established technique for producing ultrashort, TW-level peak power light pulses for probing light-matter interactions in the strong field regime [1,2]. Most OPCPA systems operating in the visible-NIR range are seeded with pulses from Ti:Sapphire oscillators and pumped by frequency-doubled Nd:YAG laser pulses. Such systems require complex solutions for stabilizing the seed pulse carrier-envelope phase (CEP), ensuring seed and pump pulse synchronization, and improving temporal contrast. We present the conceptual design and preliminary experimental results of an OPCPA setup based on Yb:KGW and Nd:YAG lasers, avoiding most of the issues of Ti:Sapphire-based OPCPA systems.

The layout of our proposed OPCPA setup is depicted schematically in fig. 1. Yb:KGW and Nd:YAG regenerative amplifiers are seeded by an Yb:KGW oscillator. Passively CEP-stabilized pulses at 1.3μm are produced in a difference frequency generator (DFG). Difference frequency pulses are focused to a sapphire plate to generate a CEP-stable supercontinuum, which, after pre-amplification in a femtosecond non-collinear optical parametric amplifier (NOPA), is used to seed the OPCPA. The DFG and fs NOPA are both pumped by second harmonic of the Yb:KGW laser. The seed pulses are stretched in a negative dispersion grism stretcher to ~70ps and sent to picosecond amplification stages, pumped by frequency-doubled Nd:YAG laser pulses. The diode-pumped Nd:YAG amplifier system delivers 532nm pulses with up to 50mJ energy at 1kHz repetition rate. Amplified pulses will be compressed using bulk glass and chirped mirrors. An acousto-optic programmable dispersive filter is used to compensate residual high-order dispersion. Upon completion, the system is expected to deliver <10fs, 10mJ pulses with 850nm center wavelength.

So far, we have developed and characterized the fs NOPA. With 400μJ pump pulses, the fs NOPA delivers pulses with >75μJ energy. The amplified pulse spectrum extends from below 700nm to over 1100nm, theoretically allowing for pulse compression to below 6fs. We have also demonstrated excellent CEP stability of the fs NOPA measured by *f*-2*f* interferometry (fig. 2). The short-term CEP noise is measured to be <67mrad during a 2 minute measurement interval. Furthermore, using a simple feedback loop, we have also demonstrated CEP noise <120mrad during periods of over 20 minutes.

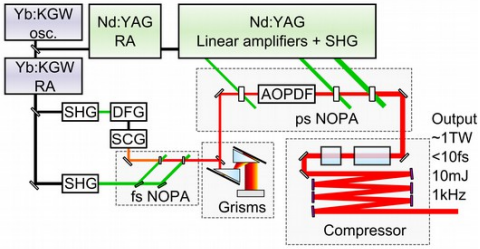

Fig. 1. Schematic of the OPCPA setup. Abbreviations: osc. - oscillator; RA - regenerative amplifier; SHG - second harmonic generator; DFG - difference frequency generator; SCG - supercontinuum generator, AOPDF - acousto-optic programmable dispersive filter

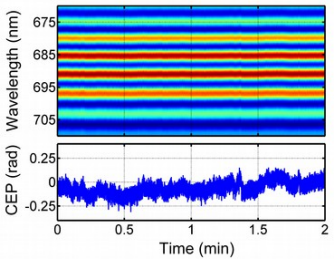

Fig. 2. Front-end CEP stability measurement. Top: *f*-2*f* interferogram; Bottom: CEP values retrieved from the interferogram. Standard deviation of the CEP values is 67mrad. No averaging was performed

Results of pulse amplification in the picosecond stages and pulse compression will be presented in the conference.

[1] A. Dubietis, G. Jonušauskas and A. Piskarskas, Powerful femtosecond pulse generation by chirped and stretched pulse amplification in BBO crystal, Optics Communications **88**, 437-440 (1992).
[2] A. Vaupel, N. Bodnar, B. Webb et al., Concepts, performance review, and prospects of table-top, few-cycle optical parametric chirped-pulse amplification, Optical Engineering **53**, 051507-1 - 051507-12 (2014).

Oral session 3

Spectroscopy, methods and devices for physical diagnostics

ELECTRON PARAMAGNETIC RESONANCE STUDY OF A MIXED VALENT METAL-ORGANIC FRAMEWORK CONTAINING Cu_2 PADDLE-WHEEL UNITS

Mantas Šimėnas[1*], Merten Kobalz[2], Harald Krautscheid[2], Jūras Banys[1], Andreas Pöppl[3]

[1] Faculty of Physics, Vilnius University, Saulėtekio av. 9, III b., LT-10222 Vilnius, Lithuania
[2] Faculty of Chemistry and Mineralogy, Leipzig University, Johannisallee 29, D-04103 Leipzig, Germany
[3] Faculty of Physics and Earth Sciences, Leipzig University, Linnestrasse 5, D-04103 Leipzig, Germany
mantas.simenas@ff.vu.lt

Metal-organic framework (MOF) compounds are a new type of porous ordered solids, which consist of metal ions connected by organic linker molecules [1]. These materials exhibit high porosity and aesthetically attractive underlying topology, drawing scientific and technological attention. The porous structure of MOFs makes them good candidates for gas adsorption, storage and separation [2]. In addition, the diverse magnetic, multiferroic, chiral and photoresponsive properties of these solids attract interest of physicist and material researchers [3].

In the presented work a novel mixed valent MOF with chemical formula $^3{}_\infty$[Cu(I)$_2$Cu(II)$_2${H$_2$O}$_2${(Me-trz-mba)$_2$thio}$_2$]Cl$_2$ is investigated by the means of the continuous-wave (CW) electron paramagnetic resonance (EPR) spectroscopy at X- and Q-band frequencies in a wide temperature range. The main building block of this compound is a so called Cu_2 paddle-wheel (PW) unit, which contains two Cu(II) ions connected via four carboxylate groups. The obtained EPR data allowed us to detect and investigate three distinct magnetic interactions which differ by the three orders of magnitude and are related to the Cu(II) pairs (see Fig. 1).

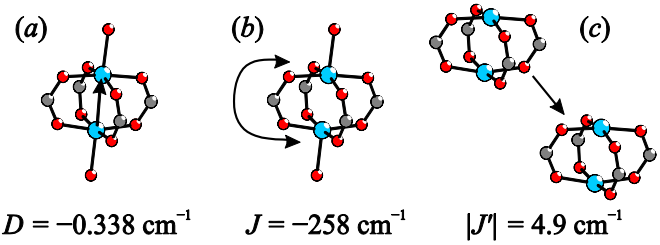

Fig. 1. Different magnetic interactions related to Cu_2 PW units determined by the EPR spectroscopy: (*a*) electron-electron interaction, (*b*) intra-PW exchange and (*c*) inter-PW exchange.

At higher temperatures the fine structure pattern was observed in the EPR spectra and by means of spectral simulations the spin-spin interaction tensor $\boldsymbol{D}$ was determined (axial zero-field splitting parameter $D = -0.338\ \mathrm{cm}^{-1}$). The origin of this pattern was assigned to the thermally populated excited triplet states of the cupric ion pairs. From the temperature dependent CW EPR experiments of the as-synthesized material it was found that these two cupric ions couple antiferromagnetically with the exchange coupling constant $J = -258\ \mathrm{cm}^{-1}$. The influence of the sample dehydration is also investigated and it is observed that the spectra of such samples show pronounced isotropic Lorentzian line indicating an inter-paddle wheel exchange. By simulating the powder pattern of this inter-dinuclear exchange line, the exchange coupling between neighboring PW units was determined ($|J'| = 4.9\ \mathrm{cm}^{-1}$).

[1] S. Kitagawa, R. Kitaura, and S. Noro, Functional Porous Coordination Polymers, Angew. Chem. Int. Ed., **43**, 2334-2375 (2004).
[2] MP. Suh, HJ. Park, TK. Prasad and D Lim, Hydrogen Storage in Metal–Organic Frameworks, Chem. Rev., **112**, 1163-1195 (2012).
[3] Zhang W and Xiong R, Ferroelectric Metal–Organic Frameworks, Chem. Rev., **112**, 1163-1195 (2012).

SPECTRAL METHOD FOR CONTROLLING OF mTHPC REDISTRIBUTION BETWEEN CYCLODEXTRINS AND BIOLOGICAL STRUCTURES

Yakovets Ilya[1*], Yankovsky Igor[1,2], Zorin Vladimir[1], Bezdetnaya Lina[2]

[1] Department of Biophysics, Belarussian State University, Minsk, Belarus
[2] CNRS, CRAN, University of Lorraine, Lorraine Cancer Institute, France
**viprorok@gmail.com*

5,10,15,20-Tetra(*m*-hydroxyphenyl)chlorin (mTHPC) is one of the most potent second-generation clinically approved photosensitizer [1]. The main limitation of its application in photodynamic therapy is a low water-solubility. mTHPC molecules form aggregates in water surroundings, that leads to disorder of sensitizer pharmacokinetics. To prevent mTHPC aggregation several special formulations, such as liposomes, polymer solutions and bioconjugates were designed. An application of specialized pharmacological formulations supposes a development of new experimental techniques to control photosensitizer distribution in biological media. Cyclic oligosaccharides, cyclodextrins, are also considered as perspective formulation for tetrapyrrolic photosensitizers.

In this work we describe fluorescent spectral technique, allowing to control mTHPC redistribution between β-cyclodextrin (β-CD) derivates and various biological structures. Fluorescence and absorbance characteristics of mTHPC in several organic solutions and in the complexes with various biological structures have been compared. It was shown, that extinction coefficient, quantum yield and fluorescence polarization degree of mTHPC bound to biological structures differ from the same parameters in organic solvents. The comparison of spectral characteristics showed that the shape of the Soret band of mTHPC absorbance spectrum and corresponding band of fluorescence excitation spectrum were strongly depended on the kind of biological structures bound with photosensitizer molecule. An inclusion of mTHPC molecule into lipid vesicles or serum proteins resulted in decreasing of shortwave shoulder of Soret band. When mTHPC formed an inclusion complex with β-CD derivatives the bands of absorbance and fluorescence excitation spectra underwent opposite changes.

For quantitative analysis of observed spectral changes we carried out a deconvolution of spectra by the Gaussians components , which are corresponded to five different bands (B_x, B_y, N_x, N_y, L) [2]. A comparison of numerical results of m-THPC absorbance and excitation spectra deconvolution allowed us to conclude that the main factor determining mTHPC spectra features in different solutions was the ratio of B_x and B_y relative weight. For monomeric unbound mTHPC molecules in organic solvents the B_x/B_y is equal to 0.9. The B_x/B_y ratio is equal to 1.05-1.67 for mTHPC-β-CD complexes. When mTHPC is bound to lipid vesicles and serum proteins value is less than 0.7.

This transformation of Soret band was explained on the basis of a conformation changes of mTHPC molecule induced by the interaction with different biological structures. By the crystallographic data [3], the planar chlorin ring of mTHPC is surrounded by two face-to-face phenyl groups, two of them making an angle of 61° with the chlorin plane and the two others an angle of 76°. If molecule of photosensitizer is located in lipid bilayer the phenyl groups rotates and dihedral angles between chlorin ring and one of the face-to-face phenyl groups are decreased. In mTHPC-β-CD complexes takes place inverse effect of increasing of the dihedral angles as a result of interaction of molecules of cyclodextrin with free phenyl groups of mTHPC.

Several kinetic experiments were carried out to show, that the variability of mTHPC Soret band shape allowed to control the redistribution of photosensitizer between cyclodextrins and biological structures, such as lipid vesicles and serum proteins. The developed method can be used for analysis of drug pharmacokinetics in an organism during photodynamic therapy.

[1] Senge, M.O. and Brandt, J.C., Temoporfin (Foscan®, 5,10,15,20-Tetra(m-hydroxyphenyl) chlorin), a Second Generation Photosensitizer, Photochemistry & Photobiology **87**, 1240-1296 (2011).
[2] Gwaltney, S. R. and Bartlett, R.J., Coupled-cluster calculations of the electronic excitation spectrumof free base porphin in a polarized basis, Journal of Chemical Physics **108** (16), 6790-6798 (1998).
[3] Krupitsky, H., Stein, Z., Goldberg, I., Molecular Structure and Intermolecular Organization in the Crystalline 1:2 Complex of Zn(II)-tetra(3-hydroxyphenyl)porphyrin with Dimethylsulphoxide, Z. Kristallogr. **210**, 665-668 (1995).

STUDY OF THE EFFECTS OF LIPID MONOLAYER COMPOSITION AND PHASE ON INTERFACIAL WATER STRUCTURE BY SUM-FREQUENCY SPECTROSCOPY

Edvardas Golovinas[1], Laura Abariūtė[1], Gintaras Valinčius[1], Gediminas Niaura[2]

[1] Vilnius University, Universiteto str. 3, LT-01513 Vilnius, Lithuania
[2] Center for Physical Sciences and Technology, A. Goštauto str. 9, LT-01108 Vilnius, Lithuania
edvardasg2007@gmail.com

Phospholipid monolayers have been studied intensely during last few decades due to their physiological importance as model systems for biological membranes. The components of biomembranes have great diversity but phospholipids constitute a major component of most cell membranes and consist of a charged headgroup connected to a pair of long acyl chains. At physiologically relevant neutral pH, some phospholipids such as phosphatidylcholine carry no net charge but are zwitterionic, whereas others such as phosphatidylserine carry a net negative charge. At interfaces, these amphiphilic molecules form Langmuir films which can attain different phases and morphologies, which depend on the identity of phospholipid headgroup and acyl chain length [1]. Natural biological membranes are most often found in an aqueous environment, as they are designed to enclose aqueous solutions, e.g. the contents of a cell.

The structure and hydrogen bonding of water molecules provides it with unique solvent properties, essential to many physical, chemical and biological processes. Intermolecular hydrogen bonding between water molecules in the bulk medium is disrupted at the interface. This disruption imparts the surface with unique structural and thermodynamic properties [2, 3]. Biological membranes form an interface with water. The interaction between water molecules and the membrane affects the structure of both the membrane and of the water associated with it [4]. Studying the influence of phospholipid monolayer composition and phase on water structure can help elucidate the nature of more complex phase behavior which takes place in biomembranes.

In this work we employed a combination of surface pressure measurements via Wilhelmy plate method and a surface-specific nonlinear optical spectroscopy, termed sum frequency generation (SFG). The lipids selected were dioleoylphosphatidylcholine (DOPC) and sphingomyelin (SM). Mixtures of aforementioned lipids and cholesterol-d7 (Chol-d7) were also studied.

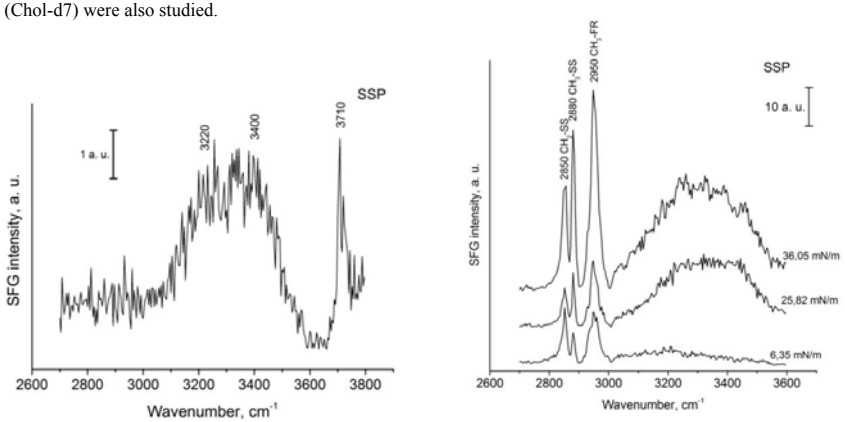

Fig. 1. SFG spectra of pure water (left) and DOPC monolayer on water surface (right).

The spectra in Fig. 1 show greater ordering of water molecules (increase in SFG signal intensity) with increasing surface pressure of DOPC monolayer. Increase in surface pressure forces DOPC molecules to attain more highly ordered structures, which then influence water molecules surrounding the charged phospholipid head groups.

[1] X. Chen, W. Hua, H. C. Allen, Interfacial Water Structure Associated with Phospholipid Membranes Studied by Phase-Sensitive Vibrational Sum Frequency Generation Spectroscopy, J. Am. Chem. Soc. 132, 11336-11342 (2010).
[2] E. A. Raymond, T. L. Tarbuck, M. G. Brown, G. L. Richmond, Hydrogen-Bonding Interactions at the Vapor/Water Interface Investigated by Vibrational Sum-Frequency Spectroscopy of HOD/H2O/D2O Mixtures and Molecular Dynamics Simulations, J. Phys. Chem. B 107, 546-556 (2003).
[3] D. E. Gragson, G. L. Richmond, Investigations of the Structure and Hydrogen Bonding of Water Molecules at Liquid Surfaces by Vibrational Sum Frequency Spectroscopy, J. Phys. Chem. B 102, 3847-3861 (1998).
[4] M. R. Watry, T. L. Tarbuck, G. L. Richmond, Vibrational Sum-Frequency Studies of a Series of Phospholipid Monolayers and the Associated Water Structure at the Vapor/Water Interface, J. Phys. Chem. B 107, 512-518 (2003).

Application of surface enhanced Raman spectroscopy for structural studies of biological fluids

Martynas Velička, Milda Pučetaitė, Vidita Urbonienė, Valdas Šablinskas

Department General Physics and Spectroscopy, Vilnius University, Lithuania
martynas.velicka@ff.vu.lt

Biological fluids have been in the centre of attention for many years, since they can be used as identification for various diseases. Only a slight change in the chemical composition could signal the existence of serious health problems. One example is uric acid which is an end product of purine metabolism. Its elevated or decreased concentration in various bodily fluids (blood, urine, tears) can suggest disorders such as gout, pre-eclamsia or cardiovascular disease. Thus, uric acid analysis in blood or urine is performed in order to evaluate kidney function. Various methods have been used for the analysis: enzymatic method, spectrophotometry, liquid chromatography, etc. [1]. However, these methods are far too rough when small concentrations of the sample molecules need to be detected.

Surface-enhanced Raman scattering (SERS) spectroscopy has been increasingly proposed as a method of choice for disease diagnosis and prevention [2]. The main advantage of SERS over conventional Raman spectroscopy is its significantly increased signal which allows detection of trace amounts of substances in the sample. Additionally, SERS can be applied in different ways which makes the experiment rather flexible. However, if one wants to use SERS spectroscopy in routine analysis, several problems, such as reproducibility of the enhancement factor, should be considered. In addition, suitable substrates should be selected according to the sample and available experimental conditions.

Using the colloidal approach of the SERS spectroscopy we have shown the advantages of this method in detection of the uric acid. This spectroscopic method is faster than conventional detection methods, as well as significantly lower concentrations of uric acid can be detected. The example of the SERS effect is shown in Fig. 1. Further application of SERS spectroscopy for intercellular fluid of the kidney tissue led us to believe, that SERS spectroscopy could be also used as a novel tool for detection of cancerous tissue areas from where the fluid is collected.

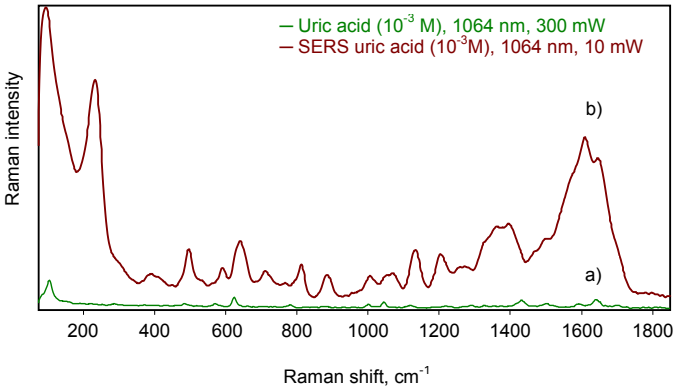

Fig. 1. Raman spectrum of uric acid (10^{-3} M) a) and surface enhanced Raman spectrum of uric acid (10^{-3} M) b).

Surface enhanced Raman spectroscopy is a promising method for analysis of chemical composition in biological fluids. Despite the difficulties of choosing optimal experimental conditions the method delivers excellent insight into the changes of the chemical composition of biological fluids and can be considered as a powerful tool for detection of various health problems.

[1] N. Misra, V. Kuma et al., Sensors Actuators B Chem. **178(0)**,371–378 (2013).
[2] W. Xie, S. Schlücker, Phys. Chem. Chem. Phys**. 15(15)**, 5329–44(2013).

Oral session 4

Chemistry and chemical physics

THE INFLUENCE OF OLIGOMERIC PROTEINS AND THEIR IMMUNE COMPLEXES ON THE PHENOTYPE OF MACROPHAGES

Asta Lučiūnaitė[1], Indrė Dalgėdienė[1], Aurelija Žvirblienė[1]

[1]VU Institute of Biotechnology, Vilnius, Lithuania
asta.luciunaite@chf.stud.vu.lt

BACKGROUND: Macrophages, cells of the immune system, play a key role in defending organism from intracellular and extracellular pathogens [1]. In certain pathologies, chronic inflammation can be a result of the immune system disorders. As a consequence, various tissues can be damaged, for example, the neurodegenerative process can occur in the central nervous system. One of these pathologies is Alzheimer's disease (AD). This disease is caused by β-amyloids (Aβ), especially $A\beta_{1-42}$ oligomers, which are detected in the brain tissue of the AD patients [2, 3]. Immunotherapy was applied in order to decrease the effects of Aβ. However, some clinical trials were discontinued due to the side effects such as meningoencephalitis [4]. The aim of this work is to investigate the influence of $A\beta_{1-42}$ oligomers and their immune complexes on macrophage phenotype.

METHODS: The study model is macrophage cell line J774, originated from BALB/c mice. The investigation of various macrophage activation states was based on the detection of markers of classically activated M1 and alternatively activated M2 macrophage populations. The variations in the levels of cellular markers – M1 markers CD86, IL-12/IL-23, TNF-α; M2 markers CD206, IL-10, TGF-β1; phagocytosis marker CD68; macrophage and cell activation marker F4/80 – were investigated by flow cytometry and enzyme-linked immunosorbent assay.

RESULTS: Treatment of J774 cells with $A\beta_{1-42}$ oligomers and their immune complexes induced an increase in the expression of cell activation markers CD68, CD86, F4/80, IL-12/IL-23 and TNF-α. However, there was no change in the expression of M2 markers.

CONCLUSION: Based on our research, activated mouse macrophages J774 show changes in CD68, CD86, F4/80, IL-12/IL-23 and TNF-α expression. This suggests that activation of macrophages with $A\beta_{1-42}$ oligomers and their immune complexes can lead to the inflammatory phenotype M1.

ACNOWLEDGEMENTS: This research was funded by a grant (No. LIG-04/2012) from the Research Council of Lithuania.

[1] D.M. Mosser, J.P. Edwards, Exploring the full spectrum of macrophage activation, Nature reviews. Immunology **8**, 958-969 (2008).
[2] H. Braak, E. Braak, J. Bohl, Staging of Alzheimer-related cortical destruction, European neurology **33**, 403-408 (1993).
[3] K.A. Jellinger, C. Bancher, Neuropathology of Alzheimer's disease: a critical update, Journal of neural transmission. Supplementum **54**, 77-95 (1998).
[4] J.M. Orgogozo, S. Gilman, J.F. Dartigues, B. Laurent, M. Puel, L.C. Kirby, P. Jouanny, B. Dubois, L. Eisner, S. Flitman, B.F. Michel, M. Boada, A. Frank, C. Hock, Subacute meningoencephalitis in a subset of patients with AD after Abeta42 immunization, Neurology **61**, 46-54 (2003).

APPLICATION OF METHYLTRANSFERASE HEN1 FOR ANALYSIS OF SMALL NON-CODING RIBONUCLEIC ACIDS

Aleksandr Osipenko[1], Alexandra Plotnikova[1], Viktoras Masevičius[1], Giedrius Vilkaitis[1] and Saulius Klimašauskas[1]

[1] Institute of Biotechnology, Vilnius University, Lithuania
aleksandr.osipenko@bti.vu.lt

Small non-coding ribonucleic acids (RNAs) such as microRNAs (miRNAs) and small-interfering RNAs (siRNAs) are among the most studied biological objects of the last decade. Present in the widest range of eukaryotes, including humans, these small molecules with its numerous functions have high importance in almost all main biological processes [1]. It is not surprising that differences in small RNA levels were determined as potential biomarkers in cancer, neurological and many other diseases [2, 3, 4]. However detection and extraction of these molecules are still challenging to scientists.

Here we present novel fast and easy one-step labeling of small RNAs (Fig. 1, A) that allows extraction of these molecules and more labile two-step labeling (Fig. 1, B) that provides wide selection of different reporter groups, such as biotin and fluorophores. Both methods use synthetic analogues of S-adenosyl-L-methionine (Fig. 1, 1 and 2) and exploit high specificity of methyltransferase HEN1 to double-stranded 21 to 24 nucleotides long RNA molecules, namely miRNA and siRNA duplexes, minimizing non-specific detection and/or extraction of deoxyribonucleic acids or irrelevant types of ribonucleic acids molecules, such as transfer RNAs or fragments of long RNAs.

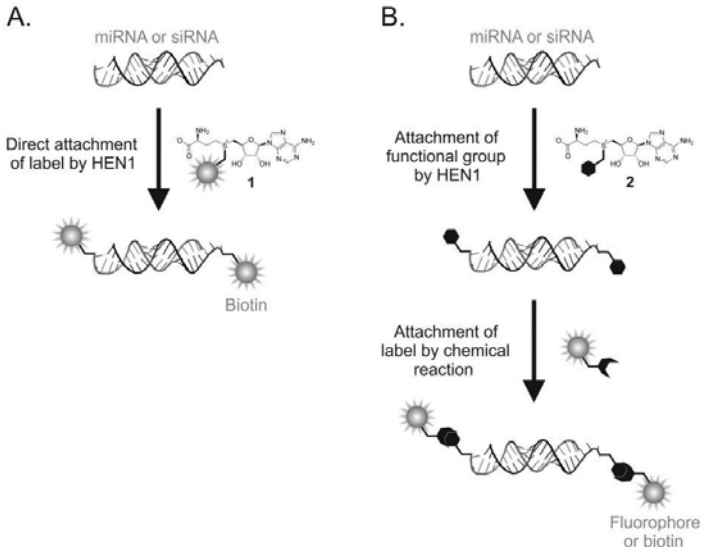

Fig. 1. One-step (A) and two-step (B) labeling of small RNAs by HEN1 methyltransferase using synthetic analogues of S-adenosyl-L-methionine (1 and 2).

[1] D. P. Bartel, MicroRNA Target Recognition and Regulatory Functions, Cell **136**, 215-233 (2009).
[2] G. Di Leva, M. Garofalo and C. M. Croce, MicroRNAs in Cancer, Annual Review of Pathology **9**, 287-314 (2014).
[3] P. J. Mishra, MicroRNAs as promising biomarkers in cancer diagnostics, Biomarker Research **2**, 19 (2014).
[4] P. Rao, E. Benito and A. Fischer, MicroRNAs as biomarkers for CNS disease, Frontiers in Molecular Neuroscience **6**, 39 (2013).

THE ANALYSIS OF FLUORINATED BENZENESULFONAMIDES BINDING TO CARBONIC ANHYDRASE VI PURIFIED FROM BACTERIA *E. COLI* AND HUMAN SALIVA

Goda Milinavičiūtė, Justina Kazokaitė, Daumantas Matulis

Department of Biothermodynamics and Drug Design, Institute of Biotechnology, Vilnius University, Lithuania

goda.milinaviciute@chf.stud.vu.lt

Recombinant proteins are produced by laboratory methods of genetic recombination. Nowadays they are found in essentially every biological research laboratory. *E. coli* is one of the earliest and most widely used hosts for the production of recombinant proteins. The main advantages of *E. coli* bacteria are rapid growth, rapid recombinant protein expression and high yields of the product. However, it is difficult to express large proteins in *E. coli*. Additionally, *E. coli* is not the best expression system for S-S rich proteins and proteins that require post-translational modifications [1]. Therefore, it is important to evaluate if the recombinant protein is a suitable model for the analysis of the certain protein found in human and assess the differences in tertiary structure and its interaction with certain compounds.

Our laboratory has been working with recombinant proteins – carbonic anhydrases (CA). They are metalloenzymes that maintain pH homeostasis by catalyzing the reversible hydration of carbon dioxide. There are 12 catalytically active CA isoforms in human differing in expression patterns, tissue localization, cellular distribution and enzymatic properties [2]. CA VI is the only secreted isozyme of the human CA family. This enzyme is found in saliva, tears, and milk. It is responsible for antireflux defense, protection from carcinogens, and taste function. Moreover, CA VI is linked with certain cancers which might be associated with salivary glands [3]. Therefore, it is important to analyze the affinity of sulfonamide inhibitors for CA VI.

Human recombinant CA VI was expressed in *E. coli*. Also, half-liter of saliva was collected from twenty volunteers. CA VI from these sources was purified by affinity chromatography. The thermodynamics of interaction between the enzyme and 4-substituted-2,3,5,6-tetrafluorobenezenesulfonamides were determined by the fluorescent thermal shift assay (FTSA). The affinity of the inhibitors designed and synthesized in our laboratory for CA VI from saliva was similar to the affinity for CA VI from *E. coli*. This study shows that CA VI purified from bacteria is a suitable model to analyze reactions between human CA VI and inhibitors and the absence of glycosylation in *E. coli* has no significant effect on inhibitor binding to CA VI.

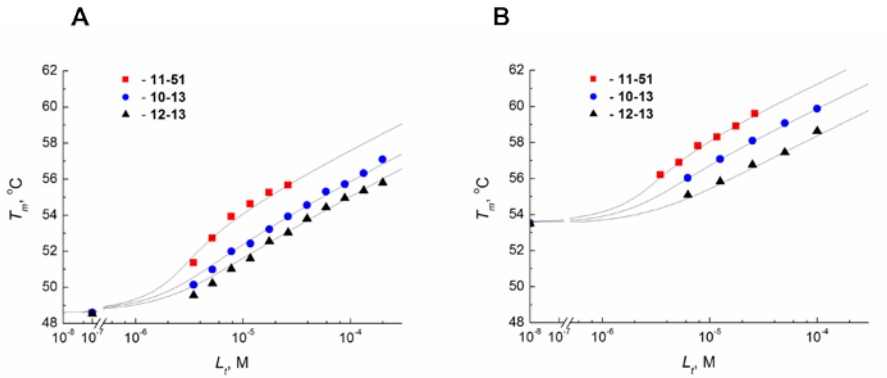

Fig 1 The FTSA data of selected compounds binding to recombinant CA VI from bacteria (A) and native CA VI from human saliva (B).

[1] Arnold L.Demain et al. Production of recombinant proteins by microbes and higher organisms. Biotechnology Advances 27, 297-306 (2009)
[2] R. McKenna et al. Insights towards sulfonamide drug specificity in α-carbonic anhydrases. Bioorganic & Medicinal Chemistry 21, 1526-33 (2013)
[3] W. Sly et al. Structure, function and applications of carbonic anhydrase isoenzymes. Bioorganic & Medicinal Chemistry 21, 1570-82 (2013)

PHOTOSTABILITY OF NITROFURAN DERIVATIVES IN SOLUTIONS

Diāna Džabijeva[1], Ilva Nakurte[1], Kārlis Bērziņš[1]

[1]University of Latvia, Faculty of Chemistry, Kr. Valdemara street 48, Riga LV 1013, Latvia
diana.dzabijeva@gmail.com

Drug degradation represents a serious problem, which relates to the loss of the pharmacological activity and the possibility of adverse effects induced by the resultant degradation impurities [1].

The problem of API degradation is discussed all over the world nowadays and is strictly controlled by internationally recognized ICH guidelines [2]. Furthermore many pharmacologically active ingredients are also photolabile and can undergo degradation initiated by electromagnetic radiation.

In this study the photodegradation of furazidin, furazolidone and nitrofurazone is discussed. These nitrofuran derivatives possess antibacterial and bacteriostatic properties and are widely used in the treatment of different diseases such as: lambliosis, salmonellosis, trichinosis, dysentery and others. The mechanism of nitrofuran influence on human organism is not completely investigated, but there is a hypothesis, that these compounds can inhibit the enzymatic processes in bacteria [3].

The photostability of furazidin, furazolidone and nitrofurazone in isopropanol and acetonitrile medium was studied using UV/VIS spectroscopy; the qualitative and quantitative analysis of furazidin photodegradation was investigated by UPLC – Tof – MS; Runge – Kutta method combined with multi-parameter optimization method was applied to obtain kinetic models for furazidin, furazolidone and nitrofurazone photodegradation and to determine kinetic parameters of the process.

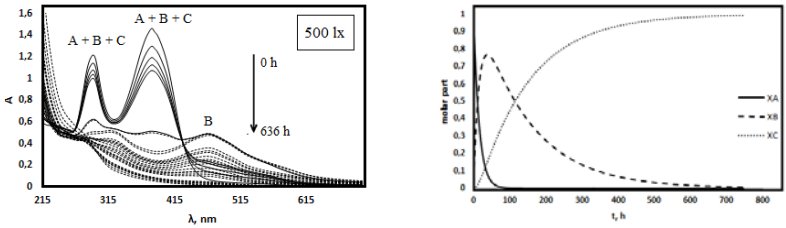

Fig. 1. UV/VIS absorption spectra and kinetic curves for photodegradation of furazidin isopropanol solution.

Chromatographic analyses were performed on a modular UPLC system, Agilent *1290 Infinity* series (Agilent Technologies). LC separations were achieved by using an X Terra MS C18 column (2.1 x 150 mm, 3.5 µm) with a mobile phase composed of deionized water (channel A) and acetonitrile (channel B) in a gradient mode at a flow rate of 0.3 mL/min. The detection was monitored at 210, 254, 292, 380, 395, 470, 550 nm.

The mass spectra (HRMS) were taken on an *Agilent 6230 TOF LC/MS* (Agilent Technologies) with electrospray ionization (ESI) in positive mode.

Electron spectroscopic analyses were performed on *Perkin Elmer Lambda 25* (PerkinElmer, Inc., United States of America) UV/VIS spectrometer. The detection was monitored in the wavelength range 190 – 700 nm.

Successful application of described methods illustrates the usefulness of photodegradation study and lets to conclude, that the methods are suitable for investigation of photostability of API and can be used in industrial drug synthesis.

[1] Lee, D.C.; Webb., M (eds.). *Pharmaceutical analysis;* 1st ed., Blackwell, 2003, pp. 16 – 20.
[2] ICH guidelines. http://www.ich.org/products/guidelines.html (viewed on 25.01.2015.).
[3] Vardanyan, R., S. *Synthesis of Essential Drugs*; Elsevier, Inc., 2006, pp. 499-523.

Analysis of the results from Car-Parrinello molecular dynamics simulations of bis(2-chloroethyl) sulfide with the help of Python programming

Joanna Lach[1,2], Pawel Rodziewicz[1]

[1] Department of Biology and Chemistry, University of Bialystok, Poland
[2] Chemistry Student's Society „Pozyton", University of Bialystok, Poland
Joana.lach@gmail.com

Bis(2-chloroethyl) sulfide (also known as sulfur mustard, SM, mustard gas, sulfur yperite, H or HD) is an organic blister agent, capable of causing short and long term morbidity. Among the chemical warfare agents (CWAs) dumped in the Baltic Sea, the amount of sulfur mustard is estimated as the highest. The laboratory analysis of CWAs are of a high risk, therefore a theoretical approach based on quantum chemistry seems to be a safe and a low cost method to investigate the nature of possible structural and spectroscopic properties.

All possible low energy conformations of the sulfur mustard molecule and their accurate relative energies were widely investigated utilizing static ab initio and DFT calculations. However these results refer to the structures at the temperature of 0K. Number of conformations results from the rotation about four bonds (two interior CH_2-S bonds and two exterior CH_2-CH_2). Every bond is represented by a dihedral angle which has three possible positions, namely trans (t), gauche+ (g+) and gauche (g-), as presented below. [1]

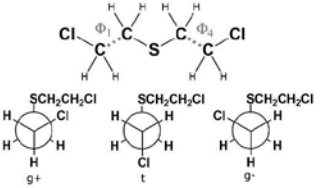

Fig. 1.Possible forms of CH_2-CH_2 bond.

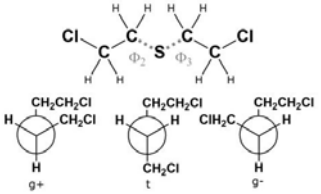

Fig. 2. Possible forms of CH_2-S bond.

Main aim of this work is to understand the nature of the conformational changes of the SM molecule in the gas phase and to study the dynamically averaged structures of the SM and their lifetime at finite temperature.

Data representing conformational changes of the molecules in the gas phase at finite temperature were obtained from Car-Parrinello molecular dynamics (CP-MD) simulations. Introduction of the finite temperature into the simulation provides a possibility to predict the behavior of this compound in a natural environment. Obtained results show that the structure with the lowest energy can easily convert to other structures with higher energies. We have reported a significant number of the rearrangements between the local minima in the trajectory from the CP-MD simulation.

Python programming was used in a post-processing population analysis of the relative low energy conformations. Lifetime of the global and local minima structures of the SM molecule and existence of the most probable rearrangements were investigated. Calculations in the gas phase are the initial step for the further computational studies in the water solution.

[1] J. Nadas, X. Zhang, B.P. Hay, Shapes of Sulfur, Oxygen and Nitrogen Mustards, J. Phys. Chem. **115**, 6709-6716 (2011).

STRUCTURALLY-MODIFIED SPIRO COMPOUNDS FOR THERMALLY ACTIVATED DELAYED FLUORESCENCE

Paulius Imbrasas[1], Gediminas Kreiza[1], Marytė Daškevičienė[2], Vytautas Getautis[2], Karolis Kazlauskas[1], Saulius Juršėnas[1]

[1] Institute of Applied Research, Vilnius University, Lithuania
[2] Department of Organic Chemistry, Kaunas University of Technology
paulius.imbrasas@ff.stud.vu.lt

Thermally activated delayed fluorescence (TADF) is a thermally-assisted process that allows triplet state harvesting with an efficiency of 100% via intersystem crossing to singlet state. Thus, TADF-based organic light-emitting devices (OLED) are capable of delivering internal quantum efficiencies reaching unity. It is an alternative and serious competitor to the state-of-the-art phosphorescent OLEDs. Avoiding the use of triplet emitters makes TADF devices cheaper and longer-lasting than their phosphorescent counterparts. Discovery and evaluation of TADF materials is therefore an important task, which could lead to the realization of new generation more efficient and cheaper OLEDs. Efficient TADF materials imply a small energy gap between the singlet and triplet excited states as well as high radiative recombination rate.

In this work, thorough investigation of structure-property relationship of novel spiro derivatives bearing either diethoxyphenylamine (V-**796**) or carbazole (V-**938**) side-moieties is presented (see Fig. 1).

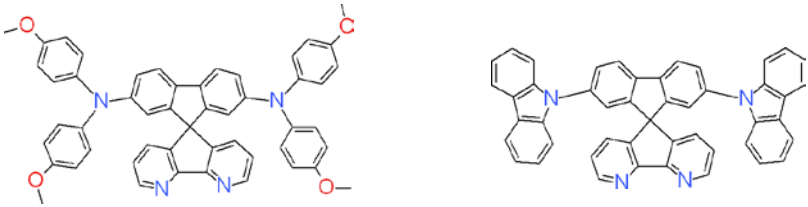

Fig. **1**.Structurally-modified spiro derivatives with diethoxyphenylamine (V-**796**, left) and carbazole (V-**938**, right) side-moieties.

Although oxygen is an effective triplet-state quencher, it also helps to identify TADF process. Efficiency of TADF is strongly affected by the amount of oxygen exposed to the sample. Since oxygen is detrimental to the process, it has to be removed. This is accomplished either by bubbling of solutions with inert gas or by preparing and encapsulating thin film samples in a nitrogen glovebox. The toluene solution of V-**796** shows an increase of fluorescence quantum yield (QY) from 1% to 3.4% after removal of oxygen. Additionally, the decay time and intensity ratio of the second component of the biexponential decay transient increases by a factor of 3.5 and 1.4, respectively. The results suggest a TADF mechanism, however the small quantum yield values deny the possibility of this material to be implemented in future organic devices. Meanwhile, the spiro compound V-**938** shows not only an enhanced fluorescence quantum yield, but also high QY values, *i.e.*, after removal of oxygen QY increases from 75% to 88%. Moreover, the excited state relaxation slows down rise to TADF decay time of 36 ns. The efficiency of TADF process in the latter compound was evaluated independently by two methods, *i.e.*, utilizing the results of both quantum yield and decay time measurements. The methods yielded TADF efficiency values of 52% and 36%, respectively. Along with the calculated reverse intersystem crossing rate constant ($1{,}27\times10^{7}$ s^{-1}), these values show a fast and efficient TADF process.

Generally, both spiro compounds V-**796** and V-**938** demonstrate TADF properties. The replacement of diethoxyphenylamine side-moieties with carbazole groups leads to the significant increase in both quantum yield and decay time, thus making V-**938** a promising TADF emitter for fabrication of OLEDs. Further supporting experiments for V-**938** are underway.

Oral session 5

Semiconductor and condensed matter physics, material sciences

GROWTH AND CHARACTERIZATION OF InGaN/GaN QUANTUM WELLS ON SHORT PERIOD SUPERLATTICE

Mantas Dmukauskas, Arūnas Kadys

Institute of Applied Research, Vilnius University, Lithuania
mantasdmuk@gmail.com

Indium gallium nitride (InGaN) - a ternary nitride compound - alloys are now widely used in commercially available blue and white light-emitting diodes (LEDs) and light detectors [1]. What makes InGaN materials attractive for their use in optoelectronics and photovoltaics is an ability to adjust their band gap by changing the ratio of indium atoms to gallium atoms. Attempts to manufacture LEDs emitting light at longer wavelength are problematic due to increased defect density, high influence of internal electric field and carrier localization. To improve the effectiveness of these structures and to develop green emitters, a more sophisticated design of the structure is required, which leads to a more complex dependence of LED parameters on the growth conditions. One of the proposed ways to reduce these problems is to use short-period InGaN/GaN superlattice (SPSL) structure in the buffer area [2].

The main objective of this work was to grow high quality blue $In_xGa_{1-x}N$ multiple quantum wells (MQWs) on GaN templates previously grown on (0001) sapphire substrates by MOCVD method. In order to reduce the resulting lattice strain – an often encountered problem – the interlayer between buffer layer and active region with InGaN/GaN SPSL was formed by changing the flow of trimethylindium metalorganic, but keeping flow of other precursors and growth temperature constant. Multiple experiments were carried out to find the best SPSL structure. Some samples investigated by X- ray diffraction measurements; the quality of grown samples was estimated by photoluminescence (PL) and atomic force microscopy measurements. The best results were obtained in samples with 8 period InGaN/GaN SPSL, where InGaN layer width of 1.7 nm and concentration of In ~ 6%, GaN layer width 2.2 nm. It is shown, that using InGaN/GaN SPSL structure, MQWs PL intensity at 450nm wavelength increase ~22 times in compare with the structure without SPSL (Fig. 1). However, SPSL layer increases the surface roughness and too high number of SPSL periods increases the dislocation density.

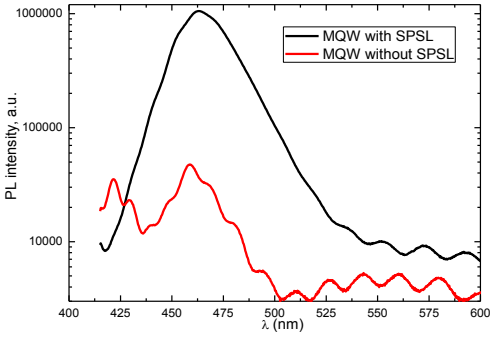

Fig. 1. PL spectra of MQW samples: with SPSL and without SPSL.

[1] H. Gilbert, Introduction to Light Emitting Diode Technology and Applications, Auerbach Publications, Taylor and Francis Group, (2009).
[2] N. V. Kryzhanovskaya, W. V. Lundin, A. E. Nikolaev, A. F. Tsatsul'nikov, A. V. Sakharov, M. M. Pavlov, N. A. Cherkachind, M. J. Hÿtch, G. A. Valkovsky, M. A. Yagovkina, S. O. Usov, Optical and Structural Properties of InGaN/GaN Short Period Superlattices for the Active Region of Light Emitting Diodes, Semiconductors, , Vol. 44, No. 6, pp. 828–834, (2010).

STUDY OF EXCESS CARRIER DYNAMICS IN NONPOLAR InGaN/GaN QUANTUM WELLS

Kristina Gelžinytė

Institute of Applied Research, Vilnius University
Kristina.Gelzinyte@ff.stud.vu.lt

Traditional growth of InGaN structures for optoelectronic devices has focused mainly on c-axis oriented material where the polar axis is perpendicular to the growth plane. For InGaN/GaN multiple quantum wells (QW) electric fields resulting mainly from piezoelectric polarizations lead to shifts in the emission wavelength associated with the quantum confined stark effect and reduced emission efficiency due to the separation of electron and hole wave functions in the QW. With the use nonpolar growth orientation, the unfavorable effects of these polarization fields can be lessened. In this work, luminescence, absorption bleaching and carrier dynamics in nonpolar m-plane $In_{0.15}Ga_{0.85}N$ single QW were studied using time resolved photoluminescence (TRPL), spectrally resolved differential transmission (DT) and light-induced transient grating (LITG) techniques. Carriers were excited selectively in InGaN QW, as pump energy was lower than a GaN barrier band gap. State filling properties, carrier lifetimes, and in-plane bipolar diffusivity over a wide excess carrier density range ($2x10^{17} – 4x10^{20}$ cm^{-3}) were investigated.

TRPL spectra were decomposed into Gaussian type components that were attributed to: (i) overlapping localized states and first two extended states (e1-hh1,2) at ~ 440 nm; (ii) high energy extended states, referring to the third QW energy level (e2-hh2), at 405 nm. The third peak appeared solitary in the absorption bleaching at 400 nm (e3-hh3) and was ascribed to the electronic transition between fourth QW energy levels. The internal quantum efficiency (IQE) was evaluated from low and high temperature PL measurements. Maximum (50 ± 10)% IQE was at $9x10^{17}$ cm^{-3} and decreased down to 4% with increased excitation (FIG. 1). Overall photoluminescence efficiency correlated with the absorption one up to $n_{th} = 3x10^{19}$ cm^{-3}. Though, radiative recombination was determined by localized states, while prior carrier excitation was to extended states, i. e. excited carrier intraband redistribution was observed. Above n_{th} IQE droop was explained by: (i) saturation of localized and lowest extended QW states and subsequent diminishing of radiative recombination from these states; (ii) enhanced carrier excitation to highest energy extended states, which was followed by increase carrier diffusivity and enhanced nonradiative recombination.

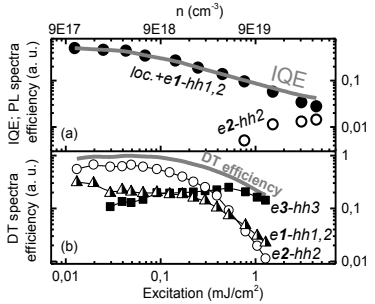

FIG. 1. IQE (line) and TRPL spectral components relative efficiency (a). General DT spectrum (line) and particular spectral components relative efficiency from Gaussian approximation at 0 ps delay (b).

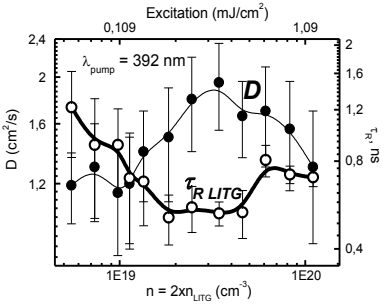

FIG. 2. Diffusion coefficients and radiation lifetimes dependence on carrier concentration.

In respect to density-activated defect recombination model used for polar plane InGaN, carrier lifetime depended on in-plane diffusion coefficient for nonpolar one exclusively for $n_{th} < 3x10^{19}$ cm^{-3}; afterwards, D saturated and immediately decreased from 2 to 1.2 cm^2/s (FIG. 2). Increase of in-plane diffusivity also could be related to enhanced carrier generation to extended states – delocalization; it is supported by τ_{LITG} drop from ~ 1200 to 500 ps, referring to the lifetime in localized or free states, respectively. Subsequently, diffusion coefficient saturated as well as: (i) absorption to the third QW energy level started to prevail; (ii) PL from the second QW energy level appeared; (iii) IQE deteriorated to ~ 10%. These trends boosted with carrier concentration, meanwhile carrier in-plane diffusivity impaired. The origin of D drop at the highest photoexcitations (above n_{th}) is not clear; tentatively, it can be attributed to additional scattering arising as the carriers occupy the high energy states and their wave functions expand into GaN barrier.

SPATIALLY RESOLVED PHOTOLUMINESCENCE OF GaBiAs EPITAXIAL LAYERS AND GaBiAs/GaAs QUANTUM WELLS

Justinas Aleknavičius[1], Darius Dobrovolskas[1], Gintautas Tamulaitis[1]

[1] Institute of Applied Research and Semiconductor Physics Department, Vilnius University, Saulėtekio Ave. 9-III, LT-10222 Vilnius, Lithuania

ju.aleknavicius@gmail.com

Recently, increasing interest has been addressed to dilute bismide semiconductor alloy GaBiAs. Introducing a small percentage of bismuth into gallium arsenide significantly reduces the band gap of the alloy. Moreover, the band gap of GaBiAs weakly depends on temperature. Charge carrier lifetimes in relaxed GaBiAs layers can be as low as 1 ps. These properties are beneficial for using GaBiAs in ultrafast infrared light emitters and detectors for optical fiber systems and terahertz applications [1]. However, growth of high quality GaBiAs is still a major challenge. GaBiAs epitaxial layers with relatively high Bi content (up to ~10%) but of rather poor crystalline quality can be grown at low temperatures (~240-380°C) [2]. Nevertheless, post-growth rapid thermal annealing (RTA) at high temperatures (~600-700°C) improves the crystalline structure of GaBiAs layers by creating bismuth-rich clusters, showing intense photoluminescence (PL) [3].

In this work, the PL properties of GaBiAs epitaxial layers and GaBiAs/GaAs quantum wells were investigated with spatial resolution. The GaBiAs structures used in this study were grown by molecular beam epitaxy (MBE) technique on GaAs substrates at the Center for Physical Sciences and Technology, Vilnius, Lithuania. Four low-temperature grown samples were investigated: three epilayers with different Bi content and a triple quantum well (QW) structure. The approximate percentage of Bi content in the samples was determined from the PL emission peak wavelength. The Bi molar fraction in the samples under study does not exceed 5%.

The samples were investigated using *WITec Alpha 300S* confocal microscope coupled to *Andor* spectrometer equipped with *iDus* InGaAs CCD detector array, capable of capturing spectra in near-infrared spectral region. The detector is thermoelectrically cooled down to -90°C. The spatial distributions of photoluminescence parameters were investigated by raster scanning randomly selected areas on the sample top surfaces with an objective of 60× magnification (NA = 0.8). PL was excited using a continuous wave HeCd laser emitting at 442 nm. All the measurements were performed at room temperature.

The epitaxial layers exhibited PL bands peaked at 1060 nm, 1110 nm, and 1210 nm. These peak wavelengths correspond to Bi content of approximately 3%, 4% and 5%, respectively. The highest PL intensity was recorded in the sample with the lowest Bi content. The PL band experienced a red shift and a decrease in intensity as the Bi content in the alloy increased. Confocal PL imaging revealed that epilayers with Bi content of 3% and 5% have a striped pattern of PL intensity distribution, which is most probably related to different surface roughness in certain orientations. The epilayer with 4% Bi showed a spotted pattern of PL intensity distribution. The emission peak position varies from ~1110 nm in bright spots to ~1140 nm in background areas. Such distribution of the PL parameters is probably related to the inhomogeneity of Bi content in the sample.

The QW sample exhibits a single PL band peaked at 1050 nm. The PL intensity distribution in this sample is homogeneous except for dark spots or lines, which were shown to be associated with crystalline defects such as crystal lattice dislocations. A peculiar response to prolonged HeCd laser exposure was observed within this sample. The PL intensity in the spots or areas exposed to a highly focused laser beam for time periods up to 25 min increased by up to 35% (see Fig. 1). Moreover, the PL band undergoes a slight blue shift. Such laser annealing effect is associated with the diffusion of Bi ions to the GaAs capping layer due to excess thermal energy of the crystal lattice. In contrast to the results obtained in QW, the PL intensity of GaBiAs epitaxial layers diminished under laser exposure. The results show that the laser annealing can be used for optimizing the GaBiAs crystal quality.

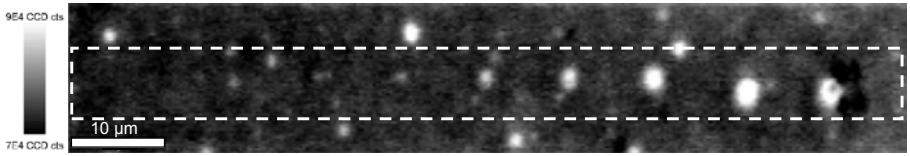

Fig. 1. Spectrally integrated intensity mapping of the GaBiAs QW sample with laser annealed spots in the marked rectangular area induced by exposure varying from 10 s at the left to 45 min at the right of the mapping.

[1] K. Bertulis, A. Krotkus, G. Aleksejenko, V. Pačebutas, R. Adomavičius, G. Molis, S. Marcinkevičius, GaBiAs: A material for optoelectronic terahertz devices, Appl. Phys. Lett. **88,** 201112 (2006).

[2] V. Pačebutas, K. Bertulis, G. Aleksejenko, R. Adomavičius, G. Molis, A. Krotkus, Growth and characterization of GaBiAs epilayers, Opt. Mater. **30** 756–758 (2008).

[3] R. Butkutė, V. Pačebutas, B. Čechavičius, R. Adomavičius, A. Koroliov, A. Krotkus, Thermal annealing effect on the properties of GaBiAs, Phys. Status Solidi C **9**, 1614–1616 (2012).

GROWTH AND CHARACTERIZATION OF QUATERNARY (GaIn)(AsBi) LAYERS ON GaAs

Sandra Stanionytė, Vaidas Pačebutas

Center for Physical Sciences and Technology, A. Gostauto 11, LT-01108, Vilnius, Lithuania
sandra.stanionyte@ftmc.lt

Diluted (GaIn)(AsBi) layers compared to other III-V compounds have weaker bandgap energy temperature dependence, which would be advantageous for the applications in optoelectronics. Alloying GaAs with InAs shifts down the conduction band edge, whereas Bi incorporation has a strongest effect on the valence band states moving up due to the band anti-crossing effect. By a proper selection of the In and Bi content, it is possible to realize the situation at which both conduction and valence bands will move towards each other symmetrically.

The aim of this work was to growth quaternary (GaIn)(AsBi) layers on semi-insulating (100) GaAs substrates in the molecular-beam-epitaxy (MBE) reactor and characterize them.

Initially, a test 30 nm thick strained (GaIn)As layers were grown at 240 ^{o}C with In concentrations range from 11% to 18% this temperature. Quaternary (GaIn)(AsBi) layers of the same thickness were grown afterwards by keeping group III elements flux unchanged. Its composition was found from the fit of X-ray diffraction (XRD) rocking curve keeping that Ga to In ratio in this layer was the same as in previously grown ternary alloy without Bi (Fig. 1).

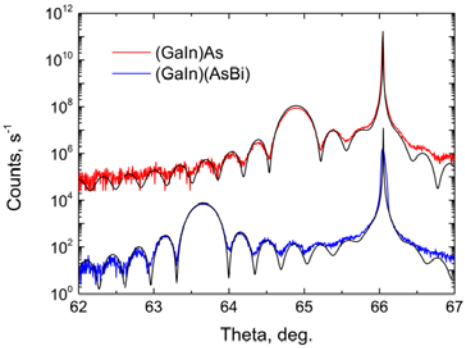

Fig. 1 ω-2θ XRD (004) rocking curves measured for the (GaIn)As and (GaIn)(AsBi) layers grown at 240^{o}C. The (GaIn)As sample has 11.6 % of In and (GaIn)(AsBi) – 11.2 % of In and 8.1 % of Bi.

Thick (GaIn)(AsBi) layers (~1,1 μm) were grown on the same conditions as the thin layers varying In concentration from 8% to 20% and Bi concentration from 3% to 12%. Thick layers were analyzed using Energy-Dispersive X-ray spectroscopy (EDX), XRD Reciprocal Space Mapping (RSM) and atomic force microscopy (AFM). AFM evaluation showed that samples were rather smooth. For 30 nm thick layers their Root Mean Square (RMS) values were less than 1 nm, for thick layers RMS was several time larger. However, when Bi/As ratio is not optimal metallic Bi droplets appears. From EDX measurement In/Bi ratio in thick quaternary layers was determined. In RSM the maximum corresponding to the layer stays near the line corresponding to a fully relaxed material what mean that only a small residual strain is present in the material. RSM also allows evaluating composition of the layer. Band gap values calculated from EDX and RSM results correlates with band gap values measured from induced THz absorption measurements. This good correlation of data obtained by employing very different experimental techniques provides an additional evidence of their reliability.

Good quality quaternary (GaIn)(AsBi) layers were grown by MBE on GaAs substrates. The layer composition was determined by XRD and EDX measurements and has evidenced an unexpectedly large, of the order of 10%, Bi incorporation resulting in narrower than 0.7 eV energy bandgaps of the material. The structural quality of the layers was even better than that of Ga(AsBi) grown on GaAs substrates with the same Bi content.

Oral session 6

Semiconductor and condensed matter physics, material sciences

COMPARATIVE SPECTROSCOPIC STUDY of InAs DOTs-in-a-WELL QUANTUM STRUCTURES WITH / WITHOUT InGaAs CAP LAYER

Andrius Rimkus, Evelina Pozingytė, Ramūnas Nedzinskas, Bronislovas Čechavičius

Semiconductor Optics Laboratory, Center for physical sciences and technology, A. Goštauto 11, LT-01108 Vilnius
andrius.rimkus@ftmc.lt

Semiconductor quantum dots (QDs) owing to their unique atomic-like quantum confinement are particularly attractive both for fundamental research and applications in optoelectronic devices such as QD infrared photodetectors (QDIPs). Recently, an advanced QDIP structure was implemented by covering self-assembling InAs QDs with a strain-relieving InGaAs layer [1]. This dots-in-a-well (DWELL) design is based on intraband optical transitions between bound QD and quantum well (QW) states. This QDIP scheme offers additional possibility to alter optical response by adjusting QW width and composition. To optimize such structures it is necessary to know their optical properties and energy spectrum which can be examined by photoluminescence (PL) and photoreflectance (PR) techniques.

The samples studied were grown by molecular beam epitaxy and consist of InAs QDs with (sample L442) or without (sample L444) InGaAs cap layer, embedded in GaAs/AlAs QWs. Spectroscopic PR/PL data can be divided into two major sets of spectral features (Fig. 1 (a)). In the 0.9–1.25 eV energy range several broadened features are caused by QD ground-state (GS) and excited-state (ES) transitions (**1–3** for L444 and **1–4** for L442). Further, in the 1.25–1.42 eV energy region features (**4–7**) for L444 sample are due to heavy- and light-hole interband transitions in WL, whereas sharp PR lines (**5–7**) for L442 structure are originated from InAs/InGaAs binary QW.

Experimental results revealed that a 5 nm-thick InGaAs cap layer significantly improves QD GS/ES signal intensity as it can be seen in Fig. 1 (a). Also, a shift of QD GS transition to lower energy by ~120 meV was observed [2].

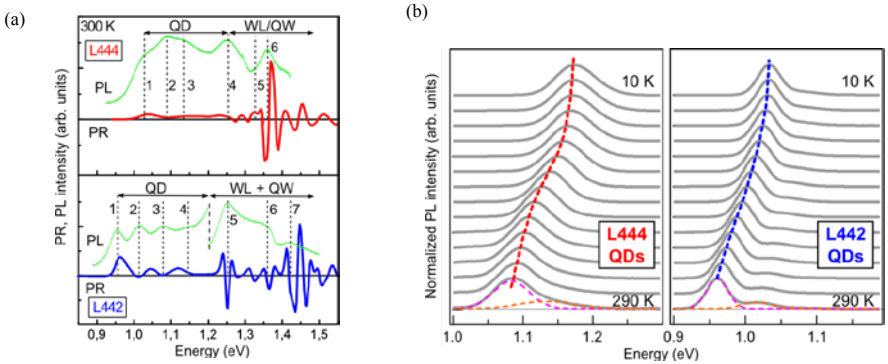

Fig. 1. a) Room temperature PR and PL spectra for DWELL structure without (sample L444) and with (L442) InGaAs cap layer; b) Temperature-dependent PL (normalized) spectra of InAs QDs for DWELL structures investigated.

To get a deeper insight, investigation of the optical properties in DWELL nanostructures was supplemented by temperature-dependent PL spectroscopy. PL bands of InAs QDs in both samples shift toward lower energies with increase in temperature (Fig. 1 (b)). At elevated temperatures (≥150 K) high energy shoulder in QD PL band can be observed, indicating thermal population of excited states. It is obvious that PL full-width at half-maximum (FWHM) parameter is much wider for uncapped DWELL structure, owing to a less uniform size distribution of QDs. This leads to thermally activated carriers escaping and retrapping in QDs of different size, thus explaining anomalous reduction of FWHM parameter registered in uncapped sample PL spectra.

Thermal quenching of PL intensity from InAs QDs was analysed using Arrhenius expression. It was estimated that thermal quenching at intermediate temperatures (120–210 K) corresponds to the reduced carrier flow into QDs, whereas at high temperatures (210–290 K) it is probably caused by the excitons escaping from the QDs.

Temperature-dependent PR measurements were applied in 3–300K temperature range in order to investigate the variation of the lineshape and associated photomodulation mechanisms. In temperature region below 150 K lower PR intensities are attributed to the doping of InAs QDs. Whereas, a decrease of intensity at elevated temperatures is related to thermal activation of the carriers from InAs QDs to InAs/InGaAs QWs.

[1] A. Barve, J. Shao, Y.D. Sharma, T.E. Vandervelde, K. Sankalp, S.J. Lee, S.K. Noh, and S. Krishna, IEEE J. Quantum Electron. **46**(7), 1105 (2010).

[2] R. Nedzinskas, B. Čechavičius, A. Rimkus, J Kavaliauskas, G. Valušis, L. Li, E. H. Linfield, *Optical features of InAs quantum dots-in-a-well structures.* Lith. J. Phys. **54**, 54–57 (2014).

TEMPERATURE-DEPENDENT PHOTOREFLECTANCE SPECTROSCOPY OF InAs DOTS-IN-A-WELL STRUCTURES

Evelina Pozingytė, Andrius Rimkus, Ramūnas Nedzinskas

Semiconductor Optics Labaratory, Center for Physical Science and Technology, Vilnius, Lithuania
evelina.pozingyte@gmail.com

Lately, there has been much interest in self-assembling InAs/InGaAs quantum dots (QDs) as active region of QD infrared photodetectors (QDIPs) [1]. This dots-in-a-well (DWELL) design allows a control of peak wavelength by changing parameters of the embedding InGaAs/GaAs quantum well (QW), and/or by adding an external electric field. However, deeper knowledge about electronic and optical properties is important for the development of QDIP devices.

This work presents a detail spectroscopic study of InAs/InGaAs/GaAs/AlAs DWELL structures grown by molecular beam epitaxy on a semi-insulating (100) GaAs substrate. Photoreflectance (PR) and photoluminescence (PL) techniques were used to explore QD- and QW-related optical interband transitions at temperatures from 3 to 300 K. Also, contactless electroreflectance (CER) and phototransmittance (PT) measurements at room temperature were performed for comparison.

Cumulative analysis of PR, PT, CER and PT in the reflection geometry revealed the influence of back-surface reflections on the PR line shape. The PR spectrum of DWELL sample with a specular GaAs substrate is actually a superposition of two components. The first component is related to photomodulated reflection from the QDs ensemble and the second one is associated with reflection from GaAs substrate. The second component is dominant and occurs due the photoabsorption (PA) effect. In order to eliminate PA in PR spectra substrate of the sample was sanded.

Temperature-dependent (3–300 K) PR spectra revealed a variety of optical transitions related to InAs QDs and binary QWs, formed by InAs wetting and InGaAs cap layers (Fig. 1a). The interband transition energies of ground- and even four exited- states for InAs QD were established. That indicates a high uniformity of QDs ensemble. Also, it was suggested that temperature-dependent lineshape in PR spectra varies with photomodulation mechanism. More detailed analysis of PR spectra disclosed that at high temperatures the line shape is influenced by the quantum-confined Stark effect. Whereas at low temperatures the line shape of PR indicated a presence of state-filling mechanisms.

Intensity and energy of InAs QD optical transitions were studied in more detail varying the temperature. PR amplitude and PL intensity of QD GS transitions (Fig. 1b) is almost identical at high temperatures. This thermal signal quenching was analyzed using Arrhenius-type expression:

$$I = \frac{I_0}{1 + a\,\exp(E_a / kT)} \qquad (1)$$

In the high temperature region, the activation energy $E_a \approx 320$ meV derived from Eq. (1) implies that a decrease of PR signal intensity is related to the excitons escaping from the QD bound-state to binary QW. Also, we observed that temperature dependence of QD-related optical transition energies follows the Varshni relation with parameters, which are between that of a bulk GaAs and InAs [2]. This indicates that the QD composition is partially changed due to Ga/In interdiffusion during the epitaxial growth.

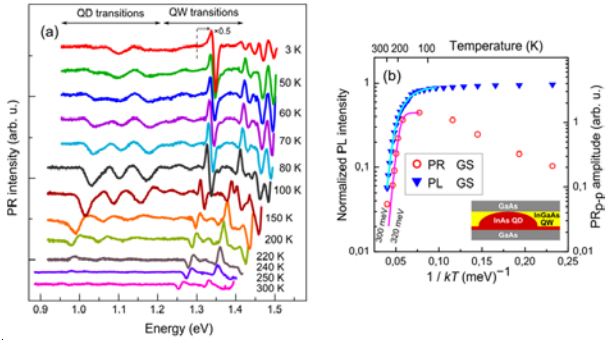

Fig.1. Temperature-dependent PR spectra for the DWELL structure (a) and Arrhenius plots of the integrated PL intensity along with PR peak-to-peak amplitude for the GS transition in the QDs (b). Inset: Scheme of the QD structure.

[1] S. Krishna, Quantum dots-in-a-well infrared photodetectors, Journal of Physics D: Applied Physics **38**, 2142-2150 (2005).
[2] F. Guffarth, R. Heitz, A. Schliwa, et al., Strain engineering of self-organized InAs quantum dots, Physical Review B, **64**, 085305 (2001).

EMISSION DYNAMICS IN THE MICRO SCALE IN TWO DIMENTIONAL NANOPOROUS ALUMINA FILLED WITH CUBIC $YALO_3:TB^{3+}$ MATRIX

Lukasz W. Golacki[1], Artur Podhorodecki[1,*], Nikolai V. Gaponenko[2], Grzegorz Zatryb[1], Igor S. Molchan[3], Liudmila S. Khoroshko[2], Jan Misiewicz[1], George E. Thompson[3]

[1]Institute of Physics, Wroclaw University of Technology, Wybrzeze Wyspianskiego 27, 50-370 Wroclaw, Poland
[2]Belarusian State University of Informatics and Radioelectronics, P. Browki str.6, 220013 Minsk, Belarus
[3]Corrosion and Protection Centre, School of Materials, The University of Manchester, The Mill, Sackville St., Manchester, M13 9PL, UK
*e-mail: artur.p.podhorodecki@pwr.edu.pl

Development of advanced light-emitting materials has received growing interest among scientists in the last decade. The goal is to create device with high emission efficiency, low cost requirements and ability of implementing into a massive production. Promising candidates are emitters obtained from sol-gel materials doped with rare earth (RE3+) ions. We investigated the optical and structural properties of terbium doped YAlO3 composites, which were fabricated by co-precipitation in porous anodic alumina films (PAA) grown on silicon. The presence of the cubic YAlO3 phase with a strong indication of ion-ion interaction has been observed. We widely discuss the distribution of Tb3+ ions in the PAA:YAlO3 structure. Additionally the emission thermal quenching and potential photonic effects has been investigated and the physical model to explain it has been proposed. Structural properties were investigated using the scanning electron microscope (SEM), equipped with backscattered electron detection (BSDE) mode and energy dispersive X-ray (EDX) detectors and using the Fourier transform infrared spectroscopy (FTIR). The optical properties were determined by measuring the photoluminescence excitation spectroscopy (PLE), time-resolved luminescence (TR-PL) and the high spatially-resolved photoluminescence and PL decay time spectra. Additionally PL time dependence was investigated and the results were analyzed using the maximum entropy method. [1]

[1] A. Podhorodecki, N. V. Gaponenko, G. Zatryb, I. S. Molchan, M. Motyka, J. Serafinczuk, L. W. Golacki, L. S. Khoroshko, J. Misiewicz, G. E. Thompson, Ion-ion interaction in two dimensional nanoporous alumina filled with cubic YAlO3:Tb3+ matrix, J. Phys. D: Appl. Phys. 46 (2013) 355302

BREATHING MODES OF ONE-DIMENSIONAL TRAPPED QUANTUM GAS

Andrii Gudyma[1], Gregori Astrakharchik [2], Mikhail Zvonarev[1]

[1]Université Paris-Sud, Laboratoire de Physique Théorique et Modèles Statistiques, UMR CNRS 8626, F-91405 Orsay, France

[2]Departament de Física i Enginyeria Nuclear, Campus Nord B4-B5, Universitat Politècnica de Catalunya, E-08034 Barcelona, Spain

Andrii.Gudyma@lptms.u-psud.fr

An interplay of interaction and statistical properties for quantum 1D gases is seen in a low-lying part of their excitation spectrum particularly well if the latter is discrete in the limit of large number of particles, N. The discreteness is ensured by confining quantum gas with the external potential. Ratio ω/ω_z of the frequency of the lowest compressional (breathing) mode, ω, and the dipole mode, ω_z, was investigated for a Lieb-Liniger gas confined by a parabolic potential in experiments [1,2]. It was observed that ω/ω_z goes through two crossovers: from 2 to $\sqrt{3}$, and then from $\sqrt{3}$ to 2 as the system goes from non-interacting to weakly interacting, and then from weakly interacting to strongly interacting regime [1]. The latter crossover has been described theoretically, by the approach based on the local density approximation (LDA). A description of the former crossover has not been done so far.

We report analytic and numerical results for ratio ω/ω_z obtained within the repulsive Lieb-Liniger gas model for the parameters accessed in experiments [1,2]. We describe a crossover from non-interacting to weakly interacting gas analytically by making use of Hartree approximation for $N \gg 1$. More specifically, ω is obtained by calculating the response of the cloud size to a change of trap frequency ω_z :

$$\omega^2 = -2\frac{\langle Q\rangle}{\partial\langle Q\rangle/\partial\omega_z^2}, \tag{1}$$

where $Q=\sum_{i=1}^{N}(z_i-Z_{\rm cm})^2$, and $Z_{\rm cm}=\sum_{i=1}^{N} z_i/N$ is the center of mass coordinate. Our Hartree solution connects smoothly with the one for weak to strong interaction crossover, obtained with LDA. We complement analytic approaches with extensive diffusion Monte Carlo simulations made for up to 25 particles, thus elaborating effects from finite N (Fig. 1).

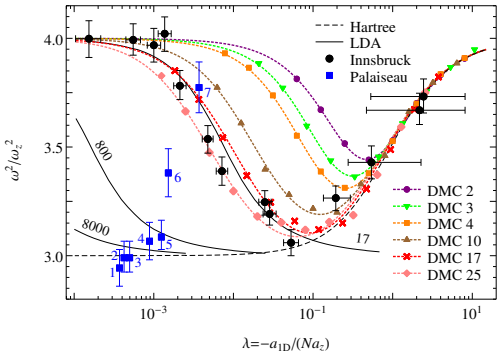

Fig. 1. Ratio ω^2/ω_z^2 as a function of Hartree parameter $\lambda=-a_{1D}/(Na_z)$. Black dashed line: Hartree approximation for $N\to\infty$. Black solid lines: LDA for $N=17$, 800, 8000. Other dashed lines: interpolations for data points obtained with diffusion Monte Carlo (DMC) simulations for $N=2,3,4,10,17,25$ particles (top to bottom). Large red circles: Innsbruck experiment [1]. Large blue boxes: Palaiseau experiment [2].

Our zero-temperature results show perfect agreement with data from Innsbruck experiment [1]. On the other hand, we found a mismatch with those data points from Palaiseau group [2] which are away from mean-field prediction $\omega/\omega_z=\sqrt{3}$.

[1] E. Haller, M. Gustavsson, M. J. Mark et al., Realization of an Excited, Strongly Correlated Quantum Gas Phase, Science **325**, 1224 (2009), 1006.0739.

[2] B. Fang, G. Carleo, A. Johnson, and I. Bouchoule, Quench-induced breathing mode of one-dimensional Bose gases, Phys. Rev. Lett. **113**, 035301 (2014), 1312.3169.

TERAHERTZ EMISSION FROM GaMnAs AND InGaAs NANOWIRES

Ieva Beleckaitė[1], Ramūnas Adomavičius[1], Aloyzas Šiušys[2], Anna Reszka[2], Janusz Sadowski[2,3] and Arūnas Krotkus[1]

[1]Semiconductor Physics Institute, Center for Physical Science and Technology, A. Goštauto g. 11, Vilnius, Lithuania
[2]Institute of Physics, Polish Academy of Sciences, al. Lotników 32/46, Warsaw, Poland
[3]MAX-Lab, Lund University, P.O. Box 118, Lund, Sweden
ieva.beleckaite@ftmc.lt

Over the last years, terahertz (THz) radiation from semiconductor surfaces illuminated by femtosecond laser pulses is finding multiple applications areas. It has recently been reported that nanowire and nanorod structures in comparison with bulk semiconductors are able to enhance THz emission from optically excited surfaces. THz emission from low temperature grown InN nanorods was about one order of magnitude greater in power than that from the bulk InN film [1]. Seletskiy et al. [2] reported that their InAs nanowires (NW) had about 15 times greater THz power efficiency than a planar InAs substrate, but this result was obtained after accounting for spatial fill factor in NW arrays. Despite the increase of the efficiency of optical–terahertz radiation conversion vertically aligned nanowire arrays have the same limitation (i. e. the main part of the radiation propagates in parallel to the surface resulting the low THz emissivity outside the sample) as bulk semiconductors. In this work THz emission of the oblique nanowires was investigated for the first time.

In the present work, THz pulse emission from samples of GaAs NW grown by molecular beam epitaxy (MBE) on high temperature (550°C) GaAs (111) and (110) substrates has been studied. One NW layer was epoxy encapsulated and removed from substrate. Experiments have been performed using Ti:sapphire oscillator generating 150 fs, 800 nm pulses at the repetition rate of 76 MHz. THz electric field transients were detected with a low temperature grown GaAs antenna.

The amplitude of the THz signal obtained from NW was from 2 to 4 times stronger than from GaAs substrate. THz pulse amplitude was insensitive to the azimuthal angle for the NW grown on (111) orientation substrates. In contrast, the azimuthal dependencies for NW layers grown on (110) substrates can be approximated by sinθ function. The dependencies can be explained by orientation of NW regarding to the GaAs substrate: it is known that the angle between the NW and the surface is 55° [3]. Photoexcited carriers moves along the NW and creates linearly polarized THz radiation. The polarization axis moves around a terahertz beam when an azimuthal angle is changing. The registered signal changes in the sinus's law as the detector registers only one polarization (Fig. 1).

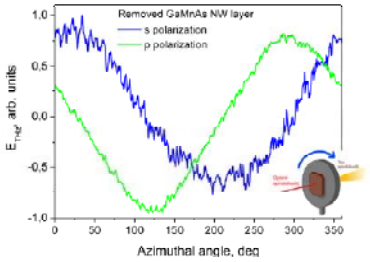

Fig. 1. THz emission azimuthal dependencies of the removed GaMnAs NW layer for s and p THz electric field polarization.

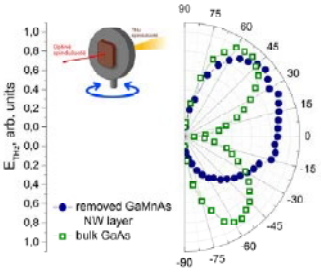

Fig. 2. THz pulse amplitude dependencies on an angle between the incident laser beam and a normal to the sample surface for the removed GaMnAs NW layer and GaAs substrate.

Fig. 2 shows dependencies of THz pulse amplitude on an angle between the incident laser beam and a normal to the sample for the epoxy encapsulated GaMnAs NW layer and GaAs substrate. No terahertz radiation is registered when laser beam falls perpendicularly to the surface of GaAs substrate because the radiation cannot propagate along axis of photoexcited electron–hole dipole. In contrast the NW layer emits the THz radiation well enough as the GaMnAs nanowires are not perpendicular to the plane of the layer.

THz emission of the tilted nanowires was investigated for the first time. The investigated layers can be used in polarization rotating terahertz emitters. This application is very important seeing that the principle of half wave plate can not be used with a wide spectrum of THz pulses.

[1] H. Ahn et al., Terahertz emission from vertically aligned InN nanorod arrays, Appl. Phys. Lett., **91**, 132108(1-3), (2007)
[2] D. V. Seletskiy et al., Efficient terahertz emission from InAs nanowires, IEEE Trans. Terahertz Sci. Technol., Phys. Rev. B , **84**, 115421(1-7) (2011)
[3] R. S. Dowdy et al., Relationship between planar GaAs nanowire growth direction and substrate orientation, Nanotechnology, **24**, 035304(1-6) (2013)

SPECTRAL CHARACTERISTICS OF (IN,GA)N QUANTUM STRUCTURES WITH DIFFERENT DESIGN AND GROWTH PARAMETERS

Kazimieras Nomeika

Department of Semiconductor Optoelectronics, Institute of Applied Research, Vilnius University, Saulėtekis Avenue 9-3, Vilnius 10222, Lithuania
Kazimieras.Nomeika@ff.stud.vu.lt

The development of light sources based on III-nitride compound semiconductors has made a great progress in a recent decade. This is because of the wide spectrum of possible applications and a demand for efficient In(Ga,N) light-emitting diodes (LEDs) with a high power output. The latter is limited by non-radiative losses, which grow noticeably at high charge carrier densities (droop effect [1]). To overcome this unwanted phenomenon and to optimize the devices (and preferably to get efficient emission in the green or even red parts of the visible spectrum) different LED structures are designed and explored.

In this work three sets of samples with different LED multilayered structures, emitting light near 450 nm, are investigated. All samples were grown at the Institute of Applied Research, Vilnius University, on sapphire substrates. The first set consists of two samples with different growth times of quantum wells (QWs), the second consists of two samples with and without short period superlattice (SPSL) and the third set consists of three samples with different growth modes of QWs.

The investigation was carried out using photoluminescence (PL) and differential transmission (DT) techniques [2] in order to track spectral changes in the samples. One of peculiarities of this study is that both techniques were carried out simultaneously, at exactly same excitation conditions. The optical parametric amplifier (OPA) allowed a selective excitation of quantum wells in the samples with a 382 nm (3.24 eV), 250 fs laser pulses.

The results of the first set of samples show that twice longer QW growth time (from 58 s to 115 s) gives a clear redshift to both the PL and DT spectra. This can be explained by a weaker quantum confinement as the QWs are wider and by a probable stronger piezoelectric field. The latter might also be responsible for the decrease of PL intensity (Fig. 1a) and possibly for the longer spectrally integrated DT charge carrier lifetime (Fig. 1b), as the electrons and holes become spatially separated. The redshift is likewise seen in the set of samples with the addition of the SPSL, along with higher PL intensity, which proves that the use of SPSL is beneficial. However, carrier lifetimes drop, and the reasons for such behavior are not completely clear.

Another set of samples exhibits longer charge carrier lifetimes and higher PL outputs with application of pulsed QWs growth instead of a non-pulse mode. These results suggest that a better crystal quality in the QWs is achievable. In addition to this, changing durations of metalorganics (MO) flow (samples F and G, MO flow 15 s on/ 5 s off and 15 s on/ 10 s off accordingly) may also alter carrier lifetimes, which indicates, that further optimizations are possible.

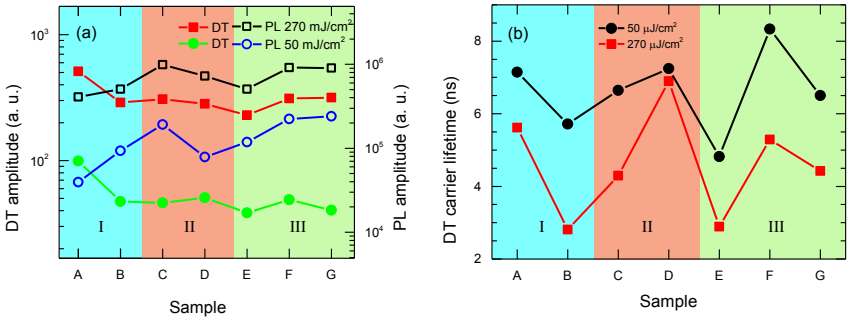

Fig. 1. PL and DT spectra intensities (a) and charge carrier lifetimes (b) of the samples. A and B stand for samples with 115 s and 58 s QWs growth, C and D- for samples with and without SPSL, E for non-pulsed, F and G- for pulsed QWs growth modes accordingly. The colored stripes mark different sets of samples.

[1] M. H. Kim, M. F.Schubert, Q. Dai et al., Origin of efficiency droop in GaN-based light-emitting diodes. Applied Physics Letters, **91**, 183507 (2007).
[2] R. Aleksiejūnas, K. Nomeika, S. Miasojedovas et al., Carrier dynamics in blue and green emitting InGaN MQWs. Phys. Status Solidi B (2015).

Oral session 7

Functional materials and derivatives, modern technologies

Metal borohydrides: the comprehensive novel functional materials.

Wojciech Wegner[1,2*], Tomasz Jaroń[2], Wojciech Grochala[2]

[1] Faculty of Physics, University of Warsaw, Poland.
[2] Centre of New Technologies, University of Warsaw, Poland.
wojciech.wegner@cent.uw.edu.pl

Metal borohydrides are versatile materials. Their traditional application is as selective reducing agents in chemical synthesis ($LiBH_4$, $NaBH_4$). Metal borohydrides contain large amount of hydrogen relative to the other groups of inorganic compounds and as such they could be used as materials for chemical hydrogen storage [1]. In addition, they could serve as precursors towards numerous refractory metal borides and *e.g.* superconducting MgB_2 which may be synthesised in thermal decomposition process of $Mg(BH_4)_2$ at temperatures above 350 ^oC [2]. Furthermore, a high lithium ion conductivity has been lately reported for $LiLn(BH_4)_3Cl$, Ln = La, Gd [3]. These features render metal borohydrides as valuable and comprehensive group of chemical compounds.

A mechanochemical approach to synthesis of borohydrides is the simplest and widespread way for obtaining homoleptic solvent-free borohydrides [4,5]. Such approach, despite being fast and efficient, shows also serious drawbacks – the most important of them are difficulties with synthesis scaling up and purification of the product. Here we present a development of a method of synthesis mixed-metal borohydrides, $M^{(3)}_yM^{(2)}(BH_4)_z$, by room temperature wet chemistry approach, as shown in Fig. 1 [6,7,8]. This method is based on solvent-mediated metathetic reaction between salt containing weakly coordinating anion, $M^{(3)}[An]$, and organic derivative of metal borohydride, containing large organic cation $[Cat]_yM^{(2)}(BH_4)_z$ (reaction **C** in Fig. 1). Here we compare both methods of synthesis, supported by IR spectroscopy, powder and single crystal x-ray diffraction, and thermal analysis including thermogravimetric analysis, differential scanning calorimetry and evolved gas analysis.

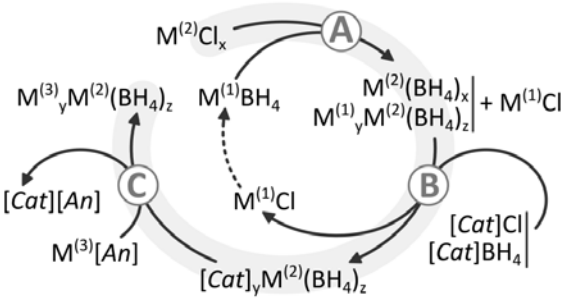

Fig. 1. New room temperature synthesis protocol for obtaining mixed metal borohydrides.

It is known, that the rare-earth metals have high magnetic moments and a diverse range of magnetic structures. Our experimental study utilizing the vibrating SQUID magnetometry revealed that rare-earth metal borohydrides may serve as novel magnetic materials as exemplified by alkali metal-lanthanide borohydrides of holmium [9] and ytterbium [10]. Our investigations indicate that strong mixing of Ln(4f) and H(1s) states, which is responsible for poor thermal stability of these materials, may, in some cases, lead to strong magnetic superexchange interactions between Ln(3+) centers via borohydride bridges.

We will also present our recent results on evaluation of organic derivatives of magnesium borohydride as precursors towards superconducting magnesium diboride coatings [11]. The experimental methods used for this study include x-ray photoelectron spectroscopy and heat capacity measurements (using the Physical Property Measurement System).

The results obtained point out to richness of possible practical applications of metal borohydride materials.

[1] W. Grochala, P. P. Edwards, Chem. Rev., **104** (2004) 1283.
[2] L. H. Rude, et al., *Phys. Status. Solidi A*, **208** (2011) 1754.
[3] M. B. Ley, et al., J. Phys. Chem. C, **116** (2012) 21267
[4] T. Jaroń, W. Wegner, M. K. Cyrański, Ł. Dobrzycki, W. Grochala, J. Solid State Chem. 2012, 191, 279–282
[5] T. Jaroń, W. Wegner and W. Grochala, Dalton Trans., 2013, 42, 6886.
[6] T. Jaroń, W.Wegner, W. Grochala, PCT/IB2014/001884.
[7] T. Jaroń, P. A. Orłowski, W. Wegner, K. J. Fijałkowski, P. J. Leszczyński, W. Grochala, Angew. Chem. Int. Ed. 2015, 54, 1236 –1239
[8] T. Jaroń, W.Wegner, K.J. Fijałkowski, P.J. Leszczyński, W.Grochala, in press, Chem. Eur. J. 2015
[9] W. Wegner, T. Jaroń, W. Grochala, Int. J. Hydrogen Energy 39 (2014) 20024-20030.
[10] W. Wegner, T. Jaroń, W. Grochala, Acta Cryst. (2013). C69, 1289–1291
[11] W. Wegner, *et al.*, in preparation.

ALKALI METAL AMIDOBORANES AS ONBOARD HYDROGEN STORAGE MATERIALS AND BORON NITRIDE PRECURSORS

Rafał Owarzany[1], Karol Jan Fijałkowski[2], Wojciech Grochala[2]

[1] Faculty of Physics, University of Warsaw, Poland
[2] Centre of New Technologies, University of Warsaw, Poland
rafal.owarzany@gmail.com

Nowadays the main energy sources for mobile aplications are based on hydrocarbons, either in gaseous or liquid state. Facing the limited amount of available hydrocarbons left one must develop new ways for onboard energy storage. In this particular field hydrogen is one of the best candidate considered [1]. In the age of growing ecological awareness it is important that the only product of hydrogen combustion is water vapour. The second great advantage of hydrogen over petroleum is its very high gravimetric energy density. Hydrogen is therefore considered as a fuel of the future.

For full replacement of hydrocarbons by hydrogen efficient ways of producing, storing, distributing and combusting hydrogen must be developed. Here, we focus on chemical hydrogen storage in solid materials. New candidates for storage materials must meet all standards defined by the U.S. Departament of Energy (DOE targets) [2]. The most important among those are the high gravimetric and volumetric densities of hydrogen in the storage systems. Ammonia borane (NH_3BH_3) and its derivatives are among the most promissing hydrogen rich materials [3,4,5]. One serious disadvantage of these materials is that contaminants (borazine, ammonia) are evolved upon thermal decomposition along with hydrogen gas [6].

We managed to synthesize and characterize (FTIR, RAMAN, TGA, PXD, NMR) all alkali amidoboranes (MNH_2BH_3, shortly MAB) [4,6,7]. We determined optimal synthetic profiles and conditions leading to the desired products (Eq. 1–3):

M = Li	$MNH_2 + NH_3BH_3 \rightarrow MNH_2BH_3 + NH_3$	(1)
M = Na, K	$MH + NH_3BH_3 \rightarrow MNH_2BH_3 + H_2$	(2)
M = Rb, Cs	$M + NH_3BH_3 \rightarrow MNH_2BH_3 + 0.5H_2$	(3)

In this presentation we show for the first time a detailed comparison of physicochemical properties of all alkali amidoboranes and then evaluate them as hydrogen storage materials with respect to DOE targets. We focus on gravimetric hydrogen capacity, temperature of hydrogen evolution and the purity of the hydrogen desorbed. Results presented here will constitute Mr. R. Owarzany's Masters thesis [8].

To broaden our knowledge about this family of compounds we also characterized products of thermal decomposition of alkali metal amidoboranes. We made an attempt to fully dehydrogenate alkali amidoboranes to obtain amorphous boron nitride (a-BN) in a way shown before for ammonia borane [9]. Our lastest results are promising, but further investigation is needed.

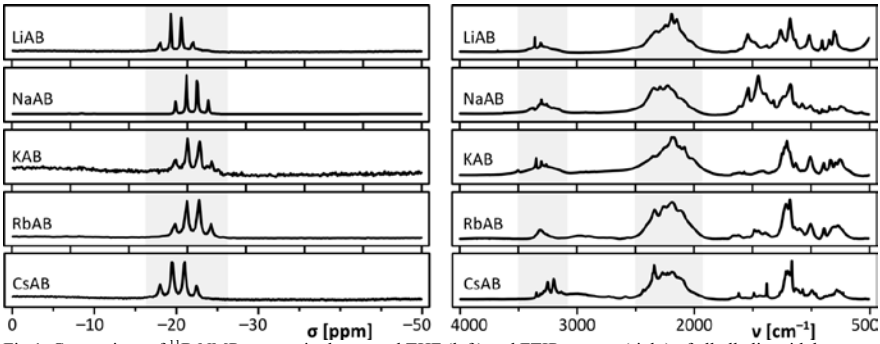

Fig 1. Comparison of ^{11}B NMR spectra in deuterated THF (left) and FTIR spectra (right) of all alkali amidoboranes.

[1] W. Grochala, P. P. Edwards, *Chem. Rev.*, 104 (2004) 1283.
[2] Targets for Onboard Hydrogen Storage Systems for Light-Duty Vehicles, US Department of Energy, September (2009)
[3] M. Bowden, T. Autrey, I. Brown, M. Ryan, *Current Applied Phys*., 8 (2008) 498
[4] Z. Xiong, C.Yong, G.Wu, P.Chen, W. Shaw, A. Karkamkar, T. Autrey, M. Jones, S. Johnson, P. Edwards, W. David, *Nature Mater.*, 7 (2008) 138
[5] K. J. Fijalkowski, T. Jaroń, P. Leszczyński, E. Magos-Palasyuk, T. Palasyuk, M.K. Cyrański, W. Grochala, *PCCP*, 16 (2014) 23340
[6] K. J. Fijalkowski, W. Grochala, *J. Mater. Chem.*, 19 (2009) 2043
[7] R. Owarzany, K. J. Fijalkowski, W. Grochala *in preperation*
[8] R. Owarzany, M.Sc. thesis, Faculty of Physics, University of Warsaw, (2015)
[9] S. Frueh, R. Kellett, C. Mallery, T. Molter, W. Willis, C. King'ondu, S. L. Suib, *Inorg. Chem.* 50 (2011) 783

TUNING GERMANIUM NANOWIRE RESONANT FREQUENCY WITH CLAMPING, MECHANICAL DEFORMATION AND MASS DEPOSITION

Jelena Kosmaca[1], Liga Jasulaneca[1], Raimonds Meija[1], Jana Andzane[1], Justin D. Holmes[2], Donats Erts[1]

[1]Institute of Chemical Physics, University of Latvia, Riga, Latvia
[2]Department of Chemistry, University College Cork, Cork, Ireland
jelena.kosmaca@lu.lv

Germanium nanowires are ideally suited for building nanoelectromechanical systems because of an advantageous combination of electric properties, high Young modulus, strength and stability. Examples of such nanoelectromechanical systems are a mass sensor [1] and a switch [2], where a single nanowire is employed as an active element. Their operation is executed by triggering frequency that matches the resonant frequency of the system. A major challenge to implementing these devices is that the nanowire resonant frequency changes significantly in response to small changes in the system, such as clamping of the nanowire end [3] or mechanical deformation. Hence it is an important parameter that should be controlled in order to perform stable operations on the nanoelectromechanical system.

This work is focused on the investigation of the origins and causes of the nanowire resonant frequency shift for these nanoelectromechanical systems and their common influencing factors. To build a nanoelectromechanical system prototype gold electrodes and germanium nanowires are configured using a nanomanipulation system staged inside a scanning electron microscope. Vibrations of the nanowire are excited electrostatically and resonance detected from scanning electron microscope images (Fig.1). The nanowire being single-clamped or double-clamped represents common configurations used in the nanoelectromechanical mass sensor and the switch.

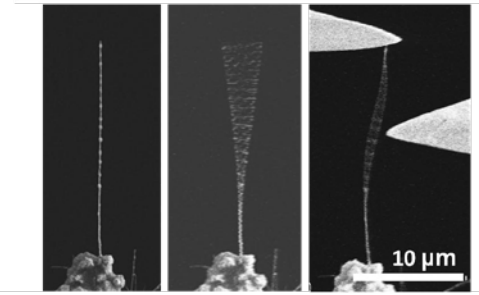

Fig.1. Scanning electron microscope images of a single-clamped nanowire (left), its resonance (centre) and a double-clamped nanowire resonance (right).

One of causes of the resonant frequency change is system mass change. The working principle of mass sensor will be demonstrated by depositing graphite microparticles onto the surface of a germanium nanowire resonator and detecting its resonant frequency shift. Another cause is the effect of nanowire deformation and permanent deflection owing to specific configurations of the electrodes and nanowire in the nanoelectromechanical system. We will demonstrate the correlation between nanowire deformation and resonant frequency. Finally, we will discuss the effect of clamping for a nanowire configured as a switch in ON state. Forcing electrical current flow through the system causes nanowire-electrode contact strengthening and a corresponding increase of the resonant frequency.

In summary, we will discuss the effects of the materials, configuration and operational conditions of nanoelectromechanical system and options for minimizing drawbacks. These results for germanium nanowires may also be applicable to other nanowire compositions.

[1] J. Kosmaca, J. Andzane, J. Prikulis, S. Biswas, J. D. Holmes, D. Erts. Application of a nanoelectromechanical mass sensor for the manipulation and characterisationof graphene and graphite flakes. Science of Advanced Materials **7**(3), 552-557 (2015)
[2] J. Andzane, R. Meija, A. I. Livshits, J. Prikulis, S. Biswas, J. D. Holmes, D. Erts. An AC-assisted single-nanowire electromechanical switch. Journal of Materials Chemistry C, **1**(43) (2013)
[3] R. Meija, J. Kosmaca, L. Jasulaneca, K. Petersons, S. Biswas, J. D. Holmes, D. Erts. Electric current induced modification of germanium nanowire NEM switch contact (2014) – manuscript submitted for publication

PHOTOELECTRIC CHARACTERIZATION OF P3HT POLYMER / PbS NANOCRYSTALS COMPOSITS

Valentas Bertašius[1], Vidmantas Gulbinas[2], Carlo Giansante[3]

[1] Faculty of Physics, Vilnius University, Saulėtekio Ave. 9-III, LT-10222 Vilnius, Lithuania
[2] Institute of Physics, Center for Physical Sciences and Technology, A. Goštauto Ave. 11, LT-01108 Vilnius, Lithuania
[3] NNL-CNR Istituto di Nanoscienze via per Arnesano, 73100, Lecce, Italy
valentas.bertasius@ff.stud.vu.lt

The need of low-cost renewable energy motivates scientific researches on looking for effective and cheap solar cells. One of potential solutions is hybrid solar cells, which can merge advantages of both organic and inorganic semiconductors, such as strong absorbance, mechanical flexibility, low specific weight of conjugated polymers, and high conductance and tunable band gap of inorganic nanocrystals [1].

In this research, we investigated photocurrent kinetics of new type hybrid solar cells created on the base of semiconductor nanocrystals doped polymer. The purpose of this research was to evaluate the mobility of electrons and holes and it dependence on composition and fabrication of samples.

Thin films (roughly 100 nm thick) with different mass ratio of poly(3-hexylthiophene) (P3HT) polymer and PbS nanocrystals were investigated by using "transcient photocurrent" and "charge carrier extraction by linearly increasing voltage" (CELIV) methods. By using the first method we registered photocurrent kinetics on several time scales (Fig. 1), and dependencies of charge carrier extraction times on applied electric field and polymer/nanocrystal composition ratios were evaluated.

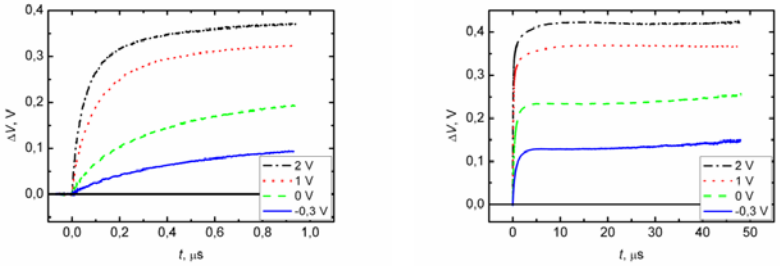

Fig. 1. Photocurrent affected voltage drop ΔV at different time scales on applied electric field.

The results of research showed that photoconductivity of samples and charge carrier extraction times were strongly dependent on the sample composition ratio and fabrication procedures. Analysis of photocurrent kinetics and their dependencies on composition ratio enabled us to distinguish the electron and hole motion. By increasing concentration of polymer the mobility of holes increases, however, the mobility of electrons decreases. The extraction times were by about 5 times shorter in samples annealed during fabrication. Furthermore, qualitative analysis of the photocurrent kinetics revealed that the charge carriers extraction time can be expressed as $1/E\mu$ in all samples, where $\mu \sim \sqrt{E}$.

By using CELIV method only few samples were measured, because others had too high conductance. The results matched with those measured by the "transcient photocurrent" method.

[1] C. Giansante, R. Mastria, G. Lerario et al., Molecular-Level Switching of Polymer / Nanocrystal Non- Covalent Interactions and Application in Hybrid Solar Cells, 1–9, 2014.

Oral session 8

Semiconductor and condensed matter physics, material sciences

TRANSPARENCY OF FINITE-THICKNESS LAYERED SUPERCONDUCTORS CONTROLLED BY DC MAGNETIC FIELD

Tetiana Rokhmanova[1], Zakhar Maizelis[1,2], Stanislav Apostolov[1,2], Valery Yampol'skii[1,2]

[1]A.Ya. Usikov Institute for Radiophysics and Electronics NASU, 61085 Kharkov, Ukraine
[2]V.N. Karazin Kharkov National University, 61077 Kharkov, Ukraine
mrokhm@gmail.com

Layered superconductors, e.g., strongly anisotropic high-T_c crystals $Bi_2Sr_2CaCu_2O_{8+\delta}$ or artificial compounds Nb/Al - AlO_x/Nb, represent materials with the periodic structure, in which thin superconducting layers (of thickness about 2-3 Å) are coupled through the thicker dielectric layers (of thickness about 15 Å) via the intrinsic Josephson effect. The interest to such structures from the fundamental science perspective is mainly related to the specific type of solid state plasma that is formed inside of them, the so-called Josephson plasma. The anisotropy of the layered superconductors supports propagation of the specific excitations, called Josephson plasma waves (see, e.g., [1] and references therein). These waves belong to terahertz frequency range, which is very important for various applications and is promising for the applied science. The possibility to control wave transmittance by means of external DC magnetic field has special interest, since the magnetic field represents a flexible tool to control the transparency of layered superconductors.

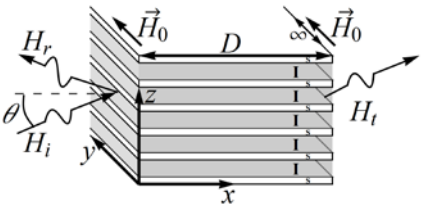

Fig. 1. Geometry of the problem.

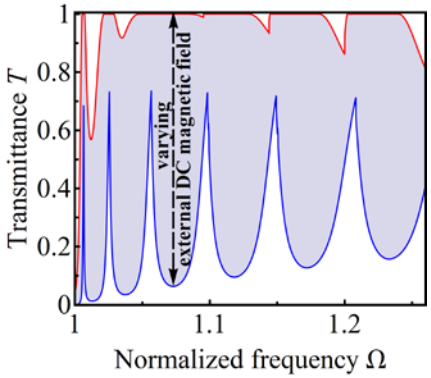

Fig. 2. The range of transmittance variation by means of external DC magnetic field (gray region) for different frequencies of incident waves, when incident angle is $\pi/4$ and the thickness of the sample is 1.2mm.

In this work, we study theoretically the transmission of transverse-magnetic (TM) waves through the finite-thickness sample of layered superconductor in the presence of the external DC magnetic field (see geometry in Fig. 1). We show that, due to nonlinear relation between electromagnetic field and the current inside of the layered superconductor, the transmittance of electromagnetic wave depends on the value of the magnetic field. We obtain the transmission coefficient and study its dependence on the problem parameters, such as the sample thickness, the angle and frequency of the incident wave. Studying all these dependencies we focus our attention on the effect produced by the external DC magnetic field.

The dependence of the transmittance on the thickness of the sample is periodical. We show, that the DC field effectively narrows the thickness and shifts the maxima of transmittance, but does not change the periodicity. When the effective thickness matches the integer number of the half-wavelengths in the sample, the complete transmission takes place. It turns out that the effect produced by the DC magnetic field depends both quantitatively and qualitatively on the values of the problem parameters. The choice of the incident angle and frequency defines the behavior of the transmittance with the change of external DC field. We show that, for frequencies not very close to Josephson plasma frequency, the complete transmission of the sample is certainly observed for definite incident angle and DC field. In addition, for any incident angle, the variation of external DC field results in significant variation of transmittance from nearly zero to one (see Fig. 2). Thus, with the proper choice of parameters, the external DC magnetic field can be a useful tool to adjust the transmittance or vary it in a wide range.

[1] S. Savel'ev, V.A. Yampol'skii, A.L. Rakhmanov, and F. Nori, Rep. Prog. Phys. **73**, 026501 (2010).

IMPACT OF LASER-INDUCED OPTICAL ANNEALING TO RECOMBINATION AND DIFFUSIVITY OF EXCCESS CARRIERS IN AlGaN

Žydrūnas Podlipskas

Institute of Applied Research and Semiconductor Physics Department, Vilnius University, Saulėtekis av. 9-III, Vilnius, LT-10222, Lithuania
Zydrunas.podlipskas@ff.stud.vu.lt

AlGaN-based devices (LEDs, LDs or HEMTs) usually perform at relatively high carrier density (in LDs case exceeding 10^{19} cm^{-3}), which can induce permanent changes in optical and electrical properties [1]. However, depending on device's application these alterations can be either harmful or desired. In this report, I used optical light induced transient grating (LITG) technique to permanently modify and then examine carrier nonradiative recombination rate and diffusivity in AlGaN within a wide range of Al content.

A set consisting of six 0.3 – 1 μm thick uncoated AlGaN epilayers was grown using migration-enhanced metalorganic chemical vapor deposition (MEMOCVD®) on c-plane sapphire substrates. Al content varied between 16% and 71%. 25 ps duration and 10 Hz repetition pulses of 213 nm wavelength were used both for excitation in optical annealing procedures and LITG measurements. All samples were annealed at the same $2\text{x}10^{20}$ cm^{-3} carrier density, taking into account from sample to sample varying absorption coefficient. After annealing for a defined duration, the LITG transients were measured at safe $3\text{x}10^{19}$ cm^{-3} carrier density, which didn't induce permanent changes in carrier dynamics. It should be noted that optical surface damage in studied AlGaN layers occurred only at carrier densities an order of magnitude larger than those used in annealing (> $1\text{x}10^{21}$ cm^{-3}). All optical annealing procedures and LITG measurements were performed at room temperature.

Optical annealing of AlGaN epilayers permanently affected three measured parameters: diffraction efficiency η, nonradiative recombination time τ_{NR}, and ambipolar diffusion coefficient D of nonequilibrium carriers. Annealing-induced diffraction efficiency drop showed no saturation with increasing annealing duration (within measured 1280 s – 12800 shots), and was most pronounced in Al rich AlGaN layers – two-fold drop in $Al_{71}Ga_{29}N$ vs none in $Al_{16}Ga_{84}N$ layer after 320 s annealing (Fig. **A**). Nonradiative recombination, carrier temperature and structural disorder (localization strength σ) were not solely responsible for annealing effectiveness rising with Al content (not shown).

Nonradiative recombination rate $1/\tau_{NR}$ increased with annealing duration at a constant pace (Fig. **B**) and accounted for diffraction efficiency diminishing within the annealing span. The $1/\tau_{NR}$ growth was most probably caused by an increased concentration of nonradiative recombination centers (possibly via activation of closed core screw dislocations), increased homogeneouity of their spatial distribution, or an easier access to them through the lowered potential barrier. Diffusion coefficient was a peaked function of annealing duration: **(i)** the amplification of D by ~2.4 times in the fast initial part could be attributed to an increased mobility of Al and/or Ga atoms, thus enhancing their intermixing, and weakening localization of nonequilibrium carriers; **(ii)** slow tail-ended part of decreasing diffusion coefficient was possibly caused by the recovering structural disorder.

In conclusion, I report permanent more than two-fold increase of excess carriers' diffusivity under intense laser illumination in AlGaN, revealing particularly attractive application in the possible performance enhancement of high electron mobility transistors (HEMTs).

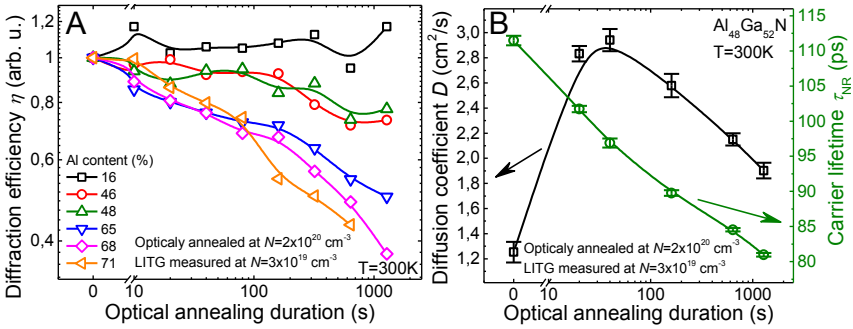

Fig. **A** Diffraction efficiency η as a function of optical annealing duration in AlGaN epilayers with different Al content. **B** Diffusion coefficient D (squares) and nonradiative recombination time τ_{NR} (circles) of nonequilibrium carriers against optical annealing duration in $Al_{48}Ga_{52}N$ layer. All samples were optically annealed at N=$2\text{x}10^{20}$ cm^{-3}, and LITG measurements were taken at $3\text{x}10^{19}$ cm^{-3} carrier densities using laser pulses of 25 ps duration, 10 Hz repetition rate and 213 nm wavelength for excitation.

[1] T. Saxena et al, Low threshold for optical damage in AlGaN epilayers and heterostructures, J. Appl. Phys. **114**, 203103 (2013).

A Monte Carlo study of an ensemble of magnetic cubic nanoparticles - the role of size, density, and anisotropy constants.

Mikołaj Sadek[1], Jacek Szczytko[1], Magdalena Woińska[1], Jacek Gosk[1,2] Andrzej Majhofer[1], Andrzej Twardowski[1]

[1]Faculty of Physics, University of Warsaw, Poland
[2]Faculty of Physics, Warsaw University of Technology, Poland
mikolaj.sadek@fuw.edu.pl

The ensemble of spatially disordered and randomly oriented spherical monodispersed single-domain magnetic cobalt nanoparticles with cubic anisotropy was studied using the Monte Carlo method.

The research focused on comparison of systems with interchanged hard and easy magnetizations axis, i.e. different signs of cubic anisotropy constants. A comparison of the simulation results for a single cluster with an infinite periodic arrangement of such clusters was performed in order to clarify the role of dipole-dipole interactions on magnetic properties of nanoparticles. In this project I was responsible for calculations and interpretation for both periodic and non-periodic systems with different nanoparticles sizes and densities. The calculations resulted in hysteresis loops and field cooling/zero field cooling (FC/ZFC) curves for these systems in different temperatures and magnetic fields.

My results show that positive value of cubic anisotropy constant provides better agreement with experiments. By comparing periodic systems with non-periodic clusters of nanoparticles I managed to approximate the size of non-periodic system, that behaves as periodic one.

NANOCRYSTALLIZATION AS A NOVEL METHOD OF OBTAINING HIGHLY EFFECTIVE LI-ION CATHODE MATERIALS

Przemyslaw Michalski[1]

[1]Faculty of Physics, Warsaw University of Technology, Poland
michalski@if.pw.edu.pl

Rechargeable lithium-ion batteries (LIBs) are the most promising candidates for applications in electric vehicles (EVs), hybrid electric vehicles (HEVs), power tools and mobile devices in terms of energy densities and power densities [1].

The important factor which limits battery performance is a quality of cathode material used. The expectations in this field are very high – the material should provide high energy and power densities described by good gravimetric capacity, high operational voltage and fast kinetics of reactions. Good thermal stability and rate capability is also important if the battery is to be into commercial production. On the other hand, the produced LIBs should be cheap and environmentally friendly.

Of course, achieving all of these goals is impossible and several compromises are required. One of methods of improving materials' parameters is the modification of their microstructure and obtaining them in a nanocrystalline form. The structural modification affects positively both electrical and electrochemical performance of the material.

During the presentation I will present the main benefits of obtaining a Li-ion cathode material in a nanocrystalline form. In addition, an interesting, novel method of synthesis - thermal nanocrystallization of glasses - will be explained and some experimental results will be shown [2].

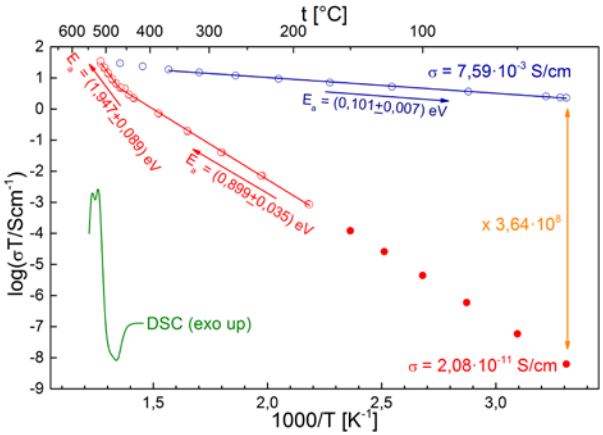

Fig. 1. The increase of electronic conductivity after heat treatment in $28.2Li_2O{\cdot}35.2FeO{\cdot}8.4V_2O_5{\cdot}28.2P_2O_5$ glass.

[1] A. S. Arico, P. Bruce, B. Scrosati et al., Nanostructured materials for advanced energy conversion and storage devices, Nature Materials **4**, 366-377 (2005).

[2] P. P. Michalski, J. L. Nowinski, T. K. Pietrzak et al., Preparation and Characterization of Li_2O-FeO-V_2O_5-P_2O_5 Glasses and Related Nanomaterials, Procedia Engineering **98**, 78-85 (2014).

SITE-SELECTIVE DEPOSITION AND APPLICATION OF GRAPHENE

Andrius Sakavičius[1]

[1]Center for Physical Sciences and Technology, Department of Physical Technologies, A. Goštauto 11, VILNIUS LT01108, LITHUANIA
andrius.sakavicius@ftmc.lt

The electronic properties of graphene, a two-dimensional crystal of carbon atoms, are exceptionally novel. For instance, the low-energy quasiparticles in graphene behave as massless chiral Dirac fermions which have led to the experimental observation of many interesting effects similar to those predicted in the relativistic regime.

Graphene can be considered as the building block of many carbon allotropes. It is a two-dimensional crystal with hexagonal structure consisting of a bipartite lattice of two triangular sublattices. Each atom is tied to its three nearest neighbors via strong σ bonds that lie in the graphene plane with angles of 120°. The σ bond is a result of the sp^2 hybridization of the 2s, $2p_x$, and $2p_y$ orbitals for the three valence electrons. The fourth valence electron is in the $2p_z$ orbital that is orthogonal to the graphene plane. A weak π bond is formed by the overlap of half-filled $2p_z$ orbitals with other $2p_z$ orbitals. The transport properties of graphene are determined by these delocalized π electrons. Also, the measured electron mobility of graphene is ultra-high and exceed 200000 cm^2/Vs [1].

$$\mathbf{F}_{\mathrm{DEP}} = (\mathbf{p} \cdot \nabla)\mathbf{E} \tag{1}$$

At this work we represent up to few layers thickness graphene application to FET transistors and terahertz imaging. The process of dielectrophoresis (Fig. 1) allows site-selective deposition of few layers graphene. One of the ways to form graphene flakes at the certain place on the substrate is employing nonuniform electric field. This method (dielectrophoresis [2]) allows the selective deposition or directed movement of spherical and one-dimensional micro and nanoscale objects in nonuniform electric fields. This includes polymer particles, cells, DNA, nanowires and bundles or individual carbon nanotubes for physical properties characterization. The dielectrophoretic force Eq. (1) is exerted on an induced dipole moment **p** of a plarizable particle in a nonuniform electric field **E**, which is proportional to the electric field gradients.

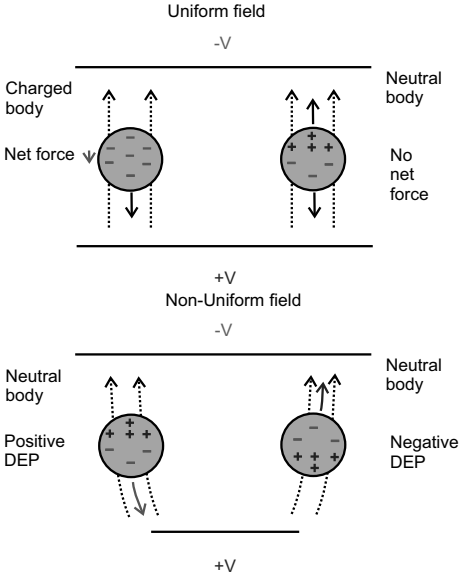

Fig. 1. A sketch of the process of dielectrophoresis.

[1] S.V. Morozov, et al., Phys. Rev. Lett. **100**, 01660 (2008).
[2] H. A. Pohl, J. Appl. Phys. **22**, 869 (1951).

DIP-PEN NANOLITHOGRAPHY FOR PATTERNING OF LIPIDS ON SELF-ASSEMBLED MONOLAYERS

Vytautas Navikas*, Martynas Gavutis, Ramūnas Valiokas
Department of Nanoengineering, Center for Physical Sciences and Technology, Vilnius, Lithuania
vytautas.navikas@ftmc.lt

Biomimetic lipid membranes are widely used *in vitro* systems to study membrane lipid or protein-protein interactions. Many effects of membrane composition, phase behavior and transport can only be studied by in vitro reconstitution. Combination of self-assembled monolayers (SAMs) on solid supports and the direct nano-patterning technique known as dip-pen nanolithography (DPN) allow controlling the composition and geometry of the biomimetic lipid assembly at the nano scale.

The aim of this study was to explore the possibilities to combine lipid DPN [1] with micro-patterned SAMs. To characterize the lipid ink (1, 2-dioleoyl-sn-glycero-3-phosphocholine) behavior, two homogeneous SAMs were used: hydrophobic eicosanthiol (C_{20}) and hydrophilic tri(ethylene glycol) - terminated thiol (EG_3). To increase the reproducibility, an ink-jet inking system was used to equalize the lipid ink amount on the tip. Furthermore, all experiments were done in a controlled humidity chamber at 50% RH and 25 ° C. Lipid patterns were investigated using imaging ellipsometry and atomic force microscopy (AFM). Combination of these techniques allowed us to perform a comparative analysis that revealed sharp contrasts in the lipid mass flow rate and phase behavior on C_{20} and EG_3 SAMs, respectively. We calculated that the transfer rate on the EG_3 SAM was about 10 times greater (depends on the contact time) than on C_{20}. However, due to the surface hydrophobicity the lipid phase behavior was completely different. Lipid patterns on the EG_3 SAM formed a monolayer less than 1 nm in height. In contrast, on the hydrophobic C_{20} SAM, lipids molded into dot-like multilayer stacks over 200 nm in height. A decrease of the contact time allowed forming lipid dots less than 50 nm in diameter and 6 nm in height. Lipid DPN on the pre-structured surfaces with areas of hydrophobic and hydrophilic SAMs revealed that lipids preferably spread along hydrophilic areas, while hydrophobic ones acted as a barrier for spreading.

Based on these observations we were able to guide DPN lipid spreading and form lipid domains of pre-defined shape and size. These results promote further development of micro and nano-patterned lipid domains for creation of a simplified biophysical model of the complex cell membrane assemblies for biophysical studies.

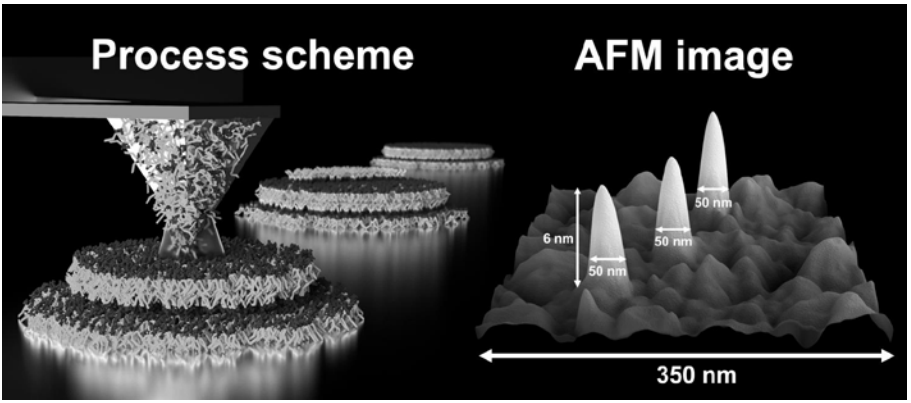

Fig.1 Experiment visualization (left, and an AFM topography image of lipid DPN patterns on a C_{20} SAM.

[1] Steven Lenhert, Peng Sun, Yuhuang Wang, Harald Fuchs, and Chad A. Mirkin, Massively Parallel Dip-Pen Nanolithography of Heterogeneous Supported Phospholipid Multilayer Patterns. Small, **3**, 71 – 75 (2007).

Oral session 9

Biophysics, medical and environmental physics

THE IMPACT OF MULDE (WENLOCK: LOWER SILURIAN) MASS EXTINCTION EVENT ON THE ECOLOGICAL DYNAMICS OF OSTRACODES

Simona Rinkevičiūtė[1], Andrej Spiridonov[1*]

[1]Department of Geology and Minerology, Vilnius University, Lithuania
simona.rinke@gmail.com

The Mulde mass extinction (~ 428 millions of years ago) was one of the most important geobiological events which affected biota of the Silurian period. Ostracodes are and always were (through the last 500 million years) an important component of benthic marine communities. Ostracodes are currently a widespread group both in the fresh and in the salt waters, which allows better understanding of the past paleobiological processes using methods of comparative analysis [1, 2]. Despite the high importance of this group in understanding global changes of the past, in general, the studies of the Silurian ostracodes and especially of their paleoecological dynamics are in incipient stage.

In order to fill the gap in our understanding of the Mulde event the upper Homerian part of the Gėluva-118 core section was studied. Overall 23 samples were taken in the depth interval between 961,5 and 1007 m. This interval spans approximately time period of one million years, starting from the beginning of the Mulde biotic event up to the final stages of recovery in the earliest Ludlow epoch. The collection of ostracode shells, their taxonomic identification and numerical analyses of frequency changes in studied samples were performed. The interpretation of Mulde event and the post-extinction recovery interval was based on the range of ecological statistical analyses of biological diversity.

The results of the study revealed, that Mulde bioevent was followed by an immediate increase in numbers of individuals (up to the maximal numbers observed in the section) and also local taxonomic richness of ostracodes. After approximately 100 thousand years the maximum in local species diversity was reached. Shannon entropy, evenness the dominance indexes show, that at the beginning of the studied time the high abundances of individuals were associated with the high asymmetry of abundance distributions, with several species dominating ostracode assambledges. This observation points to the decrease of complexity of ostracode communities in the initial post-extinction stage. However, through all of the Wenlock there was steady decline in species dominance and there was opposite increase in the entropy and the evenness of fossil ostracode assemblages. This pattern shows that during this time interval there was steady recovery in the complexity of benthic ecosystems, with fastest rates during the first 150 thousand years. Additionally, one of the most important determinants which controlled species richness and other biodiversity metrics was the change of eustatic sea level. It should be noted that during high-stands of the sea level there were higher levels of abundance, species richness and also complexity of paleocommunities. There is just one exception to this regularity – the initial phase of the recovery, which lasted approximately the first 150 thousand years from the beginning of the Mulde event.

[1] Salas M. J., Vannier J., Williams M., 2007. Early Ordovician Ostracods from Argentina: their bearing on the origin of Binodicope and Palaeocope Clades. Journal Paleontology, 81 (6): 1384 – 1395.
[2] Salas M.J., 2011. Early Ordovician (Floian) ostracods from the Cordillera Oriental, Northwest Argentina. Geological Jaurnal, 46: 637 – 650.

SEA SURFACE TEMPERATURE FRONTS IN THE BALTIC SEA

Simona Skyraitė, Donatas Pupienis

Department of Hydrology & Climatology, Vilnius University, Lithuania
skyraite@gmail.com

Ocean fronts are sharp boundaries between different water masses and different types of vertical structure (stratification) that are usually accompanied by enhanced horizontal gradients of temperature, salinity, density, nutrients and other properties [1]. Fronts and the associated currents play important roles in heat and salt transport, ocean-atmosphere interaction and ecosystem functioning. They are well known as contributors for elevated primary production areas, which are known as "hot spots" of marine life, from phytoplankton to apex predators. Moreover, the surface convergence can also lead to higher concentration of pollutants [2].

The main aim of this research is to analyze the distribution and alternation of hydrological fronts in the Baltic Sea. As fronts are high-gradient zones; therefore most objective computer-approaches to front identification are based on gradient computations. The approach used in this study is based on histogram analysis and Single Image Edge Detection (SIED) algorithm. Since a front is a boundary between two relatively uniform water masses, histograms of any oceanographic characteristic (e.g. SST) in the vicinity of the front should have two well-defined modes that correspond to the water masses divided by the front, while the latter corresponds to the frequency minimum between the modes (Fig. 1a). The front detection and tracking is conducted at three levels: window, image and pixel. The optimum window size found by Cayula and Cornillon [3] is 32 by 32 pixels. The front detection algorithm uses all pixel-based SST values within each window to compute a SST histogram for the given window. For each window that contains a front (a relatively narrow zone of enhanced SST gradient), the corresponding SST histogram would have a frequency minimum identified with the front [4].

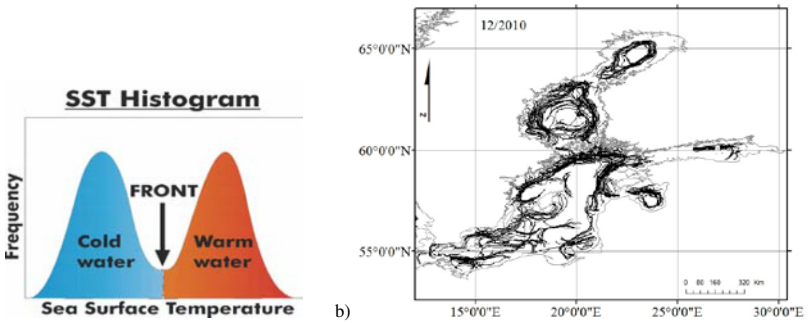

Fig. 1. a) Histogram method of front detection in the Cayula-Cornillon algorithm. b) The composition of sea surface temperature fronts (black lines) identified by Cayula-Cornillon's SIED algorithm in the GHRSST daily analysis data for December, 2010. The front detection threshold is 1.0 °C

To get a representative front distribution over the whole Baltic Sea area, it was made a composition of a few days. Numbers of images composited show us the stability and temporality of fronts. It is apparent that fronts occur much more frequently in certain areas compared to other. The large-scale distribution of fronts is aligned to the coast and follows the local bottom topography – along the Eastern Gotland basin extending north to the Western Estonian archipelago, Western Gotland basin, eastern coast of the Bothnian Sea, and in the Gulf of Finland along its northwestern coast extending southwest through Northern Baltic Proper to the coast of Sweden (Fig. 1b). Most of these fronts are distinct year-round. While others (beside Gulf of Riga, Pomeranian Bay, and Gulf of Gdansk) are frequent under the influence of a very strong stream of freshwater of rivers. Moreover, other small-scale fronts are found in the Arkona basin and Irbe Strait due to connection of two different basin with low or high salinity water.

[1] Belkin I.M., 2003. Front, in: Interdisciplinary Encyclopedia of Marine Sciences, edited by Nybakken J.W., Broenkow W.W., Vallier T.L. Grolier Academic Reference, Danbury, Conn. pp. 433–436.
[2] Belkin I. M., Cornillon P. C., Sherman K., 2009. Fronts in large marine ecosystems. Progress in Oceanography 81, 223-236
[3] Cayula J.-F., Cornillon P., 1992. Edge detection algorithm for SST images. J. Atmos. Oceanic Tech., 9(1), pp. 67–80.
[4] Belkin I. M., Cornillon P. C., 2004. Surface thermal fronts of the Okchotsk Sea. Pacific Oceanography, Vol 2, No.1–2

ACCOMMODATION LAG UNDER MONOCULAR AND BINOCULAR CONDITIONS IN SYMPTOMATIC AND ASYMPTOMATIC EMMETROPES

Karola Panke[1], Aiga Svede[1], Wolfgang Jaschinski[2], Gunta Krumina[1]

[1] Department of Optometry and Vision Science, University of Latvia, Kengaraga 8, Riga, Latvia, LV-1063

[2] Leibniz Research Centre for Working Environment and Human Factors (*IfaDo*), Research Group "Individual Visual Performance" Ardeystr. 67, D - 44139 Dortmund, Germany

karola.panke@inbox.lv

Introduction: Accommodation is the focusing mechanism that provides fast changes in the optical power of the eye in order to keep the image clear when changing the gaze from far to near distance. For each distance there is a constant theoretical accommodative demand, but real accommodation response maintain slightly lower. Difference between accommodative demand and accommodation response is called accommodative lag. The purpose of this study was to estimate the relationship between accommodation lag under monocular and binocular conditions in symptomatic and asymptomatic groups.

Method: Twenty participants (emmetropes) with mean age 24 ± 4 years participated in the study. Accommodative response was measured for dominant eye with open-field infrared autorefractometer (Shin-Nippon, SRW-5000) at 40 cm, 30 cm, and 24 cm (corresponding accommodative demands of 2.5D, 3.33D, and 4.17D) under monocular and binocular condition. Each accommodation measurement consisted of approximately 130 dynamic data points collected during consecutive 2 min time. Dissociated phoria for each distance was measured with Madox test. Convergence insufficiency symptom survey (CISS) score was used to distinguish symptomatic and asymptomatic group. Sequence of accommodation measurements were random order and all experiment was replicated twice within 7 ± 2 days.

Results: The two measurement sessions resulted in a test-retest correlation of r=0,95 for accommodative response. To indicate reliability of accommodation response, we used the standard deviation of the difference between repeated measurements (0.22 D). For asymptomatic group, monocular accommodative lag differed significantly across the distances – from 40 cm to 30 cm (0.22 ± 0.19 D, p=0.028) and from 40 cm to 24 cm (0.35 ± 0.25 D, p=0.006) showing a tendency for accommodative lag to increase with closer distance (nonparametric ANOVA: p = 0.025). For symptomatic group, monocular accommodative lag differed in a similar way – from 40 cm to 30 cm (0.20 ± 0.32 D, p=0.02) and from 40 cm to 24 cm (0.24 ± 0.31 D, p=0.02). Binocular accommodation lag was significantly smaller than monocular accommodation lag (Spearman r = 0.77*;* p < 0.001).

Conclusions: At close working distances (40 cm and closer), accommodation tends to be more variable and inaccurate for symptomatic patients both for monocular and binocular viewing conditions.

Acknowledgements

This study is supported by ESF Project No.2013/0021/1DP/1.1.1.2.0/13/APIA/VIAA/001 and also funded by "Deutsche Forschungsgemeinschaft" (DFG JA 747/5-2)

THE IMPACT OF DIABETES ON EJECTION FRACTION IN PATIENTS WITH ADVANCED CORONARY ARTERY DISEASE

Sabina Brazevič, Magdalena Grajek, Tomasz Kopyciuk

Faculty of Physics, Adam Mickiewicz University in Poznań
sabinabrazevic@yahoo.com

Morbidity due to all forms of coronary heart disease is a function of the combination of several cardiovascular risk factors: smoking, hypertension, left ventricular hypertrophy and diabetes [1]. The first signs of ischemia, infarction and heart failure faster reveal in diabetic patients, especially after a few years of the disease or with the poorly therapy. [2] In patients with diabetes and ischemic heart disease the prognosis is 2-3 times worse than the general population and the number of patients increases every year. [3] [4]

The major problem in general is the course of the disease and the selection of treatment: insulin or treatment medicaments. Due to the disease left ventricular performance is often limited and echocardiography method allows to check it out using ultrasound. Determination of ejection fraction allows to assess the state of the left ventricle.

This parameter (EF) was used to check the condition of the patient after coronary artery bypass grafting (CABG) in patients with diabetes treated with two methods: insulin or drugs.

A group of 186 patients, which included 46 patients with diabetes was studied. The main goal of this work was to check whether the ejection fraction of the left ventricle may be an important determinant of prognosis the course of convalescence after CABG surgery and thus whether it will be a good parameter determining the severity of coronary disease among people with diabetes.

[1] Koblik T., *Insulinotherapy in diabetes type 2*, Via Medica, Gdańsk 2010, ISBN 978-83-7555-214-0
[2] Cichocka A., *A practical guide to weight loss and nutritional prevention and treatment of diabetes type 2*, Medyk, Warsaw 2010, ISBN 978-83-89745-58-3
[3] Tatoń J., *Management of diabetes type 2 based on evidence - standards for doctors*, PZWL, Warsaw 2002, ISBN 83-200-2707-1
[4] American Diabetes Association, *Treatment of diabetes type 2*, Via Medica, Gdańsk 2002, ISBN 83-7258-086-3

Oral session 10

Biophysics, medical and environmental physics

OPTIMIZATION OF $NAYF_4:YB^{3+},ER^{3+}$ UP-CONVERTING NANOPARTICLES FOR CANCER CELL RESEARCH: COLLOIDAL STABILITY, CYTOTOXICITY AND CELL IMAGING

Ignas Jurčiukonis[1], Urtė Statkutė[1], Ieva Mikalauskaitė[2], Vilius Poderys[1], Vitalijus Karabanovas[1], Aldona Beganskienė[2], Ričardas Rotomskis[1,3]

[1] Biomedical Physics Laboratory, National Cancer Institute, Lithuania
[2] Department of Inorganic Chemistry, Faculty of Chemistry, Vilnius University, Lithuania
[3] Biophotonics Group of the Laser Research Centre, Faculty of Physics, Vilnius University, Lithuania
Ignas.jurciukonis@gmail.com

Numerous kinds of nanoparticles are getting increasingly popular in biomedicine. Different nanoparticles are designed considering their desired use, function, modifications. Upconverting nanophosphors (UCNPs) have the ability to absorb two or more lower energy photons to yield a single higher energy photon. This is especially useful when using them on tissues below surface. Bearing in mind an undesirably high tissue absorption in UV range, which is used to excite other nanoparticles and tissue autofluorescence under UV excitation UCNPs can be irradiated in up to 1 cm depth and prevent tissue luminescence. Using various combinations of dopant ions allows for spectral nanoparticle tuning, making it even more versatile in biomedical applications [1]. The purpose of this paper is to investigate the UCNP's ability to be absorbed into cells and used as an imaging marker, possible cytotoxicity and colloidal stability.

For these measurements we used $NaYF_4:Yb^{3+},Er^{3+}$ nanoparticles modified with F127 surface coating polymer. Nanoparticle colloidal stability was measured in relation to luminescence intensity in a solution. Different acidity solutions were compared, as well as different cell incubation mediums. Our results show increased colloidal stability in solutions set at pH 7 and 7,4 and low intensity luminescence relating to low colloidal stability in pH 6 and pH 8 phosphate buffer solutions. While comparing different cell mediums we have found that Fetal Bovine Serum (FBS) presence in Dulbecco Modified Eagle's Medium (Gibco, USA) solution extends UCNP solubility compared to DMEM solution without FBS and deionized water. Transparent cell mediums with FBS were also used to increase luminescence intensity by avoiding solution absorption (DMEM and OptiMEM), both of which allowed for higher colloidal stability.

Cell cytotoxicity evaluation was carried out using standard XTT assay. MCF 7, MDA MB 231 and MCF 10A cell lines were used. Cells were incubated using UCNP concentration, equal to that used in cell imaging, along with two and five times increased concentration. After up to 24 hour exposure to UCNPs in various concentrations cell viability dropped to no less than 80 percent in all cell lines, as evaluated by XTT assay.

Cell imaging was carried out using a custom modified Nicon Eclipse E400 microscope equipped with 980 nm continuous wave operation diode laser with emission power of 877 mW for nanoparticle excitation. Cell nuclei were stained with 4',6-diamidino-2-phenylindole DNA binding dye. Cells were incubated with UCNP solution for 1, 3,6 and 24 hours. Cell images were processed using ImageJ software (Fig. 1) (NIH, USA).

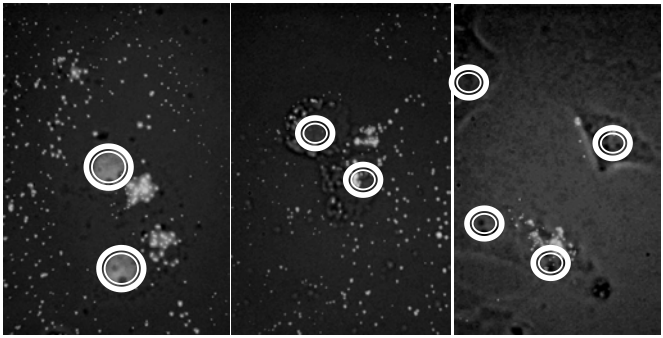

Fig. 1. MCF 7, MDA MB 231 and MCF 10A cell fluorescent images. Nanoparticles seen as white dots. White circles mark the nuclei.

[1] Chatterjee D. K., Gnanasammandhan M. K., Zhang Y. Small Upconverting Fluorescent Nanoparticles for Biomedical Applications // Small. 2010. No.6, P. 2781−2795.

QUANTUM DOT-LOADED MESENCHYMAL STEM CELLS FOR TUMOR-TROPIC THERAPY

Dominyka Dapkute[1,2], Simona Steponkiene[2], Vytautas Kaseta[2,3], Una Riekstina[4],Ricardas Rotomskis[2,5]

[1] Faculty of Natural Sciences, Vilnius University, Lithuania
[2] Laboratory of Biomedical Physics, National Cancer Institute, Vilnius, Lithuania
[3] Department of Stem Cell Biology, State Research Institute Centre for Innovative Medicine, Vilnius, Lithuania
[4] Faculty of Medicine, University of Latvia, Riga, Latvia
[5] Biophotonics group of Laser Research Center, Vilnius University, Vilnius, Lithuania
dominyka.dapkute@nvi.lt

In the past decade, stem cells, especially mesenchymal stem cells (MSCs), have been derived to track down and destroy malignant cells taking advantage of their tumor-tropic property [1]. MSCs are multipotent cells found in almost all adult tissues and have the ability to self-renew and differentiate into various cell types. MSCs are able to escape immune system and migrate to sites of lesions including tumors by using specific receptors and ligands to facilitate trafficking. Therefore, due to their tumoritropic migratory properties, MSCs can be used as delivery systems to transport nanocompounds directly to cancer cells [2].

Quantum dots (QDs) are fluorescent nanoparticles. Due to their unique optical properties and capability to form complexes and conjugates with bioactive molecules they can be used as theranostic nanoplatforms, combining both diagnostics and therapy. Low toxicity, resistance to degradation, long-term photostability and easily modified surface with drugs, photosensitizers or antibodies, enable them to be used as labels and therapeutic agents inside MSCs vehicles [3]. QDs have already been reported to be used for MSCs tracking [4], however the knowledge about QD-loaded migratory capacity of MSCs is still limited.

Before using MSCs as carriers of nanoparticles, optimal conditions for QDs loading in MSCs need to be established. In our study we, firstly, identified human skin-derived MSCs by the expression of specific surface molecules. Then we determined the optimal non-toxic concentration of QDs using cell viability test. Using confocal microscopy we detected rapid uptake of QDs and their localization in vesicles. Flow cytometric analysis showed time-dependent increase of photoluminescence intensity of QDs and the saturation point at 6 hours (Fig. 1). A more detailed analysis revealed correlation between photoluminescence intensity of QDs inside cells and the proliferation marker Ki67.

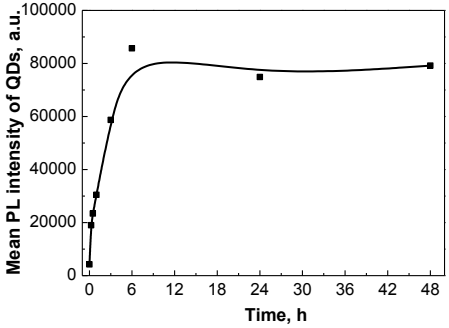

Fig. 1. Uptake of COOH-625 QDs in MSCs.

In conclusion, we optimized effective QDs concentration for labeling MSCs, found 6 hours incubation time to be sufficient to reach maximum upload of QDs and also revealed proliferation-dependent uptake dynamics.

This work was financially supported by the Joint Lithuanian-Latvian-Taiwanese Tripartite Cooperation Programme, Grant No. TAP-LLT-13-016.

[1] L. Linlin, G. Yunqian et al., Silica Nanorattle Doxorubicin-Anchored Mesenchymal Stem Cells for Tumor-Tropic Therapy, ACS Nano **5**(9), 7462-7470 (2011).
[2] C. Tang, P.-J. Russel, R. Martiniello-Wilks et al., Concise review: Nanoparticles and cellular carriers-allies in cancer imaging and cellular gene therapy? Stem Cells **28**(9), 1686-1702 (2010).
[3] B.-J. Muller-Borer, M.-C. Collins et al., Quantum dot labeling of mesenchymal stem cells, Journal of Nanobiotechnology **5**:9 (2007).
[4] A. Rak-Raszewska, M. Marcello et al., Quantum Dots Do Not Affect the Behaviour of Mouse Embryonic Stem Cells and Kidney Stem Cells and Are Suitable for Short-Term Tracking, PLoS One **7**(3), e32650 (2012).

ACCUMULATION AND TOXICITY OF MAGNETIC NANOPARTICLES Fe_3O_4 IN MOUSE EMBRYONIC FIBROBLASTS

Greta Jarockyte[1], Urte Statkute[1], Vilius Poderys[1], Vitalijus Karabanovas[1], Shan-hui Hsu[2], Ricardas Rotomskis[1,3]

[1] Biomedical Physics Laboratory of National Cancer Institute, Baublio 3B, LT08406, Vilnius, Lithuania;
[2] Institute of Polymer Science and Engineering, National Taiwan University, No.1, Roosevelt Road Sec. 4, Taipei 10617, Taiwan;
[3] Biophotonics group of Laser Research Centre, Vilnius University, Saulėtekio 9, c.3, LT-10222, Vilnius, Lithuania.
greta.jarockyte@nvi.lt

Magnetic nanoparticles are a class of nanoparticle which can be manipulated using magnetic field. Ferrous or ferric oxide is the main constituent of magnetic particles, although metals such as cobalt and nickel are used in other fields of application. Magnetic nanoparticles, with their unique magnetic properties and controllable sizes, are being actively investigated as the next generation of magnetic resonance imaging contrast agents. Furthermore they have important potential for hyperthermia therapy, anticancer drug delivery and magnetic separation [1, 2].

The aim of our work was to investigate the accumulation of Fe_3O_4 nanoparticles in mouse embryonic fibroblasts (NIH3T3) and their effect on proliferation and viability of cells.

Fe_3O_4 nanoparticles were synthesized according to previously reported procedure [3]. Atomic force microscopy measurements showed that height of Fe_3O_4 particles varies from 10 nm to 40 nm, width – from 50 nm to 200 nm. Hydrodynamic size measurements revealed that the diameter of particles in solution is approximately 50 nm.

Cellular uptake was investigated incubating with 65 ng/ml of Fe_3O_4. For uptake studies of Fe_3O_4 nanoparticles in NIH3T3 cells we used Prussian Blue staining reagent, which reacts with the iron producing a blue color. The accumulation was observed using bright-field microscope equipped with digital color camera. Fe_3O_4 nanoparticles accumulated in cells heterogeneously: in some cells Fe_3O_4 nanoparticles were localized in large vesicles spread through whole cytosol, while in other cells vesicles were localized only in the perinuclear region (Fig. 1).

Toxicity of Fe_3O_4 nanoparticles was investigated using XTT cell viability assay. The viability of NIH3T3 cells remains approximately 98% within 3-24 h of incubation, however a slight decrease of viability was observed after 48 hours of incubation.

To sum up, newly synthesized Fe_3O_4 nanoparticles are suitable for imaging of cells but the concentration and incubation times of nanoparticles should be carefully chosen in order to avoid undesirable side effects.

Acknowledge: this work was financially supported by the joint Lithuanian-Latvian-Taiwanese Tripartite Cooperation Programme, Grant No. TAP-LLT-13-016.

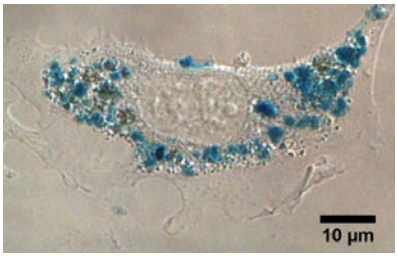

Fig. 1. NIH3T3 cell after 24 h incubation with Fe_3O_4 (stained with Prussian Blue).

[1] Q. A. Pankhurst, J. Connolly, S. K. Jones and J. Dobson.Applications of magnetic nanoparticles in biomedicine, J. Phys. D: Appl. Phys. 36 R167–R181 (2003).
[2] Akira Ito, MasashigeShinkai, Hiroyuki Honda and Takeshi Kobayashi.Medical Application of Functionalized Magnetic Nanoparticles. Journal of Bioscience and Bioengineering, 100, 1, 1–11 (2005).
[3] Shan-hui Hsu, Tung-Tso Ho, Ting-Chen Tseng. Nanoparticle uptake and gene transfer efficiency for MSCs on chitosan and chitosan-hyaluronan substrates. Biomaterials, 33(14):3639-50 (2012).

POTENTIAL DRUG RESISTANCE BIOMARKERS FOR OVARIAN CANCER

Egle Povilaityte[1], Karolina Zilionyte[2], Agata Mlynska[2], Dr. Vita Pasukoniene[2]

[1] Faculty of Medicine, Vilnius University, Lithuania
[2] Laboratory of Immunology, National Cancer Institute, Lithuania
egle.povilaityte@mf.stud.vu.lt

Ovarian cancer accounts for about 3% of cancers among women, but it causes more deaths than any other cancers of female reproductive system [1]. Due to the lack of specific symptoms, about 70% of ovarian cancer cases are diagnosed in advanced stages, when five-year survival rate is less than 40% [2] and standard treatment (cytoreductive surgery and chemotherapy) is often insufficient. It is known that ovarian cancer frequently tends to develop resistance to chemotherapy. Novel models and biomarkers are required for extensive research of drug resistance mechanisms.

The aim of this study was to identify the changes in the expression of drug resistance-related genes (*PCNA* [3], *ASS* [3], *FN1* [3], *ATPB7* [4], *ATPB11* [5], *NOTCH3* [6], *MMP3* [7], *NACC1* [8], *ABCC1* [9], *ABCC5* [9], *ABCC10* [9]) in drug-resistant sublines of human epithelial ovarian cancer cell line A2780, developed after treatment of the original cell line with the most commonly used medicaments: paclitaxel, carboplatin, cisplatin and doxorubicin.

Cell line A2780 was chosen as a model for investigation of drug resistance in ovarian cancer. Cells were maintained as monolayer in medium (RPMI) supplemented with 10% fetal bovine serum, 2 pmol/L L-glutamine and antibiotics (streptomycin and penicillin) at 37°C in a 5% CO_2 atmosphere.

Cell line was treated with different chemotherapeutic agents. The doses of the drugs were increased constantly with respect to resistance development. Different sublines were developed: A2780P, A2780Cis, A2780C, A2780D, treated respectively with paclitaxel (up to 900 ng/mL), cisplatin (up to 50 µg/mL), carboplatin (up to 15 µg/mL) and doxorubicin (up to 5 µg/mL). Flow cytometry was used to assess the cancer stem cell phenotype by staining cells with monoclonal antibodies against surface proteins CD24, CD44 and ESA.

Treated cells sublines were also analyzed for gene expression changes. After total mRNA extraction and cDNA synthesis, real time PCR was performed to evaluate the changes in expression of *PCNA, ASS, FN1, ATPB7, ATPB11, NOTCH3, MMP3, NACC1, ABCC1, ABCC5, ABCC10* genes.

The development of drug resistance was confirmed by the increase of the median lethal dose (LD50) in all treated sublines: 2,7-fold increase in A2780P, 1,75-fold increase in A2780Cis, 3,1-fold increase in A2780C and more than 5000-fold increase in A2780D.

The most pronounced changes in cell morphology were observed in sublines treated with cisplatin and doxorubicin. In addition, the major increase of stemness marker expression was also observed in these particular sublines. The expression of ESA increased from 20% in original cell line to 100% in both resistant sublines. The expression of CD44 increased from 0% in original cell line to 85% in A2780D and 95% in A2780Cis.

The major changes in gene expression were observed in *FN1, NOTCH3* and *MMP3* genes, especially in A2780Cis and A2780D sublines (Fig.1.). Proteins encoded by these genes are responsible for cell adhesion, migration, growth, differentiation, and integration in the tissue. Changes were also detected in *PCNA*, *ATPB7, ABCC1, ABCC5, ABCC10* genes. No significant changes were noted in *ASS* and *ATPB11* genes.

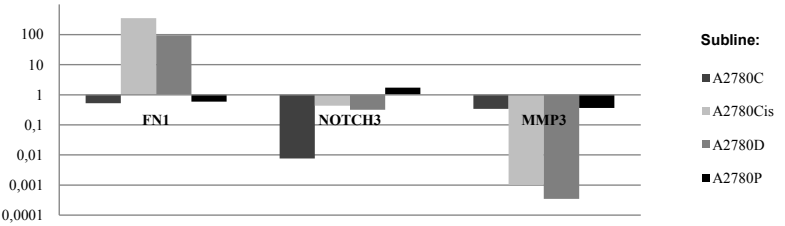

Fig.1. Gene expression changes in different ovarian cancer cell sublines in comparison to the original cell line.

The results imply that A2780 cell line is a suitable model for investigation of drug resistance in ovarian cancer. Significant increase in *FN1* gene and decrease in *MMP3* gene, together with increase in stemness marker expression and morphological change are characteristic for doxorubicin- and cisplatin-resistant sublines. It is necessary to further investigate these features in ovarian tumor specimens for confirmation and translation of the results into clinical practice.

[1] Siegel, R., Ma, J., Zou, Z., & Jemal, A. (2014). Cancer statistics, 2014. CA: A Cancer Journal for Clinicians, 64, 9–29. doi:10.3322/caac.21208
[2] Januchowski, R., Zawierucha, P., Ruciński, M., Nowicki, M., & Zabel, M. (2014). Extracellular matrix proteins expression profiling in chemoresistant variants of the A2780 ovarian cancer cell line. BioMed Research International, 2014. doi:10.1155/2014/365867

INFLUENCE OF METHYL-*β*-CYCLODEXTRIN ON *m*THPC INTERACTION WITH BLOOD COMPONENTS

Igor Yankovsky[1,2*], Ilya Yakovets[1], Ivan Khludeyev[1], Lina Bezdetnaya[2],Vladimir Zorin[1]

[1] Belarusian State University, Belarus
[2] CNRS, CRAN, University of Lorraine, Lorraine Cancer Institute, France
[*] *lubom@tut.by*

Photodynamic therapy (PDT) is a minimally-invasive photochemical-based approach that uses a combination of a light-activated drug (photosensitizer, PS) and the light of a specific wavelength to damage the target tumor tissue by generating reactive oxygen species [1]. meta-tetra(hydroxyphenyl)chlorin (mTHPC) is a highly efficient PS, clinically approved and used as a solvent-based formulation (Foscan®, Biolitec Research GmbH, Jena, Germany) for the PDT treatment of head and neck cancers [2]. Low solubility of mTHPC in aqueous solutions represents serious limitation for its application in clinical practice. mTHPC may form large-scale aggregates and precipitates just after injection [3]. It leads to reduced efficacy, induces pain upon administration and prolonged skin photosensitivity. Furthermore, mTHPC demonstrates extremely low rate of distribution between different biological structures. One of the possible ways to enhance the aqueous solubility of drugs is application of cyclodextrins (CDs). CDs are a well-known family of cyclic oligosaccharides with a hydrophobic internal cavity. CDs have already been used as carries for several drugs to improve stability against chemical and photochemical degradation and are suggested to be perspective formulation for introduction of apolar porphyrin during PDT.[4]. It is well known that mechanisms of PS transport in blood play an important role in the control PS biodistribution during PDT. PS localization in different tissues strongly depends on the its binding and distribution of the drug among blood components (serum proteins, blood cells) [5]. The aim of our study was to estimate the influence of methyl-β-cyclodextrin *(*m-β-CD) on mTHPC biodistribution in blood.

mTHPC provided by Biolitec Research GmbH (Germany). All CDs were from AraChem (Nederland). mTHPC accumulation in blood cells was measured by flow cytometer FC500 (Beckman Coulter).

mTHPC forms readily an inclusion complexes with different types of CDs. We estimated the stoichiometry ratio and apparent constant binding for this process. It was obtained that the values of the apparent constants for the complexes between mTHPC and m-β-CD are very high: $K_{1:1} \approx 1.6 \times 10^7$ M^{-1} for mTHPC : m-β-CD complexes and $K_{1:2} \approx 1.5 \times 10^6$ M^{-1} for mTHPC : 2 m-β-CD complexes.

We have studied aggregation state and distribution among different proteins of mTHPC after its introduction into human serum samples. After introduction mTHPC molecules form aggregates existing in sample for several hours. After 4-6 hours of incubation the most part of mTHPC disaggregates and bounds to serum proteins. By size-exclusion gel chromatography it was shown that in serum mTHPC preferentially (more 95%) bound to lipoproteins. Introduction of m-β-CD into serum sample significantly accelerates the process of mTHPC disaggregation. In the presence of $3*10^{-5}$ M m-β-CD mTHPC disaggregation takes only 20 minutes. CD has no influence on mTHPC distribution among different proteins. When m-β-CD concentration is above $3*10^{-5}$ M a part of mTHPC molecules redistributes from serum proteins to CDs complexes. This is in accordance with an appearance of new mTHPC peak of chromatography elution curve in the region of high exclusion volumes

We have estimated the effect of CDs on mTHPC distribution between plasma and blood cells. It was obtained that m-β-CD introduction into whole blood has different effects on the mTHPC accumulation by erythrocytes and leukocytes. Only slight increase of mTHPC accumulation is observed in erythrocytes (~1.2 times) while in the case of leukocytes a significant (~3.5 times) growth of intracellular PS accumulation is detected. This acceleration effect is strongly dependent on m-β-CD content in blood. It rises until m-β-CD concentration in blood is less then $2*10^{-5}$ M and goes down at higher concentration. When CD content in blood exceeds $2*10^{-4}$ M, mTHPC uptake by cells becomes less as compared with control sample.

The data obtained indicate that m-β-CD has different effects on mTHPC distribution in blood and can be used for modification of its pharmacokinetics. We will discuss the role of CD characteristics on kinetic and equilibrium distribution of mTHPC in vasculature and estimate an ability of improving the current PDT treatment protocols with CD.

Acknowledgements. This work was supported by Belarusian Foundation for Fundamental Research (grant М12ФП-002).

[1] Agostinis P, Berg K, Cengel KA, et al. Photodynamic therapy of cancer: an update. CA Cancer J Clin. 61(4):250–281 (2011).
[2] Senge MO, Brandt JC. Temoporfin (Foscan®, 5,10,15,20-tetra(m-hydroxyphenyl)chlorin) – a second-generation photosensitizer. PhotochemPhotobiol. 87(6):1240–1296 (2011).
[3] S. Sasnouski, V. Zorin, I. Khludeyev, M. A. D'Hallewin, F. Guilleminand L. Bezdetnaya, Investigation of Foscan interactions with plasmaproteins, Biochim. Biophys. Acta, Gen. Subj, 1725: 394–402 (2005).
[4] T. Loftsson and M. E. Brewster. Drug Solubilization and Stabilization by Cyclodextrin Drug Carriers. Drug Carriers, in Drug Delivery Strategies for Poorly Water-Soluble Drugs (eds D. Douroumis and A. Fahr), John Wiley & Sons Ltd, Oxford, UK. 67-101 (2013).

DETERMINATION OF HIDDEN PARAMETERS OF SIGNAL TRANSDUCTION IN SYNAPSES

Maryna Hliatsevich, Pavel Bulai, Taras Pitlik

Department of Biophysics, Physics Faculty, Belarusian State University, Belarus
gletsevich.marina@gmail.com

Mathematical modelling of signal transduction between neuronal cells in the brain is one of the most challenging problems in the modern neuroscience. The characteristics of this signal transduction (synaptic transmission, ST) determine the work of the neural networks and the brain as a whole. The importance of complete understanding ST has led to development of a variety of different models describing this process and each model has its own limitations and area of practical application.

Previously we have reported the deterministic model of ST which represents the system of the ordinary differential equations [1]. Each equation describes the content changes for the following biochemical participants: gates of ionic channels, calcium ions, calcium sensor – synaptotagmin protein, different pools of synaptic vesicles, proteins of exocytosis machinery, neurotransmitter – glutamate, states of neurotransmitter receptors. The Cauchy problem for the given system is solved numerically and this model can simulate the synaptic current provided by the channels of ionotropic neurotransmitter receptor.

The synaptic current can be regarded as a principal signal in ST. However experimentally ST is usually investigated with the help of microelectrode technique. This technique implies the electrical stimulation of neuronal ensemble in the definite area (CA3) of hippocampal slice. The stimulation signal undergoes ST from neuronal ensemble in CA3 to another one, placed in CA1. Synaptic currents generate action potentials on the dendrite membrane of neurons in CA1 area. The summed signal from the neuronal ensemble is registered as field excitatory postsynaptic potential (fEPSP) and one may choose conditions of stimulation when fEPSP is substantially determined by synaptic currents.

We chose the described method and conditions for experimental verification of our suggested model. To make verification procedure relevant we have taken into account the mechanism of fEPSP formation and constructed the equivalent scheme of connection between neuron and microelectrode. The synaptic current calculated in previously described model of ST was regarded as source of current in the elaborated scheme. Such approach enabled us to get good coincidence between forms of measured and simulated fEPSP.

Suggested model of ST includes many parameters that determine the result of model simulation. These parameters are rate constants of biochemical reactions, rates of binding and unbinding of agonist from receptors, surface densities of regarded proteins and so on. The majority of parameters' values can be found from the experimental measurements, but part of parameters can not be measured directly (hidden parameters). Furthermore, experimental determination of some parameters is technically complicated and does not give accurate result. Our model can suggest another way of parameters' values establishment: the exact approximation of experimentally measured fEPSP form by results of model simulation can be achieved if only the model parameters are adequate. Therefore we aimed was to find parameters' values that give the best coincidence between experimental and modelling results.

The standard deviation of simulated signal from experimentally registered one was regarded as a measure of coincidence and we searched for parameters' values that give the minimum of this objective function. The parameters' values determined with the help of such approach are listed in the Table 1.

Table 1. Determined values of model's parameters.

parameter	determined value
the bouton surface to its volume ratio	12 μm^{-1}
apparent maximal conductance of single calcium channel	8 pS
forward rate constant for active SNARE complex formation	$1.1 \cdot 10^{-3}$ ms^{-1}
forward rate constant for synaptic vesicles transition from docked to primed pool	$5.0 \cdot 10^{-6}$ ms^{-1}
time constant for inactivation of synaptic vesicles	3.3 ms
rate constant of glutamate clearance from synaptic cleft	45 ms^{-1}
rate constant of AMPAr's channel opening	1.7 $mM^{-1} \cdot ms^{-1}$
rate constant of AMPAr's channel closing	0.45 ms^{-1}

At present the main goal of our investigation is comparison of simulated effects of ST inhibitors and experimental ST inhibition. This approach is supposed to make possible the establishment or updating more biochemical parameters of ST.

Suggested model provides ways of finding the set of parameters with the help of only one experimental technique and can be useful for the approbation of neuroactive drug candidate.

This work was supported by Belarusian Republican Foundation for Fundamental Research.

[1] M.A. Hliatsevich, P.M. Bulai, T.N. Pitlik et al., Design of Deterministic Model of Signal Transduction between Neuronal Cells. Mathematical Modelling and Analysis **20**, 76-93, (2015).

Oral session 11

Astrophysics and astronomy

The search for T-type brown dwarfs

Krzysztof Domogała[1]

[1]Toruń Centre for Astronomy, Nicolaus Copernicus University, Poland
domogala@astri.umk.pl

Brown dwarfs are substellar objects which, due to their low mass, fail to initial and maintain hydrogen fusion during the initial collapse. Although it was predicted of their existing in 1960s, [1] they were discovered in the mid 1990s for the first time. The discovery of brown dwarfs brought about the increase spectral classes by three new spectral types: L, T [2] and Y [4]. In spite of intensive researching, many questions have still left without answer. Formation process and rare occurrence as as companion to star have not been solved yet. Their number and distribution in the universe are also open to question. The only way to find answer to this and other questions is a constant search for new brown dwarfs. We present the method and results of the search for brown dwarfs conducted in July 2014. Our method is based on wide-field searches and photometric properties of brown dwarfs which is now the most pupular and efficient approach.

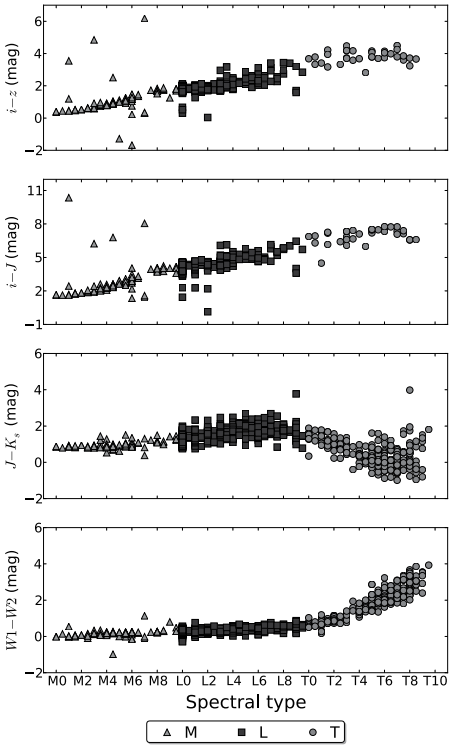

Fig. 1. Photometric colors versus spectral type for near-infrared system. The data come [5] and [6].

[1] Kumar, S. S., Models for Stars of Very Low Mass, Institute for Space Studies Report Number X-644-62-78 (1962).
[2] Kirkpatrick, J. D., New spectral types L and T, Annual Review of Astronomy and Astrophysics **43** 95-245 (2005)
[3] Kirkpatrick, J. D. et al., Further Defining Spectral Type "Y" and Exploring the Low-mass End of the Field Brown Dwarf Mass Function, The Astrophysical Journal **753** (2012)
[4] Reid, I. N. and Hawley, S. L., *New light on dark stars: red dwarfs, low-mass stars, brown dwarfs* (Springer, UK, 2005)
[5] Johnstons Dwarf Archive, Web. 2014-07-1
[6] DwarfArchives, Web. 2014-07-1

Supermassive Black Hole Accretion Disc Winds

Rokas Naujalis[1,2], Kastytis Zubovas[2]

[1]Faculty of Physics, Vilnius University, Lithuania
[2]Center for Physical Sciences and Technology, Vilnius, Lithuania
rokasn@yahoo.com

Active galactic nuclei are some of the most luminous objects in the universe and are thought to be powered by accretion of matter on to a super massive black hole (SMBH). Since accreting matter has a certain amount of angular momentum it forms an accretion disc around the SMBH instead of freely falling to the centre. Viscous forces inside the disc cause an outward transfer of angular momentum. This means that some of the matter inside the disc loses angular momentum and moves closer to the centre of the disc while the rest of the matter gains angular momentum and moves away from the centre. Viscosity also generates large amounts of heat that can be released as thermal radiation. When the radiation intensity inside the disc becomes strong enough, the force resulting from radiation pressure can accelerate matter to velocities high enough for it to escape SMBH thus creating so-called line-driven winds. Line driving happens when spectral lines of an atom absorb the momentum of radiation; this process accelerates the atom. Such winds can blow away large amounts of matter away from the disc creating massive outflows that can reach kpc scales and influence the evolution of the surrounding galaxy. Present-day galactic scale models that calculate these outflows assume that only a fixed portion of energy generated by the accretion of matter on to the SMBH is radiated away or used to drive the outflows. Our aim is to study the dependence of line-driven wind properties on different accretion rates into the disc.

To study line-driven winds we use a one-dimensional hydrodynamics code that integrates accretion disc evolution equations derived in [1]; viscosity inside the disc is calculated according to the α prescription [2]. The rate of the wind-induced matter outflow is calculated using the nozzle function derived in [3] that takes into account the geometry of the wind. Wind geometry is calculated using methods described in [4]. The wind is launched from the accretion disc in direction ranging from 16° at the centre and up to 45° at the edge of the disc with respect to the normal of the disc plane.

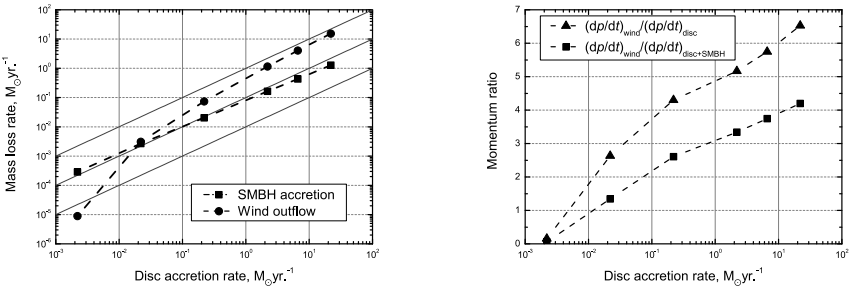

Fig. 1. (a) Maximum accretion rate on to the SMBH (squares) and mass loss rate due to wind (circles) as a function of the accretion rate into the disc. Solid lines represent 1%, 10% and 100% of the accretion rate into the disc respectively. (b) Ratio between rate of momentum carried by wind and disc radiation (triangles) or disc plus SMBH radiation (squares).

We analyze models with disc accretion rates ranging from $0.0022\,M_\odot yr.^{-1}$ to $22\,M_\odot yr.^{-1}$. The accretion rate is constant throughout each simulation and the central SMBH mass is fixed at $10^8\,M_\odot$ in all simulations. In Fig. 1a we can see that the wind becomes more important as the disc accretion rate becomes higher. At the highest disc accretion rate ($22\,M_\odot yr.^{-1}$), the wind outflow rate reaches $\sim 70\%$ of the disc accretion rate while at the lowest accretion rate it is less than 1%. This can be explained by higher densities (and in turn higher viscosity) inside the disc that result in higher temperatures and more intense thermal radiation that can accelerate larger amounts of matter. Additionally, since most of the matter is blown away by the wind only $\sim 5\%$ of the matter fed into the disc reaches the SMBH. At the same time, the momentum carried by the wind, at the highest disc accretion rates is up to ~ 6.5 times higher than the momentum of the disc radiation (Fig. 1b). This shows that the wind can be optically thick to UV radiation.

[1] Pringle J. E., 1981, ARAA, 19, 137
[2] Shakura N.I., Sunyaev R.A., 1973, A&A, 24, 337
[3] Kusterer, D. J., 2008, PhD thesis, Stuttgart
[4] Feldmeier, A., ir Shlosman, I. 1999, ApJ, 526, 344

Unusual morphologies of giant radio sources

Katarzyna Rusinek[1]

[1]Toruń Centre for Astronomy, Nicolaus Copernicus University, Poland
krusinek@astro.umk.pl

Active galactic nucleui (AGN) are compact central regions of galaxies. Their luminosities are much higher than these in normal galaxies. Moreover this parameter vary on very short timescales (less than a day) what puts tight constraints on the size of the emitting region as few light-days in diameter. The explanation is simple – the most efficient conversion of matter to energy is the accretion by a black hole which is in the center of AGN.

The picture below (Fig. 1) presents the scheme of AGN with the most popular division – the radio-loud/radio-quiet dichotomy and some subclasses of it.

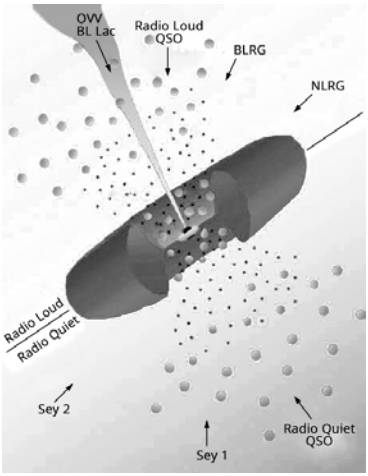

Fig. 1. Components of AGN. *Source:* [1]

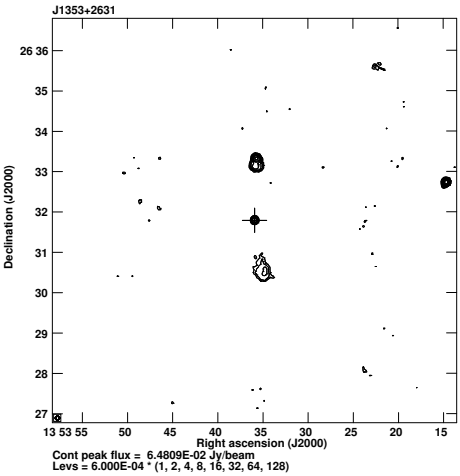

Fig. 2. J1353+2613 – an example of GRS. Radio map from FIRST made with AIPS tool.

Radio loud AGNs with radio structures of enormous linear sizes, which projected linear sizes larger than 0.72 Mpc [2], are labelled giant radio sources (GRS, Fig. 2). Using the radio images of 60 GRSs extracted from FIRST (Faint Images of the Radio Sky at Twenty-Centimeters) and NVSS (The NRAO VLA Sky Survey) surveys, we found a few objects whose radio morphologies are nonstandard.

Here, we present examples of sources whose particular components appear to be at different stages of the source's evolution – in the transition from RL to RQ state. This is a firm evidence for AGN recurrent activity. Some GRSs belong to the double-double radio galaxy, due to a pair of double lobes with a common centre. The one of subclasses, sources with a strong central component and two visible lobes (classified as Fanaroff-Riley II sources [3]), are known as core-dominated triple. The radio lobes of two of the selected objects have a strange distribution which is hard to interpret and one object is characterized by well-developed morphology.

[1] Oswalt T. D., Perlman. E. S., *Planets, Stars and Stellar Systems. Volume 6: Extragalactic Astronomy and Cosmology* (Springer, 2013).
[2] Kumicz A., & Jamrozy M., Optical and radio properties of giant radio quasars: central black hole characteristics, MNRAS, 426, 851 (2012).
[3] Fanaroff, B. L., & Riley, J. M., The morphology of extragalactic radio sources of high and low luminosity, MNRAS, 167, 31P (1974).

EVOLUTION OF INTERSTELLAR MEDIUM IN ISOLATED DWARF GALAXIES

Kostas Sabulis[1,2], Kastytis Zubovas[1]

[1]Department of Fundamental Research, Centre for Physical Sciences and Technology, Lithuania
[2]Faculty of Physics, Vilnius University, Lithuania
kostas.sabulis@ftmc.lt

Dwarf galaxies are comprised of similar components as their bigger counterparts - a stellar component, a gas component and a dark matter halo. Usually such systems are dominated by dark matter and the stellar component is the most understated. Isolated dwarf galaxies tend to have a very low star formation rate and this results in such systems being rich in gas and having a low metallicity content. This makes dwarf galaxies an ideal target to study star formation on the Hubble timescale [1]. One of the main approaches to investigating the evolution of these objects is numerical modelling. Weak or no interaction with neighbouring galaxies makes isolated dwarf galaxies easier to model since there is no need to account for interaction or mergers. Depending on the choice of technique one can follow evolution of different galaxy components, e.g. one would employ a N-body code to follow the evolution of the stellar component. Numerical modelling provides insight into long-term evolution of galaxy components, their interplay and morphology of resulting systems [2]. The end result strongly depends on physics included in the simulations and the choice of initial conditions. Which physical processes govern star formation, to some extent, remains an open question. In low mass systems, like dwarf galaxies, stellar feedback is extremely important, it heats up the gas and quenches star formation making a galaxy dormant and stopping the birth of new stellar systems. The main sources of feedback in young stellar systems are supernova explosions, photoionising radiation and stellar winds.

The main topic of this work is feedback produced by photoionising radiation. We present a new method of modelling photoionising radiation feedback in SPH (smoothed particle hydrodynamics) codes, which was implemented into an SPH/N-body code **Gadget-3** (a newer version of the publicly available **Gadget-2** [3]). We performed convergence tests in order to estimate the optimal resolution for resolving gas regions heated by photoionising radiation. Our model was checked against the analytical solution [4] and a good agreement was found. A series of test cases with different intensity of radiation source and different molecular cloud parameters were modelled. The influence of radiation feedback on various turbulent and static gas distributions was explored. These test results were used to calibrate our model and roughly estimate the effects of photoionising radiation feedback from a single source.

Next, we set up idealised initial conditions for a dwarf irregular galaxy and calculated a rudimentary model of its evolution without any form of stellar feedback. This model is our reference model and we compare all of our following calculations with additional physics against it. Next step was to compare models with additional feedback mechanisms and determine which combination of our modelled effects best reproduces an isolated dwarf irregular galaxy. The resulting morphology and spatial distribution of stellar populations of various ages is the main object of this work. Our ultimate goal is to create a realistic dynamical model of the low-mass isolated dwarf irregular galaxy Leo A and employ it to recreate the evolution of this slowly star forming galaxy.

[1] V. Vansevičius et al., *Full-Fledged Dwarf Irregular Galaxy Leo A* (ApJ, 2004)
[2] G. S. Stinson et al., *Feedback and the formation of dwarf galaxy stellar haloes* (MNRAS, 2009)
[3] V. Springel, *The cosmological simulation code GADGET-2* (MNRAS, 2005)
[4] B. Strömgren, *The Physical State of Interstellar Hydrogen* (ApJ, 1939)

Oral session 12

Theoretical physics

A STUDY OF THE FLUCTUATING INITIAL STATES OF THE HEAVY ION COLLISIONS AT LHC ENERGIES

Monika Venčkauskaitė[1], Karolis Tamošiūnas

[1] Vilnius University, Institute of Theoretical Physics and Astrophysics, A. Goštauto st. 12, 01108 Vilnius
monika.venckauskaite@gmail.com

For a first few milliseconds after the Big Bang, the Universe was filled with hot and dense matter of deconfined quarks and gluons. This state of matter is called a quark-gluon plasma (QGP). In this system strong interaction reinteracts macroscopically and is not localised in a hadron as in ordinary matter.

Similar conditions to those of the very early Universe, can be created in particle accelerators when heavy ions collide. During lead or gold nuclei collision hundreds of protons and neutrons that make up the colliding nuclei are smashed into one another at energies of up to a few teraelectronvolts per nucleon. Inside this system the QGP can be created.

QGP due to its nature cannot be detected in the particle accelerators directly. However, it is possible to study its properties from particle distributions, which are created after the hadronization of QGP.

We examine the fluctuating initial conditions of heavy ion collisions at LHC ($\sqrt{s_{NN}}=2760$ GeV) and RHIC ($\sqrt{s_{NN}}=200$ GeV) energies. We show that it is possible to separate influence of fluctuations and collective dynamics to the Fourier expansion coefficients which can be measured by the experiment. We use the initial conditions to start the hydrodynamical evolution of the system and compare calculated particle multiplicity distributions and elliptic flow rapidity dependence with the experimental data.

It will be shown, that using Glauber Monte Carlo model as the initial state (Fig. 1, Fig. 2) for the hydrodynamic evolution based on the approximate Landau solution we obtain particle multiplicity distribution and elliptic flow parameter distribution. Moreover, obtained results are in good agreement with the experimental data from LHC and RHIC colliders for a different impact parameters and at different collision energies.

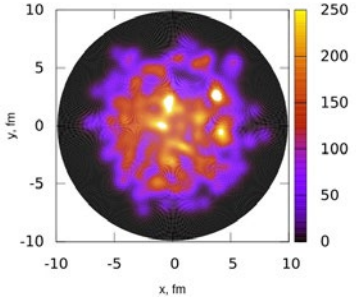

Fig. 1. Energy density distribution of central lead-lead ion collision of $\sqrt{s_{NN}}=2.76$ TeV.

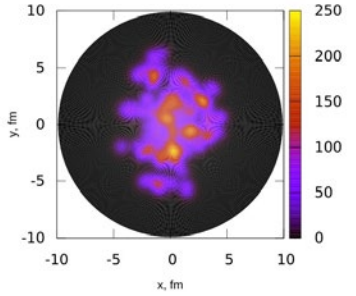

Fig. 2. Energy density distribution of peripheral lead-lead ion collision of $\sqrt{s_{NN}}=2.76$ TeV.

[1] K. Tamošiūnas, Eur. Phys. J. A (2011) 47: 121.

BFKL Formalism in Quantum Chromodynamics Applied for the Jet-Gap-Jet Processes in Hadron Collisions at High Energies

Paula Świerska[1]

[1]Faculty of Physics, Mathematics and Computer Science, Cracow University of Technology, Poland
Swierska.Paula@student.pk.edu.pl

In the majority of an events in hadron-hadron collisions an object exchanged between the interacting protons is a quark or a gluon. Such exchange typically results in a multiparticle final state distributed over several units of rapidity. These types of interactions are not the only possibilities. An object exchanged in t-channel can be also a colour-singlet. Such a process is expected to yield events containing a rapidity gap, *i.e.* a region in rapidity devoid of particles. One of the best candidates for such colour singlet is the Balitsky-Fadin-Kuraev-Lipatov (BFKL) Pomeron[1].

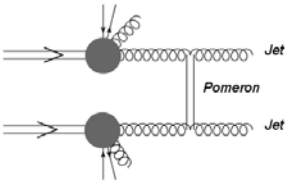

Figure 1. Diagram of the Jet-Gap-Jet production.

For more than 20 years a large effort has been devoted to understand the QCD dynamics of rapidity gaps in jet events when there is a rapidity gap between two high-pT jets. One can immediately realise that in such a process, due to the colour singlet exchange, no particles are produced between the leading jets. This gives a clear experimental signature.

Despite of the fact that the studies of Jet-Gap-Jet events were performed at the Tevatron[2], there is still no consensus on what the relevant QCD mechanism really is. The LHC accelerator opens a possibility to shed more light on this topic. In the presented work the theoretical description of this process as well as the predictions for the LHC experiments will be discussed.

To compute the JGJ process in the BFKL framework several issues need to be addressed. For example, the problem of coupling of the BFKL Pomeron to partons, has to be solved. This is usually done using the Mueller-Tang (MT) prescription[3]. Nevertheless, it is known that the original MT calculations did not describe the data properly[4]. In addition, one needs to take into account the soft interactions which in hadron-hadron collisions can destroy the rapidity gap as well as the next-to-leading-logarithmic (NLL) corrections which are known to be large[5]. In the presented work an additional need of using the full BFKL kernel with sum over the all so-called conformal spins will be explained.

Implementation of the BFKL formalism in the form of a Monte Carlo generator will be presented. In particular, the extension to jet transverse momentum up to 1000 GeV (available at the LHC energies) will be discussed.

Finally, the measurement of the ratio of the Jet-Gap-Jet cross section to the non-diffractive inclusive jet cross section, will be presented as a way to identify BFKL effects at high energies. During the talk the predictions of various theoretical models will be shown and the possibilities of their experimental tests will be discussed.

[1] L. N. Lipatov, Sov. J. Nucl. Phys. **23**, 338 (1976);
E. A. Kuraev, L. N. Lipatov and V. S. Fadin, Sov. Phys. JETP **45**, 199 (1977);
I. I. Balitsky and L. N. Lipatov, Sov. J. Nucl. Phys. **28**, 822 (1978).
[2] The D0 Collaboration, Phys. Lett. B **440**, 1998
[3] A. H. Mueller and W. K. Tang, Phys. Lett. B **284**, 123 (1992)
[4] F. Chevallier, O. Kepka, C. Marquet, C. Royon, Phys. Rev. D **79** 094019, 2009.
[5] O. Kepka, C. Marquet, C. Royon, Phys. Rev. D **83** 034036, 2011.

DEVELOPING WEYL SPINOR FORMALISM FOR SEESAW NEUTRINOS

Vytautas Dūdėnas[1,2], Thomas Gajdosik[1,2]

[1]Department of Theoretical Physics, Vilnius University, Lithuania
[2]Institute of Theoretical Physics and Astrophysics, Vilnius University, Lithuania
vytautas.dudenas@tfai.vu.lt

Despite the tremendous success of the Standard Model, there is no doubt that it cannot be a complete theory due to a numerous experimental evidences for which the SM fails to find an explanation. One part of these experimental evidences are the observation of neutrino oscillations (for a short review of these experiments see ref. [1]). This proves that at least two of the neutrinos have masses, but the original assumptions of the SM forbids these mass terms. This proves that the neutrino and (possibly) Higgs sectors should be extended with some new degrees of freedom (new particles), to allow for a possibility for neutrinos to have mass.

The simplest "building blocks" for a fermionic particle content are Weyl spinors. Thus the model building is usually done in Weyl spinor notation. However, nearly for all practical calculations the Dirac spinors are used. In chiral representation they are equivalent for two independent Weyl spinors. For the case of having one massive Weyl spinor in a theory, the formulation is done with implying a condition on the Dirac spinor to get a Majorana spinor. The main difference can be easily seen if you build these spinors from Weyl spinors:

$$\psi_D = \begin{pmatrix} \chi \\ \xi^\dagger \end{pmatrix}, \ \psi_M = \begin{pmatrix} \chi \\ \chi^\dagger \end{pmatrix},$$

where χ, ξ are Weyl spinors and ψ_D, ψ_M are Dirac and Majorana spinors, respectively. In the SM, there is no difficulty to find this correspondence of formalisms from Weyl to Dirac, since all the particles that have mass come in pairs of Weyl spinors that have the same mass term generated by Higgs mechanism. The massless neutrino comes only in the electroweak interactions and has no coupling with the Higgs, so its treatment as a massless Majorana spinor doesn't give any complications as well. But when considering how to extend the SM with neutrino masses, the correspondence between these two formalisms becomes not so trivial.

Considering one family for simplicity, the easiest way to let the neutrino have a mass is to postulate an additional neutral Weyl spinor that can interact with a SM neutrino and the Higgs. It's neutrality allows it to have an additional mass term as well, that doesn't come from the Higgs mechanism. (When this additional mass term is taken to be large, it is called the seesaw mechanism of type I. For an overview of seesaw models see ref. [2]) Without the latter mass term, we could trivially write the neutrino as a Dirac spinor (just as the electron). Without the interaction between two spinors, we would have two uncoupled Weyl spinors that can be written as Majorana spinors, but the observed neutrino wouldn't have a mass and this additional particle couldn't be observed in principle. So for this extension we have something in between of pure Dirac and Majorana case. By going into mass eigenstate basis, we can mix these spinors to write them as two Majorana neutrinos, but of course, the relation is not so simple then. The analysis could prove to be simpler if the calculations would be held using Weyl spinors.

In this work we try to fill the mentioned gap between model building and practical calculations. Using the ref. [3], where this formulation for some SUSY calculations are presented, we concentrate on the seesaw extension of the SM. For simplicity, we take only one family, and develop techniques for analyzing seesaw neutrinos. For a consistent treatment of this formalism, we recheck notations using path integral formalism. Since the mass of the neutrino is related to its self energy, we do the one loop corrections for a propagator in general R_ξ gauge and discuss the renormalization in the spirit of rescaling parameters.

[1] K. M. Heeger, "Evidence for neutrino mass: A Decade of discovery," arXiv:hep-ex/0412032.
[2] G. Senjanovic, "Neutrino mass: From LHC to grand unification," Riv. Nuovo Cim. **34** (2011) 1.
[3] H. K. Dreiner, H. E. Haber and S. P. Martin, "Two-component spinor techniques and Feynman rules for quantum field theory and supersymmetry," Phys. Rept. **494** (2010) 1

LONG-RANGE SCALING IN GENERALIZED KURAMOTO-SIVASHINSKY EQUATIONS

Vaidas Juknevičius[1]

[1]Institute of Theoretical Physics and Astronomy, Vilnius University, Lithuania
v.juknevicius@yahoo.com

The two-dimensional Kuramoto-Sivashinsky equation (KSE) for some field $h(\boldsymbol{r},t)$ with an additional nonlinear term $\nabla^2(\nabla h)^2$ and a single independent parameter α can be written as:

$$\partial_t h = -\nabla^2 h - \nabla^4 h - \alpha\nabla^2(\nabla h)^2 + (\nabla h)^2 \tag{1}$$

It has KSE as a special case when $\alpha = 0$.

Equation (1), similarly to the simple KSE, serves as a model for evolution of intrinsically unstable interfaces and has been derived as a model for solid amorphous surface growth [1]. It produces disordered cellular patterns at small scales and slow variations of $h(\boldsymbol{r},t)$ at large scales (see Fig. 1).

One of the most important macroscopic quantities [2] to observe is the *surface roughness* $w(t)$ (also called the *surface width*) defined as the rms deviation of $h(\boldsymbol{r},t)$ from its mean value $\bar{h}(t)$ at time t:

$$w(t) := \sqrt{\left\langle \left(h(\boldsymbol{r},t) - \bar{h}(t)\right)^2 \right\rangle_{\boldsymbol{r}}} \tag{2}$$

It has been established that after an initial transient period (*crossover time* $t_\times$), the evolution of the surface according to (1) saturates, i.e., becomes stationary, (at least for parameter values $0 \le \alpha < 5$) and thus the long time average w_{sat} of $w(t)$ for some $t_0 \gg t_\times$ can be defined as:

$$w_{\text{sat}} = \lim_{T\to\infty} \left\langle w(t) \right\rangle_{t\in[t_0,t_0+T)} \tag{3}$$

Since the numerical simulations are performed on the finite size systems (with periodic boundary conditions), the system size L becomes an additional parameter of the problem.

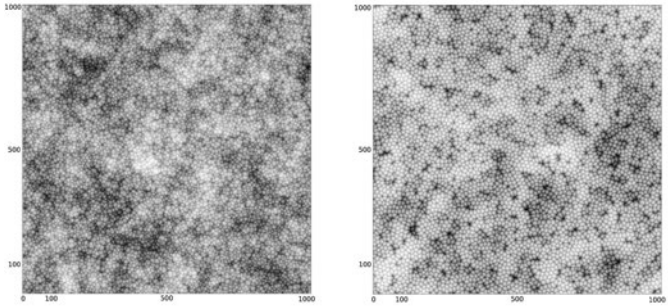

Fig. 1. Surfaces (h values coded in gray-scale) evolved according to (1) at time $t = 2\cdot 10^5$ (saturated regime) with parameter values $\alpha = 0$ (left panel) and $\alpha = 1$ (right panel). The surface spectra of these surfaces for small wave numbers has a power-law shape (4) with powers $\gamma = 1$ and $\gamma = 0.84$, respectively.

Numerical simulations of (1) exhibit dependence of w_{sat} (3) on the system size L. The results indicate power-law dependence of the spatial 'power-spectral density' $S(k)$ on the wave number k for small wave numbers (large distances):

$$S(k) \approx C k^{-\gamma} \quad \text{for} \quad k < k_{\text{s}} \tag{4}$$

This leads to a conclusion that, although cellular surface structures of definite scale dominate in the range of short distances and are independent of the system size (as long as it is at least several times larger than the average size of a single cell of the cellular pattern), there is also a scale-free long-range structuring present, as [3] suggests for KSE.

The dependence of the spectral power γ on the parameter α shows that the nonlinear term $\nabla^2(\nabla h)^2$ not only influences the evolution on small scales (the size and shape of cells in the cellular patterns), but also changes the large scale behavior in a definite way: it reduces the influence of small wave number modes, making the roughness w finite even for $L \to \infty$.

[1] M. Raible, S. J. Linz, P. Haenggi, Phys. Rev. E **64**, 031506 (2001).
[2] A.-L. Barabasi, H. E. Stanley, *Fractal concepts in surface growth* (Cambridge Univ. Press, Cambridge, 1995).
[3] C. Jayaprakash, F. Hayot, R. Pandit, Phys Rev. Lett. **71**, 12 (1993)

Influence of the strain distribution on non-radiative transitions in a quantum well-quantum dot system

Adam Mielnik-Pyszczorski, Krzysztof Gawarecki, Paweł Machnikowski

Department of Theoretical Physics, Wrocław University of Technology, Poland
adam.mielnik-pyszczorski@pwr.edu.pl

Lasers based on quantum dots (QDs) have many advantages such as low threshold current, wide spectral tunability and high temperature insensitivity. However, due to low carrier density inside the dot, the efficency of quantum dot lasers is reduced. One of the proposed solutions is a quantum well-quantum dot tunnel injection structure. The density of states in a quantum well (QW) is high, hence a QW can be used as a carrier-collecting reservoir [1,2]. The QW-QD system must be properly designed to ensure localization of its ground state in the dot. Then, with phonon-assisted processes, carriers can tunnel through the barrier from the QW to the QD.

In this contribution, we study phonon-assisted tunneling of electrons in a system composed of a dome-shaped QD placed above a QW (Fig.1). We assume the axial symmetry of the system which allows us to reduce the problem to two dimensions [3].

The strain distribution is accounted by minimization of the elastic energy of the system [4]. The electron states are calculated using **k·p** method combined with the Lödwin elimination [5]. It turns out that carriers in the QW effectively feel strain as a repulsive potential, which affects their wavefunctions.

Do not use fonts, smaller than 7 pt in figures (for example Fig. 1), graphs and tables or anywhere else in the document. All abbreviations should be fully introduced at their first appearance in the text.

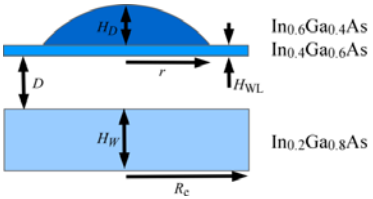

Fig. 1. The schematic cross-section of the system.

We study the effects of the electron coupling to the acoustic phonons and model the electron kinetics within the correlation expansion approach. We investigate the dependence of the phonon-assisted tunneling rate on the temperature. Our results indicate the importance of a proper design of the system geometry and composition to obtain the shortest relaxation times.

[1] W. Rudno-Rudziński, G. Sęk, K. Ryczko, M. Syperek, J. Misiewicz, E. Semenova, A. Lemaitre, and A. Ramdane, *Applied Physics Letters* **94**, 171906 (2009).
[2] Xiao-Jie Yang, Takayuki Kiba, Takafumi Yamamura, Junichi Takayama, Agus Subagyo, Kazuhisa Sueoka, and Akihiro Murayama, *Applied Physics Letters* **104**, 012406 (2014).
[3] K. Gawarecki, M. Pochwała, A. Grodecka-Grad, and P. Machnikowski, *Phys. Rev. B* **81**, 245312 (2010).
[4] C. Pryor, J. Kim, L. W. Wang, A. J. Williamson, and A. Zunger, *J. Appl. Phys.* **83**, 2548 (1998).
[5] P. O. Löwdin, *J. Chem. Phys.* **19**, 1396 (1951).

SIMULATION OF EXCITON EVOLUTION IN A SINGLE LIGHT-HARVESTING COMPLEX LH2

Tomas Marčiulionis[1], Darius Abramavičius[1], Gediminas Trinkūnas[2]

[1] Department of Theoretical Physics, Vilnius University, Lithuania
[2] Department of Molecular Compound Physics, Center for Physical Sciences and Technology, Lithuania
tomas.marciulionis@ff.stud.vu.lt

The detection of individual molecules has been applied in many areas of science – from molecular biology to quantum optics. The experimental ways of tracking the ultrafast dynamics in the molecules in time scale have emerged recently [1]. These methods have given the best opportunity yet to fully understand the processes of photosynthesis. New experimental data needs theoretical models which can explain the results of ultrafast spectroscopy experiments on single photosynthetic complex.

We have chosen to analyze the photosynthetic complex LH2 as it has very simple structure and its physical properties are well-known. Photosynthetic antenna is cylindrical, characterized by C_9 symmetry. Two rings can be seen in the structure of LH2 – the upper B850 ring and lower B800. B800 ring consist of 9 bacteriochlorophyll molecules and B850 is compounded of eighteen BChl molecules [2]. Recently the nature of electronic excitations created by photon absorption in the cyclic B850 aggregates of LH2 antenna complexes of photosynthetic bacteria has been thoroughly studied over a broad temperature range using absorption, fluorescence, fluorescence anisotropy spectra [3] as well as 2D coherent spectroscopy [4]. The steady state spectroscopic data is reproduced by consistent self-trapped exciton model which was developed on the basis of variational approach.

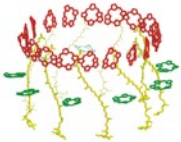

Fig 1. The structure of the LH2 light-harvesting complex. Only B850 aggregate (the upper ring) is considered in this work.

In this work, we extend the self-trapped exciton model into transient time domain. In order to follow the exciton evolution during its lifetime we assume that the slow protein dynamics at pigment sites triggered by fast exciton subsystem are governed by the Langevin equation:

$$\begin{cases} \cdots \\ M\ddot{u}_n + M\lambda\dot{u}_n + M\omega_0^2 u_n = \chi|\phi_n|^2 + \eta_n \\ (e_n + \chi u_n)\phi_n + \sum_{p\neq n} J_{np}\phi_p = E\phi_n \\ \cdots \end{cases} \quad (1)$$

Where, M is the molecular mass, u_n represents the elastic degree of freedom at site n, ω_0 is the frequency of the oscillations, χ – exciton-deformation coupling parameter. In order to describe the interaction of the deformation with the thermal reservoir at the temperature T, damping λ and noise η_n are included. E_n is the molecular site energy and J_{np} - is the excitonic interaction energy. ϕ_n is wave function's n-th element in the vector representation [5].

The simulations have showed very rich exciton behaviour which strongly depends on the environmental parameters and noise. Particularly, we have observed the rapid fluctuations of exciton size as well as its localization on different segments of the aggregate. The analysis of the corresponding simulated transient fluorescence spectra shows that they share many features observed in the experiments of single complex spectroscopy.

[1] D. Brinks, R. Hildner, E. van Dijk, F. D. Stefani, J. B. Nieder, J. Hernando and N. F. Van Hulst, Ultrafast dynamics of single molecules, Chem. Soc. Rev., Volume 43, 2476-2491 (2014).
[2] L. Valkūnas, D. Abramavičius, T. Mancal, Molecular Excitation Dynamics and Relaxation Quantum Theory and Spectroscopy, Wiley (2013).
[3] M. Pajusalu et al. ChemPhysChem 12, 634 (2011)
[4] O. Rancova, D. Abramavicius, J. Phys. Chem. B 118 7533 (2014)
[5] O. Bang, P. L. Christiansen, F. If, K. Ø. Rasmussen, Y.B. Gaididei, Temperature effects in a nonlinear model of monolayer Scheibe aggregates, Physical Review E, Volume 49, 4627-4636 (1994).

Poster session 1

TIN DIOXIDE NANOSTRUCTURES PREPARED BY TEMPLATE ASISTED SOL-GEL METHOD

Laurynas Alinauskas, Rimantas Raudonis, Edita Garskaite

Department of Applied Chemistry, Vilnius University, Lithuania
laurynas.alinauskas@chf.stud.vu.lt

Tin dioxide (SnO_2) is a n-type wide-band gap ($E_g = 3.6$ eV) semiconductor. SnO_2 porous nanostructures due to high surface to volume ratio have received considerable attention in many applications including lithium-ion batteries, photocatalysts, solar cells, medical diagnostics and chemical gas sensors [1-3].

Here we report a template assisted sol-gel synthesis route to prepare polycrystalline SnO_2 nanostructures [4, 5]. Polycarbonate membranes used as templates were removed by calcination at 550-1300 ºC. Sintering temperature, morphological features, phase composition and crystal structure of the SnO_2 nanostructures were studied by thermogravimetrical analyses (TGAs), scanning electron microscopy (FE-SEM) (shown in Fig. 1), transmission electron microscopy (TEM) and X-ray diffraction (XRD) techniques.

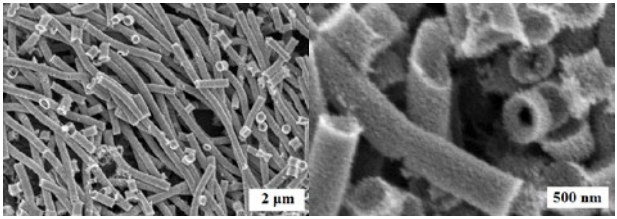

Fig. 1. FE-SEM micrographs of SnO_2 nanostructures annealed at 550 °C for 5 h.

In summary, nanostructures having narrow-size distribution and well-defined structural features were produced. Various processing conditions were examined and the initial cation concentration, organic additives, solution pH and processing temperature were found to affect the morphology and structural properties of final product. Smaller diameter and hollow nanotubes were produced from solutions of lower concentration.

[1] J. Xu et al., Synthesis, Characterizations and Improved Gas-Sensing Performance of SnO_2 Nanospike Arrays, J. Mater. Chem. **21** (47), 19086-19092 (2011).
[2] M. Batzill and U. Diebold, The surface and materials science of tin oxide. Prog. Surf. Sci. **79** (2-4) 47-154 (2005).
[3] J. Zhang et al., Reactive-Template Fabrication of Porous SnO_2 Nanotubes and Their Remarkable Gas-Sensing Performance, ACS Appl. Mater. Inter. **5** (16), 7893-7898 (2013).
[4] U. Lafont et al., Sol-Gel and Hard Template Assisted Synthesis of 3D Nanostructured SnO_2 Electrodes, J. Nanosci. Nanotechnol. **10** (7), 4273-4278 (2010).
[5] A. Stanulis et al., Sol–gel (Combustion) Synthesis and Characterization of Different Alkaline Earth Metal (Ca, Sr, Ba) Stannates, J. Sol-Gel Sci. Technol. **64** (3), 643-652. (2012).

A NOVEL POLYSTYRENE BINDING PEPTIDE FROM RANDOM PHAGE DISPLAY LIBRARY.

Dmitri Dormeshkin, Andrei Gilep, Sergey Usanov

Institute of Bioorganic Chemistry NAS Belarus, Belarus
Dormeshkin@gmail.com

Phage display technique revolutionized many areas of natural sciences from proteomics and drug design to nanomaterials and nanobioelectronics [1]. Phage display library is a useful system that allows the identification of peptidic ligands that bind directly to a wide variety of interested targets. The random sequences of the displayed peptides provide sufficient diversity, making it possible to select high affinity ligands against target protein that is routinely immobilized on polystyrene (PS) plate [2]. By an *in vitro* process known as biopanning, phage clones displaying peptides that specifically recognize the target are enriched in total phages pool.

In some cases, during the selection process peptide pool enriches by sequences binding the components of screening system. Identification of these sequences and their specific motifs help prevent false-positive results and choose the best conditions for peptide library enrichment.

The 12-mer phage display random peptide library was purchased from New England Biolabs (MA, USA). The library was generated from filamentous *Escherichia coli* phage M13, with random peptides being fused to N-terminus of the pIII coat protein. This library has the complexities of 10^9 independent phage clones and hence approximately 10^9 different peptide sequences. This is quite sufficiently in most cases for isolation specific ligands. The library was maintained and amplified in *E.coli* strain ER2738.

Peptide with amino acid sequence VHWDFRQWWQPS was observed in our lab periodically in different phage display experiments with different targets and blocking agents (bovine serum albumin, casein, peptone, non-fat dry milk). The database of target unrelated peptides SAROTUP deals with all reported and known patterns of target-unrelated peptides [3]. Web based analyses of peptide sequences using SAROTUP database does not reveal any remarkable correspondence to the polystyrene or blocking agent binders. A hydrophobic nature of peptide and its presence in peptide pool during various experiments led to the suggestion, that this peptide is a novel plastic binder, which could bind to an insufficiently blocked polystyrene.

An enzyme-linked immunosorbent assay (ELISA) and a phage elution assay confirmed that phage clone VHWDFRQWWQPS binds to polystyrene.

Such peptides can be used as affinity tags for site-directed immobilisation of proteins to plastic surfaces for example for ELISA system applications [4].

[1] G. Maruccio, A. Bramanti. Nanoelectronic Devices Based on Proteins, Nanobioelectronics for Electronics, Biology, and Medicine, 139-166 (2009).
[2] R. Derda, et al., Diversity of Phage-Displayed Libraries of Peptides during Panning and Amplification, Molecules 16, 1776-1803 (2011).
[3] J. Huang, et al., SAROTUP: Scanner and Reporter of Target-Unrelated Peptides, Journal of Biomedicine and Biotechnology, 132-139 (2010)
[4] B. Feng, Y. Dai. A novel affinity ligand for polystyrene surface from a phage display random library and its application in anti-HIV-1 ELISA system, Biologicals 37, 48-54 (2009).

SYNTHESIS OF THE OXIDE-ION CONDUCTORS AS ELECTROLYTES FOR SOLID OXIDE FUEL CELLS

Žygimantas Gricius[1], Artūras Žalga[1]

[1] Department of Applied Chemistry, Faculty of Chemistry, Vilnius University, Naugarduko Str. 24, 03225 Vilnius, Lithuania
zygimantas.gricius@chf.stud.vu.lt

During the last decade solid oxide fuel cells (SOFC's) have been intensely investigated as a next generation green energy system because they exhibit high ionic conductivity, chemical and thermal stability and also have high efficiency and generate low pollution emissions [1]. Recent SOFC's has been focused on the development of intermediate and low operating temperature range of 300-800 ºC considering long-term performance stability, high conversion efficiency, and low equipment material cost [2].

The most widely used ceramic in SOFC is yttria stabilized zirconium (YSZ) ceramic. It is a traditional fuel cell electrolyte and must typically be operated at high temperatures, due to its relatively high ionic resistivity at lower temperatures. Also this ceramic presents the metastable tetragonal phase which is essential for the structural hardening during cooling. Meanwhile, gadolinia-doped ceria (GDC, $Ce_{0.9}Gd_{0.1}O_{1.95}$) is considered to be one of the most promising electrolytes for SOFCs to be operated below 650 ºC [3]. Owing to high oxygen-ionic conductivity and good chemical compatibility, Gd-doped CeO_2-based ceramics are popularly an upcoming alternative to yttria-stabilized zirconia (YSZ) as solid electrolyte in intermediate and low temperature SOFC applications [4]. To address the significant problem with ceria based materials a number of approaches have been taken, such as finding the ideal doping level and ion to balance stability with adequate oxide ion conductivity, decreasing the operating temperature and improving materials processing etc [5].

The implement of these challenges could be successfully reached by using so-called solution-based synthetic methods, which play a crucial role in the design and production of fine ceramics, in addition, these methods have been successful in overcoming many limitations of the traditional solid-state, high-temperature methods.

In this study we report the aqueous sol-gel synthesis technique for the preparation of YSZ and GDC ceramics, which were additionally annealed at 700, 800, 900, 1,000, 1,100 and 1,200 ^{o}C temperatures. Moreover, in order to proof a difference between separate solid electrolytes the thermal decomposition of the as-prepared gels and the crystal phase stability according to the sintering temperature of the double oxides by thermogravimetric analysis, differential scanning calorimetry (TG–DTA) and X–Ray diffraction (XRD) measurements were additionally investigated. Besides, the research of the surface morphology and the characteristic vibrations of the functional groups by scanning electron microscopy (SEM) and Fourier transform infrared spectroscopy (FT–IR) were also performed.

[1] X. Zhou, J. Ma, F. Deng, G. Meng, X. Liu, Preparation and properties of ceramic interconnecting materials, $La_{0.7}Ca_{0.3}CrO_{3-\delta}$ doped with GDC for IT-SOFCs, Journal of Power Sources **162**, 279–285 (2006).

[2] Y.S. Hong, S.H. Kim, W.J. Kim, H.H. Yoon, Fabrication and characterization GDC electrolyte thin films by e-beam technique for IT-SOFC, Current Applied Physics **11**, S163-S168 (2011).

[3] C. Xia, M. Liu, Microstructures, conductivities, and electrochemical properties of $Ce_{0.9}Gd_{0.1}O_2$ and GDC–Ni anodes for low-temperature SOFCs, Solid State Ionics **152– 153**, 423– 430 (2002).

[4] Y. Dong, S. Hampshire, J. Zhou, G. Meng, Synthesis and sintering of Gd-doped CeO2 electrolytes with and without 1 at.% CuO dopping for solid oxide fuel cell applications, International Journal of Hydrogen Energy **36**, 5054–5066 (2011).

[5] M. G. Chourashiya, L. D. Jadhav, Synthesis and characterization of 10%Gd doped ceria (GDC) deposited on NiO-GDC anode-grade-ceramic substrate as half cell for IT-SOFC, International Journal of Hydrogen Energy **36** 14984–14995 (2011).

MOLECULAR DYNAMICS SIMULATION OF IONIC LIQUIDS

Kristina Jakubavičiūtė, Kęstutis Aidas

Dept. of General Physics and Spectroscopy, Faculty of Physics, Vilnius University, Lithuania
kristina.jakubaviciute@ff.stud.vu.lt

Room temperature ionic liquids (RTILs) are environmentally friendly solvents with unique chemical properties. They are chemically stable, electrically conductive, non-volatile at room temperature and their chemical and physical properties can be easily modified [1]. For applications of RTILs, it is very important to understand the relationship between the structure of the ionic compounds and properties of the underlying liquid. Molecular dynamics simulation is one of the means to find these links.

Molecular dynamics simulation is a very widely used method that allows us to model the structures and dynamics of different molecular systems. Reliability of results depends on the type of chosen force field which typically involves two types of interactions – electrostatic and van der Waals, which are described by Coulomb and Lennard-Jones potentials, respectively. The problem of force field parameterization is particularly relevant for simulating structure and dynamics of ionic liquids.

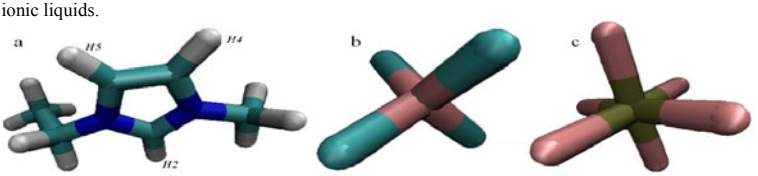

Fig. 1. Molecular structures of cation (a) 1-etil-3-metil-imidazolium [C2mim] and anions (b) tetrafluorborate [BF4] and (c) hexafluorophosphate [PF6].

In this work we have used Amber simulation software for molecular dynamics simulations. We have investigated three types of RTILs: [C2mim][BF4], [C4mim][BF4] and [C4mim][PF6] (Fig. 1). Force field parameters were taken from Z.Liu et al. [2]. The obtained results allowed us to calculate density of ionic liquids, radial distribution functions and diffusion coefficients. Estimated densities coincided with the results of [2] and the experimental results. We have typically simulated systems consisting of 128 ionic pairs, but also of 256 pairs. We have also varied the cut-off value of van der Waals interactions. In all these cases, the results were similar, which leads to the conclusion that the system consisting of 128 ion pairs is large enough to reliably estimate the structural parameters of the system.

Concerning radial distribution functions and coordination numbers, the most interesting are the H2, H4, H5 hydrogen atoms that are in the imidazole ring (Fig. 1) and the fluorine and phosphorus atoms of anions. It was noticed that the probability of finding any anion around H2, H4, H5 chemical elements is greater in [C2mim] case than [C4mim]. It is likely that this is due to a shorter alkylic chain, which in this case have a smaller impact on the movement of surrounding compounds. Coordination number of boron or phosphorus around atom H2 is almost 2. Looking at the boron or phosphorus radial distribution functions we observe more structured distribution of anions as compared to fluorine.

Table 1. Calculated diffusion coefficients of anions.

RTILs	D (10^{-11} m^2s^{-1})				
	Z. Liu et al.[2]	This work			
		128		256	
	10-50 ps	10-50 ps	40-100 ps	10-50 ps	40-100 ps
[C2mim][BF4]	0,9	3,79	4,24	2,21	1,75
[C4mim][BF4]	0,8	3,80	3,90	1,79	1,81
[C4mim][PF6]	1,0	3,10	3,53	1,80	1,73

We have also evaluated the anion diffusion coefficient (D) which allows us to evaluate how much material's center of mass per unit of surface diffuses in the time interval. The diffusion coefficient is found from the tilt of the linear part of the mean square displacement function (MSD). As shown in Table 1, our results differ from Z.Liu et al. [2] by 2 or even 4 times, depending on the number of ionic pairs participating in the simulation or the selected time interval. We can conclude that the authors of [2] for statistical diffusion coefficient calculation have chosen an insufficient amount of ionic pairs and too short time period for MSD. The best results are found by finding tilt function in MSD 40-100 ps. It is noticed that the diffusion coefficient of anions in ionic liquids is two orders of magnitude lower than the atomic ions (eg. for NaCl anion $D = 2*10^{-9}$ m^2s^{-1}), which shows that the center of gravity in ionic fluids diffuses much more slowly.

[1] Weingärtner H. Angew. Chem. Int. Ed. 2008, 47, 654-670
[2] Liu Z., Huang S., Wang W. J. Phys. Chem. B, 2004, 108 (34), 12978-12989

EVALUATION OF PRIMARY AND SECONDARY METABOLITES IN LUPINS (*LUPINUS* L.) *IN VITRO*

Rūta Laurinavičiūtė[1], Ilona Jonuškienė[2], Zita Maknickienė[3]

[1, 2]Department of Organic Chemistry, Kaunas University of Technology, Lithuania
[3]Voke Branch of Lithuanian Research Center for Agriculture and Forestry, Vilnius, Lithuania
ruta_laurinaviciute@yahoo.com

Introduction. Lupin (family *Fabaceae*) is cultivated for human nutrition because of their high protein and oil contents. Moreover, lupin is a promising candidate to be used for phytoremediation. In Europe, three species of lupin are commonly cultivated: *Lupinus angustifolius*, L. *albus* and L. *luteus*. Nowadays, the European agricultural focus is upon *Lupinus angustifolius*, the narrow-leafed lupin, due to its advantages compared to other lupin species: the highest resistance to anthracnose (fungal disease caused by *Colletotrichum gloeosporioides*), high yield and short vegetation period [1]. Plant primary and secondary metabolites are diverse group of molecules that are involved in biochemical pathways, cell growth and reproduction, adaptation of plants to their environment. Interest in plant secondary metabolites has risen dramatically in recent years of their diverse effects, include antioxidant, antiviral, antibacterial and anticancer effects. The goal of the research was to optimize the growth of lupins *in vitro*, using plant biotechnological methods and to determine primary and secondary metabolites.

Materials and methods. This research was carried out at Kaunas University of Technology, Faculty of Chemical Technology, Department of Organic Chemistry, at Biotechnology laboratory. In this research annual lupins and hybrid lupins varieties were explored: VB *Vilniai*, VB *Derliai*, *Trakiai*, *Hybrid* number 1772 (Deter), which were derived in Lithuania (Voke Branch of Lithuanian Research Center for Agriculture and Forestry, Vilnius). Protein content was explored by the Bradford method [2]. Flavonoids were determined by spectrophotometry [3].

Results. The amount of protein in lupins, which were grown in MS media *in vitro***.** The results showed that the highest protein content was determined in lupins *Trakiai*, which were grown in MS medium – 18.53 % and the lowest in *Hybrid* lupins - 4.86 %. Their amount was 3.8 times higher in *Trakiai* in comparison with *hybrid* lupins.

The amount of flavonoids in lupins *in vitro*. The results showed (Fig. 1.), that the highest flavonoid content was determined in *Hybrid* and lupins *Derliai* cultivated on MS medium *in vitro* - 0.8 mg/g, and the lowest in lupins *Vilniai* - 0.6 mg/g.

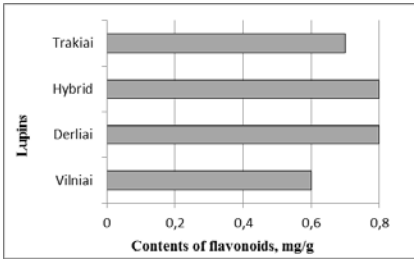

Fig. 1. Flavonoid content in lupins *in vitro*

Conclusions

1. It was established that the highest protein content was determined in lupins *Trakiai*, which were grown *in vitro* in MS medium – 32 %.
2. It was found that the highest amount of flavonoids was in *Hybrid* and *Derliai* lupins *in vitro* - 0.8 mg/g.

[1] K. Kozak, R. Galek, M. T. Waheed, E. Sawicka-Sienkiewicz, Anther culture of *Lupinus angustifolius*: callus formation and the development of multicellular and embryo-like structures, Plant Growth Regul, 145, (2012).
[2] A. L. C. Silva, C. S. Caruso, R. A. Moreira, A. C. G. Horta, Growth characteristics and dynamics of protein synthesis in callus cultures from Glycine wightii (Wight & Arn.) Verdc., Ciência e Agrotecnologia, vol. 29, n 6, 1161–1166 (2005).
[3] G. Daunoras, Pharmacopoeia collection of articles, Kaunas, Kaunas University of medicine, 203 (2001).

EFFECT OF EXTRACTION SOLVENT ON DETERMINATION OF FERULIC ACID IN *CENTAURIUM ERYTHRAEA* USING HPLC-MS-TOF

Agneta Lindmane[1], Anete Boroduske[2], Signe Tomsone[3], Madara Lazdane[3], Martins Boroduskis[2], Ilva Nakurte[2]

[1] Faculty of Medicine, University of Latvia, Raina blvd. 19, Riga, LV – 1586, Latvia
[2] Laboratory of Bioanalytical and Biodosimetry Methods, 7 Ratsupites str., Riga LV-1069, Latvia
[3]Botanical Garden of the University of Latvia, 2 Kandavas str., LV-1083, Riga, Latvia
agneta.lindmane@inbox.lv

Centaury (*Centaurium erythraea*) is a medicinal plant with numerous pharmacological effects like digestive, gastoprotective, antiinflamatory, antipyretic, hepatoprotective, diuretic, wound healing, antimicrobial, antioxidant activities [1]. Centauries contain secoiridoids, iridoids and xanthones [2].

Ferulic acid is one of active ingredients in centaury. Ferulic acid express antioxidant activity, absorbs UV radiation. It can be used in anti-age cosmetics, healing cancer. Ferulic acid also exhibits effects like decreasing blood glucose, neuroprotection, platelet aggregation inhibition, inhibition of thrombus formation.

Ferulic acid is soluble in hot water, ethyl acetate, ethanol, ethyl ether, methanol [3]. The aim of this study was to find extraction solvent suitable for most effective ferulic acid extraction of centaury using high performance liquid chromatography.

Centaury leaf samples were collected from *in vitro* shoot culture derived three week old centaury plants cultivated on modified MS medium at 23° C 16 h photoperiod. After collection plant samples were dried in 25° C for 7 days. Sample preparation involved extraction of centaury with ethanol in concentrations 0%, 10%, 30%, 50%, 60%, 70%, 96%. The separation was carried out on Agilent 1290 series UPLC system, connected with an Agilent 6230 TOF LC/MS mass spectrometer using XTerra MS C18 2.1x150mm (Waters) column. Mobile phase consisted of 0.1% formic acid in water and 0.1% formic acid in acetonitrile using 23 min gradient mode at flow rate 0.250 ml/min.Time-of-flight mass spectrometry in positive mode detection was used for high mass-accuracy compound confirmation.The identity of ferulic acid was confirmed from *m/z* values of*195.0652*.

As expected the least concentration of ferulic acid were found in extracts with 0%, 10% ethanol. In extracts with 30%, 50%, 96% ethanol ferulic acid were obtained in higher concentration.

Successful application of the method to a preliminary study of ferulic acid concentration in centaury that displays solvent effect on ferulic acid concentration illustrated the usefulness of the method.

[1]. Siler, B., Zivkovic, S., Banjanac, T. et al.Centauries as underestimated food additives: Antioxidant and antimicrobial potential, Food Chemistry, 147, pp. 367-376 (2014).
[2]. Aberham, A., Pieri, V., Croom, E.M. et al. Analysis of iridoids, secoiridoids and xanthones in Centaurium erythraea, Frasera caroliniensis and Gentiana lutea using LC-MS and RP-HPLC, Journal of Pharmaceutical and Biomedical Analysis, 54 (3), pp. 517-525 (2011).
[3]. Kumar,N., Pruthi, V. Potential applications of ferulic acid from natural sources, Biotechnology Reports, Volume 4, pp. 86-93 (2014).

INVESTIGATION OF GRAPHITE FELT WETTING WITH AQUEOUS MIXTURES OF SOME ORGANIC SOLVENTS

Brigita Macijauskienė, Egidijus Griškonis

Department of Physical and Inorganic Chemistry, Kaunas University of Technology, Radvilėnų pl. 19, LT-50254 Kaunas, Lithuania
brigita.macijauskiene@ktu.edu

The modification of the surface of graphite felt (GF) filaments with chemically or electrochemically active spaces (functional groups, nanoparticles, coatings etc.) commonly is carried out by means of so-called wet-processes in aqueous solutions. Surface pretreatment of GF filaments is one of the key procedures before modification. Since GF is highly hydrophobic material, the first stage of pretreatment is increasing of its hydrophility or wettability. Wetting properties of any solid substance are related to equilibrium of interfacial forces at the boundary of surfaces of three phases, i.e. solid, liquid and vapor. A quantitative parameter of the wettability is a contact angle measured between surfaces of interacting solid and liquid. The chemical nature and surface roughness of the solid and surface tension of the liquid play a very important role [1-3].

The aim of this investigation was to evaluate the GF wetting with some organic solvent-water mixtures of different concentrations by measuring contact angle. Organic solvents with low values of surface tension and mixable well with water: methanol CH_3OH, ethanol C_2H_5OH, 1-propanol (n-propanol, C_3H_7OH), 2-propanol (isopropanol, $(CH_3)_2CHOH$) and propanone (acetone, $(CH_3)_2CO$) were chosen the measurement of contact angle between flat surface of GF sample and above mentioned pure organic solvents was complicated since droplets of these solvents penetrated immediately into GF matrix. In certain cases contact angles lower than 30° were observed for few seconds until penetration into GF. On the other hand, this demonstrates directly a very good wettability of GF sample with these solvents. As a result of series experiments, minimum sufficient concentration of these solvents in aqueous mixtures, which show good enough and fast wettability of GF filaments matrix, were determined. Most probably, better wettability is due to almost twice lower surface tension values of the mixtures than those of pure water [4, 5]. The aqueous solutions with lower concentration of these solvents demonstrate poor wetting of GF filaments (contact angle >90°) and droplets of such solutions as well as the ones of pure water remained on the surface of GF sample for a very long time (up to few hours) (Fig. 1).

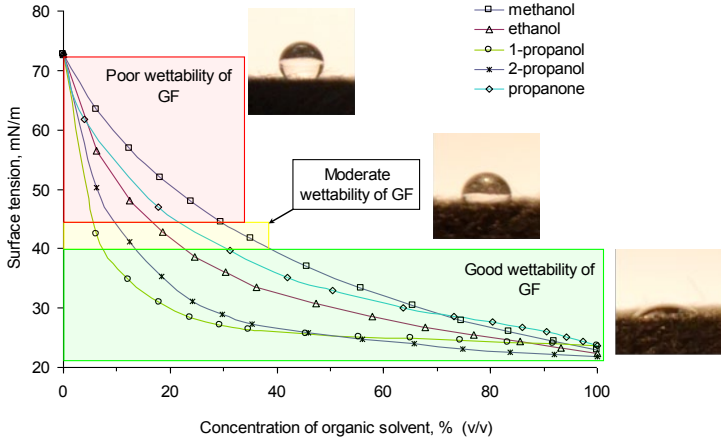

Fig. 1. Visualization of GF wettability with aqueous mixtures of some organic solvents. Data of dependence of surface tension on concentration of organic solvents-water mixtures were taken from literature [4, 5].

[1] B.-L. Ouay, Th. Coradin, Ch. Laberty-Robert, Silica-carbon hydrogels as cytocompatible bioelectrodes, J. Mater. Chem. B **1**, 606–609 (2013).
[2] I. Sas, R.E. Gorga, J.A. Joines, K.A. Thoney, Literature Review on Superhydrophobic Self-Cleaning Surfaces Produced by Electrospinning, Journal of Polymer Science Part B: Polymer Physics **50**, 824–845 (2012).
[3] B. Macijauskienė, E. Griškonis, Wetting of graphite felt with ethanol aqueous solutions, International Conference of Lithuanian Chemical Society "Chemistry and Chemical Technology 2015", ISBN 978-609-459-461-8, Vilnius University, 101-102 (2015).
[4] G. Vhquez, E. Alvarez, J.M. Navaza, Surface Tension of Alcohol+Water from 20 to 50 °C, Journal of Chemical and Engineering Data, **40(3),** 611-614 (1995).
[5] S. Enders, H. Kahl, J. Winkelmann, Surface Tension of the Ternary System Water+Acetone+Toluene, J. Chem. Eng. Data **52 (3)**, 1072–1079 (2007).

PROTEIN ANALYSIS OF EXOSOMES

Ilva Nakurte[1], Kaspars Jekabsons[1], Una Riekstina[1], Arturs Abols[2], Liga Saulite[1], Matiss Otersbergs[1], Aija Line[2], Ruta Muceniece[1]

[1] University of Latvia, Faculty of Medicine, Raina blvd. 19, Riga, LV – 1586, Latvia
[2] Latvian Biomedical Research and Study Centre, Ratsupites Str. 1, Riga, LV-1067, Latvia
ilva.nakurte@lu.lv

Exosomes are small cup-shaped vesicles of endosomal origin that are released in the extracellular space by a variety of normal cell types, including epithelial cells, mesenchymal stem cells, dendritic cells, T and B cells, and various cancers, and have been found in all human body fluids [1]. They have been shown to carry a variety of lipids, proteins, mRNAs and non-coding RNAs that can be taken up by recipient cells, where they trigger intracellular signalling resulting in diverse physiological and pathological responses [2]. This suggests that exosomes mediate a widespread mode of intercellular communication exploited by a variety of normal cells and hijacked by cancers. However, the mechanisms by which various components are sorted for loading into exosomes, as well as the factors determining recipient cell specificity and the mechanisms of exosome uptake are poorly understood.

The recent advances in mass spectrometry-based proteomics have facilitated the comprehensive analysis of exosome content and function. Proteomic analysis has revealed that exosomes contain a common set of membrane and cytosolic proteins, and they also contain distinct subsets of proteins that could be associated with cell type-specific functions [3].

The aim of this study was to characterize the biochemical profile and proteome of hypoxia and normoxia grown exosomes derived from human primary (SW480) and metastatic (SW620) colorectal cancer cells.

Peptide libraries of exosomes were obtained using XPEP1000A-1 reagent kit (SBBS Systems Biosciences, Canada). The kit comes complete to create either exosome surface protein "shaving" peptide libraries or complete exosome peptide library preparation. Totally eight different peptide libraries were obtained. Protein content was measured with the reagent kit - BCA protein assay kit No.23227 (Pierce Biotechnology, USA).

Chromatographic analyses were performed on a modular UPLC system, Agilent *1290 Infinity* series. Liquid chromatography separations were achieved by using an *Extend-C18* RRHD column (2.1x50 mm, 1.8µm). Elution solvents consist of 0.1% formic acid in acetonitrile and 0.1% formic acid in water in gradient mode at a flow rate of 0.3 mL/min. The high resolution mass spectra were taken on an *Agilent 6230 TOF LC/MS* with electrospray ionization in positive mode. Mass spectra were collected over an m/z range of 300–2500 Da.

The differences between all protein fractions were observed. Surface protein concentration in SW620 cells was 1.6 times higher extracted from hypoxia exosomes, compared with normoxia. The concentration ratio in SW480 cells was 1.78 respectively. Differences between content of total proteins extracted from hypoxia and normoxia grown exosome were less significant. First liquid chromatography-masspectrometry data shown differences between all eight chromatograms obtained from protein libraries. Differences between hypoxia and normoxia grown exosomes were observed as well.

Based on the obtained results we can conclude that the total content of proteins and protein profile varies depending on hypoxia and normoxia. Hypoxia increases the proteome. Liquid chromatography - masspectrometry method can be applied to characterise the biochemical profile and proteome of exosomes derived from various cell types in order to identify specific biochemically measurable parameters and proteins that can be used to discriminate cancer-derived exosomes form those released by normal tissues and to reveal the hypoxia-regulated exosomal components.

.

The work has been supported by Latvian Council of Science grant *Nr. 625/2014*.

[1] S. Pant, H. Hilton H, M.E. Burczynski et al.,. The multifaceted exosome: Biogenesis, role in normal and aberrant cellular function, and frontiers for pharmacological and biomarker opportunities. Biochem Pharmacol.**83**, 1484-1494 (2012).
[2] A.S. Azmi, B. Bao, F.H. Sarkar et al., Exosomes in cancer development, metastasis, and drug resistance: a comprehensive review. Cancer Metastasis Rev. **32**, 623-642 (2013).
[3] S.N. Thomas, Z. Liao et al., Exosomal Proteome Profiling: A Potential Multi-Marker Cellular Phenotyping Tool to Characterize Hypoxia-Induced Radiation Resistance in Breast Cancer. Proteomes **1**, 87-108 (2013).

LOW TEMPERATURE SYNTHESIS OF EUROPIUM-DOPED ALUMINIUM MOLYBDATE VIA AQUEOUS SOL-GEL PROCESSING

Algirdas Norkūnas[1], Artūras Žalga[1]

[1] Department of Applied Chemistry, Faculty of Chemistry, Vilnius University, Naugarduko Str. 24, 03225 Vilnius, Lithuania
algirdas.norkunas@chf.stud.vu.lt

Oxide crystals exist in any or every place of our surroundings and play an important role in our diet, environment, health, work, and so on. So there is a continuing interest in the study of the relational properties of oxide crystals from both the experiment and theory. Thus, it has been found that transition metals (Fe, Mn, and Cr) doped in oxide crystals have been shown to improve the relational properties of oxide crystals (such as domain structure, electro-optical coefficients, light absorption, refractive indices, etc.) [1]. Moreover, either transition-metal (TM) or rare earth element (REE) impurities often play a significant role in the ferroelectric, piezoelectric, photoelectric and ferromagnetic properties of compounds. A proper microscopic understanding of such properties requires knowledge of the local structure around the impurities. However, the determination of the local structural distortion of an impurity center is an interesting but difficult problem [2].

Double molybdates and tungstates of alkali and trivalent metals with the general formula $AB(XO_4)_2$ (A = alkali metal, B = trivalent element, X = Mo, W) have attracted much attention because most of the members exhibit interesting properties and applications. These compounds have attracted a great deal of interest in recent years because of their simple structure and the ability to undergo ferroelastic phase transitions in wide temperature ranges. Some of the crystals doped with ions, such as Cr^{3+} and Gd^{3+}, turned out to be promising materials for tunable laser applications in the 1 mm wavelength region and micro- and nano-sized cryogenic fluorescence thermometer. In spite of the fact that the crystals have attracted the attention of researchers for a number of years, there still seems to be a lot of doubts connected with their properties [3].

In this work aluminum molybdate and europium-doped aluminium molybdate were successfully synthesized using a simplified tartaric acid assisted aqueous sol–gel method resulting in highly crystalline, monophasic (either orthorhombic Pbcn or monoclinic P21/a depending on annealing temperature) samples. These materials could be obtained at temperatures of 400 and 700 ^{o}C after calcining for 5 hours in air at ambient pressure. Scanning electron microscopy and X-ray powder diffraction indicated that even the sample calcined at 450 ^{o}C for 5 h was free of impurities and composed of nano sized particles (100 nm), which tend to melt into the net-like structure by increase of dopant concentration. Finally, the FT-IR spectra of the samples clearly revealed the characteristic vibrations of M–O stretches in the $Al_2Mo_3O_{12}$ crystal lattice.

[1] X. Y. Kuang, A. J. Mao, and H. Wang, Local lattice structure study of the octahedral $(CrO_6)^{9-}$ clusters for Cr^{3+} ion doping in a variety of oxide crystals by simulating the corresponding EPR and optical spectra, Journal of Physical Chemistry A **112**, 737–743 (2008).

[2] C. G. Li, X. Y. Kuang, R. P. Chai, Y. R. Zhao, Theory of the ligand-correlated covalent effect on spin orbit coupling for Cr^{3+} ion doping in a variety of oxide crystals, Chemical Physics Letters **498**, 353–358 (2010).

[3] W. Zapart and M. B. Zapart, Effect of ferroelastic domain pattern changes on the EPR spectra in TDM, Phase Transitions: A Multinational Journal, **84**:9-10, 872-884, DOI: 10.1080/01411594.2011.558306 (2011).

EVALUATION OF NEW WET CHEMISTRY METHOD OF BOROHYDRIDES SYNTHESIS

Piotr Antoni Orłowski[1*], Wojciech Wegner[1], Agnieszka Starobrat[1], Michał Tyszkiewicz[2], Dawid Pancerz[1], Karol Jan Fijałkowski[2], Piotr Jerzy Leszczyński[2], Tomasz Jaroń[2**], Wojciech Grochala[2]

[1] *Faculty of Physics, University of Warsaw, Poland Hoża 69, 00-681 Warsaw, Poland*
[*] *e-mail: piotr.orlowski2@student.uw.edu.pl*
[2] *CeNT, University of Warsaw, Poland, Żwirki i Wigury 93, 02-089 Warsaw, Poland,*
[**] *e-mail: tjaron@uw.edu.pl*

For several years now metal borohydrides have been thoroughly researched for their capacity to chemically store hydrogen for powering mobile fuel cells **[1]**. Currently used methods of synthesis of new borohydrides include mostly mechanochemical solid-phase reactions **[2-3]**. This approach, though it enables to quickly obtain a variety of new materials, has many flaws, such as problems with increasing a range of production and with purifying the product which may often be just about 50% of mass fraction of a post-reaction mixture.

Recently we have developed a method of double borohydrides synthesis, $M^{(3)}_y[M^{(2)}(BH_4)_z]$, where $M^{(3)}$ and $M^{(2)}$ are metal cations **[4-6]**. This method does not have limitations typical for currently used procedures. It leads to a high-purity product and enables obtaining borohydrides that are unreachable by mechanochemical reactions. Presented synthetic method is based on double replacement reaction between a salt containing a weakly coordinating anion and a borohydride containing a large organic cation. This reaction is carried out in a non-coordinating organic dissolvent and the desired inorganic product is precipitated. The precursors are commercially accessible, or easily obtainable through well-known processes. Our method was tested for a few borohydrides including Zn, Sc, Y, *e.g.*:

$$[Ph_4P][Zn(BH_4)_3] + Na[B(C_6H_3(CF_3)_2)_4] \rightarrow Na[Zn(BH_4)_3]\downarrow + [Ph_4P][B(C_6H_3(CF_3)_2)_4],$$
$$[Bu_4N][Sc(BH_4)_4] + Li[Al(OC(CF_3)_3)_4] \rightarrow Li[Sc(BH_4)_4]\downarrow + [Bu_4N][Al(OC(CF_3)_3)_4],$$
$$[Bu_4N][Y(BH_4)_4] + K[Al(OC(CF_3)_3)_4] \rightarrow K[Y(BH_4)_4]\downarrow + [Bu_4N][Al(OC(CF_3)_3)_4], \text{ etc.}$$

Obtained products were tested via various physicochemical methods: FTIR Spectroscopy, X-ray powder diffraction, TGA/DSC/EGA analyses, and others.

Two problems that are yet to be dealt with are (i) that the organic side-products constitute a waste, and (ii) the precursors containing $[B(C_6H_3(CF_3)_2)_4]^-$ or $[Al(OC(CF_3)_3)_4]^-$ anions are quite expensive. Currently we explore the possibility of retrieval of organic constituents from the waste in order to close the reaction's cycle and increase the profitability of the method.

[1] W. Grochala, P. P. Edwards, *Chem. Rev.*, **104** (2004) 1283.
[2] D. B. Ravnsbæk, et al., *Angew. Chem., Int. Ed.*, **51** (2012) 3582.
[3] H. Hagemann, R. Černý, *Dalton Trans.*, **39** (2010) 6006.
[4] T. Jaroń, W. Wegner, W. Grochala, *patent applications*: P.405397 (2013), PCT/IB2014/001884.
[5] T. Jaroń, *et al.*, *Angew. Chem. Int. Ed. Engl.*, **54** (2015) 1236.
[6] T. Jaroń, *et al.*, *Chem. Eur. J.*, **21** (2015), in press (DOI: 10.1002/chem.201404968).

PHASE TRANSITION IN NANOCRYSTALLINE $Ca_{1-x}Sr_xMoO_4$ SYNTHESIZED BY AN AQUEOUS SOL-GEL METHOD

Giedrė Prievelytė[1], Gediminas Braziulis[1], Gytautas Janulevičius[1], Artūras Žalga[1]

[1] Department of Applied Chemistry, Faculty of Chemistry, Vilnius University, Naugarduko Str. 24, 03225 Vilnius, Lithuania
giedre.prievelyte@gmail.com

Much effort has been directed to the synthesis of nanomaterials with controlled shapes and ordered morphology because of their unique properties that are wide used in various fields [1]. Self-assembled micro- and nanostructures with specific morphology and novel physical and chemical properties have attracted great attention in science and engineering, owing to their potential applications as hosts for lanthanide activated lasers, luminescence materials, microwave applications and catalysts [2]. Lots of one-dimensional (1D), two-dimensional (2D), and three-dimensional (3D) assembled superstructures have been synthesized by using various methods. However, most routes need high temperature, catalysts, sophisticated process, or protection gases, which may result in impurity of the final product, high-cost, or inconvenience [3]. Therefore, the choice of synthesis technique usually depends on variety factors that can shorten, facilitate, and reduce the preparation way. From this point of view, the solution-based synthetic methods play a crucial role in the design and production of fine ceramics and they have been successful in overcoming many of the limitation of the traditional solid-state, high-temperature methods [4].

Metal molybdates are important inorganic materials that have a high application potential in various fields, such as photoluminescence and electro-optic applications. Alkaline earth molybdates of relatively large bivalent cations ($MMoO_4$, ionic radius > 0.99Å, M=Ca, Sr, Ba, Pb) exist in the so-called scheelite structure (scheelite = $CaWO_4$), where the tungsten atom adopts tetrahedral coordination [5].

In this work, the aqueous sol–gel synthesis method was successfully used for the preparation of the Ca–Mo–O, Sr–Mo–O and Ca–Sr–Mo–O nitrate–tartrate gel precursors with the initial composition for $Ca_{1-x}Sr_xMoO_4$ (x = 0 – 1) ceramic, which were additionally calcined at 400 – 700 ^oC temperatures. Besides, the crystalline double mixed alkaline earth metal molybdates ($CaMoO_4$, $SrMoO_4$) and as-prepared Ca–Sr–Mo–O nitrate–tartrate gels investigated by thermal analysis (TG/DTA), X-ray diffraction (XRD), scanning electron microscopy (SEM) and Fourier Transform infrared spectroscopy (FT-IR).

[1] J. Liu, X. Huang, Y. Li, Z. Li, A general route to thickness-tunable multilayered sheets of sheelite-type metal molybdate and their self-assembled films, Journal of Materials Chemistry 17, 2754–2758 (2007).

[2] Y. Jin, J. Zhang, S. Lu, H. Zhao, X. Zhang, X. J. Wang, Fabrication of Eu^{3+} and Sm^{3+} codoped micro/nanosized $MMoO_4$ (M = Ca, Ba, and Sr) via facile hydrothermal method and their photoluminescence properties through energy transfer, Journal of Physical Chemistry C **112**, 5860-5864 (2008).

[4] C. Mao, J. Geng, X. C. Wu, J. J. Zhu, Selective Synthesis and luminescence properties of self-assembled $SrMoO_4$ superstructures via a facile sonochemical route, Journal of Physical Chemistry C **114**, 1982–1988 (2010).

[4] G. Braziulis, G. Janulevicius, R. Stankeviciute, A. Zalga, Aqueous sol–gel synthesis and thermoanalytical study of the alkaline earth molybdate precursors, Journal of Thermal Analysis and Calorimetry **118**, 613-618 (2014).

[4] R. Stankeviciute, A. Zalga, Sol-gel synthesis, crystal structure, surface morphology and optical properties of Eu_2O_3 doped $La_2Mo_3O_{12}$ ceramic, Journal of Thermal Analysis and Calorimetry **118**, 925-935 (2014).

[5] J. W. Yoon, J. H. Ryu, K. B. Shim, Photoluminescence in nanocrystalline $MMoO_4$ (M = Ca, Ba) synthesized by a polymerized complex method, Materials Science and Engineering B **127**, 154–158 (2006).

Implication of drying methods of thyme (*Thymus vulgaris* L.) for antibacterial and antioxidative properties of essential oils

Arvydas Ramanauskas[1], Edita Dambrauskienė[2], Ilona Jonuškienė[1*]

[1] Department of Organic Chemistry, Kaunas University of Technology
Kaunas, Lithuania
[2]Institute of Horticulture, Lithuanian Research Centre for Agriculture and Forestry, Babtai, Lithuania
arvydas.ramanius@gmail.com

Essential oils are used for thousands of years in various cultures for medical purposes. These healing oils are rapidly growing in popularity because they act as natural medicine without side effects. Essential oils benefits come from their antiradical and antibacterial properties [1]. These parameters are affected by many factors. One of them is drying methods of raw materials.

The objective of this study was to evaluate the influence of seven drying methods (natural air, convective, forced flow dryer at ambient temperature, vacuum, infrared, microwave and freeze-drying) on essential oil antibacterial and antiradical activities of thyme (*Thymus vulgaris* L.). The essential oils were obtained by hydrodistillation from thyme. Results of antibacterial and antiradical activities of essential oil from thymus are described in Fig. 1.

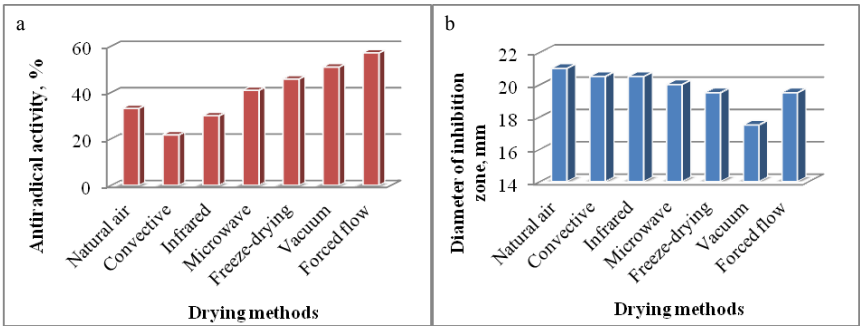

Fig. 1. Antiradical activity (a) and antibacterial activity (b) against *Rhizobium radiobacter* of essential oils from thyme (*Thymus vulgaris* L.) obtained by different drying methods

The highest antiradical activity of essential oil from thyme was then plant was dryed after flow drying at ambient temperature (57.09 %), the lowest – after convective drying (21.77 %). The strongest antibacterial activity against *Rhizobium radiobacter* was obtained after natural drying (21 mm), the weakest – vacuum drying (17.5 mm). The most suitable drying method of thyme for antiradical and antibacterial activities was flow drying at ambient temperature.

[1] Diwaker Pandey, V. S. Rao, Extraction of essential oil and its applications, Bachelor of Technology (Chemical Engineering), Orissa.

THERMAL DECOMPOSITION OF BOROHYDRIDES – AN ATTEMPT AT OBTAINING MIXED-METAL BORIDES

Agnieszka Starobrat[1*], Tomasz Jaroń[2], Wojciech Grochala[2]

[1] Faculty of Physics, University of Warsaw, Poland
[2] Centre of New Technologies, University of Warsaw, Poland
* *agnieszka.starobrat@student.uw.edu.pl*

At the time when any possible clean energy sources are intensely sought-after, metal borohydrides are intensely investigated as potential chemical hydrogen storage materials. Their thermal decomposition seems to be one of the most promising methods of release of hydrogen fuel. Looking from a different angle, hydrogen evolution from metal borohydrides may constitute a method of obtaining metal (or mixed-metal) borides. If borohydrides are distributed as a thin layer on some substrate, the resulting borides will supposedly form as coatings. Borides, as well as mentioned borohydrides, are broadly exploited materials. Their wide range of useful physicochemical properties, from high hardness as for TiB_2 to superconductivity for MgB_2, makes them one of the most widely applicable group of compounds. The mixed-metal borides are supposed to exhibit interesting electronic and magnetic properties.

Volatile borohydrides of Ti (organic derivative), Zr and Hf have already been tested as precursor materials for hard metal boride coatings prepared by a chemical vapour deposition method (CVD) [1]. However, the approach suggested above might help to reduce the harsh synthesis conditions of metal borides such as excessively high temperature.

Here we report on the synthesis of various organic scandium borohydrides, $[Cat][Sc(BH_4)_4]$, where Cat = Me_4N, Bu_4N, Ph_4P. The mechanochemical reactions were followed by solvent extraction to reduce the amount of LiCl by-product.

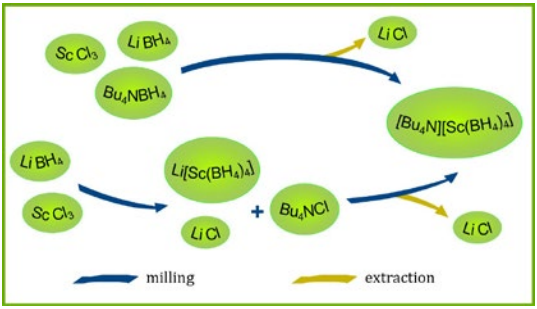

Fig. 1. Organic scandium borohydrides synthesis scheme.

The prepared borohydrides were investigated with a number of methods, including IR spectroscopy (FTIR), powder X-ray diffraction (PXD) and thermal analysis (TGA/DSC) [2]. They also served as precursors towards the lithium- scandium borohydride in solvent-mediated reactions [3,4], *e.g.*:

$$(Bu_4N)[Sc(BH_4)_4] + Li[An] \rightarrow Li[Sc(BH_4)_4]\downarrow + (Bu_4N)[An],$$

where [An] is a weakly-coordinating anion, *e.g.* $[Al(OC(CF_3)_3)_4]$ or $[B(3,5\text{-}(CF_3)_2C_6H_3)_4]$. In this case $Li[Sc(BH_4)_4]$ is obtained as a LiCl-free product, in contrast to the earlier attempts [5]. The so-obtained $Li[Sc(BH_4)_4]$ was decomposed at elevated temperature (400-800°C) in the inert gas atmosphere. The identification and characterization of solid state decomposition products were carried out on the base of FTIR, PXD, TGA/DSC, evolved gas analysis (EGA), X-ray photoelectron spectroscopy (XPS) and magnetic measurements (SQUID).

The described results of the research are the major part of the first author's master's thesis which will be defended in June 2015, which is carried out under supervision of two senior scientists.

[1] J. A. Jensen, *et al.,* Titanium, zirconium, and hafnium tetrahydroborates as "tailored" CVD precursors for metal diboride thin films, J. Am. Chem. Soc. **110,** 1643-1644 (1988).
[2] A. Starobrat, *et.al.,* manuscript in preparation (2015).
[3] T. Jaroń, W. Wegner, W. Grochala, PCT/IB2014/001884
[4] T. Jaroń, *et al.,* Hydrogen Storage Materials: Room-Temperature Wet-Chemistry Approach toward Mixed-Metal Borohydrides, Angew. Chem. Int. Ed. 2015, 54, 1236-1239
[5] H. Hagemann, *et al.,* $LiSc(BH_4)_4$: A Novel Salt of Li^+ and Discrete $Sc(BH_4)_4^-$ Complex Anions, J. Phys. Chem. A **2008**, *112*, 7551-7555.

SYNTHESIS OF SILVER NANOPARTICLES AND THEIR INFLUENCE ON OPTICAL PROPERTIES OF ORGANIC DYES

Simona Streckaitė[1], Domantas Peckus[1,2], Ramūnas Augulis[1], Tomas Tamulevičius[2], Sigitas Tamulevičius[2] and Vidmantas Gulbinas[1]

[1] Institute of Physics, Center for Physical Sciences and Technology, A. Goštauto Ave 11, Vilnius LT-01108, Lithuania
[2] Institute of Materials Science of Kaunas University of Technology, K. Baršausko Ave 59, Kaunas LT-51423, Lithuania
simona.streckaite@gmail.com

Recently, silver nanoparticles (AgNPs) have attracted much attention because of their unique size and shape dependent optical [1], electrical and magnetic properties. Possible manipulations of these properties lead to various applications of these nanoparticles in optoelectronics, biosensing, catalysis, enhanced optical spectroscopies [2], as antimicrobials [3] and other [4]. For practical use it is crucial to understand the influence of size, shape, aggregation, stability [5] and other features of nanoparticles to their optical properties.

In this work, influence of spherical and triangular AgNPs on optical properties of highly fluorescent organic dyes (rhodamine 6G (R6G), sulforhodamine 640 (SR640)) was investigated. Spherical AgNPs were prepared using few wet-chemistry techniques: reduction of silver salt ($AgNO_3 + NaBH_4 \rightarrow Ag + H_2 + B_2H_6 + NaNO_3$) – AgNPs with absorption maximum at 390 nm, Turkevich method ($4Ag^+ + Na_3C_6H_5O_7 + 2H_2O \rightarrow 4Ag° + C_6H_5O_7H_3 + 3Na^+ + H^+ + O_2$) - AgNPs with absorption maximum at 420 nm. Three different in size triangular AgNPs (absorption maxima at 630, 665 and 705 nm) were synthesized using different concentrations of $AgNO_3$, $NaBH_4$, $Na_3C_6H_5O_7$ and H_2O_2.

Thin films were made on glass, which was silanized using APTES (3-aminopropyltriethoxysilane) solution in acetone. Solutions and thin films of nanoparticles and organic dyes were investigated by using SEM imaging (Fig. 1), steady-state and ultrafast time-resolved absorption and fluorescence spectroscopy.

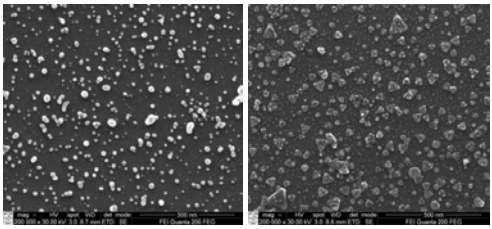

Fig. 1. SEM images of spherical (left) and triangular (right) silver nanoparticles

Steady-state absorption spectra showed that R6G causes aggregation in AgNPs solution because Cl^- ion, which disrupts the borohydride (B_2H_6) protective layer around nanoparticles, when they are synthesized from reduction of silver salt. On the contrary, SR640 stabilizes this AgNPs solution. Turkevich method gives us bigger AgNPs, which are stabilized by a protective layer of sodium citrate ($Na_3C_6H_5O_7$) and the advantage is that this reductant is non-toxic and more environmentally friendly than other methods [6]. Also it was noticed that PVP (polyvinylpyrrolidone), used for stabilization of AgNPs, cause small (~5 nm) red shift for all nanoparticles.

Analysis of ultrafast time-resolved spectroscopy measurements of thin films revealed influence of localized surface plasmon resonance of AgNPs to R6G and SR640 exited state relaxation dynamics.

[1] A.V. Sorokin, A.A. Zabolotskii, N.V. Pereverzev et al., Plasmon Controlled Exciton Fluorescence of Molecular Aggregates, J. Phys. Chem. C **118,** 7599-7605 (2014).
[2] J.R.G. Navarro, M.H.V. Werts, Resonant light scattering spectroscopy of gold, silver and gold-silver alloy nanoparticles and optical detection in microfluidic channels, Analyst **138,** 583-592 (2013).
[3] S. Agnihotri, S. Mukherji, S. Mukherji, Size-controlled silver nanoparticles synthesized over the range 5–100 nm using the same protocol and their antibacterial efficacy, RSC Adv. **4,** 3974–3983 (2014).
[4] M.U. Rashid, K.H. Bhuiyan, M.E. Quayum, Synthesis of Silver Nano Particles (Ag-NPs) and t heir uses for Quantitative Analysis of Vitamin C Tablets, Dhaka Univ. J. Pharm. Sci. **12,** 29–33 (2013).
[5] M. Franckevičius, A. Gustainytė, R. Kondrotas et al., PPI–SA and PAMAM–SA dendrimers assisted synthesis of silver nanoparticles: structure, optical properties and stability, J. Nanoparticle Res. **16,** 2343 (2014).
[6] X. Wang, F. He, X. Zhu et al., Hybrid silver nanoparticle/conjugated polyelectrolyte nanocomposites exhibiting controllable metal-enhanced fluorescence, Scientific reports **4,** 4406 (2014).

DENSITY FUNCTIONAL THEORY AND SURFACE ENHANCED RAMAN SCATTERING STUDY OF STRUCTURAL PROPERTIES OF MEMBRANE ANCHORING SELF-ASSEMBLED MONOLAYERS

Martynas Talaikis, Mindaugas Mickevičius, Gintaras Valinčius, Gediminas Niaura

Vilnius University, Institute of Biochemistry, Mokslininkų 12, LT-08662 Vilnius, Lithuania
martynas.talaikis@bchi.vu.lt

Tethered bilayer lipid membranes (tBLMs) are widely used as biological models for studies of protein-membrane interactions and development of biosensors [1]. tBLMs consists of two layers: the innermost is composed of self-assembled monolayer (SAM) which is covalently attached to metal surface and functions as anchoring site of the membrane. Functionality of tBLM is highly sensitive to conformation and structure of a SAM [2]. SAM is composed of long chain thiol derivative containing 1-mercapto(ethylene oxide)$_6$ moiety and two hydrocaron (myristoyl) chains (WC14) as well as short chain diluent deuterium marked 2-mercaptoethanol (βMEd).

Density functional calculations (DFT) at B3LYP levels of theory using 6-31++g(d,p) basis set have been carried out to investigate the conformational properties of βMEd on Au cluster consisting of 10 atoms and to obtain Raman spectra of both βMEd and WC14 molecules. Surface enhanced Raman spectra (SERS) of both molecules separately and at certain ratio were recorded as well. Experimental data and theoretical calculations are in quite good agreement.

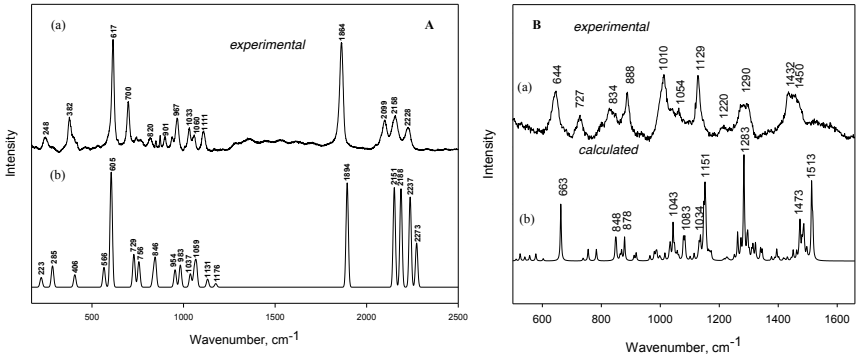

Fig 1. Comparison of experimental (a) and calculated (b) spectra of both βMEd (A) and WC14 (B) compounds.

DFT calculations reveal that *gauche* conformation of C-S bond of βMEd is more favorable over the *trans* conformation. Similar results were obtained from the experimental Raman spectra (Fig. 1A). The intense band at 617 cm^{-1} belongs to (C-S)$_G$ *gauche* stretching vibration (in the calculated spectra this band appears at 605 cm^{-1}). (C-S)$_T$ *trans* band is near 700 cm^{-1} in experimental Raman spectra and have 2.6 times lower intensity in comparison with gauche band. It should be noted, that *trans* band in calculated spectra is not shown. The detailed assignments of the Raman bands were performed from the data of calculated and experimental spectra. In particular, the strong band near 1129 cm^{-1} observed in experimental spectra was assigned to all-trans in phase stretching vibration of hydrocarbon (C-C) bonds.

[1] R.L.C. Naumann, C. Nowak, W. Knoll, Proteins in biomimetic membranes: Promises and facts, Soft Matter, 7, 9535–9548 (2011).

[2] B. Rakovska, T. Ragaliauskas, M. Mickevicius, M. Jankunec, G. Niaura, D. J. Vanderah, G. Valincius, Structure and function of the membrane anchoring self-assembled monolayers, Langmuir, 31 (2), pp 846–857 (2015).

Characterisation of polyphenolic compounds in *Lathyrus maritimus* using liquid chromatography- high resolution mass spectrometry

Jolanta Upite[1], Anete Boroduske[2], Martins Boroduskis[2], Signe Tomsone[3], Madara Lazdane[3], Elza Kaktina[2], Iva Nakurte[2]

[1] Faculty of Medicine of University of Latvia, Raina Blvd. 19, Riga, Latvia

[2] University of Latvia, Laboratory of Bioanalytical and Biodosimetry Methods, Ratsupites str. 7, Latvia

[3]Botanical Garden of the University of Latvia, 2 Kandavas str., LV-1083, Riga, Latvia

jolanta.upite@gmail.com

Legumes constitute an important source of dietary protein for large segments of the world's population, particularly in countries with a limited supply or consumption of animal protein, the latter being self-imposed because of religious or cultural habits [1]. *Lathyrus maritimus* is a relatively unknown leguminous plant which grows along the sandy and gravel shorelines of Newfoundland, Canada, and is also found along the shorelines of Artic and sub-Artic regions from Greenland to Siberia and Japan [2]. The food legumes are a rich source of protein, starch, dietary fibre, minerals, and water-soluble vitamins. Because of their importance in the human diet, the evaluation of the biological quality and availability of legume proteins have received consider able attention [3].

The presence and contents of phenolic, different types of oligosaccharides, saponin, sugars and amino acids in leaves of *Lathyrus maritimus* were determined using liquid chromatography-high resolution mass spectrometry.

Lathyrus maritimus samples were collected from *in vitro* shoot culture derived three week old plants cultivated on modified MS medium at 23° C 16 h photoperiod. After collection plant samples were dried in 25°C for 7 days.

Sample preparation involved liquid–liquid extraction of *Lathyrus maritimus* with 50 % ethanol in water. The separation was carried out on Agilent 1290 series UPLC system, connected with an Agilent 6230 TOF LC/MS mass spectrometer using XTerra MS C18 2.1x150mm (Waters) column. Mobile phase consisted of 0.1% formic acid in water and 0.1% formic acid in acetonitrile in a gradient mode.

The results showed that *Lathyrus maritimus* leaves contained a lot of different compounds, such as, glycine, alanine, aspartic acid, tyrosine, rutin, isoquercetin. All these results were obtained from *in vitro* grown plants and compared with wild *Lathyrus maritimus*. Results showed that there are differences between obtained compounds *in vitro* and in *wild Lathyrus maritimus*, most similar and dominant compounds were such as alanine, rutin, tyrosine, ferulic acid, sinapic acid and apigetrin. However in wild *Lathyrus maritimus* we did not found compounds such as kaempherol, isorhamnetin, chrisin, cinnamic acid, caffeine and chlorogenic acid.

[1] U.D. Chavan, D.B. McKenzie, R. Amarowicz, Phytochemical components of beach pea (*Lathyrus maritimus* L.), Food Chemistry 81 (2003) 61-71.
[2] F. Shahidi, U.D. Chavan, A.K. Bal, Chemical composition of beach pea (*Lathyrus maritimus* L.), Food Chemistry 64 (1999) 39-44.
[3] U.D. Chavan, F. Shahidi*, R. Hoover*, C. Perera, Characterization of beach pea (Lathyrus maritimus L.) starch, Food Chemistry 65 (1999) 61-70.

BONE SCAFFOLDS PRODUCED FROM COMPOSITE nHAp-PLA/PEG MATERIALS BY DIRECT LASER WRITING (DLW)

Justina Vaicekauskaite[1], Giedre Lubiene[2], Sima Rekštytė[3], Mangirdas Malinauskas[3], Edita Garskaite[2]

[1] Department of Chemistry and Bioengineering, Vilnius Gediminas Technical University, Lithuania
[2] Department of Applied Chemistry, Vilnius University, Lithuania
[3] Department of Quantum Electronics, Vilnius University, Lithuania
justina.vaicekauskaite@stud.vgtu.lt, edita.garskaite@chf.vu.lt.

Hydroxyapatite ($Ca_{10}(PO_4)_6(OH)_2$, HAp) is biocompatible and bioactive ceramic material widely used for dental, maxillofacial or orthopaedic applications [1]. However, pure HAp has unsatisfactory mechanical properties – it is a very brittle ceramic which is strong in compression and weak in tension [2]. To overcome this issue many different inorganic-organic composite materials with altered mechanical properties have been proposed [3]. Scaffolds – bone graft substitutes – made from such composite materials should possess precisely tunable chemical and physical properties in order to promote the migration, proliferation and differentiation of bone cells for hard tissue regeneration [4].

In this work we present a polymer-matrix mediated synthesis of nanocrystalline hydroxyapaptite (nHAp) via co-precipitation method. Prepared hybrid gels containing nHAp particles were calcined at 400-800 ºC. An effect of the polymer (poly(ethylene glycol) (PEG) and polyvinyl-alcohol (PVA)) on nucleation and growth of HAp particles, crystallinity and phase purity of calcined material has been investigated. Calcination temperature, morphology, crystallinity and phase composition of the HAp powders were studied by thermogravimetry (TG) and differential thermal analysis (DTA) (shown in Fig. 1), scanning electron microscopy (SEM), Fourier transform infrared (FTIR) spectroscopy and X-ray diffraction (XRD) techniques.

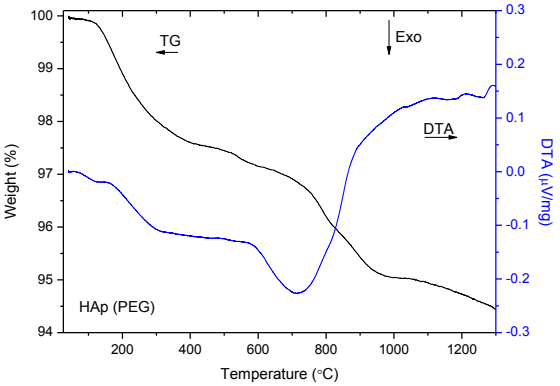

Fig. 1. TG and DTA curves of HAp-PEG powders (initial calcination was performed at 400 °C).

Synthesised nHAp powders were further used to produce inorganic-organic hybrid materials by direct laser writing (DLW) technique. Biodegradable polymers such as poly(lactic acid) (PLA) and poly(glycolic acid) (PGA) were used as an organic matrix. Various processing conditions are examined and the effect of various processing factors on the materials cross-linking and structural properties will be also presented and discussed. The proposed approach demonstrates the prospects of composite material laser fabricated scaffolds for hard tissue engineering [5,6].

[1] K. Fox, Ph .A. Tran and N. Tran, Recent Advances in Research Applications of Nanophase Hydroxyapatite, Chem. Phys. Chem., **13** (10), 2495-2506 (2012).
[2] R. I. Martin and P. W. Brown, Mechanical Properties of Hydroxyapatite Formed at Physiological Temperature, J. Mater. Sci.-Mater. M., **6** (3) 138-143 (1995).
[3] B. Thavornyutikarn, N. Chantarapanich, K. Sitthiseripratip, et al., Bone Tissue Engineering Scaffolding: Computer-Aided Scaffolding Techniques, Prog. Biomater. **3**, 61-102 (2014).
[4] R. Dimitriou, E. Jones, D. McGonagle, et al., Bone Regeneration: Current Concepts and Future Directions, BMC Medicine **9**, 66 (2011).
[5] E. Garskaite, K. Gross, S. W. Yang et al., Effect of Processing Conditions on the Crystallinity and Structure of Carbonated Calcium Hydroxyapatite (CHAp), CrystEngComm **16**, 3950-3959 (2014).
[6] M. Malinauskas, S. Rekštytė, L. Lukoševičius et al., 3D Microporous Scaffolds Manufactured via Combination of Fused Filament Fabrication and Direct Laser Writing Ablation, Micromachines **5**, 839-858 (2014).

INVESTIGATION OF CARBON ISOTOPIC RATIOS IN DIESEL AND GASOLINE FROM GAS STATIONS IN VILNIUS, LITHUANIA

Greta Bikelytė, Andrius Garbaras, Vidmantas Remeikis

Mass spectrometry laboratory, Centre for Physical Sciences and Technology,
Savanorių 231, LT-02300 Vilnius, Lithuania.
greta.bikelyte@gmail.com

Stable isotope ratio mass spectrometry method is widely used in ecology, geology, environmental and other studies [1, 2]. This method was applied to investigate stable carbon isotope ratios in fossil fuels. Samples were taken in various gas stations in Vilnius, Lithuania. The sampling was performed in fall of 2014 while analyses were made during the winter of 2015. The samples were stored in gas tide vials until analysis.

The main aim of this work was to determine differences in stable carbon isotope ratios of gasoline and diesel fuels from fuel providers available in Vilnius city (Lithuania).

28 samples (15 petrol and 13 diesel fuel) were collected from 14 different fuel stations. Stable carbon isotope ratio ($\delta^{13}C_{TC}$) was measured using EA-IRMS system (Elemental Analyser *Thermo Flash EA1112* connected to Isotope Ratio Mass Spectrometer *Thermo Delta V Advantage*via ConFlo III interface).The analysis of $\delta^{13}C_{TC}$ values revealed that diesel $\delta^{13}C$ values varied in the range from -30.71 ‰ to -30.90 ‰ with an average value of -30.76 ‰. Meanwhile gasoline had an average value of -29.96 ‰, where the $\delta^{13}C$ values were in the range from -29.57 ‰ to -30.13 ‰.

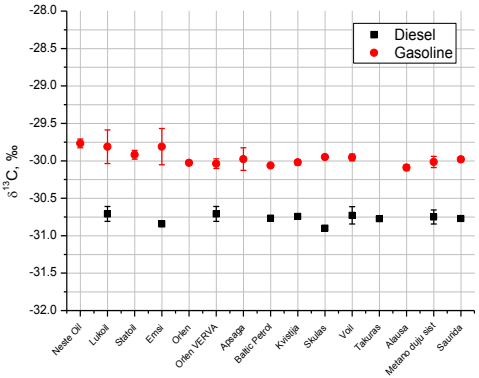

Figure 1. $\delta^{13}C$ values of gasoline and diesel from gas stations in Vilnius, Lithuania.

Carbon isotope ratio of diesel and gasoline differ by ~0.8 ‰ according to our analysis. The main cause for the difference in $\delta^{13}C$ values in diesel and gasoline could lie in the different petroleum treatment processes.

The results of stable carbon isotope analysis were used to calculate the average isotopic ratio value of crude oil based fuels and it can be useful to compare this ratio with the $\delta^{13}C$ values of other aerosol sources (biomass burning, grass burning, coal burning, etc.).

[1] Garbaras, A., A. Masalaite, I. Garbariene, D. Ceburnis, E. Krugly, V. Remeikis, E. Puida, K. Kvietkus and D. Martuzevicius (2015). "Stable carbon fractionation in size-segregated aerosol particles produced by controlled biomass burning." Journal of Aerosol Science**79**: 86-96.

[2] Mašalaite, A., A. Garbaras and V. Remeikis (2012). "Stable isotopes in environmental investigations | Stabilieji izotopai aplinkos tyrimuose." Lithuanian Journal of Physics**52**(3): 261-268.

GRAPHENE FIELD-EFFECT-TRANSISTORS FOR ROOM TEMPERATURE DETECTION OF TERAHERTZ RADIATION

Dovilė Čibiraitė[1], Alvydas Lisauskas[1,2], Jonas Matukas[1]

[1] Department of Radiophysics, Faculty of Physics, Vilnius University Sauletekio av. 9-III, LT-10222 Vilnius, Lithuania
dovile.cibiriate@ff.stud.vu.lt
[2] Physikalisches Institut, Johann Wolfgang Goethe-Universität, DE-60438 Frankfurt (Main), Germany
lisauskas@physik.uni-frankfurt.de

Terahertz (THz) radiation has a huge potential for a variety of applications, such as biomedical imaging, security imaging, spectroscopy and etc. Therefore, it is necessary to develop room-temperature terahertz sources and detectors [1].

From various novel approaches devoted for the development of high-frequency electronics, much attention has been addressed to graphene [2]. This is quite attractive material due to its high room-temperature mobility (up to 10 000 $cm^2/(Vs)$ on SiO_2 wafer) and high carrier saturation velocity with already proven ability to detect THz radiation up to 3.11 THz [3]. It was reported recently that graphene field-effect transistors (GFETs) can be used for efficient detection of 600 GHz radiation showing performance matching with the state-of-the-art detector technologies for room-temperature operation [4].

This work is devoted to the more detailed study of devices presented in [4]. Here we concentrate on the peculiarities of the response to electromagnetic radiation spanning from 100 GHz to 1 THz. Continuous wave THz system TERABEAM 1550 was used to carry out the experiment.

Figure 1a presents dependencies of resistance for three samples with different value of Dirac point (CNP). Respectively are given voltage responses at frequencies between 0.1 THz and 1 THz at Fig. 1b – d, which for the purpose of clarity are normalized to the response at one specific point of the gate bias (V_{gs} = 0 V).

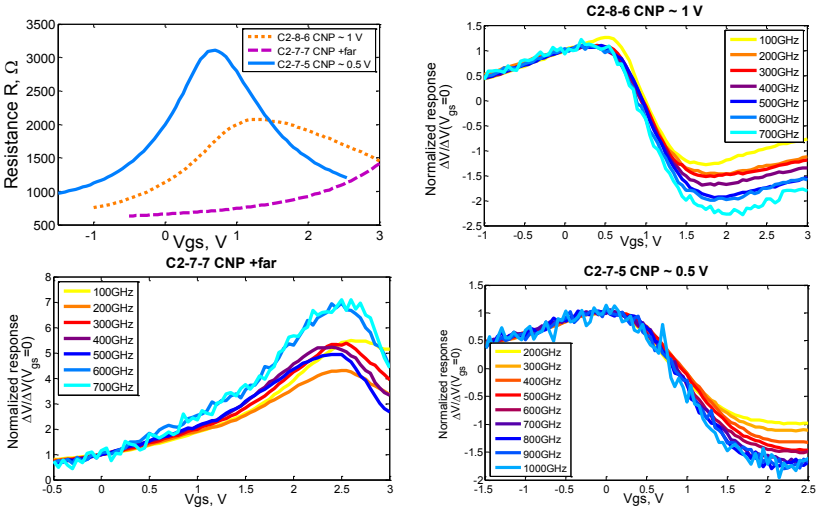

Fig. 1. Measured data: a (upper-left) – resistance of three G-FET samples with different Dirac point (CNP); Normalized voltage responses of samples with different CNP: b (upper-right) – CNP at about +1 V, c (lower-left) – far positive CNP, d (lower-right) – CNP at about +0.5 V.

In conclusion, it is notable that G-FETs can be used for the efficient detection of THz radiation at room temperature even without applied voltage V_{gs} (completely zero-bias detectors). These measurements also show that G-FETs have interesting asymmetric response, which is frequency dependent and is more pronounced at higher frequencies. Such effect could be explained by the diffusive contribution of hot carriers (hot-carrier Seeback effect).

[1] P. H. Siegel, Terahertz technology, IEEE Trans. Microwave Theory Tech., **50**(3), 910–928 (2002).
[2] A.H. Castro Neto, F. Guinea, N.M.R. Peres, K.S. Novoselov, A.K. Geim, Rev. Mod. Phys., **81**, 109−162 (2009).
[3] A.V. Muraviev, S.L. Rumyantsev, G. Liu, A.A. Balandin, W. Knap, M.S. Shur, Appl. Phys. Lett., **103**, 181114 (2013).
[4] A. Zak, M.A. Andersson et al., Antenna-Integrated 0.6 THz FET Direct Detectors Based on CVD Graphene, Nano Lett., **14** (10), 5834–5838 (2014).

RAMAN SPECTROSCOPIC STUDY OF ANION MOLAR MASS EFFECT ON ACETONITRILE VIBRATIONAL RELAXATION IN IONIC LIQUIDS [BMIM]X, (X=Cl, Br, I, BF_4)

Vida Daukšaitė[1], Vytenis Jočys[1], Jonas Kausteklis[1], Valdemaras Aleksa[1]

[1] Faculty of Physics, University of Vilnius, Lithuania
vida.dauksaite@ff.stud.vu.lt

The properties of ionic liquids (ILs) have attracted much attention from both theoretical and practical viewpoints for a long time. These liquids, being great solvents, are interesting media for vibrational relaxation study. In this work, acetonitrile (AN) molecule was used as a probe in ILs to carry out the AN C≡N stretch (also known as υ_2) vibrational relaxation investigation.

A few different imidazolium based ILs (namely 1-butyl-3-methylimidazolium bromide ([BMIM]Br), 1-butyl-3-methylimidazolium iodide ([BMIM]I), 1-butyl-3-methylimidazolium chloride ([BMIM]Cl)), 1-butyl-3-methylimidazolium tetrafluoroborate ([BMIM]BF_4)) (see Fig. 1) were chosen to enable the study of vibrational relaxation dependence on anion molar mass. Furthermore, different temperatures (295K and 328K) were used to determine AN C≡N stretch vibrational relaxation dependence on temperature. The structure of υ_2 band was analyzed using two-dimensional correlation analysis.

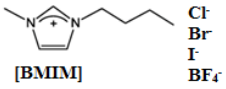

Fig. 1. Structural view of studied [BMIM] cation and anions

From the carried out experiments it was found that acetonitrile vibrational relaxation is faster in studied ILs solutions (from 2,14 ps in neat AN to 1,27 ps in AN/[BMIM]I 20% AN wt solution) and increased temperature of these solutions lead to even faster relaxation (from 1,31 ps at T = 295 K to 1,26 ps at T = 328K in AN/[BMIM]Br solution).

Decreased acetonitrile vibrational relaxation time (from 1,4 ps to 1,27 ps) when anion (of IL) was replaced by a heavier one (in this case heavier halogen) could be attributed to the change in local ionic structuring [1]. It also seems that the heavier the anion of the IL, the more red shifted C ≡ N stretch band became (see Fig. 2).

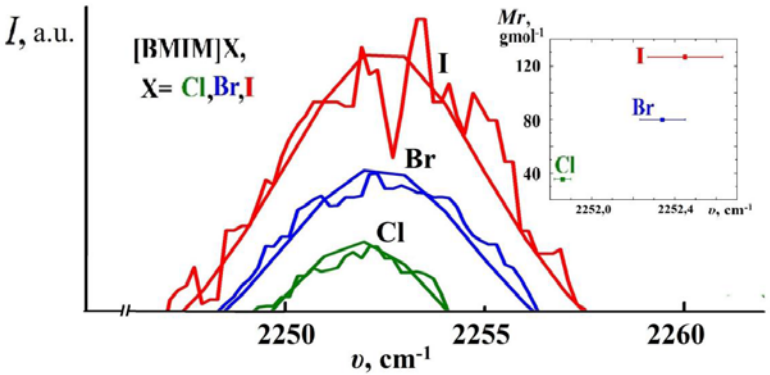

Fig. 2. AN/[BMIM]X (X=Cl, Br, I) Raman spectra of C≡N stretch peak region approximated with Lorentz profiles.

[1] V. Aleksa, V. Barkauskas, V. Pogorelov, H. Fuess, and V. Balevicius, "Raman spectroscopy of vibrational and rotational relaxation of acetonitrile molecules dissolved in ionic liquids," *Lith. J. Phys.*, vol. 47, no. 4, pp. 435–441, 2007.

INVESTIGATION OF STRUCTURE OF SINGLE-WALLED CARBON NANOTUBES BY MEANS OF RAMAN SPECTROSCOPY

Jorinta Jakubauskaitė[1], Justinas Čeponkus[1]

[1] Department of General Physics and Spectroscopy, Faculty of Physics, Vilnius University, Lithuania
jorinta.jakubauskaite@ff.stud.vu.lt

The amount of crystallographic defects is one of the most important factors when evaluating the quality of single-walled carbon nanotubes (SWCNTs). It is known to affect the physical properties of this promising nanomaterial, often reducing its suitability for potential applications. The structure of commercially produced SWCNTs is especially prone to disorder; therefore, reliable methods are needed to improve it. FT-Raman spectrometry can be successfully applied to monitor the quality of carbon nanotubes [1].

The aim of this work is to investigate the structure of SWCNTs in different environments and evaluate the impact of bombardment by argon ions. SWCNTs and KBr were mixed in various proportions, and high pressure was applied in order to prepare the samples. FT-Raman spectrometer *Bruker MultiRAM* equipped with a 1064 nm Nd:YAG laser was used to obtain the Raman spectra. By calculating the ratio of the intensities of G and D bands, it was found that the amount of defects depends on the environment surrounding the SWCNTs – it can be expected to increase as the concentration of SWCNTs decreases (Fig. 1).

After the initial measurements, some of the samples were bombarded by argon ions, and further spectrometric analysis was carried out. It can be tentatively stated that the interaction with low-energy ($E < 5$ eV) argon ions improves the structure of SWCNTs (Fig. 2), while, on the contrary, ions of higher energy can break the C–C bonds and disturb the ordered structure of the nanotubes. However, the heterogeneity of samples should be considered when evaluating the results.

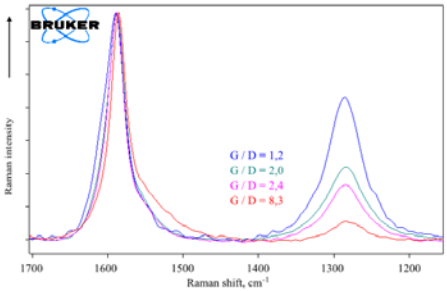

Fig. 1. G and D bands of FT-Raman spectra of SWCNT and KBr samples having mass ratios of (from top to bottom) 1:800, 1:200, 1:100, 1:1.

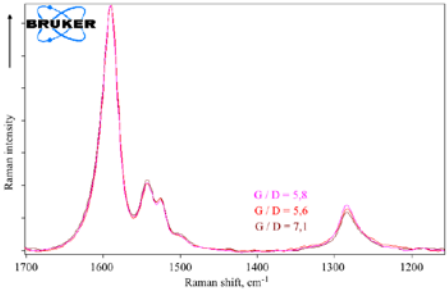

Fig. 2. G and D bands of FT-Raman spectra of a single SWCNT and KBr sample before (G / D = 5,8) and after (G / D = 7,1) the bombardment by argon ions at 5 V bias was carried out.

FT-Raman and FT-IR experiments on both chemically unaltered and functionalized SWCNTs are intended in the near future.

[1] E. C. Neyts, K. Ostrikov, Z. J. Han, S. Kumar, A. C. T. van Duin, A. Bogaerts, Defect Healing and Enhanced Nucleation of Carbon Nanotubes by Low-Energy Ion Bombardment, Phys. Rev. Lett. 110, 065501 (2013).

STUDY OF IONIC LIQUID ALKYL CHAIN LENGTH EFFECT ON ACETONITRILE VIBRATIONAL RELAXATION USING RAMAN SPECTROSCOPY

Vytenis Jočys[1], Jonas Kausteklis[1], Valdemaras Aleksa[1]

[1] Faculty of Physics, University of Vilnius, Lithuania
vytenis.jocys@ff.stud.vu.lt

Ionic liquids (ILs) have become extremely attractive study material in spectroscopy due to their tunable abilities and thus wide range of applications. Thus ILs are interesting media for the study of vibrational relaxation. In this work acetonitrile (AN) molecule was chosen as a "media sensitive" (thanks to its polarity) probe in ILs to carry out the AN C≡N stretch (also known as υ_2) vibrational relaxation investigation using polarized Raman spectroscopy. The vibrational relaxation time, or τ_{vib}, is given by the relation:

$$\tau_{vib} = (2\pi c \Delta\upsilon_{iso})^{-1}, \qquad (1)$$

were c is the speed of light and $\Delta\upsilon_{iso}$ is the half width at half maximum of isotropic spectrum, which is obtained from I_{VV} and I_{VH} (the two indices are for incident and scattered light, accordingly) Raman spectra.

Two different imidazolium based ILs (namely 1-butyl-3-methylimidazolium bromide ([BMIM]Br) and 1-decyl-3-methylimidazolium bromide ([DMIM]Br)) were chosen to enable the study of vibrational relaxation dependence on alkyl chain length. Moreover, different AN mass concentrations in AN/IL solutions (5% and 20%) and temperatures (295K and 328K) were used to assess AN C ≡ N stretch vibrational relaxation dependence on temperature and AN concentration. Two-dimensional correlation analysis was used to determine the structure of υ_2 band.

From the carried out experiments it was found that acetonitrile vibrational relaxation is faster in studied ILs solutions (see table below) probably due to local ionic structuring [1]. Increased temperature of these solutions lead to even faster relaxation (see Fig. 1). Furthermore, the lengthening of alkyl chain of IL cation (in this case from 4 carbon atoms to 10) lead to faster acetonitrile vibrational relaxation as well, which could be due to the increase in degrees of motion of the cation (i.e., the larger the cation, the more degrees of motion it has for energy to distribute).

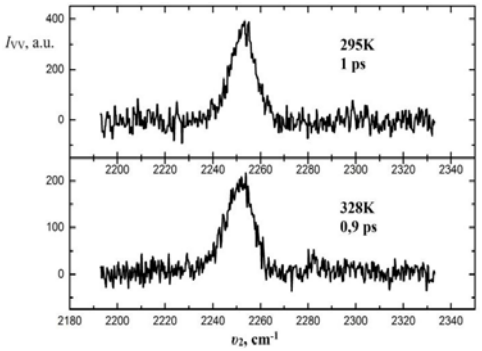

Fig. 1. AN in [DMIM]Br (upper spectrum at T = 295 K and lower at T = 328 K) solution Raman I_{VV} spectrum in υ_2 mode region with according vibrational relaxation times in picoseconds

Table 1. Measured half-widths (HWHH) of Raman mode υ_2 and calculated vibrational relaxation times (τ_{vib}) in neat AN at T = 295 K and in AN solutions (at T = 295 K and 328K in parentheses) in [BMIM]X, (X=Cl, Br, I) and [DMIMB]Br (5% and 20% AN wt)

Δ_{VV}, cm^{-1}	Δ_{VH}, cm^{-1}	τ_{vib}, ps
Neat AN		
1,65[1]	6,1[1]	3,2
2[2]	7,25[2]	2,7
2,48	6,17	2,14
AN(20 % wt)/[BMIM]Br		
4,13(4,33)	5,32(4,57)	1,31(1,26)
AN(5% wt)/[BMIM]Br		
3,71(4,18)	4,32(4,87)	1,7(1,3)
AN(20% wt)/[DMIM]Br		
5,43(6,01)	-	0,98(0,88)
AN(5% wt)/[DMIM]Br		
5(5,73)	-	1,06(0,93)

[1] V. Aleksa, V. Barkauskas, V. Pogorelov, H. Fuess, and V. Balevicius, "Raman spectroscopy of vibrational and rotational relaxation of acetonitrile molecules dissolved in ionic liquids," *Lith. J. Phys.*, vol. 47, no. 4, pp. 435–441, 2007.

[2] J. Hiraishi and K. Tanabe, "Comparative study of Raman and I.R. band widths of acetonitrile," *Spectrochim. Acta*, vol. 36A, no. 1, pp. 665–671, 1980.

MATRIX ISOLATION INFRARED ABSORBTION STUDY OF 1-BUTYL-3-METYLIMIDAZOLIUM TRIFLUORMETHANE SULFONATE IONIC LIQUID

Mindaugas Jonušas[1], Justinas Čeponkus[1]

[1] Department of Physics, Vilnius University, Lithuania
mindaugas.jonusas@ff.stud.vu.lt

Ionic liquids (IL) used as new solvents and industrial materials have been widely investigated because they have some specific properties such as high ionic conductivity, nonvolatility, and high viscosity. Researchers have been trying to understand the relationship between the properties and the anion-cation structure from the viewpoint of molecular science.

Infrared (IR) absorption vibrational spectra provide important information to determine molecular structures. However, vibrational spectra of ionic liquids are not easy to be measured. Liquid phase spectra present broad bands which are hiding important spectral information. Gas spectra are difficult to measure because vapor pressures are not high enough to obtain sufficient quality vibrational spectra [1]. These problems could be solved by using a low-temperature matrix-isolation method. The essence of the method is to trap molecules under study in low temperature (usually below 10 K) rare gas crystals.

During this study we succeeded to evaporate ionic liquid without thermal decomposition and measure IR absorption spectra (fig. 1).

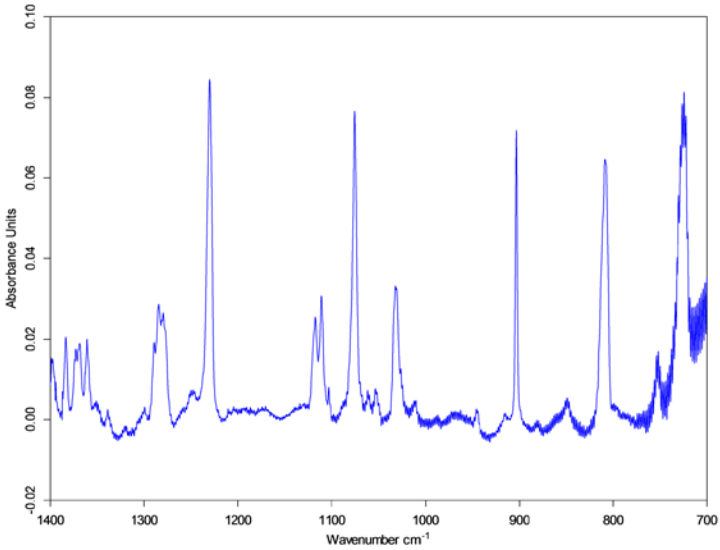

Fig. 1. IR absorption spectra of 1-butyl-3-metyl-imidazolium trifluormethane sulfonate

Sharp bands of the infrared absorption spectra with the aid of theoretical calculations allow precise assignment of each band to the vibrations of the atoms in the ionic liquid. Spectral and calculated data allows us to state that ionic liquid evaporates in pairs and not in individual ions. The annealing experiments exhibit changes in the infrared spectra, indicating possibility of conformational changes or complex formation.

[1] N. Akai, D. Parazs, A. Kawai, K. Shibuya, Cryogenic Neon Matrix-isolation FTIR Spectroscopy of Evaporated Ionic Liquids: Geometrical Structure of Cation-Anion 1:1 Pair in the Gas Phase, J. Phys. Chem. B, Vol. 113, No. 14, 4756-4762, 2009.

INVESTIGATION OF DLC:Cu NANOCOMPOSITE FILMS BY VARIABLE ANGLE SPECTROSCOPIC ELLIPSOMETRY

Aušrinė Jurkevičiūtė[1,2], Tomas Tamulevičius[1,2], Domantas Peckus[1], Šarūnas Meškinis[1], Sigitas Tamulevičius[1,2]

[1]Institute of Materials Science of Kaunas University of Technology, Baršausko str. 59, LT-51423, Kaunas, Lithuania
[2]Department of Physics, Faculty of Mathematics and Natural Sciences, Kaunas University of Technology, Studentų str. 50, LT-51368, Kaunas, Lithuania
Ausrine.Jurkeviciute@ktu.edu

Ellipsometry is a non-destructive optical method for investigation of optical properties of various materials. It is most commonly used for determination of refractive index and thickness of thin films [1]. In this work, spectroscopic variable angle ellipsometer GES5E (Semilab) and Spectroscopic Ellipsometry Analyzer (SEA, Semilab) software were employed for determination of refractive index and extinction coefficient dependences on wavelength dispersion curves, thickness of DLC:Cu nanocomposite films and copper filler content.

DLC based Cu nanocomposite films were deposited on quartz substrates using magnetron sputtering technique of Cu target with argon ions in acetylene gas atmosphere [2]. The thickness of the films were investigated using transmission electron microscope (TEM). In order to investigate optical properties, optical models of structures were created in SEA software. The optical model of the structure was varied until the measured and modelled Ψ and Δ plots had a good fit with each other [3]. Nanocomposite DLC:Cu film was described by Effective Medium Approximation (EMA). For copper filler refractive index and extinction coefficient values from database were used. DLC matrix was described by dispersion laws (Drude or Adachi).

In experimental measurement, every sample was investigated in 4-5 microspots and using parallel beam. The ellipsometric parameters were derived for 10 different angles of incidence. Since all of these angles were used to measure at the same spot, they all were fitted at the same time using the same optical model in order to obtain more reliable result.

After fitting, various parameters of the investigated nanocomposite film were obtained. The derived thickness was compared with TEM results. The differences are less than 10 %. The dispersion curves of refractive index and extinction coefficient (see fig. 1) were defined and compared with optical absorbance measurements obtained with UV-VIS-NIR spectrometer.

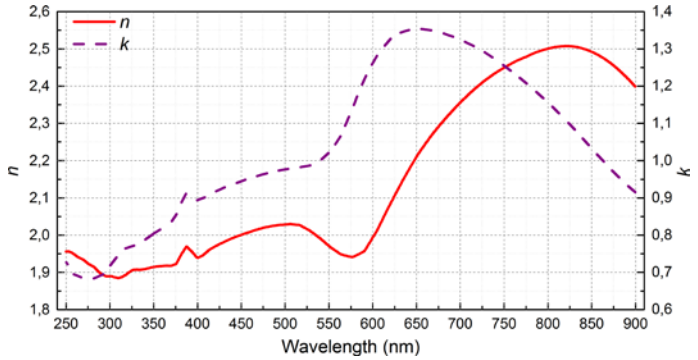

Fig. 1. The dispersion graphs of nanocomposite DLC:Cu film. Concentration of the film obtained from energy dispersive X-ray analysis: Cu 81 wt%, C 16 wt%. Thickness obtained from ellipsometry results is 29.6 nm.

Acknowledgements: This research was funded by the European Social Fund under the Global Grant measure (NIR-SOLIS Grant No. VP1-3.1-ŠMM-07-K-03-057).

[1] L. Augulis, *Taikomoji optika ir fotonika* (Vitae Litera, Kaunas, 2007).
[2] I. Yaremchuk, A. Tamuleviciene, T. Tamulevicius et al., Modelling of the plasmonic properties of DLC-Ag nanocomposite films, Physica Status Solidi A **211(2)**, 329-335, 2014.
[3] Spectroscopic Ellipsometry Analyzer User's Reference Manual. Budapest, Hungary: Semilab Co. Ltd., 2012.

2D CALCULATIONS OF OH AND CH_3 INTERNAL ROTATIONS IN ETHANOL MOLECULE

Anastasia Kapskaya, Alex Malevich, George Pitsevich.

Department of Physical Optics, Belarusian State University, Minsk, Belarus

kapskaya.anastasiya@mail.ru

In this work we study internal rotation of two not coaxial tops in CH_3CH_2OH molecule. One of this top is symmetric (CH_3) while another one (OH) – asymmetric. This tops undergo to kinematic and force interaction. Previously internal rotation in this molecule was study using B3LYP/cc-pVTZ level of theory [1]. Authors also used Podolsky transformation of Schrödinger equation from Cartesian to natural coordinates [2]. In this study more high level of theory (B3LYP/AUG cc-pVQZ) was taken. We use Wilson's $\dot{s}$ vectors [3] for transformation of Schrödinger equation from Cartesian to natural coordinates. In doing so one can get following kinetic energy operator for internal rotations of two tops in ethanol molecule if we neglect the first derivative of the wave function for torsion coordinates:

$$\begin{aligned}&\left[-B_H\left[\left(\dot{s}^{\varphi}_{r7}\right)^2+\left(\dot{s}^{\varphi}_{r8}\right)^2+\left(\dot{s}^{\varphi}_{r9}\right)^2+\left(\dot{s}^{\varphi}_{r2}\right)^2+\left(\dot{s}^{\varphi}_{r3}\right)^2\right]-B_C\left[\left(\dot{s}^{\varphi}_{r6}\right)^2+\left(\dot{s}^{\varphi}_{r1}\right)^2\right]-B_O\left(\dot{s}^{\varphi}_{r4}\right)^2\right]\frac{\partial^2}{\partial\varphi^2}+\\&\left[-B_H\left[\left(\dot{s}^{\gamma}_{r5}\right)^2+\left(\dot{s}^{\gamma}_{r2}\right)^2+\left(\dot{s}^{\gamma}_{r3}\right)^2\right]-B_C\left[\left(\dot{s}^{\gamma}_{r6}\right)^2+\left(\dot{s}^{\gamma}_{r1}\right)^2\right]-B_O\left(\dot{s}^{\gamma}_{r4}\right)^2\right]\frac{\partial^2}{\partial\gamma^2}+\\&\left[-B_H\left[2\left(\dot{s}^{\gamma}_{r2}\cdot\dot{s}^{\varphi}_{r2}\right)+2\left(\dot{s}^{\gamma}_{r3}\cdot\dot{s}^{\varphi}_{r3}\right)\right]-B_C\left[2\left(\dot{s}^{\gamma}_{r1}\cdot\dot{s}^{\varphi}_{r1}\right)+2\left(\dot{s}^{\gamma}_{r6}\cdot\dot{s}^{\varphi}_{r6}\right)\right]-B_O 2\left(\dot{s}^{\gamma}_{r4}\cdot\dot{s}^{\varphi}_{r4}\right)\right]\frac{\partial^2}{\partial\gamma\partial\varphi};\end{aligned}\qquad(1)$$

where φ and γ torsional coordinates for CH_3 and OH internal rotations respectively, $B_H = 16.7346\ см^{-1}$, $B_C = 1.4043\ см^{-1}$, $B_O = 1.0544\ см^{-1}$, $\dot{s}^{\varphi}_{r_i}$ and $\dot{s}^{\gamma}_{r_j}$ - Wilsons $\dot{s}$ for φ and γ torsional coordinates, *i,j*- atoms numbers according with Fig.1

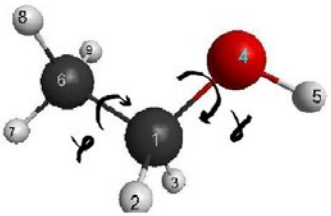

Fig. 1 Ethanol molecule with indication of atoms numbering and torsional coordinates.

2D potential energy surface (PES) was built. Energy was calculated at the nodes of 2D rectangular uniform grid with sides $0 \le \gamma \le 2\pi;\quad 0 \le \varphi \le 2\pi/3;$ with steps $\pi/6$ and $\pi/12$ respectively. Representing (1) in form:

$$F^{\gamma\gamma}(\gamma,\varphi)\frac{\partial^2\psi(\gamma,\varphi)}{\partial\gamma^2}+F^{\gamma\varphi}(\gamma,\varphi)\frac{\partial^2\psi(\gamma,\varphi)}{\partial\gamma\partial\varphi}+F^{\varphi\varphi}(\gamma,\varphi)\frac{\partial^2\psi(\gamma,\varphi)}{\partial\varphi^2};\qquad(2)$$

And expanding the kinematic coefficients and potential energy $U(\gamma,\varphi)$ in a two-dimensional complex Fourier series one can get the expression for elements of Hamiltonian matrix:

$$H_{(m'n'),(mn)} = -m^2F^{\gamma\gamma}_{m'-m,n'-n} - 9n^2F^{\varphi\varphi}_{m'-m,n'-n} - 3mnF^{\gamma\varphi}_{m'-m,n'-n} + U_{m'-m,n'-n}\qquad(3)$$

During calculations of energies and wavefunctions according with [4] we were able switch on and off kinematic and force interaction between tops. This gave us the opportunity to evaluate the influence of these interactions on frequensies of torsional vibrations. We also calculated conponents of dipol moment as functions on torsion coordinates. So intensities of torsional transition were calculated too.

[1] M. Senent, Y. Smeyers et al., Ab initio determination of the far infrared spectra of some isotopic varieties of ethanol, Journal of Chemical Physics, **112**, 5809-5819 (2000).
[2] B. Podolsky, Quantum-mechanically correct form of Hamiltonian function for conservative systems, Physical Review, **32**, 812-815 (1928).
[3] E.B.Wilson,J.C.Decius,P.C.Cross Molecular Vibrations. Dover Publications Ink, New York, 1955
[4] G. Pitsevich, V. Balevicius Hydrogen bonded pyridine N-oxide/trichloroacetic acid complex in polar media: 2D potential energy surface and O–H_ _ _O vibration analysis using exact vibrational Hamiltonian, Journal of Molecular Structure, **1072**, 38-44 (2014).

CALCULATIONS OF POTENTIAL ENERGY CURVES AND FRANCK-CONDON FACTORS OF KRb GROUND AND EXITED SINGLET STATES.

Olga Kovalkova, Maxim Shundalou, George Pitsevich.

Department of Physical Optics, Belarusian State University, Minsk, Belarus

olga.kovalkova.94@mail.ru

It is seems that calculation of the exact potential energy curves (PEC) of the diatomic molecules is routine task. But everybody who has dealt with this problem will agree that it is kind of art. Despite a number of papers on the subject [1, 2] we decided to perform a series of calculations.

The potential energy curves (PECs) for the ground and low-lying excited states of KRb are calculated by using high level *ab initio* MRPT method (XMCQDPT2/CASSCF approximation). The effective core potential (ECP) basis sets for K and Rb atoms are modified ECP10MDF and ECP28MDF respectively. CASSCF (complete active space self-consistent field) and XMCQDPT2 (extended multiconfiguration quasi-degenerate 2nd order perturbation theory) calculations were performed using the Firefly program package. The active space for the CASSCF calculations is 2 electrons in 14 orbitals. All the doubly occupied orbitals in all configurations are active in XMCQDPT2 calculations. To find energy levels values and wave functions the Schrödinger equation for vibrational-rotational motion of diatomic molecule (1) was solved using DVR and Fourier series methods [3,4].

$$-F_{KRb}\frac{d^2\Psi}{dx^2}+\{U(x)+\frac{F_{KRb}\,\mathrm{J(J+1)}}{(x+R^0_{KRb})^2}\}\Psi=E\Psi \qquad (1)$$

where $x=\frac{R_{KRb}-R^0_{KRb}}{l_0}$ - dimensionless vibrational coordinate, R_{KRb} - distance between atoms, R^0_{KRb} - equilibrium distance between atoms, l_0 =1Å, $U(\mathrm{x})$ - PEC, F_{KRb} - kinetic factors depending on the masses of the isotopes of the K and Rb atoms, J – rotational quantum number. Calculated PEC for some exited and ground singlet states are represented on figure 1.

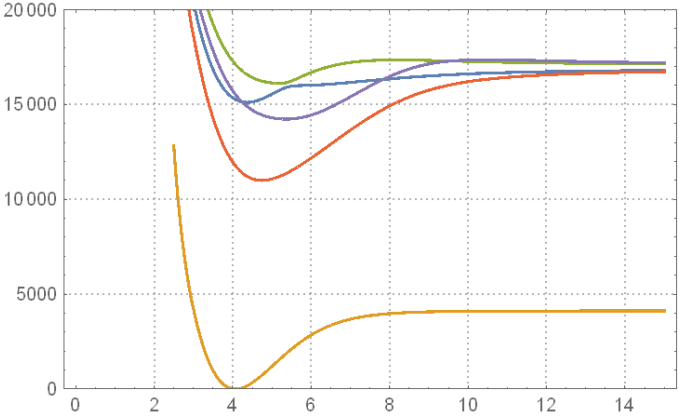

Figure 1. PES for ground (yellow color) and exited (other colors) singlet states of KRb molecule.

Vibrational-rotational energy levels values for each electronic states and J=0-10 were found. Differences between vibrational level as function of the vibrational quantum numbers for ground state extremely smooth and their values are in perfectly consistent with experimental ones. Spectroscopic constants for different singlet levels were calculated. Franck-Condon factors for transitions from ground vibrational and electronic state to exited electronic and vibrational level were calculated too.

[1] C. Amiot, J. Verges, The KRb ground electronic state potential up to 10 Å, Journal of Chemical Physics, **112**, 7068-7074 (2000).
[2] D. Borsalino, B. Londono-Florez et al., Efficient optical schemes to create ultracold KRb molecules in their rovibronic ground state, Physical Review A, **90**, 033413-1-14 (2014).
[3] G. Pitsevich, A. Malevich Simple Method of the Formation of the Hamiltonian Matrix for Some Schrödinger Equations Describing the Molecules with Large Amplitude Motions, Optics and Photonics Journal, **2**, 332-337 (2012).
[4] G. Pitsevich, V. Balevicius Hydrogen bonded pyridine N-oxide/trichloroacetic acid complex in polar media: 2D potential energy surface and O–H_ _ _O vibration analysis using exact vibrational Hamiltonian, Journal of Molecular Structure, **1072**, 38-44 (2014).

THz EMISSION FROM LARGE AlGaN/GaN HEMTs WITH GRATING ELECTRODES

Justas Laužadis, Rimvydas Venckevičius, Vytautas Jakštas, Irmantas Kašalynas

Center for Physical Sciences and Technology, Vilnius, Lithuania
justas.lauzadis@ff.stud.vu.lt, irmantak@ktl.mii.lt

The application of terahertz (THz) radiation in security and medical diagnostics besides sensitive THz detectors also requires developing compact high-power THz emitters performing at room environment. High up to 1.8 μW power emission with power conversion efficiency of 1.6×10^{-6} in the range of 0.5-4.0 THz have been observed from AlGaN/GaN field effect transistors (FETs) with sub-micron grating Ohmic contacts at room temperature [1]. The approach was left without obvious explanation and many groups worked on THz emission of the AlGaN/GaN based transistors with Schottky gate grating. In this work we perform comparative analysis of the spectra of THz emission of the AlGaN/GaN FETs with Ohmic and Schottky grating electrodes.

The electronic devices on AlGaN/GaN/sapphire grown in the VU TMI MOCVD reactor were fabricated using recently developed procedures [2]. The carrier density and mobility of two dimensional electron gas (2DEG) in high electron mobility transistor (HEMT) structures was of about $4.7\cdot10^{12}$ cm^{-2} and 2550 cm^2/(V·s), respectively. Plasmons excited in FET channel cause electromagnetic waves radiation via the 2x2 mm^2 grating of the period ranging from 6 to 150 μm fabricated as the source/drain (Ohmic type grating) and gate (Schottky type grating) contacts. The spectrum of thermally stimulated emission of the samples was measured with Fourier transform spectrometer with vacuum option, and the absolute power - with THz power meter (Thomas Keating). To see the influence of plasmonic grating, measured emission spectrum was normalized

$$(I_{HEMT} - I_{surface}/I_{surface}), \tag{1}$$

here I_{HEMT} is thermal emission spectrum from the FET with grating electrodes, and $I_{surface}$ – emission spectrum of the AlGaN/GaN/sapphire without any metal electrodes. In such a way normalized spectra are shown in Fig. 1.

The frequency of 2DEG plasma waves in transistor channel was described as [3]:

$$f = \frac{sn}{4L}\left(1 - \frac{v^2}{s^2}\right), \qquad s = \sqrt{\frac{eU_0}{m}}, \tag{2}$$

here s is plasma wave velocity, v – average electron drift velocity, L – length of transistor's channel, n – number of plasma wave mode, e – the electron charge, U_0 – applied voltage to the FET channel, m – the electron effective mass. For AlGaN/GaN 2DEG, s is around 2×10^8 cm/s and L was set by the grating period. The first 2DEG plasmon resonance was at lower frequency range 0,25-0,33 THz (9-12 cm^{-1}) for used 6-8 μm period gratins. But indistinct higher plasmon modes in radiation spectrum of the FET with 6 and 7 μm grating period only were observed at 65-100 cm^{-1} for both Ohmic and Schottky gratings (GT1, GT2, and GT8 samples). Measurement of an absolute power emission from FET with 8 μm period Schottky type grating indicated that the electrical-to-optical conversion efficiency was of about 10^{-3} in frequency range of 0-10 THz.

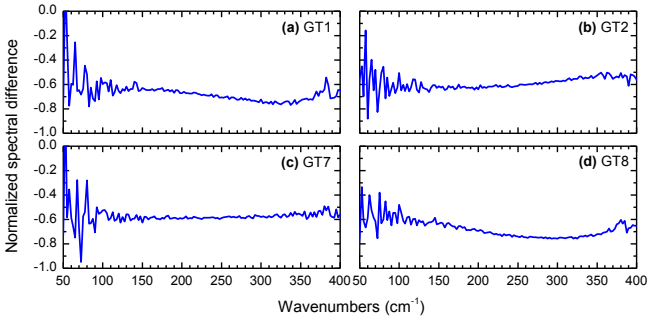

Fig. 1. Normalized emission spectrum from the FET with Ohmic (a-c) and Schottky (d) type grating electrodes. The grating period was 6 μm for GT2, GT7 and 7 μm for GT1, GT8 samples; and it was in addition modulated by period of 15 and 150 μm for sample GT2 and GT7, respectively.

[1] T. Onishi, T. Tanigawa, S. Takigawa, High power terahertz emission from a single gate AlGaN/GaN field effect transistor with periodic Ohmic contacts for plasmon coupling, Applied Physics Letters, **97**, 092117 (2010).
[2] I. Kašalynas, V. Jakštas, I. Šimkienė, V. Strazdienė, P. Prystawko, M. Leszczynski, Schottky Diodes and High Electron Mobility Transistors of 2DEG AlGaN/GaN Structures on Sapphire Substrate, Lithuanian Journal of Physics, **54** (4) 227–232 (2014).
[3] M. Dyakonov, M. Shur, Shallow Water Analogy for a Ballistic Field Effect Transistor: New Mechanism of Plasma Wave Generation by dc Current, Physical Review Letters, **71** (15), 2465-2468 (1993).

QUANTUM MECHANICS/MOLECULAR DYNAMICS PREDICTIONS OF THE ^{1}H NMR SPECTRA OF 1-DECYL-3-METHYL-IMIDAZOLIUM IN THE LIQUID PHASES

Dovilė Lengvinaitė, Kęstutis Aidas

Department of General Physics and Spectroscopy, Faculty of Physics, Vilnius University, Lithaunia
dovile.lengvinaite@ff.stud.vu.lt

Nuclear magnetic resonance spectroscopy, most commonly known as NMR spectroscopy, can provide detailed information about the structure, dynamics, reaction state, and chemical environment of molecules. Differences between isotropic values of nuclear magnetic shielding tensors, the so-called chemical shifts, are most common observables in the NMR spectroscopy. Room temperature ionic liquids (RTILs) are a class of organic salts that remain liquid at or near room temperature. Recently, RTILs have been attracting a great deal of attention of many researchers, as they have many potential applications in separations, catalysis and electrochemistry. These liquids are regarded as environmentally "green" solvents, because they are nonvolatile, thermally stable and recyclable. Furthermore, through different combinations of cations and anions, there is a tremendous variety of these so-called "designer" solvents. With great versatility of their chemical and physical properties, ionic liquids can be thus tailored and tuned for specific tasks.

The quantum chemical (QM) calculation is a valuable technique to obtain useful information without any experiments. The method has been applied to RTILs to obtain the structures of ion pairs and thermodynamic properties. Unfortunately, QM calculations are very computation-intensive and can be only implemented in very small systems. So, the intrinsic relation between the microstructure and property cannot be revealed in this way. Atomistic simulation, usually known as molecular simulation, is one of the most promising approaches to investigate structural and dynamic properties of molecules and materials. Success of molecular simulation for accurately predicting various properties depends on the quality of inter- and intramolecular potential functions, i. e., force fields.

Experimentally, a curious behavior of the ^{1}H NMR spectra of 1-decyl-3- methyl-imidazolium ([DMim]) molecule (Fig. 1) - a popular cationic component of imidazolium based ionic liquids – dissolved in solvents of varying polarity was recorded: the increasing shielding of the proton at the 2nd position of the imidazolium ring was observed with the rising polarity of the solvent [1].

In this work, we have modelled the ^{1}H NMR spectra of [DMim][Cl] ionic pair dissolved in three solvents of different polarity (dichloromethane, acetonitrile and water). We have performed molecular dynamics (MD) simulations for these systems, using AMBER based force field for the ionic pair due to Liu et al. [2]. The standard TIP3P potential was utilized for water, and GAFF force field was used for other two solvents with point charges derived using RESP procedure as implemented in the Antechamber package. GAFF is compatible to the AMBER force field and it has parameters for almost all the organic molecules. GAFF is suitable to study a great amount of molecules. MD simulations were performed in NVT and NPT ensembles. Detailed information concerning local structure was obtained by analyzing relevant radial distribution functions (RDF). Having recorded the trajectories of the systems, we turned to the combined quantum mechanics/molecular mechanics (QM/MM) based calculations of the NMR parameters. Calculations of the proton chemical shifts were performed using both polarizable and non-polarizable potentials for solvents.

Detailed account of the results will be presented at the conference.

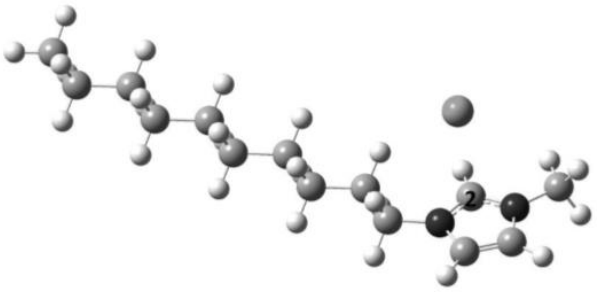

Fig 1. Structure of the 1-decyl-3-methyl-imidazolium chloride ionic pair.

[1] V. Balevicius, Z. Gdaniec, K. Aidas, J. Tamuliene, NMR and Quatum Chemistry Study of Mesoscopic Effects in Ionic Liquids, *J. Phys. Chem. A* **114**, 5365-5371, (2010).

[2] Z. Liu, S. Huang, W. Wang, A refined force field for molecular simulation of imidazolium-based ionic liquids, *J. Phys. Chem. B* **108**, 12978-12989 (2004).

DESIGN OF A MICROWAVE INTERFERENCE DETECTION SYSTEM

Karolis Mockus[1], Žilvinas Kancleris[1], Paulius Ragulis[1], Rimantas Simniškis[1]

[1] Microwave Laboratory, Department of Physical Technologies, Center for Physical Sciences and Technology, Lithuania
Karolis.Mockus@ftmc.lt

Electronic components and systems used in the industry, defense and infrastructure are becoming smaller and more complex. This means that they are becoming more susceptible to the effects of electromagnetic fields **[1]**. Furthermore the ongoing technological advancement means that high power electromagnetic radiation sources are getting smaller, cheaper and more common place. Exposure to microwave pulses may affect the operation of computers, security and communication systems and computer networks .Operation of such systems can be temporarily suspended or irreparably damaged **[2]**. Even automotive vehicles and boats may be stopped or even damaged by directed electromagnetic radiation **[3]**. Therefore it is of paramount importance to adequately protect key electronic equipment from incidental or directed electromagnetic interference.

Usually electromagnetic fields are measured using low-power and average-power measurement equipment. Such equipment cannot reliably detect short or single pulse radiation which is usually generated by compact generators trying to effect the operation of electronic equipment. By incorporating resistive sensors (RS) **[4]** high power pulses may be measured. Such detectors are very resistant to overload and can be used without attenuation therefore increasing the accuracy and reliability of the measurements.

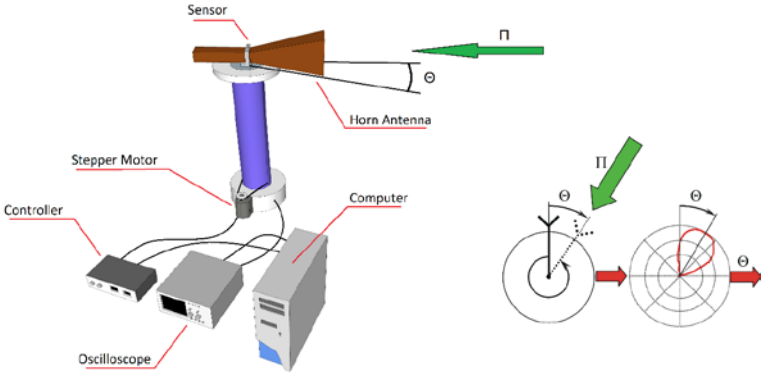

Fig. 1 Structural diagram of the microwave detection system and a polar plot of incident microwave radiation

A microwave interference detection system created incorporating an RS and a mechanically rotating positioning system is shown in figure 1. The main advantage of such an arrangement is the simplicity and precision of detecting the source of radiation the other advantages being economy of manufacture and the ability to detect strong electromagnetic fields without damage to the sensor. The system is comprised of a computer running dedicated software which controls a microcontroller operated positioning system used to rotate a highly directional horn antenna in a controlled and precise manner. The signal is detected using an oscilloscope connected to the RS. Data from the oscilloscope is collected and analyzed by software and a polar plot of the signal amplitude is generated. This plot is then used to calculate the angular position of the radiation source and the antenna is turned to that position to continue the monitoring of the interference.

The current system can precisely (<1,5) point out the source of the radiation up to 200kV/m in 1-12 GHz frequency range and has been tested in laboratory and on field trials in Norway according to the international project HIPOW, documented on NATO scientific program channel on YouTube **[5]**.

[1] M. Camp and H. Garbe, "Susceptibility of personal computer systems to fast transient electromagnetic pulses," IEEE Transactions on Electromagnetic Compatibility, vol. 48, pp. 829-833, 2006.
[2] M. Dagys, Z. Kancleris, P. Ragulis, R. Simniškis, and V. Tamosiunas, "Investigation of susceptibility of routers to high power microwave pulse radiation," 18th International Conference on Microwave Radar and Wireless Communications (MIKON), 2010, pp. 1-3.
[3] N. Picard, S. Mazen, B. Beilard, E. Martinod, J. Andrieu, J. Ch. Joly, Th. Tournardre. Radiated susceptibility of automotive eletronics: Car stopper application. *Euroem 2012* Onera-Toulouse, France July 2-6, 2012, Book of abstracts, P. 49.
[4] M. Dagys, Ž. Kancleris, R. Simniškis, E. Schamiloglu and F. J. Agee. Resistive sensor: device for high-power microwave pulse measurement. *IEEE Antennas & Propagation Magazine*, vol. 43, No 5, p. 64-79, 2001.
[5] NATO Yuotube: Suicide bombers and how to beat them, http://www.youtube.com/watch?v=56veH8-KbEM

DEVELOPMENT OF THE ALPHA-FETOPROTEIN IMMUNOASSAY BASED ON PLASMON-ENHANCED FLUORESCENCE

Alina Muravitskaya[1], Andrei Ramanenka[2]

[1] Researcher Training Institute of the National Academy of Sciences of Belarus, Belarus
[2] B. I. Stepanov Institute of Physics, National Academy of Sciences of Belarus, Belarus
alica.mur@mail.ru

Plasmon-enhanced fluorescence of molecular probes is a highly developing field providing a number of new methods in chemical and biomedical analysis. It is based on the following effects: the heightened electromagnetic fields near nanostructured metallic surfaces due to localized plasmon resonances and propagating surface plasmon polaritons enhance the excitation rate of fluorescent species placed in the near field; the close vicinity of metal nanostructures change fluorescence quantum yield drastically due to density of states effect and possible energy transfer to metal surface. So fluorescent enhancement depends on different factors, like size and shape of the metallic nanoparticles, its absorption properties, distance between them and fluorophore [1,2].

In previous works we had investigated plasmon-enhanced fluorescence of model biological conjugates BSA-FITC near silver nanoparticles deposited on glass substrates both theoretically and experimentally [3,4]. The goal of this work was to develop the fluorescent immunoassay for Alpha-Fetoprotein (AFP) that takes advantages of the plasmon-enhanced signal. For this purpose multilayer nanostructures "silver nanoparticles – polyelectrolytes – immunocomplex" were prepared by successive deposition on plastic substrates [3]. Silver sol was synthesized by the $AgNO_3$ citrate reduction technique. Complexes AFP-anti-AFP - FITC were obtained by 1) deposition of the different concentrations of the AFP to the preliminarily prepared samples with/without silver coating; 2) deposition of the BSA to block all molecules that have not connected to substrate; 3) removal of the AFP-BSA complexes; 4) deposition of anti-AFP-FITC.

Fluorescence spectra were registered with a grating spectrograph S3801 (Solar TII, Belarus) combined with a liquid nitrogen cooled silicon CCD camera (Princeton Instruments, USA). Fluorescence excitation was performed with a cheap and affordable commercial light-emitting diode with the emission spectrum peaking at 460 nm. All optical measurements were made at room temperature (~300 K).

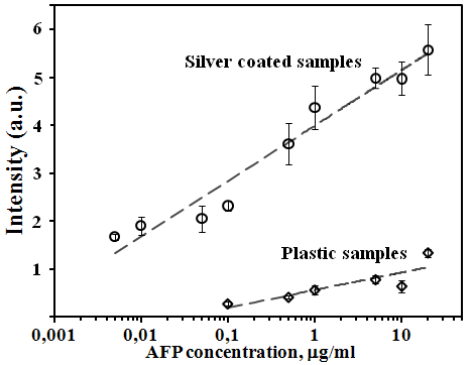

Fig. 1. Intensity of the labels fluorescence as a function of the antigen concentration on silver coated and plastic samples (concentration in logarithmic scale).

It was found that fabricated silver containing samples enhanced fluorescence in comparison to the reference signal from plastic substrates without silver coatings (Fig.1). Both concentration dependences were approximated by straight lines in logarithmic scale. The total fluorescence enhancement for AFP-anti-AFP – FITC complexes did not exceed 10 times. Linear section for silver coated samples is 5 ng/ml – 500 ng/ml (R^2=0,98) (the medical threshold point for AFP in normal conditions is 5-10 ng/ml).

[1] S. V. Gaponenko, Introduction to Nanophotonics, Cambridge University Press, Cambridge (2010).
[2] S.A. Maier, Plasmonics: Fundamentals and Applications, Springer Science, USA (2007).
[3]S. V. Vaschenko et al., "Plasmon-enhanced fluorescence of labeled biomolecules on top of a silver sol-gel film," J. Nanophoton. 6(1), 061710 (2012).
[4] D. V. Guzatov et al., "Plasmonic enhancement of molecular fluorescence near silver nanoparticles: theory, modeling, and experiment," J. Phys. Chem. C 116(19), 10723–10733 (2012).

INVESTIGATION OF NASICON NANOCERAMICS CONDUCTIVITY

Juozas Noreika

Department of Radiophysics, Faculty of Physics, Vilnius University, Lithuania
juozas.noreika@ff.stud.vu.lt

$Li_{1.3}Al_{0.3}Ti_{1.7}(PO_4)_3$ is known as a good solid electrolyte with high lithium-ion conductivity [1]. This compound crystallizes into the so called NASICON-type structure, which enables lithium migration inside solid framework [2]. Its bulk conductivity reaches 10^{-3} S/m at room temperature [3]. However, the NASICON ceramics do not show very high total conductivity because it is limited at the grain boundaries. So the modification of ceramic grain boundaries is necessary in order to improve the total conductivity of $Li_{1.3}Al_{0.3}Ti_{1.7}(PO_4)_3$ ceramics.

The aim of this work is to investigate electrical properties of $Li_{1.3}Al_{0.3}Ti_{1.7}(PO_4)_3$ ceramics prepared by different synthesis conditions. Electrical properties of the NASICON nanoceramics were investigated by two probe impedance spectroscopy method in the frequency range from 10 Hz to 3 GHz and temperatures from 300 K to 740 K. Three dispersion regions were found in the impedance spectra of the ceramics. The one at the highest frequencies is related to ionic transport in the grains of ceramics, the other in the intermediate temperature range – to the ionic transport in grain boundaries, while the dispersion at the lowest frequencies corresponds to ion blocking effects at the solid electrolyte-electrode interface. So, the impedance studies in the broad frequency range allowes one to separate grain and grain boundary conductivities of the ceramics and their temperature dependences are shown in Fig. 1.

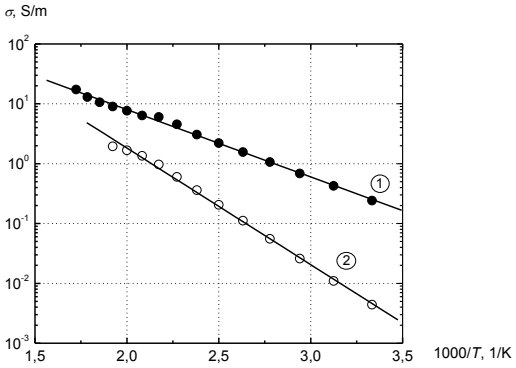

Fig. 1. Temperature dependences of grain ① and grain boundary ② conductivities of $Li_{1.3}Al_{0.3}Ti_{1.7}(PO_4)_3$ ceramics.

Both grain and grain boundary conductivities obey Arrhenius law in the investigated ceramics. The activation energies of conductivities were found from Arrhenius plots. The comparison of electrical properties for ceramics prepared by applying different their preparation conditions is presented.

[1] P. Knauth, Inorganic solid Li ion conductors: An overview, Solid State Ionics 180, 911-916 (2009).
[2] K. Arbi, M. Tabellout, M.G. Lazarraga, J.M. Rojo, J. Sanz, Non-Arrhenius conductivity in the fast lithium conductor $Li_{1.2}Ti_{1.8}Al_{0.2}(PO_4)_3$: A ^{7}Li NMR andelectric impedance study, Physical Review B 72, 094302 (8pp) (2005).
[3] T. Šalkus, E. Kazakevičius, A. Kežionis, Peculiarities of ionic transport in $Li_{1.3}Al_{0.15}Y_{0.15}Ti_{1.7}(PO_4)_3$ ceramics, J. Phys.: Condens. Matter 21, 185502 (7pp) (2009).

3D CALCULATION OF VIBRATIONS OF O-H GROUPS COMBINED TRICHLORO-ACETIC ACID AND PYRIDINENITROGONOXIDE IN ACETONIRILE

Ol'ga Novichenok[1], George Pitsevich[1*]

[1] Department of Physical Optics, Belarusian State University, Belarus
navichonak@gmail.com

As is known, light fluctuations of atoms, such as hydrogen, are especially anharmonic. This is due to the large amplitudes of oscillations of the atoms in excited vibrational states. Quadratic representation of the potential energy acceptable to describe the vibrations of most atoms is unsatisfactory. Accounting for the third and fourth derivatives of the potential energy and the use of perturbation theory makes it possible to specify the frequencies of vibrations of C-H and O-H bonds in the free molecules. However, due to the formation of hydrogen-bonded complexes, the potential surface energy associated with the vibrations of the hydroxyl group often varies significantly. This can lead to a further increase in the amplitude of the oscillatory motion. As shown by several studies [1,2], anharmonic approximation in this case is unable to correctly predict the frequencies of vibrations of O-H groups.To adequately address this problem it is necessary to obtain a more accurate representation of the potential surface energy. In line with the approach developed in [3], the calculation of vibrations of the hydroxyl group carried out under the assumption that the motion of an atom of hydrogen occurs in the field produced by the rest of the stationary atoms of the complex. Based on this approximation, the three-dimensional potential surface was calculated for different offset positions of the hydroxyl proton without geometry optimization for the other structural parameters. Energy calculation was carried out in the approximation of B3LYP / cc-pVTZ using quantum chemical package GAMESS [4]. The values of the potential energy calculated in some three-dimensional lattice sites for the displacement intervals hydroxyl hydrogen atom from its equilibrium position by 1 Å to +0.3 Å along the X axis, from -0.5 Å to +0.5 Å along the Y axis and from -0.7 Å to +0.7 Å along the axis Z. For values ΔX equal to -1 Å, -0.8 Å, -0.5 Å, -0.2 Å, 0 Å, +0.1 Å and +0.3 Å (a) energy was calculated at nodes that are in the plane perpendicular to the axis X. Thus, the potential energy was calculated over 700 points. Further, by interpolating the energy that was calculated in all nodes of a parallel pipe with dimensions $\Delta X \cdot \Delta Y \cdot \Delta Z = 1.4 \cdot 1.1 \cdot 1.5$ Å3, each axis increased 0.1 Å. Further calculations were carried out according to the procedure described in [5]. The calculated frequencies were in satisfactory agreement with the IR spectra of the complex in acetonitrile, registering at different temperatures.

[1] J. Antony, G. von Helden, G. Meijer, J. Chem. Phys., 2005, v. 123, p.014305 1-11.
[2] M. V. Vener, O. Kuhn, and J. M. Bowman// Chem. Phys. Lett., 2001, v. 349, p.562-570.
[3] G.Pitsevich,A.Malevich,V.Sablinskas,I.Doroshenko,V.Pogorelov,V.Balevicius J.Spectrosc. Dyn., 2013, 3: 19.
[4] http://www.msg.ameslab.gov/GAMESS/GAMESS.html
[5] G. A. Pitsevich and A. E. Malevich OPJ, 2012, v.2, p.332-337.

ISOTOPE METHOD APPLICATION FOR THE REVEALING OF JUICES ADULTERATION

Matas Pocevičius, Raminta Skipityte, Andrius Garbaras, Vidmantas Remeikis

Mass spectrometry laboratory, Centre for Physical Sciences and Technology,
Savanorių 231, LT-02300 Vilnius, Lithuania.
matas.pocevicius@gmail.com

Juices are important because they contain vitamins, water and sugar that are vitally important to human body. Natural juices are more valuable than concentrates with various additional components therefore dishonesty can occur in declaring this information. The ratio of ^{13}C and ^{12}C isotopes are commonly encountered in the investigation of sugar adulteration in various products like fruit juices that naturally contain sugar [1, 2].

The main reason of this research was to investigate sugar adulteration in Lithuania's juice market using stable isotope ratio difference between different parts of juice (sugar and pulp). The method is based on naturally occurring carbon stable isotope ratio differences in sugar cane and sugar beet plants. It was established that more than 1.25 ‰ difference between sugar and pulp of the same juice means sugar addition of the different type of plant [3].

Data are presented of stable carbon isotope ratio analysis on Lithuania juice market. Randomly selected 24 various juice samples were collected in freely available Vilnius supermarkets. Juice samples were chemically prepared to isolate sugar and pulp according to ISO standards ("PN-ENV 12140:2004 Fruit and vegetable juices – Determination of the stable carbon isotope ratio ($^{13}C/^{12}C$) of sugars from fruit juices – Method using isotope ratio mass spectrometry" for sugar and "PN-ENV 13070:2004 Fruit and vegetable juices – Determination of the stable carbon isotope ratio ($^{13}C/^{12}C$) in the pulp of fruit juices – Method using isotope ratio mass spectrometry" for pulp). The samples were put in the tin capsule, weighed and measured with the elemental analyzer (Thermo Flash EA1112) coupled to the isotope ratio mass spectrometer (Thermo V Advantage) via ConFlo III interface. Analysis revealed that 4 of 24 juices contained additional cane sugar. Furthemore, 3 of 4 juices according to the manufacturer did not have got any additional sugar.

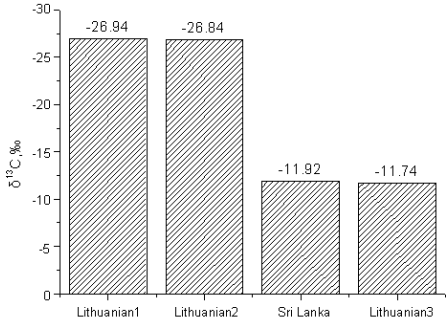

Fig. 1. $\delta^{13}C$ values of sugar from C_3 and C_4 plants.

Values of pulp ranges from -27.51 ‰ to -23.48 ‰ and sugar -26.88 ‰ to -16.98 ‰. Except one of juice's that was pineapple results clearly showed that this is C_4 plant because results were -13.16 ‰ of pulp and -12.91 ‰ of sugar.

The obtained results showed the applicability of isotope ratio mass spectrometry method for the fruit juices adulteration revealing.

[1] Ogrinc, N., K. Bat, I. J. Kosir, T. Golob and R. Kokkinofta (2009). "Characterization of Commercial Slovenian and Cypriot Fruit Juices Using Stable Isotopes." Journal of Agricultural and Food Chemistry 57(15): 6764-6769.
[2] Magdas, D. A., G. Cristea, R. Puscas and F. Tusa (2014). "The use of isotope ratios in commercial fruit juices authentication." Romanian Journal of Physics 59(3-4): 355-359.
[3] Rossmann, A. et al. (1997) "Determination of carbon-13 content of sugars and pulp from fruit juices by isotope-ratio mass spectrometry (internal reference method). A European interlaboratory comparison." Analytica Chimica Acta 340(1): 21-29.

Chemical composition of human teeth as studies by means of FT-Raman spectroscopy

Miglė Radžvilaitė, Milda Pučetaitė, Valdas Šablinskas

Department General Physics and Spectroscopy, Vilnius University
migle.radzvilaite@ff.stud.vu.lt

Early diagnosis of dental and bone diseases is a challenge in medicine as visible changes in the hard tissues only appear when the disease is already advanced. The aim of the present work was is to investigate how chemical composition and structure of human teeth depends on the dental surface, dental disease and human age. Dental enamel, dentine and cementum are biological composites made of mineral phase (apatite), organic phase, and fluid in various portions [1].

Raman spectroscopy is a method widely used for determination of chemical composition and structure of various materials [2]. In this work, Fourier transform (FT) Raman spectroscopy with near-infrared (1064 nm) excitation which allows avoiding fluorescence background in biological samples is used for the chemical analysis of the human teeth.

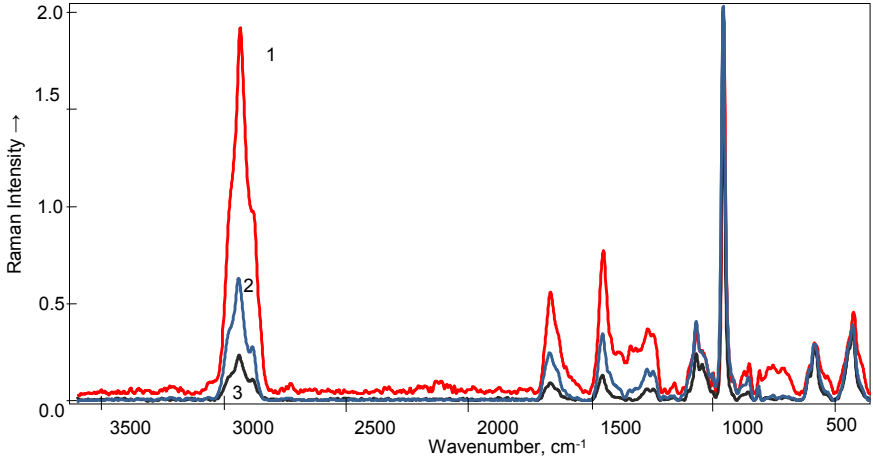

Fig. 1.Raman spectrums comparison of different tooth. 1 –dental caries spectrum, 2 – periodontal ligament spectrum, 3 – enamel spectrum

Raman spectra of different areas in the tooth are presented in Figure 1. The spectra are recorded in the area of dental caries, periodontal ligament and enamel and are normalized according to the hydroxyapatite spectral band at 961 cm^{-1} (νPO_4). It can be seen from the graph that the amount of organic compounds, mainly represented by spectral bands at 2941 cm^{-1} (νCH) and 1667 cm^{-1} (Amide I), vary according to the dental area the spectrum was recorded at. It can be concluded that the spectral differences can be used for analysis of teeth condition; however, further and more thorough investigation is required.

[1] M. Anwar Alebrahim, C. Krafft , W. Sekhaneh , B. Sigusch and J. Popp. ATR-FTIR and Raman spectroscopy of primary and permanent teeth, Biomedical Spectroscopy and Imaging 3 (2014).
[2] C. Krafft, G. Steiner, C. Beleites, R. Salzer, Disease recognition by infrared and Raman spectroscopy, J. Biophoton. 2, No. 1–2, 13–28 (2009).

Determination of thin films thickness and optical properties of periodic structures employing angular white light reflection measurements

Lukas Ramalis[1,2], Artūras Grubas[2], Linas Šimatonis[1,2], Tomas Tamulevičius[1,2], Sigitas Tamulevičius[1,2]

[1]Institute of Materials Science, Kaunas University of Technology, K. Baršausko St. 59, LT-51923, Kaunas, Lithuania,
[2] Department of Physics, Kaunas University of Technology, Studentų St. 50, LT-51368, Kaunas, Lithuania,
lukas.ramalis@gmail.com

Various applications of thins film deposition methods requires non-destructive film thickness monitoring techniques. In holographic lithography experiments with negative tone photoresist materials thickness of the cross linked polymer depends on exposure conditions and developing recipes. In the current work photoresist samples exposed with 371 nm wavelength laser employing Lloyd's mirror holographic lithography system were investigated. Residual thickness of the samples exposed with different period interference fringes were investigated employing angular polarized white light reflectance measurements. Reflectance spectra were recorded using spectrometers AvaSpec-2048 (Avantes) spectrometer covering 350-780 nm spectral ranges with 1.2 nm resolution. Measurements were performed for two polarizations (TE (s), TM (p)) and different angles of incidence varied from 20° to 50°. Reflectance spectra were calculated normalizing reflected light to the lamp spectrum and subtracting noise (dark spectra obtained when the lamp was off). Characteristic interference fringes in reflectance spectra were explained by using Fresnel's expression for system consisting of three different refractive index medium [1]:

$$R = \frac{r_{12}^2 + r_{23}^2 + 2 * r_{12} * r_{23} * \cos(\delta)}{1 + r_{12}^2 * r_{23}^2 + 2 * r_{12} * r_{23} * \cos(\delta)} \quad (1)$$

$$\delta = \frac{2 * \pi}{\lambda} * 2 * n_2 * d * \cos(\theta_t) \quad (2)$$

where R- reflectance, $r_{12,23}$ – the reflection coefficient at the boundaries between mediums 1-2 and mediums 2-3, λ – wavelength, n – refractive index, d – photoresist thickness, θ_t – angle which is found using Snell's law.

Experimental reflectance spectra (see Fig. 1) were explained varying photoresist thickness and calculating theoretical reflectance spectra with eqs. (1), (2) employing know photoresist [2] and glass substrate [3] refractive indices. Angles of refracted light were calculated employing Snell's law.

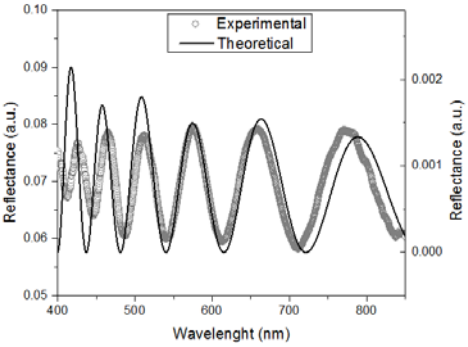

Fig. 1. Experimental and theoretical reflectance spectra obtained at 40° angle of incidence of exposed and developed photoresist film.

[1] Tomas Bernhard Haarde, Pall Ragnar Palsson, Niels Jørgen Christensen, Thin Film Rendering, Copenhagen, July 2007. 11-17 pp. (http://www.itu.dk/~pallragnar/setup/Report.pdf Last time checked 2015 02 06)
[2] http://www.microresist.de/products/negative_photoresists/pdf/po_pi_1400_400_man_08041003_en_ls.pdf, Last time checked 2015 02 06
[3] http://refractiveindex.info/?shelf=glass&book=BK7&page=SCHOTT, Last time checked 2015 02 06

RAMAN AND DFT STUDIES OF SOME ADAMANTANE BASED COMPOUNDS, POTENTIAL ANTIBACTERIAL AGENTS

Andrei Simbura[1], Anna Matsukovich[2], Maksim Shundalau[1]

[1] Department of Physics, Belarusian State University, Minsk, Belarus
[2] B.I. Stepanov Institute of Physics, National Academy of Science of Belarus, Minsk, Belarus
andrea.simbura@yandex.by

In modern chemistry one of the important problems is the synthesis of biologically active derivatives of adamantane, which can later be used as medicines. Now many derivatives of adamantane already tested for biological activity and in most cases have shown a positive result. Derivatives of adamantane have long been known for their antiviral activity against Influenza A and HIV viruses, also associated antimicrobial and anti-inflammatory activities. In this work was made analysis of the newly synthesized molecules 3-(adamantan-1-yl)-4-phenyl-1-[(4-phenylpiperazin-1-yl)methyl]-1H-1,2,4-triazole-5(4H)-thione ($C_{29}H_{35}N_5S$, compound **I**) and ethyl 4-{[3-(adamantan-1-yl)-4-phenyl-5-sulfanylidene-4,5-dihydro-1H-1,2,4-triazol-1-yl]methyl}piperazine-1-carboxylate ($C_{26}H_{35}N_5O_2S$, compound **II**) (Fig. 1). The mechanism of the antibacterial activity of those compounds is uncertain. The present study deals with the investigation of the structural and vibrational properties of those molecules to achieve a better understanding of the properties of such derivatives with the hope that the results would be helpful in the prediction of its mechanism of biological activity.

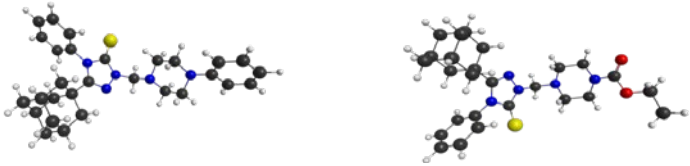

a *b*

Fig. 1. Equilibrium structures of the compound **I** (*a*) and **II** (*b*).

Raman scattering spectra (Fig. 2, *a*, *b*) have been measured using a solid-state cwNd:YAG laser (second harmonic, 532 nm wavelength), a holographic notch filter, a grating spectrometer (600 grooves per mm) Spectra Pro500i and a silicon cooled CCD-camera. Computations of the structural and spectral characteristics of the molecules (Fig. 2, *c*, *d*) were realized with the use of the quantum chemical package GAMESS-US. Optimization of the equilibrium structure, computations of force fields, Raman spectra frequencies and intensities in the harmonic approximation were performed using the standard cc-pVDZ basis by DFT methods with the help of the hybrid B3LYP functional.

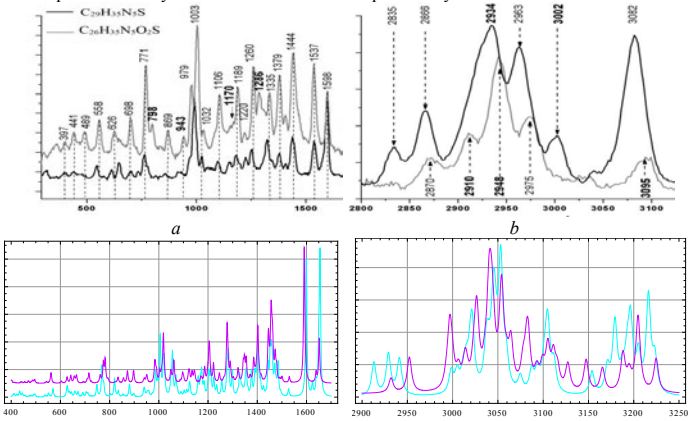

a *b*

c *d*

Fig. 2. Experimental (*a*, *b*) and calculated (*c*, *d*) Raman spectra of the compound **I** and **II**.

Based on analysis of the calculated and experimental spectra is made consistent interpretation of Raman spectra, which can be used for practical purposes objective. We identified the vibrations of different functional groups of the title molecules: adamantane, piperazine, benzyl-triazole, benzyl alcohol and carboxylate. The characteristics of the calculated Raman vibrational spectra correlate well with the experimental data.

CHARGE-SENSITIVE TRIGGERING SYSTEM FOR THE SπRIT EXPERIMENT

Aleksandra Snoch[1], Janusz Brzychczyk[2], Paweł Lasko[2], Jerzy Łukasik[3], Piotr Pawłowski[3], Christoph Schuy[4], Zbigniew Sosin[2], Christina Trautmann[4,5], Wolfgang Trautmann[4], Betty Tsang[6], Kay-Obbe Voss[4]

[1]University of Wrocław, Poland
[2]Jagiellonian University, Kraków, Poland
[3]IFJ-PAN, Kraków, Poland
[4]GSI, Darmstadt,Germany
[5]Technische Universität Darmstadt, Germany
[6]MSU/NSCL, East Lansing, USA
ola.snoch@gmail.com

Equation of state of nuclear matter has important applications in both nuclear physics and astrophysics (eg., neutron stars, or supernovae). Symmetry energy is an important part of the nuclear equation of state. A new experiment prepared by the SπRIT collaboration will be devoted to investigation of the symmetry energy in the supra-normal densities. It will be done by measurement of the π+/π- flows generated in central heavy-ion collisions. One of the essential tools needed to carry it out will be a charge-sensitive triggering system, enabling the on-line recognition of the incident-particle charge.

The triggering system is developed at the Institute of Nuclear Physics of Polish Academy of Sciences in Kraków, Poland, where during my holiday traineeship I actively participated in construction of readout electronics and assembly of the detectors, and further in first on-beam tests performed at GSI facility in Darmstadt, Germany. Currently, in frame of preparing my under-graduate thesis, I have joined the research team preparing the experiment. In the poster I will present an overview of the research questions addressed by the SπRIT experiment and the technical solutions applied in the triggering system.

ANALYSIS OF KIDNEY STONES BY MEANS OF FAR – INFRARED SPECTROSCOPY

Aldona Švelnytė, Milda Pučetaitė

Department of General Physics and Spectroscopy, Faculty of Physics, Vilnius University, Lithuania
aldona.svelnyte@ff.stud.vu.lt

Nephorolithiasis more and more becomes a worldwide health problem. Its prevalence varies from 1 % to 20 %. After treatment, kidney stones tend to recur and the probability of the recurrence is about 75 % during 20 years [1]. For the planning therapy and in order to avoid the recurrence it is important to know the chemical composition of the kidney stones.

In this work, kidney stones were analyzed by far – infrared (FIR) spectroscopy method, which has never been used before. The aim of the work was to get additional information about the stones' composition to the one that can be obtained with traditionally used physical methods. In order to record FIR absorption spectra, the samples must be prepared by polyethylene (PE) pellet technique. The grained stone is mixed with the PE powder and the mixture is pressed into a pellet under heating. Spectra of the samples were taken using VERTEX 70 (Bruker) spectrometer equipped with wide-range beamsplitter and DTGS detector. The spectral range was between 680 and 30 cm^{-1}.

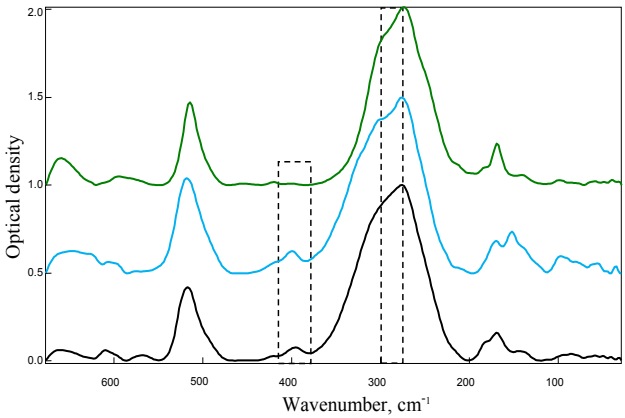

Fig. 1. Normalized absorption spectra of kidney stone containing calcium oxalate monohydrate and calcium oxalate dihydrate. Top - calcium oxalate monohydrate, middle - calcium oxalate dihydrate, bottom - kidney stone. The spectra have been vertically shifted for clarity.

Normalized spectrum of a kidney stone constituted from calcium oxalate monohydrate and calcium oxalate dihydrate and corresponding spectra of the pure components are presented in figure 1. It can be seen from the spectra that the oxalates can be distinguished from one another by a marker band at 395 cm^{-1}. Other types of stones (apatite, struvite, uric acid, brushite and their mixtures) have been analyzed as well. Comparing the results with the ones obtained earlier by means of middle-infrared spectroscopy it was determined that measurements in the FIR spectral range not only allows finding out chemical composition of the kidney stones but also complements the results of mid–infrared spectroscopy method - it becomes possible to unambiguously identify calcium oxalate dihydrate. In conclusion, FIR method is suitable to investigate the kidney stones, however, a more detailed analysis and a broader spectral library is required for the method to be used conventionally.

[1]P.G. Sofia, I. Ionescu, G. Rodica, P. Anisoara, The use of infrared spectroscopy in the investigation of urolithiasis, (2010).

Super resolution optical vortex scanning microscope

Mateusz Szatkowski[1*], Jan Masajada[1], Agnieszka Popiolek-Masajada[1]

[1] Singular Optics Group, Chair of Optics and Photonics, Faculty of Fundamental Problems of Technology, Wroclaw University of Technology, Wroclaw, Poland
mat.szatkowski@gmail.com

Optical vortex scanning microscope (OVSM) uses focused beam, carrying the optical vortex, to scan the sample. Optical vortex is stable phase dislocation [1]. We present the new setup of the OVSM (Fig. 1), which is based on the carrier frequency interferometry. In OVSM system optical vortex is generated by vortex lens, also known as spiral phase plate. Optical vortex moves inside the beam, due to vortex lens shift (shift in the x direction, perpendicular to the axis of the beam propagation) [2, 3].

The line along the vortex move, inside the beam, is called a vortex trajectory. The range of the vortex shift measured at the sample plane is reduced few hundred times, comparing to the vortex lens shift [3]. When there is no object at the sample plane, the vortex point moves along the straight line. The inclination of this trajectory depends on the observation plane position. The position of the observation plane, where the optical vortex trajectory is perpendicular to the vortex lens shift is called a critical plane [4]. At critical plane optical vortex has the highest sensitivity to small phase variations. This opens new possibilities to sample scanning.

The phase retrieval algorithm of object beam (based on the Fourier transform method) and new experimental results will be presented. We tested new design of the OVSM by measuring objects with different topography, such as: optical wedge, groove and diffraction grating.

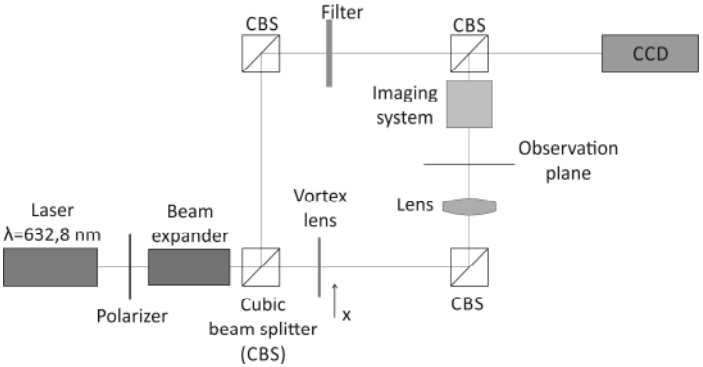

Fig. 1. System is based on the Mach-Zehnder interferometer scheme. It is illuminated with the He-Ne laser (λ=632,8 nm). Vortex lens specially designed for this wavelength, introduces the optical vortex with topological charge m=1. The interference image is registered on the CCD camera.

[1] Basisty, I. V., Soskin, M. S., Vasnetsov, M. V. Optical wavefront dislocations and their properties. Optics Communications, Vol. 119, pp. 604-612 (1995).
[2] J. Masajada, M. Leniec, I. Augustyniak, "Optical vortex scanning inside the Gaussian beam", J. Opt. 13 03571 (2011).
[3] J. Masajada, I. Augustyniak and A. Popiołek-Masajada, "Optical vortex dynamics induced by vortex lens shift – optical system error analysis", J. Opt., 15 044031 (2013).
[4] I. Augustyniak, A. Popiołek-Masajada, J. Masajada, S. Drobczyński, "New scanning technique for the optical vortex microscope", Appl. Opt. 51, C117-C124 (2012).

CEMS application for investigation of pitting corrosion

Justas Valaitis[1], Jonas Reklaitis[2], Rimantas Davidonis[2]

[1] Faculty of Physics, Vilnius University, Saulėtekio av. 9 Vilnius, Lithuania
[2] Institute of Physics, Savanorių 231, LT-02300 Vilnius, Lithuania
justas.valaitis@ff.stud.vu.lt

Buildings, bridges and vehicles all suffer from deterioration of construction materials. The total cost of corrosion and corrosion related issues only in the United States is $500 billion per year [1].

Longevity of steel in any environment is calculated measuring mass-loss after different exposure times. While the corrosion rates can be established by described method, but the data provides no information about the composition of corrosion layers. Most spectroscopic methods cannot identify early corrosion products. Thus making Mossbauer spectroscopy almost irreplaceable in corrosion research due to its ability to identify and quantify iron compounds as thin as few nanometers thick [1-2].

In this research we had samples, which were prepared form steel identical to one used in piping. Sample electrodes were put in electrolytic cells [4] each having different electrolyte. Samples were kept in electrolytic cell until visible pitting corrosion appeared.

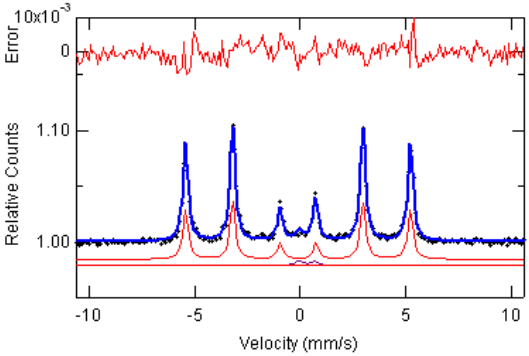

Fig. 1. Mossbauer spectrum of steel sample electrode

References

[1] Koch, G. H., Brongers, M. P. H., Thompson, N. G., Virmani, Y. P. and Payer, J. H., Corrosion cost and preventive strategies in the United States, Federal Highway Administration Technical Report No. FHWA-RD-01-156, 773 pages, March 2002

[2] A. Jagminas, R. Ragalevičius, K. Mažeika, J. Reklaitis, V. Jasulaitienė, A. Selskis, D. Baltrūnas, A new strategy for fabrication Fe2O3/SiO2 composite coatings on the Ti substrate, Journal of Solid State Electrochemistry, 14, N2, 271-277, 2010

[3] Arūnas Jagminas, Kęstutis Mažeika, Jonas Reklaitis, Vidas Pakštas, Dalis Baltrūnas, Annealing effects on the transformations of Fe nanowires encapsulated in the alumina template pores, Materials Chemistry and Physics Volume 115, Issue 1, Pages 217–222, 15 May 2009

[4] Asta Grigucevičienė, Konstantinas Leinartas, Dalia Bražinskienė, Svajus J. Asadauskas, Application of three-electrode electrolytic cell to evaluate thin films of vegetable and mineral oils, Tribology International (Impact Factor: 2.12) 44(5):557-564., (2011)

NETWORK ACCESS MANAGEMENT RESEARCH BASED ON SDN TECHNOLOGY

Gediminas Babčionis

Department of General Physics and Spectroscopy, Vilnius University, Lithuania
gediminas.babcionis@ff.stud.vu.lt

SDN - Software Defined Network is centralized network technology, where control plane is transferred from traditional network devices to special devices - controllers. SDN provides greater network security, manageability and path optimization. One of the SDN realizations is OpenFlow [1]. OpenFlow is a protocol that determines the communication between the OpenFlow switches (network devices that works with OpenFlow protocol) and controller. Using this protocol OpenFlow switches sends information about network, devices and packets to the controller. Also, this protocol is used to send rules from controller to OpenFlow switches. These rules determine how to deal with incoming packets. They are named flow entries and stored in the flow tables. Controller is a software device that manages and observes network. Its functionality spans from observing network topology changes to creating and sending flow entries to OpenFlow switches. The controller is the main part of SDN network.

The purpose of this work was to investigate performance of network access layer using SDN technology. The main focus was to compare network performance when using two different types of devices: appliances with traditional software and OpenFlow switches. Additionally, flow table capabilities were assessed in this work.

In this work, HP VAN controller and commodity Linksys WRT54GL devices with OpenWRT Backfire 10.03, r23206 [2] software which allows OpenFlow version 1.0 capability were used. Nine different network topologies were investigated. In all of them 2 PCs for ping, and 2 PCs for Iperf were used. Ping was used for delay and packet loss measurement, and Iperf – to create the load in the network. Different topologies were used to connect computers via OpenFlow (OF swi) and Cisco Catalyst 3560 (swi) switches and Linksys WRT54GL device with traditional software (WRT). In first topology computers are connected via one OF swi, in the second – via 2 OF swi, but the network load impact only one OF swi, third – same as second but network load impact both OF swi, forth – same as third with swi connected between OF swi, fifth – same as forth with one more swi interconnected, sixth is same as third, but swi is used instead of one OF swi, , seventh – computers are connected via one swi, eighth – via two swi, and in the ninth – computers are connected via WRT. Network performance: average delay and packet loss dependences on network load in different topologies are presented in Fig. 1 and Fig. 2.

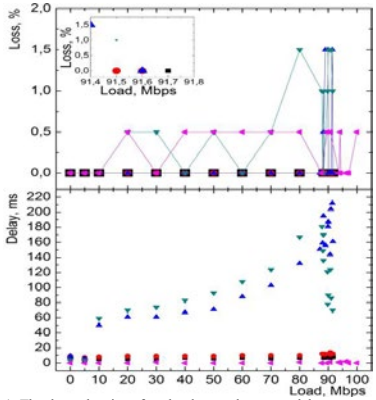

Fig. 1. The dependencies of packet loss and average delay on network load. The dots present the results for: ■ - 1st, ● - 2nd, ▲ - 3rd, ▼ - 7th, ◀ - 9th topologies.

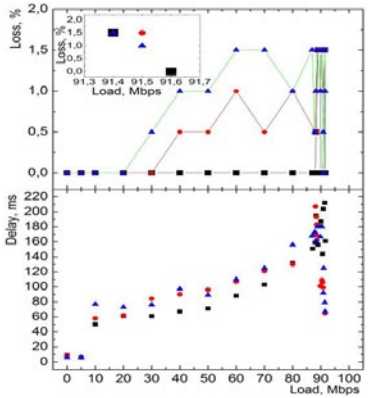

Fig. 2. The dependencies of packet loss and average delay on network load. The dots present the results for: ■ - 3rd, ● - 4th, ▲ - 5th topologies.

The results show that using mentioned devices as OpenFlow switches in access layer is fair enough for small offices, because these devices are capable of working at up to 91.5 Mbps flow rate with an acceptable network performance. The packet loss greater than 1.5 % and delay greater than 220 ms was not exceeded until network went down. Even packet loss and delay are increased when comparing to decentralized network devices, it is not critical impact to the small network. Maximum of 106 flow entries can be stored by Linksys WRT54GL devices and OpenFlow processing speed is 50 flows/s.

[1] A. Lara, A. Kolasani and B. Ramamurthy, Network Innovation Using OpenFlow: A Survey, Communication Surveys & Tutorials, IEEE **16**(1), 1–20 (2013), http://ieeexplore.ieee.org/xpl/articleDetails.jsp?arnumber=6587999.
[2] Pantou : OpenFlow 1.0 for OpenWRT, http://archive.openflow.org/wk/index.php/Pantou_:_OpenFlow_1.0_for_OpenWRT.

STUDY OF NETWORK ACCESS CONTROL IN OPENFLOW NETWORK

Mindaugas Giedraitis

Department of General Physics and Spectroscopy, Vilnius University, Lithuania
mindaugas.giedraitis@ff.stud.vu.lt

This papers goal is to introduce the concept of Software Defined Networking (SDN) and address the issues related to network access control (NAC) as well as provide a concept of network access control using OpenFlow protocol. It also consists of NAC program prototype for OpenDaylight (ODL) [1] controller.

SDN is a network architecture which changes traditional decentralized network model by separating data and control planes. Data plane is an abstraction of network components which forward the packets of the network and control plane is the entity or entities which make decisions concerning the rules of packet forwarding. In SDN network control plane is moved to a centralized entity called controller [2]. Its purpose is to instruct data plane devices on packet forwarding.

OpenFlow (OF) is one of SDN realisations. The network based on OF consist of one or few OpenFlow controllers connected to OF switches. The switches forward packets based on flow entries written by controller. When a packet matches a flow entry OF switch performs an action specified in that specific flow entry. A flow entry consists of a match field which indicates packet headers values that have to match (values can be wildcarded), priority, counters, instructions that specify the actions, timers and cookies. The lowest priority entry usually instructs switches to forward packets to controller and controller makes decisions on what should be done with the packet. The common controller's procedure is to instruct the OF switch to forward the packet and write the appropriate flow entry to the switch seeking that the switch would not forward this type of packets to the controller again.

This project proposes network access control using OpenFlow controlled access layer in the hierarchical network model. The example topology is displayed in figure 1. By replacing only the access layer with OpenFlow switches we make the least amount of changes to original network and get full benefit of OF controlled access layer as well as retain support of all traditional network protocols.

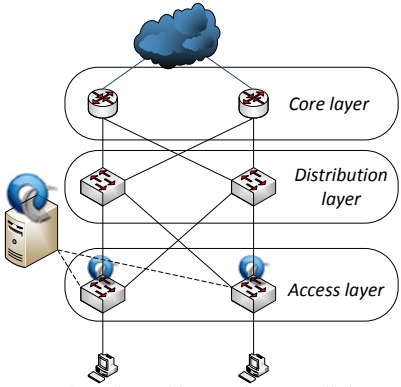

Fig. 1. Network topology with OpenFlow controlled access layer.

Port-based Network Access Control protocol (802.1x) [3] has been chosen for authentication of the users and OpenDaylight controller has been chosen for OpenFlow network management. 802.1x protocol has been adapted for OF based network access layer. A NAC program prototype has been written that uses ODLs Model-Driven Service Abstraction Layer (MD-SAL) to communicate with controller.

[1] The Linux Foundation, OpenDaylight documentation, *https://wiki.opendaylight.org/view/Release/Hydrogen/*
[2] W. Stallings, Software-Defined Networks and OpenFlow, in *The Internet Protocol Journal* 16 (1), pp. 2 – 14 (2013)
[3] IEEE, Port-Based Network Access Control, 205 p., (2010)

APPLICATION OF ARTIFICIAL NEURAL NETWORKS FOR AUTONOMOUS SELF DRIVING VEHICLE WITH EMBEDDED LINUX SYSTEM

Vadim Gerasimov[1], Vytautas Jonkus[1]

[1] Department of Radiophysics, Physics Faculty, Vilnius University, Lithuania
Vadim.Gerasimov@ff.vu.lt

Since the end of the 20th century autonomous driving was experimented on huge computers installed on heavy cars [1], as well as microcontroller [2] and field-programmable gate arrays [3]. This work describes the investigation of implementation of artificial neural networks for autonomous self driven vehicle with embedded Linux system.

The goal of this work is to investigate the compatibility of feed-forward back-propagation artificial neural network open source library on an embedded Linux system while implementing it for autonomous driving based on supervised learning. The vehicle (see Fig. 1, 2) was constructed using an RC model chassis, sonar distance sensors (1), additional servomotors (2), lead power cell (3), custom power control board (4), and two embedded Linux system boards for data relay and processing – Carambola (5) and Iteaduino Plus A10 (6). Three different neural network architectures were tested for the autonomous driving. The experiments were performed on an improvised track out of domestic objects. All of the construction, assembly and programming were performed in the M2M laboratory in the Faculty of Physics, Vilnius University.

The results yield that the neural network with 3 hidden layers out of 20 neurons in each converges better than the one with a single hidden layer out of 100 neuron architecture. 20 neurons in each hidden cells are enough for both forth and reverse wise motion, whereas only 3 neurons in each hidden layer are enough for only forward motion. The 3 hidden layer network also converges in 7 seconds on the Core 2 processor, whereas on the Allwinner A10 – in a minute. The experiments also showed that thin obstacles are barely noticeable by the vehicle both in front and profile. Reverse movement is possible only when the obstacle course is static, meaning nothing should appear behind the vehicle.

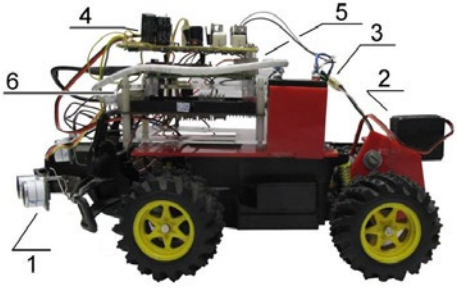

Fig. 1. Side view of the autonomous vehicle

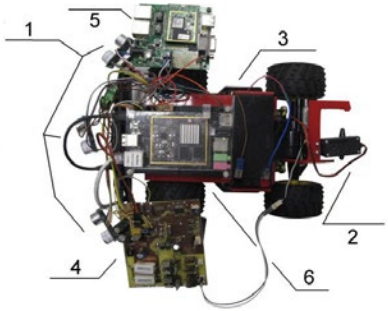

Fig. 2. Top view of the autonomous vehicle

The method used in this probe may be used in flying vehicles and man-machine interfaces [4].

[1] Progress in neural network-based vision for autonomous robot driving Intelligent Vehicles, Dean A. Pomerleau, '92 Symposium., Print ISBN: 0-7803-0747-X, IEEE Detroit, USA, p. 391 – 396. (Proc. 29 Jun – 1 Jul 1992)

[2] Dean A. Pomerliau, Neural Network Perception for Mobile Robot Guidance, Doct. Thes., app. pub. rel., p. 216 (16 Feb 1992)

[3] Amos R. Omondi, Jagath C. Rajapakse, Neural Networks in FPGAs, Proc. 9th Inter. Conf. Neural Information Processing (ICONIP'02), Vol. 2, 954-959 (2002)

[4] Alcimar Soares, Adriano Andrade, Edgard Lamounier, Renato Carrijo, The Development of a Virtual Myoelectric Prosthesis Controlled by an EMG pattern Recognition System Based on Neural Networks, Jour. Intel. Info. Sys., 2003, Vol. 21, No 2, p. 127-141.;

MUSCLE SIGNAL DECODING USING ARTIFICIAL NEURAL NETWORKS

Vadim Gerasimov[1], Vytautas Jonkus[1], Gintaras Jonaitis[2]

[1] Department of Radiophysics, Faculty of Physics, Vilnius University, Lithuania
[2] Department of Biomechanics, Faculty of Mechanics, Vilnius Gediminas Technical University, Lithuania
Vadim.Gerasimov@ff.vu.lt

Since the 80s-90s investigations have been made on muscular signal classification and virtual prosthesis control [1,2]. This work contains description of the construction of a myoelectric amplifier and the main board nodes as well as implementation of artificial neural network for the signal analysis on an embedded Linux system.

The goal of this work is to construct and test a myoelectric signal probing, amplifying, processing and recognizing apparatus. The amplifying node and the main board were constructed using photolithography printed circuit board methods. The amplifier node uses two stage operational amplifiers and precision rectifier with detector (see Fig. 1.2). The main board uses the ARM Cortex M3 (LPC1316) microcontroller. The main board is designed to ergonomically fit multiple amplifiers (see Fig. 1) and can adjust the second stage gain. It also can communicate with the processing node via the Universal Asynchronous Receiver-Transmitter. The feed-forward back-propagation artificial neural network library was implemented on the processing node – Raspberry Pi B embedded Linux system board (see Fig. 1.3). The neural network architecture consists of 20 input neurons, three hidden layers with 5 neurons each and one output neuron. The experiments included training the machine to measure the muscle's differential coordinates of motion (see Fig. 2) as well as the weight load (see Fig. 3).

The results yield that each time the system is connected to the muscles, the recognition system should be trained again. It has also been found, that the more the signal pattern matches the training data, the more precise estimation is given by the recognition system. Any electrode misfits, muscle fatigue or untimely measurements lead to an incorrect estimation of data.

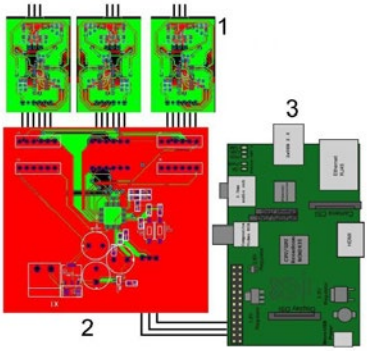

Fig. 1. A simple schematic of a myoelectric amplification and recognition system.

The muscle signal recognition system will further be used for robotic limb control.

Fig. 2. Successful attempt of coordinate measurement, thumb shows the value on the ruler and the terminal shows the recognition system output

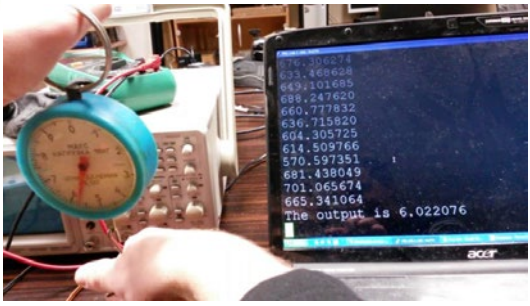

Fig. 3. Muscle load measurement, scales show the load and the terminal shows the output

[1] Micheale F. Kelly, Philip A. Parker (sen.mem. IEEE), Robert N. Scott (sen.mem. IEEE), The Application of Neural Networks to Myoelectric Signal Analysis: A Preliminary Study, IEEE Tran. Biomed. Eng., vol. 37, No 3, p. 221-230 (March 1990)
[2] Alcimar Soares, Adriano Andrade, Edgard Lamounier, Renato Carrijo, The Development of a Virtual Myoelectric Prosthesis Controlled by an EMG pattern Recogniotion System Based on Neural Networks, Jour. Intel. Info. Sys., Vol. 21, No 2, p. 127-141. (2003)

FORMATION OF MICRO AND NANO STRUCTURES EMPLOYING DIRECT LASER WRITING AND HOLOGRAPHIC LITHOGRAPHY

Linas Šimatonis[1,2], Skirmantas Norkus[1], Tomas Tamulevičius[1,2], Dainius Virganavičius[1], Sigitas Tamulevičius[1,2]

[1] Institute of Materials Science, Kaunas University of Technology, K. Baršausko St. 59, LT-51923, Kaunas, Lithuania,
[2] Department of Physics, Kaunas University of Technology, Studentų St. 50, LT-51368, Kaunas, Lithuania,
linas.simatonis@ktu.edu

Realization of planar integrated optical element with sub-wavelength feature requires advanced lithography techniques, e.g. UV contact, electron beam, nano-imprint lithography, etc. These tools are expensive and bulky. Using one UV laser light source distributed between two optical setups, i.e. Direct Laser Writing (DLW) and Lloyd's mirror interferometer systems, we were able to pattern micrometer range features together with 150 nm sized lines [1].

In a current Lloyd's mirror holographic lithography setup a continuous wave solid state UV laser (371 nm wavelength, 15 mW power) beam is expanded with micro objective and filtered with a spatial filter. Half of the laser beam illuminates the sample directly while the second half is reflected from the mirror and interferes with direct beam on the sample surface. Adjusting the angle of incidence one can control the pitch of the interference fringes. Motorized rotational stages provide precise angle control, i.e. pitch of the fringes can be varied from 300 to 500 nm. Interference fringes were recorded on flat substrates spin coated with negative tone photoresist.

Using DLW setup we have fabricated test structures with few micrometer resolution. The diameter of laser beam spot focused on the sample surface was reduced down to 5 µm. Using precise XY stages and translation of the negative tone photoresist coated sample we have exposed various tests. Exposition doses and steps between adjacent expositions were optimized to obtain micrometric resolution structures.

Automated exposure, selection of the pitch and sample translation for DLW are controlled from one software. After exposure with both optical systems light affected areas in the photoresist film are cross-linked and become insoluble after developing in appropriate solution. Microstructures were analysed employing scanning electron (SEM) and optical microscopes.

Employing described optical setup test structures including texts, simple integrated optics elements and more complex planar structures were realized. System capabilities changing the point density were demonstrated and smooth lines were obtained employing 1.825 µm step between adjacent points (see Fig. 1). Then lines with different interline distances were exposed employing optimal point density. It was demonstrated that 2.5 µm gap between 3.5 µm spaced lines can be realized (see Fig. 2).

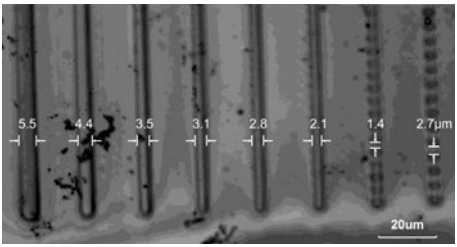

Fig. 1. Optical microscope micrograph of lines obtained using different point density (0.625-5µm, step 0.625µm)

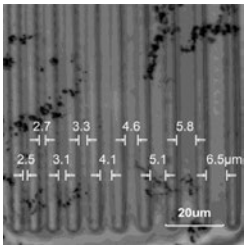

Fig. 2. Optical microscope micrograph of 3.5 µm thickness lines obtained exposing with different inter line distances (2.5-6.5 µm, step 0.625µm).

Acknowledgements:
This work was supported by European Social Funds Agency Grant No. VP1-3.1-ŠMM-10-V-02-28. Lloyd's mirror setup was financed by Research Council of Lithuania (Grant No. MIP-085/2013). L.Š., S.N. T.T. acknowledge student practice financed by Research Council of Lithuania. This research was performed within COST action MP 1205.

[1] D. Virganavičius, L.Šimatonis, A. Jurkevičiūtė, T. Tamulevičius, S. Tamulevičius, Formation of sub-wavelength pitch regular structures employing motorized multiple exposure Lloyd's mirror holographic lithography setup, Proc. SPIE **91701** (2014).

EVALUATION USING FINITE ELEMENT METHOD OF MICRONIC SCALED POLYIMIDE SCAFFOLDS FABRICATED WITH FEMTOSECOND LASER

Linas Šimatonis[1], Aušra Gadeikytė[1], Tomas Tamulevičius[1,2], Orestas Ulčinas[1], Brigita Abakevičienė[1,2], Sigitas Tamulevičius[1,2]

[1] Institute of Materials Science, Kaunas University of Technology, K. Baršausko St. 59, LT-51923, Kaunas, Lithuania,
[2] Department of Physics, Kaunas University of Technology, Studentų St. 50, LT-51368, Kaunas, Lithuania,
linas.simatonis@ktu.edu

Artificial membranes and scaffolds can be applied for drug delivery, artificial organs, tissue engineering and other medical applications [1]. Laser structured polymer films can serve as three dimensional scaffolds for different cells that can be used for targeted soft tissue replacement and engineering of soft tissues, such as cardiac muscle, blood, nerve, cartilage and retina [2].

In the current work arrays of holes in 26.7 µm thickness polyimide film (KaptonHN, DuPont) were microstructured employing Yb:KGW femtosecond laser Pharos (Light Conversion) and micromachining system FemtoLab (Altechna R&D). Biocompatible polymer film was laser patterned arrays of 30 to 45 µm spaced 14-16 µm diameter hole arrays. Quality of the structure was evaluated with scanning electron (see Fig.1) and optical microscopes, while mechanical properties of the membrane were measured experimentally with a custom build micro tensile device [3] and compared with simulated ones obtained employing finite element method (FEM, Comsol Multiphysics). Samples were stretched to strain reaching 5.5%. Fitting the experimental stress-strain curves and varying mechanical properties in the simulation software (Young modulus 0.75GPa, Initial yield stress 0.69MPa and kinematic tangent modulus 231MPa) von Misses stress were obtained.

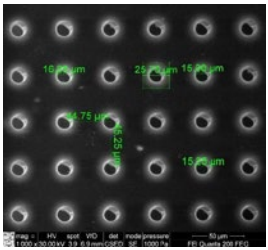

a

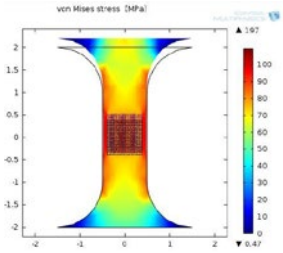

b

Fig.1. Hole arrays in polyimide film for scaffold applications fabricated employing femtosecond laser. (a) SEM micrograph (hole diameter 15.00-15.25µm, gap between two holes 45 µm). (b) 2D distribution of von Mises stress simulated with FEM.

This work was supported by European Social Funds Agency Grant No. VP1-3.1-ŠMM-10-V-02-029

[1] D. F. Stamatialis, Bernke J. Papenburg, M. Gironésa, S. Saiful, S.N.M. Bettahalli, S. Schmitmeierb, M. Wessling, Medical applications of membranes: Drug delivery, artificial organs and tissue engineering. - J. Membr. Sci.,308 ,2008 , 1-34p

[2] R. Rai, M. Tallawi, A. Grigore, A.R. Boccaccini, Synthesis, properties and biomedical applications of poly(glycerol sebacate) (PGS): A review. - Prog. Polym. Sci., 37, 2012, 1051-1078 p.

[3] http://www.sciencedirect.com/science/article/pii/S0143816603000800 Last time checked 2015 02 06

PROFILING OF CURRENT TRANSIENTS IN CAPACITOR TYPE DIAMOND DETECTORS

Darius Jotauta, Dovilė Meškauskaitė, Eugenijus Gaubas, Tomas Čeponis

Vilnius university, Institute of Applied Research, Sauletekio av. 9-III, LT-10222, Vilnius, Lithuania
j.darius1992@gmail.com

Diamond is one of the most promising wide-gap materials for applications in fabrication of high frequency sensors and radiation tolerant particle detectors [1]. The excess carrier lifetime and carrier mobility as well as diffusion coefficient are ones of the most sensitive parameters to electrically active defects in material. Also, carrier lifetime is the main limiting factor for charge collection efficiency in diamond based sensors and detectors. Manifestation of these parameters is most pronounced in operation dynamics of devices fabricated using different technology synthetic diamond [2]. The examined operation of the capacitor type detectors [3] showed possibility to fabricate fast and rather radiation resistant sensors relative to the traditional devices produced on silicon [4].

Operation characteristics of the capacitor-type type detectors based on HPHT and CVD diamond have been investigated using regimes of the perpendicular and parallel profiling of the induced current transients. Simulations of the drift-diffusion current transients have been implemented by using the dynamic models based on Shockley-Ramo's theorem, for the injected charge as the domains of surface and bulk charge. The bipolar drift-diffusion regimes have been analyzed for the photo-induced bulk domain of excess carriers. The localized surface charge domain injection by focused laser beams within the inter-electrode space leads to effects dependent on injected charge amount, their initial location as well as biasing voltage have been revealed. The screening effects ascribed to surface charge and to dynamics of extraction of the injected bulk excess carrier domain have been separated and explained. The parameters of drift mobility μ=2470 cm2/Vs, of the coefficient of carrier ambipolar diffusion Da=97 cm2/s, of carrier recombination lifetimes τR, HPHT 2 ns as well as τR, CVD 110 ns, respectively, were extracted by combining analysis of the transients of the detector current and the microwave probed photoconductivity. The obtained results are important for the prediction of the functionality of diamond based particle and photo-sensors.

[1] W. Adam et al., Radiation hard diamondnext term sensors for future tracking applications, Nucl. Instr. and Meth. A , vol. 565, iss. 1, p. 278, 2006.
[2] E. Robson, Diffusity of charge carriers in semiconductors in strong electric fields, Phys. Rev. Lett., vol. 31, no. 13, 1973
[3] M. Pomorski et al., Characterisation of single crystal CVD diamond particle detectors for hadron physics experiments, Phys. Status Solidi A, vol. 202, no. 11, p. 2199, 2005.
[4] M.Moll, Radiation tolerant semiconductor sensors for tracking detectors, Nucl. Instr. and Meth., Section A 565 (2006) 202.

The influence of radon concentration on the background spectrum measured by gamma spectroscopy.

Damian Kasyan, Krzysztof Kozak

Department of Physics, Cracow University of Technology, Poland
Laboratory of Radiometric Expertise, Institute of Nuclear Physics Polish Academy of Sciences, Poland
damian.kasyan@gmail.com

The background is very important problem in gamma spectroscopy. The accurate determination of the background guarantees more accurate result of the measurement. The reduction of the background makes it possible to lower minimum detectable activity. Unfortunately, the environmental radioactivity normally present in laboratory influences the level of background.

The main part of this radioactivity comes from building materials and radon progeny. Radon's chemical and physical properties cause its migration into laboratory building, especially located in lower floors.

The aim of this work was to study how radon concentration may influence the background gamma spectrum. Using a spectrometer with HPGe detector the background gamma spectra were collected in different radon concentrations which were continuously registered by a professional radon monitor AlphaGUARD PQ2000 PRO. Radon concentration in laboratory was changed with the application of certified radon source PYLON 1025. The comparison of the spectra is presented as well as the method for decreasing radon concentration inside the HPGe detector's shielding. This method is based on the ventilation with liquid nitrogen vapors.

The work was performed at the Laboratory of Radiometric Expertise, Institute of Nuclear Physics PAN, Krakow, Poland.

HOW TO PREPARE MATERIALS AND MEASURE THEIR PHYSICAL PROPERTIES – A BRIEF STORY

Judyta Strychalska, Katarzyna Holowacz, Paula Reczek, Mateusz Podgorski, Tomasz Klimczuk

Faculty of Applied Physics and Mathematics, Gdansk University of Technology, Poland
jstrychalska@mif.pg.gda.pl

Intermetallic compounds are a wide family of materials, among which we can find superconductors (like Nb_3Sn [1]), semiconductors, semimetals, ferromagnetics and other. One group of intermetallic materials is arranged in Y-M system (where M is a transition metal). These compounds have been the subject of many studies in the '80s of the twentieth century, especially Y-Co system. One of the most remarkable results confirmed during measuring the compounds of this system was discovering the coexistence of ferromagnetism and superconductivity of Y_9Co_7 [2]. However, there are still many materials of Y-M binary system which were not deeply studied yet.

The goal of this presentation is to show how to prepare material samples by arc-melting and study theirs physical properties basing on an example of compounds from the group of Y_3M (M = Co, Ni, Rh, Pd, Ir, Pt). Example results are presented in Figure 1. More results and their explanation will be presented.

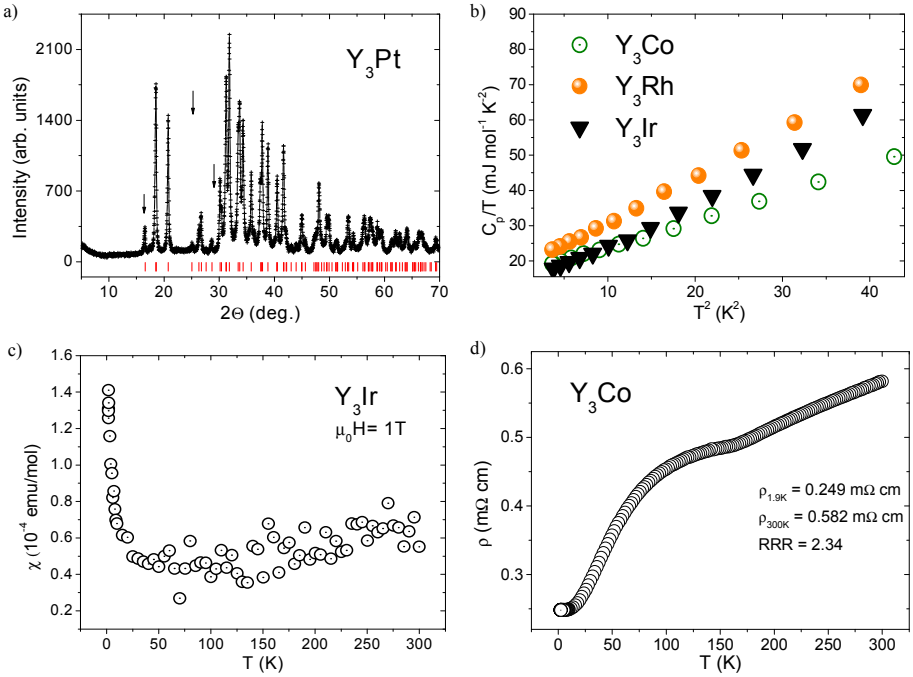

Figure 1. Selected results for compounds of the Y_3M group (where M = Co, Ni, Rh, Pd, Ir, Pt): a) X-Ray diffraction pattern for Y_3Pt, b) C_p/T versus T^2 for Y_3Co, Y_3Rh, and Y_3Ir, c) magnetic susceptibility versus temperature for Y_3Ir, d) temperature dependence of electrical resistivity for Y_3Co.

[1] B. T. Matthias, T. H. Geballe, S. Geller, E. Corenzwit, Superconductivity of Nb_3Sn, Phys. Rev. 95, 1435 (1954)
[2] A. Kolodziejczyk, C. Sulkowski, Susceptibility, magnetisation and critical behaviour of a magnetic superconductor:Y_9Co_7, J. Phys. F: Met. Phys. 15 1151 (1985)

Poster session 2

SOL-GEL SYNTHESIS OF VARIOUS METAL MOLYBDATES

G. Braziulis[1], A. Žalga[1]

[1] Department of Applied Chemistry, Faculty of Chemistry, Vilnius University, Naugarduko Str. 24, 03225 Vilnius, Lithuania
gedasv2@gmail.com

The scheelite molybdates ($MMoO_4$, M=Ba, Sr and Ca) have C_{4h} point group with two formula units per primitive cell. They have attracted particular interest in a variety of applications such as hosts for lanthanide activated lasers, luminescence materials, microwave applications and catalysts [1]. Meanwhile, $MgMoO_4$ belongs to the wolframite-type metal molybdates with triclinic structure and the [MoO_4^{2-}] oxyanion complex is the principal constitutive element. The central Mo metal ion occupies three non-equivalent positions and is surrounded by four O^{2-} ions with approximately tetrahedral coordination [2]. This compound also shows the broad and intense charge transfer absorption bands in the near-UV and it has excellent thermal and chemical stability. Moreover, as well as the crystal structure, the surface morphology also significantly affects both the optical and electrical properties of alkaline earth metal molybdates. Thus, according to this the synthesis method that could be chosen for the preparation of these ceramic materials has significant importance. Therefore, the choice of synthesis technique usually depends on variety factors that can shorten, facilitate, and reduce the preparation way. From this point of view, the solution-based synthetic methods play a crucial role in the design and production of fine ceramics and they have been successful in overcoming many of the limitation of the traditional solid-state, high-temperature methods.

In this work, the aqueous sol–gel synthesis method was successfully used for the preparation of M–Mo–O nitrate–tartrate (M = Mg, Ca, Sr, and Ba) gel precursors, which additional at 500 – 900 ^oC temperatures were calcined. In order to investigate the surface morphology of the as-prepared samples the SEM analysis was performed. In this case, the obtained pictures clearly revealed that the morphological changes of the final ceramic were significantly depending on both the annealing temperature and the nature of alkaline earth metal.

[1] T. Thongtem, A. Phuruangrat, S. Thongtem, Characterization of $MMoO_4$ (M=Ba, Sr and Ca) with different morphologies prepared using a cyclic microwave radiation, Materials Letters **62**, 454–457 (2008).

[2] L. Y. Zhou, J. S. Wei, L. H. Yi, F. Z. Gong, J. L. Huang, W. Wang, A promising red phosphor $MgMoO_4:Eu^{3+}$ for white light emitting diodes, Materials Research Bulletin **44**, 1411–1414 (2009).

VIBRATIONAL SPECTROSCOPIC AND X-RAY DIFFRACTION STUDIES OF LITHIUM MOLYBDATES PREPARED BY SOL-GEL METHOD

Austėja Diktanaitė[1], Artūras Žalga[1]

[1] Department of Applied Chemistry, Faculty of Chemistry, Vilnius University, Naugarduko Str. 24, 03225 Vilnius, Lithuania
austeja.diktanaite@gmail.com

Binary and ternary metal oxide systems have been subjects of intense interest as their characterization is essential for design of new materials of different types, like semiconductors, magnetic and optical materials or construction materials of specific thermal, mechanical or chemical properties [1]. From this point of view double molybdates of the $M^{I}M^{III}(MoO_4)_2$ family are very important compounds because of their optical, antiferroelectric and ferroelastic properties. Moreover, they are suitable hosts for transition-metal and lanthanide ions [2]. The physical and chemical properties of such kind compounds usually really depend on the surface morphology and crystallinity of the as-prepared compounds. Therefore, the choice of synthesis technique usually depends on variety factors that can shorten, facilitate, and reduce the preparation way. This is the reason why the solution-based synthetic methods play a crucial role in the design and production of fine ceramics and they have been successful in overcoming many of the limitation of the traditional solid-state, high-temperature methods [3, 4].

In this study, we report the aqueous sol-gel synthesis of the Li–Al–Mo–O nitrate–tartrate gel precursors with the initial composition for $LiAlMo_2O_8$ and $Li_3AlMo_3O_{12}$ ceramics. The crystalline compounds annealed at 400–700 ^{o}C of temperatures and as-prepared Li–Al–Mo–O nitrate–tartrate gels investigated by thermal analysis (TG/DTA), X-ray diffraction (XRD), scanning electron microscopy (SEM) and Fourier transform infrared spectroscopy (FT-IR).

[1] E. Filipek, I. Rychlowska-Himmel, A. Paczesna, Thermal stability of $In_2(MoO_4)_3$ and phase equilibria in the MoO_3–In_2O_3 system, Journal of Thermal Analysis and Calorimetry **109**, 711-716 (2012).

[2] K. Hermanowicz, J. Hanuza, M. Maczka, P. J. Deren, E. Mugenski, H. Drulis, I. Sokolska, J. Sokolnicki, Optical properties of chromium(III) in $M^{I}In(MoO_4)_2$ hosts, where M^{I} = Li, Na, K, Rb, Cs, Journal of physics: Condensed matter **13**, 5807-5816 (2001).

[3] G. Braziulis, G. Janulevicius, R. Stankeviciute, A. Zalga, Aqueous sol–gel synthesis and thermoanalytical study of the alkaline earth molybdate precursors, Journal of Thermal Analysis and Calorimetry **118**, 613-618 (2014).

[4] R. Stankeviciute, A. Zalga, Sol-gel synthesis, crystal structure, surface morphology and optical properties of Eu_2O_3 doped $La_2Mo_3O_{12}$ ceramic, Journal of Thermal Analysis and Calorimetry **118**, 925-935 (2014).

REACTION PRODUCTS OF *N*-(1-NAPHTHYL)-*N*-THIOCARBAMOYL-β-ALANINE WITH α-HALOCARBONYL COMPOUNDS

B. Grybaitė, V. Mickevičius
Kaunas University of Technology, Lithuania
birute.grybaite@ktu.edu

Recently, special attention has been paid to β-amino acids as potential precursors for bio-organic, medicinal, and natural products chemistry. Synthetic thiazole derivatives have shown various biological activities such as anti-inflammatory, antipyretic, antivirus, antimicrobial, antifungal, anticancer etc. In this work, reactions of *N*-(1-naphthyl)-*N*-thiocarbamoyl-*β*-alanine (**1**) with monochloroacetic acid, chloroacetaldehyde and α-haloketones were investigated. 3-[(4-Oxo-4,5-dihydro-1,3-thiazol-2-yl)(1-naphtyl)amino]propanoic acid (**2**) was obtained from *N*-phenyl-*N*-thiocarbamoyl-β-alanine (**1**) and monochloroacetic acid. Reaction was perfomed in aqueous solution of sodium carbonate. Reactions of **1** with α-haloketones provided *N*,*N*-disubstituted aminothiazoles **3-7.**

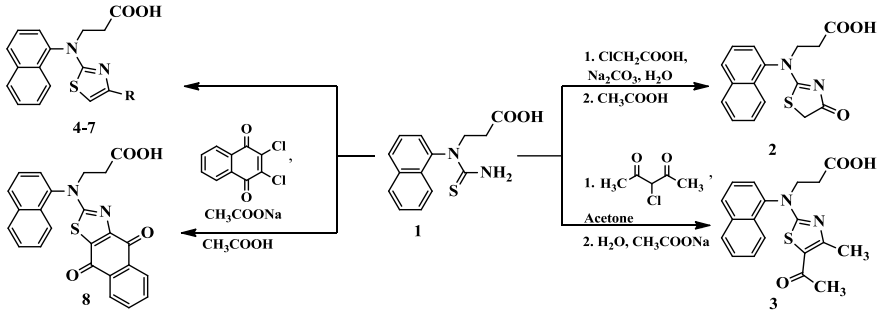

	R	Reagents
4	H	1. $ClCH_2CHO$, Na_2CO_3 2. CH_3COOH
5	CH_3	1. CH_3COCH_2Cl, Na_2CO_3 2. CH_3COOH
6	C_6H_5	1.  , acetone 2. CH_3COONa
7	naphthyl	1. 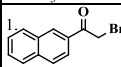 , acetone 2. CH_3COONa

3-[(4,9-Dioxo-4,9-dihidronaphtho[2,3-d][1,3]-2-yl (naphthalene-1-yl)amino] propanoic acid (**8**)was synthesized by the reaction of *N*-(1-naphthyl)-*N*-thiocarbamoyl-β-alanine (**1**) with 2,3-dichloro-1,4-naphthoquinone.

The structures of the synthesized compounds were confirmed by spectroscopic methods and elemental analysis data.

SOL-GEL SYNTHESIS AND CHARACTERIZATION OF $MgWO_4$:x%Eu

Kšištof Marcinkevič[1], Gediminas Braziulis[1], Artūras Žalga[1]

[1] Department of Applied Chemistry, Faculty of Chemistry, Vilnius University, Naugarduko Str. 24, 03225 Vilnius, Lithuania
ksiska23@gmail.com

Divalent-metal tungstates (AWO_4) are being studied with great interest because of their use as materials for scintillator detectors and laser-host crystals, as well as in acoustic and optical fiber applications. Magnesium tungstate ($MgWO_4$), the mineral hunzalaite, is part of this family. With a band gap of 3.92 eV, it is one of the most extensively studied metal tungstates because of its interest as a scintillator material for cryogenic applications used in the search for rare events in particle physics [1]. $MgWO_4$ crystallizes in a $NiWO_4$ type structure with space group P2/c (SG: 12) and has a C_{2h} point-group symmetry. Chains of Mg–O polyhedron parallel to the [001] direction are connected by W–O chains, which also lies along the [001] direction [3]. The structure consists of layers of alternating MgO_6 and WO_6 octahedral units that share edges, forming a zigzag chain and creating a close-packed structure. The presence of the light magnesium cation inhibits the tendency of the crystalline matrix to incorporate heavy radioactive nuclei and thereby reduces the inherent intrinsic radioactivity of the compound, compared with other representatives of the same family. Furthermore, $MgWO_4$ is known to be an efficient phosphor exhibiting intrinsic emission, which increases with decreasing temperature [2]. Therefore, it is a very attractive host-material that can be successfully used as phosphor for producing of light-emitting diodes (LEDs).

Considering renewed interest in the alkaline earth metal and rare earth tungstate compounds as potential hosts for Eu^{3+} activated high efficiency red phosphors [4], the $MgWO_4$ was chosen to be the host lattice in the Eu^{3+} ion-doped phosphors in this work.

The Eu-doped $MgWO_4$ ceramic was synthesized with an aqueous sol–gel method and studied for its microstructure and crystal phase formation. Therefore, the thermal analysis (TG/DTA), X-ray diffraction (XRD), scanning electron microscopy (SEM) and Fourier transform infrared spectroscopy (FT-IR) were performed for the characterization of the final materials.

[1] J. Ruiz-Fuertes, D. Errandonea, S. Lopez-Moreno, J. Gonzalez, O. Gomis, R. Vilaplana, F. J. Manjon, A. Munoz, P. Rodrıguez-Hernandez, A. Friedrich, I. A. Tupitsyna, and L. L. Nagornaya, High-pressure Raman spectroscopy and lattice-dynamics calculations on scintillating $MgWO_4$: Comparison with isomorphic compounds, Physical Review B **83**, 214112 (2011).

[2] V B Mikhailik, H Kraus, V Kapustyanyk, M Panasyuk, Yu Prots, V Tsybulskyi and L Vasylechko, Structure, luminescence and scintillation properties of the $MgWO_4$–$MgMoO_4$ system, Journal of Physics: Condensed Matter **20**, 365219 (2008).

[3] L. Y. Zhou, J. S. Wei, L. H. Yi, F. Z. Gong, J. L. Huang, W. Wang, Crystal growth, spectral properties and crystal field analysis of Cr^{3+}:$MgWO_4$, CrystEngComm **15**, 6083–6089 (2013).

[4] P. S. Duttaa and A. Khanna, Eu^{3+} Activated Molybdate and Tungstate Based Red Phosphors with Charge Transfer Band in Blue Region, ECS Journal of Solid State Science and Technology, **2** (2) R3153-R3167 (2013).

SYNTHESIS AND PROPERTIES OF *N*-(5-CHLORO-2-PYRIDYL)-*β*-ALANINE HYDRAZIDE DERIVATIVES

Beatričė Peleckytė[1], Ingrida Tumosienė[1], Ilona Jonuškienė[1], Kristina Kantminienė[2], Zigmuntas Jonas Beresnevičius[1]

[1] Department of Organic Chemistry, Kaunas University of Technology, Lithuania
[2] Department of Physical and Inorganic Chemistry, Kaunas University of Technology, Lithuania
beatrice.peleckyte@gmail.com

N-Substituted *β*-amino acids and their derivatives are structural units of a number of natural compounds, including peptides, lactones, alkaloids, and antibiotics [1]. Pyridine derivatives are found to possess a variety of biological activities including antiviral, anticancer, antimicrobial, antidiabetic, and antitubercular [2]. Acid hydrazides are precursors for the synthesis of different compounds, such as hydrazones and heterocyclic compounds. The wide array of biological activities of hydrazones includes anticonvulsive, anti-inflammatory, antithrombotic, antimicrobial, and antiproliferative [3]. Azole derivatives have demonstrated to possess antibacterial, anti-inflammatory, antitumor, antifungal, and antimicrobial activities [4].

In the present work, *N*-(5-chloro-2-pyridyl)-*β*-alanine was synthesized by the reaction of 5-chloro-2-aminopyridine with acrylic acid. The subsequent reaction of *β*-alanine with hydrazine hydrate afforded acid hydrazide **2**. Its condensation reaction with methylisothiocyanate, phenylisocyanate, and phenylisothiocyanate, in methanol at the equimolar ratio, furnished 3-[(5-chloropyridin-2-yl)amino]-*N*-[(methylcarbamothioyl)amino]propanamide (**3**), 3-[(5-chloropyridin-2-yl)amino]-*N*-[(phenylcarbamoyl)amino]propanamide (**4**), and 3-[(5-chloropyridin-2-yl)amino]-*N*-[(phenylcarbamothioyl)amino]propanamide (**5**), respectively. 1,2,4-Triazole **6** was prepared by the condensation of semithiocarbazide **5** in 20% aqueous KOH solution with the subsequent acidification of the reaction mixture with hydrochloric acid. Reaction of hydrazide **2** with different aromatic aldehydes furnished the corresponding hydrazones **7–10**.

Structures of the synthesized compounds were confirmed by ^{1}H and ^{13}C NMR spectroscopy and elemental analysis.

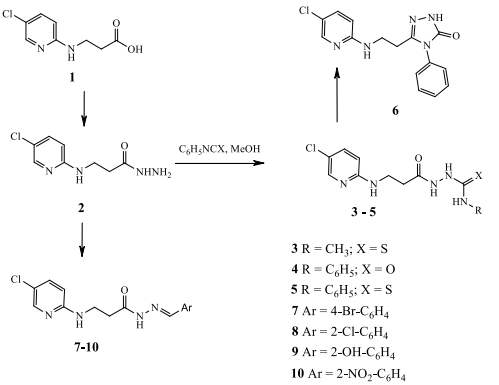

Scheme 1. Synthesis of compounds **1-10**

The antioxidative, reducing power and antibacterial properties of the synthesized compounds were screened. 3-[(5-chloropyridin-2-yl)amino]-*N*-[(methylcarbamothioyl)amino]propanamide (**3**) showed the best free radical scavenging activity, whereas 3-[(5-chloropyridin-2-yl)amino]-*N*-[(phenylcarbamoyl)amino]propanamide (**4**) and its thio analogue **5** exhibited the best reducing power properties. Among the tested compounds, only hydrazone **7** inhibited growth of *Rhizobium radiobacter, Xanthomonas campestris,* and *Escherichia coli* bacterial strains.

[1] J. Patočka, *β*-Amino acids and their natural biologically active derivatives. 5. Derivatives of unusual alicyclic and heterocyclic β-amino acids, Military Medical Science Letters **80**, 2-11 (2011).
[2] A. Chaubey, S. N. Pandeya, Pyridine a versatile nucleus in pharmaceutical field, Asian Journal of Pharmaceutical and Clinical Research **4**, 5-8 (2011).
[3] I. Tumosienė, G. Mikulskienė, K. Kantminienė, Z. J. Beresnevičius, Synthesis and structure of 3,3′-[(4-alkoxyphenyl)imino]bis(*N*′-phthaloyl- or *N*′-benzylidenepropanohydrazide) derivatives, Chemija **22**, 65-72 (2011).
[4] I. Tumosienė, I. Jonuškienė, K. Kantminienė, Z. J. Beresnevičius, The synthesis of azole derivatives from 3-[(4-methylphenyl)amino]propane-hydrazide and its *N*′-phenylcarbamoyl derivatives, and their antibacterial activity, Monatshefte für Chemie **143**, 1441-1450 (2012).

LITHIUM LANTHANUM MOLYBDATE - SYNTHESIS AND CHARACTERIZATION

Rūta Stankevičiūtė[1], Artūras Žalga[1]

[1] Department of Applied Chemistry, Faculty of Chemistry, Vilnius University, Lithuania
ruta.stankeviciute@chf.stud.vu.lt

Polytungstates and polymolybdates based either on rare earth metals (R = La, Nd, Dy, Sm, Gd etc. or alkali metals (Li, Na, K, etc.) have drawn significant attention in recent years because of their physical properties such as phase transition, ferroelectric/ ferro elastic behavior, phosphors, ionic conductivity. Oxide-ion conductors have many practical applications, such as oxygen sensors, membranes for separating oxygen and other gases, and solid electrolytes for solid oxide fuel cells [1].

Over the last ten years a new LAMOX family of oxide-ion conductors based on doped lanthanum molybdate $La_2Mo_2O_9$ with a high conductivity (0.06 S/cm at 800°C) has drawn the attention [2]. The compound exists at room temperature in the low-temperature monoclinic α phase, which passes to the cubic β phase at 580°C; in this case oxide-ion conductivity increases by almost two orders of magnitude. To stabilize the cubic phase, which has higher conductivity than the low-temperature monoclinic phase, K^{+}, Sr^{2+}, Ba^{2+}, Bi^{3+}, V^{5+}, S^{6+}, Cr^{6+}, W^{6+}, and other ions can be used to suppress the $\alpha \leftrightarrow \beta$ phase transition. As a result, a phase transition from the low-temperature cubic β phase with a statistical disorder of oxygen atoms to the high-temperature cubic β phase with a dynamic disorder of oxygen atoms occurs around 450°C [3].

What is more, the mixed molybdates of lanthanides and lithium, $LiLnMo_2O_8$, can be used as laser waveguide materials. Their preparation by conventional solid state techniques is hindered by their complex composition and the existence of numerous thermodynamically stable lanthanide molybdate phases with close metal ratios [4], because of that there is a need to use "soft" chemistry routes to create these compounds. The choice of synthesis technique usually depends on variety factors that can shorten, facilitates and reduce the preparation way. The use of solution chemistry, an agues sol-gel method in this case, can eliminate major problems, such as long diffusion paths, impurities, and agglomeration. Moreover, compared with other techniques, an aqueous sol–gel method has the advantages of a good control of the processing parameters. The use of sol–gel processing can eliminate major problems, mentioned above, which will result in products with improved homogeneity and the sintering temperature that usually strongly affects the properties of final compounds, which is crucial factor for the preparation of both nano-sized materials and thin films on different substrates [5]. From this point of view the most suitable technique to synthesize lithium lanthanum molybdate is an aqueous sol-gel synthesis method using tartaric acid as a precursor.

In this presentation, we report the synthesis of the Li-La-Mo-O tartrate gel precursor with the initial composition of the $LiLaMo_2O_8$ ceramic prepared by an aqueous sol–gel synthesis route using tartaric acid as a complexing agent. The thermal decomposition of Li-La-Mo-O was analyzed and investigated in detail. X-ray diffraction (XRD) and scanning electron microscopy (SEM) were used for the determination of crystal structure, surface morphology of the Li-La-Mo-O samples annealed at 350, 400, 450, 500, 600 ^{o}C temperatures, respectively.

[1] S. Brahma, R. N. P. Choudhary, A. K. Thakur, S. A. Shivashankar, Structural, Thermal and Electrical Property of Polycrystalline $LaLiMo_2O_8$, New Journal of Glass and Ceramics **2**, 7-12 (2012).
[2] P. Lacorre, F. Gouttenoire, O. Bohnke, R. Retoux and Y. Laligant, Designing Fast Oxide-Ion Conductors Based on La2Mo2O9, Nature **404**, 856-858 (2000).
[3] D. S. Kolesnikova, E. P. Kharitonova, V. I. Voronkova, Synthesis and Phase Transitions of Oxide-Ion Conducting Compound $La_2Mo_2O_9$ doped with Alkaline Metals, Crystallography Reports **56** (2), 315–320 (2011).
[4] V. G. Kessler, A.N. Panov, N. Y. A. Turova, A. Y. U. Borissevitch, Solution Stoichiometry Control for Pure $LiLaMo_2O_8$ Phases in Sol-Gel Preparation, Journal of Sol-Gel Science and Technology **8**, 1049–1051 (1997).
[5] R. Stankeviciute, A. Zalga, Sol–gel synthesis, crystal structure, surface morphology, and optical properties of Eu_2O_3-doped $La_2Mo_3O_{12}$ ceramic, Journal of thermal analysis and calorimetry **118** (2), 925-935 (2014).

SYNTHESIS OF NEW N,N-DISUBSTITUTED AMINOTHIAZOLE DERIVATIVES

Eglė Urbonavičiūtė, Vytautas Mickevičius

Department of Organic Chemistry, Kaunas University of Technology, Lithuania
egleurb25@gmail.com

Amino acids, their derivatives and products of cyclization play an important role in the synthesis of biologically active compounds such as pharmaceuticals, protecting agents of field plants and plant growth regulators.

The goal of the present work was synthesis of new heterocyclic compounds from *N*-(-4-methoxyphenyl)-*N*-carbamoyl-*β*-alanine (**1**).

Compound **1** reacted easily with chloroacetic acid in aqueous sodium carbonate solution, under reflux conditions and 3-[(4-methoxyphenyl)(4-oxo-4,5-dihydro-1,3-thiazol-2-yl)amino]propanoic acid (**2**) was formed. *β*-Alanine **1** was treated with 2-bromocyclohexanone in 2-propanol under reflux to afford 3-[(4-methoxyphenyl)(4,5,6,7-tetrahydro-1,3-benzothiazol-2-yl)amino]propanoic acid (**3**).

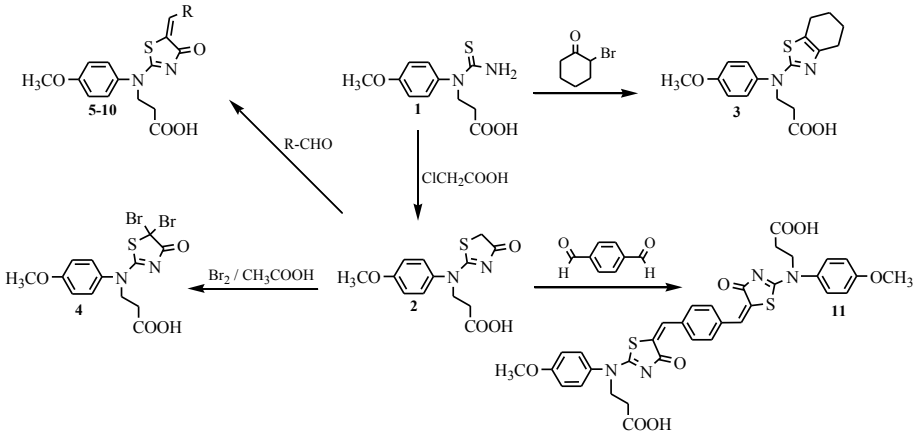

5 R= C_6H_5, **6 R**=4-Br-C_6H_4, **7 R**=4-Cl-C_6H_4, **8 R**=4-F-C_6H_4, **9 R**=2-tienyl, **10 R**=2-furil.

The reaction of compound **2** with bromine in two equimolar ratio in acetic acid at room temperature provided 3-[(5,5-dibromo-4-oxo-4,5-dihydro-1,3-thiazol-2-yl)(4-methoxyphenyl)amino]propanoic acid (**4**). The condensation of 3-[(4-methoxyphenyl)(4-oxo-4,5-dihydro-1,3-thiazol-2-yl)amino]propanoic acid (**2**) with aromatic aldehydes in aqueous solution of sodium carbonate gave thiazolones **5-11**.

The structures of the synthesized compounds were confirmed by spectroscopic methods and elemental analysis data.

DIELECTRIC PROPERTIES OF $BaTiO_3$-$KNbO_3$ COMPOSITES

Sergejus Balčiūnas[1], Maksim Ivanov[1], Jūras Banys[1], Satoshi Wada[2]

[1] Faculty of Physics, Vilnius University, Sauletekio 9/3 817k., LT10222 Vilnius, Lithuania
[2] Interdisciplinary Graduate School of Medical and Engineering, University of Yamanashi, Kofu,Yamanashi 400-8510, Japan

Sergejus.Balciunas@gmail.com

For the past 40-50 years, lead base perovskite $Pb(Zr_xTi_{1-x})O_3$ (PZT) piezoelectric ceramics have dominated the commercial market of piezoelectric devices due to their remarkable dielectric and piezoelectric properties and ability to operate in wide temperature range [1].

$BaTiO_3$ perhaps the most widely researched perovskite in the last decades. Inserting potassium niobate to BT structure creates stresses that increases domain wall count and in result piezoelectric coefficient [2] KNBT has comparable piezoelectric coefficient, thus making it a great substitute. The fact that KNBT is lead free ceramic makes it of high interest for both researchers and engineers due to environmental concerns.

KNBT composites were prepared in two steps: compact BT particles were heated to 1000^0C for 2h to create low-density ceramics, then KN were epitaxially deposited to BT structure. [3]

In this presentation dielectric properties of KNBT with different KN molar ratios will be presented. From Figure 1 we can observe that the bigger the KN/BT ratio is, the more obscured phase transitions of BaTiO3 become. Low dielectric permittivities in KN/BT with molar ratios of 0.22 and 0.5 can be explained by its low relative density. At frequencies from 10^7 to 10^{11} Hz dipole relaxation can be observed with relative relaxation time about 60-70 ps (figure 2).

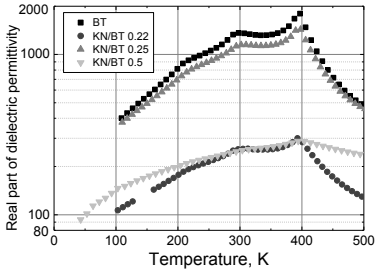

Fig. 1. Temperature dependence of real part of dielectric permittivity at 1MHz, for:
BT with 60% relative density.
KN/BT 0.22 with 53% relative density
KN/BT 0.25 with 79% relative density
KN/BT 0.5 with 60% relative density

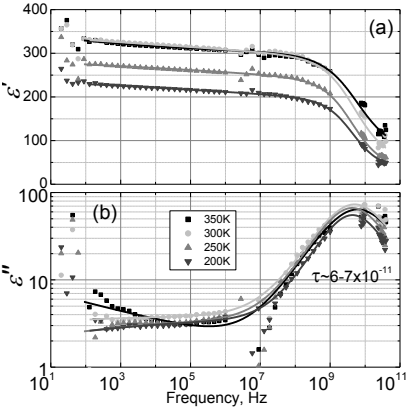

Fig. 2. Frequency dependence of real (a) and imaginary (b) part of dielectric permittivity for KN/BT 0.22 with 53% relative density.

[1] Zhang, Shujun, Ru Xia, and Thomas R. Shrout. *et al.*, *Applied Physics Letters* vol. 191.13, p. 132913 (2007):
[2] T. Higuchi, *Journal of mechanical science and technology,* vol. 24, pp. 13-18, (2010)
[3] I. Fujii, S. Shimizu, K. Yamashita, K. Nakashima, N. Kumada, C. Moriyoshi, *et al.*, *Applied Physics Letters,* vol. 99, p. 202902, (2011)

THERMOPHYSICAL AND MECHANICAL PROPERTIES OF BISPHENOL A EPOXY RESIN FILLED WITH MULTIWALLED CARBON NANOTUBES

Anna Borisova, Tatiana Glaskova, Andrey Aniskevich

Institute of Polymer Mechanics, University of Latvia, Riga, Latvia
Anna.Borisova@pmi.lu.lv

Carbon nanotubes (CNTs) are amongst the most promising nano-fillers due to their unique mechanical, thermal and electrical characteristics and have therefore been the subject of extensive research over the last few years by different methods. Issues such as the effect of CNTs volume fraction, degree of dispersion and filler/epoxy adhesion on the mechanical, thermomechanical of CNT-reinforced polymers have been addressed by a number of researchers. In view of the numerous factors that influence the microstructure of the CNT-filled polymer, reliable determination of its mechanical and thermal properties is really possible only through experiments.

Thus, the objective of the current work is to experimentally investigate the variation of the thermophysical and mechanical properties of a MWCNT/epoxy system with various loading content and to estimate correlation of the properties.

Dilatometric tests, thermal mechanical analysis (TMA), quasistatic tensile tests, hydrostatic weighting, and scanning electron microscopy (SEM) have been performed on the multiwalled carbon nanotube (MWCNT)/epoxy nanocomposite (NC) with different filler content (c = 0 - 3.8% wt.) in order to determine the influence of MWCNT content on thermophysical and mechanical properties of the NC. The experimental results show similar and nonlinear behavior of the physical properties versus nanofiller content and the existence of the optimal MWCNT content (1% wt.) in epoxy resin that maximally improves the investigated properties of the NC in comparison with unfilled epoxy. The coefficient of thermal expansion is decreased by 68%, but glass transition temperature and the tensile strength is increased by 23 oC and 18%, respectively. Comparing the results it can be seen that after exceeding optimal filler content till 1.9% wt. the properties get worse, but after adding more MWCNTs (3.8% wt.) they again improve. The correlation between investigated mechanical and thermophysical properties is estimated and reported.

The main conclusion is that addition of more CNT into epoxy resin does not mean improvement of the NC properties, because due to high viscosity the dispersion of CNT is not uniform at higher loading systems. If optimal filler content is exceeded, the composite becomes defective and its properties get worse. It happens due to small nanoparticles agglomeration which results in a bad dispersion of nanofiller that generally means that NC has defects. Optimal percentage of filler is associated with sufficient quantity of nanofiller that can improve properties of NC and have good dispersion and high aspect ratio of particles in the material.

EXAMINATION OF SMART LIGHTING WIRELESS COMMUNICATION PROTOCOLS

Miglius Budriūnas[1]

[1] Institute of Applied Research, Vilnius University, Lithuania
miglius.budriunas@ff.stud.vu.lt

Today light - emitting diodes (LED) based smart luminaires offer higher energy efficiency and also have unique properties such as instantaneous and efficient dimming, flux directionality, variable color temperature and selectable saturation/dulling ratio. With such possibilities there is a need of safe, effective, affordable and reliable communication system between luminaires and controlling devices such as smartphones and computers. Wireless communication system was selected because wired solution would require investment in data and electrical wiring infrastructure and would not be as flexible as wireless system.

After investigation, ZigBee communication protocol was selected for further applications. Alternative protocols such as Wi-Fi or Bluetooth were rejected due to too high energy consumption, possible interference with other household devices, lack of reliability or limited possibilities.

ZigBee protocol offered very low power consumption, mesh network topology which ensures high reliability and accessibility, wireless data rate of 250 kbit/s (more than enough for control commands) and secure 128 bit encryption.

Fig. 1. Smart solid state luminaires (not fully assembled for testing purposes).

Two smart luminaires with ZigBee modules were assembled for in-use examination. During testing, different configurations of modules were used. Measurements of maximum transmission distance in different environments were performed. Also communication disruptions were simulated to make sure that level of reliability is sufficient.

ZigBee communication protocol meets the requirements for smart lighting applications and was selected for further product development.

VISUAL INDICATION OF MECHANICAL DAMAGES IN POLYMER COMPOSITES

Olga Bulderberga, Andrey Aniskevich, and Sergejs Vidinejevs

Institute of Polymer Mechanics, University of Latvia, Latvia
olga.bulderberga@gmail.com

Nowadays, the use of fibre-reinforced polymer composite materials (PCM) in such industries as shipbuilding, aviation, energy, construction is common and understandable. The use of PCM is explained by their unique mechanical properties and it is growing every year. At the same time, the application area of PCM also grows, thus making the question about structural health monitoring more actual.

Unfortunately, internal damage of such material is not always visible. Non-destructive testing methods for fiber reinforced composites with epoxy matrix are very costly and usually are related to the use complex equipment.

The aim of the study was to develop fibre-reinforced polymer composite with capability of visual indication of mechanical damages.

Visualization of damaged place is provided by colour changing in the place of applied load. Approach is undertaken by integrating microencapsulated leuco dye and dye developer into the glass fabric layer. The chemical reaction between microencapsulated leuco dye and dye developer is possible, if mechanical load brings to the burst of capsule shell, dye is released, and get into the contact with colour developer. Thus the mark resembling a bruise of a human body is formed in the damaged place [1]. The following steps were made applying described approach.

Grass fibers and encapsulated components were selected for the composite manufacturing via the vacuum assisted resin transfer molding process. The worked out PCMs were tested on compression and tension to verify a capability of visual indication of mechanical damages. To decrease the threshold sensitivity of the damage visualization additional epoxy protective coatings with controlled thicknesses were used and tested. As a result relation of threshold of visualization the load vs. protective epoxy coating thickness was estimated.

Presented damage visualization method can be successfully used for composites with big surfaces, it provides the reduction of inspection time and non-equipment permanent inspection.

[1] S. Vidinejevs, O. Strekalova, A. Aniskevich, and S. Gaidukov. Development of a composite with an inherent function of visualization of a mechanical action, Mechanics of Composite Materials **49**, 77-84 (2013).

A STUDY OF LOW-FREQUENCY ELECTRICAL FLUCTUATIONS IN QUANTUM CASCADE LASERS WITH BOUND-TO-CONTINUUM DESIGN

Marek Burakevič[1,2], Alvydas Lisauskas[2,3]

[1] Department of Radiophysics, Vilnius University, Lithuania
[2]Center for Physical Sciences and Technology, Lithuania
[3]Physikalisches Institut, Johann Wolfgang Goethe-Universitat Frankfurt, Germany
marekburakevic@gmail.com

Terahertz (THz) frequency range which spans from 0.3 THz to 10 THz is still quite undeveloped and rarely used part in the spectrum of electromagnetic radiation. This is due to technological difficulties of creating a reliable and convenient sources and sensors of this radiation [1]. So far there are only a few alternatives of terahertz sources: backward wave oscillator, frequency multipliers, photo mixing devices, quantum cascade lasers and etc., none of them, however can operate in the whole THz frequency range. This work focusses on quantum cascade lasers.

Quantum cascade lasers (QCL) - are semiconductor devices that are characterized by high efficiency, small size, low price and can be produced in large quantities. They are grown by molecular beam epitaxy of alternating layers with different bandgaps and requires band structure engineering. QCL operation principle is based on intraband transitions. Charge carriers rolling down a potential staircase while sequentially emitting photons at the steps [2]. The steps consist of coupled quantum wells in which population inversion between discrete excited states is achieved.

Different types of noise can easily distort the expected characteristics of the laser, so one should make an effort to reduce their affect [3]. In order to do so, the noise research should be performed. Investigation of noise characteristics under varying parameters (like temperature or circuit current) allows to determine certain processes inside of the device, reveal the main origins of fluctuations, as well as to figure out some routes to improvement of noise characteristics of the device.

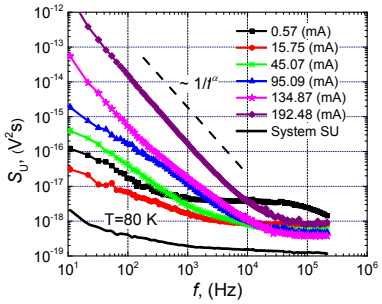

Fig. 1. Spectral density of voltage fluctuations at liquid nitrogen temperature, under various circuit current conditions.

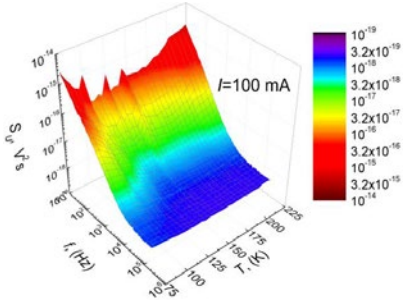

Fig. 2. Spectral density of voltage fluctuations at various temperatures, and constant 100mA circuit current.

Figure 1 presents low-frequency noise spectra for a 3.41 THz QCL with bound-to-continuum design, with different bias current at 80 K temperature. The dependencies of noise spectra on the ambient temperature for fixed 100 mA bias are presented in Figure 2. Our studies have shown that in the investigated QCL devices low-frequency noise exhibit strong 1/*f* type character, which at high frequency range goes into the white noise.

We use two models to describe white noise in nonlinear systems: the shot noise model superposed with thermal noise of shunting elements sources and Gupta theorem. This comparison of experimental and modelled data indicates that Gupta theorem with the premise of the substantially higher electronic temperature than the lattice temperature can be used to describe experimental values more accurately than the shot noise model.

[1] Peter. H. Siegel, *Terahertz technology*. (IEEE Trans. Microwave Theory Techn., vol. 50, no. 3, pp. 910–928, 2002).
[2] Jerome Faist. et al. *Quantum Cascade Laser.* (Science, Vol 264. 1994).
[3] Thomas Südmeyer et al. *Investigation and reduction of frequency noise in quantum cascade lasers.*

PROPERTIES OF POLYCARBONATE LAYERS WITH AZOPHENYLCARBAZOLE DURING OPTICAL POLING

Juozas Getautis[1], Rolandas Tomašiūnas[2], Armandas Balčytis[3], Gražina Medeišienė[4]

[1] Faculty of Physics, Vilnius University, Lithuania
[2] Institute of Applied Research, Vilnius University, Lithuania
[3] Swinburne Univ. of Technology, Australian National Fabrication Facility, Australia, Ctr. for Physical Sciences and Technology, Lithuania
[4] Institute of Applied Research, Vilnius University, Lithuania
juozasget@gmail.com

It is possible to modify the orientation isotropy and centrosymmetry of chromophores made from organic polymers thus creating optical anisotropy, second and third degree optical nonlinearity.

This allows us to use polymers with chromophores in variety of applications in photonics, signal measuring technologies, creating of large density optical or holographic storage devises, functional surfaces, optical frequency converters, modulators or switches in optical devices. [1] [2]

One of the most important and actively researched photochemical reaction is trans→cis photoisomerization. It is observed in molecules that have double bonds, for example: C=C, N=N, and C=N. Optical poling is a new method which allows us to create second order nonlinearity $\chi(2)$ in thin sheets of polymer. [3]

This work studied the parameters of polycarbonate induced with different chromophores and the influence different structures of the polymer has on the dynamics of optical poling. To achieve this poling kinetics of polymers with different structures were measured. Conclusions were drawn from linking the difference in poling kinetics to the difference in the structure of the polymer and by comparing them together.

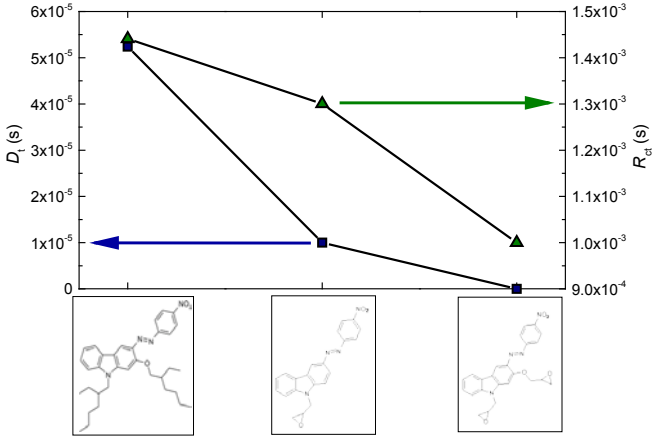

Fig. 1. Poling relaxation parameters of polymers with different structures.

Successfully achieved writing of second order nonlinearity and confirmed that the decay is governed by 2 processes: isomerization of cis→trans (fast decay) and orientational diffusion of trans isomers that are not activated. The results show that adding more anchor structures to the polymer has a tendency to decrease the orientiational diffusion of chromosomes or eliminate it at all as seen in Fig 1.

[1] Z. F. Liu, K. Hashimoto and A. Fujishima, Nature, vol. 347, p. 658, 1990.
[2] T. Ikeda and O. Tsutsumi, Science, vol. 268, p. 1873, 1995.
[3] C. Fiorini, F. Charra, J.-M. Nunzi and P. Raimond, J. Opt. Soc. Am. B, vol. 14, p. 1984, 1997.

INVESTIGATION OF PHOTOISOMERIZATION OF AZOPHENYL SELF-ASSEMBLED MONOLAYER ON GaN SURFACE

Edgaras Gurauskas, Vitalijus Bikbajevas

Institute of Applied Research, Vilnius University, Saulėtekio av. 10, 10223 Vilnius, Lithuania
edgaras.gurauskas@ff.stud.vu.lt

Molecular switches can be shifted between states in response to external stimuli. The trigger used to switch between the states can be an electrical current, a change in temperature, chemical environment, or light. This property makes them an attractive component in sensor design.

In this work we studied light photoisomerisation of various azophenylcarbazole compounds chemsorbed to gallium nitride. When exposed to a source of light photo-excitation causes azophenylcarbazole compounds to switch between trans and cis states. The change in geometry of a molecule modifies its dipole moment. When azophenylcarbazole compounds are chemsorbed to GaN surface change in dipole moment causes a corresponding change of work function[1, 2].

A self-assembled monolayer on GaN was formed by hydroxylating GaN by piranha etch and then immersing into solution containing azophenylcarbazole compound. Work function difference measurements were performed using Kelvin probe. Switching is performed by illuminating samples with λ = 440nm light source. These measurements were compared with measurements performed on unmodified GaN in order to find work function differences between cis-trans and trans-cis conformations and corresponding time constants.

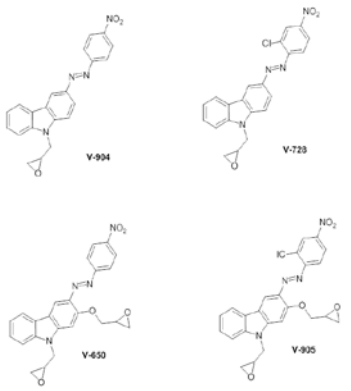

Fig. 1.Azophenyl compounds used in experiment

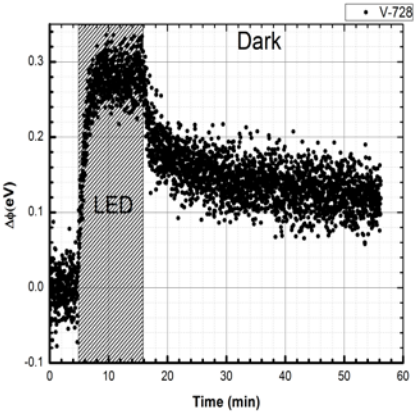

Fig. 2.Change in work function due to photoisomerization

[1] K. Asadi, F. Gholamrezaei, E. C. P. Smits, P. W. M. Blom andB. de Boer, J. Mater. Chem., 2007, 17, 1947–1953
[2] N. Crivillers et al., Photoinduced work function changes by isomerization of a densely packed azobenzene-based SAM on Au: a joint experimental and theoretical study, Phys. Chem. Chem. Phys., 2011,13, 14302-14310

INFLUENCE OF CHARGE TRANSFER STATE TO OPTICAL PROPERTIES OF NAPHTHALIMIDE DERIVATIVES

Mantas Jakučionis[1], Regimantas Komskis[1], Saulius Juršėnas[1]

[1] Institute of Applied Research, Vilnius University, Saulėtekio al. 9-III, LT-10222 Vilnius, Lithuania
mantasjk@gmail.com

1,8-Naphthalimide derivatives are already being widely used in organic light-emitting diode devices, as nerve cell markers, metal, ion and other detector devices due to strong photophysical properties and customizable molecular structure with wide variety of different substituents. Better understanding of the charge transfer state recombination would allow naphthalimide derivatives to be used for more precise and controlled probe devices and in OLED technologies.

In this work fluorescence and phosphorescence properties of naphthalimide derivatives with fenil, naphthalene, pyrene, fluorene and carbazole substituents (Fig. 1) were optically investigated. At first, the fluorescence emission spectra dependency on solvent dielectric constant of 1,8-naphthalimide modified with carbazole moiety (**5**) was found to exhibit a very pronounced solvatochromic effect, redshifting emission peaks from 437 nm when dissolved in cyclohexane to 625 nm in dilute dimethyl sulfoxide solution. 1,8-naphthalimide with fluorene substituent demonstrated almost linear fluorescence quantum yield (QY) dependency on solvent dielectric constant in the range from 2.4 (90.5%) to 46.7 (14%). We found that decreased QY is related to the drastically increased non-radiative recombination rate (from 37.5 ns in cyclohexane to 0.6 ns in DMSO). In our previous works it was shown that the introduction of fluorene fragment into 1,8-naphthalimide backbone (**4**) exhibited reversed tendencies compared to 1,8-naphthalimide-carbazole compound (**5**). Changing solvent dielectric constant from 2.4 to 46.7 resulted in QY increase from 50% to 84% and non-radiative fluorescence recombination rate decrease from 2.4 ns to 27 ns.

A detailed analysis of the photoluminescence properties were completed by determining emission spectra intensity dynamics in time. 1,8-Naphthalimide derivatives with fenil, naphthalene, pyrene, fluorene and carbazole substituents (Fig. 1) were investigated at 15K temperature under helium atmosphere. Several charge transfer state recombination channels were determined. Initially, all compounds showed the fluorescence spectra, resulting from the charge transfer from HOMO band, concentrated on an attached moiety, to LUMO band on 1,8-naphthalimide core. Fluorescence spectra peaks shifted from 412 nm, of the least π-conjugated 1,8-naphthalimide-fenil derivative (**1**), to 480 nm of 1,8-naphthalimide-carbazole compound (**5**) and lasted for up to 80 ns. Redshifted by up to 50 nm the delayed fluorescence was observed continuing for about 100 μs and it is governed by the triplet-triplet annihilation (TTA) [1] process. All of these structures, apart from demonstrating the phosphorescence emission spectra ranging from 572 nm for 1,8-naphthalimide-fenil structure (**1**) to 593 nm for 1,8-naphthalimide-carbazole compound (**5**) and lasting beyond the 100 ms mark, also exhibited an intermediate triplet type emission spectra ranging from 477 nm for 1,8-naphthalimide-fenil derivative (**1**) to 510 nm for 1,8-naphthalimide-pyrene compound (**3**). We have shown that this emission maxima is correlated with the substituent π-conjugation length. Intensities of the spectra, generated by triplet state recombination processes, were compared in non-polar and polar solvents for (**4**) and (**5**) compounds allowing to deduce that the charge transfer state recombination through triplet type processes is not the main pathway for non-radiative recombination.

In conclusion, naphthalimide derivatives exhibits not a straightforward QY dependency on solvent dielectric constant, 1,8-naphthalimide-fluorene structure (**4**) and 1,8-naphthalimide-carbazole derivative (**5**) being the most pronounced examples of the high sensitivity on charge transfer energy state and charge transfer recombination rate.

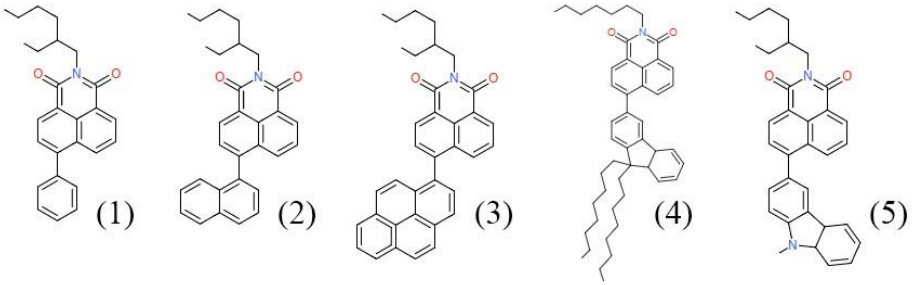

Fig. 1. Naphthalimide derivatives with fenil, naphthalene, pyrene, fluorene and carbazole substituents

[1] H. Sternlicht, G. C. Nieman, G. W. Robinson, *Triplet—Triplet Annihilation and Delayed Fluorescence in Molecular Aggregates,* J. Chem. Phys. **38**, 1326 (1963).

MICRO PARTICLE ARRANGEMENT VIA CAPILLARY FORCE ASSISTED PARTICLE DEPOSITION ON REPLICATED POLYMER TEMPLATES

Mindaugas Juodėnas[1*], Dainius Virganavičius[1], Tomas Tamulevičius[1]

[1] Institute of Materials Science, Kaunas University of Technology, Lithuania
mindaugas.juodenas@ktu.edu

Over recent years a big increase in usage of nanoparticles, varying in size and shape, is evident. In many applications where nanoparticles are used it is necessary to have them in defined positions on the surfaces. Therefore, efficient methods of well-controlled deposition have to be investigated. One of such methods is capillary force assisted assembly from colloidal solutions [1]. During this process, a small volume of nanoparticle colloidal solution is translated over a substrate with or without nanostructures at a certain temperature. Depending on the substrate surface properties, nanorelief and deposition conditions, nanoparticles can organize themselves in well-defined designated positions or in tightly packed monolayers on the substrate surface. Such arrays of micro and nanoparticles are used as drug delivery systems [2], SERS sensors [3], security features [4], etc. This paper presents results achieved using a capillary force assisted assembly system and polystyrene micro particles.

The setup applied in this work consists of precise motorized linear translator, controlled temperature sample holder and imaging system. Everything is set up on an anti-vibration optical table. Motorized translation stage that is able to move at speeds <0.001 mm/s, is assembled under the optical microscope with CCD camera on manual XY positioning stages for comfortable positioning under the microscope. The drop of colloidal solution is placed under the glass piece that can be manipulated adjusting the distance to the sample and angle of inclination. Controlled temperature sample holder fixed on the motorized translation stage slides with respect to the glass slide. The temperature control is performed employing a thermoelectric thermostat via software for temperature control input and monitoring. Results were investigated using optical and scanning electron microscopes.

The micro particle deposition from colloidal solution was carried out on patterned polymeric substrates that were formed using soft lithography replication processes from the silicon shim. Periodic structures of 560 nm width pits repeated with 1.8 μm pitch were patterned in poly-dimethyl-siloxane (PDMS). 700 nm polystyrene microbeads from 0.77 wt% colloidal solution were deposited at 12 μm/s translation speed and 40ºC temperature on the polymer template with reasonable reproducibility. Further investigation is required to increase yield of controlled particle deposition.

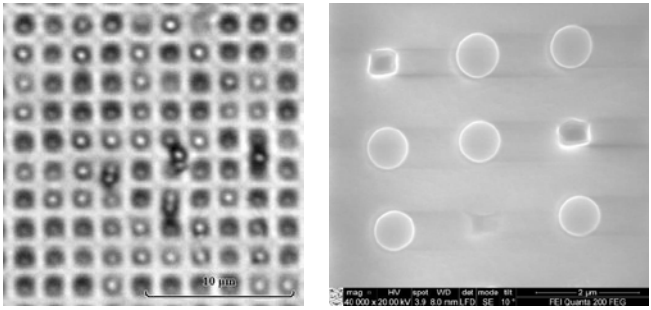

Fig. 1 Optical microscope (a) and SEM (b) micrographs of micro particles on a PDMS replica with pits assembled employing capillary force assisted depositions

This work was supported by the European Social Funds Agency Grant No. VP1-3.1-ŠMM-10-V-02-028.

[1] Laurent Malaquin, et al., *Controlled Particle Placement through Convective and Capillary Assembly*, Langmuir, 2007, 23 (23), pp 11513–11521
[2] Sang Joon Lee, et al., *Self-Organized Nanoparticles of Caffeic Acid Conjugated Polysaccharide and Its Anticancer Activity,* Journal of Nanoscience and Nanotechnology, 2015, 15 (2), pp 1130-1134(5)
[3] Joel Henzie, et al., *Oriented assembly of polyhedral plasmonic nanoparticle clusters,* Proceedings of the National Academy of Sciences of the United States of America, 2013, 110 (17), pp 6640-6645
[4] Songbo Ni, et al., *Capillary assembly of cross-gradient particle arrays using a microfluidic chip,* Microelectronic Engineering, 2014, 141, pp 12-16

Synthesis and characterization of silica with embedded silver nanoparticles

Algimantas Lukša, Marius Treideris, Virginijus Bukauskas, Alfonsas Rėza, Viktorija Nargelienė, Irena Šimkienė, Arūnas Šetkus

Center for Physical Sciences and Technology, A. Goštauto 11, Vilnius LT01108, Lithuania
algimantas.luksa@ff.stud.vu.lt

Photovoltaics is a promising large scale technology for the electrical power generation. However, the cost should be reduced to make it competitive with fossil fuel technologies. On one hand, there is a great interest in developing nanomaterial transparent conductive electrodes to replace conventional indium tin oxide films, in order to enable low-cost and mechanical flexibility while maintaining low sheet resistance and high transmittance [1]. On the other hand, the cost of photovoltaics could be reduced using thin film technology. A great limitation in all thin film solar cell technologies is that the absorbance of near-bandgap light is small, in particular for the indirect-bandgap semiconductor Si, and conventional pyramid surface structuring is not suitable for thin film solar cells. The use of metallic nanostructures that support surface plasmons is a promising method for achieving light trapping in thin film solar cells [2].

Silica sol-gel process is a versatile method allowing precise control of the structure. This method became widespread because of its simplicity and ability to change properties of the structure by embedding additional substances during the process. In sol-gel process silica is synthesized using monomer alkoxide precursor tetraethyl orthosilicate in a solution during polycondensation reactions. After the synthesis of silica sol, a thin film of sol is coated on glass plate by spin coating method followed by drying in a furnace.

This work focuses on modification of silica thin films by embedding silver nanoparticles (NP). For the preparation of silver NP, reduction of silver ions in a solution was used. Two approaches of NP embedding into silica were used: (i) addition of NP to the silica sol and (ii) addition of silver ions to the silica sol and reduction during film drying. To prevent growth of silver NP and to increase stability a polymer stabilizer was added. The formation of silver NP was confirmed by color change of silica films, atomic force microscopy and UV-VIS-NIR spectrophotometry. Absorbance spectra of silica film without (dotted line) and with (solid line) embedded silver NPs spin coated on fused silica wafer are shown in Fig.1. The peak centered at 424 nm is due to the localized surface plasmon resonance in silver NP.

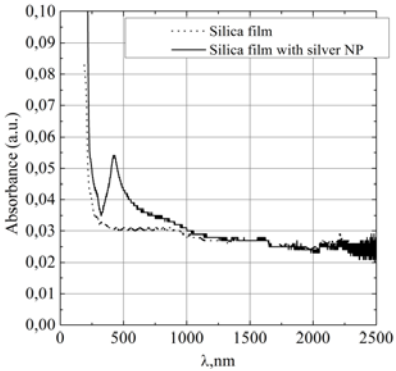

Fig. 1. Absorbance spectra of silica thin film (dotted line) and silica thin film with silver NP (solid line).

Acknowledgement

The work was carried out within the project VP1-3.1-ŠMM-08-K-01-009 that is partly supported by the National Programme "An improvement of the skills of researchers" launched by the Lithuanian Ministry of Education and Science.

[1] P.-C. Hsu et al., Performance enhancement of metal nanowire transparent conducting electrodes by mesoscale metal wires, Nature Communications **4,** 2522 (2013).

[2] H. A. Atwater, A. Polman, Plasmonics for improved photovoltaic devices, Nature Materials, **9** (3), 205-213 (2010).

Investigation of Electromagnetic Compatibility of MMDS Broadcast with LTE System

Marius Marinskas[1], Jurgis Aleksandravičius[1]

[1]Department of Radiophysics, Vilnius University, Lithuania
marius.marinskas@ff.stud.vu.lt

Every day we use mobile internet in smartphones and tablets. Growing need for fast and reliable internet connection requires implementation of 4G LTE network which can offer download speeds up to 300 Mbit/s and upload speeds up to 75 Mbit/s [1]. However, when implementing or expanding LTE networks, providers have to take into account, that LTE (2300-2400 MHz) is spectrally adjacent to MMDS (Microwave Multichannel Distribution Service) system (2200-2300 MHz). MMDS is used for general-purpose broadband networking, but more commonly for transmission of digital television. Since these two systems are near each other, there is a possibility that this proximity can cause interferences between MMDS and LTE systems. Interferences to MMDS are more significant, since this system uses receivers that are designed to work in frequencies overlapping with LTE frequency band, while LTE devices work only in their frequency range [2].

In this work electromagnetic compatibility of MMDS broadcast with LTE system was investigated. Also, frequency separation, needed to receive television transmission properly, was determined. The investigation was carried out using DVB-T (Digital Video Broadcasting – Terrestrial) and DVB-C (Digital Video Broadcasting – Cable) signals in MMDS system. Fixed signal power values were set for MMDS and LTE signals and the minimum frequency separation, when transmission without interferences could still be seen, was found.

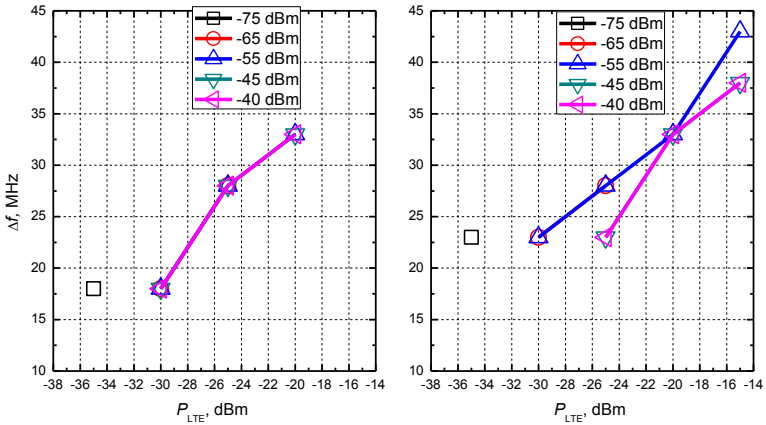

Fig. 1 Minimal frequency separation between LTE and DVB-T signals.
LTE bandwidth 10 MHz (left) and 20 MHz (right).

After investigating compatibility, we discovered that MMDS resistance to LTE interference had very little relation to MMDS signal power itself (Fig. 1). The resistance to interference was determined by LTE signal power and frequency separation between these two systems, meaning that LTE signal causes saturation in MMDS receiver. Moreover, after comparing results with DVB-T and DVB-C signals in MMDS system we determined that both DVB standards have very similar level of protection against interferences.

[1] E. Dahlman, S. Parkvall, J. Skold: *4G LTE/LTE-Advanced for Mobile Broadband* Elsevier, 105-107 (2011).
[2]G. Baruffa, M. Femminella: *Protection Ratio and Antenna Separation for DVB–T/LTE Coexistence Issues* IEEE COMMUNICATIONS LETTERS, VOL. 17, NO. **8**, 1588-1591 (2013).

DETERMINATION OF MECHANICAL PROPERTIES FOR 3D PRINTED POLYLACTIC ACID OBJECTS VARYING MICRO-ARCHITECTURE

Deividas Mizeras[1], Edvinas Skliutas[2], Andžela Šešok[3], Mangirdas Malinauskas[2]

[1]Department of Materials Science and Welding, Vilnius Gediminas Technical University, Lithuania
[2]Department of Quantum Electronics, Vilnius University, Lithuania
[3]Department of Biomechanics,Vilnius Gediminas Technical University, Lithuania
andzela.sesok@vgtu.lt; mangirdas.malinauskas@ff.vu.lt

3D printing based on fused filament fabrication (FFF) is emerging as a tool for rapid prototyping as well as additive manufacturing. Recently its equipment cost has dropped to the level affordable for hobby usage at home. At the same time it offers 3D micro-structuring potential impactfull for scientific research in microfluidics, micromechanics and biomedicine. Commercially available and widely used FFF 3D printers enable straightforward patterning of objects having internal micro-architecture out of biodegradable polylactic acid (PLA or polylactide). It opens wide prospects for the creation of custom made biodegradable templates which are of great interest for cell growth and tissue engineering applications [1]. So far there has been no systematic study on mechanical properties of micro-printed PLA. Thus, in this work we aim to determine the mechanical properties of 3D printed PLA objects having various orientation log-pile microarchitectures applying standard testing equipments and following ISO defined procedures. We employ FFF 3D printer "Ultimaker" for the manufacturing of log-pile structures having 1.2 mm lattice period and ∼50% fill factor as shown in Fig. 1(a). Bending and compressive response of the specimens tests are examined using universal "TIRAtest2300" machine, the corresponding principle measuring schemes are depicted in Fig. 1(b,c). Note that non-100% filling factor means the object itself is respectively lighter and at the same time requires proportianally less material to produce it. Employing additive manufacturing techniques it is inherently micro-porous having pores of defined shapes and dimensions.

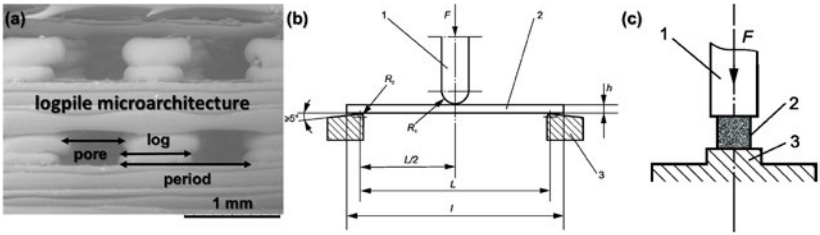

Fig. 1. (a) - an SEM micrograph of a typical 3D printed PLA specimen having log-pile micro-architecture [2]. (b,c) - principle schemes of flexural and compressive measurement setups [3]. In (a) 1 - striking edge, 2 - test specimen, 3 - support, L - distance between supports (mm); R_1 - striking edge's radius of roundness (5 mm ±0.2 mm), R_2 - support's radius roundness (5 mm ±0.1 mm); l - specimen length (mm); h - specimen thickness (mm); F - applied force (N). In (b) 1,3 - compression inducing holders; 2 - specimen; F - applied force (N).

Table 1. Experimentally obtained load/displacement properties values of PLA sample varying micro-architecture.

Type of micro-architecture	Flexural modulus (MPa)	Elastic modulus (MPa)	Stiffness (N/m $\times 10^5$)
Log-pile body-centered cubic	55	9.2	2.3
Log-pile face-centered cubic	380	7.8	1.9
Log-pile rotating 60 deg	410	23.1	5.7

In this work we 3D printed objects having internal log-pile geometries and experimentally measured stress-strain and load/displacement curves of such specimens. Within the limitation of the study we show that micro-architecture (variation of log orientation in respect to each other) can significantly modify the mechanical properties. Thus we prove that employing low-cost equipment and applying the same raw material one can create objects of desired rigidity. By means of additive manufacturing one can produce objects with specific micro-architectures which allows exploitation the structural advantages of stretching and compression constructions as well as size dependent strengthening effects [4].

[1] M. Malinauskas et al., 3D Microporous Scaffolds Manufactured via Combination of Fused Filament Fabrication and Direct Laser Writing Ablation, Micromachines **5**, 839-858 (2014).
[2] D. Mizeras et al., Tailoring mechanical properties of 3D printed objects of polylactic acid varying internal micro-architecture, **submitted** (2015).
[3] ISO 178-2003. Plastics - Determination of flexural properties; ISO 604-2002. Plastics - Determination of compressive properties.
[4] J. Bauer et al., High-strength cellular ceramic composites with 3D microarchitecture, Proc. Nat. Acad. Sci. **111**, 2453-2458 (2014).

FUSED FILAMENT FARBRICATION OF BIODEGRADABLE POLYLACTIC ACID THREE-DIMENSIONAL MICROSTUCTURES

Edvinas Skliutas, Mangirdas Malinauskas

Department of Quantum Electronics, Vilnius University, Saulėtekio Ave 9, Vilnius LT-10222, Lithuania

edvinas.skliutas@ff.stud.vu.com

Fused filament fabrication (FFF also known as fused deposition modeling or FDM) allows rapid and accurate materialization of computer aided design (CAD) models into real objects out of polylactic acid (PLA). This technology is simple, cheap and flexible, thus can be implemented in a wide range of applications: from rapid sculpting of new product prototypes or custom counterparts to printing of microstructured objects owning internal architecture. The later one is particularly promising for cell culturing research and tissue engineering practice.

Three-dimensional porous micro-woodpile geometry structures can be successfully applied as templates for cell proliferation [1] and further be used for tissue engineering as well as regenerative medicine applications. Tissue engineering develops biological substitutes that restore, maintain or improve tissue function or a whole organ [2]. The aim of our research was production of various porosity microstructures for restoration of hard tissue (bone) by employing commercially available low-cost 3D printer and standard material. It is known, that the pore size usually has to be within the range of 0.1-1 mm to be suitable for osteoblast cell growth. To manufacture such objects we used a widespread 3D printer (3DP) "Ultimaker Original". This device empowers fabrication of free-form shapes out of thermoplastic using FFF technology. Our chosen thermoplastic was biocompatible, biodegradable, transparent PLA. Also we applied colored (for additional functionality) and photosensitive PLA (highly luminescent under UV light).

Cell growth in the 3D microstructure woodpile depends on its microstructure and porosity. For this reason we produced various log orientation and different pore sizes micro-woodpiles. Both of these parameters corresponds to the final porosity of the object (*material volume/whole structure volume*). Their scanning electron (SEM) images are shown and described in Fig. 1. Be tuning the fabrication parameters such as heating nozzle temperature, flow rate, fan speed and optimizing the CAD model, we reached a result that the 3DP can reproducibly manufacture structures with up to 0.6 mm or larger pore sizes. In agreement to literature the produced micro-structures objects showed durability and flexibility in comparison to bulk PLA.

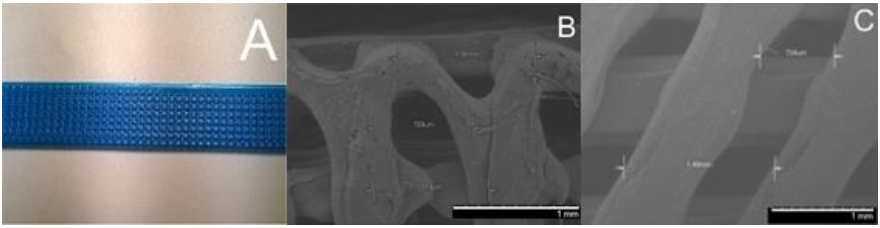

Fig. 1. Micro-woodpile structures. A – a 3DP woodpile with 0.8 mm pore size out of blue stained PLA. B – a 3DP woodpile with 0.6 mm pore size. C – a 3DP woodpile with 0.8 mm pore size, micro-logs are rotated 60 deg angle in respect to the ones of previous layer. A – optical image, B and C micrographs are obtained with SEM.

Samples of different types were given to the researchers from Vilnius University Institute of Biochemistry. Currently cell growth and tissue formation experiments on 3D micro-printed woodpiles are in progress. Additionally, ISO standardized mechanical characterization of microstructured PLA is being carried out [3].

In brief, our proposed approach employing tabletop 3D printer of "*hobby"* level enables creation of personal microfabrication laboratory at home offering production of custom made 3D structured templates of biocompatible as well as biodegradable PLA thermoplastic material. In comparison to material subtraction (milling) or lithography techniques – FFF additive manufacturing provides possibility of straightforward 100% material usage. This is highly promising to be implemented in constantly growing and emerging fields like biomedicine, Lab-on-Chip based sensing, microfluidics and integrated micromechanics.

[1] M. Malinauskas, S. Rekštytė, L. Lukoševičius, S. Butkus, E. Balčiūnas, M. Pečiukaitytė, D. Baltrukienė, V. Bukelskienė, A. Butkevičius, P. Kucevičius, V. Rutkūnas, S. Juodkazis, „3D Microporous Scaffolds Manufactured via Combination of Fused Filament Fabrication and Direct Laser Writing Ablation", Micromachines **4**(**5**), 839–858 (2014).

[2] A. Selimis, V. Mironov, M. Farsari, "Direct laser writing: Principles and materials for 3D scaffold printing", Microelectronic engineering, **132**, 83-89, (2015).

[3] D. Mizeras, E. Skliutas, L. Jonušauskas, A. Žukauskas, A. Šešok, A. Piskarskas, M. Malinauskas, "Tailoring bulk mechanical properties of 3D printed objects of polylactic acid varying internal micro-architecture", to be published (2015).

SORPTION OF PLUTONIUM IN DIFFERENT SOILS

Laima Nedzveckienė[1], Benedikta Lukšienė[1], Nikolaj Tarasiuk[1], Evaldas Maceika[1], Stasys Tautkus[2]

1 A State Research Institute Center for Physical Sciences and Technology, Savanorių ave. 231, LT-02300 Vilnius, Lithuania

2 Vilnius University, Faculty of Chemistry, Naugarduko st. 24, LT-03225 Vilnius, Lithuania

E-mail: laimakaza@gmail.com

Plutonium isotopes are present in the environment as a result of nuclear weapon testing, nuclear fuel reprocessing and nuclear facility accidents. Much attention has been paid to the evaluation of radiation risk of Pu in the environment due to its strong radiological toxicity and long-term persistence [1]. Dissolved radionuclide ions bind to solid surface because of a number of processes often classified under the broad term of sorption. Although a significant progress has been made in describing sorption on heterogeneous solids as a weighted result of sorption on the homogeneous surface, models for describing the radionuclide sorption are still mostly based on empirical values of solid-liquid distribution coefficients (K_d, $L \cdot kg^{-1}$). This is the simplest sorption model and consists of the ratio of the concentration of the radionuclide sorbed on a specific solid of the radionuclide in a specified liquid phase at equilibrium.

The distribution coefficient K_d is one of the most significant parameters in predicting the fate of a radionuclide in the environment, it is a common input in risk assessment models. Some efforts have been made to create a K_d database for soils and to establish ranges of values for a specific radionuclide and soil type and its features [2]. The K_d value was calculated using the following equation:

$$K_d = \frac{(C_i - C_e)}{C_e} \cdot \frac{W_1}{W_s} \qquad (1)$$

Where C_i is the initial radionuclide concentration (BqL^{-1}), C_e is the radionuclide equilibrium concentration in the liquid phase ($Bq\ L^{-1}$), W_1 is the solution volume (L) and W_s is the soil dry weight (kg) [3].

To determine empirical values of the solid-liquid distribution coefficient of ^{236}Pu, we conducted laboratory experiments with loam, clay, peat and two types of sand samples (sand BLZ and sand BDG). The amount of organic matter, micro and macro elements (Cu, Mn, Co, Pb, Fe, Ca, Mg, K) and total density were determined in all soil samples. Sand samples contained different concentrations of tested elements, where of different color and texture, also had different pH_{KCl} values. The dynamic flow method was used in the investigation of the sorption and transport of plutonium (^{236}Pu) in soils from distilled water. The ^{236}Pu uptake from aquatic medium by tested soils was evaluated following radiochemical analysis of the sorbent and effluent. The plutonium analyte of each studied aliquot was electrochemically deposited onto the stainless steel disc and measured with the alpha spectrometer.

Calculated K_d values showed the different permeability of tested soils to ^{236}Pu from distilled water of pH 1.6. According to K_d values tested soil samples may be distributed in the following sequence: peat> clay> loam> sand BLZ>sand BDG. It can be concluded that the amount of principal macroelements, Ca and Mg, basically defines the magnitude of the K_d value under tested conditions. The higher the amount of these elements in the soil, the higher value of the solid-liquid coefficient K_d. The differentiation in K_d values was observable depending on the amount of Ca and Mg in sand samples. The Ca and Mg concentration in sand BLZ was 8.5 $mg \cdot g^{-1}$and 1.25 $mg \cdot g^{-1}$, respectively, and the solid-liquid distribution coefficient K_d value was 292.0 $L \cdot kg^{-1}$. The Ca amount was above the determination limit and Mg concentration was 0.25 $mg \cdot g^{-1}$ in the sand BDG. The solid-liquid coefficient K_d value was significantly lower in the sand BDG compared to that in sand BLZ, it was only 54.6 $L \cdot kg^{-1}$. Obviously K_d values in sand samples demonstrated the feature of probably high accumulation capacity of Ca and Mg compounds present in soil.

[1]. Wenting Bu, Jean Zheng. Vertical distribution and migration of global fallout Pu in forest soil in southwestern China, Journal of Environmental Radioactivity **136**, 174-180 (2014**)**

[2]. C. Gil-Garcia, A. Rigal. New best estimates for radionuclide soil- liquid distribution coefficients in the soils, Part 1: radiostrontium and radiocaesium Journal of Environmental Radioactivity, **100**, 690-696 (2009)

[3]. Nao.K. Iskihawa, Shigeo Uchida. Estimation of soil-soil solution distribution coefficient of radiostrontium using soil properties, Applied Radiation and Isotopes, **67,** 319-323 (2009)

STUDY OF RADIOCESIUM AND PLUTONIUM SORPTION-DESORPTION PROCESSES APPLYING BIO- AND SYNTHETIC MATERIALS

Zita Žukauskaitė[1], Benedikta Lukšienė[1], Nikolaj Tarasiuk[1], Evaldas Maceika[1]

[1] State Research Institute Center for Physical Sciences and Technology, Savanorių ave. 231, LT-02300 Vilnius, Lithuania
zita9458@gmail.com

For many years, a considerable effort has been made to develop a comprehensive understanding of the behavior of plutonium and radiocesium in the freshwater system. Studies of plutonium and cesium required analyses of many large-volume water samples for the accurate assessment of the variation in concentrations in the aquatic system. The assessment of activity concentrations of ^{137}Cs and ^{239,240}Pu, ^{238}Pu in fresh water systems requires minimum 10-20 L [1] and 300-400 L [2] of water, respectively. To avoid transportation of large volumes of water samples to the laboratory and long lasting chemical treatment of these samples, we applied methods which allowed us to preconcentrate radionuclides on solid matrices. Various methods (precipitation, extraction, ion exchangeable, absorption, bioaccumulation) were used to remove radionuclides from environmental water bodies [3].

There is a big variability of materials, whose sorption capability for the removal of heavy metals and radionuclides from aqueous medium is investigated [3, 4]. Bentonite [5], mesoporous silica functionalized with copper ferrocyanide [6], zeolite, montmorillonite, aerogel, silica gel [7] and other are often used as sorbents.

The main aim of this study was to investigate some kind of bio- and synthetic materials considering them as promising alternatives to commercialized sorbents and to investigate the uptake behavior of ^{137}Cs and ^{236}Pu from the radionuclide-bearing fresh water under laboratory and natural conditions.

The flow method was used for studying the dynamic sorption properties of various sorbents toward Pu and Cs radionuclides by analyzing the radiocesium and plutonium distribution in the solid phase of the sorbent. The dynamic sorption characteristics are determined by measuring the activity of sorbent layers after passing definite volumes of the solution. Some laboratory and *in situ* desorption experiments were also carried out.

Environmental assays of moss (*Ptilium crista-castrensis*), lichen (*Cladonia rangiferina*), mushrooms (*Chanterella)*, pine needles, raw clay and synthetic sorbents such as filter material AFA-RMP-20 and granular activated carbon were selected and used for ^{137}Cs and ^{236}Pu sorption from the lake water. Desorption of ^{137}Cs and ^{236}Pu from moss and lichen in distilled and lake water was carried out.

The sorption-desorption capacity was evaluated based on results of α- and γ- spectrometric measurements. The raw clay as sorbent exhibited the largest sorption capacity for ^{236}Pu (lake water, pH 6, ambient conditions). The magnitude order of sorption capacity of other sorbents for ^{236}Pu was: moss>filter material>mushrooms>lichen>granular activated carbon>pine needles.

^{137}Cs was significantly sorbed by the granular activated carbon. The percentage of the ^{137}Cs desorption efficiency from moss and lichen approximately depended on the volume of water, which filled sorbents and removed ^{137}Cs. The flowing lake water of 300 L volume through the moss column desorbs 35.6 % of ^{137}Cs within 100 min. and desorbs 71.2 % of ^{137}Cs within 200 min. The same moss columns as for ^{137}Cs, showed the sorption capacity for plutonium when lake water of the 300 L volume was flowing through them.

Generalizing the obtained experimental results the following items can be pointed out. The evaluation of the initial radionuclide activity of biomaterials is required. Complex sorption-desorption process was observed when the same moss column was applied for the dynamic flow of a large lake water volume. The flowing lake water of 300 L volume caused a significant desorption of the initial ^{137}Cs activity concentration from moss while ^{239,240}Pu and ^{238}Pu were sorbed in the moss matrix from the lake water.

[1] N. Tarasiuk, A. Moisejenkova, E. Koviazina et al., On the radiocesium behavior in a small humic lake (Lithuania), Nukleonika **54(3),** 211-220 (2009).
[2] K. M. Wong, G.S. Brown, V. E. Noshkin, A rapid procedure for plutonium separation in large volumes of fresh and saline water by manganese dioxide coprecipitation, Journal of Rrioanalytical Chemistry **42**, 7-15 (1978).
[3] Li Ping, Yin Zhuoxin, Lin Jianfeng, Jin Qiang, Du Yaofang, Fan Qiaohui, Wu Wangsuo, The immobilization of U (VI) on iron oxyhydroxides under various physicochemical conditions, Environmental Science.: Processes Impacts **16**, 2278–2287 (2014).
[4] Soetaredjo F.E., Kurniawan A., Ong L. K., Widagdyo D. R., Ismadji S., Investigation of the continuous flow sorption of heavy metals in a biomass-packed column: revisiting the Thomas design model for correlation of binary component systems. RSC Adv., 4, 52856–52870 (2014).
[5] J. D. Begg, M. Zavarin, S. J. Tumey, A. B. Kersting, Plutonium sorption and desorption behavior on bentonite, Journal of Environmental Radioactivity **141**, 106-114 (2015).
[6] T. Sangvanich, V. Sukwarotwatb, R. J. Wiacek et al., Selective capture of cesium and thallium from natural waters and simulated wastes with copper ferrocyanide functionalized mesoporous silica, Journal of Hazardous Materials **182**, 225–231 (2010).
[7] I. S. Shaban, V. Mikulaj, Sorption-desorption of radiocesium on various sorbents in presence of humic acid, Journal of Radioanalytical and Nuclear Chemistry **208(2)**, 593-603 (1996).

BIREFRINGENT FRESNEL ZONE PLATE AND BESSEL BEAM GENERATOR INDUCED BY FEMTOSECOND LASER DIRECT WRITING

Laimonas Jacunskas[1, 2], Antanas Laurutis[1, 2], Titas Gertus[3], Valerijus Smilgevičius[1]

[1] Department of Physics, Vilnius University, Lithuania
[2] Altechna, Lithuania
[3] Workshop of Photonics, Altechna R&D, Lithuania
laimonas.jacunskas@altechna.com

Femtosecond laser direct writing is method of inducing self-assembled nanogratings in fused silica glass volume. This phenomena orients them in two directions, while one of them is perpendicular to incident light polarization of the laser beam. These nanogratings creates birefringent structure in the volume, thus passing light polarization expierences retardation up to 260 nm. Retardation and slow axis can be controlled by altering pulse energy and incident light polarization accordingly. Femtosecond laser direct writing technology allows to create various optical elements while changing light's polarization state. Such as radial or azimuthal polarization converters, optical vortex generators [1], random polarization converters or diffractive gratings.

a) b) c)

Here we present fabrication of various spatially variant birefringent optical elements, such as Fresnel zone plate with 8 mm clear aperture (Figure 1, a), same Fresnel zone plate structure view in microscope between crossed polarizers (Figure 1, b), Bessel beam generated after fabricated birefringent optical element (Figure 1, c). Induced patterns can substitute currently used methods for Bessel beam generation as well simplify manufacturing of Fresnel lens. Generated Bessel zone is longer than in same characteristics axicon generated Bessel zone. Investigation in birefringent optical element for Fresnel zone plate showed that beam diameter at focal spot is same as for spherical lens. However, can be improved by generating radial and azimuthal polarization in the same element.

[1] M. Beresna, M. Gecevičius, P. G. Kazansky, T. Gertus, "Radially polarized optical vortex converter created by femtosecond laser nanostructuring of glass", Appl. Phys. Let. 98 (20), 201101–201103, (2011).

Analysis of picosecond laser radiation effect on thin-film CIGS solar cell absorber layer

Andrius Žemaitis[1]

[1]Center for Physical Sciences and Technology, Savanoriu ave. 231, LT-02300, Vilnius, Lithuania
andrius.zemaitis@ff.stud.vu.lt

In recent years thin-film solar cells became very popular due to many advantages including low cost, flexibility and high efficiency. One of the most promising solar cells are based on $CuIn_xGa_{(1-x)}Se_2$ (CIGS) with efficiency as high as 21,7 % [1].

The high efficiency of large thin-film solar cell can be maintained if cell is divided into smaller segments interconnected in series in order to reduce photocurrent and resistance losses. In fabrication process three types of scribes have to be used to form a connection between two adjacent cells. Scribes are made after back contact deposition (P1), after semiconductor layers (P2) and after front contact layer deposition (P3). There is a simpler way to pattern a solar cell, when P2 micro-welding scribe is made after the last layer deposition, thus shortening the fabrication time and saving production costs. When CIGS compound is exposed with laser radiation it melts and welds a connection between front contact and back contact layers. Semiconductor CIGS after melting process change its crystal structure and recrystallize becoming metallic compound due to partial selenium evaporation and Cu-rich zones formation [2].

In this work we used picosecond laser to form molten scribes in CIGS layer. There has been chosen 1 MHz repetition rate to achieve high pulse overlap about 99 %. Using optical and scanning electron microscopes (SEM) we found the best laser system parameters for most molten scribes without back contact and substrate damages. Energy dispersion spectroscopy (EDS) analysis together with Raman spectroscopy was applied to investigate the composition of chemical elements and crystal structural changes along various laser scribes made in CIGS absorber layer. It has been found that in laser affected zone forms Cu-rich area (Fig. 1) and CIGS changed its crystal structure (Fig. 3). SEM, EDS and Raman spectroscopy results analysis lets us consider that CIGS has changed its electrical properties and became conductive compound.

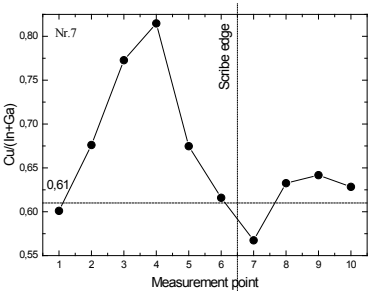

Fig.1 Ratio of Cu/(In+Ga) along laser scribe in ZnO/Cds/CIGS/Mo structure. In laser affected area the ratio is higher. 0,61 is counted reference value.

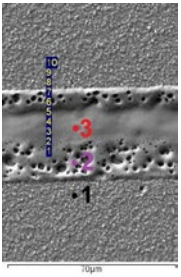

Fig. 2 Numbers in SEM micrograph shows measurement points of EDS and Raman spectroscopy.

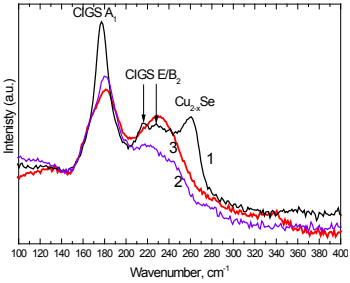

Fig.3 Raman spectroscopy measured in three points shows structural change of CIGS in laser affected area with new peak at 230 cm^{-1} in scribe center.

[1] ZSW, New best mark in thin-film solar performance with 21.7 percent efficiency, Press Release, 1–2 (2014).
[2] P.-O. Westin, U. Zimmermann, M. Edoff, Laser patterning of P2 interconnect via in thin-film CIGS PV modules, Sol. Energy Mater. Sol. Cells 92, 1230–1235 (2008).

FORMATION OF PERIODICAL STRUCTURE ON SILICON USING DIRECT LASER INTERFERENCE ABLATION AND SURFACE ETCHING PROCESSES

A. Žukauskas[1], B. Voisiat[1], M. Gavutis[1], G. Račiukaitis[1]

[1]Center for Physical Science and Technology, Savanorių Ave. 231, LT-02300, Vilnius, Lithuania
a.zukauskas@ftmc.lt

Silicon remains as the main material used in microelectronic and solar cell industry, because of its low cost, abundance in nature and well-established technologies. To control material wettability [1] and [2], optical properties [3], or field emission efficiency, structuring of the silicon surface was performed. One of the technique used for surface structuring is direct laser ablation. Most of the studies on such Si structuring deal with the formation of self-organized surface structures like sub-wavelength laser-induced periodic structures [4] created by irradiating silicon with multiple femtosecond laser pulses of near-IR radiation.

In this paper, we present the results on patterning of crystalline silicon surface using Direct Laser Beam Interference Patterning (DLIP) technique. This technique uses the interference of several beams to directly pattern the material surface [5]. This technology allows structuring big surface area using only one laser impulse. Ablation with interfering beam was implemented using interference of four and six beams. The laser beam was split into four and six beams by the diffractive optical element (DOE), then those beams were directed on the sample surface using two lenses arranged in 4F system.

"EKSPLA" 532 nm picosecond laser with a maximum pulse energy of 1.5 mJ and 2-axes positioning system "Aerotech" were used. 1 cm^2 silicon plates were ablated using different number of pulses with various energies and after that silicon plates were etched with KOH solution. After etching the plates were examined using SEM, AFM and optical microscope. Results show that after etching, silicon surface forms periodical inverted pyramids (Fig. 1).

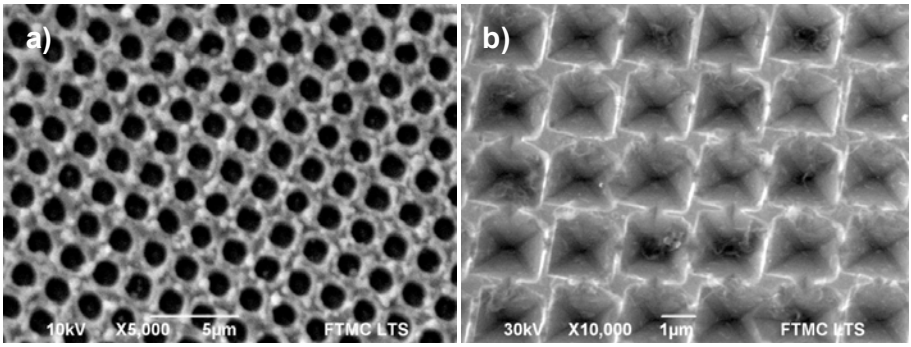

Fig. 1, SEM image of silicon surface after using 4 beam laser interference ablation technique (a) and the same silicon surface etched in KOH solution (b).

[1] T. Baldacchini, J. E. Carey, M. Zhou and E. Mazur, Superhydrophobic Surfaces Prepared by Microstructuring of Silicon Using a Femtosecond Laser, Langmuir **22**(11), 4917-4919 (2006).
[2] B. Nunes, A.P. Serro, V. Oliveira, M.F. Montemor, E. Alves, B. Saramago, et al., Ageing effects on the wettability behavior of laser textured silicon, Applied Surface Science **257,** 2604–2609 (2001).
[3] C. Wu, C.H. Crouch, L. Zhao, E. Mazur, Visible luminescence from silicon surfaces microstructured in air, Applied Physics Letters **81,** 1999–2001 (2002).
[4] F. Costache, S. Kouteva-Arguirova, J. Reif, Sub-damage-threshold femtosecond laser ablation from crystalline Si: surface nanostructures and phase transformation, Applied Physics A: Materials Science and Processing 79, 1429–1432 (2004).
[5] Voisiat, B., M. Gedvilas, S. Idrišiūnas and G. Raciukaitis, Flexible Microstructuring of Thin Films Using Multi-beam Interference Ablation with Ultrashort Lasers, Journal of Laser Micro/Nanoengineering **6**(3), 185-190 (2011).

HOT ELECTRON ELECTROCHEMISTRY INDUCED BY FEMTOSECOND LASER PULSES

Hannes Pöhl, Oskar Armbruster, Wolfgang Kautek*

Department of Physical Chemistry, University of Vienna, Austria
wolfgang.kautek@univie.ac.at

High intensity laser pulses can generate high densities of electrons in matter [1]. One technologically important follow-up process (Fig. 1) is the deterministic multiphoton-electron coupling [2-4]. In the present work, the generation of high densities of electrons in a solid by high intensity femtosecond laser pulses, the subsequent emission of hot electrons into an electrolyte and the thusly triggered electrochemistry of intermediates are studied as a function of laser and electrochemical parameters [5-8]. Results may lead to a new understanding of the fundamentals of fast hot electron electrochemical kinetics, intermediate species electrochemistry, and nanomedicine [9]. Furthermore, the influence of hot electron emission on materials machining with femtosecond laser pulses is investigated. This may lead to further understanding of laser pulse induced periodic surface structure formation processes [10].

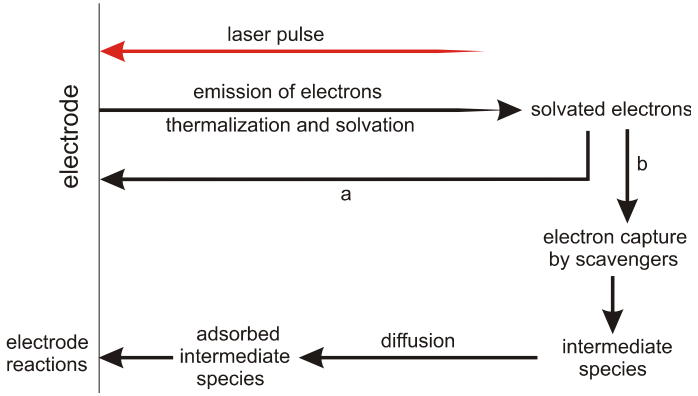

Fig. 1: Sequence of processes initiated by photo-thermoemission of electrons from metal into an electrolyte solution.

[1] D. Bäuerle, Laser Processing and Chemistry (Springer Verlag Berlin Heidelberg New York 2000).
[2] W. Kautek, J. Krüger, M. Lenzner, S. Sartania, C. Spielmann, F. Krausz, Appl. Phys. Lett. 69, 3146 (1996).
[3] M. Lenzner, J. Krüger, S. Sartania, Z. Cheng, C. Spielmann, G. Mourou, W. Kautek, F. Krausz, Phys. Rev. Lett. 80, 4076 (1998).
[4] J. Krüger, W. Kautek, Advances in Polymer Science, Vol. 168 (Springer Verlag Heidelberg 2004), p. 247.
[5] A.G. Krivenko, J. Krüger, W. Kautek, and V.A. Benderskii, Ber. Bunsenges. Phys. Chem. 99 (1995) 1489.
[6] A.G. Krivenko, W. Kautek, J. Krüger, and V.A. Benderskii, Russian J. Electrochem. 33 (1997) 394
[7] A.G. Krivenko, V.A. Benderskii, J. Krüger, and W. Kautek, Russian J. Electrochem. 33 (1998) 1068.
[8] V.A. Benderskii and A.V. Benderskii, Laser Electrochemistry of Intermediates, CRC Press 1995.
[9] A. Vogel, J.Noack, G. Hüttman, G. Paltauf, Appl. Phys. B 81 (2005) 1015.
[10] E.V. Zavedeev, A.V. Petrovskaya, A.V. Simakin, G.A. Shafeev, Quant. Electron. 36 (2006) 978.

PREPARATION OF NICKEL NANOPARTICLES IN AQUEOUS SOLUTION BY LASER IRRADIATION

Niusha Lasemi[1], Ulrich Pacher[1], Jaqueline Friedmann[2], Dietmar Pum[2], Wolfgang Kautek[1]*

[1] University of Vienna, Department of Physical Chemistry, Austria
[2] University of Natural Resources and Applied Life Sciences (BOKU), Centre for NanoBiotechnology, Vienna, Austria
wolfgang.kautek@univie.ac.at

Sonochemical processing proved to be an interesting approach to the preparation of core-shell nanopowders, such as Ni/polymer structures on the basis of conventional homogeneous redox processes [1]. The power of the ultrasonic device can control the size, morphology, and growth process of the final product.

The advantages and potential of laser-assisted nanoparticle productions are: high purity, simple starting materials, high efficiency, laser parameters control NP-size and shape [2,3].

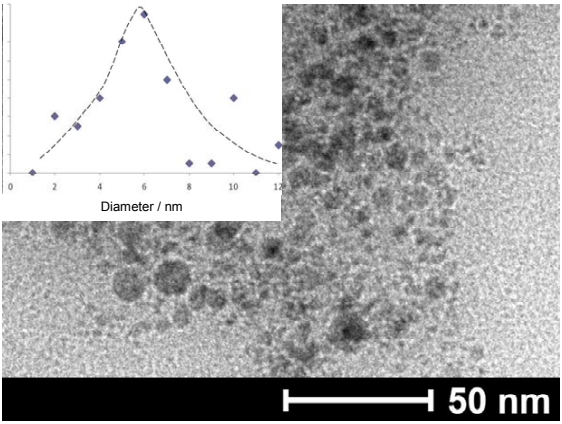

Fig. 1: TEM Micrograph of Ni-nanoparticles laser-generated in water.
5 ns, 48 mJ @ 532nm, 20Hz. 10 min/site, 6 sites. (FEI Tecnai G2 20. 200kV).

In this work, direct laser assisted production of stable Ni nanoparticles without reducing additives was investigated. Special attention was given at the strong agitation by bubble formation and cavitation processes in comparison to sonochemical mechanisms studied before [1].

[1] S. Moradi, P. Abroomand-Azar, N. Lasemi, J. Applied Chemical Researches (2008), 43.
[2] S. C. Singh, H. B. Zeng, C. Guo and W. Cai. Nanomaterials: Processing and Characterization with Lasers (2012).
[3] G. Yang (ed.), Laser Ablation in Liquids: Principles and Applications in the Preparation of Nanomaterials, Pan Stanford Publishing (2012).

DEPTH PROFILING OF GALVANO-ALUMINIUM-NICKEL COATINGS ON STEEL BY UV AND VIS LASER-INDUCED BREAKDOWN SPECTROSCOPY

Ulrich Pacher, Tristan Nagy, Björn Bielec, Wolfgang Kautek*

University of Vienna, Department of Physical Chemistry, Austria
wolfgang.kautek@univie.ac.at

Laser-Induced Breakdown Spectroscopy (LIBS) has become a method for rapid, contact-free elemental analysis of various kinds of surfaces and bulk materials. In combination with a laser's ability to perform controlled, step-by-step ablation, stratigraphic analysis is a logical option as well. In order to gain the highest possible amount of information from such an experiment, detailed knowledge of the ablation process, as well as a reliable way of tracing the spectral emissions, is necessary.

In the experiments presented here, a sample consisting of a galvanic coating of aluminium on steel, separated by a thin nickel layer, was analysed using both the second (532 nm) and fourth (266 nm) harmonic of a Nd:YAG laser for ablation and plasma generation. SEM imaging and EDX line scans were used to gain independent information about the layer formation.

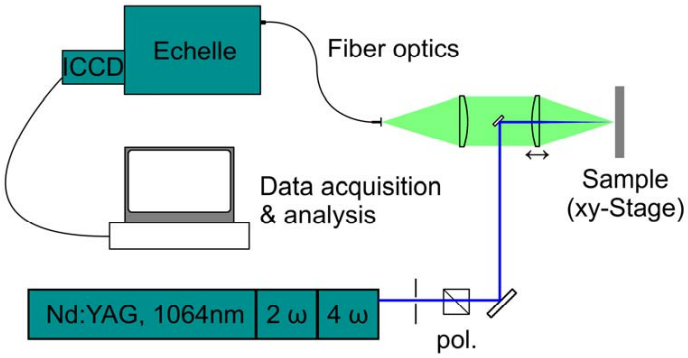

Fig. 1: Schematic of the LIBS setup.

Rather than tracing individual emission lines, the LIBS signal was generated by calculating the linear correlation coefficient, *r* between each recorded spectrum and previously recorded high-resolution standard spectra of the expected elements. This method has the advantage of compensating for influences by fluctuations in laser fluence, as well as effects such as self-absorption in the generated plasma [1]. The empirical fitting functions used to describe the signal give an excellent description of the analytical results [2]. Comparison of the signal onset for Ni and Fe with the position of the layer interfaces determined via EDX traces allows calculation of the ablation rate *h*.

[1] M.P. Mateo, J.M. Vadillo and J.J. Laserna, Journal of Analytical Atomic Spectrometry, 2001, 16, 1317.
[2] T.O. Nagy, U. Pacher, A. Giesriegl, O. Armbruster, W. Kautek, Applied Surface Science, 302 (2014) 189.

SUB-30fs PULSE LASER IRRADIATION AREA DEPENDENCE OF THE MODIFICATION BEHAVIOUR OF STEEL, SILICON AND POLYSTYRENE

Aida Naghilou[1], Oskar Armbruster[1], Markus Kitzler[2], Wolfgang Kautek[1*]

[1] University of Vienna, Department of Physical Chemistry, Austria
[2] Vienna University of Technology, Photonics Institute, Austria
wolfgang.kautek@univie.ac.at

Modification fluence thresholds are core parameters in laser materials processing [1] as well as for optical components [2] and telecommunication systems [3]. The thresh-old energy density (fluence) was found to be an unambiguous material property for a given set of experimental parameters such as pulse duration, wavelength, number of pulses, and pulse repetition rate. The modification threshold fluence however shows a dependence on the irradiated area, both for femtosecond [2,4] and nanosecond [3] pulses. However, existing models cannot explain this crucial phenomenon.

The modification threshold dependence of steel, silicon, and polystyrene on the spot area under sub-30 fs-laser irradiation was investigated. The results show incubation behaviours depending on the material class.

[1] F. Brandi, N. Burdet, R. Carzino and A. Diaspro, Optics Express, 2010, 18, 23488-23494.
[2] N. Sanner, B. Bussiere, O. Utéza, A. Leray, T. E. Itina, M. Sentis, J. Y. Natoli and M. Commandré, Proc. SPIE, 2008, 6881, W8810-W8810.
[3] G. Mann, S. Pentzien and J. Krüger, Applied Surface Science, 2013, 276, 312-316.
[4] S. Martin, A. Hertwig, M. Lenzner, J. Krüger and W. Kautek, Applied Physics A, 2003, 77, 883-884.

LASER ABLATION OF METAL FOILS VIA FEMTOSECOND LASER PULSE FOCUSING IN WATER

Tomas Baravykas[1],Simas Butkus[1], Domas Paipulas[1] and Valdas Sirutkaitis[1]

[1]Laser Research Center, Vilnius University, Saulėtekio av.10, Vilnius 10223, Lithuania
Tomas.Baravykas@ff.stud.vu.lt

Fast microfabrication of metal foils is becoming essential due to the increasing industrial requirements of nano-micro meter scale high-quality devices and materials especially in the automobile, making shadow-masks for display devices from Invar alloys [1]. Conventional laser systems (nanosecond or longer pulse duration) are applicable, however, additional post-processing treatments are required to improve quality, in addition ablation in air or vacuum creates more residue around the cutting path as a portion of the material is ejected from the irradiated area [2]. By using femtosecond pulse lasers we can achieve better precision and greater quality cuts and there is no need for post-processing of the cut samples, however residue around the area is still unavoidable. By using a thin film of water above the metal the ejected material is contained in in the water and does not stick back to the material, in addition, the fabrication throughput increases dramatically. The aim of this article is to demonstrate a method for precise, efficient and high quality processing of thin metal foils.

The experiments were done using a Pharos laser (up to 20 W), pulse duration- 280 fs, repetition rate- up to 660 kHz, pulse energy- up to 400 μJ, wavelength 1030 nm. An f-theta lens (f=100mm) was used for focusing of the beam, the beam was guided using a Scanlab® galvanometric scanner. The experiments were produced when pulses were focused in air and in water. For the case of water the metal foil (0.04 mm copper) was cowered by a thin (0.5 mm) water layer [3]. An investigation was performed on how scanning speed of the beam and focal position relative to the surface of the sample influence the process (in water and air). The focal position is changed using a stepper motor stage (that translates along the z direction). The laser parameters used in the experiment were: power 5W, pulse time 280 fs, repetition rate 25 kHz. The time required to make a through cut along a 10 mm line was measured.

Our results show that cutting without water takes approximately 5 times longer to cut through the material and the quality is considerably worse compared to cutting with water. The quality is also impacted by the scanning speed (is gradually worse at low speeds). Through cuts without the water layer are produces after approximately 0.75s (for a total length of 10 mm) this corresponds to an effective 13 mm/s cutting speed. With water the cutting time equals approximately 0.15s (effective cutting speed is ~65mm/s). The differences in quality can be seen in Fig. 1.

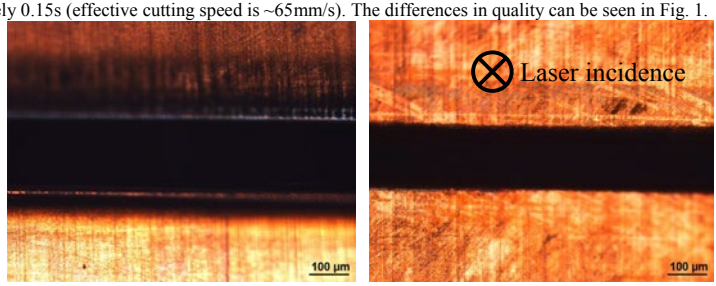

Fig. 1. Topside of the irradiated metal foil in air (left) has heat affected zone and in water (right). (1030 nm, 280 fs, 5 W, 25 kHz)

As it can be seen from Fig. 1 the use of water eliminates color change near the edges of the cut, i.e. the heat affected zone must be greatly decreased, in addition, water-ablated lines possess less or no residue, contrary to when ablation was done in air.

Further tests could lead to better quality and process speed as better parameters for processing are found. Ablation in water could be used in the micromachining of Invar alloys. The most valuable property of Invar is its very low coefficient of thermal expansion , which makes it a great resource in the making of high precision instruments like clocks, seismic creep gauges, television shadow-mask frames, valves in motors and antimagnetic watches.

[1] IL-Young Chung, Jae-Do Kim, and Kyung-Ho Kang, Ablation drilling of invar alloy using ultrashort pulsed laser, INTERNATIONAL JOURNAL OF PRECISION ENGINEERING AND MANUFACTURING Vol. 10, No. 2, pp. 11-16.
[2] N.G. Semaltianos, W. Perrie, V. Vishnyakov, R. Murray, C.J. Williams, S.P. Edwardson, G. Dearden, P. French, M. Sharp, S. Logothetidis, K.G. Watkins, Mater. Lett. **62**(14), 2165 (2008).
[3] S. Butkus, E. Gaižauskas, D. Paipulas, Ž. Viburys, D. Kaškelytė, M. Barkauskas, A. Alesenkov, V. Sirutkaitis, Rapid microfabrication of transparent materials using filamented femtosecond laser pulses**,** Applied Physics A**,** Volume 114, Issue 1 , pp 81-90

SHAPE CONTROL OF PICOSECOND PULSES BY CASCADE SECOND HARMONIC GENERATION

Arminas Butkus[1], Jonas Adamonis[2], Tomas Stanislauskas[1], Rimantas Budriūnas[1], Arūnas Varanavičius[1]

[1] Department of Quantum Electronics, Faculty of Physics, Vilnius University, Lithuania
[2]UAB Ekspla, Savanorių pr. 237, Vilnius, Lithuania
arminas.butkus@ff.stud.vu.lt

High intensity laser physics scientific group is developing optical parametric chirped pulse amplification (OPCPA) system NAGLIS in Vilnius university, laser research center. In OPCPA, the efficiency of amplification process, the gain bandwidth and the pulse contrast strongly depends on the temporal profile of the pump pulse and the ratio between pump and seed pulse duration. It is known that rectangular (super-Gaussian) spatiotemporal shape pump pulse is optimal for OPCPA system, therefore, it is necessary to be able to manage and control these pump pulse characteristics [1, 2].

The basic principle of shape control of picosecond pulses by cascade second harmonic (SH) generation is based on three-wave interaction in the nonlinear media (see Fig. 1 (a)). At the first cascade SH generator stage fundamental harmonic (FH) pulse undergoes significant changes, which depends on the pump pulse temporal profile (in our case Gaussian shape) and SH conversion efficiency. At a certain pump intensity value FH temporal profile may become flat-top or even with a dip. Afterwards, the second cascade SH generator stage is pumped by the modified FH pulse. The temporal profile of the SH pulse generated at the second stage depends on the modified FH pulse and maintains similar temporal profile [3].

We have explored modification of picosecond pulses temporal profile by cascade SH generation (the first stage – 9 mm length LBO crystal, the second stage – 8 mm length KTP crystal). The cascade SH generator was pumped by 75 ps Gaussian shaped pulses from the 1 kHz Nd:YAG amplification system. The measurements were performed by using the modified third-order cross-correlator „Sequoia“. The SH signal was measured at the center of the beam to eliminate effects due to the beam intensity distribution. At pump intensity $I_P = 570$ MW/cm^2 formed pulse duration is about $\tau_{FWHM} = 150$ ps, temporal range in which intensity drops 15% of its maximum value is about 105 ps, while conversion to SH efficiency at the first stage was 58%. These kind of pulses are suitable to pump the first OPCPA stage.

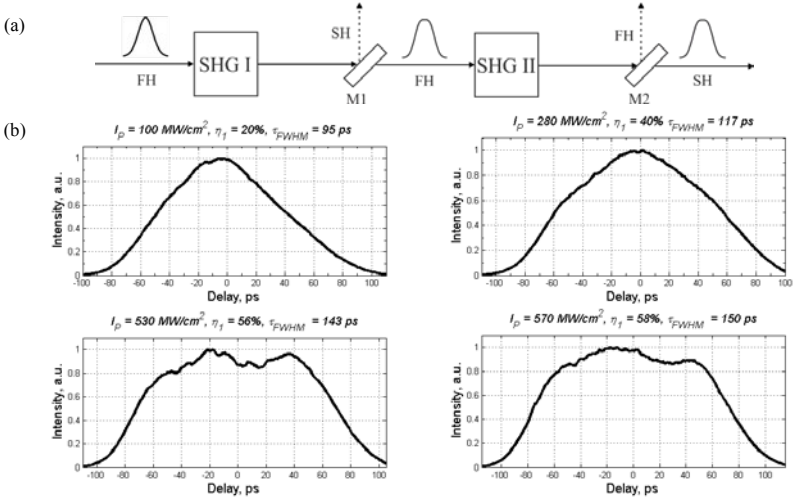

Fig. 1. (a) Principal scheme of the cascade second harmonic generator (FH – first harmonic pulse, SH – second harmonic pulse, SHG – second harmonic generator, M – mirror, dashed line – separated and blocked redundant signal); (b) Picosecond pulse temporal profiles in the center of the beam at different pump intensities from the cascade SH generator (I_P – pump intensity at the first stage, η_1 – SH conversion efficiency at the first stage, τ_{FWHM} – pulse duration).

[1] V. Pyragaite, A. Stabinis, R. Butkus, R. Antipenkov and A. Varanavičius, Parametric amplification of chirped optical pulses under pump depletion, Optics communication **283**, 1144–1151 (2010).
[2] S. Witte and K. S. E. Eikema, Ultrafast Optical Parametric Chirped-Pulse Amplification, IEEE Journal of Selected Topics in Quantum Electronics **18**, 296–307 (2012).
[3] J. Adamonis, Didelės galios pikosekundinis Nd:YAG lazeris čirpuotų impulsų parametrinių stiprintuvų kaupinimui, Vilniaus universitetas, 59–74 (2013).

PROPERTY ASSESSMENT OF WHITE LIGHT CONTINUA GENERATED BY ULTRA-SHORT LASER PULSES

Darius Dementavičius, Kipras Redeckas, Vladislava Voiciuk, Mikas Vengris

Department of Physics, Vilnius University, Lithuania
dementaviciusd@gmail.com

White light continuum (or supercontinuum) generation is a nonlinear optical phenomenon. During the generation the narrow spectrum of the initial laser pulse can spread many times and as a result a broad and smooth continuum is formed. The obtained white light can be applied in many different fields: telecommunication, medicine, material science. Many different nonlinear processes contribute to the broadening of the spectrum, therefore mathematical modeling of continuum generation is problematic. Most research on the properties of supercontinuum is carried out by experiments. Many publications on this topic can be found [1-3].

In this work, the properties of white light continuum, generated in sapphire, calcium fluoride (CaF_2) and water were examined and evaluated. A small experimental setup was constructed for the measurements. Several laser sources were used: first and second harmonics of Coherent Libra laser (800 nm, 50 fs pulses with 1 kHz repetition rate) and also first and second harmonics of Light Conversion Pharos laser (1030 nm, approximately 300 fs laser pulses with 25 kHz repetition rate).

With each material and laser source the relative intensity and relative noise of every generated spectral component were measured. As an example of the measurement results, in Fig. 1 relative intensity of continua (left) generated with the used materials with the first harmonic of Coherent Libra laser are shown along with the relative noise (right).

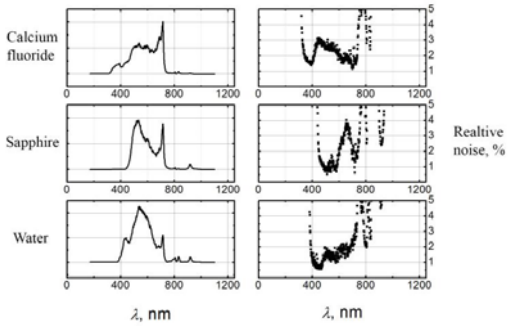

Fig. 1. White light continua generated in calcium fluoride, sapphire and water using 800 nm, 50 fs laser pulses with 1 kHz repetition rate.

Comparing all the measurements, it can be said that calcium fluoride provides continuum spread furthest down the blue side of the spectrum. Using the second harmonic of the Libra laser, the obtained spectrum reached 260. This is due to the fact that calcium fluoride has the largest band gap of the all the used materials. In all of the measurements, the relative stability of the spectrum generated in calcium fluoride was less stable than in other materials, because the fluoride is quite sensitive to optical breakdown and the crystal had to be rotated in order not to damage it.

Using the 1030 nm pulses of the Pharos laser, one interesting result is that the pump wavelength is further from the center of the generated continuum. Thus, when trying to filter out the remains of the pump pulse from the continuum, less of the generated spectrum is lost. Using this laser the measured spectra were generally less stable, probably due to the laboratory conditions, which were not ideal. Also, due to the longer pulses and higher repetition rate, continuum was not obtained in water and calcium fluoride. In water due to the fact that the point where pulse would self-focus would begin to boil not long after the start of the exposure to the laser light and in calcium fluoride due to the increased risk of damaging the crystal.

The knowledge of the spectra gained in these materials using mentioned laser sources can be used in material science, specifically pump-probe experiments, where supercontinuum is used to measure absorption kinetics of various materials.

[1] A. Brodeur, S. L.Chin, Ultrafast white light continuum generation and self-focusing in transparent condensed media, Journal of the optical society of America B Vol. 6, No. 4, 637-650 (1999).
[2] A. K. Dharmadhikari, F. A. Rajgara, D. Mathur, Systematic study of highly efficient white light generation in transparent materials using intense femtosecond laser pulses, Applied Physics B, 80, 61-66 (2005)
[3] T. Imran, G. Figueira, Intensity-phase characterization of white light continuum generated in sapphire by 280 fs laser pulses at 1053 nm, Journal of Optics 14 035201

Beam Shaping with Axisymmetric Photonic Crystals

Darius Gailevicius[1], Vytautas Purlys[1], Lina Maigyte[2], Martynas Peckus[1], Roaldas Gadonas[1], Kestutis Staliunas[2,3]

[1]Laser Research Center, Department of Quantum Electronics, Vilnius University, Lithuania
[2]Departament de Fisica i Enginyeria Nuclear, Universitat Politecnica de Catalunya, Spain
[3]Institucio Catalana de Recerca i Estudis Avancats (ICREA), Spain
darius.gailevicius@ff.stud.vu.lt

Photonic crystals (PhCs) have been shown to exhibit unique properties that can result in some interesting phenomena, such as negative refraction, flat lensing, non-diffractive propagation of light, super-prism effect, chromatic and spatial filtering of light, etc, all of which can be realized through selective dispersion engineering. Here we discuss an alternative method of spatial beam shaping, enabled by the gap-less spatial filtering phenomenon [1]. Previously, such PhC filters of 2D rectangular geometry were demonstrated [2], facilitating the deflection of potentially unwanted spectral components to diffraction maxima, however some applications may require high quality beams with an uniform angular spectrum in all radial directions.

We present results of our recent study on design, experimental realization and performance of axisymmetric photonic crystals [3]. Such PhCs are comprised of modified refractive index concentric rings with a periodically varying radius, arranged in periodic layers in a sequential negative-positive manner Fig. 1 (a). PhCs were fabricated using the direct laser writing technique in a soda-lime glass medium and characterized by measuring the angular transmission spectrum of a 633 nm HeNe laser beam. The resulting PhC structures had a 25 mrad wide filtered out areas of 65 mrad central filtering angle (Fig. 1 (b)), which can be tuned by varying the PhC's period lengths (even employing chirping [4] to increase widths of the filtered out areas Fig. 1 (c)). Gap-less spatial filtering is advantageous due to the experimentally achievable PhC period lengths, which in our case were 2 μm for transversal and 13.4 μm for longitudinal directions.

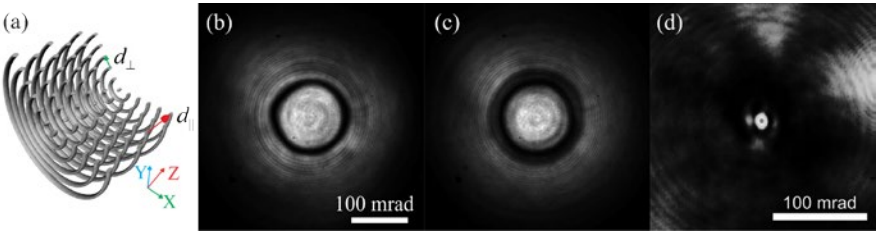

Fig. 1. (a) axisymmetric photonic crystal geometry, experimental far field images showing axisymmetric filtering (b), axisymmetric filtering with a chirped PhC (c), and super-collimation effects (d).

Additionally, the super-collimation [5] effect has been experimentally observed. It leads to an accumulation of intensity for the near optical axis beam components by depleting the higher spatial frequency components. This effect is visible for PhCs that are of approximately double length compared to PhC filters, and requires near axis spatial filtering. Experimental observation of energy concentration near axis in axisymmetric PhC showed, that a collimated beam was formed. Said beam had a divergence of 20 mrads and an intensity increase of 7 times Fig. 1 (d). Numerical calculation show that a more than 20 times intensity increase can be expected if fabrication conditions could be optimized. We emphasize, that this effect is not observed in conventional 2D or 3D woodpile PhCs.

The results of our studies in combination of numeric optimization techniques might be utilized in miniature spatial beam filters or shapers, possibly replacing current rather bulky filters, consisting of two lenses and a pinhole.

[1] K. Staliunas and V. Sanchez-Morcillo, Spatial filtering of light by chirped photonic crystals, Phys. Rev. A **79**, 053807 (2009).
[2] L. Maigyte et al., Signatures of light-beam spatial filtering in a three-dimensional photonic crystal, Phys. Rev. A **82**, 043819 (2010).
[3] V. Purlys et al., Spatial filtering by axisymmetric photonic microstructures, Opt. Lett. **39**, 929-932 (2014).
[4] D. Gailevicius et al., Chirped axisymmetric photonic microstructures for spatial filtering, J. Nanophoton **8**(1), 084094 (2014).
[5] V. Purlys et al., Super-collimation by axisymmetric photonic crystals, Appl. Phys. Lett. **104**, 221108 (2014).

HIGH QUALITY "WHITE" VORTEX GENERATION BY RADIAL POLARIZATION S-WAVE PLATE CONVERTER

Mindaugas Gecevičius[1,2], Maksym Ivanov[4], Martynas Beresna[2], Titas Gertus[3], Aidas Matijošius[1], Peter Kazansky[2] and Valerijus Smilgevičius[1]

[1] Vilnius University Laser Research Center, 10 Sauletekio avenue, LT-10223, Vilnius, Lithuania
[2] Optoelectronics Research Centre, University of Southampton,SO17 1BJ, Southampton, United Kingdom
[3] UAB „Altechna", 6A Mokslininku st., LT-08412, Vilnius, Lithuania
[4] Taurida National V.I.Vernadsky University, 4 Vernadsky Ave., 95007 Simferopol, Ukraine
maks.ivannov@gmail.com

Recently a significant advance was achieved in development of coherent and in-coherent broadband light sources leading to growth of applications ranging from attosecond pulse generation to optical coherence tomography. However, control of phase and polarization of such light sources exhibits a significant challenge as most of conventional optical elements exhibit strong dependence on wavelength. Here we exploit ultrafast laser nanostructuring for implementing broadband phase elements in particularly for "white" vortex generation.

Femtosecond laser imprinted birefringent optical element, S-wave plate, depending on the input light polarization, allows generation of azimuthally/radially polarized beams or optical vortex beam [1], with efficiency close to 99%.The S-wave plate is fabricated in the widespread silica glass, which exhibits high damage threshold level and wide transparency window. Until recently, this polarization and phase control method was considered as strongly wave length dependent with a typical bandwidth of tens of nanometers. However, we demonstrated that the S-wave plate, which is manufactured for the certain (e.g. 530 nm) wavelength, can be also used with other wavelengths, since the residual light, occurring due to wavelength mismatch, is orthogonally polarized to the optical vortex. As a result, after a polarization sensitive filtering with an achromatic quarter-wave plate and linear polarizer, the output beam results into a perfect high contrast optical vortex at any given wavelength. Moreover, this method can be successfully implemented for in-coherent light sources. To demonstrate this, the S-wave plate (manufactured by Altechna Ltd. for 532 nm) was illuminated with the halogen lamp with continuous spectrum from 400 nm till 830 nm. The collimated light was circularly polarized and then converted into optical vortex by the S-wave plate. The output beam was filtered as described above. At the output we obtained an optical vortex with deep node of intensity in the centre, which preserved its doughnut shape upon long distance free space propagation (Fig. 1).The resulting white vortex did not exhibit any spatial or spectral dispersion. The position of the node and structure of the beam was thoroughly examined with the narrow band interference filters (402-753 nm). Real colour images show no spectral components dispersion. To confirm the presence of the phase singularity and show the value of topological charge in the white vortex beam, it is being focused by cylindrical lens (description of the method see in the [2]).

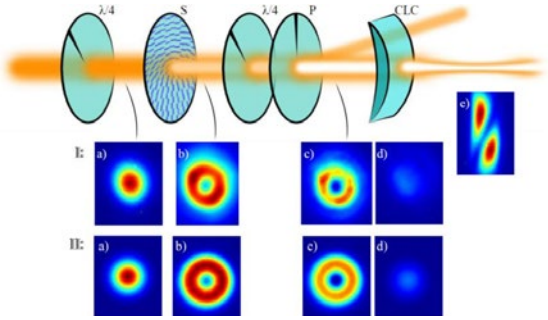

Fig. 1. Simplified experimental set-up: λ/4 – quarter-wave plates, S – S-wave plate fabricated for 523 nm, P – polarizer, CLC – cylindrical lens converter; I: experimental results; II: theoretical modeling; a) circularly polarized collimated while light beam, b) beam after S-wave plate, c) vortex part of the beam, d) orthogonally polarized noise part of the beam, e) intensity distribution after cylindrical lens converter-analyzer.

The white vortex generated by radial polarization S-wave plate converter has no disadvantages, that present in other methods on generation of white light optical vortices from non-coherent light sources, like spatial-, chromatic-, topological charge-dispersions.

[1] M. Beresna, M. Gecevičius, P. G. Kazansky, "Polarization sensitive elements fabricated by femtosecond laser nanostructuring of glass [Invited]" Opt. Mater.Express, 1(4), 783 (2011).
[2] V. Denisenko, V. Shvedov, A. S. Desyatnikov, D. N. Neshev, W. Krolikowski, A. Volyar, M. Soskin, and Yu. S. Kivshar, "Determination of topological charges of polychromatic optical vortices" Opt. Express 17, 23374-23379 (2009)

SUPERCONTINUUM GENERATION IN SOLID-STATE DIELECTRIC MEDIA WITH PICOSECOND LASER PULSES

Milda Skeivytė[1], Ieva Gražulevičiūtė[1], Justinas Galinis[1], Gintaras Tamošauskas[1], Vytautas Jukna[2], Audrius Dubietis[1]

[1]Department of Quantum Electronics, Vilnius University, LT-10222 Vilnius, Lithuania
[2]Centre de Physique Theorique, CNRS, Ecole Polytechnique, F-91128 Palaiseau, France
** milda.skeivyte@ff.stud.vu.lt*

Supercontinuum (SC) generation in bulk dielectric media is a very efficient method for production of broadband radiation with excellent spatial and temporal coherence properties at various parts of the optical spectrum. During the last decades, SC generation was widely studied in a variety of solid-state media with femtosecond (100 fs and shorter) laser pulses, using amplified Ti:sapphire lasers as predominant pump sources [1]. Recent advances in the development of novel solid-state laser systems, such as based on Yb-doped lasers in particular, see e.g. [2], prompted experimental investigations of SC generation in solid-state dielectric media using picosecond laser pulses. Most of these efforts are directed toward development of ultrabroadband table-top optical parametric chirped pulse amplification (OPCPA)-based systems, where picosecond SC seeding markedly simplifies the overall setup, excluding the need of employing optically synchronized broadband laser oscillator source [3].

In this contribution we present a detailed numerical and experimental study of SC generation by self-focusing and filamentation of 1.1 ps, 1055 nm laser pulses in YAG crystal. Numerical simulations based on solving the unidirectional nonparaxial propagation equation uncover that spatiotemporal dynamics of self-focusing picosecond pulses is more complex and markedly different from that observed in femtosecond filamentation regime [4]. In particular, we show that free electron plasma plays a dominant role in spatiotemporal reshaping of picosecond laser pulses, producing a Bessel-like spatial intensity distribution at the pulse tail, which thereafter undergoes temporal splitting and produces an octave-spanning supercontinuum, covering wavelength range from 460 nm to 1.8 μm, in excellent agreement with experimental data. Moreover, our measurements demonstrate that SC is generated without the onset of optical damage. Its spectral shape is highly reproducible from pulse-to-pulse, with a standard deviation of spectral intensity fluctuations less than 3% throughout the major part of the SC spectrum.

This research was funded by the European Social Fund under the Global Grant measure, grant No. VP1-3.1-SMM-07-K-03-001.

[1] M. Bradler, P. Baum, E. Riedle, Appl. Phys. B **97**, 561 (2009).
[2] A. Vaupel, N. Bodner, B. Webb, L. Shah, M. Richardson, Opt. Eng. **53,** 051507 (2014).
[3] R. Riedel, A. Stephanides, M. J. Prandolini, B. Gronloh, B. Jungbluth, T. Mans, F. Tavella, Opt. Lett. **39**, 1422 (2014).
[4] V. Jukna, J. Galinis, G. Tamošauskas, D. Majus, A. Dubietis, Appl. Phys. B **116**, 477 (2014).

INVESTIGATION OF SUBSURFACE DAMAGE IMPACT ON RESISTANCE TO LASER RADIATION OF FUSED SILICA SUBSTRATES

Saulė Abbas[1,2], Kęstutis Juškevičius[1,2]

[1] Center for Physical Sciences and Technology, Lithuania
[2] Department of Physics, Vilnius University, Lithuania
saule.abbas@ff.stud.vu.lt

It is well known that the conventional CeO_2 abrasive polishing techniques cause subsurface damage of fused silica (FS) glass, which is the main limiting feature of light absorption, especially in ultraviolet wavelength region of laser radiation [1-2]. Subsurface damages are defined as residual digs and scratches filled with polishing slurry and covered with the so-called Bielby layer (polished layer) [3-4].

In this study surface treatment by wet etching in fluoride-based solutions (HF/HNO_3) was applied to remove Bielby layer and "clean out" digs and scratches containing residual polishing materials.

The dissolution of silicate glasses results in the formation of the stable hexafuorosilicate (SiF_6^{2-}) anion [5]. When hydrofluoric acid is used, the overall reaction can be summarized as:

$$SiO_2 + 6HF \rightarrow SiF_6^{2-} + 2H_2O + 2H^+ \quad (1)$$

Surface roughness (RMS) of polished FS substrates before and after the etching process using different HF/HNO_3 solution concentrations was measured. Laser induced damage threshold (LIDT) tests (1-on-1) were used for all samples. Measurements were performed for 355 nm, 100 Hz, 4.8 ns laser radiation (Fig. 1).

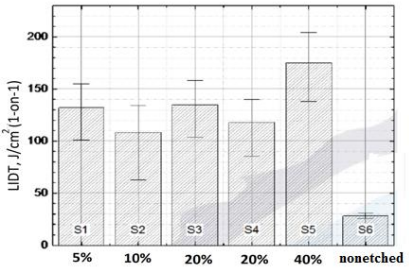

Fig. 1.The LIDT@355 dependence on HF/HNO_3 concentration.

Though measured roughness of etched FS substrates was higher than the ones that were not etched, LIDT results of bare etched FS samples were successfully increased ~4 times (from 28.20 J/cm^2 to 133.70 J/cm^2). This could be the result of removing said subsurface damage during the etching process.

[1] C.L. Battersby, L.M. Sheehan, M.R. Kozlowski, SPIE, Boulder, CO, USA, 1999, pp. 446-455.
[2] L. Hongjie, H. Jin, W. Fengrui, Z. Xinda, Y. Xin, Z. Xiaoyan, S. Laixi, J. Xiaodong, S. Zhan, Z. Wanguo, Opt. Express, 21 (2013) 12204-12217.
[3] P.E. Miller, T.I. Suratwala, L.L. Wong, M.D. Feit, J.A. Menapace, P.J. Davis, R.A. Steele, SPIE, Boulder, CO, USA, 2005, pp. 599101-599125.
[4] J. Lambropoulos, Optical Society of America, 2000, pp. OMA6.
[5] L. Wong, T. Suratwala, M. D. Feit, P. E. Miller, R. E. Steele, "The distribution of subsurface damage in optical glasses," J. Eur. Opt. Soc. **6**(2011).

ALL-OPTICAL SURFACE PATTERNING IN AMORPHOUS CHALCOGENIDE AND AZOPOLYMER THIN FILMS

Ugis Gertners, Janis Teteris, Andrejs Gerbreders

Institute of Solid State Physics, University of Latvia, Latvia
gertners@gmail.com

This work will be based on all-optical surface patterning, which objective is to do a research on the amorphous chalcogenide (and for other light sensitive materials) susceptibility to light. As one of the research methods, a direct holographic record will be used, i.e., creating surface relief micro/nanostructures or holographic gratings in light sensitive materials directly during the recording without any additional processing, like etching. Complete development of this method opens wide range of usage possibilities in optical element production and utilization, as well as in introduction of new and innovative technologies. There is still a lot of interesting phenomena that are not well understood and explained in a microscopic level and so this work will be directly involved in the process of research. Record efficiency dependence from its parameters (intensity, polarization) and recording conditions will be examined and recording process in microscopic level will be explained. Optical properties for obtained nanostructures will be studied, such as transmission, reflection, diffraction efficiency, etc. The obtained structures will be viewed by atomic force microscopy, determining their shape and size.

PLASMONIC ENHANCEMENT OF RAMAN SCATTERING FOR POTASSIUM BROMATE

Anna Matsukovich

B. I. Stepanov Institute of Physics, NASB, Nezavisimosti Ave., 68, 220072 Minsk , Belarus

a_matsukovich@tut.by

Analysis of the composition of drinking water is actual problem. Bromates are contaminants that develop in drinking water mainly as the disinfection byproducts [1].The bromate ion BrO_3^- may exist in a number of salts, the most common of which are potassium bromate $KBrO_3$ and sodium bromate $NaBrO_3$.

This work shows the surface-enhanced Raman scattering for potassium bromate ($KBrO_3$) with two types of substrates. The substrates have been prepared by gold nanoparticles immobilizing on the glass surface via layer-by-layer electrostatic deposition during 1 hour and 24 hours. The monodisperse gold sol have been prepared by Turkevich technique [2]. Optical density spectrum of the gold sol shown the maximum on 532 nm. The average size of nanoparticles was about 12 nm.

The potassium bromate water solutions have been deposited on the SERS-active substrates and dried at the room temperature in the horizontal position. Concentration of the solutions was 10^{-1} M. The solutions in the same manner were also deposited on the reference metal-free substrates.

The YAG:Nd^{3+} laser (532 nm) was used to excite the Raman spectra. Registration spectrum occurred range 200-1000 cm^{-1}. The registration system consisted of a spectrograph (Spectra Pro-500i, Acton, USA) with a diffraction grating 600 lines/mm and a CCD matrix. For Raman measurements exposure time was 75 s.

Raman spectra for the potassium bromate on the glass surface and the gold substrates are shown in (Fig. 1). We can see asymmetric band E at 366 cm^{-1}, symmetric band A_1 at 430 cm^{-1}, symmetric stretching A_1 at 793 cm^{-1} and band at 835 cm^{-1} [3, 4]. The bands at 366, 430 and 793 cm^{-1} correspond to vibrations of bromate anion (BrO_3^-) [3].

In both cases the enhancement of the bands corresponds to 366, 793 and 833 cm^{-1}. The enhancement of the bands for the gold substrate (1 hour) is 2.8-3.5 times (Fig. 1a) and for the gold substrate (24 hours) is 1.5-2.3 times (Fig. 1b). The maximum gain in both cases is for the band 793 cm^{-1}: 3.5 for the gold substrate (1 hour) and 2.3 for the gold substrate (24 hours).

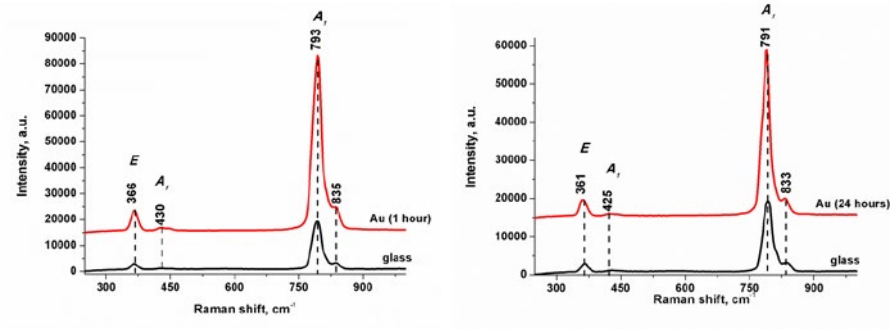

a) **b)**

Fig. 1. Raman spectra of potassium bromate on the surface of the Au (1 hour) substrate (a) and on the Au (24 hours) substrate (b).

[1] Bromate in Drinking-water. Background document for development of World Health Organization Guidelines for Drinking-water Quality. World Health Organization 2005.
[2] J. Turkevich et al., A study of the nucleation and growth processes in the synthesis of colloidal gold. Discuss. Faraday Soc. **11**, 55–57 (1951)
[3] Alves, Wagner A., and Roberto B. Faria, Vibrational investigation of the stretching region of bromate ion in solution. Spectrochimica Acta Part A: Molecular and Biomolecular Spectroscopy **58.7,** 1395-1399 (2002).
[4] Gardiner, D. J., R. B. Girling, and R. E. Hester, Vibrational spectra and force constants of chlorate, bromate and iodate ions in aqueous solution. Journal of Molecular Structure **13.1,** 105-114 (1972).

RESEARCH OF NANOPHOTONIC RING RESONATOR FOR OPTICAL BIOSENSORS

Greta Naujokaitė[1], Darius Urbonas[2], Raimondas Petruškevičius[2]

[1] Vilnius University Faculty of Physics, Sauletekio ave. 9, LT-10222 Vilnius, Lithuania
[2] Center for Physical Sciences and Technology, Savanoriu ave. 231, LT-023300 Vilnius, Lithuania
naujokaite.greta@gmail.com

Optical biosensors are an emerging detection and analysis tools for biomedical research, pharmaceuticals and environmental monitoring [1]. The sensing mechanism of micro ring resonator is based on the change of mediums refractive index which surrounds the resonator.

Two most important parameters for biosensors are sensitivity and quality factor. Sensitivity and quality factor - noise to signal ratio, determines the detection limit of the sensor. However, with the increase of sensitivity the quality factor decreases and in order to get the optimal combination of these parameters optimization of resonators is required. One of the most simple and promising resonators is ring resonator.

Thus, in this work, ring resonator structure with effective parameters was modeled and investigated by FDTD method. The evanescent field which is present at the ring resonator surface is influenced by analytes which distributed in surrounding bulk. To see the interaction between light and analytes the transmission spectrum was investigated at the out port of the ring resonator. The spectrum showed that ring resonator supports many resonance modes (Fig. 1. (a)) The position of these resonances are influenced by effective refractive index which depends on the properties of analytes and their distribution. When refractive index changes the resonances shift. The amount of resonance shift that can be monitored is limited by the free spectral range – distance between nearby resonances.

To eliminate this limit ring resonator was decorated with gold nanoparticle. Au nanoparticles create second order Bragg grating modulated by losses. Metal nanoparticles also support localized surface plasmons [2]. In this case ring resonator supports only one resonance (Fig. 1. (b)) which means that there is no detection limit which is present in ring resonator with no Au nanoparticles.

We have concluded that ring resonator decorated with gold nanoparticles have unique and advantageous properties that show great potential for biosensors applications.

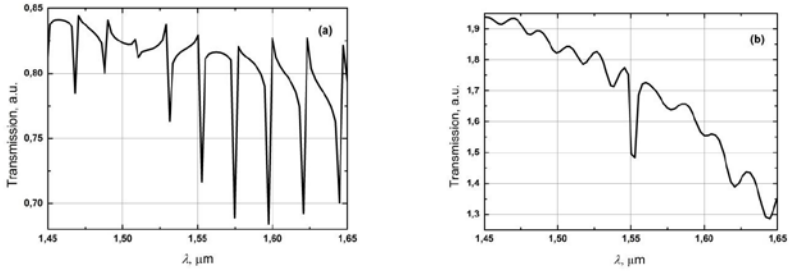

Fig.1. Measured transmission spectrum of (a) ring resonator and (b) ring resonator decorated with Au nanoparticles.

[1] X. Fan, I. M. White, S. I. Shopova, H. Zhu, J. D. Suter, and Y. Sun, Sensitive optical biosensors for unlabeled targets: a review., Anal. Chim. Acta **620**, 8–26(2008).
[2] J. Homola, S. S. Yee, and G. Gauglitz, Surface Plasmon Resonance, Sensors and Actuators **54**, 3–15 (1999).

Lanthanide(Ce , Eu , La) doped –tin dioxide nanoparticles-carbon nanotube composite thin films deposited by MAPLE technique

Niculescu Ana-Maria[1], Claudiu T. Fleaca[2], Marius Dumitru[1], Eugen Vasile[2], IonMorjan[1], Maria Dinescu[1]

[1] National Institute for Lasers, Plasma and Radiation Physics, 409 Atomistilor Str., 77125 Bucharest- Magurele, Romania

[2] University POLITEHNICA of Bucharest, Faculty of Applied Chemistry and Material Science, Department of Oxide Materials and Nanomaterials, No. 1-7 Gh. Polizu Street, 011061 Bucharest, Romania

SnO_2-based nanoparticles were obtained by glycine combustion technique starting from organometallic tetrabutyl-bis(acetyloxi) distanoxane precursor and rare earth nitrates *of* of Ce , Eu , La as dopants sources . The dopant concentration was controlled to obtain a Sn/La atomic ratio of 95/5. The reference powder (undoped SnO_2) and the doped ones were dispersed in aqueous media together MWCNTs at different concentrations with the aid of a Na-CMC (hydrophilic polyelectrolyte) using ultrasonication. Their hydrodynamic size distributions were evaluated by DLS (Dynamic Light Scattering). The water-based mixtures were frozen in liquid nitrogen and deposited using MAPLE (Matrix Assisted Pulsed Laser Evaporation) on silicon substrates. The resulted films were characterized by XRD, AFM, EDAX, DLS. Their properties are discussed in relation with sensors application.

INVESTIGATION OF SURFACE-ENHANCED RAMAN SCATTERING EFFECTS IN DIAMOND LIKE CARBON SILVER NANOCOMPOSITE THIN FILMS

Orestas Ulčinas, Tomas Tamulevičius, Asta Tamulevičienė, Domantas Peckus, Šarūnas Meškinis, Sigitas Tamulevičius

Institute of Materials Science of Kaunas University of Technology, K. Baršausko Str. 59, Kaunas LT-51423, Lithuania, Orestas.Ulcinas@ktu.edu

Diamond like carbon (DLC) films have unique properties such as extremely high hardness, very low friction coefficient, negative electron affinity and optical transparency in the visible and infrared range [1]. Metal doped DLC films possess interesting optical properties due to surface plasmon resonance (SPR) and are promising materials for developing the element base of laser physics, opto- and micro-electronics devices. The SPR feature depends on the size, shape as well as concentration of nanoparticles embedded in DLC host matrix [2]. It is known that Ag nanoparticles can enhanced the Raman scattering signal and the enhancement factor depends on the size and shape of nanoparticles, interparticle distance and their arrangement [3]. The research was aimed on further elucidation of the role of silver nanoparticles in enhancing Raman spectra of DLC as well on influence of nanoparticles on the growth mode of nanocomposites.

In the present research, two types of films were formed: DLC based silver nanocomposites (DLC:Ag) and DLC:SiO_x films with different thickness on 20 nm thickness Ag layer (as coated and annealed). DLC:Ag films were synthesized employing unbalanced reactive magnetron sputtering of silver target with Ar ions in acetylene atmosphere. By changing the gas ratio (C_2H_2/Ar: 10-30%) and bias voltage, films with Ag concentration from 2.8 at.% to 14.8 at.% were deposited. DLC:SiO_x films of 11-190 nm thickness were deposited employing closed drift ion beam source. As a precursor hexamethyldisiloxane with hydrogen carrier gas was used.

The structure of the films was determined employing Raman scattering spectrometer InVia (Renishaw), 532 nm wavelength laser. Surface of the films was analyzed with SEM Quanta 200 FEG (FEI) and AFM Nanowizard 3 (JPK) working in AC mode. Ultrafast processes were performed employing transient absorption spectrometer HARPIA (Light Conversion).

Such kind of experiments enabled us to differentiate between the role of nanoparticles in production of sp^3 bonded carbon and sp^2 clusters as well to study role of silver in surface enhanced Raman spectroscopy measurements (Fig. 1).

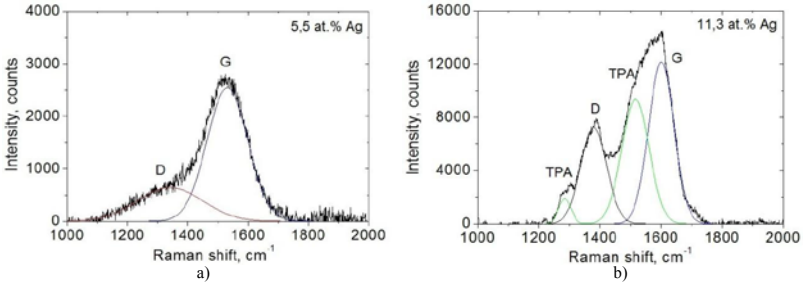

Fig. 1. Raman spectra of DLC:Ag nanocomposite films with different Ag concentration: a) 5.5 at.% and b) 11.3 at.%

Due to incorporation of Ag nanoparticles in DLC matrix, these nanocomposites show plasmonic response in visible wavelength range. Increase of Ag concentration gives more pronounced SPR peak. Raman scattering spectroscopy results show that DLC:Ag nanocomposite films with larger Ag concentration (> 7 at.%) could be used as plasmonic substrates. Ag layer induces biggest enhancement for DLC:SiO_x films of 190 nm thickness. The annealing of Ag layer resulted in the highest enhancement for 22 nm thickness DLC:SiO_x film. Particles area analysis of the DLC:Ag SEM micrographs showed that the silver interparticle distance have a significant impact on Raman enhancement. Transient absorption spectra dynamics revealed the existence of two transient absorption relaxation components: negative and positive. Negative transient absorption signal decays during ~1 ps, while positive signal can have two relaxation components which decay ~1 and ~100 ps. Evidently, positive transient absorption signal can show two relaxation processes: fast because of electron-photon interaction and slower phonon-phonon relaxation processes.

This research was funded by a grant (no. MIP-070/2013) from the Research Council of Lithuania.

[1] L.-Y. Chen et al., Applied Physics Letters, 82, 3526-3528 (2003)
[2] I. Yaremchuk et al., Physica Status Solidi A, doi 10.1002/pssa.201330067
[3] K.G. Stamplecoskie et al., The Journal of Physics Chemistry C, 115, 1403-1409 (2011)

Investigation of superfluorescence in high gain femtosecond Non-collinearly phase matched Optical Parametric Amplifier

Ignas Balčiūnas[1], Tomas Stanislauskas[1], Arūnas Varanavičius[1]

[1] Department of Quantum Electronics, University of Vilnius, Lithuania
ignas.balciunas@ff.stud.vu.lt

Optical parametric chirped pulse amplification (OPCPA) [1] is a well established method to produce high-energy, sub-10~fs pulses. This technique allows one to reach a gain of more than 10^6 in single few millimetre long crystal. However, this gain applies not only to injected signal but also to generated parametric fluorescence. Further, amplified parametric fluorescence or superfluorescence (SF) degrades the signal stability and the contrast ratio of compressed pulse, due to transfer of pump energy to the incoherent pedestal. The pulse contrast ratio is the major concern for high-field experiments.

We are using Yb:KGW diode-pumped solid state laser system (Pharos, Light Conversion, Ltd.) which delivers 1 mJ, 200 fs pulses at 1030 nm. Small part of the pulse energy ~1 μJ are focused into a 4 mm sapphire plate to generate a white light continuum which is used as seed for non-colinnear parametric amplifier. The main portion of the pulse was frequency doubled in a 0.7 mm thick BBO crystal and then used to pump the two stages of the NOPA.

In this work we experimentally investigated properties of SF generated in BBO crystal in the first stage of the NOPA. The signal beam was focused with a spherical mirror (R = 1 m) onto a crystal to a spot size of 200 μm. Direction of the signal beam was adjusted to match the apex angle of the amplified parametric fluorescence cone emitted by the BBO crystal when illuminated by a pump pulse to achieve the best phase matching possible. SF amplitude was registered at the output of the system with pump intensities ranging from 80 *G*W/cm^2 to 190 *G*W/cm^2 (Fig. 2).

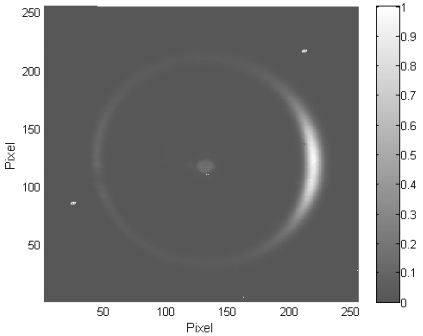

Fig. 1. SF cone imaged on the CCD camera.

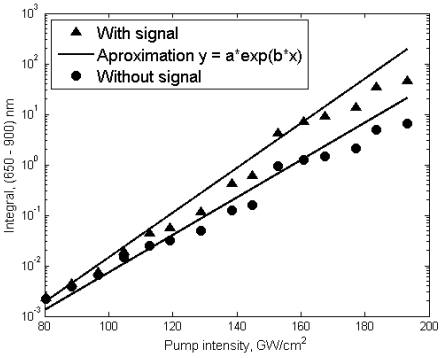

Fig. 2. SF measured with a spectrometer at the top of the cone.

[1] A. Dubietis and G. Jonušauskas and A. Piskarskas, Powerful femtosecond pulse generation by chirped and stretched pulse parametric amplification in BBO crystal, Optics Communications, **88**(4-6), 437-440 (1992), ISSN 00304018, doi:10.1016/0030-4018(92)90070-8.

GENERATION OF ULTRASHORT PULSES FROM PASSIVELY MODE-LOCKED YB FIBER OSCILLATOR UTILIZING LOW DISPERSION CHIRPED FIBER BRAGG GRATING

Tadas Bartulevičius[1,2*], Saulius Frankinas[1,2], Rokas Danilevičius[1,2], Nerijus Rusteika[1,2]

[1] EKSPLA, Ltd., Vilnius, Lithuania
[2] Department of Laser Technology, Center for Physical Sciences & Technology, Vilnius, Lithuania
tadas.bartulevicius@gmail.com

Fiber lasers are extensively applicable in variety of fields such as medical diagnostics, laser material processing, imaging, spectroscopy and scientific research. High power, high repetition rate ultrashort pulse fiber lasers are usually realized using chirped pulse amplification (CPA) technique [1]. However, it is necessary to choose system parameters correctly to suppress nonlinear effects which are very significant comparing to solid state laser systems and scale rapidly with higher optical intensities causing spectral distorsions and reduced pulse contrast at the system output. Final pulse duration and spectrum could be strongly affected by the seed source output parameters.

Passively mode-locked all-in-fiber oscillators operating at average soliton pulse regime are simple, stable and reliable seed sources for CPA. The pulse duration of such source could be easily controlled choosing Chirped Fiber Bragg Grating (CFBG) with correct dispersion value in the laser resonator [2]. In previous work, we demonstrated CPA system with all-in-fiber seed source which generated 2 ps pulses [1]. This system lacked of pulse contrast at the output without using additional nonlinear phase compensation components. One of the solutions of such system improvement is to generate shorter pulses in fiber oscillator. The purpose of this work was to find the main parameters of CFBGs used in the seed source in order to generate broad spectrum transform-limited sub-picosecond and femtosecond pulses. In this work we experimentally investigated specially designed and manufactured CFBGs with different dispersion values. We introduce the oscillators using 0,25-0,62 ps/nm CFBG which generates 373-931 fs duration pulses. Intensity autocorrelation traces of oscillators utilizing mentioned CFBGs is shown in Fig.1. As well as theoretical simulations of pulse spectrum at different fiber Bragg grating dispersion values at different CFBG reflection bandwidth are presented in this work. Detailed calculations compared with experimental results will be presented at the conference.

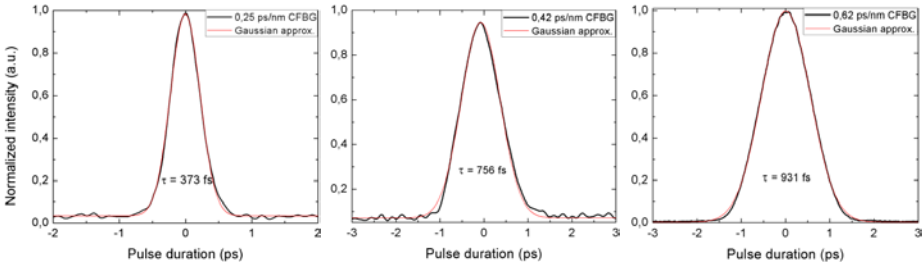

Fig. 1. Experimentally measured intensity autocorrelation traces of oscillators using 0,25-0,62 ps/nm CFBG.

[1] S. Frankinas, R. Danilevičius, N. Rusteika, High Power Femtosecond CPA System With TOD Compensating Chirped Fiber Bragg Grating Stretcher, 16th International Conference Laser Optics 2014.
[2] M. Baumgartl, B. Ortaç, J. Limpert, A. Tünnermann, Impact of dispersion on pulse dynamics in chirped-pulse fiber lasers, Appl Phys B **107**, 263-274 (2012).

TEMPERATURE TUNING CHARACTERISTICS OF THE KTP OPTICAL PARAMETRIC OSCILLATOR PUMPED BY 532 NM RADIATION

Karolis Jurkus, Daniel Žitkovskij, Vygandas Jarutis, Valerijus Smilgevičius

Vilnius University Laser Research Center, Vilnius, Lithuania
jurkusk@gmail.com

In this work we present results of investigation of KTP optical parametric oscillator (OPO) pumped by second harmonic of Nd:YAG laser. In [1] it was shown that the doubly resonant OPO output energy drastically depends on the cavity length and has periodically changing maxima/minima. This phenomenon was explained as interaction of signal and idler waves in a doubly resonant OPO cavity. The same situation arises in all doubly resonant OPOs. The main attention in our research was devoted to temperature stability of the OPO output radiation because wavelengths of signal and idler waves change by tuning OPO crystal temperature which alters OPO resonator quality.

We investigate KTP OPO pumped by second harmonic of commercial microchip laser STA-01 (UAB "STANDA): wavelength – 1064 nm, pulse energy – 200 μJ, pulse duration 3,2 ns, repetition rate – 1 kHz. OPO resonator consisted of two flat input (HR 1064 nm, HT 532 nm) and output (R=44%@1064 nm, R=18%@532 nm) mirrors. Resonator length was 19 mm. As the nonlinear crystal, 8 mm long KTP crystal was used. OPO generation threshold was 24 μJ and maximum energy for 70 μJ pump was 22 μJ which signifies 31% conversion efficiency.

It was shown that at certain temperatures, well separated spectral clusters arise. Cluster spacing was calculated to be 0.83 nm. In Fig.1 the OPO output energy dependence on the KTP crystal temperature, along with spectra, is presented. The experimental results are in good agreement with theoretical calculations.

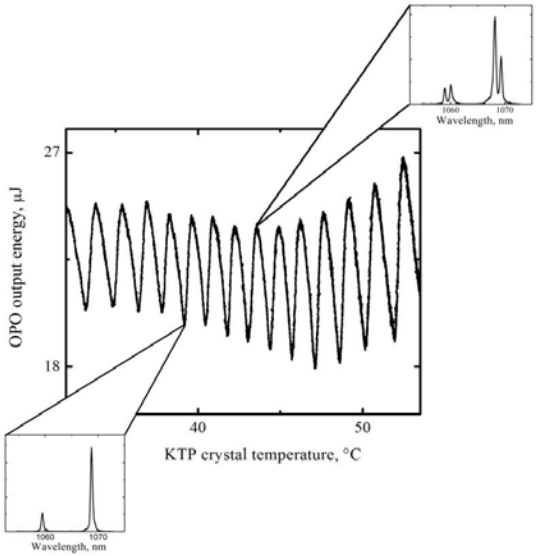

Fig. 1. OPO output energy dependence on temperature. Insets show spectra of output (signal and idler) beams at energy maxima and minima.

[1] G. Aristholm, E.Lippert, G.Rustad and K.Stenersen, "Effect of resonator length on a doubly resonant optical parametric oscillator pumped by a multilongitudinal-mode beam", Optics Letters **25**, 1654-1656 (2000).

Control of thermal effects in high harmonics generator of solid-state femtosecond laser

Simas Sobutas[1,2], Eglė Gabrytė[1,2], Romualdas Danielius[2]

[1]Laser Research Center, Department of Quantum Electronics, Faculty of Physics, Vilnius University, Sauletekio Ave. 10, LT-10223 Vilnius, Lithuania
[2]Light Conversion Ltd., Keramiku 2B, LT-10233 Vilnius, Lithuania
simas.sobutas@ff.stud.vu.lt

While generating high peak intensity ultrashort pulses in the ultraviolet (UV) spectral range linear and nonlinear (two-photon – TPA) absorptions could become significant in transmitting optical components (lenses, beamsplitters, etc.) [1]. TPA also occurs in nonlinear crystals such as beta barium borate ($\beta - BaB_2O_4$, BBO) [2], which are used in conversion of radiation frequency, resulting in decrease of conversion efficiency to UV spectral range radiation. The crystal absorbs some of generated UV radiation where it transforms into heat – causing an increase of crystal temperature and a change of phase matching angle.

The thermal effects prolong the warm-up time of the high harmonics generator (UV radiation). In order to reduce the influence of these effects, it is important to compensate the change of phase matching angle of nonlinear crystal. The crystal tilt angle is alternated using the motorized rotation stage which trajectory is based on the time-dependent function.

To explore and discuss the thermal effects on phase matching angle a system generating high average power femtosecond laser pulses of UV spectral range was designed. A sum of two exponential functions was used to define the temperature change of the crystal when cooling. This allowed the calculations of the crystal cooling constants. The same pair of exponential functions, using cooling constants, was applied to the motorized control of nonlinear crystal angle. The result is the finding of the optimal motion trajectory which in turn compensates the influence of thermal effects and reduces the warm-up time of high harmonics generator.

The method demonstrates a significant reduction in the warm-up time of the fourth (257,5 nm) and the fifth (206 nm) harmonics from 25 s to 5 s and from 30 s to 7 s respectively without experiencing any power loss (see Fig. 1). The findings show that this method can be applied to the high harmonics generator of solid-state femtosecond laser. This laser system could be used in applications, such as ophthalmic surgery, where the speed of the laser-assisted microfabrication of materials is of very high importance.

Though the findings are promising, the method remains open for further development and improvement.

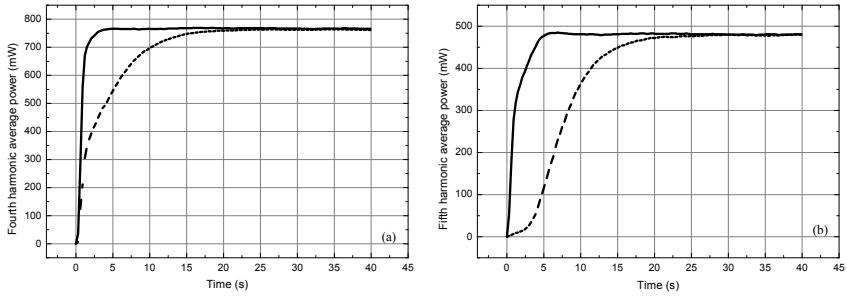

Figure 1. Time dependence of average power of the fourth (a) and the fifth (b) harmonics. Solid lines represent harmonic generation with motorized control of nonlinear crystal tilt angle, while the dashed lines represent harmonic generation excluding the motorized control.

[1] S. A. Slattery, D. Nikogosyan, Two-photon absorption at 211 nm in fused silica, crystalline quartz and some alkali halides, Optics Communications **228**(1-3), 127–131 (2003).
[2] A. Dubietis, G. Tamošauskas, A. Varanavičius, G. Valiulis, Two-photon absorbing properties of ultraviolet phase-matchable crystals at 264 and 211 nm, Applied Optics **39**(15), 2437–2440 (2000).

Simulation of Raman Spectra of Carotenoid Molecules

Jonas R. Umaras[1], Juozas Šulskus[1]

Department of Theoretical Physics, Faculty of Physics, Vilnius University, Saulėtekio al. 9-III, LT-10222 Vilnius, Lithuania

jonas.umaras@ff.stud.vu.lt

Carotenoids are organic molecules which can be found in cells of plants. These molecules are actively involved in photosynthesis acting as light-absorbers which protect photosystems. It can as well counteract the exited singlet oxygen molecule which has detrimental impact on biological systems. Carotenoids are organic pigments which determine colors of living organisms and reflect processes within living cells. The spectroscopic properties of carotenoids are mainly conditioned by polyene chain in the molecules but at the same time they are sensitive to the position of ending structures connected to ends of polyene chain and surrounding environment.

In recent years experimental methods for observing minor deformations in carotenoids' molecules while investigating electronic and vibrational resonance in Raman spectrum were developed. Resonance Raman spectrum enables researchers to distinguish specific modes related to molecule's conformation and structure.

The main objective of this research was to find frequencies of harmonic modes in a known active region of resonance Raman spectrum of β-carotene (Fig. 1), determine significance of anharmonicity for these modes and the change of frequencies in the second excited electronic state of molecule[1].

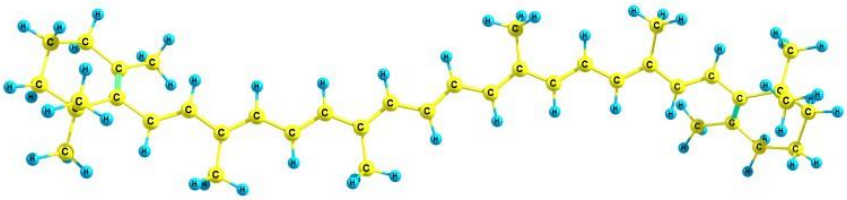

Fig. 1: β-carotene

Gaussian09 [2] and Gamess [3] quantum chemistry packages at Vilnius University "HPC Saulėtekis" supercomputer[4] were used in this work for the simulation and determination of these properties at DFT and TDDFT b3lyp/6-311G(d,p) level along with MacMolPlt [3] and Chemcraft [5] visualization programs for data analysis.

The modes corresponding to C=C and C-C valence oscillations of polyene chain mainly related to resonance Raman spectra during the first active PI-PI* electronic excitation were analyzed. The anharmonicity of particular modes were evaluated by numerical solving of vibrational Schrodinger equation along a particular mode. Evaluation of relative deviation from harmonic approximation showed that anharmonicity of vibrations in the ground electronic state is not significant.

As the harmonic approximation of vibrational spectrum is qualitatively applicable a further research on resonance Raman spectrum of β-carotene is possible in order to find out how rings at the ends of polyene chain and interactions with environment alter frequencies of highest intensities in the spectrum.

[1] Macernis, M.; Sulskus, J.; Malickaja, S.; Robert, B.; Valkunas, L. Resonance Raman Spectra and Electronic Transitions in Carotenoids: A Density Functional Theory Study. J. Phys. Chem. A 2014, 118, 1817−1825;
Macernis, M.; Sulskus, J.; Malickaja, S.; Robert, B.; Valkunas, L. Resonance Raman Spectra of Carotenoid Molecules: Influence of Methyl Substitutions. J. Phys. Chem. A, 2015, 119, 56–66.
[2] http://www.gaussian.com/g_prod/g09.htm
[3] http://www.msg.ameslab.gov/gamess/
[4] http://supercomputing.ff.vu.lt
[5] http://www.chemcraftprog.com/

Calibration of the Hadron Calorimeter of the CERN CMS Detector

Jonas R. Umaras[1], Paulius Juodsnukis[1], Andrius Juodagalvis[2]

[1]Department of Physics, Vilnius University, Vilnius, Lithuania
[2]Institute of Theoretical Physics and Astronomy, Vilnius University, Vilnius, Lithuania
jonas.umaras@ff.stud.vu.lt

In 2012 two particle physics experiments at the Large Hadron Collider (LHC) at the laboratory of European Organization for Nuclear Research (CERN), ATLAS (A Toroidal LHC Apparatus) and CMS (Compact Muon Solenoid), announced a discovery of a new bosonic particle [1, 2]. Later it was confirmed to be the sought Higgs boson, with the properties predicted by the Standard Model [3]. The mass and the couplings of the Higgs boson to other particles had to be measured, and the hadron calorimeter played an important role for this goal. These precise physics measurements would not be possible without an adequately calibrated instrumentation. Currently the LHC experiments are getting ready for the next round of proton-proton collisions at an increased collision energy of 13 TeV ("Run 2"). A strategy for the calibration of the particle-detecting systems is being revised.

The CMS hadron calorimeter, made of brass and scintillator, has a poorer energy resolution than other subsystems of the detector, including the electromagnetic calorimeter. This can be taken into account considering the possibilities of its calibration. The accuracy of the measured hadronic energy could be improved analyzing the results of the physical processes where all available energy is measured by the detector. Some products of proton-proton collisions escape undetected due to the construction of the detector that needs to have holes at the ends along the symmetry axis in order to allow entrance of the colliding particles (the "beam axis"). This creates an ambiguity of the momentum measured along the beam axis. The CMS detector registers all known particles with an exception of neutrinos. Neutrino-less reactions allow accurate measurement of the momentum in the plane that is transverse to the beam axis, since there is no movement in this plane before the protons collide. The simplest case is to have two physical objects that would move in the opposite directions in the transverse plane after their production in a proton collision. Their measured transverse momenta should be equal.

Two physics processes are being considered, namely, the production of two jets and the simultaneous photon and jet production. (An example of a photon and jet event in the CMS detector is shown in Fig. 1.) Momentum balancing was previously used to calibrate the measured jet energy (see e.g. [5]). It can also be employed to derive the calibration coefficients for the hadron calorimeter. The presented discussion focuses on the calibration in rings that are defined as a set of ranges of the radial angle from the beam axis, θ (transformed into a pseudo-rapidity variable η). A ring uniformity around the beam axis is assumed.

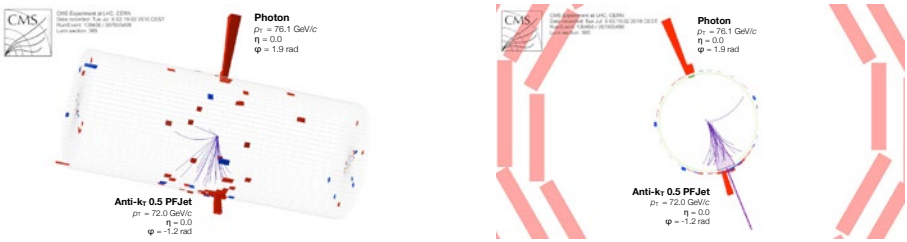

Fig. 1. A photon+jet event from 7 TeV proton-proton collision [4].

[1] ATLAS Collaboration, Observation of a new particle in the search for the Standard Model Higgs boson with the ATLAS detector at the LHC, Physics Letters **B 716**, 1-29 (2012).
[2] CMS Collaboration, Observation of a new boson at a mass of 125 GeV with the CMS experiment at the LHC, Physics Letters **B 716**, 30-61 (2012).
[3] CMS Collaboration, Precise determination of the mass of the Higgs boson and tests of compatibility of its couplings with the standard model predictions using proton collisions at 7 and 8 TeV, arXiv:1412.8662, *submitted to* Eur. Phys. J. C.
[4] A photon+jet event from 7 TeV proton-proton collisions used for gamma+jet balance in CMS PAS JME-10-003, obtained on February 05, 2015 from `https://twiki.cern.ch/twiki/bin/view/CMSPublic/PhysicsResultsJME` .
[5] CMS Collaboration, Jet energy calibration with photon+jet events, CMS-PAS-JME-09-004, 2009.

INVESTIGATION OF RESONANT MODES IN TWO-DIMENSIONAL ARRAY OF SPLIT-RING RESONATORS

Birutė Leiputė[1,2], Dalius Seliuta[2], Gediminas Šlekas[2], Andžej Urbanovič[2], Dovilė Zimkaitė[2], Žilvinas Kancleris[2]

[1]Department of Physics, Vilnius university, Saulėtekio Ave 9-III, LT-10220 Vilnius, Lithuania
[2]Center for Physical Sciences and Technology, A. Goštauto St 11, LT-01108 Vilnius, Lithuania
birute.leipute@ff.stud.vu.lt

This work explores the possibilities of creating new optically tunable metamaterials to fill the so-called terahertz gap. The purpose of the investigation was to experimentally and theoretically examine electromagnetic properties of metamaterial samples in the terahertz regime and find how those features are influenced by applying photoexcitation to GaAs substrates (using 780 nm laser).

The chosen type of the metamaterial for investigation was a two-dimensional array of uniform split-ring resonators consisting of one, two or no gaps, placed on GaAs substrates. Transmission curves (1 GHz - 1600 GHz) measured via terahertz time domaimn spectroscopy were compared with the results gathered by using commercially available modeling software. In addition to that the resonant modes of magnetic and electric origin are discussed and the surface current patterns in resonators are shown. The most promising are the results of high tunability exhibited in transmission spectra by optically exciting the surface of the investigated samples.

Poster session 3

PHOTOELECTRIC PROPERTIES OF GAAS P-N-JUNCTION UNDER ILLUMINATION OF INTENSE LASER RADIATION

Steponas Ašmontas, Jonas Gradauskas, Algirdas Sužiedėlis, Aldis Šilėnas, Viktoras Vaičikauskas, Ovidijus Žalys, Gytis Steikūnas and Angelė Steikūnienė

Center for Physical sciences and Technology, Gostauto 11, LT-01108 Vilnius, Lithuania

ovidijus.zalys@gmail.com

We present the results of an experimental investigation of photoelectric properties of GaAs p-n-junction illuminated with short laser radiation pulses of 1.06 μm wavelength. The p-n- junctions were fabricated by liquid phase epitaxy grown p-type 10 μm-thick layer on n-type substrate. The photoresponse voltage was induced across the junction when it was illuminated with the laser radiation. Typical oscilloscope traces of laser pulse and photoresponse pulse are presented in Fig.1. The observed photoresponse voltage U consisted of two components, $U = U_f + U_{ph}$, where U_f is the fast component caused by the free carriers heating. The polarity of U_f corresponds to that of thermoelectromotive force of hot carriers. The slow component, U_{ph}, has polarity opposite to that of U_f and is caused by electron-hole pair generation. Measurements of the dependence of photoresponse voltage on laser intensity P revealed that the fast component linearly depends on P, whereas U_{ph} is proportional to P^2. This fact indicates that the electron-hole pair generation is caused by two-photon absorption since the laser photon energy is less than the forbidden energy gap of GaAs.

It is worth to note that the influence of carrier heating on formation of photovoltage decreases with reverse bias applied on the p-n-junction. The same situation was observed earlier in narrow-gap semiconductor p-n-junctions under the action of intense pulses of CO_2 laser radiation. [1]

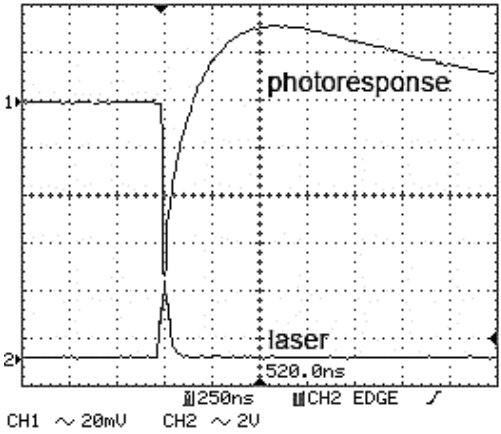

Fig. 1. Oscilloscope traces of laser pulse (bottom) and photoresponse.

[1] J.Gradauskas et. al., Peculiarities of High Power Infrared Detection on Narrow-Gap Semiconductor p-n Jungtions, Acta Physica Polonica A, Vol.119(2), p. 237-240 (2011).

EXPERIMENTAL MODELING OF GEOMETRICAL PARAMETERS OF DEFECTS IN SEMICONDUCTOR LAYERS

Laurynas Andrulionis, Algirdas Mekys

Department of Semiconductor Physics, Vilnius University, Lithuania
l.andrulionis@gmail.com

The main task for this experiment was to investigate how quantity and orientation of large-scale structural defects influence measurements of Hall and magnetoresistance (MR) mobilities.

With reference to earlier done experiments [1–4], an attempt was made to experimentally model similar characteristics of samples and to measure them. Large-scale defects can form naturally during growth process or made artificially. It is possible to face distortions of measured parameters when trying to evaluate charge carry parameter – mobility. In this experiment lead telluride (PbTe) was chosen due to its high mobility value. Thin layers were etched in certain patterns which distorted potencial profile. Therefore, measured characteristics (resistance, Hall voltage) were affected. Samples were made using thermal vacuum evaporation method. Ohmic contacts were made out of lead and bismuth mix. AV characteristics were measured to check whether ohmic contacts were good. During experiment, PbTe samples were placed in cryostat and Hall and MR measurements were taken. After that a single defect was etched in the sample by needle under a microscope and measurements were repeated again. Experiment was repeated several times to have more statistical data.

Figure 1 shows substantial difference visible between Hall and MR signals. Large-scale defects influence Hall signals much more than MR signals. It could be explained that to make Hall voltage signal electrons are needed to concentrate in their respective contacts. Defects create obstacles, thus fewer electrons reach contacts. However, to create MR signal, a few electrons are needed because relative change of resistance in magnetic field is being registered.

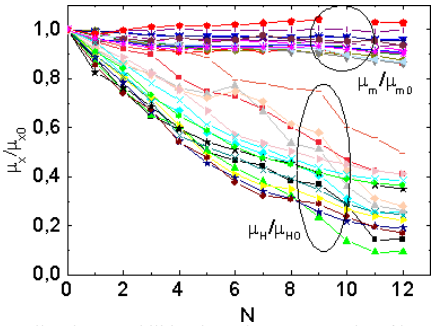

Fig. 1. Relative Hall and MR mobilities dependence on quantity of large-scale defects

[1] R. Vasiliauskas, a Mekys, P. Malinovskis, S. Juillaguet, M. Syväjärvi, J. Storasta, and R. Yakimova, "Impact of extended defects on Hall and magnetoresistivity effects in cubic silicon carbide," *J. Phys. D. Appl. Phys.*, vol. 45, p. 225102, 2012.

[2] R. Vasiliauskas, A. Mekys, P. Malinovskis, M. Syväjärvi, J. Storasta, and R. Yakimova, "Influence of twin boundary orientation on magnetoresistivity effect in free standing 3C-SiC," *Mater. Lett.*, vol. 74, pp. 203–205, 2012.

[3] P. Malinovskis, A. Mekys, E. Dvinelis, V. Rumbauskas, J. Storasta, and R. Vasiliauskas, "Magnetovaržinio efekto pasireiškimas 3C-SiC defektuotuose kristaluose," in *39- oji Lietuvos Nacionalinė Fizikos Konferencija*, 2011.

[4] J. V. Vaitkus, A. Mekys, and J. Storasta, "Analysis of microinhomogeneity of irradiated Si by Hall and magnetoresistance effects," 2007.

SIMULATION OF CHARGE CARRIER TRAPPING BY DEFECTS LOCATED IN SPHERICAL CLUSTERS

Nastya Arslanova, Elena Levchuk, Leonid Makarenko

Department of Applied Mathematics and Computer Science, Belarusian State University, Minsk, Belarus
anastacia.arslanova@gmail.com

It is expected the formation of defects when high-energy Si knock-on atoms are created and cluster effects are likely to be quite important for radiation damage of silicon devices. However, the understanding of electrical characteristics of such defects in materials irradiated with heavy particles is insufficient as compared to the knowledge on the role of isolated point defects.

Two characteristic features of clustered defects are well established by DLTS method. First, it is temperature dependence of DLTS peak amplitude $S_{\max}(T)$ and closely related to this feature the inequivalent heights of divacancy peaks [1 – 3]. And second, the stretched kinetics for filling of clustered traps [3, 4]. This work focuses on studies of the second effect. Numerical simulation of trapping kinetics by clustered single charged traps has been performed. A mathematical model for this simulation can be formulated as follows:

$$\frac{\partial n^*}{\partial t} = -D_n^* n^* \left(1 - n^* - n_T^*\right) + D_n^* \frac{\partial n^*}{\partial r}\frac{\partial u}{\partial r} + D_n^* \frac{\partial^2 n^*}{\partial r^2} + D_n^* \frac{2}{r}\frac{\partial n^*}{\partial r} + A n_T^* - n^* \left(N_T^* - n_T^*\right), \quad r > 0,\ t > 0, \tag{1}$$

$$\frac{\partial^2 u}{\partial r^2} + \frac{2}{r}\frac{\partial u}{\partial r} = -\left(1 - n^* - n_T^*\right), \quad r > 0,\ t > 0, \tag{2}$$

$$\frac{\partial n_T^*}{\partial t} = n^* \left(N_T^* - n_T^*\right) - A n_T^*, \quad r > 0,\ t > 0, \tag{3}$$

$$n^*\big|_{t=0} = 1, \quad n_T^*\big|_{t=0} = 0, \quad r > 0, \tag{4}$$

$$\left.\frac{\partial u}{\partial r}\right|_{r=0} = 0, \quad u\big|_{r\to\infty} = 0, \quad t > 0, \tag{5}$$

$$\left.\frac{\partial n^*}{\partial r}\right|_{r=0} = 0, \quad n^*\big|_{r\to\infty} = 0, \quad t > 0, \tag{6}$$

where n^* is normalized concentration of charge carriers, u is normalized electrical potential, n_T^* is normalized concentration of the traps filled with electrons, A is normalized emission rate, D_n^* is normalized coefficient of electron diffusion, N_T^* is the trap distribution in the cluster

$$N_T^*(r) = \frac{M_T}{R_0^3 \pi^{3/2} N_D} \exp\left(-\frac{r^2}{R_0^2}\right), \tag{7}$$

where M_T is the total number of defects in the cluster, R_0 is the characteristic radius of the cluster, r is the distance from the cluster center. Scaling parameters are: Debye length L_D for r and R_0, $\tau_0 = \frac{1}{C_n N_D}$ for t, N_D (donor's concentration) for all concentrations, $\varphi_T = \frac{kT}{e}$ for potential.

The simulations have been performed using the finite difference method. It has been shown that explicit time integration scheme is unstable when the trap concentration is high. A simplified model has been suggested taking into account the fact that Maxwellian relaxation time can be very small in several cases.

Our simulation results show that the stretched kinetics is arisen as a result of the barrier distribution for traps located at different distances from the cluster center. Numerical relations have been obtained between the R_0 and M_T values and parameters of this distribution. Results of our model are compared to those ones for models suggested in [3] and [4].

[1] I.V. Antonova et al, Phys. Tekhn. Poluprovodn. **22**, 998 (1988).
[2] M. Kuhnke. ROSE/TN/2003-01.
[3] E. V. Monakhov et al, Phys. Rev. **B 65**, 245201 (2002).
[4] R. M. Fleming el al, J. Appl. Phys., **102**, 043711 (2007).

STRUCTURAL, OPTICAL AND ELECTRICAL CHARACTERIZATION OF InGaN LED ON SPSL BUFFER GROWN BY PULSED MOCVD

Kazimieras Badokas[1,2], Tadas Malinauskas[2]

[1] Faculty of Physics, Vilnius University, Saulėtekio av. 9, Bld. III, LT-10222 Vilnius, Lithuania
[2] Institute of Applied Research, Vilnius University, Saulėtekio av. 10, LT-10223 Vilnius, Lithuania
badokas.k@gmail.com

In recent times, nitride-based optoelectronic devices have been experiencing fast technological improvements. Blue light emitting diodes frequently use an active layer made of InGaN/GaN multiple quantum wells (MQW) [1]. However, InGaN/GaN short period superlattice structures (SPSL) have been found to further improve quality and performance of such LEDs.

The complete LED structure (Fig. 1) was grown using metalorganic chemical vapor deposition (MOCVD) technology in a close-coupled 3x2" showerhead reactor (AIXTRON). The pulsed growth regime was applied to grow quantum well in order to enhance diffusion of atoms.

Structural, optical and electrical characterization was performed using X-ray diffraction, photoluminescence and electroluminescence techniques. To study thickness and chemical composition of QWs XRD measurements were performed (Fig. 2). For PL measurements continuous wave laser (405 nm) was used as excitation source. Internal quantum efficiency (IQE) was calculated as a ratio of PL intensity at low temperature (8K) and room temperature (300K) as shown in Fig. 3. The lowest possible excitation intensity was used [2]. The external efficiency and its droop were characterized by measuring electroluminescence intensity at various injection currents (Fig. 4).

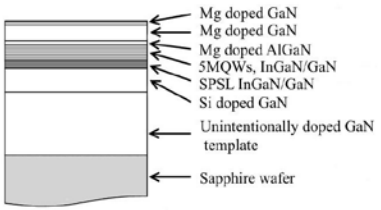

Fig. 1. Structure of LED.

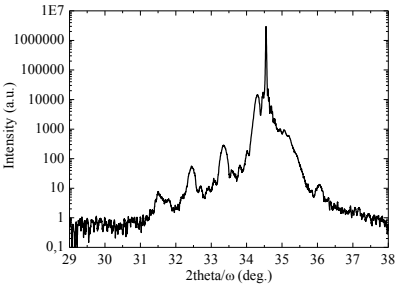

Fig. 2. XRD diffraction (0002) 2theta/ω scan used for structural characterization.

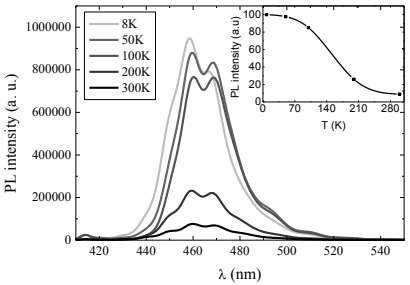

Fig. 3. Photoluminescence signal dependence on temperature used for estimation of IQE.

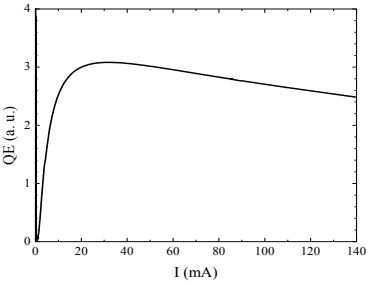

Fig. 4. Efficiency of electroluminescence dependence on injection current.

[1] Jia C. et al., Performance improvement of GaN-based LEDs with step stage InGaN/GaN strain relief layers in GaN-based blue LEDs, Opt. Express **21,** 8444-8449 (2013).
[2] Y.-L. Li, Y.-R. Huang, Y.-H. Lai, Efficiency droop behaviors of InGaN/GaN multiple-quantum well light-emitting diodes with varying quantum well thickness, Applied Physics Letters **91**, 181113 (2007).

RADIATIVE AND NONRADIATIVE RECOMBINATION OF PYRROLO[2,3-D]PYRIMIDINE DERIVATIVES

Tadas Bučiūnas[1], Regimantas Komskis[1], Lina Skardžiūtė[1], Saulius Juršėnas[1]

[1] Institute of Applied Research, Vilnius University, Saulėtekio al. 9-III, LT-10222 Vilnius, Lithuania
tadas.buciunas@gmail.com

In the recent years the technologies of organic semiconductors have drawn much scientific attention for their great variety of compounds demonstrating valuable fluorescence and phosphorescence abilities. The industry of the organic optoelectronic devices, such as field transistors, OLED's and solar cells, is based on molecular properties of the organic compounds. A novel research on thermally activated delayed fluorescence mechanism granted a record efficiency of a blue light OLED, which was achieved by varying the positions of the singlet and triplet states. Thus, it is of great interest to understand and, eventually, control the singlet and triplet energy states by supplementing different substitutions of compounds and its surroundings.

In this work the pyrrolo-pyrimidine derivatives with tert butoxycarbonyl (**1**) and methoxymehane (**2**) substitutions were investigated. After a detailed analysis of the emission spectra dynamics in time, three emission channels were pointed out. Initially, the fluorescence is observed, which is thought to be prevailed by the emission of the charge transfer state. Regarding the **1** compound, the emission from singlet state peaks at 390 nm and shifts to 420 nm, lasting for about 100 ns. As for the **2** compound the fluorescence is located at 415 nm and also shifts to 450 nm, while continuing for about 120 ns. Afterwards, the slightly redshifted (due to reabsorption) delayed emission is registered from 120 ns to 440 µs. For both compounds the phosphorescence spectra express vibronic structure lasting several seconds. The maxima of **1** and **2** compounds are positioned at 540 nm with 1% mass ratio of compound to the host matrix and 580 nm with 5% mass ratio. The bathochromic effect of the fluorescence and phosphorescence in the samples with higher concentration is caused by the enhanced interactions between the molecules.

The emission decay time characteristics of the pyrrolo-pyrimidine derivatives with different substitutes at pyrrolo–nitrogen position demonstrated one-exponential molecular fluorescence decay. Meanwhile, the non-linear delayed fluorescence decay time for both compounds implies to the triplet-triplet annihilation (TTA) [1] process. The TTA process is known to be highly dependent on concentration, however, the pyrrolo-pyrimidine derivatives exhibited no such dependency. Moreover, the **1** compound demonstrated more expressed phosphorescence and less rapid TTA rate then the **2** compound. The most efficient emission from triplet states was registered in the samples with 1% mass ratio.

Considering the results achieved, the photoluminescence emission is influenced only by the singlet energy states and polarity of the substitutes. Nonetheless, the surroundings of a compound have a minor effect on the triplet energy states.

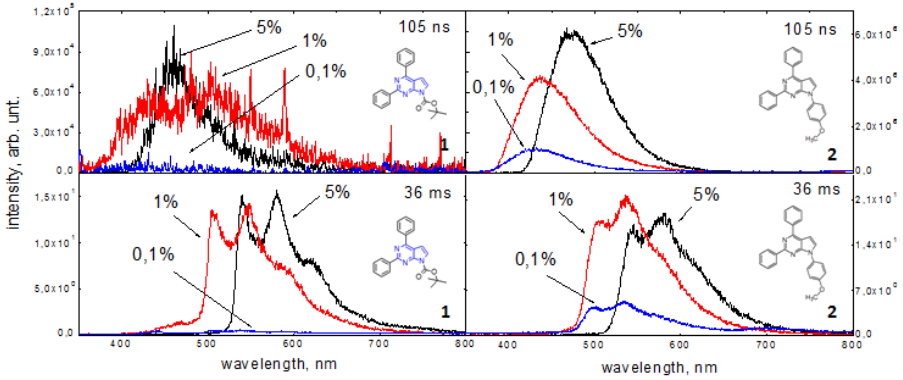

Fig. 1. Emission spectra of Pyrrolo-pyrimidine with methoxymehane and tert butoxycarbonyl derivatives.

[1] H. Sternlicht, G. C. Nieman, G. W. Robinson, *Triplet—Triplet Annihilation and Delayed Fluorescence in Molecular Aggregates,* J. Chem. Phys. **38**, 1326 (1963).

Graphene nanoribbon

Paweł Bugajny[1]

[1] Institute of Physics, Wroclaw University of Technology, Poland

pawel.bugajny@onet.eu

Graphene, a two dimensional crystal made of carbon atoms, has driven a lot of research in condensed matter, for its mechanical, electrical and topological properties. However, its discovery was only the beginning of a new and exciting adventure in the world of two dimensional crystals, where many other systems are being discovered. With them, novel and exotic properties are no longer material science fiction.

In this work we investigate electrical properties of graphene nanoribon using Hubbard model and the Kane-Mele spin-orbit coupling[1]. I show the transition from two-dimensional semimetallic state to a quantum spin Hall insulator in graphne (fig. 1). Topological insulators are special electronics systems which show insulating bulk properties, but protected metallic edge properties.

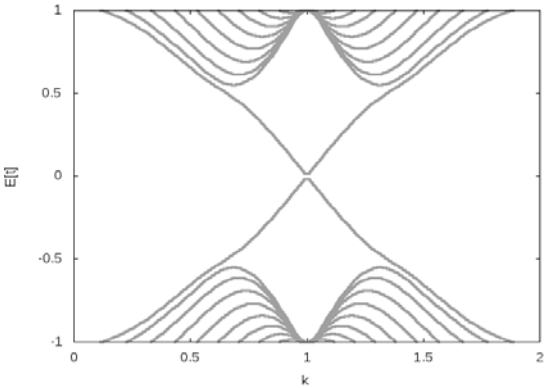

Fig. 1. One-dimensional energy bands for a nanoribbon of graphene. The bands crossing the gap are spin filtered edge states[1].

[1] C. L. Kane and E. J. Mele, Quantum Spin Hall Effect in Graphene, PRL **95**, 226801 (2005).

INVESTIGATION OF THE SURFACE ELECTRICAL POTENTIAL DISTRIBUTION IN PHOTOVOLTAIC ELEMENTS BY SCANNING PROBE MICROSCOPY

Tomas Daugalas[1,2*], Virginijus Bukauskas[2], Aldis Šilėnas[2], Arūnas Šetkus[2]

[1] Faculty of Physics, Vilnius University, Lithuania
[2] Center for Physical Sciences and Technology, Lithuania
Tomas.daugalas@ff.stud.vu.lt

Few last decades electronic components, such transistors, diodes and even components of solar cells, are being scaled down to nanometer dimensions, due to the cost of materials and possible use of new previously unknown physical phenomena such memory resistance or memristance [1]. These actions require a subtle technique in order to measure electrical parameters of these elements with the least possible effect on the component. A growing use of scanning probe microscopy (SPM) based techniques enables new ways to build and investigate nanoscaled electronic devices [2]. Despite of the wide use of SPM in nanoscale surface characterization, the interpretation of the electrical signal and extraction of common electrical parameters of the device remains challenging. SPM usually measures electrical signal at the sample surface (up to few nanometers) but not the bulk.

In our work we used several SPM electrical characterization modes to measure electrical characteristics of the freshly cleaved multilayer $Al_XGa_{1-X}As$ photovoltaic element in room temperature in air. The results were compared with a simple theoretical model. This comparison showed a mismatch between the experimental values and the theoretical ones (Fig. 1). The mismatch was explained in terms of the surface effects, which cause energy band bending at the surface.

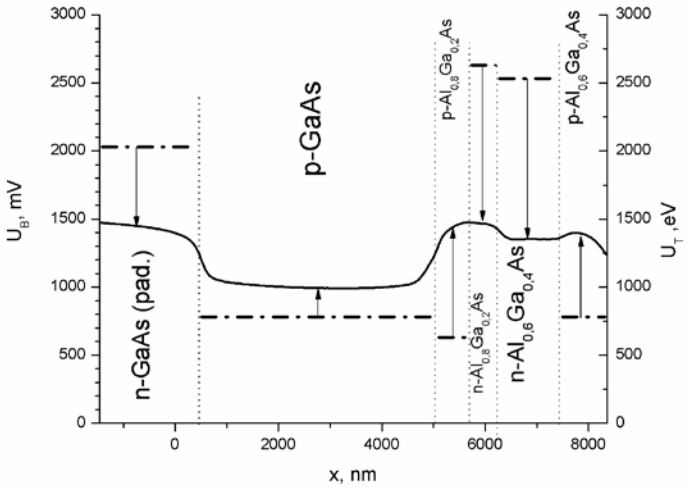

Fig. 1. The cross section of the $Al_XGa_{1-X}As$ solar cell surface potential signal: experimental (solid line) and theoretical values (dashed and dotted lines).

Acknowledgement

The work was carried out within the project VP1-3.1-ŠMM-08-K-01-009 that is partly supported by the National Programme "An improvement of the skills of researchers" launched by the Lithuanian Ministry of Education and Science.

[1] D. B. Strukov, G. S. Snider, D. R. Stewart, R. S. Williams, The missing memristor found, Nature. Letters, 453, 80–83 (2008).
[2] G. Benstetter, R. Biberger, D. Liu, A review of advanced scanning probe microscope analysis of functional films and semiconductor devices, Thin Solid Films, **517**, 5100-5105 (2009).

INTERBAND OPTICAL TRANSITIONS OF THE MONOCRYSTALLINE ZINC

Adomas Eikevičius, Saulius Tumėnas

Semiconductor optics laboratory, Center for Physical Sciences and Technology, Vilnius, Lithuania
a.eikevicius@gmail.com

The optical investigations of zinc were started in 1950s [1] and were, in principle, directed to confirm the Drude theory – predicted IR response of simple metals. When using pseudo-potential method the band structure of the Zn have been calculated [2], was made an attempt to modeling the optical response (optical conductivity), but good agreement with experimental date was not reached. In this work we present spectroscopic ellipsometry (SE) study and analysis of interband optical transitions of monocrystalline zinc.

The main experimental problem is that a determination of both the ordinary and extraordinary components of the dielectric function tensor in uniaxial metals requires measurements from several crystallographic planes. Refractive index of zinc in the VIS spectral range is very high, and Zn is also very active for cohesion with oxygen. Due this reasons measurements of optical response of Zn is quite complicated. By a cleavage can be easily disclosed clean (001) surface, whereas preparation of the (110) surface requires more attention. We used combined preparation technology involving mechanical polishing and chemical etching, and for final step Ar^+ ion etching in UHV chamber. The optical response of Zn was measured by the generalized spectroscopic ellipsometry technique [3], using two ellipsometers (both J. A. Woollam Co, Inc.), a dual rotating compensator RC2 (0.73 – 6 eV) and rotating compensator Fourier transform ellipsometer IRSE (2000 – 5000 cm^{-1}). Ellipsometric data were recorded in the 0.25 – 6 eV spectral range, in the steps of 1 nm at various incidence ϑ and azimuthal φ angles in the intervals of 45 – 80º and 0 – 90º, respectively. At each incidence and azimuthal angle, the experimental ellipsometric parameters Ψ and Δ were simultaneously recorded.

The optical response of Zn in the IR spectral range is dominated by the intraband, Drude-type, optical transitions, whereas in VIS spectral range occur the interband transitions across the pseudogaps, which open at intersections of the Fermi surface with 002 and 101 families of Bragg planes. Interband optical transitions across pseudogaps depends significantly on the polarization of the probing light beam. This can be clearly observe in ε_2 spectrum (Figure 1), which was deduced from analysis of SE data employing semi-infinite uniaxial substrate model. Depending on the polarization of light there are two or one absorption peaks in the ε_2 spectrum. For light polarization perpendicular to an optical, C_6, axis, the interband optical transitions occur only across Δ_{101} pseudogaps. For light polarization parallel to an optical axis, optical transition occur both across the Δ_{101} and Δ_{002} pseudogaps. Optical response of monocrystaline zinc was described using nearly free electron approximation (NFE) and two band model (two band model of NFE spectrum presented in Fig. 1 inset). In the IR spectral range optical conductivity was described using Drude theory (two variable parameters – relaxation time and static conductivity), whereas in the VIS region by the interband optical transitions of the valence electrons (four variable parameters – Δ_{101}, Δ_{002} and broadening parameters for each pseudogaps). The determined width of the pseudogaps values are Δ_{101}=1.55 eV and Δ_{002}=0.9 eV.

The calculation of density of the states allowed us for a determination of Fermi level (ε_F = 9.12 eV) and Sommerfeld parameter (γ = 0.61 mJ K^{-2} mol^{-1}), which is in good agreement with the experimental values [4].

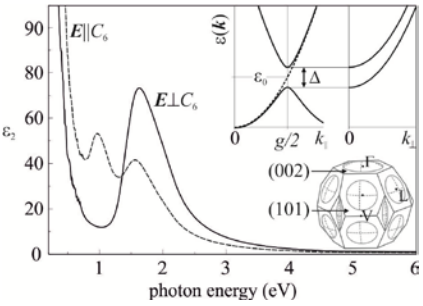

Figure 1. Ordinary (solid) and extraordinary (dashed) imaginary part of dielectric function tensor of Zn, inset – two band model of NFE spectrum and second Brillouin zone.

[1] J. N. Hodgson, The Infra-red Properties of Some Metallic Films, *Proc. Phys. Soc. B* 68, 593 (1955)

[2] W. A. Harrison, Band Structure and Fermi Surface of Zinc, *Phys. Rev.* 126, 497 (1962)

[3] R. M. A. Azzam, N. M. Bashara, *Ellipsometry and Polarized Light* (Amsterdam: North-Holland, 1999)

[4] U. Mizutani, Low Temperature Specific Heats of Pure. Zinc, *Jpn. J. Appl. Phys.* 10, 367 (1971)

SOI MOSFETS AS A WAY TO INCREASE THE OPERATING TEMPERATURE

Fursau Dzmitry

Departament of micro- and nanoelectronics, Belarusian State University of Informatics and Radioelectronics, Republic of Belarus
raven610@yandex.ru

Semiconductor silicon is still the basic material of solid-state electronics for over 50 years. Experts predict that it will keep its leadership in the next 40 years in microelectronics, power electronics and such new high-growth areas such as telecommunication electronics, solar energy, micromechanics and others. Problems with heating in the high silicon integrated circuits (IC's) with increasing a clock frequency in the GHz region have led to the consideration of the technology of silicon-on-insulator (SOI) as the main alternative to ordinary silicon technology. In recent years, the United States, Japan, France and some other far abroad countries carried out a focused intensive scientific and technical search in the development of high-tech manufacturing multifunctional systems based on SOI structures. SOI technology of the world's leading companies (IBM, AMD) selected a general direction of development of silicon microelectronics, which provides the greatest benefit while creating ultrafast transistors.

Carried out researches of the properties of the SOI MOSFETs allow to study the influence of high temperature on the electrical characteristics of transistors, such as the drain current, the drain-source resistance, the threshold voltage and the cutoff voltage, slope, the active component of the output conductance, and input, transfer and output capacities.

As a result of the project implementation, the next objectives are achieved:

- there have been studied the different configurations of the MOSFETs on SOI structures, their properties, advantages and disadvantages;

- described methods and measurement circuit characteristics of transistors, as well as methods of processing the results;

- carried out experimental measurement of characteristics of transistors using a specially assembled measuring stand, the obtained dependences of the graphs.

Following conclusions were made: in the field of submicron dimensions due to complete dielectric isolation, SOI transistors have several advantages over their analogues on the bulk silicon - lower power consumption, high breakdown voltages high performance. In the nanometer range the attractiveness of the SOI is due to, especially the possibility of solving a number of problems peculiar to short-channel transistors, as well as the ability to create new devices working on quantum size effects.

SELECTED MAGNETIC PROPERTIES OF NANOPARTICLES FOR EXAMPLE FERRITIN

Elżbieta B. Gotfryd

Cracow University of Technology,Department of Physics, Mathematics and Computer Science, Poland

elzbietagotfryd@gmail.com

The aim of presentation is to show selected magnetic properties of nanoparticles and to demostrate results of some measuments, which were taken in Department of Magnetic Research in Institute of Nuclear Physics Polish Academy of Science. The measurements were performed for horse-spleen ferritin (HoSF) by using MSMP SQUID magnetometer.

HoSF is protein with very interesting properties such as superparamagnetism [1], so since `40 it is subject of many scientific research in fields like nanotechnology, molecular biology or chemistry. It is responsible for storage and transportation of iron in body. Besides small particles are more economical: they need less energy to overcome the crystal-field anisotropy and lower thermal energy to reverse spin [2].

Due to its two-phase iron core (highly crystalline core and disordered surface layer), it produces spin frustration, which destabilizes simple collinear model of Stoner-Wohlfarth [3]. In consequence nanoparticles (ferritin also) exhibit lack of saturation. The hysteresis loops are very narrow and usually above 3 T become closed.

Interest in magnetic properties of ferritin is connected with possibility to use it in resonsans tunelling.

The presentation will show results of AC and DC susceptibility as well as output of Dynamic Light Scattering, which determine the size of particles, because for nanoparticles properties change depending on their size.

That data allows to state such values as spin relaxation time or blocking temperature in which magnetization vector is blocked in energy minimum [2].

[

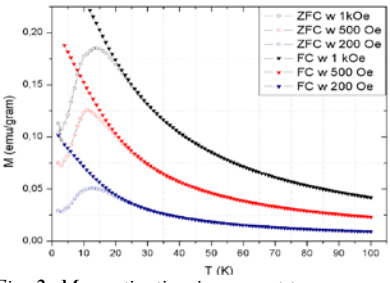

Fig. 2: Magnetization in respect to temperature for different magnetic fields.

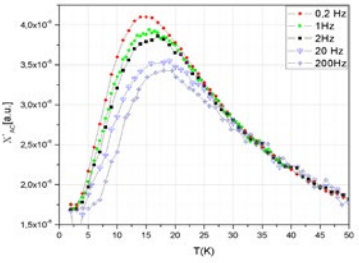

Fig 1: AC susceptibility (X`) in respect to temperature for different frequencies.

[1] S.H. Kilcoyne, R. Cywinski, Ferritin: a model superparamagnet, *Journal of Magnetism and Magnetic Materials, 140-144 (2009)*
[2]G.C. Papaefthymiou, *Nanoparticle magnetism, Nano Today (2009)*
[3] U. Vodkoboynik, *Anomlous field dependance of blocking temperature of natural horse-spleen ferritin*,Acta Phys, ,S-43,. Pol. A , (1997)

Optical properties of molybdenum ditelluride ($MoTe_2$)

Magdalena Grzeszczyk[1], Katarzyna Gołasa[1], Karol Nogajewski[2], Marek Potemski[2] and Adam Babiński[1]

[1]Faculty of Physics, University of Warsaw, Pasteura 5, 02-093 Warsaw, Poland
[2]LNCMI, CNRS-UJF-UPS-INSA,25 rue des Martyrs, 38042 Grenoble, France
mgrzeszczyk@student.uw.edu.pl

Molybdenum ditelluride ($MoTe_2$) belongs to a large group of layered transition metal dichalcogenides (LTMDs). Such materials exhibit unique physical properties that results from the transitaion from bulk to two-dimensional materials, which makes them interesting research subjects. Like other LTMDs, $MoTe_2$ is an inorganic compoundwith hexagonal crystalline structure, with a weak interlayer van der Waals bonding and strong intralayer ionic–covalent bonding. A single layer of this material consists of one plane of molybdenum atoms sandwiched between two planes of telluride atoms with trigonal prismatic coordination, and is a direct-gap semiconductor with a band gap of around 1.1 eV, while bulk material is a semiconductor with an indirect band gap of about 1.0 eV [1].

In this communication, we report our research on the optical properties of MoTe2 crystals, thinned down by exfoliation with a high–quality backgrinding tape and transferred onto a Si/SiO_2 substrate with the aid of an all–dry, non–deterministic, polydimethylsiloxan-based stamping technique [2]. We found such an approach to be especially well suited for cleaving LTMDs, which as compared to graphite are much more brittle, and thus turning them into a form of thin flakes with an area that is sufficient to be probed with a laser beam, represents a challenging task. The optical properties of our sample were studied by micro–Raman spectroscopy

The Raman scattering measurements have been carried out in two excitation modes using wavelengths of λ = 632.8 nm and λ = 532.07 nm as a function of layer number of $MoTe_2$ (Fig. 1). Due to the first–order Raman scattering processes a few peaks, including the in–plane E^1_{2g} mode ($\sim$234 cm^{-1}) and the out–of–plane A_{1g} mode ($\sim$ 170 cm^{-1}) for monolayer and few layer $MoTe_2$ can be seen. It can be noted that both E^1_{2g} and A_{1g} modes are sensitive to the MoTe2 layer thickness, which can be used to unambiguously identify single–layer material. An inactive mode B^1_{2g} ($\sim$ 289 cm^{-1}) in bulk can be noted for bi–, tri– and four–layer $MoTe_2$ which may be due to the breaking of translation symmetry [1] and has the highst intensity for two–layer material, then we can observe the intensity to decrease with the increasing number of layers of $MoTe_2$.

This study may lead towards further understanding the lattice dynamics and optical processes in LTMD materials, such as $MoTe_2$.

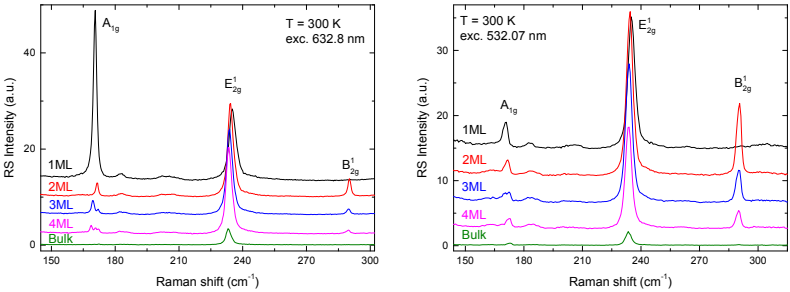

Fig. 1. : Raman spectra of $MoTe_2$ layers under the 532.07 nm and 632.8 nm laser excitation.

[1] C. Ruppert et al., „Optical Properties and Band Gap of Single- and Few-Layer $MoTe_2$ Crystals", Nano Letters **14**, 6231 (2014).
[2] S. Goler et al., „Self-assembly and electron-beam-induced direct etching of suspended graphene nanostructures", Journal of Applied Physics **110**, 064308 (2011).

EFFECT OF THE SUPERLATICE ON GAN/ALGAN STRUCTURES PERFORMANCE VIA SCHOTTKY DIODE STUDIES

Vytautas Janonis[1], Vytautas Jakštas[1], Irmantas Kašalynas[1]

[1]Semiconductor Physics Institute of Center for Physical Sciences and Technology
vytautas.janonis@ftmc.lt

Gallium nitride (GaN) is one of the most promising semiconductor materials for high frequency and high power electronics applications, where silicon faces fundamental challenges. High electron mobility, high saturation velocity and breakdown voltages, also very high thermal and mechanical stability are main parameters that encouraged fast GaN-based devices development during recent years [1]. Formation of GaN/AlGaN heterojunction allows two dimensional electron gas (2DEG) to appear at the interface without an intentional materials doping. High carrier mobility and density of the 2DEG are suitable for development of the field effect transistors (FETs) used in radiofrequency power electronics [1]. Moreover, parameters of 2DEG in GaN/AlGaN make possible recent progress of plasmonic THz emitters for efficient operation at room temperature [2]. All of the mentioned applications require good performance of Ohmic and Schottky contacts.

The aim of this work was the investigation of GaN/AlGaN/sapphire structures grown with and without internal super-lattice in Vilnius University Institute of Applied Research (VU TMI) MOCVD reactor. Specific ohmic contact resistance, 2DEG layer sheet resistance and Schottky barrier diode parameters were investigated. Fabricated Ohmic Ti/Al/Ni/Au and Schottky Ni/Au contact structures are shown in Fig1. The structures were fabricated in Semiconductor Physics Institute of Center for Physical Sciences and Technology employing recently developed procedures [3].

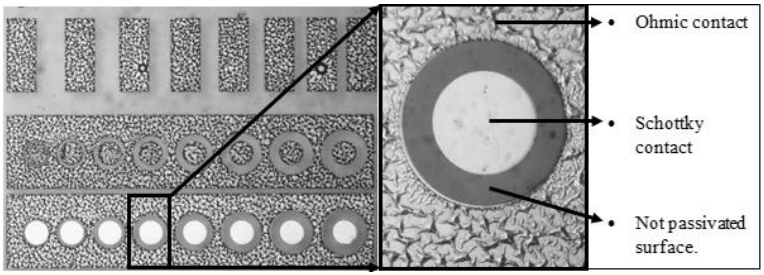

Fig.1. The optical view of the investigated Ohmic and Schottky contact structures.

Resistance and IV measurements were carried out in room temperature, using probe station and Keithley 2400 source meter. CV measurements were carried out using Agilent 2494A Precision Impedance Analyser. Schottky barrier diode IV characteristics were measured in the range of -2 to +2V in DC regime.

Measurements using Circular Transmission Line Method (CTLM) revealed the specific Ohmic contact resistance of about 10^{-5} Ωcm. Such value was acceptable for investigation of parameters of the Schottky diodes. The sheet resistance of 2DEG was 674Ω/□ in the investigated sample without superlattice and 616Ω/□ in the sample with the superlattice design. Obtained carrier mobility was also slightly smaller in the superlattice design sample.

Schottky barrier diode IV characteristics revealed that the formation of the superlattice degrades the leakage currents as it increases the concentration of lattice defects and acts as a second conductivity channel. Existence of the second conductivity channel was also proved by the measured CV characteristic of the Schottky diode. The barrier heights (1 ÷ 1,1eV) and the ideality factors (1,2 ÷ 1,4) were found from the IV experiments, performed at room temperature, and correlation between these two parameters, indicating parasitic tunnelling channel, was obtained.

All in all it was concluded, that the introduction of the superlattice in the GaN/AlGaN structures creates a second conductivity channel and an increase of the defect concentration. It is harmful in respect of the production of electronic devices therefore the growth of the superlattice requires further optimisation process.

[1] Trew, R. J. SiC and GaN transistors - is there one winner for microwave power applications? Proc. IEEE 90, 1032–1047 (2002).
[2] Shur, Michael Shur, Michael, AlGaN/GaN plasmonic terahertz electronic devices, Journal of Physics: Conference Series, 486, 012025 (2014).
[3] Jakštas, V. et al. Schottky diodes and high electron mobility transistors made of 2DEG AlGaN/GaN structures on sapphire. Lith. J. Phys. 54, 227–232 (2014).

PLASMONIC FILTERING OF INGAN MQW LUMINESCENCE

Agnė Kalpakovaitė [1], Tomas Grinys [1], Arūnas Kadys [1]

[1] Institute of Applied Research, Vilnius University, Saulėtekio av. 10, 10223 Vilnius, Lithuania
agne.kalpakovaite@ff.stud.vu.lt

Recently nanometer scale self organized metal particles attracted much interest due to their interesting physical properties [1]. At the interface between conductive particles and insulator or semiconductor the excitation of collective electrons known as localized surface plasmons (LSP) can be observed. The electromagnetic waves can be efficiently absorbed and scattered by metal nanoparticles at a resonant interaction with LSP. The changes: such as size and shape of metal nanoparticles as well as local dielectric environment is responsible for shift in resonance of LSP.

The most common method for sensing of analyte absorption on metal nanoparticles is the monitoring changes in local dielectric environment [2]. This can be achieved by measuring resonant wavelength shift of LSP. The radiation spectrum of InGaN multi quantum wells shows good agreement with LSP resonance of silver nano-islands on sapphire substrate. Therefore silver nanoparticles on sapphire with GaN based LED structure can be successfully applied for spectrum filtering and thus analyte sensing.

In this work the plasmonic filtering of light radiation from InGaN multi quantum wells (MQW) was studied by photoluminescence (PL). Prior plasmonic filters were formed size and shape of silver nanoparticles was optimized by manipulating technological parameters. Metallic nanostructures were formed on sapphire substrates by annealing silver thin films. Typical scanning electron microscope (SEM) image (Fig. 1 a)) showed that size of nanoparticles was less than 100 nm. Two sharp peaks in transmittance spectrum were observed which can be attributed to different LSP resonance mode: dipole (DP) and higher order such as quadrupole mode (QP) (see Fig. 1 b)).

The buffer GaN following by active layer of InGaN MQW was formed on sapphire substrate by metal organic chemical vapor deposition (MOCVD). The PL spectrum of such structure excited by picosecond laser of wavelength 354 nm is shown in Fig. 1 c). Two peaks can be apparently distinguished in the spectrum. The first at 369 nm corresponds to the near band edge emission of the GaN, while the second one at 440 nm to radiation of InGaN MQWs. The sharp absorption of light is observed in the range of 400-550 nm if the PL light is passed through silver plasmonic filter integrated on the sample with MOCVD grown GaN based structure (see Fig. 1 c)). The maximum of absorption shows good agreement with DP resonance mode of LSP.

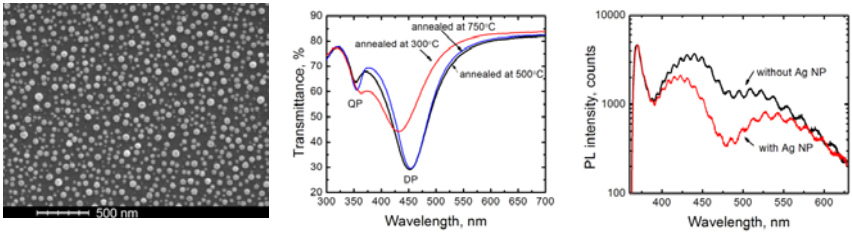

a) b) c)

Fig. 1. a) typical SEM image of silver nanoislands, b) transmittance spectra of nanoislands prepared at different temperatures, c) photoluminescence spectrum of InGaN MQW structure with and without Ag nanoparticles (NP).

[1] X. Gu, T. Qiu, *Nanoscale Research Letters* **6**(199), (2011).
[2] Z. Zalevsky and I. Abdulhalim, *Integrated Nanophotonic Devices* (2010).

DIELECTRIC AND IMPEDANCE SPECTROSCOPY OF $Bi_5FeTi_3O_{15}$ and $Bi_{4.25}$ $La_{0.75}Ti_3FeO_{15}$ ceramics

R.M.Katiliūtė[1], M.Ivanov[1], J. Banys[1], J. Bobič[2], B. D. Stojanovič[2]

[1]Faculty of Physics, Vilnius University, Sauletekio 9/3 817, LT-10222, Vilnius, Lithuania
[2]Institute for Multidisciplinary Research, University of Belgrade, Kneza Viseslava 1, Belgrade, Serbia
ringaile.katilute@ff.vu.lt

Bismuth layer structured ferroelectrics (BLSFs) have attracted a great deal of attention from technological and scientific points of view. It is recognized that the entire displacement of the perovskite blocks with respect to the Bi_2O_2 layers induces ferroelectric nature. [1]

The compound $BiFeO_3$ (BFO) is one of the most intensively studied multiferroic materials because of the simultaneous presence at room temperature of ferroelectricity and antiferromagnetic order.[2] When $BiFeO_3$ is doped by La (BLFO), the dielectric parameters is improved.[3]

Therefore, an idea of combining both BFO or BLFO and BLSFs together to form new type of multiferroics is particularly interesting.[2] However, they are quite poorly investigated. That is why we aim is to characterize $Bi_5FeTi_3O_{15}$ (BFTO) and $Bi_{4.25}$ $La_{0.75}Ti_3FeO_{15}$ (BLFTO) ceramics, which could potentially be of interest to a wide scientific community.

Measurements were performed using precision LCR meter HP 4284A in 20 Hz – 1 MHz frequency range and 300 K – 1000 K temperature interval in a SNOL 0,2/1250 furnace during cooling cycle with 1 K/min temperature variation rate.

Dielectric spectra for BLFO shows dielectric anomaly at high temperatures, while at BFTO conductivity dominates. Ceramics exhibit several charge relaxation processes observed in different temperature and frequency ranges. All of them are well described by Arrhenius law with different activation energies. A more detailed investigation will be presented during the conference.

[1] M. Suzuki, Y. Noguchi, T. Uchikoshi, and M. Miyayama, "Polarization and piezoelectric properties of grain-oriented ferroelectric Bi5FeTi3O15 ceramics prepared by magnetic-field-assisted electrophoretic deposition method," *J. Electroceramics*, vol. 24, no. 2, pp. 91–96, Jun. 2008.
[2] X. Y. Mao, W. Wang, and X. B. Chen, "Electrical and magnetic properties of Bi5FeTi3O15 compound prepared by inserting BiFeO3 into Bi4Ti3O12," *Solid State Commun.*, vol. 147, no. 5–6, pp. 186–189, Aug. 2008.
[3] P. Priyadharsini, A. Pradeep, B. Sathyamoorthy, and G. Chandrasekaran, "Enhanced multiferroic properties in La and Ce co-doped BiFeO3 nanoparticles," *J. Phys. Chem. Solids*, vol. 75, no. 7, pp. 797–802, Jul. 2014.

CONDUCTIVITY INVESTIGATION IN MULTIFERROIC $Bi_{1-x}Dy_xFeO_3$ CERAMICS

Aurimas Kirelis[1], Edita Palaimiene[1], Jan Macutkevic[1],Juras Banys[1], Dzimtri Karpinsky[2], Andrei Kholkin[2]

[1] Vilnius University, Faculty of physics, Sauletekio av. 9, III b., LT-10222 Vilnius, Lithuania
[2] Department of Ceramics and Glass Engineering & CICECO, University of Aveiro, P-3810-193 Aveiro, Portugal
aurimas.kirelis@ff.stud.vu.lt

The Bismuth ferrite, $BiFeO_3$, (BFO) is one of few materials exhibiting ferroelectric (FE) and antiferromagnetic (AFM) ordering above room temperature [1]. $BiFeO_3$ has high temperatures of ferroelectric-paraelectric ($T_C \approx 1100$ K) and antiferromagnetic-paramagnetic ($T_N \approx 643$ K) transitions. It is also a multiferroic material, in which electric and magnetic ordering can coexist in a single phase, because of that, it and its derivatives have attracted a lot of attention, particularly Dy-substituted bismuth ferrite.

This work presents broadband dielectric spectroscopy results of dysprosium bismuth ferrite ceramic, $Bi_xDy_{1-x}FeO_3$ (x=0.1, 0.15, 0.2). Dielectric measurements were performed as a function of both temperature and frequency in the temperature range 25 K – 1000 K and in the frequency range 20 Hz – 1 M Hz. The $Bi_xDy_{1-x}FeO_3$ ceramic were prepared by a two-stage solid-state reaction method using the oxides Bi_2O_3, Dy_2O_3 and Fe_2O_3 [2].

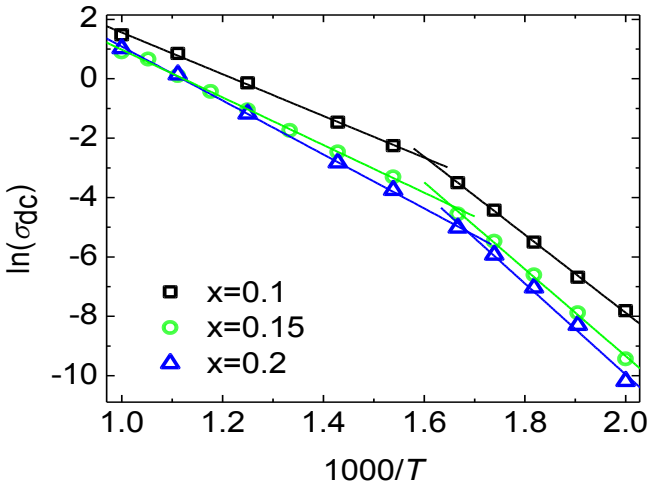

Fig. 1. $\ln(\sigma_{DC})$ *vs.* $1/T$ of $Bi_{1-x}Dy_xFeO_3$ (x=0.1, 0.15, 0.2). (Lines are results of the Arrhenius fit: $\sigma_{DC} = \sigma_0 \exp(E_A/kT)$)

The electrical conductivity was calculated from frequency dependence of the resistance. At higher temperatures (above 400 K) in all investigated ceramics the huge electrical conductivity values was observed (Fig. 1). In all ceramics the temperature of DC electrical conductivity has some change in the slope close to T=590 K, therefore DC electrical conductivity was fitted with the Arrhenius law separately below and above this temperature. The conductivity activation energy increases with the concentration of dysprosium.

[1] K. Melcher, L.-M. Ng, E. Zhou et al., A gate-latch-lock mechanism for hormone signaling by abscisic acid receptors, Nature **462**, 602-608 (1990).
[2] V. A. Khomchenko, D. V. Karpinsky, A. L. Kholkin, N. A. Sobolev, G. N. Kakazei, J. P. Araujo, I. O. Troyanchuk, B. F. O. Costa, and J. A. Paixão. Rhombohedral-to-orthorhombic transition and multiferroic properties of Dy-substituted $BiFeO_3$, J. Appl. Phys. **108**, 074109 (2010).

ANALYSIS OF LUMINESCENCE DECAY KINETICS IN InGaN MQW's MEASURED IN THE FREQUENCY DOMAIN

Rolandas Kudžma[1], *Ignas Reklaitis*[1], *Jūras Mickevičius*[2]

[1] *Institute of Applied Research, Vilnius University, Lithuania*
[2] *Faculty of Physics, Vilnius University, Lithuania*
rolandas.kudzma@gmail.com

In this work carrier lifetimes of three different InGaN multi quantum well (MQW) structures have been measured in the frequency domain [1]. Sample's numbered #1 #2 #3 had emission peaks at 460 nm, 500 nm and 530 nm respectively. The excitation source for the study was laser diode (LD) emitting at 405 nm, it allowed us to measure luminescence in resonant excitation regime (barrier material of MQW's is GaN absorbing at 378 nm) and to cover wide range of excitation power densities, ranging from 1 mW/cm^2 to 500 mW/cm^2. The LD was modulated in the wide frequency range – from 1 Hz to 200 MHz, enabling to measure carrier lifetimes from seconds to nanoseconds.

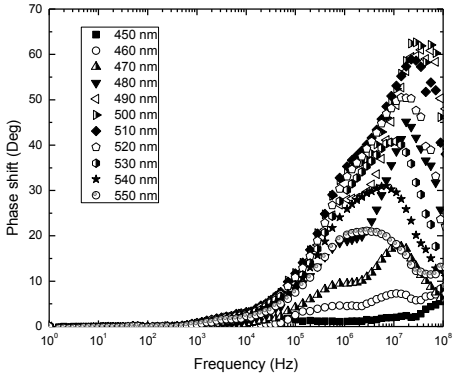

Fig. 1.Sample's #2 frequency response curve as a function of luminescence wavelength.

All samples, showed complex multi-component decays, which can be described using well know stretch exponential decay law [2]:

$$I(t) = \exp[-(t/\tau)^{\beta}] \qquad (1)$$

During presentation, values of stretching parameter β and carrier lifetime τ values for all three samples will be announced.

[1] J. Mickevicius, Carrier dynamics in GaN at extremely low excited carrier densities, Solid State Commun. **145,** *312 (2008).*
[2] M.Popgristic, Long.Time-resolved photoluminescence measurements of quantum dots in InGaN multiple quantum wells and light-egmitting diodes, J. Appl. Phys. **86**, *2 (1999).*

INVESTIGATION OF TiO2 THIN FILMS DENSITY OBTAINED BY DIFFERENT MAGNETRON SPUTTERING METHODS

Raimundas Kumža, Jevgenij Višniakov, Audružis Mironas, Algirdas Selskis, Artūras Suchodolskis

Semiconductor Physics Institute of Center for Physical Sciences and Technology, A. Goštauto Str. 11, LT-01108, Vilnius, Lithuania

raimiskma@gmail.com

Titanium oxide presents many interesting properties in various fields. The most remarkable that titanium oxide is transparent in visible range of the electromagnetic spectrum, it has extraordinarily high dielectric constant and presents three polycrystalline phases, in particular rutile, anatase and brookite [1].

Magnetron sputtering (MS) technique was employed for TiO2 thin films deposition using direct current (DC), radio frequency (RF) and high impulse power MS (HiPIMS) methods. MS deposition is a widely used process for depositing metal and ceramic films for semiconductor applications, optical coatings, magnetic media and etc. High deposition rates and the possibility to carry out ion assisted growth are primary advantages of this technique [2]. High power impulse magnetron sputtering is an emerging physical vapor deposition technology. It is characterized by a high pulse power density at the sputtering target, which is typically two orders of magnitude greater than the average power density [3]. Measurement were carried out by scanning electron microscopy for layer mass thickness parameter and spectroscopic ellipsometry for its thickness.

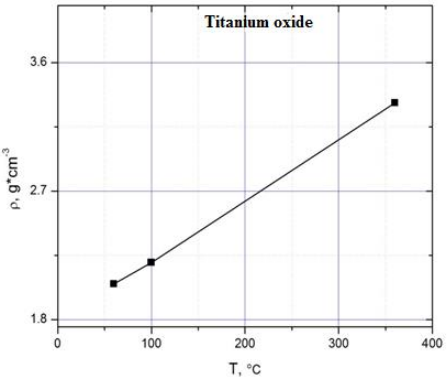

Fig. 1. DC deposited TiO2 film density at different temperatures.

Higher density of the titanium oxide film can be achieved by varying the conditions of the deposition process. Increased temperature of substrate during the sputtering shows higher density even for standard DC process. It's shown in figure 1.

Obtained densities using HIPIMS technology are denser than other compared magnetron sputtering methods of the same power applied to the target.

[1] S. Konstantinidis, J.P. Dauchot , M. Hecq, Titanium oxide thin films deposited by high-power impulse magnetron sputtering, Thin Solid Films 515 (2006) 1182–1186.

[2] Karol Macak, Vladimir Kouznetsov, Jochen Schneider, and Ulf Helmersson, Ionized sputter deposition using an extremely high plasma density pulsed magnetron discharge, American vaccum society 2000 1533-1537.

[3] André Andersa and Joakim Andersson , High power impulse magnetron sputtering: Current-voltage-time characteristics indicate the onset of sustained self-sputtering, JOURNAL OF APPLIED PHYSICS 102, 113303 2007

PHOTOLUMINESCENCE STUDIES OF $RESE_2$ SINGLE CRYSTALS

Joanna Kutrowska[1], Joanna Jadczak[1], Leszek Bryja[1*]

[1] Faculty of Fundamental Problems of Technology, Wrocław University of Technology, Poland
j.kutrowska@gmail.com

Bulk rhenium diselenide is supposed to be indirect band gap semiconductor belonging to the family of transition-metal dichalcogenides (TMDs) [1]. TMD are exciting class of materials due to layered structure which allow to obtain individual layer using e.g. micromechanical cleavage technique. Most of them are indirect bandgap semiconductors in bulk and direct in monolayer.

Rhenium diselenide ($ReSe_2$) is one of the least well-known members of the layered TMD family. In contrast to most of TMDs rhenium diselenide crystallize in a structure with low symmetry (it is triclinic and has a bulk space group $P\bar{1}$). Re atoms in each layer are displaced from the centre of octahedral coordination units and form zigzag chain along the b-axis. The surface of $ReSe_2$ is corrugated on the lateral length scale of unit cell [1]. Lattice distortion leads to the anisotropy of optical and electrical properties in van der Waals plane.

In our measurements we focus on the optical properties of pure $ReSe_2$ single crystals. They were grown directly from the composite elements (Re: 99.99% pure; Se: 99.999%) by the vapor transport method using I_2 as transport agent. Transitions of studied material were measured using polarization-dependent photoluminescence spectroscopy in the temperature range of 16-70 K. The observed spectra reveal anisotropic physical properties – observed transitions are polarization-dependent (Fig.1).

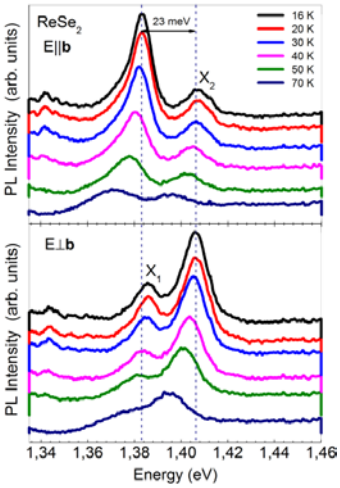

Fig. 1. Temperature-dependent PL spectra of $ReSe_2$ for two orthogonal polarizations.

In this work we compare a photoluminescence spectra of bulk rhenium diselenide and very similar to that – rhenium disulphide. Our results confirmed a strong, opposite polarization dependence of observed excitons: the X_1 is not allowed for light polarized perpendicular to b axis, whereas the X_2 is not allowed for light polarized along the b-axis. This situation is very similar to the case of ReS_2. Furthermore we present ways in which $ReSe_2$ may extend the potential of the TMD materials.

[1] D. Wolverson, S. Crampin, A. S. Kazemi et al., Raman Spectra of Monolayer, Few-Layer, and Bulk $ReSe_2$:An Anisotropic Layered Semiconductor, ACS Nano **8**, 11154-11164 (2014).

EFFECT OF A MAGNETIC FIELD ON CONTROL OF SHALLOW DONOR STATES NEAR SEMICONDUCTOR SURFACE

Elena Levchuk[1], Leonid Makarenko[1]

[1] Department of Applied Mathematics and Computer Science, Belarusian State University, Independence Ave. 4, 220030 Minsk, Belarus

liauchuk.alena@gmail.com

Single dopant impurities in semiconductors under control of electric and magnetic fields are among the most promising physical systems for implementing a quantum computer [1]. This problem has stimulated much theoretical studies and numerical simulations on the quantum states of donors localized near a semiconductor surface in a magnetic field [2-4]. However, in previous works the system has been considered without external electric field [2-3] or under uniform electric field [4]. In the given work, we additionally assume a disc-shaped gate as a source of the external electric filed, and study characteristics of electron shuttling from the donor to the gate in the presence of uniform magnetic field.

We consider the donor near semiconductor surface, at which the disc-shaped gate is situated. Two kinds of boundary conditions for the field applied by the gate are used. Firstly, we consider that the gate is surrounded by a dielectric material. Secondly, we assume that the gate is surrounded by a metal, at which the potential equals zero. Magnetic field is applied perpendicular to the semiconductor surface. Then, the stationary Schrödinger equation for the impurity electron in cylindrical coordinates is given by

$$\hat{H}\Psi = E\Psi \tag{1}$$

with the Hamiltonian operator

$$\hat{H} = -\frac{1}{\rho}\frac{\partial}{\partial\rho}\left(\rho\frac{\partial}{\partial\rho}\right) - \frac{\partial^2}{\partial z^2} - \frac{1}{\rho^2}\frac{\partial^2}{\partial\varphi^2} - i\mu\frac{\partial}{\partial\varphi} + \frac{\mu^2\rho^2}{4} + \hat{V}_D + \hat{V}_{D'} + \hat{V}_{im} + \hat{V}_G, \tag{2}$$

where μ is considered as a measure of the magnetic field strength, $\hat{V}_D$, $\hat{V}_{D'}$, $\hat{V}_{im}$ are the interactions between the electron and the donor, the donor image and electron image respectively, $\hat{V}_G$ describes the potential landscape in the semiconductor due to the gate. The problem for the equation (1) – (2) has been solved using finite element method (FEM).

We have investigated the effect of magnetic field on the structure of electron energy spectrum of near-gate states, i.e. when the donor is infinitely distant from the semiconductor interface (Fig. 1). The system in this case can be considered as a quantum dot induced by electric field. On the basis of FEM results, we also propose a trial function of a simple form for variational method to take into account magnetic field effect for near-gate states. The energy spectrum of near-gate states is compared with energy spectrum of near-donor states (Fig. 1).

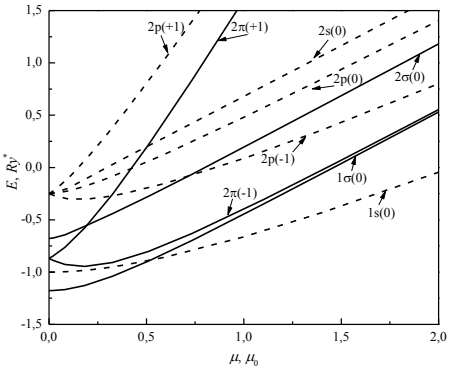

Fig. 1. Energies of near-gate (solid lines) and near-donor (dashed lines) states as a function of magnetic field, $\mu_0 = \hbar/\left(a^*\right)^2 e$, a^* and Ry^* are effective Bohr radius and effective Rydberg.

Two main characteristics of electron shuttling from the donor to the gate have been studied: critical gate potential at which the shuttling takes place and minimum gap $\left(g_{\min}\right)$ between ground and first excited σ-state, which can be used to estimate the tunneling time. It has been found that the presence of magnetic field leads to increasing of the critical potential. The dependence of $g_{\min}$ on μ has been found to reveal nonmonotonic behavior: the value of $g_{\min}$ increases on ~20% for $\mu < 0.2$ and decreases for larger magnetic fields.

Differences between the cases of uniform and nonuniform external electric fields have been studied.

We have also studied the effect of image charges, gate diameter, donor position on donor states in electric and magnetic fields.

[1] B.E. Kane, A silicon-based nuclear spin quantum computer, Nature **393**, 133-137 (1998).

[2] B. Li et al., Effect of a perpendicular magnetic field on the shallow donor states near a semiconductor-metal interface, Phys. Rev. B **87**, 075313 (2013).

[3] A. Bruno-Alfonso, L. Candido, G.-Q. Hai, Two-dimensional electron states bound to an off-plane donor in a magnetic field, J. Phys.: Condens. Matter **22**, 125801 (2010).

[4] M.J. Calderon, B. Koiller, S. Das Sarma, External field control of donor electron exchange at the Si/SiO_2 interface, Phys. Rev. B **75**, 125311 (2007).

NONEQUILIBRIUM CARRIER DYNAMICS IN GaN EPILAYERS IN A WIDE RANGE OF EXCITATION POWER DENSITIES

Mažena Mackoit[1], Jūras Mickevičius[1], Jonas Jurkevičius[1], Gintautas Tamulaitis[1], M. Shatalov[2], J. Yang[2], R. Gaska[2]

[1]Semiconductor Physics Department, Vilnius University, Saulėtekio ave. 9-III, LT-10222 Vilnius, Lithuania
[2]Sensor Electronic Technology, Inc., 1195 Atlas Road, Columbia, SC 29209, USA
mazena.mackoit@ff.stud.vu.lt

GaN and its derivatives have a wide variety of applications in modern optoelectronics. Despite the rapid progress in the development of III-nitride-based light-emitting diodes and laser diodes during last two decades, the details of the radiative and non-radiative recombination processes are still not well understood. Moreover, the carrier dynamics in III-nitride compounds is usually studied without taking into account the equilibrium carriers, even though their densities are quite substantial, especially in the n-type III-nitrides.

In this report, the carrier dynamics in GaN epilayers is investigated using the dependence of the photoluminescence (PL) intensity on excitation power density. The dependence was measured in a wide excitation power density range covering nine orders of magnitude.

A number of n-type nominally undoped GaN epitaxial epilayers grown using standard metal-organic chemical vapor deposition (MOCVD) technique on c plane sapphire substrates were studied.

To cover the wide range of excitation power densities, two measurement modes were used. The spectra were recorded by a CCD camera at a continuous-wave (CW) excitation using the He-Cd laser radiation (λ_{exc} = 325 nm) with power density varying from 4 mW/cm^2 to 16.1 W/cm^2 for low excitation intensities. Meanwhile, the luminescence at high excitation intensities was measured in quasi-steady-state mode, under excitation by the fourth harmonic (266 nm) of a YAG:Nd mode-locked laser radiation (pulse duration of 4 ns) with attenuator providing optical excitation power densities between 0.8 kW/cm^2 and 19.7 MW/cm^2. The PL spectra were recorded using a spectrometer equipped with a CCD camera. All of the measurements were performed at room temperature.

The spectrally-integrated PL intensity dependences on excitation power density measured in the two modes were matched and fitted with model calculations.

It is shown that the fit between the experimental results with the corresponding dependence calculated using the common ABC model is acceptable only in a narrow range of excitation power densities. At low excitation power densities, a super-linear PL intensity dependence on excitation power density was observed. The acceptable fit was achieved using a set of differential rate equations usually referred to as the Brandt model. Our results show that the equilibrium carriers have to be taken into account to properly describe the photoluminescence efficiency and to accurately extract the rate coefficients for radiative and nonradiative recombination.

INVESTIGATIONS OF Zn_2Mg OPTICAL RESPONSE

Paulius Mackonis, Saulius Tumėnas

Semiconductor Optics Laboratory, Center for Physical Sciences and Technology, Vilnius, Lithuania
paulius.mackonis@ff.stud.vu.lt

Magnesium dizinc is an intermetallic hexagonal crystalline compound (a = 5.233 Å, c = 8.566 Å [1]) of the Laves phase. Primitive cell of Zn_2Mg Laves phase contains twelve atoms, eight zinc atoms of which occupy two inequivalent sites, and four magnesium's atoms are in equivalent sites. The atomic composition of Zn_2Mg and atoms local neighboring surrounding are similar to icosahedral fci-$Zn_{60}Mg_{30}RE_{10}$ quasicrystals (RE = rare earth elements), and magnesium dizinc presents a convenient physical reference system for studies of both the atomic, and the electronic structure of the fci-ZnMgRE quasicrystals. From other side Zn_2Mg structure is comparable to monocrystalline Zn, they both have hexagonal crystal symmetry and Zn_2Mg consist of 67% zinc.

In this work we present spectroscopic ellipsometry (SE) study and qualitative analysis of interband optical transitions of Zn_2Mg. Optical response from uniaxial metals depends on polarization of probing light. The main issue for reliable determination of both ordinary and extraordinary dielectric functions requires careful optical surface orientation and preparation. The (110) surface of Zn_2Mg prepared using careful mechanical polishing and Ar^+ sputtering in a UHV chamber. The optical response measured using a dual rotating compensator ellipsometer RC2 (J. A. Woollam Co., Inc.) in the 0.6 – 3.5 eV spectral range at various incidence and azimuthal angles in the intervals of 45–75° and 0–90°, respectively. At each angle the experimental ellipsometric parameters Ψ and Δ were simultaneously recorded.

Experimental ellipsometric parameters were analyzed using the CompleteEASE (J. A. Woollam Co., Inc.) software, which can perform data analysis at all wavelengths. From experimental ellipsometric parameters were determined both ordinary and extra-ordinary components of Zn_2Mg dielectric function, obtained spectra presented in Fig. 1. As see from figure, dielectric function have two optical features related to interband optical transitions. Interband optical transitions depends significantly on the polarization of the probing light beam. Optical transitions occur at pseudogaps, which opens at intersections of Bragg planes with Fermi surface. In hexagonal crystals pseudogaps opens at intersection with (002) and (110) Bragg planes. In Fig. 1 we clearly see two or one absorption peaks in the dielectric function spectrum, for $E \| C_6$ optical transitions occurs across Δ_{101} and Δ_{002} pseudogaps, for $E \perp C_6$ occurs only across Δ_{101} pseudogap. Employing nearly free electron approximation and two band model we determined width of the pseudogaps values, which are Δ_{101}=1.45 eV and Δ_{002}=0.89 eV.

In order to reveal similarities we compared Zn_2Mg optical conductivity with Zn and ZnMgY [3] optical conductivities. Results showed that electronic subsystem of zinc-based intermetallic compounds correlates between, comparing crystalline Zn with binary Zn2Mg crystal and the ternary icosahedral $Zn_{62}Mg_{29}Y_9$.

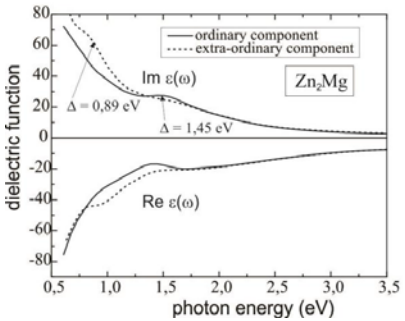

Fig. 1. Dielectric function of Zn_2Mg

[1] T. Ohba, Y. Kitano, Y. Komura, The charge-density study of the Laves phases, MgZn2 and MgCu2, Acta Crystallogr. C 40, 1–5 (1984).
[2] B. Johs, J. S. Hale, Dielectric function representation by B-splines, physica status solidi a 205, 715–719 (2007).
[3] S. Tumėnas, V. Karpus, H. Arwin, W. Assmus, Optical conductivity of fci-ZnMgRE quasicrystals, Thin Solid Films 519(9), 2951–2954 (2011).

OPTICAL CHARACTERIZATION OF NON-POLAR ZnO FILMS

Simona Paurazaitė, Saulius Tumėnas

Semiconductor Optics Laboratory, Center for Physical Sciences and Technology, Vilnius, Lithuania
simona.paurazaite@ff.stud.vu.lt

Zinc oxide is a multifunctional material with possible application in optoelectronic, ZnO has wide direct band gap of 3.37eV and large exciton binding energy of 60 meV at room temperature. Due to the hexagonal structural symmetry, ZnO exhibit a strong lattice polarization field along the polar c-axis. This polarization field, called Quantum Confined Stark Effect [1], significantly degrades the internal quantum efficiency of the emitting devices. Several groups have used different approaches to solve this problem. A useful approach is to grow ZnO along different crystallographic directions.

We investigated the optical properties of polar c-plane and non-polar a- and m-plane ZnO epitaxial films grown on $LiGaO_2$ (LGO) substrate. The ZnO films were grown by chemical vapor deposition (CVD) directly on the LGO substrate without any buffer layer. Optical characteristics of polar and non-polar ZnO thin films were investigated employing transmission, temperature-dependent photoluminescence (PL) and spectroscopic ellipsometry (SE) techniques. Transmission spectroscopy was carried out using UV-3600 Shimadzu Spectrophotometer, for the PL investigations sample was excited by a diode-pumped Nd: YAG solid state laser working at 266 nm wavelength. Transmission and PL measurements are not sensitive to sample optical anisotropy, to reveal polarization dependent properties we used generalized spectroscopic ellipsometry technique. SE measurements were carried out by dual rotating compensator ellipsometer RC2 (J. A. Woollam Co, Inc.) in the 0.73 – 6 eV spectral range, at the incident angles from 45 to 75 degrees.

Experimental absorption spectra, presented in Fig. 1 (a), allowed us to reveal fundamental absorption edge, which was 3.276 eV for c-ZnO, 3.325 eV and 3.280 eV for a- and m- samples. Room temperature PL spectra, presented in Fig. 1 (b), show exciton emission maximum at 3.284 eV for c- sample and 3.296 for a- and m- samples. Small exciton emission peak blue shift of about 12 meV related to different exciton binding energy and different band gap values [2]. Spectroscopic ellipsometry allowed for reliable determination of film thickness: a-ZnO and m-ZnO were 124 nm and 408 nm thick and sample c-ZnO - 167 nm. Experimental SE data were analyzed in terms of three phase model, where ZnO dielectric function was characterized as B-spline function [3]. Deduced imaginary part of the ordinary dielectric function presented in Fig. 1 (c). As seen from a figure, all three samples exhibit optical feature at 3.378 eV, which is related to optical transition at Γ point. Optical feature at 3.316 eV energy is related to exciton absorption and correspond exciton binding energy of 62 meV. Sample a- and m- show more suppressed exciton absorption than c- one. Determined values of optical band gap and exciton binding energies are in a good agreement with literature data [2].

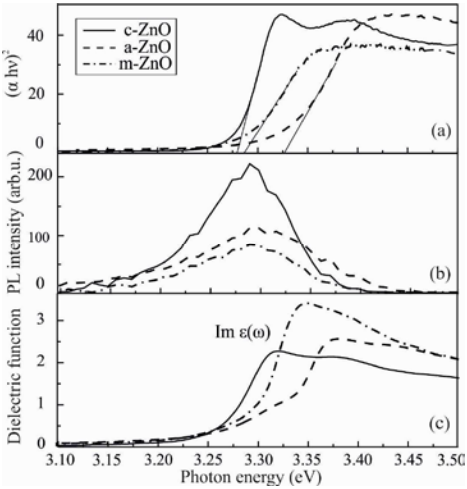

Fig. 1. Absorption spectrum (a), RT-PL spectrum (b), and imaginary part of ordinary dielectric function (c).

[1] G. Vaschenko, D. Patel, C. Menoni, N. Gardner, J. Sun, W. Gotz, C. Tome, B. Clausen, Significant strain dependence of piezoelectric constants in $In_xGa_{1-x}N$/GaN, Physical Review B **64**, 241308 (2001);
[2] T. Kang, H. Lee, W.I. Park, G. Yib, Ellipsometry on uniaxial ZnO and $Zn_{1-x}Mg_xO$ thin films grown on (0001) spphire substrate, Thin Solid Films **455**, 609-614 (2004);
[3] B.Johns, J.S. Hale, Dielectric function representation by B-splines, Physica Status Solidi A **205**, 715-719 (2008).

INVESTIGATION OF AGEING EFFECTS IN NANOSTRUCTURED La-Sr-Mn-O FILMS

Vakaris Rudokas[1,2], Nerija Žurauskienė[2]

[1] Vilnius University, Faculty of Physics, Saulėtekio ave. 9, LT-10222, Vilnius, Lithuania.
[2] Center for Physical Sciences and Technology, Semiconductor Physics Institute, A. Goštauto 11, LT-01108, Vilnius, Lithuania.
vakaris.rudokas@ff.stud.vu.lt

Recently it was demonstrated that nanostructured $La_{0.83}Sr_{0.17}MnO_3$ (LSMO) films which exhibit the colossal magnetoresistance effect (CMR) can be successfully used for the development of magnetic field sensors [1]. They exhibit low anisotropy of magnetoresistance (*MR*) and the *MR* of these films does not saturate up to the megagauss limit [1,2]. This property of thin nanostructured manganite films was used for the design of so-called CMR-B-scalar sensors which can measure the magnitude (*B*) of magnetic flux density in very small volumes. These sensors were applied to study the magnetic diffusion processes in railguns and to measure magnetic field distribution in non-destructive pulsed-field magnets [3,4]. The operation of these devices is based on electrical resistivity change of manganite film due to external magnetic field action. However, the resistivity and magnetoresistance of manganite films is very sensitive to the ambient temperature variations [2,5,6]. For this reason the temperature drift during operation of the CMR-B-scalar sensors is very important and has to be taken into consideration during design and calibration of such devices. Moreover, the stability of the electrical resistance and magnetoresistance over the time (ageing effects) plays an important role. In this work, the accelerated ageing by annealing the films at higher than operation temperature is applied, and the effects induced by this annealing on film properties are investigated and discussed.

The kinetics of resistivity and magnetoresistance change was studied during ageing of thin nanostructured $La_{0.83}Sr_{0.17}MnO_3$ manganite films grown on lucalox (99.9% Al_2O_3 + 0.01% MgO) substrate by PI MOCVD method. It was obtained that accelerated ageing of the films annealing them in Ar atmosphere at temperature of 100 °C leads to the significant increase of film resistivity (see Fig 1a). The obtained results are analyzed using typical for topologically-disordered systems model of hierarchically limited relaxation dynamics described by stretched exponent [7]. The analysis of resistivity *vs*. temperature dependence in paramagnetic state by using Mott's variable range hopping (VRH) model showed that localization length of charge carriers decreases during annealing. At the same time it was found that the accelerated ageing process decrease the demagnetization field of thin LSMO films (see Fig 1b), however, it insignificantly influences the magnetoresistance in magnetic fields higher than 0.7 T. The possible reasons of observed changes are explained by oxygen diffusion and its depletion in the grain boundaries of the films.

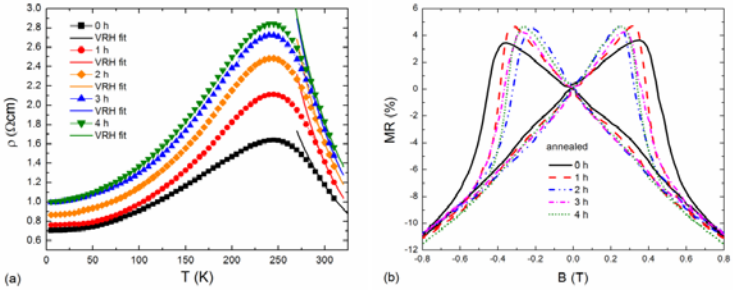

Fig. 1. The resistivity vs. temperature dependences (a) and magnetoresistance vs. magnetic flux density dependences (b) of nanocrystalline LSMO film annealed at 100 °C for different time periods.

[1] S. Balevičius, N. Žurauskienė, V. Stankevič, S. Keršulis, V. Plaušinaitienė, A. Abrutis, S. Zherlitsyn, T. Herrmannsdorfer, J. Wosnitza, F. Wolff-Fabris, Nanostructured Thin Manganite Films in Megagauss Magnetic Field, Appl. Phys. Lett. **101**, 092407-1-4 (2012).
[2] N. Žurauskienė, S. Balevičius, V. Stankevič, S. Keršulis, M. Schneider, O. Liebfried, V. Plaušinaitienė, A. Abrutis, B-Scalar Sensor Using CMR Effect in Thin Polycrystalline Manganite Films, IEEE Trans. Plasma Sci. **39**, 411-416 (2011).
[3] M. Schneider, O. Liebfried, V. Stankevič, S. Balevičius, N. Žurauskienė, Magnetic diffusion in railguns: Measurements using CMR – based sensors, IEEE Trans. Magnetics, **45**, 430-435 (2009).
[4] S. Balevičius, N. Žurauskienė, V. Stankevič, T. Herrmannsdörfer, S. Zherlitsyn, Y. Skourski, F. Wolff-Fabris, J. Wosnitza, CMR-B-Scalar Sensor Application for High Magnetic Field Measurement in Nondestructive Pulsed Magnets, IEEE Trans. magnetics, **49**, 5480-5484 (2013).
[5] C. Israel, M.J. Calderón, N.D. Mathur, The current spin on manganites, Mat. Today, **10**, 24-32 (2007).
[6] K. Daoudi, T. Tsuchiya , T. Kumagai, Growth and characterization of epitaxial $La_{0.7}Ca_{0.3}MnO_3$ thin films by metal-organic deposition on $(LaAlO_3)_{0.3}$–$(SrAlTaO_6)_{0.7}$ substrates, Thin Solid Films **516**, 6325-6329 (2008).
[7] V. O. Balitska, B. Butkievich, O. I. Shpotyuk, M. M. Yakiv, On the analytical description of ageing kinetics in ceramic manganite-based NTC thermistors, Microelectron. Reliab. **42**, 2003-2007 (2002).

X-RAY ANALISYS OF DIFFERENT POLYMORPHS USING HIGH-PRESSURE CRYSTALLOGRAPHY

Szymon Sutula[1], Roman Gajda[2], Krzysztof Woźniak[2]

[1] Department of Physics, University of Warsaw, Poland
[2] Department of Chemistry, University of Warsaw, Poland
szymon.sutula@gmail.com

Polymorphism is the ability of solid state of matter to create different crystal structures (also amorphous state) depending on the external conditions. Although substances at normal conditions exist mostly in their stable form, it is possible to examine their behaviour by changing, for example, the pressure and temperature.

Using standard Diamond Anvil Cell (DAC) very high pressures can be obtained, even exceeding 15 GPa. The ability of DAC to create tiny homogenous environment for an examined substance results in requiring very small quantities of studied compound. This makes DAC an ideal tool for experiments. However, using DAC decreases the number of reflections that can be measured as a consequence of reducing angular acces to the sample.

In typical DAC (shown in Fig. 1), sample and a chip of ruby are put inside a small hole in a gasket made of alloy of hard metals and compressed by two diamond culets [1]. Diamonds are pushed towards by screws that control the stability of pressure.

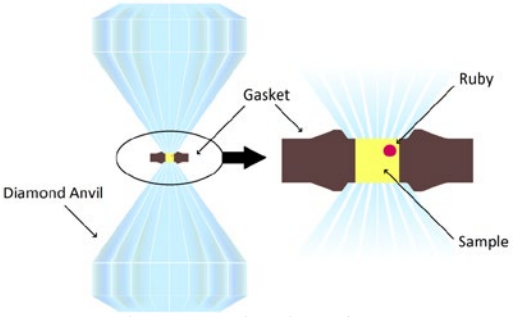

Fig. 1. Construction scheme of DAC

Procedure of preparing DAC involves using a fluorescent pressure sensor, usually a ruby chip. Illuminated by a laser, ruby fluoresces giving two R-line peaks and their shift depends on the pressure inside the cell [2][3].

Two methods can be used while loading DAC. If the initial substance is in the solid state, it is important to fill the hole in the gasket with hydrostatic fluid to ensure that forces propagate isotropically. However, if a sample is a liquid at normal conditions, it is essential to melt the polycrystalline mass that appears after the compression and slowly grow a monocrystal with as few dislocations as possible. Placing the sample between polarizer and analizer gives a great insight into homogeneity of the crystals and allows for notification if any unwanted twinning occurs.

Mostly, anodes in diffractometers are made of molybdenium or copper, which have the wavelength of emission lines Kα 0,71 Å and 1,54 Å, respectively. However, using shorter wavelength enables to spot more reflections in the reciprocal space and closer crystal planes may be measured, according to the Bragg equation, Eq. (1). Silver has the wavelenght of Kα 0,56 Å, which makes this metal significant for constructing the anodes in X-ray tubes to study diffraction of monocrystals inside DAC.

$$n\lambda = 2d_{hkl}\sin\theta \qquad (1)$$

Aside from analyzing the crystal structure, one of the goals of the high-pressure crystallography is looking for high-pressure polymorphs of low-temperature crystal structures and obtaining single crystals of compounds which are difficult to crystallize at ambient conditions. Substances which I analyze are simple organic compounds, mostly benzene substituted in different positions with methyl, hydroxyl group and halogens. These compounds are liquid at normal conditions, but their melting point is slightly lower than room temperature. Although some chemicals I examine in DAC exhibit clear phase transition, the other form amorphous phase with no long-range order. I will show a few examples of such studies.

[1] M. McMahon, High-Pressure Crystallography, Top Curr Chem **315**, 69-110 (2012).
[2] A. Chijioke, W. Nellis, A. Soldatov, I. Silvera, The ruby pressure standard to 150 GPa, J. Appl. Phys. **98** (2005).
[3] H. Yamaoka et al., Ruby pressure scale in a low-temperature diamond anvil cell, J. Appl. Phys. **112** (2012).

LUMINESCENCE IN CE^{3+} DOPED BaSiO AMORPHOUS GLASS AND GLASS CERAMICS

Augustas Vaitkevičius[1], M.Korjik[2], D. Dobrovolskas[1], E. Trusova[3], and G.Tamulaitis[1]

[1]Institute of Applied Research and Semiconductor Physics Department, Vilnius University, Saulėtekio av. 9, building III, 10222 Vilnius, Lithuania
[2]Research Institute for Nuclear Problems, Belarus State University, 11 Bobruiskaya str., 220030, Minsk, Belarus
[3]Belarusian State Technological University, 13a Sverdlova str., 220006, Minsk, Belarus
augustas.vaitkevicius@ff.stud.vu.lt

During the last decade, an impressive progress in the lighting technology based on the light-emitting diodes (LEDs) was achieved. Currently, the white LEDs have a considerable share of the light source market. Nevertheless, study and implementation of novel phosphors acting as wavelength converters in white LEDs is still one of the key issues in further development of these devices.

From the point of view of development of high power LEDs, glass ceramic materials have several advantages combining the properties of crystals and glasses. High thermal conductivity is of special importance. Recently, BaSi2O5 doped with Eu2+ and Eu3+ was found to be a good phosphor emitting in blue and red spectral ranges [1, 2]

We studied the influence of crystallization on the luminescence properties of Ce^{3+}–doped stoichiometric glass $BaO\text{-}2SiO_2$ at different stages of transformation from amorphous phase to glass ceramics. The samples were prepared by using 99.99% purity barium carbonate ($BaCO_3$) and silicon oxide (SiO_2) at stoichiometric molar ratio $BaO\text{-}2SiO_2$. Cerium was added at the amount of 1 weight % over the crystal stoichiometry in the form of $Ce_2Si_2O_7$, i.e., in the compound containing Ce in a trivalent state, in contrast to the conventional Ce^{2+} introduction using CeO_2. Two samples were cut of the glass after fabrication and annealed in different conditions: 15 min. at 900 °C and 30 min. at 850 °C. Unannealed sample was also studied for reference. The samples were prepared in Belarus State University.

The samples were investigated using confocal luminescence spectroscopy. The mapping and study of spatial variation in photoluminescence (PL) spectra were performed using WITec Alpha 300 S microscope system operating in confocal mode. An objective with numerical aperture NA = 0.6 ensured the in-plane spatial resolution of ~250 nm. The microscope was coupled by optical fiber with a spectrometer followed by a thermoelectrically cooled CCD camera. A CW laser diode, emitting at 405 nm was exploited for excitation.

Typical defects of the glass have been detected and studied in the unannealed sample. The bandwidth of PL band from the areas surrounding structural defects is lower, and the peak position is slightly redshifted, when compared to PL from defect free areas (Fig. 1). The same features have been observed, when comparing the spatially averaged PL spectra from annealed samples with those from the reference sample. In both cases, the change in PL parameters is a result of crystallization: either around the structural defects acting as crystallization centers in unannealed glass or in the bulk of the sample due to annealing.

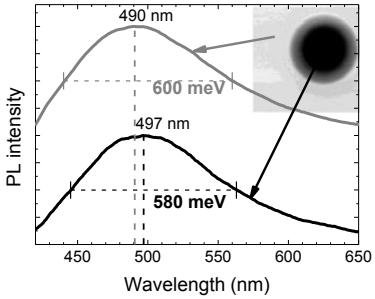

Fig. 1 PL spectra from area surrounding a structural defect (dark) and defect free area (grey). In the inset, typical PL intensity mapping around a structural defect.

Comparison of PL from samples annealed in different conditions showed that the luminescence properties of these samples are similar. This indicates that the influence of crystallization on Ce^{3+} ion emission is insensitive the investigated annealing conditions. These features are favorable for application of this glass system as phosphor material with low sensitivity of spectral parameters to fabrication conditions.

[1] J. W. Chung et al., Luminescence Properties of Eu2+ and Eu3+ Activated BaSi2O5 Phosphor Thin Films Grown by The Pulsed Laser Deposition, J. Korean Phys. Soc., **55**, 1965 (2009)
[2] A. Herrmann, A. Simon, and C. Rüssel, Preparation and luminescence properties of Eu2+-doped BaSi2O5 glass-ceramics, J. Lumin.,**132**, 215–219 (2012).

NITROGEN DEPTH PROFILE INVESTIGATION IN NITRIDED 65G STEEL

Audrius Valavičius [2], Vitoldas Kopustinskas[1], Mindaugas Andrulevičius [1,2]

[1] *Institute of materials science of Kaunas University of technology, savanorių Av. 271, LT-50131 Kaunas, Lithuania*

[2] *Department of physics, Kaunas University of technology, studentų St. 50, LT51368, Kaunas, Lithuania*

E-mail: audrius.valavicius@gmail.com

Ion nitriding have number of advantages over another conventional nitriding processes such as gas nitriding or nitriding in salt bath [1]. This process is widely used in the manufacturing and machining industries, primarily to treat tools for hot and cold work [2]. Studies of nitridation carried out in the past shown that microstructure of the surface layer can be affected by changing temperature, time and gas mixture ratio [1, 2]. In this paper we represent the investigation of 65G spring steel nitrogen concentration distribution on the depth after nitridation process.

Samples of 65G spring steel of dimensions 37.5x8x1mm were used for this study. The alloy studied here has the following composition (wt. %): C, 0.62 - 0.7; Si, 0.17 – 0.37; Mn, 0.9 – 1.2; P, 0.035; S, 0.035; Cr, 0.25; Ni, 0.25; Cu, 0.2; and Fe, balance [3]

The samples surfaces were carefully mechanically grinded and polished. Before nitridation all samples were cleaned with ethanol and boiled in acetone. Nitridation processes were accomplished using „Usi-Ionic“ equipment. Process was continued 30 min in nitrogen atmosphere (N_2 99.6%) and temperature of samples was approximately 100 ^oC. Direct ion-nitriding was implemented at low-pressure nitrogen gases (0.7 Pa). Six samples were ion-nitrided at three different energies of nitrogen ions: 100, 250, and 400 eV while ions current density was 0.08; 0.15; 0.24 mA/cm^2 respectively.

65G spring steel depth profiling spectra was acquired by “Escalab 250 xi” XPS spectrometer. The profiling was realized using “ESCALAB 250Xi MAGCIS” ion gun [4] where argon (Ar^+) ions energy was 500 eV. The sputtering was done by three difference regime - the sample surface was sputtered 9 times for 5, 10 and 100 second respectively in each regime. Sputter rate for metal oxide and metal was calculated using sputter yield ratio [5, 6]. Atomic concentrations were calculated using software “Fityk” [7]. Results of calculated nitrogen, carbon and oxygen concentrations are represented in Figure 1.

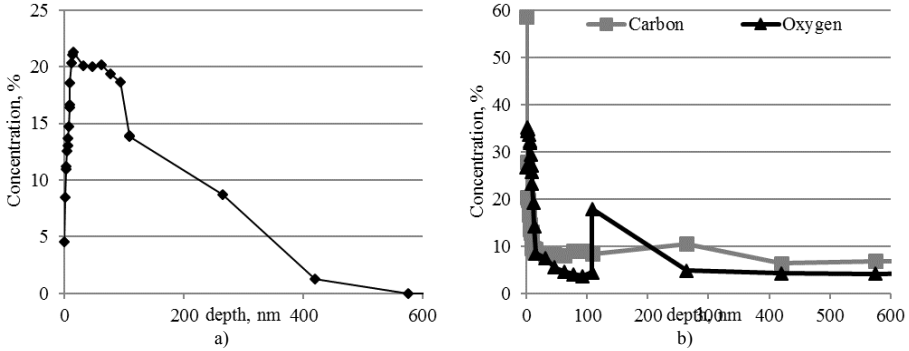

Fig. 1 a) Nitrogen, b) carbon and oxygen concentration dependence of sputtered depth (ion energy 400 eV)

As one can see from this picture, nitrogen penetration depth exceeds 400 nm. Highest value of nitrogen centration was observed at 15 nm depth after 75 s of sputtering. Also there is plateau-type part of the curve were concentration value is approximately 20 %. This plateau-type of curve may be cause of ion-implantation and diffusion influence.

[1] F. ASHRAFIZADEH. Influence of plasma and gas nitriding on fatigue resistance of plain carbon (Ck45) steel – Surf. Coat. Tech.. V173-174. 2003. 1196 – 1200 p.

[2] ALSARAN. A. CELIK. C. CELIK. Determination of the optimum conditions for ion nitriding of AISI 5140steel – Surf. Coat. Tech.. V160. 2002. 219 – 226 p.

[3] http://www.splav.kharkov.com/mat_start.php?name_id=265 manual of steel (status of 2015-01-24)

[4] http://xpssimplified.com/escalab_250xi.php official equipment site. (status of 2015.02.04)

[5] http://www.neyco.fr/pdf/Materials_D_Targets.pdf elements sputter yields (status of 2015.02.04)

[6] G. J. STOKKERS, A. VAN SILFHOUT, G. A. BOOTSMA, T. FRANSEN, P. J. GELING, Interaction of oxygen with an aisi 314 stainless steel surface studied by ellipsometry and auger electron spectroscopy in combination with ion bombardment – Corr. Scien. V 23. 1983. 195 – 204.

[7] http://fityk.nieto.pl/ official software site (status of 2015.02.04)

Photocatalytic properties of nanostructured titanium oxide

Anton Yermalovich[1]

[1] Department of Micro and Nanoelectronics, Belarussian State University of Informatics and Radioelectronics, Minsk, Belarus
anton.yermalovich@gmail.com

The goal of the current paper was to investigate electronic and photacatalyctic processes on the surface of nanostructured titanium oxide. A vast amount of practical and theoretical work done in the field of nanophotonics supports the need for further investigations in the field [1, 2].

The object of the work is a structure based on nanostructured titanium oxide. Today there are several types of nanostructures based on titanium oxide widely used in microelectronics industry: nanostructured titanium films, noble metal nanostructures on a titanium oxide substrate, and composite nanostructures comprised of both titanium oxide and noble metals. A number of practical works supplies data about electronic and optical properties and said materials. But there is no single model that describes and accurately predicts the processes that take place on the surface of the nanosized structures. Developing such model or models will allow designing nanosized devices with required optical and electronic properties.

A model describing processes in nanostructured titania was developed. The model includes quasistatic approximation and accounts for localized damping of surface plasmons. This model allows predicting various properties of nanostructured titanium oxide, namely electric field enchancement near the surface depending from the wavelength of the incident radiation and geometric properties of the material. Absorption and scattering factors where determined, as well as resonance conditions.

The received theoretical data was compared to actual measurements performed on similar structures. Theoretical data exceeds experimental numbers of absorption and scattering factors by about 32% but otherwise the values match quite closely.

Thus the created model can be used for modelling properties of nanostructures based on titanium oxide, but it requires further tuning and it's applicability to other structure types still needs to be explored.

[1] I. D. Mayergoyz, Z. Zhang and G. Miano. Analysis of dynamics of excitation and dephasing of plasmon resonance modes in nanoparticles. Phys. Rev. Lett. **98,** 147401 (2007).

[2] S. Mohapatra, Y. K. Mishra, D. K. Avasthi, D. Kabiraji, J. Ghatak and S. Varma. Synthesis of gold-silicon core-shell nanoparticles with tunable localized surface plasmon resonance. Appl. Phys. Lett. **92** 103105 (2008).

OPTICAL PROPERTIES OF NANOSTRUCTURED FILMS OF InN

Alexander Mudryi [1], Vadim Zhivulko [1], William Schaff [2]

[1]Scientific-Practical Materials Research Centre NAS of Belarus, Republic of Belarus
[2]Department of Electrical and Computer Engineering, Cornell University, USA
vad.zhiv@gmail.com

The InN compounds in comparison with other known AlN, GaN and InN nitride semiconductors with direct-gap energy structure are least studied [1,2].This is caused by the fact that growth of material with qualitative structure and electronic properties is difficult due to passivity of molecular nitrogen relative to metal indium and low temperature stability (~620 – 630º C) of InN compound. In the present study, we investigated the electronic structure of high-quality thin films of nanostructured InN, grown on sapphire substrates by molecular beam epitaxy method. Studies were carried out in a wide temperature range 4.2 – 300 K using various spectroscopic techniques: optical transmittance, reflectance, luminescence and registration of luminescence excitation spectra. According to the optical transmission and reflection measurements it was revealed that the films with the lowest concentration (n-type conductivity), $n_e \sim 3.6 \cdot 10^{17}$ and $5.4 \cdot 10^{17}$ см$^{-3}$, for InN compounds, have band gap at room temperature equal to $E_g \sim 0.624$ eV and $E_g \sim 0.636$ eV, and at 4.2 K – $E_g \sim 0.675$ eV and $E_g \sim 0.679$ eV, respectively (Fig. 1).

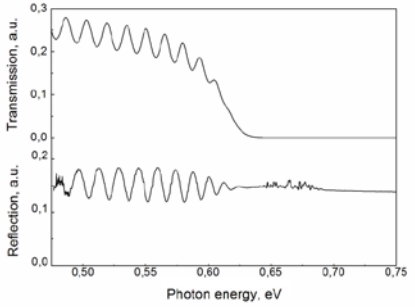

Fig. 1. Transmission and reflection spectra of InN films ($n_e \sim 3.6\ 10^{17}$ cm $^{-3}$) at 300 K.

For the first time in the near-band edge absorption region at cryogenic temperatures in the range of ~ 4.2 – 30 K the fine structure of the bands in photoluminescence spectra has been resolved. Luminescence bands were assigned to certain types of recombination centers formed during molecular beam epitaxial growth of InN thin films. In particular, it is shown that the appearance of two photoluminescence bands in the spectral range of 0.59 – 0.63 eV is related to the existence of two types of acceptor levels in the band gap of InN. The energy levels of the acceptors are determined and possible natures of defects related with these levels are discussed for InN nanostructured films.

[1] V. Yu. Davydov et al., Absorption and emission of hexagonal InN. Evidence of narrow fundamental band gap, Phys. Stat. Sol. (b), **229**, R1 – R3 (2002).
[2] J.Wu, When group-III nitrides go infrared: New properties and perspectives, J. Appl. Phys. **106**, 011101 (2009).

Gas Sensor Using Surface Absorbed Channel Modulated MoS_2 Structure

[1]Shifur Rahman Shakil, [2]Sabbir Ahmed Khan*

[1]School of Engineering and Computer Science, BRAC University, Bangladesh
[2]Department of Physics, Lund University, Sweden
fyk14mk1@student.lu.se

In recent years researchers have been focused on the material used in electronic devices considering on structural, mechanical and electronic properties. Two dimensional (2D) characteristics of Graphene and MoS_2 hence therefore grabbed the attention of scientists and huge numbers of research have been conducted introducing these materials as sensing medium [1]. In this research, the electrical transport characteristics of Molybdenum disulphide (MoS_2) is investigated by using Non Equilibrium Green's Function (NEGF) formalism; the consequences of adsorption effect of NO_2 on pristine, defect and doped MoS_2 (Fig.1) is analyzed over current-voltage (I-V) characteristics, Device Density of States (DDOS) (Fig.2). The strong interaction of NO_2 and doped with transitional metals on MoS_2 is observed vigorously. The electron transport behaviors reveals that in case of designing chemical sensor Fe doped MoS_2 shows higher sensitivity in contrast to pristine-,defect-, Si-MoS_2 . It has been observed in our work that, for detecting gas molecules, MoS_2 can be used as sensing medium and the increment of sensitivity is occurred by introducing appropriate doping.

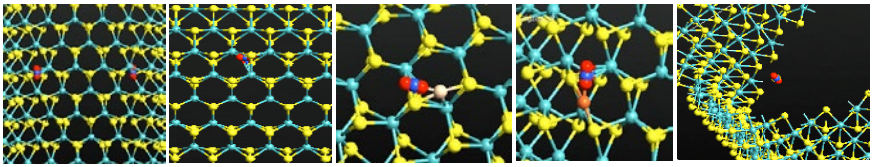

(a) (b) (c) (d) (e)

Figure 1 Different view of the relaxed structures of different adsorption configurations for NO_2/MoS_2 **(a-b),** $NO_2/Si–MoS_2$ **(c)**, $NO_2/Fe–MoS_2$ **(d)**, different position of absorbing gas molecule **(e).**

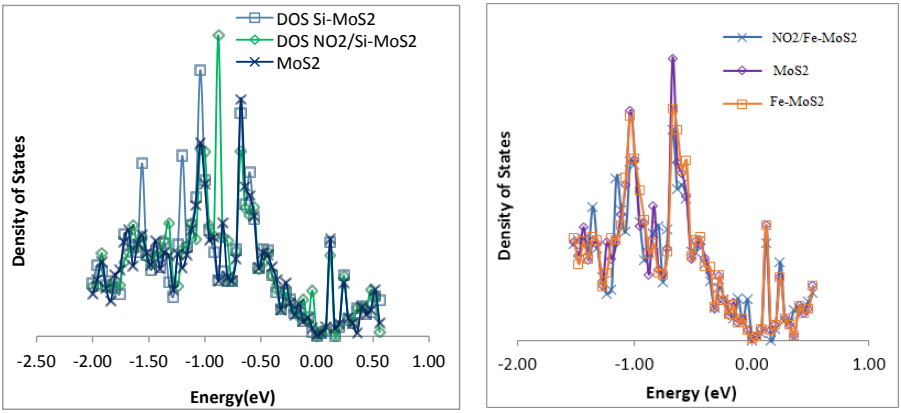

(a) (b)

Fig.2.The spin-up electronic density of states for (a) pristine, Si-MoS_2 and NO_2/Si-MoS_2 (b) pristine, Fe-MoS_2 and NO_2/Fe-MoS_2

[1] H. Wang, L. Yu, Y.H. Lee, Y. Shi, A. Hsu, M.L. Chin, L.J. Li, M. Dubey, J. Kong, T. Palacios, Integrated circuits on bilayer MoS_2 transistors, Nano Lett.**12**, 9(2012)

* This work has been produced during my scholarship period at Lund University, thanks to Swedish Institute (SI.) scholarship.

A Comparative Study of Trade off for FET Materials and their Nano-scale Performance

M. H. Rubel [1], Sabbir Ahmed Khan[2]*, Shifur Rahman Shakil [3], Sheikh Ziauddin Ahmed [4]

[1] Department of Electrical and Computer Engineering, Boise State University, Boise, ID, USA
[2] Department of Physics, Lund University, Sweden
[3]BRACU Robotics, School of Engineering and Computer Science, BRAC University, Bangladesh
[4]School of Engineering and Computer Science, BRAC University, Bangladesh
fyk14mk1@student.lu.se

Over the years, researchers have been focused on FETs considering it as a promising device in the electronics industry as a result much concentration are given on to use different FETs material. Different dominant factors like reduced dimension, device density, switching speed and energy improvements are being considered while fabricating for nano electronic applications. To cope up with the revolution of electronic devices, microprocessor chips have become smaller day by day which suggests to place large numbers of transistor in single chip which results some problems including higher power consumption and heat dissipation. According to our study, we have presented a comparative analysis where we have explained the sequential comparison of using differ material as FETs in nano-electronic applications and their unique characteristics.

Carbon Nanotubes (CNT) are long, thin cylinders of carbon, which were first discovered in 1991 by S. Iijima. They may either consist of a single shell known as single wall nanotube (SWNT) or of several shells called multi wall nanotube (MWNT) [1]. Carbon Nanotube devices can operate in the ballistic regime due to the nanotube's one-dimensional structure, which greatly decreases the scattering probability [2]. But while solving the coupled Schrodinger-Poisson equations within the device cross sections and fully considering for quantum mechanical effects, an experiment was done for 65 to 45 nm technology nodes which showed an unexpected conclusion that for a predetermined threshold voltage, the gate-all-around CNTFET offers only a slightly better performance with respect to fully depleted cylindrical silicon nanowire FETs and four gate rectangular nanowire (4G RNW) FETs. As a consequences of research, Graphene was first explored by A. Geim, K. Novoselov and co-workers when they found the elusive free-standing graphene films [3]. Graphene can be used as superconducting FETs and transparent electrodes [4]. Despite having better mobility than typical silicon material and high –k, the performance of graphene devices can be limited by a critical issue which is poor contact resistance because currently the contact resistance values are in the order of kilo-ohms. Another problem of using graphene as an alternative material to silicon that has been explored is the absence of a bandgap between its conduction and valence band, literally which makes graphene based electronics to achieve low power dissipation in the OFF state [5]. At the end of 20th century, most of the efforts of nanowire devices have been focused on producing nanowire FETs. European research groups have made noteworthy contributions in the area including wrap gated Si [7] and InAs [6] nanowires and they attempted to engineer the bandgap of the channel of the device. It is a problem that the nanowire length and diameter need to be controlled within the much closed limits. When a material having a high dielectric constant serves as a gate dielectrode, nanowire surfaces should be properly passivated by either thermal oxidation or conformal atomic layer deposition [6]. Nowadays researchers have introduced two dimensional (2D) character of Molybdenum Disulfide (MoS_2) like another grapheme material has attracted significant amount of attention due to its unique characteristics.

[1] Franklin,N. R. et al., "Integration of suspended carbon nanotube arrays into electronic devices and electromechanical systems" ,Appl. Phys. Lett. **81**, 913–915 (2002).
[2] Kong, J. et al., Quantum interference and ballistic transmission in nanotube electron wave-guides, Phys. Rev. Lett. **87**, 106801 (2001)
[3] Britnel,L.et al, Field-Effect Tunneling Transistor Based on Vertical Graphene Heterostructures, Science **335,** 947–950(2012)
[4] G. Fiori, G. Iannaccone "Code for the 3D Simulation of Nanoscale Semiconductor Devices, Including Drift-Diffusion and Ballistic Transport in 1D and 2D Subbands, and 3D Tunneling", Journal of Computational Electronics **4**, 63-66 (2005).
[5] B. Obradovic, R. Kotlyar, F. Heinz, P. Matagne, T. Rakshit, M. D. Giles, M. A. Stettler, and D. E. Nikonov, "Analysis of graphene nanoribbons as a channel material for field-effect transistors," Applied Physics Letters **88**, 142101.1-142101.3 (2006).
[6] Bryllert, T.,et al., Vertical High-Mobility Wrap-Gated. InAs Nanowire Transistor, IEEE Electron Device Lett. **27**, 323(2006)
[7] Mårtensson, T.,et al., Epitaxial III-V nanowires on silicon , Nano Lett. **4** (2004)

* This work has been produced during my scholarship period at Lund University, thanks to Swedish Institute (SI.) scholarship.

MAGNETIC PROPERTIES OF TRANSITION-METAL-DOPED ZnO

Maryia Zialenina, Veranika Skachkova, Olga Kozlova

Department of Micro- and Nanoelectronics,
Belarusian State University of Informatics and Radioelectronics, Belarus
veranika.burko@gmail.com

Research have been performed with the aim to detect physical features of properties of ZnO crystals with transition metal impurities. It was carried out via *ab initio* simulation for seeking the conditions and parameters of the optimal technology for creation of the materials with required functional properties for spintronics and sensor devices.

Zinc oxide is the wide-gap semiconductor, which demonstrates properties of high-temperature ferromagnetic both in its pure form and in the presence of magnetic impurities, such as Fe, Co, Ni and Cu. These impurities are the transition elements with incompleted d-orbital.

Computation have been performed using density functional theory (DFT) via the programm complex VASP, which is intended for quantum (QM) and molecular mechanics (MM) simulation.

On the first stage the structure relaxation of the investigated systems have been performed. Zinc oxide super-cell has been constructed. It contains 128 atoms. Some atoms in super-cell were replaced on transition metal atoms (Fe, Co, Ni, Cu).

The second stage is static calculation, where local density approximation was used with Hubbard correction of 7.5 eV for zinc d-orbital and of 2 eV for oxygen p-orbital.

In the case of Ni and Fe, magnetic moment increases monotonically with an increase in the number of introduced atoms. In the case of Co and Cu, value of magnetic moment of super-cell with four introduced atoms is lower than it for super-cell with three introduced atoms. In the case of specified ferromagnetic states, clusters consisting of three and four Cu atoms and of four Co atoms aren't advantageous energetically.

ZnO: Fe (3,13), ZnO: Co (2,34) have the largest magnetic moment (9,5 μB, 8.1 μB for super-cell of 128 atoms) and these systems are the most stable among the studied ones..

During the simulation of the ZnO:Ni(x) systems with different variations of x value it was established that systems are stable at the antiferromagnetic state. Figure 1 is a graph showing the DOS of the system ZnO: Ni (1,56).

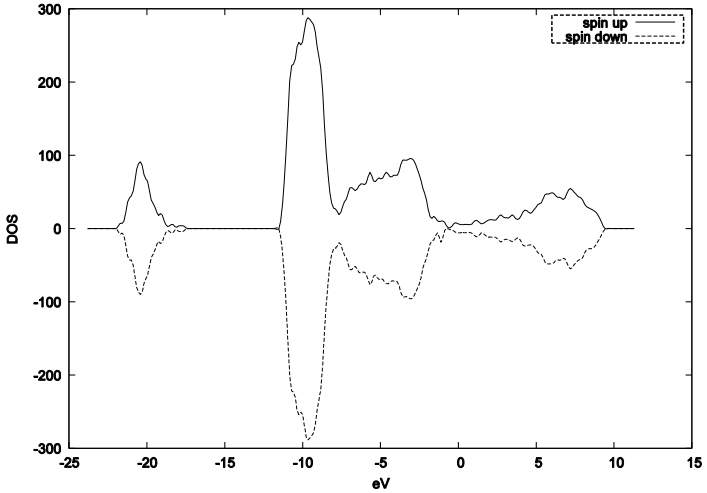

Fig. 1. Electronic density of states of ZnO:Ni(1,56)

It is easy to notice that narrow d - bands are mirrored relatively to the x-axis. A small perturbation in the form of the asymmetry of two curves, is notably on the border of sp-zone. Supposedly this can be associated with the stoichiometry violation during the introducing of the impurity atoms.

[1] Kresse, G.and Joubert, J. From ultrasoft pseudopotentials to the projector augmented-wave method / G. Kresse // Phys. Rev. B - 1999. - Vol.59- P.1758-1765

[2] Kresse, G. VASP the guide: tutorial / G. Kesse // Austria, University of Vienna. – 2003.

Electronics properties of quasi-two-dimensional TiX_2 (X=S, Se) type structures

Olga Kozlova[1]

[1] Department of Micro and Nanoelectronics, Belarussian State University of Informatics and Radioelectronics, Minsk, Belarus
olga.bsuir@gmail.com

The aim of this paper was to investigate quasi-two-dimensional structures based on TiS_2 and $TiSe_2$. Structures were modified by injection of monovacancies and its clusters. It has been studied how the different configuration of the vacancies lead to local structural deformation that were shown on STM pictures [1].

Layered materials of titanium disulfide and diselenide (TiX_2, where X = S, Se) are typical representatives of quasi two-dimensional structures (2D) of 3d — 5d dichalcogenides of transition metals. Due to it layered structure and strong anisotropy of interatomic bonds in TiX_2 it is possible to to create various intercalated and nanostuctured systems. Electronic properties in such systems can depend on the presence of different atomic defects [2].

The super-cell was built for the simulation of the described structures consisted of 6x4 unit cells. 8 main structural defects were investigated: points defects, cluster of the defects, and Frenkel defects (Fig. 1).

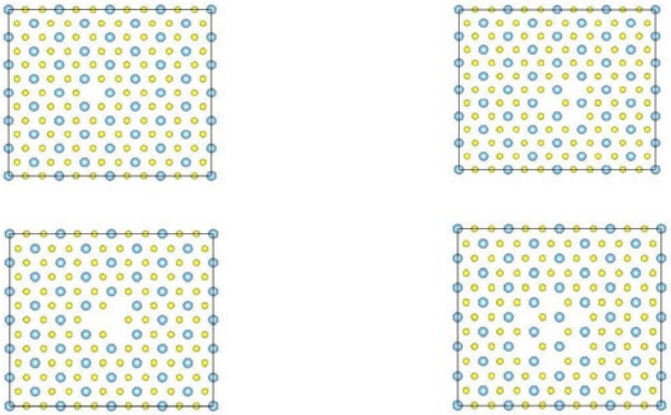

Fig. 1. Quasi-two-dimensional structures of 1T-TiX2 with different defects

Analyzing the calculation data of the investigated structures of TiX_2 the results of vacancies stability, densities of electron states, and band diagrams were calculated. As a result of conducted analysis the values of band gab were obtained. Quasi-two-dimensional structures of 1T-TiX_2 with prismatic coordination of Ti atoms exhibits semiconductor properties with band gap values ranges from 0,12 to 0,15 eV. Further investigation in this area will allow to investigate a deeper level of understanding and explaining of the electronic properties patterns of nanostructured materials.

[1] A. N. Enyashin and A. L. Ivanovskii, Inorgan. Mater., **41**, No. 10, 1118-1123 (2005).
[2] A. N. Enyashin, S. Gemming, and G. Seifert, Eur. Phys. J. ST, **149**, No. 1, 103-125 (2007).

FORMATION OF A NICKEL CONTACT ON POROUS SEMICONDUCTORS BY ELECTROPLATING

Vladimir Agafonov[1], Marius Treideris[1], Arūnas Šetkus[1], Irena Šimkienė[1], Virginijus Bukauskas[1], Audružis Mironas[1], Viktorija Strazdienė[1], Renata Butkutė[1]

[1] Center for Physical Sciences and Technology, A. Goštauto 11, Vilnius LT01108, Lithuania
vladimir.agafonov@ff.stud.vu.lt

One of the main problems in our world is increasing energy demand and exhaustion of non- renewable resources. The key solution is usage of renewable energy source like solar cell. However, solar cells have relatively high price comparing with other energy resources. To drive silicon solar cells for the further competition in the solar cell market the efficiency must be increased and the price decreased. There is a possibility to increase efficiency and lower the price by using 3D solar cell concept [1]. Another approach to reduce solar cell price is to replace front silver contact (silver price increases so the cell price increases) with other front contact like Ni/Cu [2]. In this work, we analyze the electroplated Ni contact on electrochemically etched porous silicon (por-Si) as 3D solar cell matrix.

As it is shown in *fig. 1* main problem in forming contact on por-Si by vapor sputtering is that metal atoms do not fill porous structure inside pores. The advantage of electrolysis is that firstly liquid fills pores with metal ions and then during electrolysis metal can easily cover pores form inside.

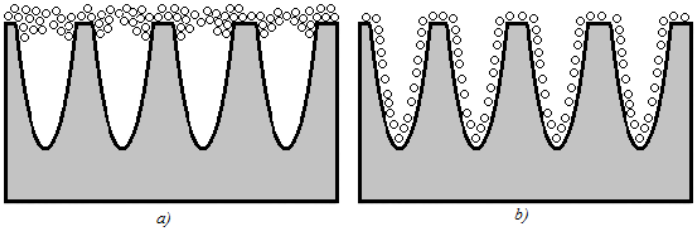

Fig. 1 Metal plated on porous silicon by a) vapor sputtering, b) electroplating

Firstly, the dependence of NiSi formation on annealing temperature was analyzed. Thin nickel layer was by magnetron sputtering deposited on *p* type silicon wafers. NiSi was formed firing wafers in RTA furnace at different temperatures. I-V characteristics of the samples showed that the ohmic contact was formed for samples annealed at 700°C.

Nickel based electrochemical contact formation was investigated on *p* type silicon wafers and por-Si samples. I-V characteristics after depositions showed that all formed contacts were schottky type. Samples were annealed at different temperatures and I-V characteristics were measured again. After annealing nickel layer became adhesive to silicon and contact type of all samples changed to ohmic. After measurement of resistivity, it seems that lowest resistivity is for samples annealed at temperatures between 500 – 600°C. It was noted that ohmic with lowest resistivity contacts are formed at lower annealing temperatures than for contacts formed by magnetron sputtering. This is due the silicon oxide removal from the sample surface during electrochemical Ni deposition.

Acknowledgement

The work was carried out within the project VP1-3.1-ŠMM-08-K-01-009 that is partly supported by the National Program "An improvement of the skills of researchers" launched by the Lithuanian Ministry of Education and Science.

[1] D. Ambrazevicius, G. and Zaicevas, G. and Jasutis, V. and Lescinskas, D. and Lideikis, T. and Simkiene , I. and Gulbinaite, "Layered structure of luminescent porous silicon," *J. Appl. Phys.*, vol. 76, no. 9, pp. 5442–5446, 1994.

[2] J. Kanungo, C. Pramanik, S. Bandopadhyay, U. Gangopadhyay, L. Das, H. Saha, and R. T. T. Gettens, "Improved contacts on a porous silicon layer by electroless nickel plating and copper thickening," *Semicond. Sci. Technol.*, vol. 21, no. 7, p. 964, 2006.

ELECTROCHEMICALLY ETCHED 3D MATRIX FOR SI SOLAR CELLS

Justinas Banelis, Marius Treideris, Irena Šimkienė, Viktorija Strazdienė, Alfonsas Rėza, Andrius Maneikis, Arūnas Šetkus

Center for Physical Sciences and Technology
A. Goštauto 11, Vilnius LT01108, Lithuania tel.: +370-5-2626737
jbanelis@gmail.com

With increasing focus in energy efficiency solutions for the benefit of the environment, solar power is becoming one of the main renewable energy sources. Expected growth in this field to reduce costs and increase efficiency on currently used solar cells requires new technological developments.

Novel possibilities for promising improvements of Si-based solar cells are based on the three-dimensional (3D) solar cell concept with the light trapping on the surface [1]. This concept is promising for the solar cell efficiency increase due to high p-n junction surface. The main objective of this study was to fabricate a porous silicon matrix for 3D solar cell with controllable pore diameter coincident with the visible light wavelength for solar cells and by reduction in this way of reflectance.

The Por-Si was made using standard electrochemical etching setup [2] on a p-type silicon substrate. The electrochemical etching was performed in different ratio of HF and dymethylformamide (DMF) (0.1-1) with the current density 10-40 mA/cm^2 for 1-15 min in the dark. The influence of the intensity of the cell vibration on etching process of por-Si was investigated (Fig. 1). Optical and surface analysis methods were used for the examination of formed porous 3D matrix structural parameters.

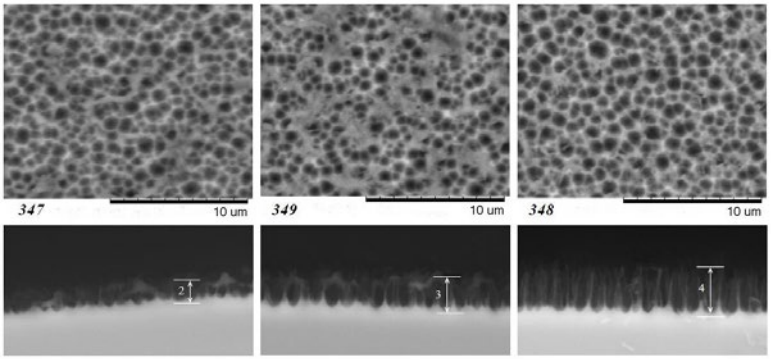

a *b* *c*

Fig. 1. Top and cross-sectional view SEM micrographs of por-Si produced by etching: a) without shaking b) shaking with an ultrasonic bath c) using the vibration generator.

In the structure, the pores were perpendicular to the surface, the diameter was 500-850 nm and depth was 0.5-4 μm. Regardless of the intensity of the cell vibration, the reflection coefficient was evenly spread throughout the visible light wavelength range and its value decreased depending on the depth of the pores. The minimum reflection coefficient of the 3D por-Si structure with pore depth ~ 4 μm and the pore diameter (750 - 850) nm reaches ~ 8.2% (reflectance reduced by 75% compared to bulk Si).

Acknowledgement

The work was carried out within the project VP1-3.1-ŠMM-08-K-01-009 that is partly supported by the National Programme "An improvement of the skills of researchers" launched by the Lithuanian Ministry of Education and Science.

[1] A. Setkus, I. Šimkiene, M. Treideris, V. Bukauskas, A. Reza, A Nano-Hole Array Based 3D C-Si Solar Cell with Enhanced Light Conversion Characteristics, 28th European Photovoltaic Solar Energy Conference and Exhibition Proceedings, 312 – 315, 2013, doi:10.4229/28thEUPVSEC2013-1AV.2.20.
[2] I. Šimkienė, Porous dielectric and semiconductor films in nanotechnology, Lithuanian J. Phys, 2003, 43.5: 319-334.

Cr^{3+} DOPED ITRIUM AND GALLIUM GARNET PHOSPHOR FOR PHOSPHOR-CONVERSION LIGHT EMITTING DIODES

Henrikas Dapkus,[1,*] Akvilė Zabiliūtė-Karaliūnė,[1] Rokas Paulius Petrauskas,[2] Skirmantė Butkutė,[2] Artūras Žukauskas,[1] and Aivaras Kareiva[2]

[1] Institute of Applied Research, Vilnius University, Lithuania

[2] Department of General and Inorganic Chemistry, Vilnius University, Lithuania

*Corresponding author: *henrikas.dapkus@ff.vu.lt*

Plant cultivation in greenhouses with artificial lighting is an important technology. Nowadays high pressure sodium, metal halide and fluorescent lamps are mostly used for this application. However, solid state lighting allows achieving higher productivity and nutritional quality due to the reason that the spectral power distribution (SPD) of LEDs can be modified and chosen to meet the physiological needs of plants. There are three main photophysiological processes in plants: phototrophy photosynthesis and photomorphogenesis that require blue (400-500 nm), red (620-680 nm) and far-red (700-760 nm) light respectively [1]. Blue and red components can be provided by a high quality InGaN and AlGaInP LEDs respectively. However, AlGaAs LEDs that emit light in a far-red spectral range, degrade fast, are sensitive to humidity and temperature variations [2]. A solution to this problem could be a phosphor converted LED (pcLED) composed of a blue InGaN LED and a far-red phosphor converter, for example $Y_3Ga_5O_{12}:Cr^{3+}$ (YGG:Cr) [3].

In this work, using an YGG:Cr phosphor described in ref. 3 and a blue InGaN LED a solid state lamp for greenhouse lighting was designed and its spectral properties were measured. Furthermore, the morphological: x-ray diffraction (XRD), scanning electron microscopy (SEM), and luminescent properties: diffuse reflection, photoluminescence (PL), PL excitation (PLE), and PL quantum efficiency (QE) of YGG:Cr phosphor tablets, annealed at different temperatures (1000 °C-1400 °C) were measured.

The converter of the designed far-red lamp was made of YGG phosphor powder doped with 8 mol% Cr^{3+} and annealed at 1300 °C temperature and transparent silicone. The composition of the converter and the spectral properties of the lamp are given in table 1. The SPD of the pcLED is given in Fig. 1. The designed far-red lamp prototype was transferred to "Institute of Horticulture Lithuanian Research Centre for Agriculture and Forestry" for further research on the plant growth in greenhouses.

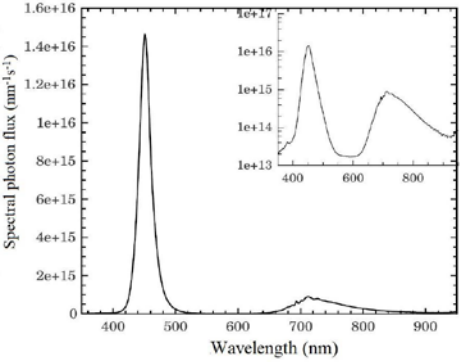

Fig. 1. Spectral power distribution of lamp prototype.

Table 1. Spectral properties of the lamp.

	Photon flux (I = 350 mA)
Concentration of YGG:Cr powder in the silicone converter	5.7 wt%
Blue LED without lens	2.2489 μmol/s
Blue LED with lens	2.2074 μmol/s
Blue LED covered with a converter	0.6361 μmol/s
Phosphor PL	0.1367 μmol/s
The Sum of blue LED and phosphor PL in the lamp	0.7728 μmol/s
Converter efficiency	35%

The XRD spectra of tablets confirmed that the structure of YGG:Cr is garnet. SEM images clearly show that higher annealing temperatures increase the uniformity of the samples. Moreover, it is observed that for higher annealing temperatures a crystal structure of phosphor particles are more pronounced. The measurements of the diffuse reflection showed absorption in the regions of 400-520 nm and 580-680 nm, which matched well with the PLE spectra that peaked around 420 nm and 600 nm. The PL spectra of the tablets showed a broad band in a far-red region that peaked around 700 nm. The measurements of QE showed that pressing YGG:Cr phosphor powder to tablets can significantly increase the efficiency of phosphors. The highest obtained value of QE was 55% for YGG phosphor tablet doped with 8 mol% Cr and annealed at 1300 °C temperature.

[1] M. S. McDonald, Photobiology of Higher Plants (Wiley, 2003).

[2] G. Tamulaitis, P. Duchovskis, Z. Bliznikas, K. Breivė, R. Ulinskaitė, A. Brazaitytė, A. Novičkovas, and A. Žukauskas, "High-power light-emitting diode based facility for plant cultivation",J. Phys. D: Appl. Phys. 38, 3182–3187 (2005).

[3] A. Zabiliūtė, S. Butkutė, A. Žukauskas, P. Vitta, A. Kareiva, *Appl. Opt.* 2014, Vol. 53, 907-914.

Improving charge carriers' mobility in MEH-PPV by affecting inner structure with external electric field

Romualdas Dargužis[1], Andrius Aukštuolis[1]

[1]Department of Solid State Electronics, Vilnius University, Vilnius, Lithuania
ramiux.dar@gmail.com

Organic materials, especially conjugated polymers are getting a lot of attention in the field of electronics. Conjugated polymers enable us to make flexible and transparent coatings, make it possible to integrate them into textile, in fact there are so many variations of them that they can be applied in most electronic devices. OLEDs (organic light emitting diodes) are being already widely made for such devices as TV's or mobile phones, but to make efficient solar cells or OFETs (organic field effect transistors) there are still ways to go. One of the possibilities is to somehow alter the inner structure of the formed film in order to improve charge carriers mobility.

Strong perpendicular electric field is applied on undoped MEH-PPV (Poly[2-methoxy-5-(2-ethylhexyloxy)-1,4-phenylenevinylene])) polymer film during the process of evaporation of the solvent. Applied external electric field causes MEH-PPV polymer chains to orient. As the result, the improvement in holes mobility is obtained.

MEH-PPV were dissolved in toluene, the solution dropped on ITO plate, which then was held in glove box under electric fields of 9.5 x 10^3 V cm^{-1} and stronger. To measure holes mobility, TOF (time of flight) [1] and photo – CELIV (photogenerated charge carriers extraction by linearly increasing voltage) [2] methods were used. Results showed that films of about the same thickness differ in holes mobility, which was 1.3 – 3 times larger in films with applied electric field. It is known that the position of the current maximum depends on charge carriers mobility as $\mu \sim t^{-2}$ when using photo-CELIV method. So improvement in holes mobility can be clearly seen from the shift of current maximum position in Fig. 1.

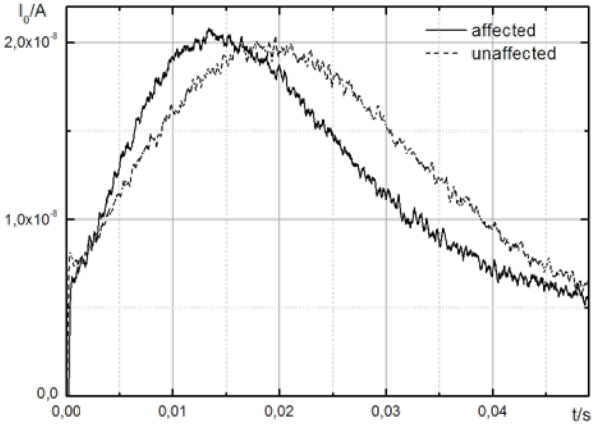

Fig. 1. Current transients measured using photo-CELIV method. Affected – current transient of film affected by external electric field, unaffected - current transient of unaffected film.

[1] M. Weis, J. Lin, D. Taguchi, T. Manaka, M. Iwamot. Analysis of Transient Currents in Organic Field Effect Transistor: The Time-of-Flight American Chemical Society, Japan (2009).
[2] G. Juška, N. Nekrašas, V.Valentinavičius, P. Meredith, A.Pivrikas. Extraction of photogenerated charge carriers by linearly increasing voltage in the case of Langevin recombination, Physical review, Vilnius University, Vilnius, Lithuania (2011).

MOCVD GaN BASED CAPACITOR-TYPE RADIATION DETECTOR

Arnoldas Jasiūnas, Eugenijus Gaubas, Tomas Čeponis, Dovilė Meškauskaitė, Jevgenij Pavlov

Vilnius University, Institute of Applied Research, Vilnius LT-10222, Lithuania
arnoldas.jasiunas@ff.stud.vu.lt

A variety of the wide band-gap semiconductors, for example GaN, are promising materials in design and fabrication of radiation tolerant particle detectors. The applicability of these materials is grounded on their low leakage currents, effective pair production of secondary charge carriers and radiation hardness [1-2]. Crystalline GaN layers show additionally the rather efficient luminescence properties under the impact of the high energy particle beams. Moreover, it can be also employed not only as scintillating, but also as a charge collecting device [3]. Although efficient GaN p-n junctions are still a pursued objective, the capacitor-type detectors made of the homo-epitaxial GaN layers can already be implemented.

In this work, the tentative capacitor- type device has been manufactured using a 25 μm thick GaN nitride epi-layers grown by MOCVD method on a sapphire substrate (Fig. 1 a). In order to make a capacitor-type device structure, the as-grown layer was plasma etched in three sub-sequential steps using a mask to expose a local sample area to plasma etching. Electrodes were formed by metallization on these etched (three separate) contact spots (marked „1“, „2“ and „3“). Barrier evaluation by linearly increasing voltage (BELIV) technique [4] and C-V characterization have been employed in order to evaluate the electrical characteristics of the structure and the influence of the contacts to the overall performance of the device. The role of the additional background illumination has been investigated using a UV source.

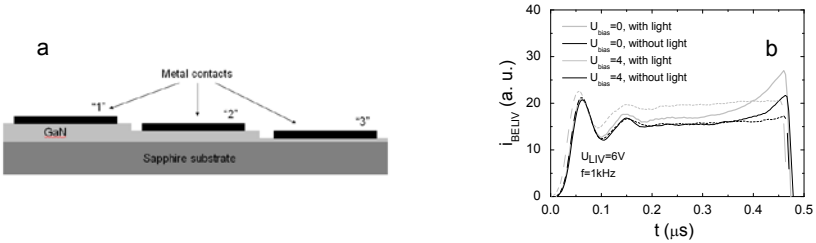

Fig. 1. a-A scheme of the device structure. b -BELIV current transients recorded with/without cw illumination and using different dc, pedestal biasing voltages.

Fig. 1b illustrates the typical responses of the capacitor charging currents under the linearly increasing voltage pulse. As can be deduced from figure 1b, the character of the BELIV transient is dependent on the applied pulsed and dc voltages (U_{LIV}, U_{bias}) and on the additional cw illumination. The square-wave shape BELIV transient i_{BELIV}, inherent for the capacitor-type device under a single LIV pulse with rearward generation current component, is observed. The initial square-wave component of the BELIV transient is specific for the GaN capacitor. The background UV illumination leads to the increase of both current components within transient, determined by increase of the capacitance of the structure due to the injected charge and that caused by thermal emission via de-trapping from deep levels. This effect proves the possibility to detect the injected charge and temporal variations due to carrier drift and trapping, and functionality of the capacitor-type sensor. The impact of thermal emission current can be modified by dc voltage pedestal combined with a pulsed LIV voltage. Thereby, operational characteristics of the sensor and its sensitivity relative to carrier drift signal can be externally manipulated. In summary, the functionality of the capacitor-type sensor made of the MOCVD GaN has been demonstrated. The results of the comparative study of the GaN detector capacitance-voltage (pulsed and dc) and the capacitance-frequency (for harmonic test signals) characteristics will be presented and discussed.

[1] E. Gaubas, S. Jursenas, R. Tomasiunas, J. Vaitkus, A. Zukauskas, A. Blue, M. Rahman ir K. M. Smith, Nucl. Instrum. Methods in Phys. Res. A **546**, 247 (2005).
[2] P. J. Sellin ir J. Vaitkus, Nucl. Instrum. Methods Phys. Res. A **557**, 479 (2006).
[3] E. Gaubas, T. Ceponis, A. Jasiunas, V. Kovalevskij, D. Meskauskaite, J. Pavlov, V. Remeikis, A. Tekorius ir J. Vaitkus, Applied Phys. Lett. **104**, 062104 (2014).
[4] E. Gaubas, T. Ceponis, S. Sakalauskas, A. Uleckas ir A. Velicka, Lihuanian Journal of Physics, **51**, No. 3, 230-236 (2011).

OPTIMIZATION OF DRY ETCHING PROCESS FOR BLACK SILICON FABRICATION

Morta Marcinkutė[1], Armandas Balčytis[1,2], Ignas Reklaitis[1]

[1] Institute of Applied Research, Vilnius University, Lithuania
[2] Center for microphotonics Swinburne university of technology, Australia
morta.marcinkute@gmail.com

Black silicon (b–Si) can be described as a semiconductor material which surface is covered with huge amount of densely stacked silicon nano-needles. Black silicon has high absorption of visible light and respectively very low reflectance [1]. This material has wide application – from bacteriological researches [2] to optoelectronic industry [3].

The aim of this research was to optimize technological parameters of reactive ion etching (RIE) process for black silicon fabrication. Optimization was executed in several stages. At first, series of samples were manufactured using dry etching process by adjusting lower electrode's temperature and flow of heat transferring helium gasses in to the etching chamber. Secondly, measurements of an optical reflection spectrum where made for each of the samples (for example Fig. 1), to reveal how optical properties is being influenced by alternating process parameters. Finally, samples were characterized using electrons scanning microscope (SEM) at Swinburne University of technology in Australia (for example Fig. 2), to assess how sample's optical properties is distinguished by nano-needles length and density. After systemizing results of the research a control sample was etched and optically characterized.

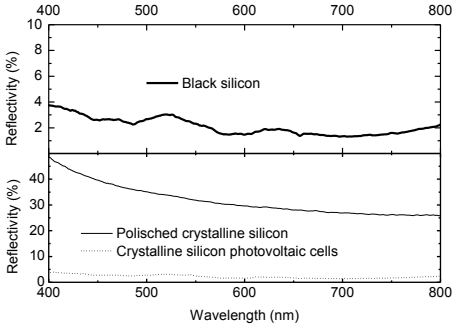

Fig. 1. Reflectance spectra of one of the black silicon sample (upper part) and reflectance spectrum of polished crystalline silicon and micro-pyramid patterned crystalline silicon photo-voltaic cell as a reference (lower part).

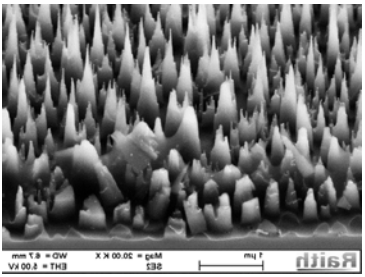

Fig. 2. SEM micrograph of one of the sample fabricated, showing surface covered by nano-needles.

Results of the research will be adduced during the presentation.

[1] Z. Cheng, Electrical properties of Black Silicon, Proc. of SPIE **8419**, 18 (2012).
[2] E. Ivanova, Bactericidal activity of black silicon, Nature Communications **4**, 2838 (2013).
[3] X. Liu, Black silicon: fabrication methods, properties and solar energy applications, Energy and Environmental Science **7**, 3223 (2014).

MIRRORLESS LASING IN BENZOFLUORENE COMPOUNDS

Edvinas Radiunas, Gediminas Kreiza, Ona Adomėnienė, Povilas Adomėnas, Karolis Kazlauskas

Institute of Applied Research, Vilnius University, Lithuania
eradiunas@gmail.com

The demonstration of stimulated emission in conjugated polymers and low-molecular-weight compounds makes these materials promising as high gain media for solid-state lasers [1–3]. To date, optically pumped lasers based on conjugated organic materials have been demonstrated in both solution and thin films. With continuous efforts in pursuing electrically pumped organic lasing, luminescent organic semiconductors with improved characteristics, such as lower thresholds of stimulated emission, enhanced carrier mobility, and further improved thermal stability are constantly desired. Organic lasers can be potentially compact and ready for integration with other optoelectronic devices since amorphous films permit deposition on a variety of substrates. Broad gain spectra accompanied by the numerous choice of organic lasing materials offer wide emission-wavelength tunability across the entire visible range. Another great advantage of organic lasers is negligible temperature dependence of stimulated emission threshold, output power and emission wavelength [3], which is a result of molecular origin of the electronic transitions, i.e., strongly localized excited states (excitons), involved in light emission. Such organic laser sources may eventually compete with inorganic semiconductor lasers in a number of fields, *e.g.*, spectroscopy, optical data communication, memory, sensing and displays [3].

The current work focuses on the investigation of benzo[c]fluorene class of compounds (see Fig. 1) and their suitability as gain media. The measurements of amplified spontaneous emission (ASE), a type of mirrorless lasing, for a series of benzofluorene derivatives possessing different peripheral moieties were performed in dilute tetrahydrofuran (THF) solutions and polystyrene matrix at different compound concentrations (0.5-100 wt%). Polystyrene films were prepared by spin-coating technique on glass substrates. ASE measurements were carried out in the edge configuration, *i.e.*, a cylindrical lens was employed to focus the excitation beam into a thin stripe with dimensions of $0.04\times12\ mm^2$ onto the sample near its edge, whereas the amplified emission were collected from the sample edge (in the direction perpendicular to the excitation beam). The emission spectra were measured as a function of the pumping intensity by using an optical fiber, which was coupled to a CCD spectrometer. The additional optical techniques such as absorption and fluorescence spectroscopy, fluorescence quantum yield (Φ_F) and fluorescence lifetime were employed to reveal the structure-property relationship of the compounds.

Concentration quenching measurements of all the benzofluorenes revealed very low quenching of Φ_F with increasing compound concentration in polystyrene matrix. An increase of the concentration from 0.5% to 100% resulted in a less than 2-fold drop of Φ_F (roughly from 75% to 45%) and of fluorescence lifetime (roughly from 1.5 to 1.0 ns). Estimated radiative relaxation rate was up to $0.7\times10^9 s^{-1}$, which is considered as high and promising for lasing materials. ASE threshold as a function of compound concentration for the studied benzofluorenes is shown in Fig. 2. Importantly, some of the benzofuorenes demonstrated the lowest threshold (down to 900 W/cm^2) in the neat films. This value is considered as one of the lowest ASE threshold values up to date achieved in the neat films.

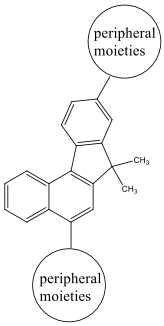

Fig. 1. General chemical structure of the studied benzo[c]fluorene compounds

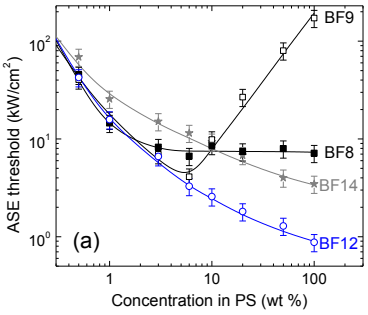

Fig. 2. Amplified spontaneous emission threshold dependence on compound concentration in polystyrene matrix.

[1] F. Hide, M. A. Díaz-García, B. J. Schwartz, M. R. Andersson, Q. Pei, A. J. Heeger, *Science* **1996**, *273*, 1833.
[2] G. Kranzelbinder, G. Leising, *Rep. Prog. Phys.* **2000**, *63*, 729.
[3] I. D. W. Samuel, G. A. Turnbull, *Chem. Rev.* **2007**, *107*, 1272.

Ga+ RESISTLESS LITHOGRAPHY ON Si

Ignas Reklaitis[1], Armandas Balčytis[1,2]

[1] Institute of Applied Research, Vilnius University, Lithuania
[2] Center for microphotonicsSwinburne university of technology, Australia
ignas.reklaitis@gmail.com

A direct writing lithography technique, via Ga+ ion implantation into the surface of silicon sample, is proposed. Ion implantation is carried out using focused ion beam (FIB) irradiation and subsequent etching is done by an inductively coupled plasma reactive ion etching (ICP-RIE) (SF_6 and O_2 based plasma). While FIB offers patterning capabilities with sub-micron resolution and ICP-RIE produces highly anisotropic etching profile with high selectivity between ion irradiated and non-irradiated silicon [1], planar (2D) microstructures can be fabricated. The linear selectivity versus implanted Ga density and FIB grayscale micromachining ability enables creation of spatial (3D) structures,which will be shown during presentation.This resistless lithography approach is shown to be suitable for micro electro mechanical systems (MEMS) fabrication.Finally, the removal of masking layer with implanted gallium ions is presented, as well.

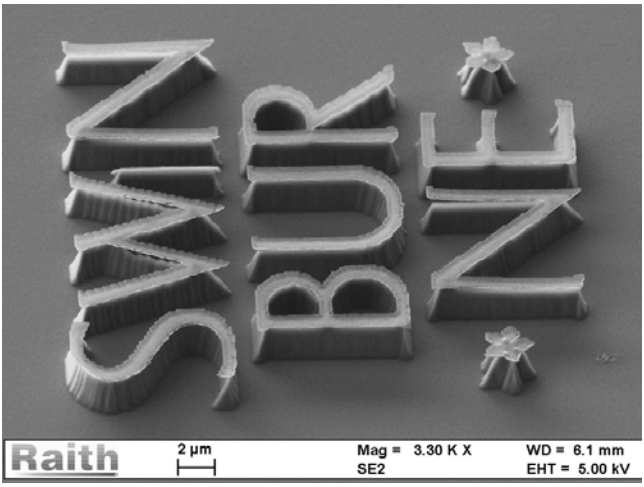

Fig. 1.Example of planar structure fabricated using Ga+ resistless lithography.

[1] MDHenry, Ga+ beam lithography for nanoscalesilicon reactive ion etching, Nanotechnology **21**, 245303 (2010)

HIGHLY SELECTIVE FLUORESCENT METAL SENSOR BASED ON 1,8-NAPHTHALIMIDE DERIVATIVE

Rokas Skaisgiris, Saulius Juršėnas

Institute of Applied Research, Vilnius University, Saulėtekio 9-III, LT-10222 Vilnius, Lithuania
rokas.skaisgiris@ff.stud.vu.lt

Mercury ions (Hg^{2+}) are one of the most hazardous environmental pollutants because they can be bioaccumulated through the food chain and cause great damage to the nervous system even in low concentrations [1]. Due to its specific properties it is widely used in industry where pollution is sometimes inevitable. Another transitional metal ion that is important to human health is iron (Fe^{2+}) which is abundant in mammals. The lack of iron can result in anemia, hemochromatosis, liver damage, diabetes and cancer, while the excess of iron can induce several serious diseases, such as Alzheimer's, Huntington's and Parkinson's diseases [2]. Therefore it is important to sense Hg^{2+} and Fe^{2+} in environment and living organisms. High sensitivity, rapid response, low cost and easy operation makes fluorescence sensors exceptional in this field. Naphthalimide derivatives have gained increasing interest as fluorescent probes for metal ions because of their unusual photophysical properties [3].

In this paper we investigated photophysical properties of 4-(4-dimethylaminophenyl)-N-(2-ethylhexyl)-1,8-naphthalimide (NI) in the absence and in the presence of the salts of several transition metal ions. The naphthalimide derivative was synthesized by prof. J. V. Gražulevičius group at Kaunas University of Technology (KTU).

The UV-vis absorption spectra of NI in tetrahydrofuran (THF) solution (4×10^{-6} M) were investigated in the presence of transitional metal ions Mn^{2+}, Fe^{2+}, Co^{2+}, Ni^{2+}, Cu^{2+}, Zn^{2+}, Zr^{4+}, Hg^{2+}, Pb^{2+} (Fig. 1. a). With none cations the absorption spectrum exhibits large peak at 423 nm which is typical for charge transfer (CT) state and a small peak at 345 nm typical for 1,8-naphthalimide. Addition of mercury or iron ions to the solution led to some drastic changes of absorption spectrum while other transitional metals did not influenced it. Complexation of Hg^{2+} or Fe^{2+} ions with NI led to quenching of CT state absorption (423 nm) and enchantment of 1,8-naphthalimde absorption (345 nm) therefore leading to visible color change of the solution.

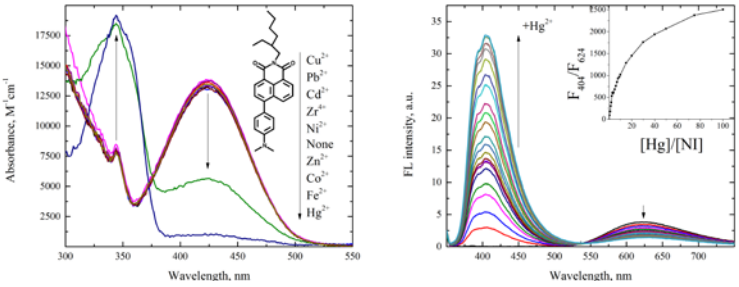

Fig. 1. (a) Absorption spectra of 4-(4-dimethylaminophenyl)-N-(2-ethylhexyl)-1,8-naphthalimide in THF solution (concentration 4×10^{-6} M) with different metal ions present (concentration of metals is 4×10^{-5} M). (b) Fluorescence spectra of NI in THF solution ($C = 4 \times 10^{-6}$ M) with different concentrations of mercury ions present. Concentration of Hg^{2+} is increased from 0 to 4×10^{-4} M. Inset graph represents the proportion of fluorescence intensities at 404 nm and 624 nm with the proportion of metal ion and naphthalimide derivative concentrations.

Further we investigated fluorescence spectra of NI without and with the presence of metal ions in THF solution when exciting at 345 nm. The obtained data revealed CT state fluoresce peak at 623 nm and a small peak typical for 1,8-napthalimide at 404 nm. The introduction of transitional metals to solution again showed that NI reacts only with iron and mercury ions hence quenching CT fluorescence and enchanting locally excited state fluorescence up to 1000 times. When increasing the concentration of metal ion gradually, the fluorescence is enchanted coherently (Fig. 1. b) thus giving a linear sensitivity to concentration of ions in range from 0.5 to 10 equivalents of NI concentration.

The results show that 4-(4-dimethylaminophenyl)-N-(2-ethylhexyl)-1,8-naphthalimide is very sensitive to iron and mercury ions and therefore can be used as highly selective sensor of these ions.

[1] J. B. Nevado, R. R. Martin-Doimeadio, M. J. Moreno, J. M. do Nascimento, A. Herculano, M. Crespo-Lopez, Mercury speciation analysis on cell lines of the human central nervous system to explain genotoxic effects, Microchemical Journal, **93**, 12 - 16 (2009).
[2] W. Le, Role of iron in UPS impairment model of Parkinson's disease Parkinsonism & Related Disorders, **20**, S158 - S161 (2014).
[3] J.-H. Xu, Y.-M. Hou, Q.-J. Mab, X.-F. Wub, X.-J. Wei, A highly selective fluorescent sensor for Fe^{3+} based on covalently immobilized derivative of naphthalimide, Spectrochim. Acta A: Mol. Biomol. Spectrosc. **112**, 116-124 (2013).

EVALUATION OF ANISOTROPIC InP AND Si ETCHING POSSIBILITIES FOR THE FABRICATION OF THE DIFFRACTIVE THz PHOTONIC COMPONENTS

Andrius Vaitkūnas[1, 2], Linas Minkevičius[1, 2], Vincas Tamošiūnas[1, 2]

[1] Center of Physical Sciences and Technology, A. Goštauto 11, LT-01108 Vilnius, Lithuania
[2] Vilnius University Faculty of Physics, Saulėtekio al. 9, bldg. III, LT-10222 Vilnius, Lithuania
andrius.vaitkunas@ff.stud.vu.lt

Terahertz (THz) radiation is a frequency range between microwave and far infrared of the electromagnetic radiation spectrum. Properties of THz radiation (non-ionizing radiation, characteristic material spectral lines, propagation through materials which are opaque for other frequency ranges) make it relevant for material science, security systems and medical applications. For the purpose of implementing compact THz imaging systems there is a necessity of compact passive optical elements [1]. The problem of manipulation of THz radiation can be solved by using refractive (mirrors, lenses) or diffractive (Fresnel zone plates) optics. Since zone plates have a flat surface, it is simplier to construct compact systems based on them in comparison to conventional lenses with added advantages of reduced weight.

In this work, properties of phase-changing Fresnel zone plates (FZP) were simulated numerically for 0,6 THz frequency. It was assumed that the zone plates were formed on Si and InP substrates by anisotropic etching. Finite-difference time-domain simulations were run using MIT Meep software to predict properties of the grooved zone plates and compare them with the conventional (metalized) zone plates. Our simulations predict a nearly twofold increase of the electric field amplitude in the focal point in case of phase-changing plates (Fig. 1). In addition, anisotropic chemical wet etching was employed to evaluate possibilities to obtain structures required for creating simulated zone plates. InP samples were etched in HCl and H3PO4/HCl acid solutions [2]. After the experiment the etching profiles were investigated with optical and scanning electron microscopes (Fig. 2).

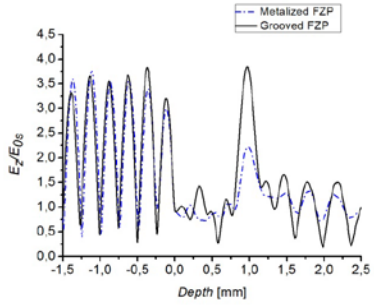

Fig. 1. Distribution of normalized electric field amplitudes for simulated FZP.

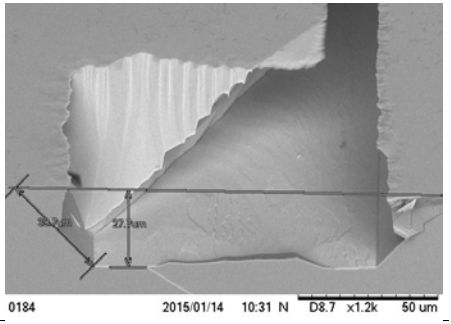

Fig. 2. SEM image of InP sample anisotropically etched in H_3PO_4/HCl solution. Sample is rotated 45° in respect to the sample surface.

In conclusion, the results of simulations have showed better focusing properties for the grooved zone plates in contrast to metalized ones. Results of anisotropic wet chemical etching confirm the possibility of obtaining the required structures and depths of the order of tens of microns.

Andrius Vaitkūnas acknowledge support by project "Promotion of Student Scientific Activities" (VP1-3.1-ŠMM-01-V-02-003) from the Research Council of Lithuania. This project is funded by the Republic of Lithuania and European Social Fund under the 2007-2013 Human Resources Development Operational Programme's priority 3.

[1] Minkevičius, L., et al. "Terahertz zone plates with integrated laser-ablated bandpass filters." *Electronics Letters* 49.1 (2013): 49-50.

[2] Eliáš, P., et al. "Wet-etch bulk micromachining of (100) InP substrates."*Journal of Micromechanics and Microengineering* 14.8 (2004): 1205.

ION TRACK ETCHING THRESHOLDS FOR CREATION POROUS *a*-SiO_2

Dzmitry Yakimchuk, Egor Kaniukov

Scientific-Practical Materials Reseach Center of NAS of Belarus, Belarus
yakimchuk.dima.nas@gmail.com

In the last years a large interest to investigations of various nanosized objects has been developed in concern with their exhibition of interesting characteristic properties, being indistinctive for materials with macro- and microscopic properties. The most simple and logical method of a creation of nanomaterials is the use of nanoporous matrices (templates), as natural conditions of self-organization of nanosized objects are realized in the pores. Using of the pores makes it possible to obtain nanoparticles and nanofibres of semiconductors [1], metals [2], multilayers of metals [3], etc. Some structures of this kind possess a sensitivity to light, humidity, organic substances, and could be used as sensors [4]. Depending on the nature of the material placed in pores, the obtained nanostructures could be used for a construction of resistors, capacitors, diodes and inductors [5]. At present, porous Al_2O_3, TiO_2, polycarbonate and polyimide membranes are used for a creation of nano-objects [6, 7]. Still, from the point of view of an implementation of nanosystems on the base of silicon in modern technological processes, most prospective are the use of templates on the base of silicon oxide. Pores in *a*-SiO_2 layer can be obtained with the implementation of the swift heavy ion (SHI) track technology, which includes irradiation with the SHIs and chemical etching [8].

The process of chemical etching in solutions of hydrofluoric acid of swift heavy ion tracks in *a*-SiO_2 depends on the energy of electronic loss $(dE/dx)_e$ and has a threshold character. At the $(dE/dx)_e$ value less than 1.5 keV · nm^{-1}, pores formation is impossible. At the $(dE/dx)_e$ values in the range ~ 1.5 – 4 keV · nm^{-1} the etching process is possible, but obtained pores are characterized by various diameters and angles of the etching cone, as well as by a not high etching efficiency (not all the ion tracks are transformed into pores). The energy value of about 4 keV · nm^{-1} is a necessary condition for the obtaining of pores with a uniform distribution of forms and dimensions with the etching efficiency ~ 100 %. At the electronic loss energies of more than 4 keV · nm^{-1}, the pore diameters depend on the $(dE/dx)_e$ value and their sizes increase with the rise of this loss at the same etching conditions [9].

We have given a proposition that at large energy loss energies (> 15 keV · nm^{-1}) pore diameters will not depend on the $(dE/dx)_e$ value at the same etching conditions. This assumption could be justified on the base of the following arguments. The transfer of energy of the bombarding ion to the lattice by means of the equilibrium thermodynamic processes takes place in nanoscopic scales during particularly short period of time. Since the temperature equilibrium is achieved after the ten atomic collisions during the time period 10^{-13} s, the local temperature equilibrium at such a high temperatures and short time scales can take place only in the limit of 0.5 nm. As the energy can propagate on small distances, first a melting and evaporation of material inside the ion track, and only then its diameter will increase. It should be noted that an absence of the dependence of the pore diameter on the electron energy loss at $(dE/dx)_e$> 15 keV/nm has been noted as well in the work [9].

A systematic investigation of results of the ion track etching in the *a*-SiO_2 layer, obtained at the irradiation by ^{132}Xe, ^{152}Sm, ^{197}Au and ^{238}U ions with $(dE/dx)_e$ values in the range from 16 to 23 keV · nm^{-1} has made it possible to introduce the new threshold value $(dE/dx)_e$ > 15 keV · nm^{-1}. With that the pore diameters have a constant size independently on the value of electronic loss energy. Results of the present investigation make it possible to forecast obtaining of the *a*-SiO_2-based porous templates with a pre-determined geometrical parameters, independently of the irradiating ion with a high precision.

[1] D. Xu, Y. Xu, D. Chen et al., Preparation of CdS single-crystal nanowires by electrochemically induced deposition, Adv. Mater. **12** №7, 520-522 (2000).
[2] V. A. Sivakov, E. Yu. Kanukov, J. Mühlenstädt et al., Silver nanostructures formation using swift heavy ion track technology, J. Cryst. Growth **400**, 21-26 (2014).
[3] L. Sun, Y. Hao, C. L. Chien et al., Tuning the properties of magnetic nanowires, J. Res. Dev. **49**, 1-5 (2005).
[4] S.E.Demyanov, E.Yu.Kaniukov, A.V.Petrov et al., Positive magnetoresistance in Si/SiO_2/(Cu/Ni) structures, Sens. Actuat. A **216**, 1-5 (2014).
[5] D.Fink, P.S.Alegaonkar, A.V.Petrov et al., High Energy Ion Beam Irradiation of Polymers for Electronic Applications, NIMB **236**,11-20 (2005).
[6] Y. Liu, J. Goebl, Y. Yin, Chem. Soc. Rev., **42**, 2610-2653 (2013).
[7] C.R. Martin, Nanomaterials: A Membrane-Based Synthetic Approach, Science 266, 1961-1966 (1994).
[8] D. Fink, *Fundamentals of Ion-Irradiated Polymers* (Springer Series in Materials Science, Heidelberg, 2004).
[9] A. Dallanora, T. L. Marcondes, G. G. Bermudez et al., Nanoporous SiO_2/Si thin layers produced by ion track etching: Dependence on the ion energy and criterion for etchability, J. Appl. Phys. **104**, 024307 (2008).

INHOMOGENEOUS MAGNETIC STATE IN THE NANOSIZE $Sr_2FeMoO_{6-\delta}$ PREPARED BY CITRATE-GEL METHOD

Marta Yarmolich[1], Nikolai Kalanda[1], Jon Ustarroz[2], Herman Terryn[2]

[1] Scientific-Practical Materials Research Centre, NAS of Belarus, Minsk, Belarus
[2] Research Group Electrochemical and Surface Engineering (SURF), Vrije Universiteit Brussel
jarmolich@ifttp.bas-net.by

$Sr_2FeMoO_{6-\delta}$ (SFMO) is half-metallic ferromagnet with variety of magnetic states and physical properties, which are caused by interrelation of orbital, charge, spin and lattice degrees of freedom. These materials have a significant magnetoresistance (MR) ~ 38% in a relatively weak magnetic field (B ≈ 1T) at T = 50K, high values of Curie temperature (Tc = 400-450K) and almost 100% degree of spin polarization [1-3]. Increasing the superstructural ordering of Fe and Mo cations increases the density of free charge carriers at the Fermi level D (E_f), thereby enhancing the intensity of ferromagnetic and metallic properties of double perovskite [2, 3]. During the point defects formation in double perovskites iron cations may exist in different spin states: the low-spin, intermediate and the high [1-3]. The presence of zero-defects in the structure SFMO is determined primarily by the synthesis conditions and microstructure of samples and especially for nanoscale grain size. So the magnetic properties of the double perovskite affect particle size and shape of their morphology, particle interaction with each other.

Nanosize powder of SFMO with an average grain size of 50-350 nm was obtained using citrate-gel method. Based on the information obtained through the analysis of pH (pH=2, 4, 6, 9) and temperature effect on the phase composition and morphology during SFMO synthesis, an improved procedure was designed. Temperature dependences of SFMO magnetization were measured in next modes: pre-cooled from 300 to 4.2K in a magnetic field (FC-field cooling) or without (ZFC-zero field cooling) followed by heating to 300K at various magnetic fields [Fig.1.].

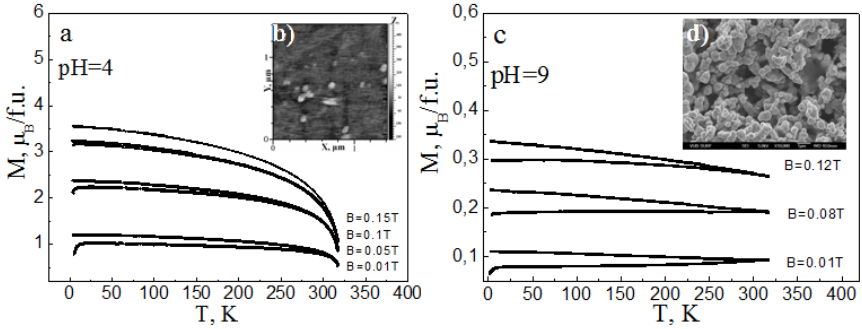

Fig. 1. Temperature dependencies of SFMO: pH=4 (a), and pH=9 (c)) magnetization measured in the magnetic field at ZFC and FC regimes (powders annealed at 1120K for 10 h in a continuous stream of 5%H_2/Ar gas mixture at 2 deg/min heat rate); (b)-AFM image of SFMO with pH=4, (d)-SEM image of SFMO with pH=9.

According to the magnetization data measured in ZFC and FC regimes it was found that the magnetic state of the samples correlates with their heterogeneity in sizes and shapes of SFMO grains. Thus, the presence of nanoscale spherical shape grain in SFMO nanopowders in which exchange forces provide uniform magnetization contributes to realization of superparamagnetic state, as indicated by the temperature dependence of ZFC in the low temperature region at T = (4.2 - 19) K. An important advantage of obtaining SFMO powders using such method is the possibilities of further use of these compounds in the injectors of spin polarized electrons, as electrode for SOFC, for spin transistors, for sensors of weak magnetic fields, for recording and processing information, etc [4, 5].

[1] D. Serrate, J. M. De Teresa, M.R. Ibarra, Double perovskites with ferromagnetism above room, J. Phys.: Condens. Matter, 19 (2007) 1–86.
[2] E. Hemery, Magnetic and Transport Studies of Strongly Correlated Perovskite Ceramics, Ph. D. Thesis, Victoria University of Wellington (2007).
[3] N. Kalanda, S. Demyanov, W. Masselink, A. Mogilatenko, M. Chashnikova, N. Sobolev, O. Fedosenko, Interplay between phase formation mechanisms and magnetism in the $Sr_2FeMoO_{6-\delta}$ metal-oxide compound, Cryst. Res. Technol., 46(5) (2011) 463–469.
[4] L.V. Kovalev, M.V. Yarmolich, M.L. Petrova, J. Ustarroz, H. Terryn, N.A. Kalanda, M.L. Zheludkevich, Double Perovskite Sr_2FeMoO_6 Films Prepared by Electrophoretic Deposition/ Leonid V. Kovalev et al// ACS Appl. Mater. Interfaces. – 2014, – Vol 6 (21), – P. 19201–19206.
[5] G.G.Goroh, S.E. Demyanov, N.A. Kalanda, M.V. Yarmolich, A.A. Lozovenko, E.A. Sochneva, Films of strontium ferromolybdate in porous anodic alumina matrix: preparation and properties, Proceedings of the VIII International Conference "Fullerenes and Nanostructures in Condensed Matter" (PNS- 2014), Minsk, Belarus, 64 -70 (2014).

AlN and AlGaN Growth by MOCVD and Characterization

Marek Kolenda, Tadas Malinauskas, Jūras Mickevičius, Darius Dobrovolskas, Arūnas Kadys

Institute of Applied Research and Semiconductor Physics Department, Vilnius University, Saulėtekio al. 9-III, Vilnius 10222, Lithuania
mkolendaus@gmail.com

Metalorganic chemical vapor deposition (MOCVD) is recognized as the method of choice for the large-scale production of nitride based optoelectonic and electronic devices [1]. The group-III-nitride semiconductors (AlN, GaN and InN) and their alloys are promising materials for many optoelectronic device applications such as blue-green and UV light-emitting diodes (LEDs), laser diodes (LDs) and high-temperature, high power electronic devices. The growth conditions affect the Al incorporation and quality of AlGaN epilayer. For these devices, one important thing is to obtain high-quality AlGaN epilayer with high Al content [2].

The main goal of this work was to obtain high crystalline quality AlGaN epilayers with different Al concentration.

AlN and AlGaN epilayers were grown on c-plane sapphire substrate by MOCVD (AIXTRON 3x2 FT) reactor. Trimethylgallium (TMGa), Trimethylaluminum (TMAl) and ammonia (NH3) have been used as precursors for gallium, aluminum and nitrogen respectively. All AlGaN samples were grown on 280 nm AlN buffer layer deposited at 1135 ^{o}C under hydrogen (H_2) atmosphere. The summary of AlGaN growth parameters is shown in Table 1.

Table 1. AlGaN growth parameters.

Sample	Template	P, mBar	T, ^{0}C	NH_3, mol/min	TMG, mol/min	TMA, mol/min	Growth time, s	Thickness, nm
452	Sapphire/AlN	100	1090	$1,8\times10^{-1}$	$9,5\times10^{-6}$	$2,9\times10^{-5}$	4500	280
460		100			$2,9\times10^{-5}$	$2,9\times10^{-5}$	3300	420
461		100			$6,6\times10^{-5}$	$2,9\times10^{-5}$	4500	1120
463		100			$1,6\times10^{-4}$	$1,7\times10^{-4}$	3300	1120
464		85			$6,6\times10^{-5}$	$6,7\times10^{-5}$	2700	700

The crystal quality of AlGaN layers and Al concentration has been evaluated using high resolution X-ray diffraction measurements (HRXRD) (Fig. 1). The obtained value of aluminum composition in the layers varied from 26% up to 72%. The value of the full width at half maximum (FWHM) of XRD peaks shows the distribution uniformity of aluminum and gallium in the layer. The dependence of FWHM versus Al concentration revealed that the metal distribution in AlGaN alloys becomes most uneven when Al and Ga concentrations in the layer are similar (Fig. 2).

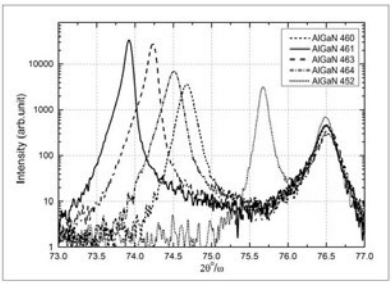

Figure 1. AlGaN layers' HRXRD measurements.

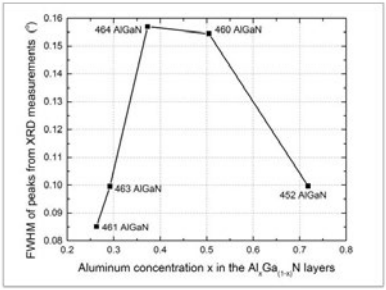

Figure 2. Peaks' FWHM dependence on Al concentration.

The surface morphology and roughness of AlN and AlGaN have been studied by atomic force microscopy. Root mean square roughness values have been found to increase from 0.9 nm up to 30 nm with the increase of Al concentration in the AlGaN alloys.

The optical properties of AlGaN/AlN layers have been investigated by room temperature photoluminescence. It was found that with increasing Al content, the AlGaN photoluminescence emission peak shifts towards higher photon energies. A bowing parameter *b* of -0.61eV was obtained from the band gap variations as a function of Al composition.

[1] Stacia Keller, Steven P. DenBaars. Metalorganic chemical vapor deposition of group III nitrides—a discussion of critical issues. Journal of Crystal Growth **248,** 479–486 (2003)

[2] M. Jayasakthi, R. Ramesh, et al. Effect of Al-mole fraction in Al(x)Ga(1-x)N grown by MOCVD. AIP Conference Proceedings **1591** (2014)

SYNTHESIS AND MAGNETIC PROPERTIES OF THE $MN_{1-X}GD_XSE$ SYSTEM SOLID SOLUTIONS

Sergey Aplesnin[1], Aliona Panasevich[1,2], Kazimir Yanushkevich[2]

[1]Siberian State Aerospace University named after academician M.F.Reshetnev, 660014 Krasnoyarsk, Russia
[2]Scientific-Practical Materials Research Centre of NAS of Belarus, P.Brovki Str.19, Minsk, Belarus
alyona_panasevich@mail.ru

The substances, electric and magnetic properties of which have a strong correlation, are promising for applications in microelectronics [1]. Solid solutions with cation substitution in the $Mn_{1-x}Gd_xSe$ system, having semiconducting properties, can be attributed to such substances. The purpose of this work is a synthesis of $Mn_{1-x}Gd_xSe$ solid solutions, studying the characteristics of their magnetic properties depending on the composition and temperature.

The compositions of $Mn_{1-x}Gd_xSe$ ($0 \leq x \leq 0.9$) were obtained by solid state reaction method from powders of based limit compounds.

The specific magnetization of received compounds is studied by ponderomotive method in the 77 - 900K temperature range in a magnetic field with induction B = 0.86 T [2, 3]. The temperature dependence of the specific magnetization of $Mn_{1-x}Gd_xSe$ solid solutions for compositions with x = 0.05 and x = 0.7 are shown in Fig. 1.

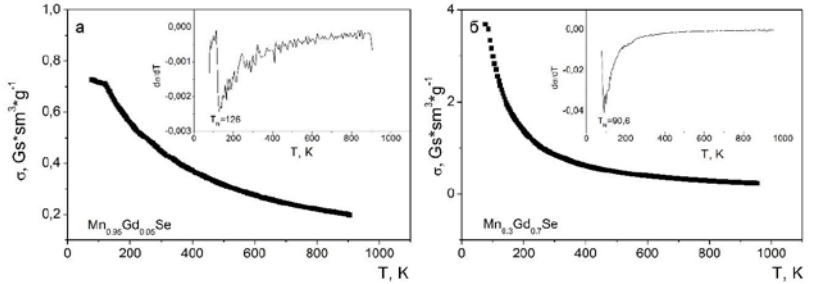

Fig. 1. The specific magnetization σ and derivative of magnetization with respect to temperature dσ/dT (insert) for solid solutions a) $Mn_{0.95}Gd_{0.05}Se$; b) $Mn_{0.3}Gd_{0.7}Se$

It is found that the heating of solid solutions up to a temperature of 900 K does not lead to irreversible changes in the magnitude of the magnetization. Dependences $\sigma = f(T)$ in "heating-cooling" regime measurements are identical.

As a result of the research is found that the substitution of manganese by gadolinium in solid solutions of $Mn_{1-x}Gd_xSe$ system leads to an increase in the average magnetic moment. It is revealed a slight decrease in the phase transformation "magnetic order - magnetic disorder" temperature with increasing concentration x of gadolinium. This is most likely due to a disturbance of the exchange interactions with cationic substitution [4].

[1] Aplesnin S. S. Magnetic and electrical properties of strongly magnetic semiconductors with four-interaction and orbital ordering (Moscow, 2013. 167p.)
[2] Chechernikov V.I. Magnetic measurements (Moscow State University Press. Moscow, 1969, 387p.)
[3] Yanushkevich K.I. Methods of measurement of the magnetization and magnetic susceptibility (Minsk, 2009, 19p.)
[4] Yanushkevich K.I. Solid solutions monochalcogenides 3d-metal (Minsk, 2009. 256p.)

ANALYSIS OF LOW-ENERGY SURFACES OF THE α-SILICON NITRIDE (α-Si_3N_4) UTILIZING DENSITY FUNCTIONAL THEORY

Ewa Martyniuk[1]

[1] University of Bialystok, Department of Biology and Chemistry, Establishment of Physicochemical Methods
ewa.martyniuk91@gmail.com

Molecular modelling is a theoretical method, used to projection, modelling or anticipation of the molecules in the system ranging from small chemical systems to large biological molecules and material assemblies thanks to powerful computer programs. Nowadays this method is becoming increasingly popular in various fields of computational chemistry, drug design, computational biology and materials' science, because it allows to save a lot of time, money and manpower. The simplest calculations can be performed by hand, but more complicated calculations require computers with high performance computing and time to perform calculations. Therefore every method is selected on the basis of optimal computing time relative to the accuracy. So if research requires high precision, the best method will be Quantum Mechanics (QM), but then computational operation will be prolonged and system will consist of a few atoms with brief period of system's life. There would be opposite situation, if research requires low precision, then the system may exist of large number of atoms (even 10^8 atoms) and computing time will not be long. The best option then will be Molecular Mechanics (MM). There are other methods less or more accurate such as Density Functional Theory (DFT) or Tight-Binding beetween those two.

Silicon nitride (Si_3N_4) has three polymorphs: α, β and γ phases. The crystal structures of the α and β phases are hexagonal. Their structures are closely related to each other. In both of two phases, Si and N atoms have tetrahedral (fourfold) and trigonal (threefold) coordinates, respectively. The unit cells of the α and β phases are characterized by planar structure parallel to (0001), a basal plane. α-Si_3N_4 (nierite) crystallizes in the trigonal system, with lattice parameters a=7.766 Å and c=5.615 Å, space symmetry group P31c and density 3,16–3,19 g/cm^3. And β-Si_3N_4 crystallizes in the hexagonal system similar to α-Si_3N_4, with reticular parameters a=7.608 Å and c=2.911 Å and density 3,19–3,20 g/cm^3. [11] β-Si_3N_4 has a periodic stacking structure such as ABAB... in the direction of the c axis. In the case of α- Si_3N_4, ABCDABCD... Therefore, the lattice constant of α- Si_3N_4 in the c axis is approximately two times longer than that of β- Si_3N_4. The trigonal pyramidal unit, N-Si_3, with N atom at 2a and 2b sites in α- Si_3N_4, and that with N atom at 2c site in β- Si_3N_4, lay parallel to basal plane. The other N-Si_3 units are vertically placed to the basal plane. Both the α and β phases can be synthesized under the ordinary pressure by direct nitridation of silicon or decomposition of precursors such as silicon diimide. On the other hand, the γ phase is a high pressure product. It forms a cubic spinel structure. All of N atoms have tetrahedral coordination. There are two kinds of coordination numbers for Si atoms, i.e. tetrahedral (fourfold) and octahedral (sixfold). All three phases are found to be dynamically stable. β- Si_3N_4 shows lower Helmholtz free energy than α-Si_3N_4 in the temperature range from 0 to 2000K. In other words, α-Si_3N_4 is not a low-temperature phase but a metastable phase under the ordinary pressure. The presence of planer N-Si_3 units and their strong Si-N bonds in the two hexagonal polymorphs, α- and β- Si_3N_4, is the origin of the high-frequency phonon band at above 25THz, which is absent in γ- Si_3N_4. It plays key roles for anisotropic local vibration of N atoms. The different temperature dependence of specific heat between α/β and γ phases can also be ascribed to the structure. The transition pressure from β to γ phase is computed as a function of temperature. It is found to increase with the rise of temperature. Furthermore, both of them, α and β phases can be synthesized and stably existent under ambient conditions. Millimeter-sized single crystals are available for both of them. Submicron-sized powders of the α phase are often selected for sintering of high-strength ceramics. α→β transformation generally occurs when sintered with some oxide additives as liquid phase formers. No back transformation of β→α occurs except for highly concentrated alloys that prefer the formation of the α phase. These phenomena seem to suggest that β is more stable than α at high temperatures. However, it is still unknown whether the α phase is really a metastable phase at all temperatures and it is formed by a kinetic reason.

This work will show stability of the α-Si_3N_4 surface utilizing Density Functional Theory. This kind of research is very useful, when new nanocomposites are designed, because silicon nitride is very popular material in production of bearing elements, centering pins and semiconductors. Hence knowledge of surface allows to find the best connection between stability and surface properties.

[1] A. Kuwabara, K. Matsunaga, I. Tanaka; *Lattice Dynamics and thermodynamical properties of silicon nitride polymorphs*; PHYSICAL REVIEW B **78**, 064104 (2008)

[2] S. Veprek, A. S. Argon, R. F. Zhang; *Origin of the hardness enhancement in superhard nc-TiN/α-Si3N4 and ultrahard nc-TiN/α-Si_3N_4/$TiSi_2$ nanocomposites*; Philosophical Magazine Letters; Vol. 87, No. 12, December 2007, 955-966

THE RAMAN SPECTRA OF NORMAL ALCOHOLS IN LONG-WAVE REGION

Oksana Rudaya[1], George Pitsevich[1*]

[1] Department of Physical Optics, Belarusian State University, Belarus
rudaya_oksana@mail.ru

The researchers attention is attracted intermolecular vibrations in hydrogen-bonded complexes in the gas [1], in the liquid [2] and in the matrix isolation [3]. However, the spectral range of their manifestation (the long-wave region of the spectrum) are still poorly understood. Often, the frequency range 30-500 cm-1 can be registered in the Raman spectra. At the same time, we can expect that the intermolecular vibrations must be accompanied by a significant change in the components of the polarizability tensor. We have registered a number of long-wave Raman spectra of normal alcohols in the liquid phase (Figure 1).

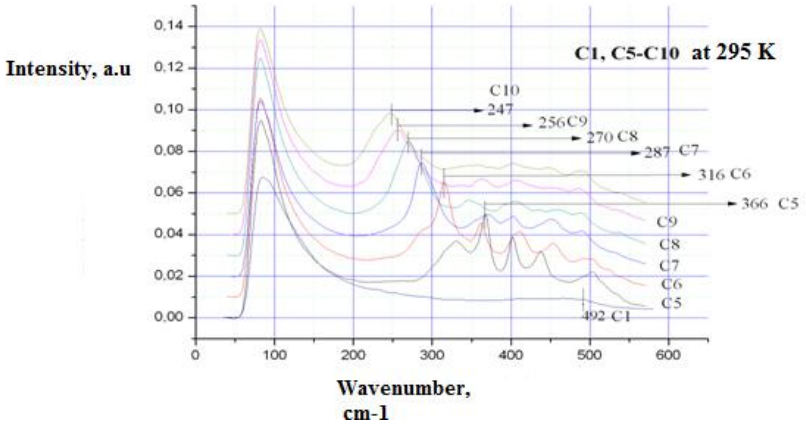

Figure 1. The long-wave Raman spectra of some normal alcohols

We can see that Raman lines shift to lower frequencies monotonically in the range 400-200 cm-1 (Figure 1) and sizes of alcohol molecules increase.

For the interpretation of spectral data we made calculations of the structures and the Raman spectra of dimers of some alcohol molecules using a package [4] in the approximation-NII B3LYP / cc-pVTZ. We determined frequencies of intermolecular vibrations and calculated their intensities in the Raman spectra.

[1] C.Lassegues,J.Lascombe in J.R.Durig Vibrational Spectra and Structure v.11, (1982), Elsevier, p.51-106.
[2] H.Ratajczak Molecular Interection v.1 John Wiley and Son, (1980), p.231-269.
[3] A.Engdahl Intermolecular Interections in Hydrogen bonded molecular complexes.A matrix Isolation Study.University of Lund, Sweden,(1997).
[4] http://www.msg.ameslab.gov/GAMESS/GAMESS.html

INFLUENCE OF WO_3 LAYERS GROWN BY ELECTRON-BEAM METHOD ON THE PROPERTIES OF ORGANIC LIGHT EMITTING DIODES

Julius Danišauskas[1], Tomas Tolenis[2], Bronė Lenkevičiūtė[1], Giedrius Juška[1]

[1]Vilnius University, Faculty of Physics, Department of Solid State Electronics
[2]Center for Physical Sciences and Technology, Laboratory of Optical Coatings
julius.danisauskas@ff.stud.vu.lt

Quantum dot, semiconductor Tungsten Oxide (WO_3) and layers of organic materials of inverted structure hybrid quantum dots organic light emitting diodes (QD OLEDs) were vacuum deposited and spin coated onto Fluorine doped Tin Oxide (FTO) covered glass and their electrical, photoluminescence (PL) and electroluminescence (EL) features were investigated.

The structure of samples was changed by using different WO_3 layer: with inclined and vertical to the substrate nanowires and by using different hole transporting layer (HTL): 4,4′-Bis(*N*-carbazolyl)-1,1′-biphenyl (CBP) or *N,N*′-Bis(3-methylphenyl)-*N,N*′-diphenylbenzidine (TPD).

It was found that $Ir(Fppy)_3$ and WO_3 layer with vertical nanowires cannot be used for making inverted structure QD OLEDs due to difficulty of forming quantum dot monolayer on it.

When layer of TPD was used as hole transporting layer in QD OLED it had formed a barrier for holes between $Ir(Fppy)_3$ and TPD layers and we could not observe any EL.

In conclusion we showed that for QD OLEDs application it is better to use WO_3 with inclined nanoparticles. Electroluminescence was observed in the sample with WO_3 layer which had inclined nanowires and CBP hole injection layer when threshold voltage of 23 V was applied. The complete structure of this sample was - FTO/WO_3′/RQD/$Ir(Fppy)_3$/CBP/LiF/Al.

INVESTIGATION OF LLTO NANOCERAMICS CONDUCTIVITY

Justas Subatavičius[1]

[1] Department of Radiophysics, Faculty of Physics, Vilnius University, Lithuania

Justas.subatavicius@ff.stud.vu.lt

LLTO (lithium lanthanum titanate) nanoceramics are conductors with high grain conductivity and low grain boundary conductivity, but the total conductivity depends mostly from grain boundary conductivity.LLTO nanoceramics could be used to make lithium ion batteries, high capacity capacitors.

In our investigation we used $Li_{3x}La_{2/3-x}TiO_3$, where x=0,1, nanoceramic.Impedance measurements were made in 10Hz – 3GHz frequency range and 300K to 700K temperature range. In our investigation we used two different measurement methods – two electrodes and four electrodes.[1]

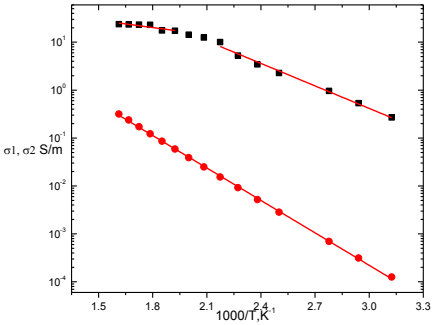

Fig. 1Grain and grain boundary conductivity dependence from inversed temperature

Fig. 1 shows that grain boundary conductivity obeys Arrhenius law and we can calculate activation energy ΔE_{gb}= 0.451eV.

Grain conductivity obeys Arrhenius law in two different ranges with two different activation energies:

from 320K to 480K -$\Delta E_{b1} = 0.1eV$.

from 540K to 620K - $\Delta E_{b2} = 0.312$eV.

[1]A.Kežionis , E.Kazakevičius , T. Šalkus and A. Orliukas , Solid state Ionics 188 (2011) 110-113

Poster session 4

FLUCTUATIONS OF BROWNIAN PARTICLE IN INHOMOGENEOUS MEDIA AS A SOURCE OF 1/f NOISE

Rytis Kazakevičius and Julius Ruseckas

Institute of Theoretical Physics and Astronomy, Vilnius University, Lithuania
rytis.kazakevicius@tfai.vu.lt

One of the characteristics of the signal is the power spectral density (PSD). Signals having the PSD at low frequencies f of the form $S(f) \sim 1/f^{\beta}$ with β close to 1 are commonly referred to as "1/f noise". The nonlinear stochastic equations generating signals with $1/f$ spectrum in a wide range of frequencies have been used so far to describe socio-economical systems [1]. The derivation of the equations has been quite abstract and physical interpretation of the assumptions made in the derivation is not very clear. We present a physical model where such an equation can be relevant. We expect that this derivation leads to a better understanding of which systems can be described using such an equation. We start from Langevin equations for one-dimensional motion of a Brownian particle

$$\frac{\mathrm{d}}{\mathrm{d}t}v(t) = -\gamma v(t) + \frac{1}{m}F(x) + \sqrt{\frac{2\gamma}{m}\frac{1}{\beta(x)}}\xi(t) \tag{1}$$

$$\frac{\mathrm{d}}{\mathrm{d}t}x(t) = v(t)\,. \tag{2}$$

Here x is particle position, v is velocity, m is mass, γ is relaxation rate of velocity, $F(x)$ is external force and $\xi(t)$ is white noise. These equations describe the motion of a Brownian particle in an inhomogeneous environment. The inhomogeneous environment can be a result of a linear potential affecting the Brownian particle together with the steady state heat transfer due to the difference of temperatures at the ends of the medium. In high friction (also called overdamped) limit the relaxation rate is large, $\gamma \gg |dv/dt|$. Performing adiabatic elimination of the velocity as in [2], we obtain equation

$$\frac{\mathrm{d}}{\mathrm{d}t}x(t) = \frac{1}{\gamma m}F(x) + \sqrt{\frac{2}{\gamma m}\frac{1}{\beta(x)}}\xi(t)\,. \tag{3}$$

We assume that external force potential is $U(x) = \left(\frac{\nu}{\theta} - 1\right)/\beta(x)$ and inverse temperature is $\beta(x) = bx^{-\theta}$ and obtain stochastic differential equation

$$\frac{\mathrm{d}}{\mathrm{d}t}x = \sigma^2\left(\eta - \frac{1}{2}\nu\right)x^{2\eta-1} + \sigma x^{\eta}\xi(t)\,. \tag{4}$$

Here $\eta = \theta/2$ and ν is power law exponent of steady state distribution. It can be shown that Eq. (1) generate signals with $1/f$ noise and power law steady-state probability densities (PDF), $P(x) \sim x^{-\nu}$.

$$S(f) \sim \frac{1}{f^{\beta}}\,, \qquad \beta = 1 + \frac{\nu - 3}{2(\eta - 1)}\,. \tag{5}$$

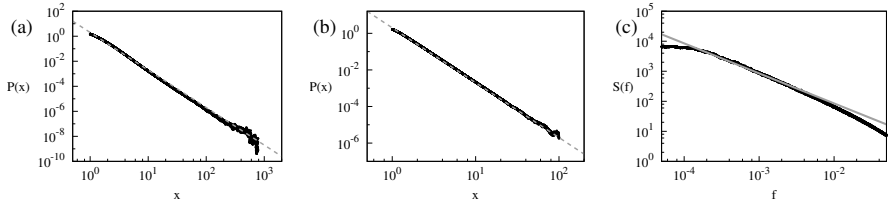

Fig. 1. The steady-state PDF of the signal generated by the Langevin equations Eq. (1) and Eq. (2) with reflective boundaries at $x_{\min}$ and $x_{\max}$ and the parameters: (a) $\theta = 1$, $\nu = 3$, $x_{\min} = 1$, $x_{\max} = 1000$, (b) $\theta = 0$, $\nu = 3$, $x_{\min} = 1$, $x_{\max} = 100$. The dashed line shows the power-law with the exponent -3. (c) The PSD of the signal corresponding to the parameters in (b) case. The gray line shows the slope f^{-1}.

Fig. 1 shows good agreement between numerical solution of Eq. (1) and Eq. (2) system and analytical predictions Eq. (5). This confirms that Langevin equation can be approximated by Eq. (4) in high friction limit. Also power law statistics remains for a case of colored environmental noise instead of white noise. In conclusion, we have derived the equation generating with $1/f$ noise and power law statistics from Langevin equations.

[1] V. Gontis, J. Ruseckas and A. Kononovičius, A long-range memory stochastic model of the return in financial markets, Physica A **389**, 100-106 (2010).

[2] J. M. Sancho, M. San Miguel and D. Dürr, Adiabatic elimination for systems of Brownian particles with nonconstant damping coefficients, J. Stat. Phys **28**, 291-305 (1982).

DEVELOPMENT OF CODE PACKAGE FOR PARSING THE ATOMIC STRUCTURE AND FOR CALCULATING AND REPRESENTING THE INTENSITY SPECTRA

Gintaras Kerevičius

Department of the Theory of Atom, Institute of Theoretical Physics and Astronomy, Vilnius University, A. Goštauto st. 12, LT-01108, Vilnius, Lithuania
gintaras.kerevicius@tfai.vu.lt

This thesis marks a little more than a year of development of programs for parsing and classifying the input data of atomic structure, for calculating and in different ways representing the intensity spectra of that structure. The Python [1] programming language (PL) and Spyder [2] integrated development environment (IDE) were used to achieve this task. Most of the code is based on standard and built-in Python packages and modules. The default functions and methods on data-types were used extensively throughout the code. However, more specific packages written with PLs following the static typing discipline were used also, as the subroutines written in this manner perform a lot faster during a program runtime. Special variables, special and standard mathematical functions and interpolation subroutine were used from the NumPy [3] package. Quadrature subroutine from the SciPy [4] package was used for numerical integration. The Matplotlib package (year 2013, version 1.3.1), which is described in the original paper [5], was used for a graphical representation of intermediate and final results.

The parsing package and its modules were developed and tested using the atomic structure data calculated by the Flexible atomic code (FAC) [6] and my supervisor's programs. The latter programs calculate polarization and angular anisotropy parameters of various objects participating in the initial and final state of an atomic process. Matrix elements of the parameters are calculated in Born or distorted-wave approximation using the basis of intermediate coupling Hartree-Fock [7] eigenfunctions. Whereas, the former program [6] was used for calculation of the level energies, excitation cross sections and decay probabilities of discrete states of an atom. FAC uses the Dirac-Fock-Slater [6] approximation for calculating various atomic structure parameters. Described input data is parsed and stored by using the same code package, i. e. the package is not bound to the data. The parsing package consists of a number of modules. One of the modules splits raw-data into special and real data groups by looking for special identifiers, e. g. any type of assignment symbol or special symbols described in the define module. The other module determines the form of data, i. e. how it is presented in the file (structured, divided into blocks or typically tabulated). The third module is responsible for gathering global and local information about each subset of the data and discerning between numerical and symbolic data-types. Based on predefined rules and gathered information, each data subset is recognized as belonging to a particular atomic quantity. Then, the data is stored in an adaptive data-structure (list or dictionary), which builds up after each new data is encountered. New subsets of data belonging to the same atomic quantity as stored ones are robustly checked to stay consistent with each other. One of modules performs an unambiguous 1-to-1 and full classification of the states of an atom based on the absolute value or position of the expansion coefficient in an eigenstate expansion.

Some parts of the program are based on a command line interface, where the code queries a user for parameters to change the work-flow of the following procedure. Some queries are optional, e. g. there is a possibility to shift the specified lines of a given spectrum. The latter spectrum is presented in the graphical user interface (GUI). Hopefully, in later stages of development all program capabilities will be represented in the GUI. There are queries with a necessary answer, e. g. a user needs to specify at least one input parameter of the excitation energy and energy resolution of spectra, respectively. But, there are also queries that have default parameter values if these are not specified. For example, at the beginning of program runtime there is a query about the relative destination (or path) of theoretical data in an operating system. A path can be described by atom's name and its number of electrons. If one or all parameters are not specified, the program searches for theoretical data in the default path based on the specified parameters.

Packages responsible for calculating and representing the intensity spectra of atoms use the query answers and data-structure to extract needed information. There can be an arbitrary number of spectra calculated and presented together with experimental digitized spectra at each program runtime. If required, the GUI can show a real-time calculation of each intensity spectrum. A publication [8] on classification of the states and intensity spectrum of Cs was submitted. This code package was used to achieve the latter results.

[1] G.-V. Rossum and the Python Software Foundation, Python (version 2.7.6) (2013). Available at https://www.python.org/download/releases/2.7.6/
[2] P. Raybaut and the Spyder Developer Community, Spyder: Scientific PYthon Development EnviRonment (version 2.2.5) (2013). Available at https://pypi.python.org/pypi/spyder/2.2.5
[3] T. Oliphant ant the NumPy Developers, NumPy: array processing for numbers, strings, records and objects (version 1.8.2) (2014). Available at https://pypi.python.org/pypi/numpy/1.8.2
[4] T. Oliphant, P. Peterson, E. Jones and the Community library project, SciPy: Scientific Library for Python (version 0.13.3) (2014). Available at https://pypi.python.org/pypi/scipy/0.13.3
[5] J.-D. Hunter, Matplotlib: A 2D Graphics Environment, Comput. Sci. Eng. **9**, 90-95 (2007).
[6] M.-F. Gu, The flexible atomic code, Can. J. Phys. **86**, 675-689 (2008).
[7] C.-F. Fischer, General Hartree-Fock program, Comput. Phys. Commun. **43**, 355-365 (1987).
[8] G. Kerevičius and A. Kupliauskienė, Classification of the $5p^5nln'l'$ *LSJ* energy levels of Cs excited by 30 eV electrons, submitted to Lith. J. Phys. (2015).

Long-range memory in nonlinear GARCH(1,1) models

Aleksejus Kononovicius[1], Julius Ruseckas[1]

[1] Vilnius University, Institute of Theoretical Physics and Astronomy, Lithuania
aleksejus.kononovicius@tfai.vu.lt

Econophysics started out as purely empirical science. Physicists around the world analyzed huge amounts of financial market data and discovered certain statistical regularities, which is now often referred to as stylized facts[1, 2]. One of these regularities is long-range, decaying as power-law, correlations often referred to as long-range memory [2]. Power spectral density (PSD) of the time series with long-range memory behaves as $1/f^{\beta}$ with β values being close to 1.

At the same time economists proposed, applied and further developed auto-regressive conditionally heteroskedastic (ARCH) models [3]. The basic idea behind ARCH models lies in an assumption that certain heteroskedastic economical observables, z_t, may be modeled as being composed of two parts - stochastic part, ω_t, and time dependent volatility, σ_t:

$$z_t = \sigma_t \omega_t. \tag{1}$$

Stochastic part may be usually assumed to follow Gaussian distribution (though it may depend on actual application), while time dependent part may be assumed to be driven by the following generalized GARCH(p,q) process (though there are numerous other possibilities, once again dependent on actual applications):

$$\sigma_t^2 = a + \sum_{i=1}^{p} b_i \sigma_{t-i}^2 \omega_{t-i}^2 + \sum_{i=1}^{q} c_i \sigma_{t-i}^2. \tag{2}$$

In this case if $p = q = 1$, then new σ_t values depend only on the immediate prior σ_{t-1} value. As σ_t does not depend on further history, any σ_{t-i} $(i > 2)$, the model appears to be memory-less - it exhibits Markov property.

GARCH(1,1) process, Eq. (2) with $p = q = 1$, may be rewritten in continuous time as stochastic differential equation (SDE):

$$\mathrm{d}y = (A - Cy)\mathrm{d}t + |B| y \mathrm{d}W_t, \tag{3}$$

where W_t is Wiener process (standard one dimensional Brownian motion) and with the following relation of parameters: $Ah = a$, $B^2 h = 2b_1^2$ and $Ch = 1 - b_1 - c_1$ (in the infinitesimally small time step limit, $h \to 0$). The obtained SDE may be further compared to a general class of SDEs exhibiting power law statistics, including $1/f^{\beta}$ PSD:

$$\mathrm{d}x = \sigma^2 \left(\eta - \frac{1}{2}\lambda \right) x^{2\eta - 1} \mathrm{d}t + \sigma x^{\eta} \mathrm{d}W_t, \tag{4}$$

which was proposed in[4]. From the comparison it is evident that linear GARCH(1,1) will not be able to reproduce $1/f^{\beta}$ noise as $\eta = 1$. Though it is able to reproduce another interesting statistical feature - power-law distribution.

We consider two possible nonlinear modifications of Eq. (2), with $p = q = 1$:

$$\sigma_t^2 = a + b_1 \sigma_{t-1}^{\mu} \omega_{t-1}^{\mu} + c_1 \sigma_{t-1}^2, \tag{5}$$

where $\mu > 2$ is an odd integer, and

$$\sigma_t^2 = a + b_1 \sigma_{t-1}^{\mu} |\omega_{t-1}|^{\mu} + \sigma_{t-1}^2 - c_1 \sigma_{t-1}^{\mu}, \tag{6}$$

where μ may be any positive real number. Both of these nonlinear GARCH(1,1) processes are able to reproduce power-law distributions, with exponent $\lambda = \mu$, as well as PSD of the $1/f^{\beta}$ form, with $\beta = 1 + \frac{\mu - 3}{\mu - 2}$, [5].

[1] A. Chakraborti, I. M. Toke, M. Patriarca and F. Abergel, Econophysics review: I. Empirical facts, Quantitative Finance **7**, 991-1012 (2011).
[2] R. Cont, *Long range dependence in financial markets* (Springer, 2005).
[3] T. Bollerslev, *Glossary to ARCH (GARCH)* (CREATES, 2008).
[4] B. Kaulakys and J. Ruseckas, Stochastic nonlinear differential equation generating $1/f$ noise, Physical Review E 70, 020101 (2004).
[5] A. Kononovicius and J. Ruseckas, Nonlinear GARCH model and $1/f$ noise, to appear in Physica A (2015). arXiv: 1412.6244 [q-fin.ST].

EXCITATION DYNAMICS IN SINGLE-WALLED CARBON NANOTUBES

Jonas Narkeliūnas, Leonas Valkūnas, Jevgenij Chmeliov

Department of Theoretical Physics, Faculty of Physics, Vilnius University, Lithuania
Jonas.Narkeliunas@ff.stud.vu.lt

Carbon nanotubes are large molecular systems made entirely of carbon atoms. Structurally, they can be viewed as a graphene sheet rolled-up in some particular direction to make a tube. Their interesting shape gives a variety of interesting properties like tunable energy gap and incredible tensile strength, therefore carbon nanotubes could be used in many different machines and devices. However, till this day many of their properties aren't fully understood, and thus, to unlock their full potential, a theoretical description is needed.

In our research, we tried to explain ultra-fast transient absorption measurements in carbon nanotubes by modeling kinetics of excitation dynamics [1]. As many experiments confirm that non-linear excitation's relaxation is being observed, many models are based on the exciton-exciton annihilation. Such models gave good approximation in femtosecond scale, when most of the excitation decays, but failed to explain the asymptotic behavior. Thus improvements needed to be done.

We showed that these problems can be solved by additionally introducing exciton diffusion [2]: $\gamma(t) = \begin{cases} \gamma_0, & t \le \tau \\ \frac{\gamma_0}{\sqrt{t}}, & t > \tau \end{cases}$, and phase space-filling factors [3]: $f_i(n_i) = 1 - \dfrac{n_i}{n_{i,max}}$. While diffusion process is supposed to slow down exciton-exciton annihilation, the phase space-filling factor is mainly responsible for saturation effects as seen at higher pumping intensities [4]. With these effects being taken into account, the time evolution of excitons can be described by following kinetic equations:

$$\frac{\mathrm{d}n_1}{\mathrm{d}t} = G_1(t)\cdot f_1(n_1) - \frac{1}{2}\left(1+\alpha\cdot f_2(n_2)\right)\gamma(t)\,n_1^2 + k_{21}n_2\cdot f_1(n_1) - Kn_1,$$
$$\frac{\mathrm{d}n_2}{\mathrm{d}t} = G_2(t)\cdot f_2(n_2) + \frac{1}{2}\alpha\gamma(t)\,n_1^2\cdot f_2(n_2) - k_{21}n_2\cdot f_1(n_1).$$

While it is impossible to solve the system of equations analytically, we were able to obtain a solution using computational methods. And after optimizing it to give the best fit with experimental data, we were able to reproduce experimental excitation dynamics at the whole timescale, ranging from femtoseconds to tens of picoseconds, as seen in Fig. 1 (left).

Using this model, we were able to explain other experimental observations that were measured at room temperature (Fig. 1 right). However, for low temperature experiments we saw a substantial deviation from experiment, thus we presume that other processes might also take place in carbon nanotubes. In the end, we concluded that its necessary to include exciton diffusion and phase space-filling factors, while modeling excitation dynamics in carbon nanotubes, though other effects, such as local heating, could be happening at the same time.

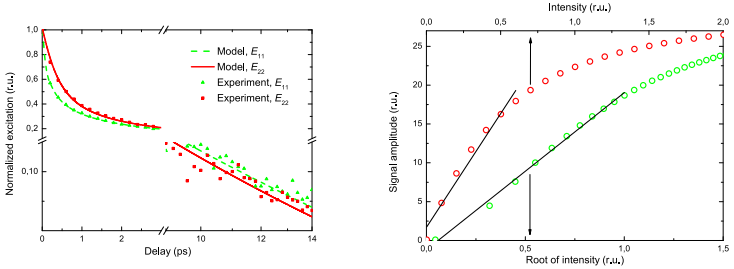

Fig. 1. Left: Normalized excitation opposed to time delay between pumping and probing impulses. Experimental data (triangles and squares) compared to the best fit of our model (full and dashed lines). Right: Excitation amplitude versus pumping intensity and root of pumping intensity, when pumping to E_{22} (upper) and E_{11} (lower) energy levels, respectively.

[1] T. Koyama, S. Yoshimitsu, Y. Miyata, H. Shinohara, H. Kishida, A. Nakamura, Transient absorption kinetics associated with higher exciton states in semiconducting single-walled carbon nanotubes: Relaxation of excitons and phonons, The Journal of Physical Chemistry C **117**(39), 20289–20299 (2013).

[2] L. Luer, S. Hoseinkhani, D. Polli, J. Crochet, T. Hertel, G. Lanzani, Size and mobility of excitons in (6, 5) carbon nanotubes, Nat. Phys. **5**(1), 54–58 (2009).

[3] M. W. Graham, J. Chmeliov, Y.-Z. Ma, H. Shinohara, A. A. Green, M. C. Hersam, L. Valkunas, G. R. Fleming, Exciton dynamics in semiconducting carbon nanotubes, J. Phys. Chem. B **115**(18), 5201–5211 (2011).

[4] L. Valkunas, Y.-Z. Ma, G. R. Fleming, Exciton-exciton annihilation in single-walled carbon nanotubes, Phys. Rev. B **73**, 115432 (2006).

Local void in polymer systems: different approaches

Wojciech Radosz

Faculty of Fundamental Problems of Technology, Wroclaw University of Technology, Poland
wojtekradosz@wp.pl

Polymer materials are nowadays applicable to many areas of modern technologies. It is motivation for investigation and understanding their internal processes. Resulst of experiments connected with nonlinear optics effects of host (polymer) - guest (dipoles, photochromic dyes,) systems are difficult to explain. Also the investigation of polymer systems behavior and properties for various temperatures (glass transition, diffusion of: particles, center of mass, guests,) seems to be a complex task.

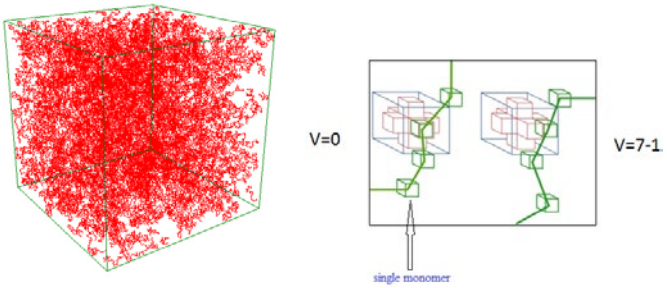

Figure 1. Snapshot polymer system (left) and method for evaluation of void parameter - value in each cell is based on amount of free space nearby (right). [1]

Through computer simulations we attempt to explain those problems. Description of model and system's preparation will introduce into so-called local void problem - roughly speaking empty space in the system. Approaches from literature will be compared with the one we want to apply.

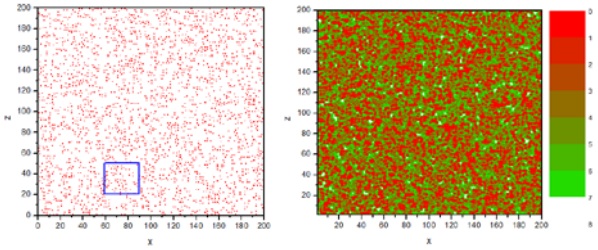

Figure 2. Cross section of the polymer system during the simulation: spatial distribution of monomers in $x-z$ plane (left) and local void parameter V (right). [2]

Results obtained with local void parameter show that there is strong correlation between monomers positions and regions of red color (Fig. 2, left), what is a straightforward consequence of its definition. What is more important, areas of white/green color are correlated with empty space in the system (Fig. 2, right). Groups of empty cells are the key for optical effects explanation and proper system's description.

[1] G. Pawlik, R. Orlik, W. Radosz, A.C. Mitus, and M.G. Kuzyk, Proc. SPIE 8474, 84740A (2012).
[2] G. Pawlik, W. Radosz, A. C. Mitus, J. Mysliwiec, A. Miniewicz, F. Kajzar, and I. Rau, Cent. Eur. J. Chem. RICCCE 18 (2014).

Efficient 9j symbol and harmonic oscillator transformation brackets evaluation for binary cluster calculation

Augustinas Stepšys[1], Saulius Mickevičius[2,3], Darius Germanas[4], Ramutis Kazys Kalinauskas[4]

[1]Department of Theoretical Physics,Faculty of Physics of Vilnius University, Saulėtekio Avenue 9,build. 3, 10222, Vilnius , Lithuania
[2]Vytautas Magnus University, K. Donelaičio str. 58, LT-44248, Kaunas, Lithuania
[3]Kaunas University of Technology, Physics Department, Studentu str. 50, LT-51368 Kaunas, Lithuania
[4]Center for Physical Sciences and Technology, Savanoriu 231, LT-02300 Vilnius, Lithuania
augustinas.stepsys@ff.stud.vu.lt

It is well known that in order to represent the bound state of the system formed of identical particles, including the nuclei of atom, the use of binary cluster model depends heavily on 9-j symbol [1] and harmonic oscillator transformation coefficients (3HOB) [2]. In particular for creating the desirable wave-function the use of angular momenta algebra which in order to couple four angular momentum vectors relies heavily on re-coupling coefficients, which are directly related to purely mathematical 9j symbol. 9j symbol is also very widely used in atomic and molecular calculations. In these calculations, depending on the system which is researched, the number of evaluations can construct the main portion of the whole algorithm, thus effectively requiring large computing resources.

In order to construct wave function to describe the bound state of the system consisting of identical fermions must obey the principle of Pauli. Also, not taking into account other significant properties of this type of wave function, it has to be strictly translational invariant. It can be achieved by using translational invariant wave-function expansion which splits the components into symmetric and antisymmetric according to permutations in separate subsystems. This type of wave-function will be dependant only from intrinsic (Jacobi) coordinates which describe only system local degrees of freedom, thus making the wave-function of system independent from the freely moving centre of mass coordinate. This type of transformation requires the use of Talmi-Moshinsky transformation and corresponding brackets . In general these transformations describe an explicit transformation from one set of Jacobi coordinates to another upon passing to different coupling schemes.

This type of approach creates high interest in the accurate and fast calculation routines. Moreover, use of faster algorithms for evaluation of aforementioned transformation coefficients often result in loss of precision which could limit the scope of created algorithm and create uncertainties in results. Therefore, it is essential to have efficient methods for fast evaluation of given coefficients. Moreover, evaluation of given kind are often repetitive, requiring the values, which were already used. Therefore, on purpose to reduce the effective calculation to the maximum, one by can store the evaluated coefficients in the memory of computer. However, by increasing the maximum value of angular momenta for 9-j symbol and energy quanta for 3HOB, it can be observed that the number of calculated coefficients is rising very rapidly, as a result making the the storage and retrieval of needed values a moot point.

One of obvious solutions to employ the symmetries of 9-j symbol and 3HOB, thus effectively reducing the amount of values which require storage. Although use of all symmetry properties of 9-j symbol is quite complex and require large amount of binary calculations, by using only selective symmetry properties one can significantly speed up the process of acquiring required values. Also this type of approach allows use of complex and slow, but very accurate calculation methods for initial coefficient evaluation, thus extending the range of stability of whole algorithm and providing with more accurate results.

In presentation we address the problem for fast Harmonic oscillator transformation brackets for Talmi-Moshinsky transformation and 9-j symbol evaluation requirements. Our approach lets us considerably reduce calculation time of nuclear calculations (Fig.1).

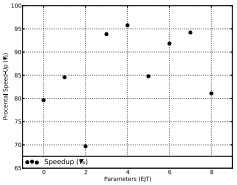

Fig. 1. Speedup of calculations achieved by using symmetries of 9j symbol and 3HOB

[1] A. P. Jucys, A. A. Bandzaitis, Judėjimo kiekio momento teorija kvantinėje mechanikoje (Vilnius, Mokslas, 1977).
[2] G.P Kamuntavicius, R.K. Kalinauskas, B.R. Barrett, S. Mickevicius, D. Germanas, The general harmonic-oscillator brackets: compact expression, symmetries, sums and Fortran code, Nucl. Phys. A **695**, 191-201 (2001).

COMPARISON OF NON-RELATIVISTIC AND QUASIRELATIVISTIC APPROACHES IN THE CASE OF IRON IONS

Darius Stonys, Pavel Bogdanovich

Institute of Theoretical Physics and Astronomy, Vilnius University, Lithuania
darius.stonys@tfai.vu.lt

Over many years in the Department of the Theory of an Atom at ITPA VU, broad theoretical research of atom and ion spectral parameters has been conducted. In order to calculate these spectral characteristics, two approaches that differ by their radial orbitals (RO) are most often used. By solving the Hartree-Fock equations (HFE) [2,3] in the case of non-relativistic approach (NRA), we determine the RO that describe investigated atom configurations. Similarly, in the case of quasirelativistic approach (QRA), we acquire the RO by solving the quasirelativistic HFE. In both these approaches the relativistic effects are taken into account by defining the Hamiltonian matrix in the framework of the Breit-Pauli approximation. We account for the correlation corrections by the configuration interaction (CI) method. For this reason we construct a broad base of transformed radial orbitals (TRO) [4] that guarantee the maximal energy correlation corrections. Afterwards TRO are applied to generate an extensive list of all possible admixed configurations, so we adopt a small variable parameter w as a criterion to select only those admixed configurations that make the greatest contribution to the adjusted configuration (AC) wavefunction. Finally, this selected configuration base is employed to calculate AC energy level spectra, radiative transition parameters and electron collision data.

Although both methods under consideration have been used for a long time, no research has been performed to compare their effectiveness. There is only one publication [5] in which the convergence of QRA with the variation of the selection parameter w is analyzed.

In this work we examine and compare the dependence on w of various physical characteristics, calculated in NRA and QRA in the case of the iron ions (Fe^{10+}, Fe^{12+}, Fe^{18+} and Fe^{20+}). We have selected these ions because of available experimental data [6] and the suitability of NRA, since their ionization degree is not too high.

One of the most reliable indicators that verify the accuracy of CI calculations is a correspondence between experimental data and theoretical results. To evaluate the discrepancy between theory and experiment we use the mean square deviation σ. We present some deviations from experiment [6] of NRA and QRA with different w values in Table 1.

Table 1. The mean square deviations σ of the Fe ion energy spectra (in cm^{-1}) with selection parameters w in bold.

		w					
Ion	Method	**1**	**10^{-4}**	**10^{-5}**	**10^{-6}**	**10^{-7}**	**10^{-8}**
Fe^{10+}	NRA	4395	1326	715	700	706	701
	QRA	4289	591	622	495	502	500
Fe^{12+}	NRA	11955	3618	2194	2314	2255	2262
	QRA	11697	4039	1858	1667	1604	1594
Fe^{18+}	NRA	17981	11702	11192	10402	10110	9961
	QRA	11891	6397	12075	6087	6002	6000
Fe^{20+}	NRA	42249	20721	20586	19758	19671	19638
	QRA	17442	14324	15124	14123	13929	13776

The dependence on w was evaluated for various characteristics: the size of configuration bases, computation times, spectral parameters (radiative lifetimes, transition probabilities) and etc. Furthermore, we also examined the dependence of theoretical level energies accuracy on the size of CI base and on the number of active AC shells.

It is evident from Table 1 that both approaches fluctuate while converging, however, QRA converges to a smaller deviation value compared to NRA deviation. Consequently, QRA facilitates calculation of more accurate results than NRA while using the same computer resources.

[1] V. Fock, Näherungsmethods zur Lösung des quantenmechanischen Mehrkörperproblems, Zr. für Phys., B. **61**, 126 (1930).
[2] P. Bogdanovich, O. Rancova, Quasi-relativistic Hartree-Fock equations consistent with Breit-Pauli approach, Phys. Rev. A, **74**, 052501 (2006).
[3] P. Bogdanovich, O. Rancova, Adjustment of the quasirelativistic equations for *p*-electrons, Phys. Rev. A, **76**, 012507 (2007).
[4] P. Bogdanovich, R. Karpuškienė, Transformed radial orbitals with a variable parameter for the configuration interaction, Lith. J. Phys **39**, 193 (1999).
[5] P. Bogdanovich, D. Majus, T. Pakhomova, Investigation of accuracy of configuration interaction for oxygen isoelectronic sequence, Phys. Scripta, **74**, 558 (2006).
[6] A. Kramida, Yu. Ralchenko, J. Reader and NIST ASD Team (2014). *NIST Atomic Spectra Database* (ver. 5.2), [Online]. Available: http://physics.nist.gov/asd [2015, February 5]. National Institute of Standards and Technology, Gaithersburg, MD.

PLANE EM WAVE DIFFRACTION THROUGH A FINITE SET OF METAL CYLINDERS WITH 1 AND 2 SLITS

Giedrius Tušinskis[1]

[1] Department of Theoretical Physics, Vilnius University, Lithuania
giedrius.tusinskis@ff.vu.lt

The array of parallel cylinders is a convenient object while investigating complex structures, which possess properties that can be used in electronics. Structures from periodic cylinders - photonic crystals - are used in optics as elements of objects which control a beam. Photonic crystals of macroscopic elements are convenient because one can easily manipulate them without any special equipment and the requirements for the precision of processing of the surfaces are lower [1]. Periodic dielectric or metallic structures are a subject of continuing interest because of their wide use for practical devices in microwaves and optical waves [2]. The problem of electromagnetic wave scattering by a finite cylinder set is once again interesting due to the possibility of modeling different type structures [3]. These structures should have perspective properties for their application in electronics and be made from materials with high absorption. Also further development should be made for the problems arising in the range of THz waves [4]. Calculating the intensity of diffraction on a screen is important due to the possibility of creating better optical instruments that can produce higher resolution. This can be used in creating improved microscopes. Calculating techniques allow us to solve boundary problems of complex two-dimensional structures made from cylinders [5], [6].

After solving the boundary problem we find magnitudes of cylindrical waves. With a set of field values one can characterize the system with the required accuracy. It isn't convenient because we have to operate with large amounts of data. Here we investigate the intensity of an EM wave diffracting through a finite set of cylinders with 1 and 2 slits of width 2λ, here λ is the wavelength of the incident wave. We study these parameters with different distances between the cylinders, distance from the screen and slit width. By doing calculations with different parameters we try to find qualitative features of the phenomenon.

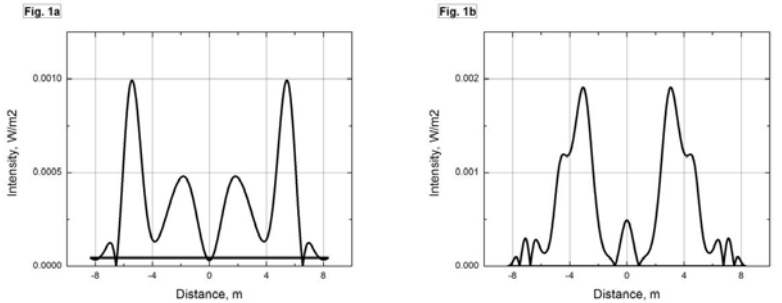

Fig. 1. Intensity of EM wave on a screen with different distances of the screen 0.3m (a) and 0.1m (b), polarization of the wave is parallel to the cylinders.

In Fig. 1 we present the dependencies of the intensity of an EM wave observed on a screen placed at different distances from the set of cylinders. There are N=36 metal cylinders placed perpendicular to the propagation of the wave. The cylinders are of radius R=2mm the cylinders are touching each other but not overlapping. The cylinders are perpendicular to the XoY plane and placed parallel to the Y axis. The screen on which we observe the intensity is placed parallel to the Y axis with the given distance from the cylinders. The frequency of the incident wave f=12GHz. As one can see depending on the distance of the screen from the set of cylinders under investigation the place where we observe the maximum of intensity changes (see Fig. 1 a and b).

[1] F. J. Valdivia-Valero and M. Nieto-Vesperinas, Resonance excitations and light concentration in sets of dielectric nanocylinders in front of a subwavelength aperture. Effects on extraordinary transmission. Optics Express, Vol. 18, No 7, 6740 (2010).
[2] K. Yasumoto, Electromagnetic Theory and Applications for Photonic Crystals, CRC Press, New York (2005).
[3] J. D. Joannopoulos, S. G. Johnson, J. N. Winn, R. D. Meade. Photonic Crystals, Princeton university press (2008).
[4] H. Toyama and K. Yasumoto, Electromagnetic scattering from periodic arrays of composite circular cylinder with internal cylindrical ccatterers. Progress in Electromagnetics Research, PIER 52, 321-333 (2005).
[5] A. K. Ozturk and R. Paknys Analysis of Propagation Between Rows of Conducting Cylinders That Model Solid Surfaces Using the Same Surface Area Rule. IEEE Transactions on Antennas Propagation, VOL. 60, NO. 5, 2602-2606, (2012).
[6] G. Tušinskis, Investigation of absorption in a finite set of cyinders. Open Readings (2014).

Quantum mechanics - molecular dynamics study of UV absorption of acridine yellow bound to human serum albumin

Martynas Velička, Kęstutis Aidas

Department of General Physics and Spectroscopy, Vilnius University, Lithuania
martynas.velicka@ff.vu.lt

In this work a possible human serum albumin binding site for chromophore acridine yellow was investigated via quantum mechanics - molecular dynamics calculations (QM/MM). This was done by calculating the excitation energies of acridine yellow and by comparing the maximum absorption energy shift, going from aqueous to protein environment, with experimental results.

The geometry of acridine yellow was optimised in vacuum of the HF/6-31G* level of theory via "Gaussian09" program [1] and atom charges were assigned using RESP (Restrained Electroscatic Potential) method for HF/6-31G* based electrostatic potentials using "Antechamber". Afterwards, molecular dynamics simulations were run in a rectangular cuboid box with periodic boundary conditions to sample the phase space of acridine yellow in water solution. Molecular dynamics simulations were done with "Amber12" [2] package and consisted of equilibration and production runs, the latter lasting 1200 ps. Non-polarizable TIP3P potential for water was used in these simulations.

The fatty acid binding site in sub-domain IA of human serum albumin was chosen due to a high number of hydrophobic species present in the vicinity compared to the previously analysed binding sites [3]. Out of fourteen possible docking configurations found in this site, two, with most hydrogen bonds formed between acridine yellow and human serum albumin, were selected for the molecular dynamics calculations. The position of acridine yellow in the human serum albumin is presented in Fig. 1. Molecular dynamics simulations in the protein environment were also composed of extensive equilibration and production runs which lasted 3 ns and 2 ns respectively.

Hundred configurations from the last part of molecular dynamics simulations were selected for the quantum mechanical calculations and accordingly hundred excitation energies were calculated using QM/MM techniques. These calculations were run using "Dalton" program [4]. The density functional theory based calculations were run with CAMB3LYP functional and bases set 6-31+G* and aug-cc-pVDZ for calculations in water and bases set 6-31+G* for calculations in protein environment. The calculated excitation energies were summed up using a Gaussian contour and the absorption energy shift was analysed and compared with experimental results.

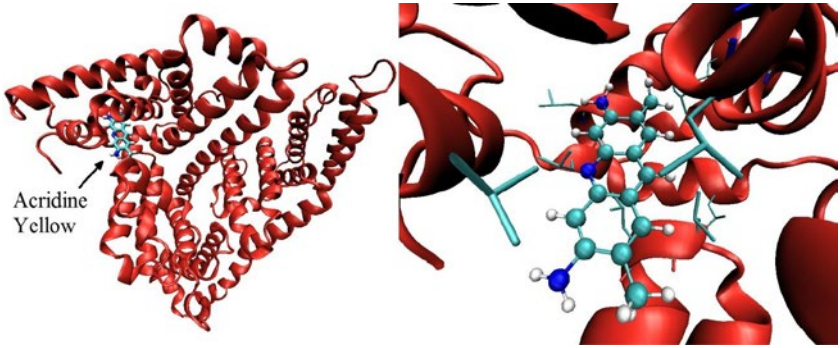

Fig.1. Acridine yellow in its binding site of human serum albumin (left), acridine yellow and neighbouring leucine amino acids (right).

After comparing the experimental results with the results obtained from quantum mechanics – molecular dynamics calculations during this and previous work, it was seen, that the absorption energy shift was slightly higher than previously calculated in different binding sites. The values of absorption energy shifts for the two orientations were 0,15 eV and 0,19 eV. However, the shift is too small compared to the experimental 0,3 eV shift. Thus, from these results it cannot be stated, that the fatty acid binding site in sub-domain IA of human serum albumin is the one, that acridine yellow binds to. Further analysis must be made in order to certify this result.

[1] Gaussian09, Revision D.01, M. J. Frisch, G. W. Trucks, H. B. Schlegel, et. al. Gaussian, Inc., Wallingford CT, 2009.
[2] D. A. Case, V. Babin, J. T. Berryman, R. M. Berz, et. al., Amber 14, University of California, San Francisco, 2014.
[3] K. Aidas, J. Magnus, H. Olsen, J. Kongsted and H. Agren, Photoabsorption of Acridine Yellow and Proflavin Bound to Human Serum Albumin Studiedied by Means of Quantum Mechanics/Molecular Dynamics, J. Phys. Chem. B, 2013, **117(7)**, 2069-2080.
[4] K. Aidas C. Angeli, K. L. Bak, et. al. "The Dalton quantum chemistry program system", WIREs Comput. Mol. Sci., 2014, **4,** 269-284.

PRODUCTION OF m=28 a.m.u. FRAGMENTS FROM THE TRYPTOPHAN, PROLINE AND VALINE MOLECULES BY LOW ENERGY ELECTRONS

Laura Baliulytė[1,2], Jelena Tamulienė[2]

[1]*Vilnius University, Faculty of Natural Sciences, M.K. Ciurlionio st. 21/27, LT-03101 Vilnius, Lithuania*
[2]*Vilnius University, Institute of Theoretical Physics and Astronomy, A. Gostauto 12, LT-01108 Vilnius, Lithuania*
E-mail:Laura.Baliulyte@gf.stud.vu.lt

The studies of the damages amino acids, resulted from the influence of ionizing radiation, are being the hot topic of a series of investigations within last decades. The majority of the above damages are not usually due to the primary high-energy radiation but results from the effect of the secondary low-energy charged particles produced in the course of ionization [1].

The structures of the most stable conformers of tryptophan ($C_{11}H_{12}N_2O_2$), proline ($C_5H_9NO_2$) and valine ($C_5H_{11}NO_2$) were studied using the generalized gradient approximation for the exchange–correlation potential in the density functional theory (DFT) as it is described by the Becke's three-parameter hybrid functional, using the non-local correlation provided by Lee, Yang and Parr. The DFT method is commonly referred to as B3LYP [2]– a representative standard DFT method. The cc-pVTZ basis set has been used as well [3]. The Gaussian 03 Rev D.01 program packages were applied here. The appearance energies of ionic fragments were calculated as the difference between the total energy of the molecule and the sum of the energies of the fragments predicted.

The chemical structure of the amino acids investigated are very different, i.e. they can not be represented as a core molecule with different substitutions. However, in the mass-spectrum of these amino acids, the fragments, which mass is equal to m=28 a.m.u., are found. These fragments could be $C_2H_4^+$ or CH_2N^+, which structure should be C-NH_2, H_2C-N or HC-NH. Hence, the goal of our studies are to determine the structure and chemical composition of the m=28 a.m.u. fragments, which are produced under the above amino acids impact by low energy electrons.

Referring to our results obtained, the most stable composition of the CH_2N^+ ion is HC-NH one. The binding energy per atoms indicates the higher stability of the CH_2N^+ ion than that of the $C_2H_4^+$ one. The energy of the appearance of the $C_2H_4^+$ fragment is larger than that of the CH_2N^+ ion in the all cases investigated. The observations allow us to state that the production of the CH_2N^+ fragments is more probable than $C_2H_4^+$ under low energy electron impact of the tryptophan, proline and valine molecules. This ion could be produced during fragmentation reactions presented in Table 1.

Table 1. Fragmentation reactions and energy of the apperance of the CH_2N^+ fragments formed under low electron impact of the tryptophan, proline and valine molecules

Fragmentation reactions	Appearance energies, eV
$C_{11}H_{12}N_2O_2 + e \rightarrow CH_2N^+ + (COOH+C_9H_8N)^- + e$	9.64
$C_5H_9NO_2 + e \rightarrow CH_2N^+ + C_4H_7O_2^- + e$	10.40
$C_5H_{11}NO_2+e \rightarrow CH_2N^+ + (COOH+H+C_3H_7)^- + e \rightarrow CH_2N^+ + (C_4H_7O_2+H_2)^- + e$	9.10
$C_5H_{11}NO_2+e \rightarrow CH_2N^+ + (COOH+H+CH(CH_3)_2)^- + e \rightarrow CH_2N^+ + (C_4H_7O_2+H_2)^- + e$	10.11

Acknowledgment
The authors are thankful for the high performance computing resources provided by the Information Technology Open Access Center of Vilnius University.

[1] S. Cristoni, L.R. Bernardi, Mass. Spectr. Rev. **22**, 369 (2003).
[2] A.D. Becke, J. Chem. Phys., **98**, 5648 (1993).
[3] R.A. Kendall, T.H. Dunning., R.J. Harrison, Electron affinities of the first-row atoms revisited. Systematic basis sets and wave functions, J. Chem. Phys., **96**, 6796–6806 (1992).

UP-CONVERTING NANOPARTICLES: SYTHESIS AND PROPERTIES

Zofia Felcyn[1], Piotr Samol[1], Izabela Kamińska[2], Vicente Montes Jiménez[3]

[1]Faculty of Physics, Adam Mickiewicz University, Poland
[2]Institute of Physics, Polish Academy of Sciences, Poland
[3]Department of Organic Chemistry, Universidad de Córdoba, Spain
zofia.felcyn@gmail.com
samol.piotr@gmail.com

The generation of higher energy radiation from exciting radiation of lower energy is called up-conversion. This phenomenon describes the transition of the radiation of low energy to a higher energy radiation by multiphoton absorption and subsequent luminescence.

Up-converting nanoparticles have many applications but our main goal is a synthesis of nanoparticles that can be used in fluorescent imaging. Typically to excite fluorophores UV light is used but UV light has plenty of disadvantages (especially to living organisms) which will be listed in the poster. But by using up-converting nanoparticles we can prevent potential damages to organisms since the nanoparticles are excited with near-infrared radiation[1]. There is also hypothesis concerning biofunctionalization of these nanoparticles to use them in treatment e.g. of cancer but it is not exactly our research goal.

In this poster we focus on synthesis of nanoparticles emitting visible light from infrared radiation in two-photon absorption. We used Gd_2O_3 as a matrix doped with rare earth elements: Yb and Er. We synthesized them by simple precipitation method. We investigated how time and addition of Mo atoms affect fluorescence intensity and emission spectrum.

Structure and size of nanoparticles were also determined. These measurements were taken on scanning electron microscope (SEM). Exemplary photo below:

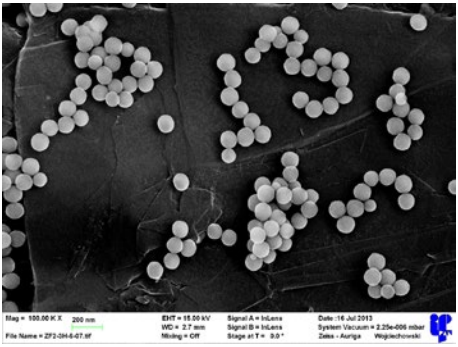

Fig. 1. Photo of Gd_2O_3:$Yb^{3+}Er^{3+}$ nanoparticles made by SEM.

[1] B. Sikora, Transport of $NaYF_4$:$Er^{3+}Yb^{3+}$ up-converting nanoparticles into HeLa cells, Nanotechnology **24** (2013)

ANALYSIS OF PROSTATE CANCER EPIGENOME - IDENTIFYING NEW DNA METHYLATION MARKERS

Agnieška Mackoit[1], Kristina Daniūnaitė[2] and Sonata Jarmalaitė[2]

[1] Faculty of Medicine, Vilnius University, Lithuania
[2]Human Genome Research Centre, Faculty of Natural Sciences, Vilnius University, Lithuania
agnieska.mackoit@mf.stud.vu.lt

Epigenetic mechanisms associated with DNA methylation at CpG loci play a fundamental role in both normal development and disease. Assessment of DNA methylation using microarray technology enables the quantitative analysis of DNA methylation throughout an entire genome[1]. Methylation profiling may potentially improve our understanding of epigenetic events that regulate gene expression and influence development of complex diseases such as cancer.

Despite significant increase in knowledge of genetic and epigenetic changes causing prostate cancer (PCa) during the last decade, it still is a major cause of cancer-related morbidity in men living in Western countries[2]. Identification of new potential epigenetic biomarkers could greatly enhance our ability to diagnose PCa and predict its biochemical recurrence (BCR) after surgery.

The main goal of our study – is to investigate global DNA methylation profile of PCa using DNA methylation microarrays and evaluate the diagnostic and prognostic value of the selected epigenetic markers for PCa detection. We will examine epigenetic changes in genes in order to gain new insights into underlying molecular mechanisms of PCa development.

For microarray analysis, immunoprecipitated and reference DNA was labeled with cyanine 5-dUTP and cyanine 3-dUTP respectively. Then labeled DNA was purified and hybridized onto 1x244K format microarray slide. Selection of target genes was based on methylation array data analysis (Fig.1). DNA methylation profile was analyzed according to ≥212000 probes localized in promoters or exons and introns of known and predicted genes. Targets for further analysis were selected from more than 1000 genes that showed significant differences in methylation profile. Candidates were selected according to the following criteria: gene methylation difference between the groups (prostate tumors vs nontumors; progressed vs nonprogressed cases), statistical significance, and data from literature and databases

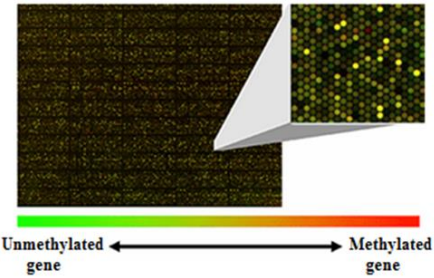

Fig. 1. Microarray data analysis for selection of the significantly differentially methylated genes

For further investigation, selected epigenetic markers will be analyzed using molecular genetic techniques such as methylation-specific polymerase chain reaction (MSP) to validate their methylation status in cancerous and benign prostate samples. MSP results will be linked to clinical-pathological characteristics of the patients in order to evaluate the diagnostic potential of selected genes as biomarkers.

We expect that biomarkers would identify early stages of the disease and increase our ability to distinguish indolent and aggressive tumors of PCa patients.

[1] Baylin, S., Jones, P.A. (2011). A decade of exploring the cancer epigenome — biological and translational implications. *Nature Reviews Cancer* 11, 726-734.
[2] Hatcher, D., Daniels, G., Osman, I., Lee, P. (2009). Molecular mechanisms involving prostate cancer racial disparity. *Am J Transl Res*:1(3):235-248.

CELLULAR UPTAKE AND CYTOTOXICITY OF PHOTOLUMINESCENT Au-MES NCs IN MCF-7 CANCER CELLS

L. Budėnaitė[1], M. Matulionytė-Safinė[1,2], R. Rotomskis[1,2]

[1]Biomedical Physics Laboratory, National Cancer Institute
[2]Biophotonics Group of Laser Research Centre, Vilnius University
budenaite.laima@gmail.com

Gold nanoparticles (Au NPs) exhibiting unique optoelectronic properties, easy surface modification and low toxicity are one of the newest strategies in nanomedicine. Au NPs in diameter from 4 nm to several hundreds of nanometres demonstrate plasmonic absorption, therefore they can be used in photothermal cancer therapy. Due to nanoscale size comparable to the Fermi wavelength of electrons (~0.7 nm) recently synthesized photoluminescent ultrasmall gold nanoclusters (Au NCs) can easily bypass natural barriers and accumulate in cells and tissues which makes them very promising fluorescent markers. Knowledge about internalization, cellular uptake and cytotoxicity of NPs is essential before these nanomaterials can be used in nanomedicine. Unfortunately, there is still not enough information about it, therefore, more research is required. In this work cellular uptake and toxicity of 2-(N-morpholino)ethanesulfonic acid coated gold nanoparticles (Au-MES NPs) in epithelial breast cancer cells MCF-7 were investigated

NCs were synthesized according to modified synthesis protocol proposed by Bao et.al. [1] by mixing chloroauric acid solution HAuCl4 (0.29 M) and aqueous MES buffer solution (1 M, pH 6.3) to the volume ratio of 1:5. The synthesis was performed for 21.5 hours at 37 °C temperature under vigorous stirring. The synthesized colloidal solution exhibited photoluminescence at 476 nm indicating formation of ultrasmall Au-MES NCs below 1 nm in diameter [2].

To investigate uptake of photoluminescent Au-MES NCs in MCF-7 breast cancer epithelial cells laser confocal microscopy was used. The cells were incubated with Au-MES NCs (45 mg/ml) for 3, 6 and 24 hours. After 3 hours of incubation the diffuse distribution of photoluminescent Au-MES NCs within the cells was observed. After longer times of incubation photoluminescence intensity of Au-MES NCs within the cells increased. Au-MES NCs distribute evenly in total volume of a cell, including nucleus. It can be clearly seen that nanoparticles were not encapsulated in vesicles. Due to small size Au-MES NCs might have accumulated in cells via a non-endocytic pathway. Nuclear pore size for passive diffusion of molecules is about 9 nm [3], therefore particles that are smaller than the pore size, including photoluminescent Au-MES NCs, could cross envelope of nucleus.

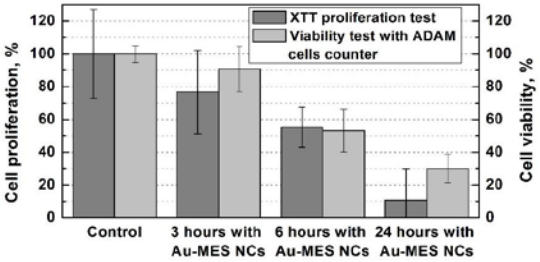

Fig. 1. XTT proliferation and ADAM viability tests of MCF-7 cells after incubation with Au-MES NCs for 3, 6 and 24 hours.

Toxicity of Au-MES NCs to MCF-7 cells was evaluated by XTT proliferation test and with ADAM cell counter. Both tests showed decreased viability and proliferation with increased time of incubation (Fig. 1). Control values were considered as 100 %. ADAM viability test after 3 hours of incubation showed 91 % viability. After 6 hours of incubation viability decreased to 53 %. After 24 hours of incubation viability was less than 31 %. XTT proliferation test after 3 hours of incubation showed 77 % proliferation. After 6h proliferation was less than 55 % and after 24 hours of incubation – 19.2 %. Propidium iodide dye stained dead cells were observed using confocal fluorescence microscope and confirmed results that longer time of incubation with Au-MES NCs has stronger toxic effect on MCF-7 cells. Photoluminescent Au-MES NCs show high cellular toxicity levels in breast cancer epithelial cells MCF-7.

[1] Y. Bao, H.-C.Yeh, Ch. Zhonget. al., Formation and Stabilization of Fluorescent Gold Nanoclusters Using Small Molecules, J. Phys. Chem. C 114, 15879–15882 (2010).
[2] M. Matulionytė, R. Marcinonytė, R. Rotomskis. PhotoinducedspectralchangesofphotoluminescentgoldnanoclustersJournalofBiomedicalOptics 20, 51018 (2015).
[3] P. L. Paine, L.C. Moore, S.B. Horowitz.Nuclear-Envelope Permeability.Nature.254,109–114 (1975).

Study of Fe-S centers and Free Radical Processes in Prostate tumors by EPR Method

Ana Khazaradze, Liana Ramishvili, Nanuli Kotrikadze

Department of Biology, Faculty of Exact and Natural Sciences, Iv. Javakhishvili Tbilisi State University
any_khazaradze@yahoo.com

Electron Paramagnetic Resonance (EPR) spectroscopy has a big potential in the study and identification of individual iron-sulphur (Fe-S) clusters of whole macromolecular protein complexes, as well as organelles such as mitochondria and chloroplasts [1, 2].

The goal of the given work was the study of Fe-S centres and free radical processes in benign and malignant human prostate tumour tissues and in mitochondrial suspensions, respectively.

The studies have shown that in case of prostate cancer the decrease of Fe-S cluster EPR-signal intensity (g=1.94, g=2.01) occurs in parallel to the intensification of free radical processes. Intensification of free radical processes and the accompanying damage of Fe-S clusters in prostate cancer tissue indicate the disruption of respiratory chain complex I and II function.

In case of the mitochondrial suspension, the increase of cytochrome P450 EPR-signal (g=2.25) indicates the disruption of steroidogenesis in prostate epithelium and the decrease of the superoxide dismutase EPR-signal (g=2.14) indicates the weakening of its activity, as a mitochondrial antioxidant system, in case of prostate malignant tissue.

[1] Malkin R, Bearden AJ, Primary reactions of photosynthesis: photoreduction of a bound chloroplast ferredoxin at low temperature as detected by EPR spectroscopy,Proc Natl Acad Sci USA 68:16–19 (1971)
[2] Evans MCW,Sihra CK, Bolton JR, Cammack R, Primary electron acceptor complex of Photosystem I in spinach chloroplasts, Nature 256:668–670 (1975)

ANALYSIS OF AUTO-FLUORESCENCE OF GYNECOLOGICAL SAMPLES IN GYNOPREP

Vilmantas Gėgžna[1, 2], Ignas Čiplys[1], Lukas Gudiškis[1],
Rūta Kurtinaitienė[3], Aurelija Vaitkuvienė[2]

[1] Faculty of Natural Sciences, Vilnius University, Vilnius, Lithuania
[2] Institute of Applied Sciences, Vilnius University, Vilnius, Lithuania
[3] Vilnius Unversity Hospital Santariskiu Klinikos, Vilnius, Lithuania

Ignas.Ciplys@gf.stud.vu.lt

Fluorescence spectroscopy has a huge potential to be used in the field of medical diagnostics. One of the possible branches of application is diagnostics of cervical pre-cancer. To adopt spectroscopy-based technologies in medicine appropriate methods for data analysis are required for each type of medical specimen. In the previous research [1] auto-fluorescence spectra of liquid cervical smears preserved in fixation liquid called GynoPrep were investigated. Data formalization technique based on curve fitting with multiple Gaussians was implemented. Unfortunately, this method requires a bunch of subjective decisions of an investigator to be made as well as rules of convergence are not clear. To avoid these drawbacks current research is directed towards optimization of cervical smears in GynoPrep auto-fluorescence spectra analysis by means of applying more rigid methods for data formalization.

Methods. 76 auto-fluorescence spectra of medical cervical smear samples belonging to 3 medical groups (*normal* – no pathology found, *cervicitis* – inflammation of cervix, *CIN2+* – pre-cancerous condition) were investigated. The medical groups were determined by histological test, which is considered to be a gold standard in medicine. Data analysis algorithms including principal component analysis (PCA) *varimax* rotation, multivariate curve resolution alternating least squares (MCR-Als) and mutual information based least dependent component analysis (MILCA), curve-fitting techniques were applied to extract 12 components as it was done in the earlier mentioned investigation [1]. Receiver operating characteristic (ROC) test was used to assess performance of medical group classification.

Results. The best result in terms of AUC (area under the ROC curve) acquired using combination of MCR-ALS algorithm which uses the result of PCA with *varimax* rotation as initial conditions. The components extracted by this method are shown in Fig.1 and the graphical representation of the results are drawn in Fig.2. As expected, the best discrimination qualities (AUC > 0.75) were achieved comparing normal and pre-cancerous CIN2+ groups.

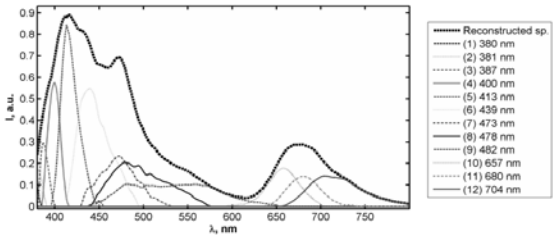

Fig. 1. Components extracted by using combination of MCR-ALS, PCA and *varimax* algorithms.

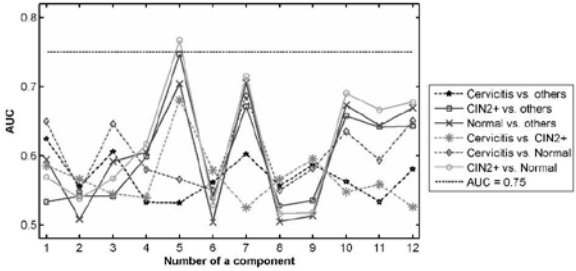

Fig. 2. Graphical representation of the results acquired by using combination of MCR-ALS, PCA and *varimax* algorithms.

[1] A. Vaitkuviene, V. Gegzna, R. Kurtinaitiene, and J. V Vaitkus, Cervical smear photodiagnosis by fluorescence, *Photomed. Laser Surg.*, **30**(5), 268–74, (2012).

MULTIVARIATE ANALYSIS OF HUMAN INTERVERTEBRAL DISC SAMPLES' NATIVE FLUORESCENCE

Vilmantas Gėgžna[1, 2], Lukas Gudiškis[1], Darius Varanius[1, 2], Ignas Čiplys[1], Gunaras Terbetas[3], Aurelija Vaitkuvienė[2]

[1] Faculty of Natural Sciences, Vilnius University, Vilnius, Lithuania
[2] Institute of Applied Sciences, Vilnius University, Vilnius, Lithuania
[3] Clinics of Neurology and Neurosurgery, Faculty of Medicine, Vilnius University, Vilnius, Lithuania

Vilmantas.Gegzna@gf.stud.vu.lt

This research is directed towards the multivariate analysis of native fluorescence (also known as auto-fluorescence) of human intervertebral disc samples for medical classification purposes.

During operations of intervertebral disc hernia in Clinics of Neurology and Neurosurgery pieces of intervertebral disc tissue were removed as a part of conventional procedure. Autofluorescence of these samples were excited in-vitro with 355 nm radiation (microlaser STA-01-TH, Standa, ltd.) and registered with spectrometer OceanOptics USB2000 through a system of fiber optics. The specimens were classified to three medical groups in accordance with localization of tissue (D – specimen from inner part of a disc, S – free sequester, P – herniation from subligamentous space). In this investigation 527 spectra (group D – 38%, group P – 41%, group S – 21%) were investigated.

Spectral data reduction was carried out by means of multivariate curve resolution methods (such as multivariate curve resolution-alternating least squares and principal component analysis) utilizing 11 component model, which gave the highest performance in the previous investigation (unpublished data). The performance of group identification was performed pairwise (D vs. P, D vs. S, P vs. S, and S vs. all remaining groups, i.e., others, P vs. others, D vs. others.) applying receiver operating characteristic (ROC) method.

Results. Component nr. 11 was considered to be a noise due to extremely low amplitude. The best performance to discriminate groups was achieved using the long-wave side components. Despite the fact that the amplitudes of components are overlapped the tendencies to separate spectra can be noticed in the graphical representation of results (Fig.1). The accuracy higher than the minimum requirement for medical tests (i.e. area under the ROC curve, the AUC, is greater than 0.75) was achieved.

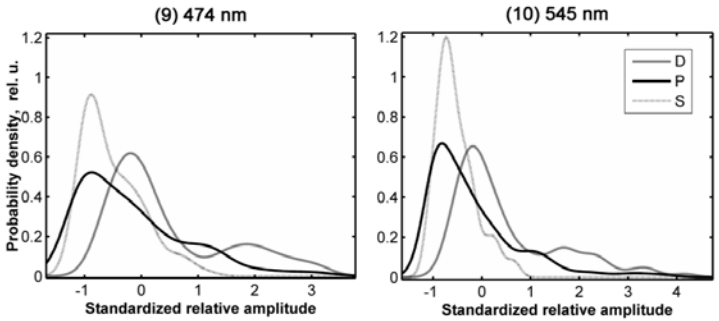

Fig. 1. Smoothed probability density functions of the standardized relative amplitudes of the 9th (left) and the 10th (right) components which peak positions are at 474 and 545 nm respectively.

PHOTOINDUCED BLEACHING AND DEGRADATION OF CHLOROPHYLLS IN FRESHWATER ALGAE

Agnė Kalnaitytė, Saulius Bagdonas

Quantum Electronics Department, Faculty of Physics, Vilnius University, Lithuania
agne.kalnaityte@ff.stud.vu.lt

Chlorophylls (Chls) are among the most important biomolecules in the organic world, which allow plants' cells to absorb energy from light and to use it in photosynthesis. However, a small fraction of absorbed light is re-emitted as fluorescence (FL), which can be used for relatively easy spectroscopic detection of photosynthetic pigments. The yield of FL in plants' cells is influenced in a complex manner by factors that are directly or indirectly related to photosynthesis. Thus, Chls can be regarded as intrinsic fluorescent probes in plants' study, for example, in physiology [1]. Algae cells can be used as model organisms for investigation of higher plants, because they have similar mechanisms of photosynthesis including Chls pigments and store starch as an energy reserve.

Excessive amount of absorbed light can cause fluorescence bleaching of Chls indicating an adaptation response in green plants. It can also impair photosynthesis by inducing photodamage to the photosynthetic reaction centres and degrading Chls. While chemical structures, biosynthesis and function of the chlorophylls are known in detail [2], mechanisms of Chls degradation have remained among the least well understood biological processes.

This study reports on spectroscopy and microscopy measurements that were performed on freshwater microalgae *Scenedesmus* in aqueous medium under exposures to the blue light of different intensity. Photoinduced bleaching and degradation of chlorophylls were investigated in the living algae cells.

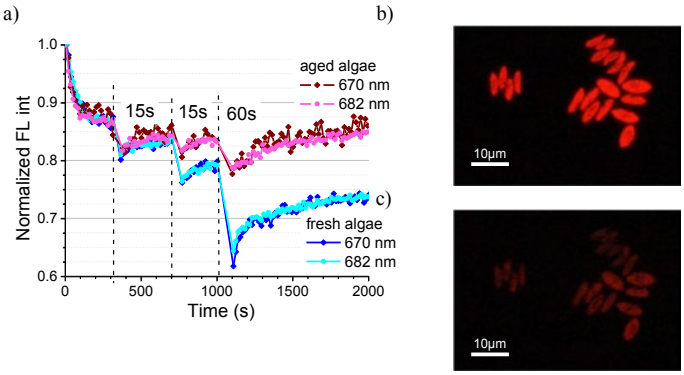

Fig. 1. Kinetics of fluorescence bleaching (at 670 nm and 682 nm wavelengths, λ_{ex}=405 nm) in algae cells from fresh (ten days) and aged (two months) populations. During the measurement cells were additionally exposed to the blue diode (404±9 nm (FWHM), 90 mW/cm^2) light twice for 15 s and once for 60 s (a). Fluorescence view (λ_{ex}=380-420 nm) of algae cells before (b) and after (c) exposure with a similar irradiation dose as that used for (a).

When exposed to blue light, chlorophylls fluoresce brightly in the red region of the spectrum (Fig. 1). In samples of algae from aged population the FL intensity of chlorophylls at 682 nm and 670 nm decreased relatively less than in samples of algae from fresh population (Fig. 1a). Additional irradiation with a blue diode caused short-term reversible photobleaching of microalgae FL that depended on the age of algae population. The bleaching of red-fluorescing algae cells was clearly observed after the exposure to a similar irradiation dose (Fig. 1b, c).

The exposures through the 100x oil immersion objective using three different excitation ranges (λ_{ex}=330-380 nm, λ_{ex}=380-420 nm and λ_{ex}=510-560 nm) allowed monitoring the step-wise decrease of intensity of red fluorescence leading to its total disappearance in algae cells. At first their red fluorescence turned into whitish in the area of a sample exposed at λ_{ex}=380-420 nm, and then – into the blue fluorescence. The green algae cells became transparent on the phase contrast images. Thus, a number of photoproducts with different fluorescence properties can be distinguish in algae cells by means of fluorescence microscopy during degradation of chlorophylls induced by the exposure to the blue light.

[1] G. H. Krause, E. Weis, Chlorophyll fluorescence as a tool in plant physiology. II. Interpretation of fluorescence signals, Photosynthesis Research **5**, 139-157 (1984).
[2] G. Karp, Cell and Molecular Biology, 6th edition, 211-220, (2010).

INACTIVATION OF *SALMONELLA ENTERICA* USING PHOTOACTIVATED CHLOROPHYLIN-CHITOSAN COMPLEX

Viktorija Lukševičiūtė, Živilė Lukšienė

Institute of Applied Research, Vilnius University, Lithuania
viktorija.lukseviciute@tmi.vu.lt

S. Enterica – one of the most common food born pathogens. According to European food safety authority this gram negative bacteria causse 100 thousand illnesses in EU each year. Conventional food decontamination methods are not always safe and effective. It enforces reserchers across the world explore inovative methods for food safety. One of the most promising and environmentally friendly methods is photosensitization [1]. Thus the aim of this work was to evaluate inactivation of *Salmonella Enterica* using photoactivated chlorophylin-chitosan complex (Chl-CHS).

Chlorophylin (Chl) is a green food colorant, also known as food additive E141 [2] and chitosan (CHS) is biodegradable, nontoxic biopolymer widely-used as an antimicrobial agent [3]. Both materials are considering safe for people and compatible with food. It was shown that photosensitization itself is effective against gram positive pathogens but not against gram negative [4]. CHS was used to ensure close Chl localization to the target since close vicinity is crucial for the effectiveness of photoactive dye.

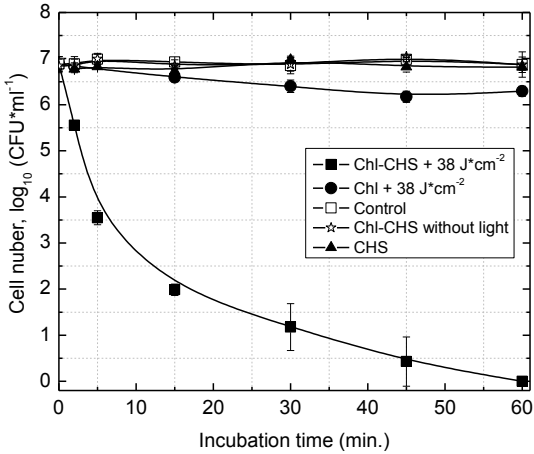

Fig. 1. *S. Enterica* inactivation dependence of incubation time using 0.1% CHS, photoactivated $1.5 \cdot 10^{-5}$ Chl (light dose 38 J·cm^2) and photoactivated 0.001% Chl–0.1% CHS complex (light dose 38 J·cm^2).

Samples with bacteria and Chl or Chl-CHS complex were illuminated by 405 nm light, dose 38 J·cm^{-2}. Spread plate method was used to evaluate the effectiveness of 0.001 % Chl alone, 0.1 % CHS alone, and 0.001% Chl–0.1% CHS complex. Results are presented in Fig. 1. CHS alone did not affect *S. Enterica* since the result is the same as control. Chl alone has a small effect on *S. Enterica,* it shows 0.5 log reduction from control samples. In contrast Chl-CHS complex shows *S. Enterica* inactivation until undetectable level. These results demonstrate synergetic antibacterial effect of Chl and CHS which could rely on complexation. Soluble conjugates of Chl-CHS contain positive charge and bacterial cell wall contains slightly negative charge. Such conditions let them bind through electrostatic forces.

Since this food decontamination method is non thermal, cost effective and uses non hazardous compounds it has a huge perspective to be applied for food safety.

[1] Z. Luksiene and L. Brovko, Antibacterial Photosensitization-Based Treatment for Food Safety, Food Engineering Reviews **5**, 185–199 (2013).
[2] G. Lopez-Carballo and M. J. Ocio, Photoactivated Chlorophyllin-based gelatin films and coatings to prevent microbial contamination of food products, International Journal of Food Microbiology **126**, 65–70 (2008).
[3] M. Kong, X. G. Chen, K. Xing and H. J. Park, Antimicrobial properties of chitosan and mode of action: A state of the art review, International Journal of Food Microbiology **144**, 51-63 (2010).
[4] Kairyte K., Lapinskas S., Gudelis V. ir Luksiene Z., Effective inactivation of food pathogens *Listeria monocytogenes* and *Salmonella enterica* by combined treatment of hypericin-based photosensitization and high power pulsed light, Journal of Applied Microbiology **112**, 1144–1151 (2012).

MODERN MICROBIOLOGICAL DIAGNOSTICS USING BY MASS SPECTROMETRY MALDI-TOF MS-MS

[1]Emil Paluch

[1]Department physicochemistry of microorganisms, Institute of Genetics and Microbiology, University of Wroclaw, Poland.

mikro.paluch.emil@gmail.com

Microbiological research conducted at the Institute of Genetics and Microbiology in cooperation with the Wroclaw Zoo in Poland (2012-2014) on a variety of species lizards (n= 24). Research confirmed the significant carriers reptiles for *Enterobacteriaceae* strains. Cloacal swabs were taken during the study, from healthy animals. Two techniques are applied in this study, the first is based on the identification of microorganisms on the basis of their biochemical characteristics using microbiological media- bacteria were grown on media: Lisogeny Broth, Mac Conkey Agar, Shigella Salmonella Agar and a second which is tandem mass spectrometry MALDI-TOF MS/MS. [1]

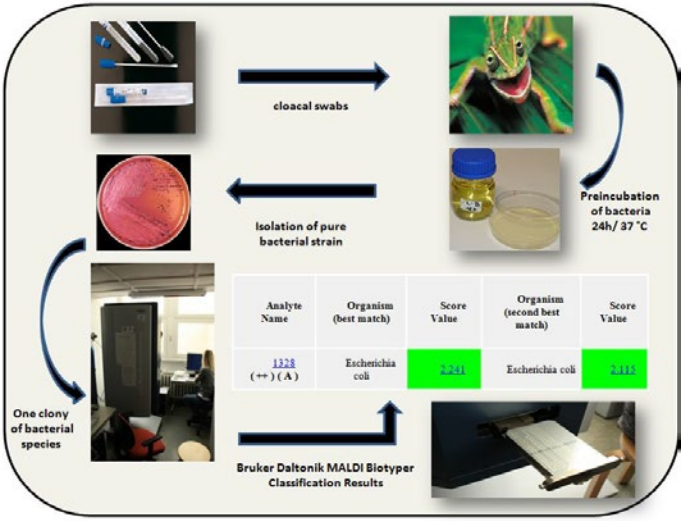

Fig. 1 The process of isolation and identification of microorganisms using by mass spectrometry MALDI TOF MS/MS.

In the study 11 bacterial species were isolated within the family *Enterobacteriaceae*, including species (*Klebsiella variicola*), which up until this study there has been no recorded cases of isolating these from reptiles. For each different genus of the family *Enterobacteriaceae*, studies have shown the following carriers among lizards such: *Salmonella* (33%), *Klebsiella* (23%), *Citrobacter* (17%), *Proteus* (10%), *Escherichia* (10%), *Enterobacter* (10%) and *Morganella* (3%). The obtained isolates will be included in the PCM (Polish Collection of Microorganisms) in IITD Polish Academy of Sciences. [2]

[1] Seng P., Drancourt M., Gouriet F., Scola B., Fournier P., Rolain J., Raoult D. Ongoing revolution in bacteriology: Routine identification of bacteria by Mastrix-Assisted Laser Desorption Ionization Time-of-Flight Mass Spectrometry. CID 49. Pp. 543-551, 2009.

[2] Miętka K, Książczyk M., Paluch E., Dudek B., Korzekwa K., Korzeniowska-Kowal., Tobiasz A., Ratajszczak R., Fabiszewska-Jerzmańska M., Bugla-Płoskońska G. Antybiotykooporność pałeczek *Enterobacteriaceae* i *Pseudomonaceae* wyizolowanych w latach 2012-2014 od gadów przebywających w Ogrodzie Zoologicznym .Ogólnopolska konferencja naukowa „Wektory i Patogeny", Wrocław 2014.

INVESTIGATION OF THE COLOUR DISCRIMINATION USING SMART SOLID-STATE LIGHTING

Justina Aglinskaitė[1], Lurdė Andrijauskaitė[1], Andrius Petrulis[1]

[1] Institute of Applied Research, Vilnius University, Lithuania
justinaaglin@gmail.com, lurde.andrijauskaite@gmail.com

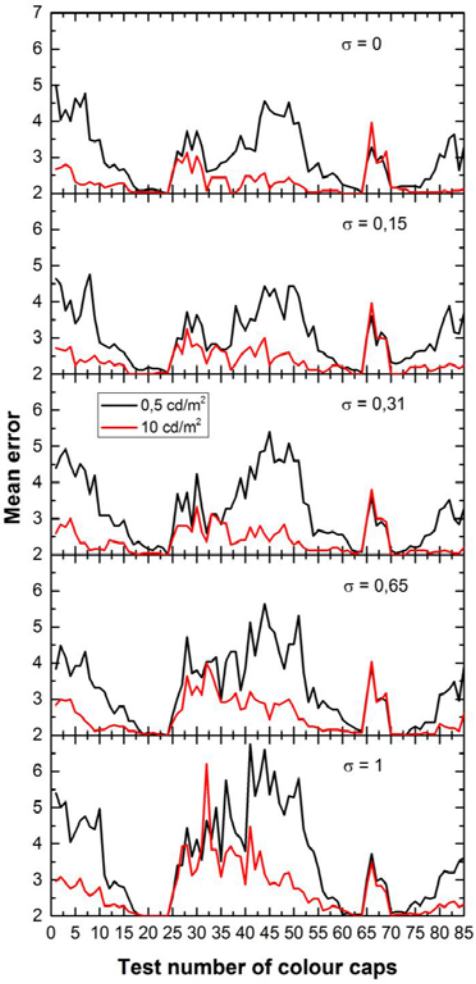

Fig. 1 Investigation results at 5 sets of different colour quality (σ) with 2 levels of luminance.

Nowadays one of the most important parameters for the light source is an excellent colour rendition. Ideal light source should render colours with the highest colour fidelity in general case. Illuminated objects with a similar reflectance spectrum should be discriminated and hue distortion must be minimal [1].

The main objective of this investigation was to research human colour discrimination ability under different conditions of the same solid-state lightning source. Farnsworth–Munsell 100 Hue Test [2] (FM test) was chosen. It contains 85 different hue caps of the same saturation which are divided into four colour areas. Test subjects are asked to arrange coloured caps according to their chromatic vision. The number of errors made during the test correlates with a human ability to discriminate colours.

Six participants (3 men and 3 women with average age of 23) took 5 sets of FM tests under two different luminances (0,5 cd/m^2 and 10 cd/m^2). Each set represents a different level of colour quality: $\sigma = 0$ – dulling lighting; $\sigma = 0{,}15$ – natural (the highest fidelity) lighting; $\sigma = 0{,}31$ – preferential lighting; $\sigma = 0{,}65$ – slightly saturated; $\sigma = 1$ – fully saturated. Sets were generated in random order by the tetrachromatic metameric solid-state light source consisted of red, amber, green and blue light-emitting diodes with colour rendering index of 93 at 3000 K natural lighting.

Results of the colour discrimination are showed in Fig. 1. Black line shows mean error for each colour cap at low luminance, red line – for high luminance. Under the 0,5 cd/m^2 luminance (mesopic vision) mean error score is considerably higher than under 10 cd/m^2 luminance (photopic vision). Colour quality sets reveal that the highest number of errors are when $\sigma = 1$ and the lowest at $\sigma = 0{,}15$ and $\sigma = 0$. This shows that colour discrimination is the best under natural or slightly dulling lighting. Research revealed that human ability to discriminate colours is the poorest in greenish (caps from 25 to 55) and reddish (caps from 75 to 15) visible spectrum regions. The best discrimination is in the yellowish and purplish regions. Errors repeated in every set from 65 to 70 caps are originated by the incorrect FM test caps reflectance and degradation. Decreased errors at green-blue colours region with increased luminance are conditioned by the eye sensitivity shift from cyan to green colour. Finally, this investigation shows that when metameric light source increases gamut area of illuminated objects, it decreases the ability to discriminate colours.

[1] M.S. Rea and J.P. Freeyssinier-Nova, "Color Rendering: A Tale of Two Metrics" Color Res. Appl. 33(3), 192-202 (2008).
[2] D. Farnsworth, "The Farnsworth-Munsell 100-Hue and Dichotomous Tests for Color Vision", Journal of the Optical Society of America 33, 568–574 (1943).

INFLUENCE OF EMOTIONAL PICTURES ONTO MICROSACCADIC RATE

Ieva Vaišnoraitė[1], Aleksandras Pleskačiauskas[2], Osvaldas Rukšėnas[2*]

[1] Department of Neurobiology and Biophysics, Vilnius University, Lithuania
ieva.vaisnoraite@gf.stud.vu.lt

Microsaccades - the biggest and fastest fixational eye movements. It is small involuntary saccades that occur during fixation. Last decade many research works showed link between microsaccades and perception. Researches show that microsaccadic rate depends on covert attention - biphasic response with sudden drop and increase of microsaccadic rate after stimulus presentation.
Involuntary microsaccades and voluntary saccades can be an index of human brain activity in attention and oculomotor behavior tasks. The question is if they can reflect human's emotional attention. There is no accurate and objective way to evaluate quantitatively attention to emotional stimuli. Proper method would help to diagnose mental disorders.

Emotions by Charles Darwin are evolutionary adaptation because it is essential that emotional stimuli would be sensed faster than neutral stimuli. One of the theories is that we perceive emotional information faster due to attention directed to emotional stimuli which allows discriminating important information from less important. Brain structures responsible for attention displacement, emotions, microsaccades and saccades generation are connected. It would be logical to search links between these eye movements and emotional attention.

In our research we searched how reaction to emotional pictures from IAPS (*International Affective Picture System*) affects microsaccadic rate. We found that microsaccadic response inhibition for about 100 – 300 ms after stimulus onset and at 400 – 600 ms we found reliable difference in social unpleasant stimuli comparing to pleasant ones. Also we noticed that microsaccadic rate was lower for social stimuli. For all emotional pictures female microsaccadic rate was higher than for male suggesting that women attention to stimuli is higher than men.

Microsaccades research is a new and promising direction and it can be perspective method to explore emotional attention mechanisms.

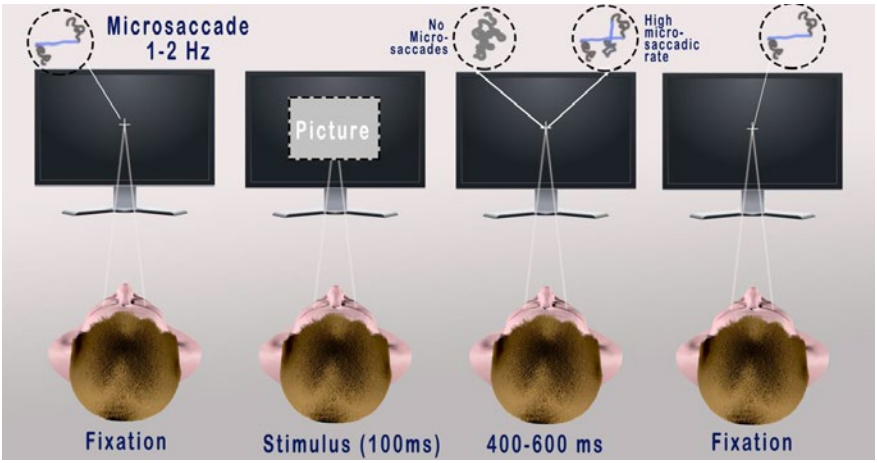

Fig1. Abstract experiment scheme. Microsaccadic rate drops sudden after the stimulus onset with following increase after it.

[1] K. Kashihara, K. Okanoya, N. Kawai, Emotional attention modulates microsaccadic rate and direction. Psychol Res 2013 Mar 28.
[2] R. Engbert, R. Kiegl, Microsaccades uncover the orientation of covert attention. Vision Res 2003 Apr.

IMMERSION LIQUID FOR ULTRASONIC THROMBOLYSIS

Yekelchyk Michail[1], Nosan Darya[2]
[1] Department of Physics, Belarusian State University, Belarus
[2] Medical Faculty, Belarusian State Medical University, Belarus
yekelchyk@yahoo.com

Cardiovascular diseases are the leading cause of morbidity and mortality in the world. Intervention methods are traditional in the ischemic conditions treatment. However, in spite of the good results obtained, intervention methods have some disadvantages: low efficiency of angioplasty in vessels with intracoronary thrombus and restenosis. One of the most perspective methods of interventional cardiology is the intravascular use of low-frequency high-intensity ultrasound [1]. But it was found that in addition to effective restoration of arterial patency ultrasound exposure has a negative impact on the vascular wall [2]. Therefore it is important to search for optimal parameters of ultrasonic exposure and use of the immersion medium.

Objective of work is to investigate the effectiveness of immersion liquids use with ultrasonic thrombolysis.

Methods:

1) Elmors chemical condensation method was used for immersion liquids creation;
2) Toxic investigation methods were used for bio neutrality tests;
3) Mass degradation method was used for investigations of clot destruction efficiency;
4) Calorimetric and luminescent methods were used for cavitation threshold investigations.

Results:

1) The cavitation threshold in immersion liquids is much lower than the cavitation threshold in blood (8-14 times less), so less energy needed for cavitation.

2) Three different immersion liquids had developed (based on 0,9% NaCl solution, based on dextran, based on an aqueous solution of 10 % citric acid). Immersion liquids showed an extremely high performance of bio neutrality (experiments *in vitro* on erythrocytes and *in vivo* on laboratory mice).

3) The experiments of clot mass degradation *in vitro* showed an increase of degradation using immersion (MF) liquids (relative to the control sample); *(without magnetic field)* 9.3 - 27.4% for immersion based on dextran; 14.1 - 31.6% for immersion based on 10% citric acid solution (Fig. 1); *(with magnetic field)* 9.8 - 42.5% for immersion based solution 0,9% NaCl; 9.5 - 47.3% for immersion based on dextran; 12.3 - 45.9% for immersion based on 10% citric acid solution; 6.3 - 44.8% for immersion based on solution 0,9% NaCl.

4) Immersion liquid based on 10% citric acid solution showed the best results in clot destruction.

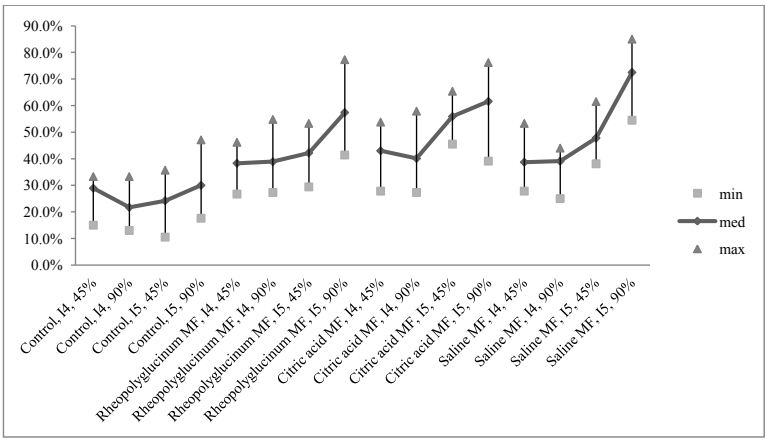

Fig. 1. Thrombus destruction *in vitro* (no magnetic field).

[1] Adzeriho, I.E. Ultrasound thrombolysis in the treatment of arterial thrombosis : MD PhD dissertation: 14.00.06 / I.E. Adzeriho. - Minsk 2004. - 322 p.

[2] Efimova N.N. "Effect of ultrasound on the efficiency and thrombolysis hemostasis using waveguides of different designs (experimental study)." MD PhD dissertation: 14.00.06. - Minsk, 2009. – 115 p.

Implementation of optimal illuminants for retinal imaging using a spectrally tunable light source based on a digital micromirror device

Piotr Bartczak[1], Pauli Fält[1], Daiga Čerāne[2], Niko Penttinen[1] Markku Hauta-Kasari[1]

[1]School of Computing, University of Eastern Finland, Finland
[2]Department of Optometry and Vision Science, University of Latvia, Latvia
daiga.cerane@lu.lv

White light illumination (e.g. Xenon flash) is typically used for the optical imaging of human retina. However, these broadband light sources are not necessarily optimal for getting the best possible visibility of different features-of-interest in retinal images. The use of optimal light sources, which have optimized spectral shapes for the contrast-enhancement of various retinal features or lesions in fundus images, would therefore be preferred.

In order to implement these optimal illuminants, a spectrally tunable light source based on a digital micromirror device (DMD) was constructed, and retinal images were captured. The images taken with optimal illuminants were compared with red-free fundus images.

RECEPTOR MODELS APPLICATION IN LONG-RANGE TRANSPORT OF CARBONACEOUS AEROSOL PARTICLES IN COASTAL ENVIRONMENT

Vadimas Dudoitis, Steigvilė Byčenkienė, Kristina Plauškaitė,
Nina Prokopčiuk, Genrik Mordas, Vidmantas Ulevičius

Department of Environmental Research, SRI Center for Physical Sciences and Technology, Lithuania
vadimas.dudoitis@ftmc.lt

Aerosol emissions from biomass and fossil fuel burning have a huge impact on air quality and climate. These processes together with atmospheric oxidation of biogenic and anthropogenic volatile organic compounds are the main sources for carbonaceous aerosol particles [1].

The knowledge of long-range transport origin and contribution to pollution level can help outspread the understanding of the nature of local air pollution at a given location. Long-range air mass backward trajectories are evaluated using HYSPLIT4 model [2]. For estimating potential pollution source areas, different receptor modelling approaches, i.e. air mass cluster analysis and concentration weighted trajectory (CWT) analysis, were applied [3].

Measurements were conducted at the Atmospheric Research Station located in Preila (55°55'N; 21°04'E) from 1st to 31st of March 2014. Two instruments were used during the measurement campaign. Aerosol Chemical Speciation Monitor (ACSM) provided continuous measurement of aerosol chemical components: organics, SO^{2-}_4, Cl^-, NH^+_4 and NO^-_3 [4]. The Aethalometer (Magee Scientific model AE31) was deployed to measure carbonaceous aerosol particle light-absorption properties and black carbon (BC) concentration.

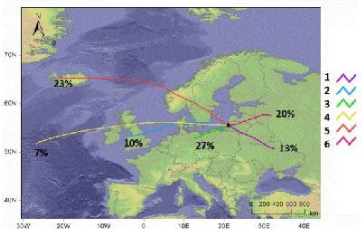

Fig. 1. Air masses backward trajectory (duration 72 h) cluster representation in Preila.

Table 1. The clusters and their mean aerosol concentrations of organic aerosol, nitrates, sulphates, ammonium, chloride and black carbon.

Clusters	Org., μg m^{-3}	SO^{2-}_4, μg m^{-3}	NO^-_3, μg m^{-3}	NH^+_4, μg m^{-3}	Cl^-, μg m^{-3}	BC, μg m^{-3}
1	8.94	2.25	0.56	1.68	0.23	1.29
2	5.64	0.91	1.10	1.34	0.18	0.51
3	3.30	1.20	3.23	1.03	0.21	0.50
4	6.81	2.21	1.42	1.28	0.06	0.25
5	1.60	0.71	1.26	0.30	0.08	0.80
6	4.62	1.12	1.54	1.35	0.23	0.60
Mean	4.25	1.56	1.71	1.21	0.12	0.82

Clustering of air masses is representation of similar trajectories by movement and direction. The air masses from W and NW direction, represented in clusters 2, 4 and 5 (Fig. 1), were longer and moved faster, while trajectories in clusters 1, 3 and 6 were shorter and moved slower.

The 1st cluster represented the SE air mass trajectory pathway with the highest mean concentrations for the whole measurement period (Table 1). In this cluster, the influence of biomass burning in Belarus and Ukraine was indicated due to high CWT values. The trajectories of the 3rd cluster were the shortest, therefore air masses spent more time over the small area (i.e. Kaliningrad and Poland). It could be indicated that the accumulation of pollutants from the grass fires, which had occurred at that time of the year. In this cluster, the highest BC concentration reached up to 12.00 μg m^{-3} and average total loading of ACSM was 7.20 μg m^{-3}, organics contributed to more than half of the aerosol mass. The 4th and 5th clusters were represented by clean and fast moving air masses from the W and NW and resulted in BC concentrations equal or lower than estimated mean value of 0.75 μg m^{-3} in Preila.

Acknowledgements. The research leading to these results has received funding from Lithuanian-Swiss cooperation programme to reduce economic and social disparities within the enlarged EU under project agreement No CH-3-ŠMM-01/08.

[1] T. C. Bond, S. J. Doherty et al., Bounding the role of black carbon in the climate system: a scientific assessment, Journal of Geophysical Research: Atmospheres **118(11)**, 5380–5552 (2013).
[2] R. R. Draxler, G. D. Rolph, HYbrid Single-Particle Lagrangian Integrated Trajectory Model, http://ready.arl.noaa.gov/HYSPLIT.php (2014)
[3] V. P. Kabashnikov, A. P. Chaikovsky et al., Estimated accuracy of three common trajectory statistical methods, Atmospheric Environment **45 (31)**, 5425–5430 (2011).
[4] N. L. Ng, S. C. Herndon et al., An Aerosol Chemical Speciation Monitor (ACSM) for routine monitoring of the composition and mass concentrations of ambient aerosol, Aerosol Science and Technology **45(7)**, 780–794 (2011).

CHARACTERIZATION OF AEROSOL OPTICAL PROPERTIES AT PETERHOF (RUSSIA) STATION

Olga Juralevičiūtė[1], Yury M. Timofeev[2], Anatoly V. Poberovsky[2], Inna Frantsuzova[2], Brent N. Holben[3], Alexander Smirnov[3], Ilya Slutsker[3]

[1] Faculty of Physics, Vilnius University, Lithuania
[2] Faculty of Physics, Saint Petersburg State University, Russia
[3] NASA's Goddard Space Flight Center, USA
olga.juraleviciute@ff.stud.vu.lt

Aerosols contribute to atmospheric pollution and affect human health. Additional scattering and absorption of light caused by aerosols has cooling effects on climate. Aerosol particles act as seeds for cloud droplets influencing the albedo of a cloud in addition to affecting its ability to produce precipitation.

Since March 2013 a Cimel sunphotometer is running at Peterhof (Russia). Two years of aerosol measurements have been analyzed. Sun photometer was used to measure the columnar aerosol optical depth (AOD) at the wavelengths of 340, 380, 439, 500, 675, 869, 937, 1019 and 1638 nm.

Figure 2 shows the monthly mean AOD at 500 nm from March 2013 to August 2014. The mean AOD varies on a monthly basis reaching minimum value in October (0,081 ±0,026) and March (0,092±0,031) indicating that the atmosphere at that period was relatively clean. The lower mean AOD in autumn, which is the rainiest season of all, may be due to wash-out by rains. Growth of AOD in winter season may be associated with heating. Biomass burning, anthropogenic aerosols during winter (January, February) enhanced the AOD twice in comparison with October. However, due to the lack of sunny days in winter, data is less accurate. Generally speaking, the AOD values were smaller in fall and the biggest in summer.

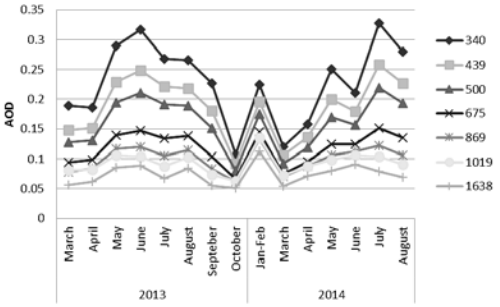

Fig. 1. Monthly means of AOD at 340, 439, 500, 675, 869, 1019, 1638 nm at Peterhof

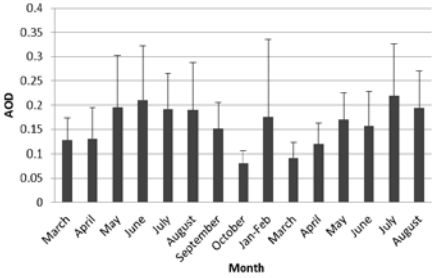

Fig. 2. Monthly means of AOD at 500 nm at Peterhof, calculated using AERONET level 1.5 monthly mean values. Error bars indicate standard deviation

Diurnal variability of AOD is important for various applications, including satellite aerosol data validation, radiative forcing computations, studies of aerosol interaction with humidity and clouds, and public health [2]. AOD increases by 10-40% during daytime at most urban sites [2]. This trend is observed in Peterhof too. AOD increases in the morning, reaching the maximum value and then decreased. In 2013 in spring, summer and autumn maximum values are reached approximately from 12:00 to 16:00 (GMT+3). We observed that in 2014 AOD maximum value distribution during daytime was seasonally dependent. In winter AOD reached the maximum value at 15:00 and in spring at 12:00.

We correlated the optical depths for different wavelengths in Peterhof and nearby stations: Kuopio (Finland), Hyytiala (Finland), Helsinki (Finland), Helsinki Lighthouse (Finland) and Toravere (Estonia). In 2013 Peterhof station data correlated best with the data from Toravere station (0,64-0,68) and a similar trend was observed in 2014 with Helsinki station (0,64-0,68). Values of AOD in Peterhof and Toravere are considerably bigger than in other stations.

Acknowledgment:

The authors are grateful for the right to use the data from the following stations: 1. Toravere and personally Erko Jakobson; 2. Helsinki and personally Gerrit de Leeuw; 3. Helsinki Lighthouse and personally Giuseppe Zibordi; 4. Hyytiala and personally Gerrit de Leeuw; 5. Kuopio and personally Antti Arola.

[1] Jianjun Liu, Youfei Zheng, Zhanqing Li, Rongjun Wu, Ground-based remote sensing of aerosol optical properties in one city in Northwest China, Atmospheric Reserch 89 (2008) 194-205

[2] Smirnov A., Holben B. N., Eck T. F., Slutsker I., Chatenet B., Pinker R. T., 2002. Diurnal Variability of aerosol optical depth observed at AERONET (Aerosol Robotic Network) sites. Geophysical Research Letters 29 (23), 2115. doi:10.1029/2002GL016305

STABLE SULFUR ISOTOPE RATIO IN AEROSOL PARTICLES

Inga Rumskaitė[1], Andrius Garbaras[1] and Vidmantas Remeikis[1]

[1] Institute of Physics, Center for Physical Sciences and Technology, Lithuania
inga.rumskaite@ftmc.lt

The concentration of anthropogenic aerosols in the Earth's atmosphere has grown rapidly since the industrial revolution. Sulfur containing aerosols has a cooling effect on our planet through their ability to scatter incoming solar radiation and increase cloud formation and reflectivity. Also, they take an important part of increasing acidity of precipitation and affecting terrestrial ecosystems. Sulphates represent a significant part of sulfur containing aerosols. They are formed most from the oxidation of sulfur dioxide (SO_2) produced in the combustion of fossil fuels and industrial processes [1].

To investigate the origin and the movement of sulfur through the atmosphere the sulfur isotope ratio in aerosol particles was measured by using IRMS (Isotope-ratio mass spectrometry). Two stable sulfur isotopes were chosen to examine their ratio $^{34}S/^{32}S$ in meaning of $\delta^{34}S$ (Eq. (1)) in aerosol particles.

$$\delta^{34}S = \left[\frac{\left({}^{34}S/{}^{32}S \right)_{SAMPLE}}{\left({}^{34}S/{}^{32}S \right)_{STANDARD}} - 1 \right] \times 1000, ‰ \qquad (1)$$

Atmospheric aerosol particles were collected on a quartz fiber filter using High Volume Autosampler. Then water soluble sulphates were extracted and precipitated as barium sulphate ($BaSO_4$) by adding barium chloride to the solution. Membrane filters with sulphate were analyzed using elemental analyzer – IRMS system for $^{34}S/^{32}S$ isotopic ratio.

Obtained differences in sulfur isotope ratio in air masses coming from the Baltic Sea and continent revealed the potential of stable sulfur isotope ratio applicability in atmospheric aerosol source apportionment studies.

[1] C.T. Lin, A.R. Baker, T.D. Jickells, S. Kelly, T. Lesworth. An assessment of the significance of sulphate sources over the Atlantic Ocean based on sulphur isotope data, Atmospheric Environment 62, 615–621 (2012).

SPATIAL AND TEMPORAL VARIATIONS OF AEROSOL CHEMICAL COMPOSITION IN LITHUANIA

Julija Pauraitė[1,2], Genrik Mordas[2], Vidmantas Ulevičius[2]

[1]Faculty of Physics, Vilnius University, Lithuania
[2]Institute of Physics, Center for Physical Sciences and Technology, Lithuania
julijapauraite@gmail.com

Aerosol particles affect global climate, ecosystems and human health. The influence of aerosol depends on particle chemical composition and physical properties. Mass concentration trends of the main aerosol components and their correlations with black carbon (BC) were investigated to assess the contribution of the main carbonaceous sources in three different environments.

An Aerosol Chemical Speciation Monitor (ACSM) was used for continuous measurements of aerosol composition during 2013 – 2014 years. ACSM measures aerosol mass concentration and chemical composition of non-refractory submicron aerosol particles in real-time. It provides information about composition for particulate ammonium, nitrate, sulfate, chloride and organics. A Magee Scientific Company Aethalometer^{TM}, Model AE31 Spectrum, manufactured by Aerosol d.o.o., Slovenia, provided real-time, continuous measurements of the BC mass concentration. The optical transmission of carbonaceous aerosol particles was measured sequentially at 7 wavelengths (λ= 70, 450, 520, 590, 660, 880 and 950 nm). The concentration of BC corresponds to the 880 nm. Measurements were carried out in Preila, Rūgšteliškis and Vilnius which represent marine, rural and urban environments, respectively.

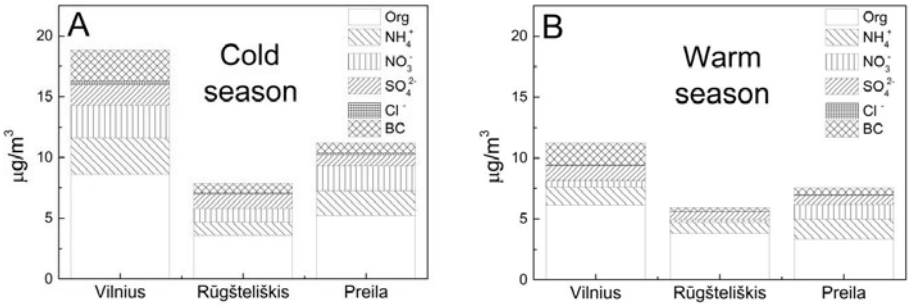

Fig 1. Aerosol particle chemical composition during (A) cold and (B) warm seasons.

The annual data of main chemical components concentrations in three environments were divided into cold and warm seasons. The aerosol particles in Vilnius, Rūgšteliškis and Preila consisted mainly of organics (45.7%, 46.0% and 46.9%, respectively), NO_3^- (14.3%, 14.8% and 18.4%, respectively) and NH_4^+ (15.9%, 13.1% and 18.0%, respectively) during the cold season. The BC concentration in Vilnius was twice higher than in Preila and Rūgšteliškis. Meanwhile, during the warm season organic relative contribution increased to 54.8% and 64.3% in Vilnius and Rūgšteliškis, respectively. The BC relative contribution decreased up to 5.5% and 6.0% in Rūgšteliškis and Preila, respectively.

Thus, it can be concluded that the main chemical component in all three environments during both seasons is organics. Moreover, during the cold season the BC concentration was affected by local sources (mainly domestic heating and traffic) and during the warm season the contribution of the local sources is lower.

[1] N. L. Ng, S. C. Herndon, et al., An Aerosol Chemical Speciation Monitor (ACSM) for Routine Monitoring of the Composition and Mass Concentrations of Ambient Aerosol, Aerosol Science and Technology **45**, 780-794 (2011).
[2] S. Byčenkienė, V. Ulevičius, S. Kecorius, Characteristics of black carbon aerosol mass concentration over the East Baltic region from two-year measurements, Journal or Environmental Monitoring **13**, 1027-1038 (2011).

QUANTITATIVE ANALYZE OF WATER REUSE RELATED TO ENERGY SAVING

Marina Valentukevičienė

Department of Water Management, Vilnius Gediminas Technical University, Lithuania
marina.valentukeviciene@vgtu.lt

The main aim of this study was estimation - how water reuse can save energy provided for water supply at students dormitories. The research was carried out by exchange students studying at Vilnius Gediminas Technical University (Lithuania). The quantity of the water reuse was measured as follows: daily (L/d) and weekly L per 7 days. The energy quantity for water supply was calculated and estimated using installed water pump technical characteristics.

Water reuse is one of the key strategies of Green University recycling system in Lithuania. Water reuse can help realize that energy-efficient and sustainable equipment is required at students dormitories and class-rooms. At present, reusability of water and energy is determined only by the materials functional situation or the economic cost evaluation analysis. It does not cover all triangle of sustainability, including environmental, economic and social point of views. In this study, the sustainable integrated method, hands-on possibilities assessment, is employed to measure reusability of water and energy saving. The references [1 and 2] were used for the comparison research needs. Water reuse experience at other contries was usefull when all measurements and statistical calculations were carried out.

Measured and statistically evaluated results of possible water reuse at students' dormitory (presented in Fig. 1), were found to be different following all students activities evaluated in this research. All abbreviations in the Figure 1 means: Ma-morning activities (showers, toothbrush, breakfast); Mi-midday activities (lunch); Gi-sport related activities; Sa- sauna-related activities; Ve – evening related activities (dinner); Ba - (bath).

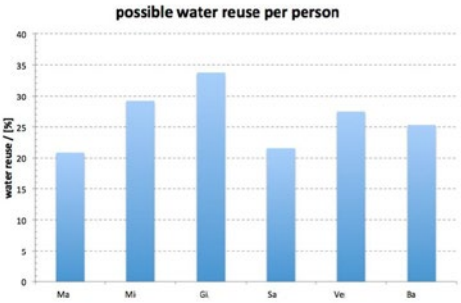

Fig. 1. Percentage of possible water reuse at different facilities.

Annually approximately 1839 m^3 water can be reused in case of implementing water saving devices at students dormitory. Estimated and calculated saved energy quantities supposed to be approximately 232 kWh annually per academic year. The results of case studies show that, energy saving based reusability of shower water and bath water will help improve water supply facilities at student's dormitories.

[1] Li, F.; Wichmann, K.; Otterpohl, R. Review of the technological approaches for grey water treatment and reuses, Science of the Total Environment 407: 3440–3447 (2009).

[2] Li, Z.; Boyle, F.; Reynolds, A. Rainwater harvesting and greywater treatment systems for domestic application in Ireland, Desalination 260, (2010).

NONEXTENSIVE STATISTICS FOR RELATIVISTIC PROTON-PROTON AND HEAVY ION COLLISIONS

Greta Ambrazevičiūtė, Karolis Tamošiūnas[1]

[1] Vilnius University, Institute of Theoretical Physics and Astronomy, Goštauto g. 12, 01108 Vilnius, Lithuania
greta.ambrazeviciute@ff.stud.vu.lt

High energy physics studies strongly interacting matter at extreme temperatures and densities. The Large Hadron Collider, at CERN, is the particle accelerator with the highest energy per nucleon presently available.

The transverse momentum spectra of hadrons produced in collisions involving protons and also heavy ions at RHIC and LHC energies have recently been successfully investigated through nonextensive statistical mechanics. Nonextensive statistics is recently introduced generalization of Boltzmann-Gibbs statistics. Four decades ago a statistical-mechanical approach to analytically describe transverse momentum spectra was already used. It was done using Boltzmann-Gibbs statistics. This classical approach works well at low beam-energies. However, the experiments at higher energies have produced data that depart more and more from a standard thermal behavior, giving rise to power-law distributions in the high transverse momentum regime. These properties, as seen in Fig. 1, are well reproduced using nonextensive statistics (Eq. 1). It will be shown that nonextensive statistics reproduces transverse momentum spectra for wide energy range and different collisions i.e. p-p, Pb-Pb, p-Pb.

$$f(p_T) = A\, exp_q\left(\frac{m_T}{T}\right) = A\left(1 + (q-1)\frac{m_T}{T}\right)^{\frac{1}{1-q}} \tag{1}$$

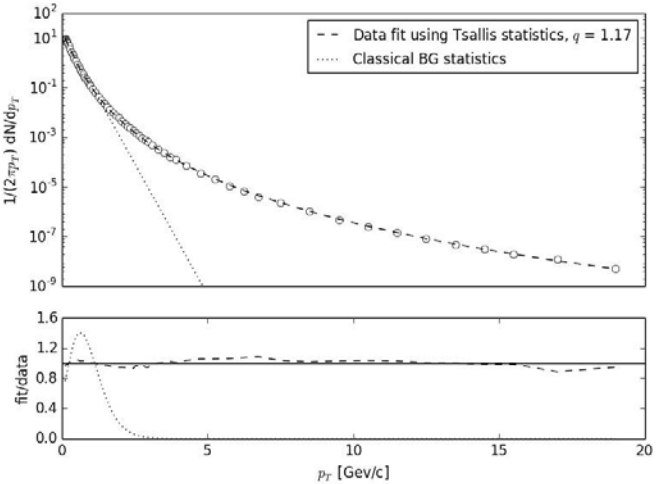

Fig. 1. Comparison of experimental transverse momentum distribution data (circles) of pions in pp collisions fits, using classical (dots) and Tsallis (dashes) statistics. The ratios fit/data are shown at the bottom. Data from [1].

[1] B. Abelev et al. (ALICE Collaboration), Production of charged pions, kaons and protons at large transverse momenta in pp and Pb-Pb collisions at $\sqrt{s_{NN}}$= 2.76 TeV (2014), arXiv:1401.1250

HYDRODYNAMIC METHOD TO ESTIMATE INITIAL STATE OF HEAVY ION COLLISION

Tomas Babelis[1], Karolis Tamosiunas[1]

[1]Institute of Theoretical Physics and Astronomy, Vilnius University, Gostauto g. 12, 01108 Vilnius, Lithuania
tomas.babelis@ff.stud.vu.lt

It is believed, that for a first few milliseconds after the Big Bang the universe was an incredible dense plasma consisted most of deconfined quarks and gluons. This state of matter is called quark-gluon plasma (QGP) [1]. QGP is also supposed to exits in the core of neutron stars. In the Earth, QGP can be produced in particle accelerators by colliding two heavy ions at sufficiently high energy. In heavy ion collision experiments, QGP cannot be detected directly, and its properties must be inferred from the spatial distribution of formed particles.

The purpose of this study is to describe new method to estimate initial state of heavy ion collisions. Collective dynamics of QGP is best described by hydrodynamics and approximate Landau solution of hydrodynamics equations gives a good description for the evolution of quark-gluon plasma in relativistic heavy-ion collisions [2]. The rapidity distribution of number of produced particles for the central collisions in the center-of-mass system to be

$$\frac{dN}{dy} \propto \exp\sqrt{y_{beam}^2 - y^2}, \tag{1}$$

where $y_{beam} = \ln(\sqrt{s_{NN}/m_N})$ is the beam rapidity, m-mass of the nucleon, $\sqrt{s_{NN}}$ - c.m. energy per nucleon. The analytical relation between rapidity distribution and initial state parameters gives a possibility to make calculation back in time from experimental data to QGP formation [3]. So, having experimental Event-by-Event data it is possible to find initial state parameters: thermalization thickness and energy gradient function. Knowledge of these parameters will help to understand QGP formation dynamics.

After heavy ion collision the volume of produced QGP rapidly expands with decreasing its temperature and energy density. Another purpose of this study is to investigate kinetic Freeze-Out radius influence on the outcome of hydrodynamic calculations. Using simple Wounded Nucleon model [4] for initial state, we have shown that Freeze- Out radius has very small impact on the distribution of particle multiplicity in transverse and longitudinal planes. Consequently it will be shown, that modified Landau solution can be used as a new method to investigate initial state of heavy ion collision directly from experimental data.

[1] H. Bohr and H. Nielsen, "Hadron production from a boiling quark soup," 1977.
[2] C.-Y. Wong, "Lectures on Landau Hydrodynamics," Phys. Rev. C, vol. 78, p. 54902, 2008.
[3] K. Tamosiunas, "Longitudinal Scaling of Elliptic Flow in Landau Hydrodynamics," Eur. Phys. J., vol. 47, p. 121, 2011.
[4] A. Bialas, M. Bleszynski, and W. Czyz Nucl. Phys., 1976.

GLAUBER MODEL FOR RIDGE-LIKE CORRELATIONS IN HIGH-MULTIPLICITY PROTON-PROTON COLLISIONS

Patryk Kubiczek[1], Stanisław D. Głazek[2]

[1] Faculty of Physics, Astronomy and Applied Computer Science, Jagiellonian University in Krakow, Poland
[2] Faculty of Physics, University of Warsaw, Poland
patryk.kubiczek@student.uj.edu.pl

Recently, the CMS collaboration reported an unexpected long-range in rapidity, near-side ("ridge-like") angular correlations in very high multiplicity proton-proton collisions, so called ridge effect [1]. This surprising observation suggests the presence of a collective flow that resembles the one believed to produce a similar correlation hydrodynamically in heavy-ion collisions.

If the hydrodynamic description is valid then the effect should be triggered by the initial spatial anisotropy of the colliding matter. The estimation of this anisotropy within different models of the proton internal structure and verifying whether it leads to the agreement with the experimental data could in principle constitute a test for such models.

Inspired by [2,3] we proposed several phenomenological models of the internal structure of proton. Subsequently we calculated the expected initial eccentricity and triangularity of the dense matter formed in proton-proton collisions within the formalism of the Glauber model, commonly used in the description of heavy-ion collisions [4]. We indeed found that the initial anisotropy can account for the ridge effect, though our considerations do not lead to a very stringent test of the models.

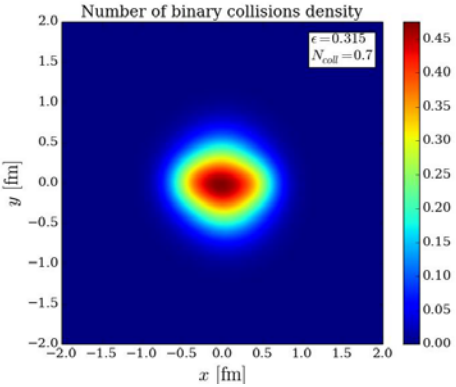

Fig. 1. Density of colliding matter (precisely, number density of protons' constituents binary collisions) for a sample proton-proton collision. The numerical value of eccentricity ϵ for this event is presented.

[1] V. Khachatryan et al. [CMS Collaboration], Observation of Long-Range Near-Side Angular Correlations in Proton-Proton Collisions at the LHC, JHEP **1009**, 091 (2010), arXiv:1009.4122 [hep-ex].
[2] S. D. Glazek, Hypothesis of quark binding by condensation of gluons in hadrons, Few-Body Syst. **52**, 367 (2012), arXiv:1110.1430 [hep-ph].
[3] J. D. Bjorken, S. J. Brodsky, A. S. Goldhaber, Possible multiparticle ridge-like correlations in very high multiplicity proton-proton collisions, Phys Lett. **B 726**, 344 (2013), arXiv:1308.1435 [hep-ph].
[4] R. J. Glauber in *Lectures in Theoretical Physics* ed. W. E. Brittin and L. G. Dunham (Interscience Publishers, New York, 1959), 1-315 (1959).

RECOVERING STAR FORMATION HISTORY OF GALAXIES

Marius Čeponis[1], Donatas Narbutis[2]

[1] Faculty of Physics, Vilnius University, Lithuania
[2]Center for Physical Sciences and Technology, Lithuania
marius.ceponis@ff.stud.vu.lt

Understanding galaxy star formation histories is crucial to constrain cosmological parameters and galaxy evolution scenarios in general. Here we present a method developed to recover star formation histories based on simple stellar population approach applied for the interpretation of stellar photometric data of the resolved galaxies.

Photometric measurements of a star sample in a galaxy are compared to a theoretical model bank of simple stellar populations to derive age and mass probability density distribution functions of individual stars. Assuming that the star sample consists of star subsamples of various ages, the total mass of stars born at particular time in the past (i.e. star formation history) is recovered.

Performance of the method was tested on simulated observations of simple stellar populations (7 age and 4 mass nodes) of the quality that is achieved with Subaru telescope in the M33 galaxy using *BVRI* filter system. Padova isochrones [1] and Kroupa initial stellar mass function [2] were used to simulate 20 populations per each node. The half-width of the interval between 15th and 85th percentiles of the recovered parameter distributions divided by the true parameter (age or mass) value are displayed as accuracy in each node of Fig. 1.

The method is applicable to the ground-based wide-field survey observations of nearby resolved galaxies, like M31 and M33, and also for the Hubble Space Telescope and forthcoming James Webb Space Telescope data of a more extensive sample of distant galaxies.

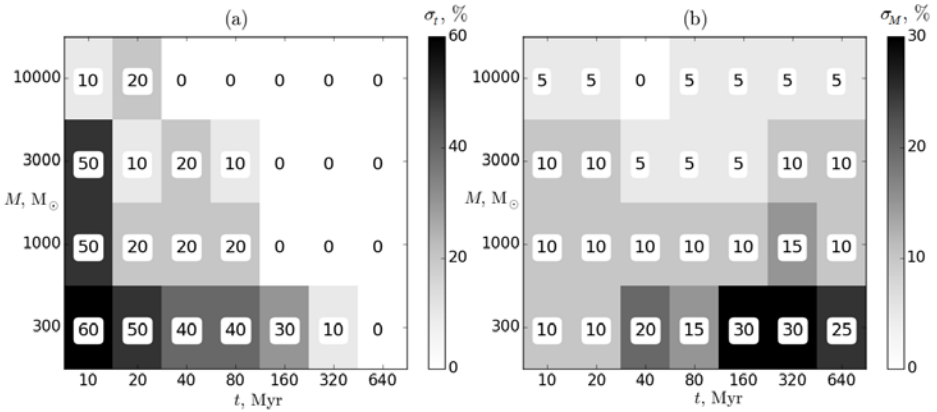

Fig. 1. The accuracy (grey scale corresponds to the percent indicated in each node) of the method tested to derive age (a) and mass (b) of simulated simple stellar populations. In total 20 simulations were made per each node of the grid of 7 ages, t, and 4 masses, M.

[1] L. Girardi, "CMD 2.7": http://stev.oapd.inaf.it/cgi-bin/cmd.
[2] P. Kroupa (2001) "On the variation of the Initial Mass Function" *Mon. Not. Roy. Astron. Soc. 322, 231.*

ASTROPHYSICAL MASERS TYPE II

Marta Dziełak

Centre for Astronomy, Nicolaus Copernicus University, Toruń
mmaerta@gmail.com

Stimulated emission is not only present in technology. This phenomena we can observe both - at optical wavelengths (known as a laser) and at microwaves (called a maser).

We can observe astrophysical masers from many astronomical objects. For some of these sources, this is only a way to determine in details their nature and physical properties.

Astrophysical masers of type II are connected with regions where the intensive formation of massive stars is taking place. Using interferometric observations, it is possible to conclude kinematic and structural features of protostar's neighborhood, when long-term monitoring of maser spectrum can provide crucial information about the evolution of the source.

FRAGMENTATION OF GAS AND STAR FORMATION IN GALAXY-WIDE OUTFLOWS

Eimantas Ledinauskas[1], Kastytis Zubovas[2]

[1]Faculty of Physics, Vilnius University, Lithuania
[2]Department of Fundamental Research, Centre for Physical Sciences and Technology, Lithuania
eimantasl@gmail.com

In recent years observations in active galaxies revealed highly ionized relativistic winds [1] and kiloparsec-scale outflows [2] which are evidence for galaxy-wide outflows induced by active galactic nuclei (AGN).

According to the model of AGN wind feedback [3] if the mass of the supermassive black hole (SMBH) exceeds some, particular for a galaxy, critical mass then its wind shocks can propagate to large distances from SMBH where it is not efficiently cooled by Compton scattering any more and then hot (~10^7 K) and fast (~10^3 km/s) energy-drivenoutflows form. These violent outflows can blow gas and dust away from a galaxy and therefore stop the star formation in it. However, since after the shock and cooling the matter density in an outflow can be about million times higher than the pre-shock density, these outflows could also induce gravitational fragmentation of gas and star formation similarly like expanding shells of supernovae do, but on larger scale.

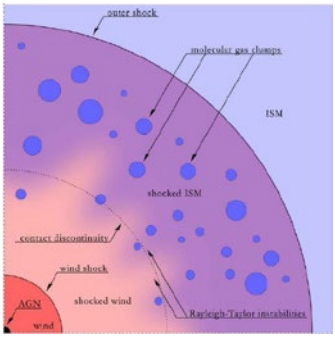

Fig. 1. Schematic view of the outflow (source: [4]).

This work is concerned with determination of the statistical distribution of masses of gas clouds that should form in the outflow, the star formation rate in these clouds when they gravitationally collapse and observational properties of these processes. To achieve this the ideas of the analytical models of turbulent gas fragmentation, collapse and star formation derived for more standard star formation regions are used (e.g. [5,6]) with some refinements which are required in the more extreme environment that is studied. The resulting properties differ from those in standard environments. For example, the mass function of gas clouds is found to be flatter, that is, a bigger fraction of clouds that form are massive.

[1] Pounds, K. A.; Vaughan, S., An extended XMM-Newton observation of the Seyfert galaxy NGC 4051 - II. Soft X-ray emission from a limb-brightened shell of post-shock gas, MNRAS **415**, 2379-2387 (2011).
[2] Feruglio, C.; Maiolino, R. et al., Quasar feedback revealed by giant molecular outflows, Astronomy and Astrophysics **518**, id.L155 (2010).
[3] Zubovas K., King A., Clearing Out a Galaxy, The Astrophysical Journal Letters **745**, 5 (2012).
[4] Zubovas K., King A., Galaxy-wide outflows: cold gas and star formation at high speeds, MNRAS **439**, 400-406 (2014).
[5] Padoan P., Nordlund A., The Stellar Initial Mass Function from Turbulent Fragmentation, The Astrophysical Journal **576**, 870-879 (2002).
[6] Hennebelle P., Chabrier G., Analytical Theory for the Initial Mass Function: CO Clumps and Prestellar Cores, The Astrophysical Journal **684**, 395-410 (2008).

SELF-PROPAGATING STAR FORMATION IN M33 GALAXY

Alina Leščinskaitė[1,2], Rima Stonkutė[2]

[1] Faculty of Physics, Vilnius University, Lithuania
[2]Centre for Physical Sciences and Technology, Lithuania
alina.lescinskaite@ff.stud.vu.lt

Star formation process plays an important role in determining the dynamics and chemical evolution of the galactic disks. Physical mechanisms for triggering star formation and evolution of star forming regions have long been subjects of research in astrophysics, however, the overall picture of the star formation process still remains obscure. Observations of the Milky Way and other spiral or irregular galaxies show that shell-like structures are abundant in the interstellar medium [1]. Actually, they are giant cavities of hot ionised gas created by strong stellar feedback from OB associations. Their sizes are from 100 pc to as large as 1 kpc, being the largest structures created by the star formation process. As the shell expands it either disrupts the existing structures of the interstellar gas or accumulates the surrounding matter creating a layer of gas of increased density or an uneven distribution of clumpy gas clouds at the rims of the shell. These accumulations of matter create favorable conditions for induced star formation, as the compression and collisions of the gas clouds occur here more frequently [2].

Here we study the large-scale star formation in the disk of M33 galaxy. The supershells of ionised gas are considered to be the main providers of a physical mechanism for triggered star formation. A detailed analysis of a 2.3x2.9 kpc^2 field, covering a large star forming complex in the Southern arm of the galaxy, is presented. In total 19 supershells were identified by using data of multi-wavelength observations. These structures range in size from ~200 to ~900 pc and mean size is of ~500 pc (see Fig. 1, panel c). Ages of the supershells were estimated using resolved multi-band stellar photometry data of the M33 galaxy derived from the Suprime-Cam observations with the 8 m Subaru telescope and stellar isochrones. The average expansion velocity of the supershells of ~4 km s^{-1} was derived. An uneven distribution of gas and dust is observed at the rims of the supershells with some secondary star formation being evident. The latter process is the most efficient within the fronts of "colliding" supershells, suggesting that collisions of dense gas clouds play an important role in the process of induced star formation.

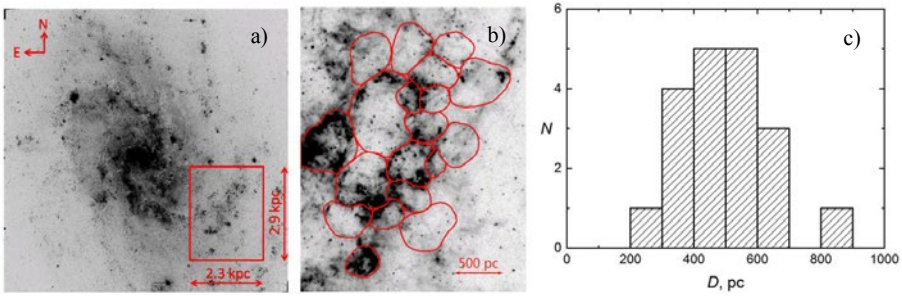

Fig. 1. (a) an *U*-filter image of M33 galaxy, boxed area marks the field analyzed in this study; (b) an 8 μm image of the boxed area in (a), red contours mark the identified supershells; (c) a size distribution of the supershells.

[1] Y.-H. Chu, *Bubbles and Superbubbles: Observations and Theory*, IAUS, **250**, 341-354 (2008).
[2] J. R. Dawson, *The Supershell–Molecular Cloud Connection: Large-Scale Stellar Feedback and the Formation of the Molecular ISM*, PASA, **30**, 25 (2013).

Globular clusters

Mateusz Narożnik

Institute of Physics, Nicolaus Copernicus University, Poland
mateusznaroznik1@gmail.com, 267228@fizyka.umk.pl

The main thema of my research is one of the greatest globular clusters of our celestial sphere, for sure the most spectacular on the northern sky. It is Hercules globular know as M13 for all astronomers. In my presentation I would like to show you some possibilities of amateur setup: primary telescope- Newton 150/750, primary cameras: Canon600d and Atik383L+, guider- refractor 70/400, guiding camera- SS Autoguider, mount- HEQ5+extension tube and for visual observation Newton 254/1200. The aim of my observation and research is appoint apparent magnitude of variable stars RR Lyrae (Cepheid) and light curve, for use their standard candle's properties from one of the most important equation in the history of astronomy. I assume that absolute magnitude is known and equal 0,61mag[1].

Next step is to calculate distance to globular cluster, angular and real size of that object. So, if we know the location of M13 (not the plane of the Galactic disk) on the sky, location of our Solar System, size of Galactic disk (1kly) and distance to globular cluster I can conclude that M13 is located in Milky Way's galactic halo. Another thing which we can do is calculating lightness distribution globular cluster. I will discuss two theoretical models and results of my measurements, which prove these models for several clusters of our sky[2].

1 G. Kopacki, Z. Kołaczkowski, and A. Pigulski, *Variable stars in the globular cluster M13,* Astronomy & Astrophysics February 2, 2008

2 Andrzej Branicki, *Obserwacje i pomiary astronomiczne*, Wydawnictwo Uniwersytetu Warszawskiego, Warszawa 2012

DICE OPTICAL LATTICE AS EXTENSION OF HALDANE MODEL TO QUASI-SPIN-1

Tomas Andrijauskas[1], Egidijus Anisimovas[1], Mantas Račiūnas[1], Algirdas Mekys[1], Viačeslav Kudriašov[1], Ian Spielman[2,3] and Gediminas Juzeliūnas[1]

[1]Institute of Theoretical Physics and Astronomy, Vilnius university, A. Goštauto 12, Vilnius LT-01108, Lithuania
[2]Joint Quantum Institute, University of Maryland, College Park, Maryland 20742-4111, 20742, USA
[3]National Institute of Standards and Technology, Gaithersburg, Maryland 20899, USA
tomas.andrijauskas@ff.stud.vu.lt

We consider ultracold atoms in a two-dimensional optical lattice of the dice geometry in a tight-binding regime. The atoms experience a laser-assisted tunneling between the nearest neighbour sites of the dice lattice accompanied by the momentum recoil. This allows one to engineer staggered synthetic magnetic fluxes over plaquettes, and thus pave a way towards a realization of topologically nontrivial band structures. In such a lattice the real-valued next-neighbour transitions are not needed to reach a topological regime. Yet, such transitions can increase a variety of the obtained topological phases. The dice lattice represents a triangular Bravais lattice with a three-site basis consisting of a hub site connected to two rim sites (See figure 1).

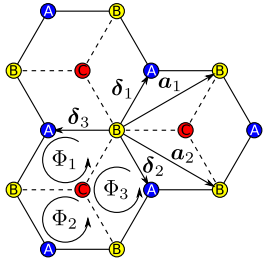

Fig. 1. Dice lattice. The blue, green and red sites correspond to three different triangular sub-lattices A, B and C. Solit lines show coupling between the sites A and B. Dashed lines show couplings between the sites B and C.

As a consequence, the dice lattice supports three dispersion bands. From this point of view, our model can be interpreted as a generalization of the paradigmatic Haldane model [1] which is reproduced if one of the two rim sub-lattices is eliminated. We demonstrate that the proposed upgrade of the Haldane model creates a significant added value, including an easy access to topological semimetal phases relying only on the nearest neighbour coupling, as well as enhanced topological band structures featuring Chern numbers higher than one leading to physics beyond the usual quantum Hall effect. The numerical investigation is supported and complemented by an analytical scheme based on the study of singularities in the Berry connection [2].

[1] F. D. M. Haldane, *Model for a Quantum Hall Effect without Landau Levels: Condensed-Matter Realisation of the "Parity Anomaly"*, Phys. Rev. Lett. **61**, 2015 (1988).
[2] T. Andrijauskas, E. Anisimovas, M. Raciunas, A. Mekys, V. Kudriasov, I. B. Spielman, G. Juzeliunas, *Dice lattice and Haldane-like model for quasi-spin-1*, arXiv:1501.00425 (2015).

DYNAMIC CHIRAL-π MODEL ON A SQUARE LATTICE

Mantas Račiūnas[1,2], Giedrius Žlabys[1,2], Egidijus Anisimovas[1,2], André Eckardt[3]

[1]Faculty of Physics, Vilnius University, Lithuania
[2]Institute of Theoretical Physics and Astronomy, Vilnius University, Lithuania
[3] Max-Planck-Institut für Physik komplexer Systeme, Dresden, Germany
mantas.raciunas@tfai.vu.lt

Optical lattices are periodic potential distributions created by a set of interfering laser beams. Systems of ultracold atoms trapped in optical lattices provide a clean and controllable environment to reproduce a variety of quantum phenomena [1] known from other branches of physics, and often provide insights beyond the conventional knowledge. In our work, we analyze a square lattice where an artificial magnetic flux is created by means of periodic laser phase modulation (known as lattice shaking). The sign of the flux alternates in a checkerboard pattern. In this setup, relatively flat topological energy bands are formed and thus the fractional quantum Hall effect (FQHE) may be induced without an external magnetic field.

The structure of the dynamic chiral-π lattice is shown in Fig.1. To induce complex hopping amplitudes between nearest neighbors (NN) the lattice is periodically shaken and a static energy shift for B sites (open dots) sites is introduced. The static energy shifts are cancelled by a gauge transformation, and the resulting tight-binding Hamiltonian features only time dependent-hopping amplitudes.

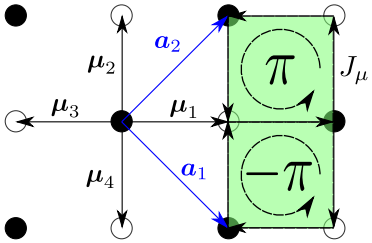

Fig. 1. Checkerboard lattice (sites A – black dots, sites B – open dots) and artificial fluxes.

Application of the Floquet analysis produces an effective time-independent Hamiltonian which describes the long term dynamics of the system. Diagonalization of the effective Hamiltonian reveals the presence of topologically nontrivial energy bands which give rise to the integer quantum Hall effect (IQHE) and paves the way towards the fractional quantum Hall states.

The essential requirement for FQHE to occur is strong interaction between the particles. The interaction strength must significantly exceed the single-particle bandwidth. We construct the Hubbard Hamiltonian with three tunable parameters – the shaking frequency, shaking amplitude and the interaction strength, and set out to search for the parameter region where the degenerate ground state is separated from the rest of states by a large many-body gap and thus stable FQHE states may be formed.

To reduce the volume of numerical computations we have used interaction operator projection [2] into the relevant energy band and simplified method for calculation of topological properties [3].

[1] P. Windpassinger, K. Sengstock, Engineering novel optical lattices, Rep. Prog. Phys. **76**, 086401 (2013).
[2] E. J. Bergholtz, Z. Liu, Topological flat band models and fractional Chern insulators, Int. J. Mod. Phys. B **27**, 1330017 (2013).
[3] T. Neupert, L. Santos, C. Chamon, C. Mudry, Elementary formula for the Hall conductivity of interacting systems, Phys. Rev. B **86**, 165133 (2012).

SIMULATIONS OF MOLECULAR SYSTEMS USING TRAPPED ATOMS AND IONS

Marta Sroczynska[1], Krzysztof Jachymski[1], Zbigniew Idziaszek[1], Tommaso Calarco[2], Rene Gerritsma[3]

[1] Faculty of Physics, University of Warsaw, Poland
[2] Institute for Complex Quantum Systems, University of Ulm, Germany
[3] Institute of Physics, University of Mainz, Germany
m.sroczynska@student.uw.edu.pl

Recent experimental progress in the field of trapped atoms and ions allows us to study the properties of such systems. They can potentially be used for quantum simulations [1]. Ions aligned in a chain can be thought of as an analogue of a crystal structure, so it may simulate condensed matter systems, where the atoms play the role of electrons [2].

Here we theoretically study the properties of system consisting only of two tightly trapped ions interacting with a single atom. Our simple model has features characteristic for H_2^+ molecule. More complex systems can be constructed by adding more atoms and ions in a controllled way.

[1] A. Harter, J. Hecker Denschlag, Contemporary Physics **55**, 33-35 (2014).
[2] U. Bissbort et al., Phys. Rev. Lett. **111**, 08051 (2013).

SELF-ASSEMBLY OF DNA-COATED VESICLES AND THEIR PHASE PORTRAITS

Michał Bogdan[1]

[1] Department of Physics, University of Cambridge, United Kingdom
mjb271@cam.ac.uk

The presentation will discuss phase portraits and properties of infinite networks of DNA-coated vesicles.

Giant unilamellar vesicles (GUVs) are artificial lipid bilayers, of spherival shape. Similiar basic structure governes cell membranes and membranes of many cell organelles.

Individual vesicles have been a subject of research for a long time, as drug carriers (due to their biocompatibility) and as bacteria detectors.

A relatively new line of research is examining the behavior of networks of vesicles. Vesicles' surfaces are coated with single strand DNA (attached to the surface by, for example, cholesterol), which causes an attractive interaction between vesicles coated with complementary DNA strands. A theory regarding the behavior of two adhering vesicles has already been designed, predicting the equilibrium contact angle's dependence on temperature and number of DNA strands [1]. Physically, this is a specific and experimentally accessible realization of a system of soft spheres, connected with entropic springs.

The presentation describes efforts to create a theory describing the behavior of infinite networks of liposomes in various two- and three- dimensional geometries, taking into account elastic energy of membrane deformation, entropic and energetic contributions from confinement of the DNA during interactions, to predict under what circumstances percolation occurs in such systems., and what geometries will be preferred in self- assembly under natural conditions. Understanding the behavior of such systems could lead to novel strategies of drug delivery and production of precious biocompatible materials.

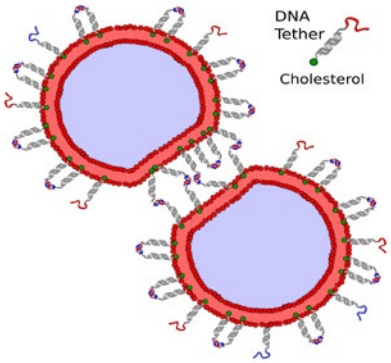

Fig. 1. Adhering giant unilamellar vesicles (GUVs)

[1] Lucia Parolini, Bortolo M. Mognetti, Jurij Kotar, Erika Eiser, Pietro Cicuta & Lorenzo Di Michele, Volume and porosity thermal regulation in lipid mesophases by coupling mobile ligands to soft membranes, Nature Communications 6, Article number: 5948 doi:10.1038/ncomms6948 07 January 2015

ALIGNMENT OF MAGNETIC SOLENOID LENS FOR MINIMIZING TEMPORAL DISTORTIONS OF ULTRASHORT ELECTRON PULSES

Deividas Sabonis[1], Daniel Kreier[2,3], Peter Baum[2,3]

[1] Faculty of Physics, Technical University Munich, Germany
[2]Faculty of Physics, Ludwig-Maximilians-Universität München, Germany.
[3]Max-Planck-Institut für Quantenoptik, Germany
Deividas.Sabonis@tum.de

Always present focusing elements for charged particles are the magnetic solenoid lenses, capable of focusing continuous beams or ultrashort pulses in a similar way. However the perfect alignment of magnetic lens in real experiments is hardly possible. Recently it was noted that misalignment of the lens assembly, i.e. displacement or tilt around axis of symmetry, causes significant temporal aberrations on a femtosecond time scale. This misalignment destroys the symmetry of magnetic lens system and electron pulse, because the central electrons now are being deflected by the magnetic lens instead of propagating unaffected, due to this misalignment effect. The pulse lengthening is only minimized if the lens is aligned central and perpendicular to the electron beam. Therefore the purpose of this work is to identify influence of magnetic lens misalignment effects to the temporal resolution of ultrashort pulses in ultrafast diffraction. This question is not easily treated due to complexity of modern electron optical devices. Therefore discussion goes along with the model case of a simple solenoid lens. A simplified electron source was studied to understand the basic mechanisms of temporal distortions in magnetic lens. To investigate effect of lens on ultrashort pulses it is needed to disregard all other mechanisms for temporal distorsions and assume infinitely short pulses entering the magnetic lens. It is also necessary to disregard any possibility of tilted pulses and restrict discussion to incoming pulses of flat shape. Here an experimental procedure is presented based on periodic reversal of the magnetic field for aligning position and tilt with sufficient precision for reducing the aberrations to less than one femtosecond [1]. The principles used here for a solenoid is intended to be a starting point for more specific studies of realistic lenses in modern electron microscopes and diffraction apparatuses to reach ultimate temporal resolutions, potentially to the attosecond regime of electronic motion.

[1] Daniel Kreier et al,., Alignment of magnetic solenoid lenses for minimizing temporal distortions, J. Opt. 16 075201 (2014)

DVR AND FOURIER APPROACH TO STUDY STATIONARY STATES OF ELECTRON IN HEXAGONAL POTENTIAL WELL

Anya Radko, Alex Malevich, George Pitsevich.

Department of Physical Optics, Belarusian State University, Minsk, Belarus

radko.anya@mail.ru

In solid-state physics and semiconductors is very urgent problem of calculating the energy of the stationary states of an electron in the potential wells of different configurations. The height of the barrier can be finite or infinite. For some simple configuration of the well an analytic solution exists. But in general case numerical solution of the Schrödinger equation is necessary. The main problem is the correct representation of the vertical potential step. Really if we want to find values of the stationary states of electron in hexagonal well we can set values of potential energy in nodes of the regular 2D grid equals to zero if node within hexagonal and equals to U_0 if node outside (Fig.1).

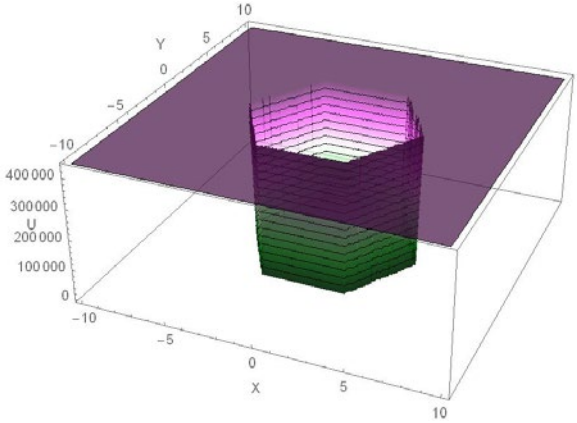

Fig.1 Hexagonal potential well with electron inside.

Then analytic representation of this 2D PES is necessary. At first we tried to do this using Fourier series. But because of the Gibbs beats to get an exact solution is impossible mission. So we applied DVR method because it does not need analytical representation of the PES at all. Note that the slope of the step is determined by the grid spacing at a constant barrier. So in doing so we were able to reproduce well existing analytical solution for square well, and to get solution for hexagonal well. Wave functions for some of exiting stationary states of electron in hexagonal well is shown on Fig.2

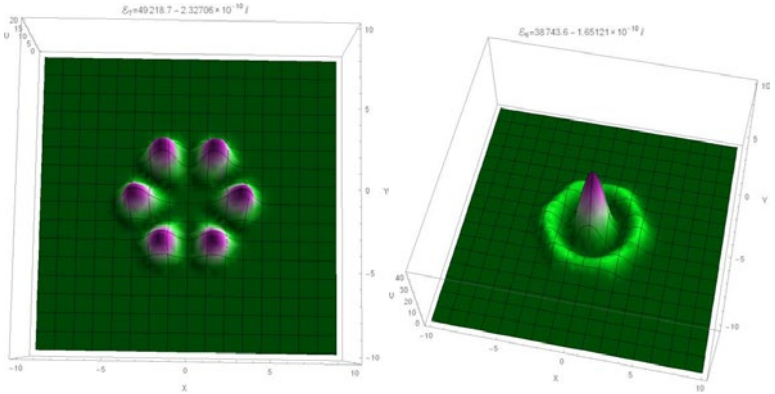

Fig.2 Wave functions of some exiting states of electron in hexagonal potential well.

Evolution of wavefunctions through topological phase transition in HgCdTe quantum dots

Maciej Bieniek, Paweł Potasz, Arkadiusz Wójs

Departament of Theoretical Physics, Wrocław University of Technology, Poland
maciej.bieniek@pwr.edu.pl

Topological insulators are new fascinating materials that are insulating in the bulk while having topologically protected conducting edge states. First predicted in 2005 by Kane and Mele [1] for graphene and then for CdTe/HgTe/CdTe quantum wells [2], they were experimentally observed by König et al. [3] in 2007. First theoretical and experimental studies of this quantum systems were focused almost exclusively on ribbon geometries, while other remain relatively unexplored [4].

In the following work CdTe/HgTe/CdTe quantum dot electronic structure is studied within tight-binding approximation framework. Particular attention is given to the behavior of electronic states near bulk band gap and corresponding wavefunctions. Evolution of edge states through topological phase transition (TPT) steered by quantum well thickness is shown.

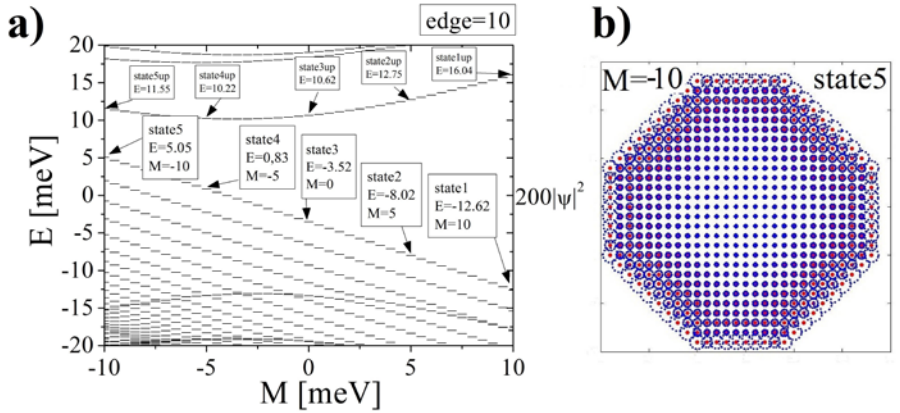

Fig. 1. (a) Evolution of energy levels (E) through topological phase transition. M is so-called mass parameter in effective Dirac equation describing studied systems and it changes with changing quantum well thickness. (b)Wavefunction corresponding to M=-10 meV (edge state inside bulk band-gap). Red (central) points are discrete lattice points of a quantum dot and corresponding circle's radius is proportional to magnitude of the wavefunction in a specific point.

Figure 1(a) shows how electronic states of a quantum dot evolve through topological phase transition. For M>0 system is in topologically trivial state and electron density is in the center of the system. During TPT M changes sign and electron density shifts to the edge, which means that one of the states becomes edge state (as in Fig. 1(b)). By studying spin splitting double degeneracy of states is presented along with preliminary results of magnetic field effect on these states.

[1] Kane, C. L., and E. J. Mele, Quantum Spin Hall Effect in Graphene, Phys. Rev. Lett. 95, 226801 (2005).
[2] B. A. Bernevig, T. L. Hughes and S.-C. Zhang, Quantum Spin Hall Effect and Topological Phase Transition in HgTe Quantum Wells Science 314, 1757 (2006).
[3] M. König, S. Wiedmann, C. Brüne, A. Roth, H. Buhmann, L.W. Molenkamp, X.-L. Qi, and S.-C. Zhang, Quantum Spin Hall Insulator State in HgTe Quantum Wells, Science 318,766
(2007).
[4] K. Chang and W.-K. Lou, Helical Quantum States in HgTe Quantum Dots with Inverted Band Structures, Phys. Rev. Lett. 106, 206802 (2011).

THEORETICAL ANALYSIS OF THE LARGE AMPLITUDE BENDING VIBRATIONS IN BH_3 MOLECULE USING EXECT FORM OF THE KINETIC ENERGY OPERATOR.

Maryia Zhuk, Alex Malevich, George Pitsevich.

Department of Physical Optics, Belarusian State University, Minsk, Belarus

zhuk_maryia@mail.ru

Large amplitude motions (LAM) of atoms take place for some specific molecular vibrations. To describe these movements more precise representation of the kinetic and potential energy is needed. Since the borane molecule (see Fig.1) contains three light H atoms they can take part in LAM in particular in bending H-B-H vibration. Similar situation took place in case of UO_3 molecule due to double well potential [1].

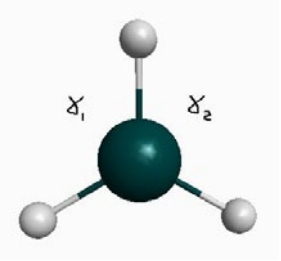

Fig.1 Borane molecule with introducing bending coordinates γ_1 and γ_2.

Borane - BH3 - is the simplest boron hydride. It is difficult enough to observe borane is as it rapidly dimerizes in a more stable molecule - diborane (B_2H_6). Keeping in mind the instability of the molecule borane it is not surprising that the first report of its registration IR spectrum [2] appeared only in 1971. In more recent experimental studies [3,4] some of assignments proposed in [1], has been called into question. Data on the Raman spectrum of this molecule are absent in the literature. These facts underscore the need for theoretical studies of this molecule. Recently [5] stretching B-H vibrations were studied theoretically. Equilibrium configuration of borane molecule is planar and belong to D_{3H} point group symmetry. Six normal mods of this molecule represented by following symmetry types: $\Gamma_v = 1A_1' + 1A_2'' + 2E'$. The only totally symmetric mode is stretching B-H vibration. The only out of plane mode (A_2'') is bending B-H vibration. The mode in hand has E' symmetry type and active only in IR spectrum. Following [1] we can represent exact kinetic energy operator:

$$\hat{K} = h_{\gamma_1}\frac{\partial}{\partial\gamma_1} + h_{\gamma_2}\frac{\partial}{\partial\gamma_2} + G_{\gamma_1\gamma_1}\frac{\partial^2}{\partial\gamma_1^2} + G_{\gamma_2\gamma_2}\frac{\partial^2}{\partial\gamma_2^2} + G_{\gamma_1\gamma_2}\frac{\partial^2}{\partial\gamma_1\partial\gamma_2}$$

where

$$h_{\gamma_1} = -\frac{\hbar^2 ctg\gamma_1}{\mu_{BH}l^2} + \frac{\hbar^2}{M_B l^2 \sin\gamma_1};\ h_{\gamma_2} = -\frac{\hbar^2 ctg\gamma_2}{\mu_{BH}l^2} + \frac{\hbar^2}{M_B l^2 \sin\gamma_2};$$

$$G_{\gamma_1\gamma_1} = \frac{\hbar^2}{\mu_{BH}l^2} - \frac{\hbar^2\cos\gamma_1}{M_B l^2};\ G_{\gamma_2\gamma_2} = \frac{\hbar^2}{\mu_{BH}l^2} - \frac{\hbar^2\cos\gamma_2}{M_B l^2};\ G_{\gamma_1\gamma} = -\frac{\hbar^2}{\mu_{BH}l^2} + \frac{\hbar^2(\cos\gamma_1 + \cos\gamma_2 - \cos(\gamma_1+\gamma_2))}{M_B l^2}$$

l -is length of the B-H bond, M_B mass of the B atom, μ_{BH} - reduce mass of the B and H atoms. 2D potential energy surface for γ_1, γ_2 coordinates using B3LYP/cc-pVTZ approximation.

[1] G. Pitsevich, I. Doroshenko et al., 2D study of the bending vibrations in nonrigid UO_3 molecule using exact kinetic energy operator. Book of abstracts 32 European Congress on molecular spectroscopy Dusseldorf, Germany p.267 (2014).
[2] A. Kaldar, R. Porter, Infrared Spectra of the Pyrolysis Products of Borane Carbonyl in an Argon Matrix JACS **93**, 2140-2145 (1971).
[3] K. Kawaguchi, J.E. Butler et al., Observation of the gas-phase infrared spectrum of BH_3 J.Chem.Phys., **87**, 2438-2442 (1987).
[4] K. Kawaguchi . Fourier transform infrared spectroscopy of the BH_3 ν_3 band J.Chem.Phys. **96**, 3411-3416 (1992).
[5] G. Pitsevich, A. Malevich et al., Not empirical anharmonic analysis of the vibrational states of BF3 and BH3 molecules using symmetry coordinates J. Appl. Spectr. **82**, 50-56 (2015).

AN ASSESSMENT OF URBAN DRAINAGE VELOCITY AND DISCHARGE AND ITS ENVIRONMENTAL PROBLEMS IN CHITTAGONG CITY, BANGLADESH

Md. Monirul Islam[1], Md. Iqbal Sarwar[2]

[1] Department of Physical Geography and Ecosystem Science, Lund University, Sweden
[2] Department of Geography and Environmental Studies, University of Chittagong, Bangladesh
md_monirul.islam.506@student.lu.se

In Bangladesh, Professional planning is being practiced in urban areas but unfortunately drainage planning is the most neglected part of our urban planning and development activities [1]. The Study has been carried out on an assessment of urban drainage velocity and discharge and its environmental problems in Chittagong City. The Master plan sets out a staged development program of storm water, drainage and flood control works of the above drainage area up to the year 2015 to meet the Storm Water Drainage and Flood Control problems [2]. In this research, Chittagong Metropolitan Master Plan (CMMP) drainage area 5a and 5b was selected as a study area. The study demonstration that, although velocity and discharge rate of the *khal* varies spatially (figure.1, figure.2) but this leads to various environmental problems adjacent to drainage areas in the city. With urban runoff siltation load from hills and building construction, solid waste and garbage from residential and bazar areas, meandering shape of the canal, culvert are main drivers to decrease velocity and discharge rate of the study area. For this reason, environmental problem (table.1) such as disruption of water flow, waterlogging, flash flood, tidal flood are common occurring event in the city especially in the rainy season. The results also suggests that regular dredging operation, development of garbage and solid waste management system, culvert re-construction, public awareness and appropriate steps of concerned authorities are ultimate solution to control drainage velocities and discharge for better urban drainage management in the study area.

Khal No.	Sample Location	Problem Types	Drainage Area
H1	Chaktai *Khal* mouth	Siltation, water logging	5a
H2	Raja *khal* mouth	siltation,	5a
H3	Fishari *Khal* mouth	Water flow disruption, Siltation	5a
H4	Mirza Khal mouth	solid waste blockage, water logging	5b
H5	Chasma *Khal* mouth	Siltation	5b
H6	Hijra *khal* middle	Solid waste blockage	5a & 5b
H7	Badarpatti	Disruption of water flow	5a
H8	Jamalkhan *khal* mouth	-	5a
H9	Chatteswari *khal* mouth	Siltation	5a
H10	Korbaniganj *Khal* mouth	Disruption of water flow	5a
H11	Tulatoli *Khal mouth*	Disruption of water flow	5b
H12	Mia khan *khal* mouth	Inundation	5a & 5b
H13	Shutikhipetri *khal mouth*	water logging with Tidal Flood	5a
H14	Open channel 1	Flashflood	5b
H15	Open Channel 2	Tidal Flood	5b

Table.1. Sample location, khal number, problem types in the study area (drainage area 5a and 5b); Source: field Survey

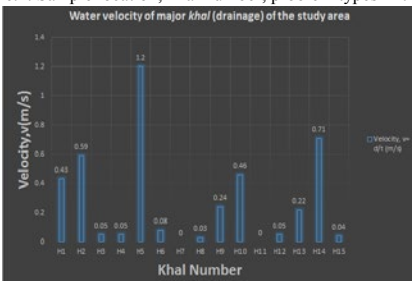

Figure.1.water velocity of major *khal* in the study area

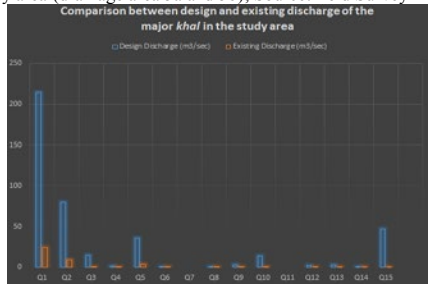

Figure.2.Design and Existing Discharge of major *khal*

[1] M. A. Ashraf, M. S .A. Chowdhury, Drainage planning in the Cities of Bangladesh: Case Study of Drainage and Water Logging in Chaktai Commercial area, Chittagong, BIP **2,** 49-60(2009)
[2]Chittagong Storm Water Drainage and Flood Control Master Plan, Volume-2: Main Report (Published by Chittagong Development Authority)

TESTING OF NEW ALFA TRIGGER INTERFACE

Bartosz Dziedzic[1]

[1] Institute of Physics, Tadeusz Kościuszko Cracow University of Technology, Poland
bd13.01.89@gmail.com

ALFA is a subdetector of ATLAS experiment on LHC used to measure Absolute Luminosity For ATLAS. In Run2, ALFA uses new trigger interface for Central Trigger Procesor (CTP) of ATLAS. Before comissioning of the new interface, physicists need to test modernized systems, but they haven't any tools to check communication between ALFA trigger and CTP. In my presentation I'll tell few words about testing procedures and submit the device that I developed with my supervisor in Niewodniczanski Institute of Nuclear Physics in Cracow.

[1] K. Korcyl, *ALFA detector: timing and trigger*, Proc. of SPIE Vol. 8903 89032K-1.
[2] S. Jakobsen, *Commissioning of the Absolute Luminosty For ATLAS – detector at the LHC*, CERN-THESIS-2013-230

The nature of folding of knotted proteins inside a chaperone

Emiliano Carvalho[12], Patrícia Faísca[12]

[1] Condensed Matter Physics Centre, Portugal
[2] Department of Physics, Faculty of Sciences of the University of Lisbon, Portugal
emiliano.lip@gmail.com

Proteins are synthesized inside the cell in the form of linear chains that then self organize, folding to their functional shapes by reaching the energy minimum for a given temperature. *In vitro* studies are performed with proteins outside their normal biological context, but in the cell this process often happens inside a chaperone, a molecular "cookie jar". Here is presented the impact of excluded volume – one of the main physical implications of the process happening inside a chaperone – in the folding of a protein with a 3-1 knot, using Monte Carlo simulations in a lattice model, with Parallel Tempering and WHAM analysis.

ANTIMICROBIAL PROPERTIES OF HUMAN β DEFENSIN-2

Izabela Konieczna

Department of Pathogen Biology and Immunology, University of Wrocław, Poland
izabela.anna.konieczna@gmail.com

The twenty-first century has brought humanity huge technological development but also many of the problems associated with interference in the natural environment. One of these problems is the bacterial antibiotic resistance caused by excessive use of antibiotics. Exploring the potential of natural antimicrobial peptides is very important in combating multi-drug resistance of microorganisms.

Human β defensin-2 (HBD2) is a cysteine-rich cationic, small (2-6 kDa), antimicrobial peptide that is considered to be important antibiotic-like effectors of innate immunity [1]. HBD2 is produced by epithelial cells inter alia in response to contact with microorganisms. It exhibits potent antimicrobial activity against gram-negative bacteria and Candida but was less effective against gram-positive *Staphylococcus aureus* [2]. The mechanism by which microorganisms are killed by defensins is not understood completly but there is a huge potential and hope in these small peptides to combat multi-drug resistance microorganisms.

[1] D. Yang, A. Biragyn, L. W. Kwalk, J. J. Oppenheim, Mammalian defensins in immunity: more than just microbicidal, TRENDS in Immunology, Vol.23 No.6 June 2002
[2] H-Y. Lee, A. Andalibi et al, Antimicrobial activity of innate immune molecules against Streptococcus pneumoniae, Moraxella catarrhalis and nontypeable Haemophilus infuenzae, BCM Infectious Diseases 2004, 4:12
[3] J-M. Schroder, J. Harder, Human beta-defensin-2, The Intrernational Journal od Biochemistry & Cell Biology, Vol. 31, June 1999

GENERALIZED HYPERBOLIC METAMATERIALS

Vladislav Popov[1], Andrey Novitsky[1]

[1] Department of Theoretical Physics and Astrophysics, Belarusian State University, Belarus
physics.vlad@gmail.com

Hyperbolic metamaterials (HMMs) represent the ultra-anisotropic limit of traditional uniaxial crystals, and one of the principal components of either their permittivity $\boldsymbol{\varepsilon} = diag[\varepsilon_o,\varepsilon_o,\varepsilon_e]$ or permeability tensors $\boldsymbol{\mu} = diag[\mu_o,\mu_o,\mu_e]$ is opposite in sign to the others. Here, the subscripts *o* and *e* indicate components parallel and perpendicular to the anisotropy axis, respectively. Nowadays, there are two types of HMM: Type 1 with $Re(\varepsilon_o) > 0$, $Re(\varepsilon_e) < 0$ and Type 2 with $Re(\varepsilon_o) < 0$, $Re(\varepsilon_e) > 0$. Unique properties of HMMs stem from the hyperbolic form of their isofrequency surface for extraordinary wave [1]. In this study we deal with electric hyperbolic structures, i.e. with $\mu_o = \mu_e = 1$.

We propose the concept of generalized hyperbolic metamaterials (GHMMs) which high-wavevector isofrequency surface has more complex form than a hyperboloid. A layered metal-dielectric structure composed of alternating slabs of a biaxial absorbing crystal and a biaxial conducting crystal is an example of GHMM. We predict the effective medium permittivity tensor of the layered GHMMs using Maxwell-Garnett approach [1], which is valid in the long wavelength limit. We restrict ourselves on the case when the effective medium permittivity tensor is biaxial, i.e. in the system of its principal axes one takes form $\boldsymbol{\varepsilon}_{\mathbf{eff}} = diag[\varepsilon_{xx},\varepsilon_{yy},\varepsilon_{zz}]$. It means that we deal with high symmetry crystals.

Consider the set of alternating dielectric and metallic slabs. Dielectric slab is a slab of "uniaxial" absorbing crystal of thickness d_d with permittivity tensor $\boldsymbol{\varepsilon}_{\mathbf{d}} = diag[\varepsilon_o,\varepsilon_o,\varepsilon_e]$ and metallic slab is a slab of isotropic metal of thickness d_m with permittivity ε_m. Let us work in the system of absorbing crystal's principal axes, i.e. when $\boldsymbol{\varepsilon}_{\mathbf{d}} = diag[\varepsilon_o,\varepsilon_o,\varepsilon_e]$ and the direction of the anisotropy axis coincides with the normal to the slabs' interface. If the absorbing crystal and the isotropic metal are chosen properly then we can "move" the negative sign along the diagonal of the effective permittivity tensor by means of the rotation of the absorbing crystal's anisotropy axis. For instance, let $\boldsymbol{\varepsilon}_{\mathbf{d}}$ and ε_m be chosen properly and when $\boldsymbol{\varepsilon}_{\mathbf{d}} = diag[\varepsilon_o,\varepsilon_o,\varepsilon_e]$ components of the corresponding effective medium permittivity tensor are such that $Re(\varepsilon_{xx}) > 0$, $Re(\varepsilon_{yy}) > 0$ and $Re(\varepsilon_{zz}) < 0$. When we rotate the anisotropy axis of the absorbing crystal so that its permittivity tensor in the chosen coordinate system takes form $\boldsymbol{\varepsilon}_{\mathbf{d}} = diag[\varepsilon_o,\varepsilon_e,\varepsilon_o]$ then $Re(\varepsilon_{xx}) > 0$, $Re(\varepsilon_{yy}) < 0$ and $Re(\varepsilon_{zz}) > 0$. We have shown that there are a lot of appropriate parameters for a "uniaxial" absorbing crystal and an isotropic metal.

Isofrequency surfaces of an effective medium are determined by its permittivity tensor. From the above mentioned follows that we can literally choose a place of signs on the effective permittivity tensor's diagonal. This fact gives us the opportunity to obtain such isofrequency surfaces as we would get if we could rotate the anisotropy axis of HMM. Moreover, behavior of the transmission coefficient for such GHMMs is almost the same as for HMMs with "rotated" anisotropy axis. There are several interesting intermediate isofrequency surfaces, i.e. when the absorbing crystal's principal axes do not coincide with basis vectors of the above chosen coordinate system and neither $\boldsymbol{\varepsilon}_{\mathbf{d}}$ nor $\boldsymbol{\varepsilon}_{\mathbf{eff}}$ takes diagonal form. Fig. 1 shows examples of obtained isofrequency curves of the effective medium which corresponds to the layered metal-dielectric structure with $\boldsymbol{\varepsilon}_{\mathbf{d}} = diag[1.7, 1.7, 1.5+3i]$, $d_d = 9.778$nm, $\varepsilon_m = -2+0.7i$ and $d_m = 8$nm, when angle between the absorbing crystal's anisotropy axis and normal to the interface equals 0.3 rad. It is evident that axial symmetry is lost and transmission coefficient now depends both on the angle of incidence and plane of incidence.

We have shown that the effective medium indeed describes corresponding layered metal-dielectric GHMM (for propagating modes) by comparing their transmission and reflection properties.

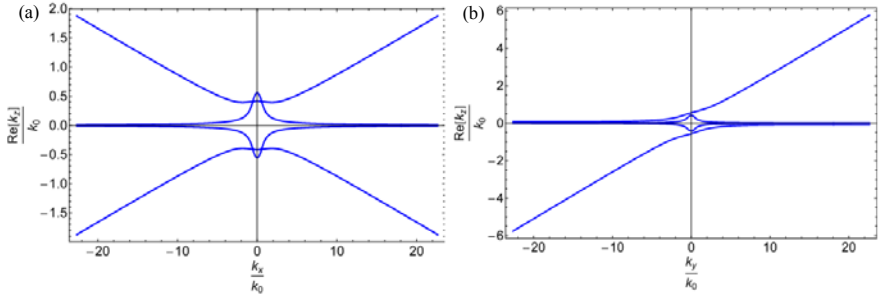

Fig. 1. Isofrequency curves, plane of incidence is orthogonal (a) and coincides (b) with the plane of the absorbing crystal's anisotropy axis and normal to the interface (angle between them equals 0.3 rad.).

[1] Shekhar et al.: Hyperbolic metamaterials: fundamentals and applications. Nano Convergence 2014 1:14.

Recreating Darwinian ligand evolution in vitro – cell-SELEX technique as an efficient way of aptamers selection

Konrad Zabłocki

Department of Biotechnology, University of Wrocław, Poland
zablockikonrad@gmail.com

Aptamers – nucleic acids with molecular recognition, have over the past twenty years emerged as a versatile tool in biochemistry, medicine and nanotechnology. To find a specific sequence that folds into a three dimensional structure that is able to bind the chosen target, Systematic Evolution of Ligands by EXponential enrichment (SELEX), also referred to as in vitro evolution (or simply selection), is usually applied. The method enables isolating an aptamer of interest from a pool of randomized molecules by repeated steps of incubation with the target, partitioning and amplification, until the pool of molecules becomes enriched in a particular clone.[1]

Many variants of that technique was described recently – some of them are able to decrease the number of selection rounds, while others imply the use of modified nucleobases to enlarge the diversity of selected oligos, or modifications of the nucleic acid's backbone to prevent enzymatic degradation by nucleases.[2] Another variation is cell-based aptamer selection, termed cell-SELEX which is particularly promising strategy for various applications, including cancer research and therapy.

Bearing in mind that prior knowledge of the target molecules is unnecessary in cell-SELEX, the technique seems to be perfect for the discovery of native-state biomarkers.[3] During the lecture, we will track the entire selection process – from setting up a cancer cell culture up to the sequencing and preliminary analysis.

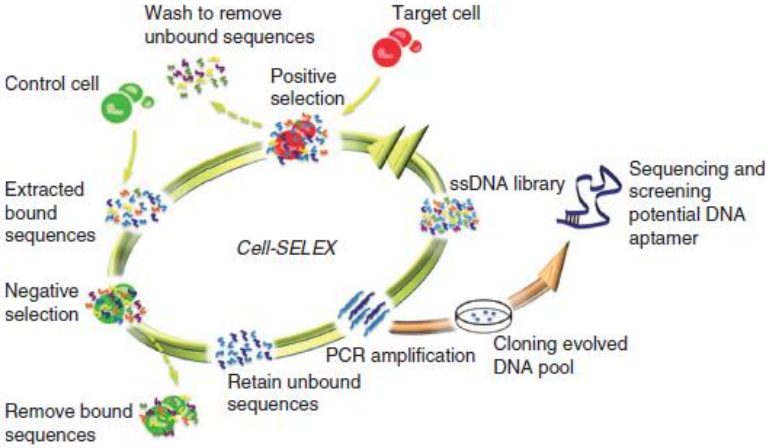

Fig. 1. Schematic representation of DNA aptamer selection using the cell-SELEX strategy.[3]

[1] Radom F., Jurek P., Mazurek M., Otlewski J., Jeleń F. „Aptamers: Molecules of great potential", Biotechnology Adv, Dec. 2013.
[2] Y. Lin, Q. Qiu, S. C. Gill, and S. D. Jayasena, "Modified RNA sequence pools for in vitro selection," *Nucleic Acids Res.*, vol. 22, no. 24, pp. 5229–5234, 1994.
[3] Kwame Sefah, Dihua Shangguan, Xiangling Xiong, Meghan B O'Donoghue, Weihong Tan, „Development of DNA aptamers using Cell-SELEX", Nature Protocol, 3 June 2010.

Author index

H

I

J

K

L

M

N

O

P

R

S

T

U

V

W

Y

Z

Altechna

UAB Altechna is a laser technology company operating in the fields of photonics and laser research since 1996.

Altechna is a reliable supplier of laser products: laser optics, crystals, lasers and optomechanics.

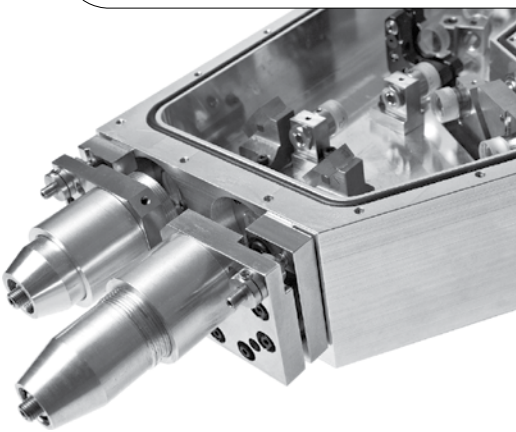

Our products:

- Lasers and laser equipment
- Spectroscopy equipment
- CCD cameras
- Positioning systems
- Laser crystals and optics
- Other laboratory equipment

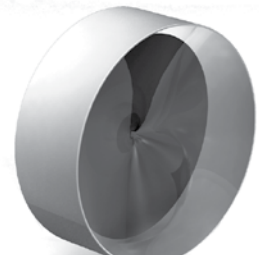

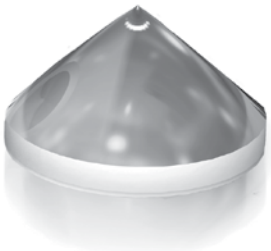

Altechna represents:

AEROTECH
www.aerotech.com

INNOLAS
www.innolas.com

MIYACHI
MIYACHI EUROPE CORPORATION
www.miyachi.com

ANDOR™
TECHNOLOGY
www.andor.com

Laser Quantum
www.laserquantum.com

Ocean Optics
www.oceanoptics.com

First Contact™
Photonic Cleaning Technologies
www.photoniccleaning.com

LASOS
For worldwide photonics
www.lasos.com

Semrock
www.semrock.com

UAB Altechna • Mokslininkų st. 6A, 08412 Vilnius, Lithuania
Tel. +370 5 2725738 • Fax +370 5 2723704 • E-mail: info@altechna.com

EKSMA OPTICS

A manufacturer and Your partner for Laser and Photonics components

- Nd:YAG LaserLine components
- FEMTOLine components
- Pockels cells for Q-switching and pulse picking
- Laser Optics for high power lasers
- Frequency conversion and laser media crystals
- Opto-mechanics mounts and optical positioners

Reliable supplier
for R&D and OEM customers
for more than 30 years!

Visit our website
www.eksmaoptics.com

EKSPLA

Advanced Scientific Lasers and Systems

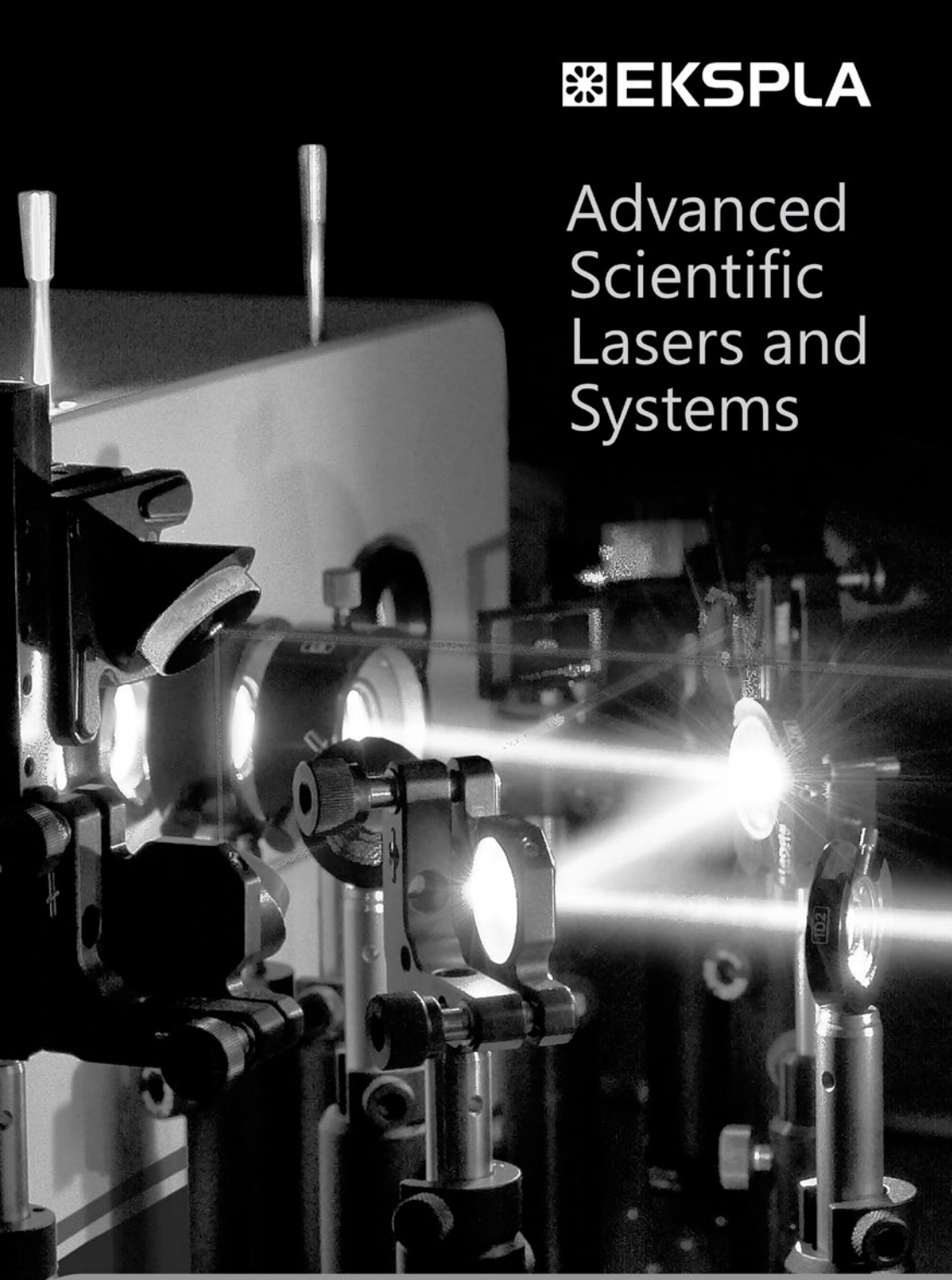

Lasers | Laser systems | Optoelectronics

www.ekspla.com

LIGHT CONVERSION

Light Conversion is a leading developer and manufacturer of wavelength tunable OPA based ultrafast light sources and advanced diode laser pumped femtosecond ytterbium laser systems

TOPAS SERIES MODELS

TOPAS white
Optical Parametric Amplifier

HE-TOPAS
Optical Parametric Amplifier

TOPAS-C
Optical Parametric Amplifier

PHAROS SERIES PRODUCTS

PHAROS
High-Power Femtosecond Lasers

CARBIDE
Femtosecond Laser for Industrial & Medical Applications

ORPHEUS
Collinear Optical Parametric Amplifier

HARPIA
Off-the-Shelf Pump-Probe Spectrometer

Keramiku 2, LT-10233 Vilnius, Lithuania
Tel.: +370 5 2491830
E-mail: sales@lightcon.com

www.lightcon.com

Ruptela

GPS TRACKING

SOFTWARE DEVELOPER AND HARDWARE MANUFACTURER

1 GPS MONITORING **PLATFORM IN 24 LANGUAGES**

8 HIGH ADDED VALUE **SOLUTIONS**

5 GPS TRACKING **DEVICES**

PARTNERS IN **87 COUNTRIES**

0 LOST CUSTOMERS

24x7 TECHNICAL SUPPORT

7 YEAR EXPERIENCE

EUROPEAN **EXPORT CHAMPIONS** AWARD

40 367 OBJECTS ON TRUSTTRACK

TRUST US

Coca-Cola

NATO OTAN

orange™

vodafone

IN **5** LANGUAGES

LT RU PL EN ES FR AR DE HI UR IT PA

OFFICE SPEAKS IN **12** LANGUAGES

RESULTS IN 2013

AWARDS

TOP 5 TECHNOLOGY COMPANY

IN CENTRAL-EASTERN EUROPE, **NO.1 IN THE BALTICS** BY DELOITTE

THE MOST PROMISING COMPANY

BY "LITHUANIAN TRANSPORT LEADERS 2013"

10TH FASTEST GROWING COMPANY

IN LITHUANIA **BY "GAZELLE 2012"**

AMONG **FINANCIALLY MOST STABLE COMPANIES**

IN LITHUANIA BY CREDITINFO

ECO-DRIVE - THE BEST SERVICE

FOR TRANSPORT INDUSTRY BY ICC LITHUANIA

Photonics Tools

- Optomechanics
- Motion Controls
- Tunable Lasers
- Advanced Imaging
- OCT Systems
- Optics
- Fibers

You Speak, We Listen.....

THORLABS

www.thorlabs.com
scandinavia@thorlabs.com

Scientific investigations in physics, chemistry and technologies as well as experimental development research are carried out

Scientists capable of performing high level research and solving scientific problems on their own are trained

Scientific expertise is performed, scientific consultations are given

Post graduate studies and post-doctoral fellowships are organized

Research is performed as well as methodological, met hodical and other assistance is rendered to order of business enterprises

Scientific knowledge is disseminated to the public, the innovation-based economy development and knowledge-based society education are promoted

CENTER
FOR PHYSICAL SCIENCES
AND TECHNOLOGY

State Research Institute Center for Physical Sciences and Technology

Savanorių ave. 231, LT-02300 Vilnius, Lithuania. Ph. +370 5 264 9211,
fax. +370 5 260 2317, e-mail: office@ftmc.lt, http://www.ftmc.lt

INTERNATIONAL YEAR OF LIGHT 2015

www.light2015.org

OSA The Optical Society

UNESCO

INTERNATIONAL YEAR OF LIGHT 2015

EPS

SPIE.